

Adolfo Avella  
Ferdinando Mancini *Editors*

# Strongly Correlated Systems

Numerical Methods

# **Springer Series in Solid-State Sciences**

## **Volume 176**

### ***Series Editors***

Manuel Cardona, Stuttgart, Germany

Peter Fulde, Dresden, Germany

Klaus von Klitzing, Stuttgart, Germany

Roberto Merlin, Ann Arbor MI, USA

Hans-Joachim Queisser, Stuttgart, Germany

Horst Störmer, New York NY; Murray Hill NJ, USA

For further volumes:

<http://www.springer.com/series/682>

The Springer Series in Solid-State Sciences consists of fundamental scientific books prepared by leading researchers in the field. They strive to communicate, in a systematic and comprehensive way, the basic principles as well as new developments in theoretical and experimental solid-state physics.

Adolfo Avella · Ferdinando Mancini  
Editors

# Strongly Correlated Systems

Numerical Methods

With 106 Figures



Springer

*Editors*

Adolfo Avella

Dipartimento di Fisica “E.R. Caianiello”

Università degli Studi di Salerno

Fisciano (SA)

Italy

Ferdinando Mancini

Dipartimento di Fisica “E.R. Caianiello”

Università degli Studi di Salerno

Fisciano (SA)

Italy

ISSN 0171-1873

ISBN 978-3-642-35105-1

ISBN 978-3-642-35106-8 (eBook)

DOI 10.1007/978-3-642-35106-8

Springer Heidelberg New York Dordrecht London

Library of Congress Control Number: 2013930016

© Springer-Verlag Berlin Heidelberg 2013

This work is subject to copyright. All rights are reserved by the Publisher, whether the whole or part of the material is concerned, specifically the rights of translation, reprinting, reuse of illustrations, recitation, broadcasting, reproduction on microfilms or in any other physical way, and transmission or information storage and retrieval, electronic adaptation, computer software, or by similar or dissimilar methodology now known or hereafter developed. Exempted from this legal reservation are brief excerpts in connection with reviews or scholarly analysis or material supplied specifically for the purpose of being entered and executed on a computer system, for exclusive use by the purchaser of the work. Duplication of this publication or parts thereof is permitted only under the provisions of the Copyright Law of the Publisher's location, in its current version, and permission for use must always be obtained from Springer. Permissions for use may be obtained through RightsLink at the Copyright Clearance Center. Violations are liable to prosecution under the respective Copyright Law.

The use of general descriptive names, registered names, trademarks, service marks, etc. in this publication does not imply, even in the absence of a specific statement, that such names are exempt from the relevant protective laws and regulations and therefore free for general use.

While the advice and information in this book are believed to be true and accurate at the date of publication, neither the authors nor the editors nor the publisher can accept any legal responsibility for any errors or omissions that may be made. The publisher makes no warranty, express or implied, with respect to the material contained herein.

Printed on acid-free paper

Springer is part of Springer Science+Business Media ([www.springer.com](http://www.springer.com))

# Preface

This volume “Numerical methods for Strongly Correlated Systems”, together with the set “Methods and Techniques for Strongly Correlated Systems” it belongs to, builds upon the long-standing experience we have acquired in organizing the “Trainings Course in the Physics of Strongly Correlated Systems” in Vietri sul Mare (Salerno, Italy) since 1996 and our working scientific experience in the field. Running a school for advanced graduate students and junior post-docs, we realized that this field of condensed matter and solid-state physics was missing adequate textbooks and that the whole Strongly Correlated Systems community would benefit by a systematic exposition of the field. The present volume consists of a series of monographs on the most relevant numerical methods currently used to tackle the hoary problem of correlations. Authors have been selected, consulted major experts in the field, among the most world-wide famous scientists who invented or greatly helped to improve/spread the specific method in the community. Each chapter presents the method in a pedagogical way and contains at least one case-study where the method has proved to give a substantial leap forward in the knowledge and a very rich bibliography. The book is mainly intended for neophytes, who will find in one single volume all pieces of information necessary to choose and start learning a numerical method. Also, more experienced researchers would benefit from this volume as they would gain a deeper understanding of what any single technique can really tell them and what cannot. Accordingly, the accent is more on the ideas behind (origins, pros/cons, perspectives, ...) than on the technical details, which are left to the comprehensive bibliography.

We wish to thank all authors of this volume as they all joined this editorial project with enthusiasm and provided the whole community with what we hope will become a relevant resource for any researcher in the field as comprehensive and extended reference.

Salerno, Italy, March 2013

Adolfo Avella  
Ferdinando Mancini

# Contents

<b>Foreword</b> . . . . .	xvii
Elbio Dagotto	
<b>1 Ground State and Finite Temperature Lanczos Methods</b> . . . . .	1
P. Prelovšek and J. Bonča	
1.1 Introduction . . . . .	1
1.2 Exact Diagonalization and Lanczos Method. . . . .	3
1.2.1 Models, Geometries and System Sizes . . . . .	3
1.2.2 Lanczos Diagonalization Technique . . . . .	5
1.3 Ground State Properties and Dynamics . . . . .	7
1.4 Static Properties and Dynamics at $T > 0$ . . . . .	8
1.4.1 Finite Temperature Lanczos Method: Static Quantities . . . . .	9
1.4.2 Finite Temperature Lanczos Method: Dynamical Response . . . . .	12
1.4.3 Finite Temperature Lanczos Method: Implementation . . . . .	14
1.4.4 Low Temperature Lanczos Method. . . . .	16
1.4.5 Microcanonical Lanczos Method . . . . .	18
1.4.6 Statical and Dynamical Quantities at $T > 0$ : Applications . . . . .	19
1.5 Reduced Basis Lanczos Methods . . . . .	22
1.6 Real Time Dynamics Using Lanczos Method. . . . .	27
1.7 Discussion . . . . .	28
References . . . . .	29
<b>2 The Density Matrix Renormalization Group</b> . . . . .	31
Adrian E. Feiguin	
2.1 Introduction . . . . .	31

<b>2.2</b>	<b>Truncated Diagonalization: The Numerical Renormalization Group Idea . . . . .</b>	32
2.2.1	Two-Spin Problem . . . . .	32
2.2.2	Many Spins . . . . .	33
2.2.3	A Simple Geometrical Analogy . . . . .	35
2.2.4	The Case of Spins . . . . .	37
2.2.5	The Block Decimation Idea . . . . .	38
<b>2.3</b>	<b>The Density Matrix Truncation: The Kernel of the DMRG . . . . .</b>	40
2.3.1	The Reduced Density Matrix . . . . .	41
2.3.2	The Singular Value Decomposition . . . . .	42
2.3.3	The Schmidt Decomposition . . . . .	43
2.3.4	Optimizing the Truncated Wave-Function . . . . .	44
<b>2.4</b>	<b>Infinite-Size DMRG . . . . .</b>	44
2.4.1	Adding a Single Site to the Block . . . . .	46
2.4.2	Building the Super-Hamiltonian . . . . .	47
2.4.3	Obtaining the Ground-State: Lanczos Diagonalization . . . . .	47
2.4.4	Density Matrix Truncation and the Rotation to the New Basis . . . . .	49
2.4.5	Storing Matrices and States . . . . .	50
<b>2.5</b>	<b>The Finite-Size DMRG . . . . .</b>	50
2.5.1	Obtaining Quasi-Exact Results with the Finite-Size DMRG . . . . .	52
2.5.2	Measuring Observables . . . . .	53
2.5.3	Targeting States . . . . .	55
2.5.4	Calculating Excited States . . . . .	55
2.5.5	Wave-Function Prediction . . . . .	56
2.5.6	Generalization to Higher Dimensions and Complex Geometries . . . . .	57
<b>2.6</b>	<b>When and Why Does the DMRG Work? . . . . .</b>	58
2.6.1	Entanglement . . . . .	58
2.6.2	Entanglement and the Schmidt Decomposition . . . . .	59
2.6.3	Quantifying Entanglement . . . . .	60
2.6.4	The Area Law . . . . .	61
2.6.5	Entanglement and the DMRG . . . . .	63
<b>2.7</b>	<b>Outlook: DMRG and Tensor Network Methods . . . . .</b>	63
	References . . . . .	64
<b>3</b>	<b>Matrix Product State Algorithms: DMRG, TEBD and Relatives . . . . .</b>	67
	Ulrich Schollwöck	
3.1	Introduction . . . . .	67
3.2	Ground State Calculations in One Dimension . . . . .	68
3.2.1	Matrix Product States . . . . .	68

3.2.2	Matrix Product Operators . . . . .	75
3.2.3	The Variational MPS or Finite-System DMRG Algorithm . . . . .	79
3.2.4	iDMRG—Infinite-System DMRG Revisited. . . . .	81
3.2.5	Why Does it Work and Why Does it Fail? . . . . .	86
3.3	Time Evolution of Matrix Product States. . . . .	87
3.3.1	Conventional Time Evolution: Pure States. . . . .	88
3.3.2	Conventional Time Evolution: Mixed States . . . . .	91
3.3.3	tMPS, tDMRG, TEBD: Variations on a Theme . . . . .	95
3.3.4	How Far Can We Go? . . . . .	96
	References . . . . .	97
<b>4</b>	<b>Quantum Criticality with the Multi-scale Entanglement Renormalization Ansatz</b> . . . . .	99
	Glen Evenbly and Guifre Vidal	
4.1	Introduction . . . . .	99
4.2	Entanglement Renormalization and the MERA . . . . .	102
4.2.1	Foundations of Entanglement Renormalization. . . . .	102
4.2.2	Foundations of the MERA. . . . .	105
4.2.3	Choice of MERA Scheme . . . . .	108
4.3	Symmetries in Tensor Network States. . . . .	108
4.3.1	Spatial Symmetries. . . . .	110
4.3.2	Global Internal Symmetries . . . . .	112
4.4	Scale-Invariant MERA . . . . .	113
4.4.1	Basic Properties . . . . .	114
4.4.2	Transitional Layers. . . . .	114
4.4.3	Local Density Matrix . . . . .	114
4.4.4	Scale-Invariant Objects . . . . .	116
4.5	Benchmark Results . . . . .	119
4.5.1	Comparison with MPS . . . . .	121
4.5.2	Evaluation of Conformal Data: The Ising Model . . . . .	125
4.6	Conclusions . . . . .	128
	References . . . . .	129
<b>5</b>	<b>The Time-Dependent Density Matrix Renormalization Group</b> . . . . .	131
	Adrian E. Feiguin	
5.1	Introduction . . . . .	131
5.2	The Adaptive Time-Dependent DMRG (tDMRG). . . . .	133
5.2.1	The Suzuki–Trotter Approach . . . . .	133
5.2.2	Evolution Using Suzuki–Trotter Expansions . . . . .	135
5.3	The tDMRG Algorithm. . . . .	135
5.4	Time-Step Targeting Method . . . . .	137
5.5	Sources of Error. . . . .	139

5.6	Comparing Suzuki–Trotter and Time-Step Targeting . . . . .	141
5.7	Evolution in Imaginary Time . . . . .	141
5.8	Applications. . . . .	143
5.8.1	Transport. . . . .	144
5.8.2	Time-Dependent Correlation Functions . . . . .	146
5.9	The Enemy: Entanglement Growth . . . . .	148
5.9.1	Global Quench: Qualitative Picture. . . . .	149
5.9.2	Local Quench: Qualitative Picture . . . . .	150
5.9.3	Computational Cost . . . . .	150
5.10	Discussion . . . . .	151
	References . . . . .	151
<b>6</b>	<b>Loop Algorithm . . . . .</b>	<b>153</b>
	Synge Todo	
6.1	Introduction . . . . .	153
6.2	Path Integral Representation . . . . .	154
6.2.1	Mapping to Classical System . . . . .	154
6.2.2	Single Spin-1/2 in a Magnetic Field . . . . .	155
6.2.3	Continuous Time Path Integral Representation . . . . .	156
6.2.4	World-Line Representation of XXZ Spin Model . . . . .	159
6.2.5	Negative Sign Problem . . . . .	160
6.3	Loop Algorithm . . . . .	162
6.3.1	Markov Chain Monte Carlo . . . . .	162
6.3.2	Swendsen–Wang Algorithm . . . . .	162
6.3.3	Kandel–Domany Framework . . . . .	163
6.3.4	Continuous Imaginary Time Limit and Rejection Free Scheme . . . . .	165
6.3.5	Loop Algorithm for XXZ Model . . . . .	167
6.3.6	Implementation and Technical Aspects . . . . .	170
6.3.7	Generalizations. . . . .	171
6.4	Measurements . . . . .	173
6.4.1	Diagonal Operators and Correlation Functions . . . . .	173
6.4.2	Susceptibilities and Dynamical Structure Factors . . . . .	174
6.4.3	Correlation Length and Excitation Gap . . . . .	175
6.4.4	Energy and Specific Heat . . . . .	176
6.4.5	Spin Stiffness. . . . .	177
6.5	Loop Representation . . . . .	178
6.5.1	Improved Estimators . . . . .	178
6.5.2	Pure Loop Representation . . . . .	180
6.5.3	Pure Loop Algorithm . . . . .	181
6.6	Conclusion. . . . .	182
	References . . . . .	183

<b>7 Stochastic Series Expansion Quantum Monte Carlo . . . . .</b>	185
Roger G. Melko	
7.1 Introduction . . . . .	185
7.2 Quantum Monte Carlo Formalism. . . . .	187
7.2.1 Finite-Temperature Representation . . . . .	188
7.2.2 Zero-Temperature Projector Representation . . . . .	190
7.2.3 Local and Non-Local Updating Schemes. . . . .	191
7.3 Spin-1/2 Heisenberg Model . . . . .	193
7.3.1 Finite-Temperature SSE in the $S^z$ Basis. . . . .	194
7.3.2 Zero-Temperature Projector in the Valence Bond Basis. . . . .	197
7.4 Transverse Field Ising Model. . . . .	199
7.4.1 Finite-Temperature SSE in the $S^z$ Basis. . . . .	200
7.4.2 Zero-Temperature Projector in the $S^z$ Basis . . . . .	203
7.5 Discussion . . . . .	204
References . . . . .	205
<b>8 Variational Monte Carlo and Markov Chains for Computational Physics . . . . .</b>	207
Sandro Sorella	
8.1 Introduction . . . . .	207
8.2 Quantum Monte Carlo: The Variational Approach . . . . .	208
8.2.1 Introduction: Importance of Correlated Wave Functions . . . . .	208
8.2.2 Expectation Value of the Energy . . . . .	211
8.2.3 Finite Variance Property . . . . .	213
8.3 Markov Chains: Stochastic Walks in Configuration Space. . . . .	216
8.3.1 Detailed Balance and Effective Hamiltonian . . . . .	218
8.4 The Metropolis Algorithm. . . . .	223
8.5 Stochastic Minimization of the Energy . . . . .	225
8.6 Conclusion. . . . .	230
References . . . . .	235
<b>9 Coupled Cluster Theories for Strongly Correlated Molecular Systems . . . . .</b>	237
Karol Kowalski, Kiran Bhaskaran-Nair, Jiří Brabec and Jiří Pittner	
9.1 Introduction . . . . .	237
9.2 Single Reference CC (SRCC) Methods . . . . .	239
9.2.1 Standard Approximations. . . . .	241
9.2.2 Solvability of the CC Equations . . . . .	243
9.2.3 Perturbative Inclusion of Higher-Order Clusters . . . . .	244
9.2.4 Parallel Implementations of the SRCC Methods. . . . .	248
9.3 Multireference CC Theories. . . . .	251
9.3.1 Wave Operator Formalism and Bloch Equation . . . . .	252

9.3.2	State-Universal MRCC Formulations . . . . .	253
9.3.3	Intruder State Problem . . . . .	255
9.3.4	Incomplete/General Model Spaces . . . . .	256
9.3.5	State-Specific Methods . . . . .	257
9.3.6	Inclusion of High-Order Clusters in MRCC Formalisms . . . . .	259
9.3.7	Parallel Calculations with the MRCC Methods: Reference-Level Parallelism . . . . .	264
9.4	Conclusions . . . . .	266
	References . . . . .	267
<b>10</b>	<b>Diagrammatic Monte Carlo and Worm Algorithm Techniques . . . . .</b>	<b>273</b>
	Nikolay Prokof'ev	
10.1	Introduction . . . . .	273
10.2	Diagrammatic Monte Carlo . . . . .	274
10.2.1	Updates . . . . .	276
10.2.2	Advantages and Potential Problems . . . . .	278
10.3	Worm Algorithm . . . . .	280
10.3.1	Ising and XY Models . . . . .	281
10.3.2	Path-Integral Representation . . . . .	285
10.3.3	Wandering Amongst the Feynman Diagrams . . . . .	289
	References . . . . .	291
<b>11</b>	<b>Fermionic and Continuous Time Quantum Monte Carlo . . . . .</b>	<b>293</b>
	Emanuel Gull and Matthias Troyer	
11.1	Introduction . . . . .	293
11.2	Diagrammatic Monte Carlo . . . . .	296
11.2.1	Monte Carlo Basics . . . . .	296
11.2.2	Diagrammatic Monte Carlo . . . . .	298
11.2.3	The Negative Sign Problem . . . . .	300
11.3	Interaction Expansion . . . . .	302
11.3.1	Partition Function Expansion . . . . .	302
11.3.2	Updates . . . . .	304
11.3.3	Measurements . . . . .	304
11.3.4	Generalizations . . . . .	305
11.4	Hybridization Expansion . . . . .	306
11.4.1	Partition Function Expansion . . . . .	306
11.4.2	Updates . . . . .	308
11.4.3	Measurements . . . . .	308
11.4.4	Generalizations . . . . .	310
11.5	Applications . . . . .	310
11.5.1	Nanoscience . . . . .	310
11.5.2	Single Site Dynamical Mean Field Theory . . . . .	311
11.5.3	Cluster DMFT . . . . .	312

Contents	xiii
11.5.4 Diagrammatics Beyond DMFT . . . . .	313
11.5.5 Lattice and Large Cluster DMFT Calculations and Extrapolations to the Infinite System . . . . .	314
11.5.6 Applications to Real Materials . . . . .	315
11.5.7 Real-Time Dynamics . . . . .	316
11.6 Outlook . . . . .	317
References . . . . .	317
<b>Index . . . . .</b>	<b>321</b>

# Contributors

**K. Bhaskaran-Nair** William R. Wiley Environmental Molecular Sciences Laboratory Battelle, Pacific Northwest National Laboratory Richland, Washington 99352, USA, e-mail: kiran.bhaskarannair@pnnl.gov

**J. Bonca** J. Stefan Institute, 1000 Ljubljana, Slovenia; Faculty of Mathematics and Physics, University of Ljubljana, 1000 Ljubljana, Slovenia, e-mail: janez.bonca@ijs.si

**J. Brabec** J. Heyrovský Institute of Physical Chemistry, Academy of Sciences of the Czech Republic, 18223 Prague 8, Czech Republic, e-mail: jiri.brabec@jh-inst.cas.cz

**E. Dagotto** Department of Physics and Astronomy, The University of Tennessee, Knoxville 37996, TN, USA; Materials Science and Technology Division, Oak Ridge National Laboratory, Oak Ridge 37831, TN, USA, e-mail: edagotto@utk.edu

**G. Evenbly** Institute for Quantum Information and Matter, California Institute of Technology, 1200 E. California Blvd, Pasadena, CA 91125, USA, e-mail: evenbly@caltech.edu

**A. E. Feiguin** Department of Physics, Northeastern University Boston, Boston, MA 02115, USA, e-mail: a.feiguin@neu.edu

**E. Gull** Department of Physics, University of Michigan, Ann Arbor, MI 48109-1040, USA, e-mail: egull@umich.edu

**K. Kowalski** William R. Wiley Environmental Molecular Sciences Laboratory Battelle, Pacific Northwest National Laboratory Richland, Washington 99352, USA, e-mail: karol.kowalski@pnnl.gov

**R. G. Melko** Department of Physics and Astronomy, University of Waterloo, Waterloo, ON N2L 3G1, Canada; Perimeter Institute for Theoretical Physics, Waterloo, ON N2L 2Y5, Canada, e-mail: rgmelko@uwaterloo.ca

**J. Pittner** J. Heyrovský Institute of Physical Chemistry, Academy of Sciences of the Czech Republic, 18223 Prague 8, Czech Republic, e-mail: jiri.pittner@jh-inst.cas.cz

**P. Prelovsek** J. Stefan Institute, 1000 Ljubljana, Slovenia; Faculty of Mathematics and Physics, University of Ljubljana, 1000 Ljubljana, Slovenia, e-mail: peter.prelovsek@ijs.si

**U. Schollwock** Department of Physics, University of Munich, Theresienstrasse 37, 80333 Munich, Germany, e-mail: schollwoeck@lmu.de

**S. Sorella** SISSA, Via Bonomea n.245, Trieste, Italy, e-mail: sorella@sissa.it

**S. Todo** Institute for Solid State Physics, University of Tokyo, 7-1-26-R501 Port Island South, Kobe 650-0047, Japan, e-mail: wistaria@issp.u-tokyo.ac.jp

**M. Troyer** Institut f. Theoretische Physik, ETH, 8093 Zurich, Switzerland, e-mail: matthias.troyer@itp.phys.ethz.ch

**G. Vidal** Perimeter Institute for Theoretical Physics, 31 Caroline St, Waterloo, ON N2L 2Y5, Canada, e-mail: gvidal@perimeterinstitute.ca

# Foreword

**Elbio Dagotto**

**Abstract** The perspective of the author on the important and rapidly growing role of computational techniques in Theoretical Condensed Matter Physics is provided. A brief summary of each of the chapters of the book is also included in this Foreword.

## 1 Introduction

In elementary courses on Condensed Matter Physics, students learn that a good description of the electronic properties of simple metals, such as copper or silver, can be obtained via the one-electron approximation. The main assumption of this approximation, which works remarkably well for good metals, is that you can solve the quantum mechanical problem of a particle in a large box, mimicking the crystal, and then simply fill the individual levels with spin-up and spin-down electrons until all the electrons that you wish to have are properly located in states of the box, namely filling levels up to the Fermi energy. Alert students often wonder how this miracle occurs since obviously electrons interact with one another via repulsive Coulombic forces, thus invalidating the one-electron approximation. Elaborated rationalizations are then invoked, based on the Fermi liquid ideas, to justify the neglect of those interactions. But then typically, these students will sooner or later attempt to follow a similar rationale to study other more complex materials, discovering with surprise that this “one electron”

---

E. Dagotto (✉)

Department of Physics and Astronomy, The University of Tennessee, Knoxville 37996, TN, USA; Materials Science and Technology Division, Oak Ridge National Laboratory, Oak Ridge 37831, TN, USA

e-mail: edagotto@utk.edu

approximation fails miserably in most cases. A famous example is provided by the copper-oxide high temperature superconductors where naive one-electron estimations would predict the parent compound to be a metal while in reality it is a Mott insulator precisely due to the importance of those repulsive forces among the electrons. Then, in general it is crucial to be able to move beyond “one electron” ideas to properly describe the physics of a wide variety of materials that are both of crucial conceptual relevance and technical importance.

However, properly taking into account the correlations between electrons is much easier said than done. Students also know, from their quantum mechanical classes, how difficult it is to be accurate in problems of atomic physics beyond the hydrogen atom, precisely due to that “pesky” Coulomb repulsion between the electrons. Heroic attempts are being made to address the full quantum mechanical Schrödinger equation of electrons in clusters of atoms via Quantum Monte Carlo (QMC) methods in the continuum, but these techniques are not sufficiently developed to satisfy the vast needs that condensed matter theorists have at present to describe the myriad of interesting novel phenomena that our experimental colleagues almost daily unveil. Then, the most common path is to work with model Hamiltonians. These models are constructed by hand under the assumptions that they must satisfy the known symmetries of the system, they must involve local or quasi local interactions, and in general they have to be “reasonable” such as containing “electron hopping” terms only among atoms at short distances from each other, and involving the proper orbitals for electron tunneling to occur. The construction of these models is typically a fun adventure, but then sooner or later the task of solving the model arises and things rapidly become complicated: if we have trouble studying say light atoms with a few electrons, the problem can only get worse if the number of electrons is of the order of Avogadro’s number.

It is fair to say that clever approximations have been developed over the years to study interacting many-body systems. For instance, the BCS theory of superconductivity based on a simple variational state and the assumption that a weak electron–electron attractive interaction arises from the time-retarded interactions with phonons, addresses successfully a complex many-body problem. But in general only a small subset of interesting materials admits such simple descriptions. Moreover, an important motive of present-day Condensed Matter Physics is the “competition” of states in families of compounds with rich phase diagrams. These states can be reached in the laboratory by adding or removing electrons, increasing pressures, turning on and off electric or magnetic fields, etc. Having a single “pen and pencil” formalism that allows the study of competing, say insulating and metallic states, is very difficult, particularly if we aim to reach an accurate description of both states. Dealing with complex many-body problems can indeed be frustrating.

Fortunately, the fast development of computers in recent times allows for some hope. How about solving the quantum mechanical many-body problems, with all the important interactions incorporated, using the help of computers? Computers can manipulate large arrays of numbers in tiny amounts of time, way beyond what any human can hope to do in a lifetime. In fact, we are witnessing the slow

evolution of the traditional theoretical physics mainly based on pen and pencil calculations unto a more sophisticated enterprise that often involves large-scale computer simulations. While older generations carved their intuition based on integrals over momentums and frequencies, new generations often think in real space and time and learn to visualize intuitively the physics under discussion from the analysis of complex plots of data arising from the study of model Hamiltonians using elaborated computational techniques. In fact, in my lifetime I have seen the rise of computational physics from an early “supporting actor” role to a much more fundamental role in the study of models and materials. Nowadays nobody blinks when a publication is almost entirely based on results coming from computational efforts. Hopefully, the new generations will appreciate that this did not happen overnight, and will thank in their hearts the pioneers that established computational physics as a well respected, and currently rapidly growing, area of theoretical physics.

In this book, edited by Professors Adolfo Avella and Ferdinando Mancini, the state of the art of computational methods to study model Hamiltonians is presented. This volume is actually one component of a set of three books on the general area of “Strongly Correlated Systems: Methods and Techniques,” all of them edited by Avella and Mancini. The first volume, already published recently by Springer, has the title “Theoretical Methods for Strongly Correlated Systems,” and the focus is on analytical studies of correlated electrons. A personal observation here about the title of this first book: note that computational physics is a rapidly growing subset of theoretical physics. Thus, describing analytical methods as “theoretical” and computational methods as a separate entity often called “numerical” is incorrect. Both analytical and numerical methods are different methods used to address theoretical physics. The second book in this series is the one you have in your hand now. The third will address “Experimental Techniques for Strongly Correlated Systems.” Having a global view of correlated electrons, via its analytical and computational theoretical perspectives and also the experimental component will be very beneficial to young scientists entering into this field.

Returning to the Foreword for this book, note that having powerful computational techniques to carry out the numerical investigations is crucial, because although my casual writing above (“let the computers do the work”) may imply that this is relatively easy, in practice it is certainly not. To start with, most of the computational studies are carried out using finite small systems, with the hope of performing a systematic study of many sizes and then an extrapolation to the bulk limit. For this reason, accurate and powerful methods are needed that can handle large clusters. Moreover, sometimes there are subtleties, such as the effect known as the “sign problem” that is widely discussed in several chapters of this book. This effect can certainly spoil the fun of a project. Thus, it is important to be aware of the sort of techniques that are available in the literature for the handling of a particular problem of interest to the reader. Let me make this point clear: there is no single computational technique at present that can handle any problem of your choice, but each method presented in the many chapters of this book has a limited

range of applicability. Young theoretical physicists reading this text should become familiar with all of the methods presented here, and particularly remember the type of problems that each technique is good for.

In the rest of this foreword, I will present a brief description of each of the many chapters of this book (following the order in which they appear), aiming to summarize the essence of each method. But, of course, readers should use my writing only as a stepping stone into the real important portion of the book that are the individual chapters. I will also resist the temptation of citing literature in this foreword, so that readers will have to consult the many chapters to gather that important information.

## 2 Lanczos Exact Solution of Small Clusters

In [Chap. 1](#), Prelovšek and Bonča describe the Lanczos method, often casually referred to as Exact Diagonalization, both at zero and finite temperature. The essence of this technique is to solve exactly a small cluster of the model Hamiltonian that is under study. While the exponential growth of Hilbert spaces often limits the applicability of this technique to very small systems, the reason for its popularity is that it can be applied to all the families of models that are frequently used in the correlated electron context, although with a cluster size that shrinks fast with the number of degrees of freedom per site. In these regards the technique is flexible and moreover it is truly unbiased: the exact properties of the model in the small cluster used will be obtained as an answer, as opposed to a crude approximation to those properties. Typically, after a Lanczos analysis unveils a particular tendency to spin, charge, or orbital order at the short distances that fit into the small cluster that was solved exactly, then other computational techniques or mean-field approximations can be employed to address larger systems. Reciprocally, the Lanczos method can also be used to confirm ideas, such as proposed variational states, or to gather numerical information to be used as benchmark to judge the accuracy of other computational methods. Lanczos has the important advantage over other algorithms in that it can also be used to gather dynamical information, both in the form of spectral functions or as real-time evolutions of states, the latter including studies far from equilibrium.

Prelovšek and Bonča also describe in [Chap. 1](#) variations of the Lanczos technique, such as the High Temperature expansion method where a reduced set of randomly chosen states are used, as in Monte Carlo procedures. The calculations are carried out for all temperatures simultaneously. Applications of this finite-temperature Lanczos method include the study of the famous two-dimensional  $t$ - $J$  model for Cu-oxide high temperature superconductors, addressing subtle issues such as the presence of non-Fermi liquid behavior, the exotic linear resistivities unveiled at optimal hole doping in the cuprates, the existence of pseudogap regions in the underdoped regime, and others. Also, recent variations of the Lanczos technique are presented in this chapter, such as the “low temperature” and

“microcanonical” Lanczos methods, and even the use of a reduced or truncated basis set, illustrated with the example of adding phonons, which is in the spirit of the Density Matrix Renormalization Group (DMRG) technique described in the subsequent chapters of this book.

### 3 Density Matrix Renormalization Group, Matrix Product States, and the Multi-scale Entanglement Renormalization Ansatz

To improve on the severe size limitations of the Exact Diagonalization or Lanczos method, the DMRG technique was developed by S. White, and four chapters of this book are devoted to this technique (three of them being reviewed here in this subsection simultaneously), including recent variations and improvements. In [Chap. 2](#), Feiguin introduces the reader to the DMRG method by first explaining the fast growth of Hilbert spaces with the number of spins using the spin-1/2 Heisenberg model as illustration. This example clearly shows that to study large systems, a clever basis truncation procedure is needed. In the early days, the Renormalization Group method of K. Wilson was used to construct an approximate basis and the technique worked nicely in several cases. But consider for instance the simple problem of just one electron hopping between nearest-neighbor sites along a chain of length  $L$  with open boundary conditions, and suppose we wish to get a good approximation to its ground state by knowing the properties of a chain of length  $L/2$ . The ground state wave function of the  $L/2$  chain has the shape of a cosine function, with nodes at both ends of the chain. If we naively assume that the ground state for the case of length  $L$  can be approximated by gluing the two ground states of length  $L/2$ , then we are generating a spurious node at the center, since we know that the ground state of  $L$  only has nodes at the extremes of the chain. Then, the energy alone cannot be the best indicator for how to select a proper truncated basis. As Feiguin explains, it is much better to use the reduced density matrix to select that reduced basis since in this quantity the connection between the two portions of the problem, and their potential quantum mechanical entanglement, is included. Based on these ideas the DMRG method emerges and certainly this technique is the method of choice for quasi one-dimensional electronic model Hamiltonians.

Feiguin explains also the limitations of the DMRG method. For instance, in the early days it was common practice to use the “infinite” system variation of DMRG, but nowadays it is known that addressing finite systems and then extrapolating to the bulk is the best way to go. And of course, carefully analyzing how the results change with the number of states  $m$  is a must, since sometimes the behavior of observables with increasing  $m$  is not smooth, due to occasional “tunneling” into regions of the Hilbert space that were not included for a smaller  $m$ . Another limitation is the generalization to two-dimensional systems: in fact if

we order the sites of a finite ladder or truly two-dimensional lattice via a “snake” procedure to reduce it to a one-dimensional arrangement, it is clear that in the 1D language the hopping terms and interactions, that are not on-site, will develop a long-range character that always complicates any algorithm. Fortunately, considerable progress is being made via the concept of entanglement entropy that allows to understand why the DMRG number of states  $m$  that is needed in 2D grows very fast with the number of sites (following an “area law”, see also [Chap. 3](#) by Schollwöck). The entanglement entropy is an important concept that establishes that two systems  $A$  and  $B$  are disentangled when the wave function of the system is merely the product of the wave functions of the individual components, while they are maximally entangled when the state of  $A$  uniquely establishes the state of  $B$  and vice versa. DMRG in fact minimizes the loss of information related with the entanglement of the components.

The DMRG-related novel area based on the “Matrix Product States” (MPS) is presented in detail by Schollwöck in [Chap. 3](#) (this topic is also mentioned in [Chap. 2](#) by Feiguin). Starting with the mathematical discussion of the main ideas, an example based on the Heisenberg model helps in clarifying the formalism. The MPS perspective establishes DMRG as a variational method in the space of matrix product states, allowing for extensions of the method and a deeper conceptual understanding. The connection between the MPS perspective and the original DMRG algorithm is explained in this chapter. Overall, it is clear that although the novel approaches are not yet in practice better than the original DMRG, surprises may be found in the near future as research in this active field continues progressing based on the MPS perspective.

In [Chap. 4](#), Evenbly and Vidal describe the notion of “tensor network states” as variational states to characterize lattice quantum many-body systems. The number of parameters in this case is much smaller than the exponentially large dimension of the Hilbert space with increasing lattice size. These tensor network states can be classified based on the physical geometry of the system or via the holographic geometry, where an additional dimension parameterizing different lengths or energy scales is introduced. The focus of [Chap. 4](#) is on the latter, in particular on the Multi-scale Entanglement Renormalization Ansatz (MERA) to study critical systems in one-dimensional geometries, aiming to properly capture the scale invariance of these systems. The authors describe in detail all the properties of the MERA method and compare with other techniques, and they also explain how to deal with symmetries. In addition, benchmark results are provided using the critical Ising model and other critical systems, and comparison with results of other methods are discussed. The conclusion of these comparisons is that the MERA method indeed produces better correlators at large distances for critical systems, as the method was originally designed to achieve.

## 4 Time-Dependent DMRG

In [Chap. 5](#), Feiguin explains the time-dependent DMRG method (this topic was also discussed in [Chap. 3](#) by Schollwöck). This technique allows for the study of real-time dynamics (i.e. not imaginary time but real) and it can provide spectral functions with frequency dependence and also results far from equilibrium. Feiguin explains that as time grows adapting (i.e. changing) the basis is crucial, because the “truncated” or optimal basis for the ground state is not necessarily the same basis that is needed for the state during the time evolution. For instance, this becomes clear for the case of strong perturbations that will drive the system away from the equilibrium state that existed before the perturbation was turned on. In this case, other areas of the Hilbert space may become relevant as, for example, occurs when a steady current develops due to a strong electric field. Thus, it is important to keep track of the entire time-evolution of the wave function: in fact, the propagation of the wave functions becomes the main purpose of the algorithm.

Feiguin explains that the Suzuki–Trotter approach is a natural procedure to break the time evolution operator. It introduces a discretization, i.e., a “Trotter error” that is under reasonable control in practice since this error can always be reduced by reducing the time-step length, of course at the cost of increasing the computer time of the study. In addition, the advantages of the Runge–Kutta integration for these types of methods are discussed in this chapter via concrete examples. Moreover, a similar evolution but in imaginary time can be used to obtain results at finite temperatures, showing the formal similarities with the real-time evolution.

The time-dependent DMRG technique is widely applied these days to problems that range from transport through quantum dots to non-equilibrium physics in the context of cold atoms. In the former, the introduction of a sudden bias to generate a current is often employed, and a plateau in the current versus time is formed in a finite window of time (due to the open boundary conditions, eventually the current will bounce back). Thus, the I–V curve can be studied for those quasi-stationary currents. Several other time-dependent correlation functions can be calculated as well. Feiguin also describes the “enemies” of these methods: they are related with the entanglement entropy, and with the abrupt versus adiabatic introduction of modifications in the Hamiltonian. For instance, to study the effects of a strong perturbation it may be advantageous to turn on this perturbation “slowly” so that the system has time to select the proper basis to describe the new system.

## 5 Loop Algorithm

In [Chap. 6](#), Todo explains how a quantum model can be mapped into a classical model by adding another dimension related with temperature, which is then discretized in steps. This is equivalent to working in imaginary time. Moreover, Todo

also explains that there is a continuous-time path-integral representation that can be alternatively used. The world-line configurations are introduced for the stochastic sampling, involving products of matrix elements, and it is emphasized that millions of spins can be handled by this procedure. However, note that these matrix elements can be negative, thus leading to “sign problems” which of course introduces a limitation in the type of models that can be handled with these techniques. While this is a complication difficult to avoid, Todo discusses that another typical problem of Monte Carlo simulations, the slowing down of the simulations at low temperatures or near criticality, can actually be improved upon or eliminated altogether via cluster algorithms where groups of spins are simultaneously flipped, instead of using individual spins for the updates. This reduces critical slowing down near continuous phase transitions, particularly if the cluster sizes are chosen based on the correlation lengths of the problem. Another procedure to avoid the lack of ergodicity addresses global constraints in the simulation, via a generalization of phase space. In this case auxiliary variables are introduced that represent constraints in the spin system, to fight conservation rules that make the single site update procedure useless. For instance, if the total spin  $S_z$  must be conserved, the flip of a spin will always be rejected. For this reason, procedures involving bonds as opposed to single sites are sometimes more natural. Thus, the ability of the programmer is needed to identify the correct variables to use to carry out the simulations in an efficient manner. In the case of the spin-1/2 antiferromagnetic Heisenberg chain, introducing the imaginary time direction leads to a representation in terms of loops that thus becomes an integral part in the updating process.

## 6 Stochastic Series Expansion

In [Chap. 7](#), Melko discusses the Stochastic Series Expansion (SSE) technique, which is a very efficient QMC method for quantum lattice models. This technique was originally devised by A. Sandvik as a finite-temperature simulation based on a Taylor expansion of the partition function. The method is easy to implement and applies to quantum spins and bosons, as long as they do not have the “sign problem.” As simple examples, Melko discusses the spin-1/2 isotropic Heisenberg model and the Ising model in a transverse field. In general a quantum  $D$  dimensional problem must be mapped into a  $D + 1$  dimensional classical representation incorporating an imaginary time axis to allow for its implementation in classical computers. In the SSE method the trace of products of the Hamiltonian are evaluated stochastically, formally via path integral or world-line representations. Cluster and loop algorithms are used to speedup the simulation and allow for ergodicity. More recently, the method has been reformulated to become applicable to the zero-temperature projector method, where a large power of the Hamiltonian is applied to a trial wavefunction to project out the ground state. Both methods are in principle conceptually quite different, but their implementation via non-local

loop or cluster algorithms reveals an underlying similarity, as discussed by Melko via the example of the Heisenberg model in a valence bond basis.

## 7 Quantum and Variational Monte Carlo

In [Chap. 8](#), Sorella discusses the very powerful QMC technique and the associated Variational Monte Carlo (VMC) method. For model Hamiltonians and in regions of parameter space where QMC “works”, namely where there are no “sign problems” or other technical inconveniences, the QMC method is very powerful and addresses exactly (within statistical errors) the physics of the model under investigation. Sorella explains that the somewhat tedious process of gathering statistics to reduce error bars can be easily parallelized by running different realizations of the Monte Carlo evolution at different nodes of a computer cluster. For instance, after arriving to an equilibrium configuration, at each node a different “random number set” can be used to continue the runs with that configuration as a start. The results of the many Monte Carlo time evolutions at those different nodes can be eventually gathered at the end of the runs to construct averages. Considering that there are supercomputers with  $\sim 100,000$  nodes these days, clearly this procedure is advantageous since its scalability adapts to the number of nodes available. Of course we must be aware of the complications that arise in QMC and similar algorithms when we are near criticality since in these cases the self-correlation time diverges (namely the number of Monte Carlo steps needed to generate statistically independent equilibrium configurations diverges at second order transitions). And of course we must worry about sign problems, as explained before. But where it works, QMC is indeed very powerful and unbiased.

With regard to the VMC method, the relation with QMC arises from the need to calculate the expectation values in the variational state via a Monte Carlo stochastic process. Definitely starting with a “good” wave function is a must for accuracy, and Sorella uses the case of the Gutzwiller wave function to illustrate how a simple projector operator that removes doubly occupied sites can make an important difference for the case of the famous (or infamous depending on your view) Hubbard model. Dealing with many-body variational wave functions often illuminates the physics under discussion, thus VMC tends to provide qualitative insight into the problem studied even if it is not as precise and unbiased as QMC is. Since the Nobel prizes for the BCS theory of superconductivity and the Fractional Quantum Hall effect were essentially given for proposing an excellent (and simple) multi-electronic variational wave function, it is clear that variational approaches have some appeal. These days VMC can be carried out with a very large number of free parameters to optimize, and moreover, there are proposed methods to systematically improve a starting wave function.

## 8 Coupled Cluster Technique for Quantum Chemistry and Nuclear Physics

In [Chap. 9](#), Kowalski et al. describe the coupled cluster (CC) formalism. This is a widely employed and accurate method for the solution of the Schrödinger equation in molecules and other intrinsically finite systems. For instance, the technique is mainly applied in the context of computational chemistry but it is also used in nuclear physics. Correlation many-body effects are properly captured by the CC formalism, contrary to perturbative methods. These correlation effects are crucial to understand molecular structures, chemical reactions, and bond-forming/bond-breaking processes.

The CC method starts with an exponential Ansatz involving the exponential of the cluster operator  $T$  acting over a single Slater determinant, such as the one arising from the Hartree-Fock approximation.  $T$  is a sum over the many-body components. The authors explain that including higher order excitations in the process comes at a high numerical price, leading to severe limitations of the straightforward procedure even for relatively small systems. But the authors also explain that there are several interesting improvements to deal with this problem, including the use of leadership class computer architectures. Often the cases of the  $\text{H}_2\text{O}$  and  $\text{CO}_2$  molecules are used as examples to judge the accuracy of the results, and in some tests, up to 210,000 cores of supercomputers have been used. Extensions to the always complex case where there are quasi-degenerate states are also presented by the authors. In the rest of the chapter, the several variations of the methodology are reviewed in considerable detail. It is concluded that at present accurate calculations can be carried out for 200–300 correlated electrons with 1,300–1,500 basis set functions.

## 9 Monte Carlo Methods for Diagrammatic Series

[Chapter 10](#) by Prokof'ev reviews the basic principles of the Diagrammatic Monte Carlo (DiagMC) and Worm Algorithm techniques. With regard to DiagMC, the simpler case that comes to mind are the Feynman diagrams as they appear in standard perturbative formulations of Quantum Electrodynamics, or in similar diagrammatic formulations of problems of Condensed Matter Physics. The DiagMC method discussed in this chapter is generic and simply aims towards an accurate estimation of a sum of multiple integrals. However, Prokof'ev clarifies that DiagMC is fundamentally different from simply listing all diagrams of order say less than a maximum number, and then evaluating via Monte Carlo each integral one by one. In fact, in DiagMC the order of the diagram, their topology, and internal and external variables are all treated on equal footing, and each diagram represents a “point” in a generalized configuration space. A unique feature of DiagMC is that instead of addressing finite systems with increasing size

as in most computational techniques described in this book, the technique applies directly to the Feynman diagram series. Thus, results are obtained already in the thermodynamic limit and at any temperature.

Prokof'ev addresses the “sign blessing” issue (as opposed to the “sign problem” issue widely discussed in other chapters): due to the fact that the Feynman diagrams can be positive or negative, the apparent fast growth of the number of diagrams with their order, and the associated impression that the series are just asymptotic, is removed by the sign alternation. In fact, it is thanks to the sign blessing in this context that the series do converge.

With regard to the Worm Algorithm, this technique allows for a better sampling of configuration space in cases where this space has a complex topology and/or global constraints, which usually induce complications in standard Monte Carlo methods based on local updates, since the Monte Carlo time evolution leads to nominal equilibrium states that are actually trapped in a portion of the configuration space. In this case, there are ergodicity problems since not all sectors of configuration space are equally sampled. In practice, the method is based on enlarging the original configuration space with the original constraints into a larger space without those constraints. This facilitates the “tunneling” between different sectors. Examples dealing with the Ising, XY, and bosonic models are discussed in this chapter.

## 10 Continuous Time Quantum Monte Carlo

In [Chap. 11](#), Gull and Troyer provide an introduction to “continuous time quantum Monte Carlo” (CT-QMC) methods for fermions. The description includes both lattice models, such as the Hubbard model, and quantum impurity problems, such as the Anderson impurity problem describing a magnetic atom embedded in a non-interacting medium. Impurity problems formally appear also in the solution of the Dynamical Mean Field Theory (DMFT) equations, and it is in this area where CT-QMC methods are used the most frequently at present. CT-QMC is based on the stochastic sampling of time-dependent diagrammatic perturbation theory, as described by Prokof'ev in [Chap. 10](#). Time is continuous from the beginning, since there is no need to discretize this dimension, contrary to what is done in many other techniques presented in this book. Gull and Troyer explain that at present there are already several types of extensions of this method (called hybridization, interaction, and auxiliary method) with different areas of applicability. These three variations are explained in detail in the bulk of the chapter. The authors include an introduction to the general diagrammatic Monte Carlo formulation, with sums involving not only the order of the diagrams but also their topology in order for ergodicity to be satisfied (see [Chap. 10](#) by Prokof'ev). The issue of the sign problem is also discussed, and it is concluded that in impurity problems, this complication is not as severe as in finite-sized lattice models.

In the second half of the chapter, the authors provide several examples that illustrate the wide range of applicability of the continuous-time methods. The examples include Kondo problems and quantum dots, single-site and cluster DMFT, the three-dimensional Hubbard model above the critical temperature for antiferromagnetism, LDA + DMFT approaches to real materials, and even real-time dynamical methods.

## 11 Summary

In this Foreword, my goal has been to transmit to the readers my profound enthusiasm for the field of research centered at the computational studies of model Hamiltonians. With just a few exceptions, it is difficult to find analytical techniques that are reliable for the study of a particular model in the area of Strongly Correlated Electrons since usually there is no small parameter to use in an expansion. Thus, after applying those techniques we always have the uneasy feeling of not really knowing if the results are accurate. However, with the use of computational methods, calculations can have a much more robust foundation. Employing the computer for the study of a model has the feeling of an experiment: you can ask clever “questions” to the “sample” under study, analyze data, and come up with an intuitive picture of what is happening. Very often the computer results are not what we were expecting a priori, thus there is a neat back and forth process until a convergence to a firm conclusion is reached. The many chapters in this book illustrate on how sophisticated the computational methods have become in recent years, with plenty of interesting new tricks and perspectives being developed and applied to address challenging issues in the study of a variety of model Hamiltonians. And in the meantime, while we work hard on these types of problems, the computer industry is constantly improving the machines that we use in our effort! For all these reasons, I am convinced that this area of research has a promising future and hopefully it will continue to attract outstanding researchers such as the many authors of the chapters contained in this book.

**Acknowledgments** The author thanks Adriana Moreo for a careful reading of this foreword. The work of the author was supported by the US Department of Energy, Office of Basic Energy Sciences, Materials Sciences and Engineering Division, and also by the National Science Foundation under Grant No. DMR-11-04386.

# Chapter 1

## Ground State and Finite Temperature Lanczos Methods

P. Prelovšek and J. Bonča

**Abstract** The present review will focus on recent development of exact-diagonalization (ED) methods that use Lanczos algorithm to transform large sparse matrices onto the tridiagonal form. We begin with a review of basic principles of the Lanczos method for computing ground-state static as well as dynamical properties. Next, generalization to finite-temperatures in the form of well established finite-temperature Lanczos method is described. The latter allows for the evaluation of temperatures  $T > 0$  static and dynamic quantities within various correlated models. Several extensions and modification of the latter method introduced more recently are analysed. In particular, the low-temperature Lanczos method and the micro-canonical Lanczos method, especially applicable within the high- $T$  regime. In order to overcome the problems of exponentially growing Hilbert spaces that prevent ED calculations on larger lattices, different approaches based on Lanczos diagonalization within the reduced basis have been developed. In this context, recently developed method based on ED within a limited functional space is reviewed. Finally, we briefly discuss the real-time evolution of correlated systems far from equilibrium, which can be simulated using the ED and Lanczos-based methods, as well as approaches based on the diagonalization in a reduced basis.

### 1.1 Introduction

Models of strongly correlated systems have been one of the most intensively studied theoretical subjects in the last two decades, stimulated at first by the discovery of compounds superconducting at high-temperatures and ever since by the emergence

---

P. Prelovšek (✉) · J. Bonča  
Jožef Stefan Institute, 1000 Ljubljana, Slovenia  
e-mail: peter.prelovsek@ijs.si

P. Prelovšek · J. Bonča  
Faculty of Mathematics and Physics, University of Ljubljana, 1000 Ljubljana, Slovenia  
e-mail: janez.bonca@ijs.si

of various novel materials and phenomena which could be traced back to strongly correlated electrons in these systems. Recently, cold atoms in optical lattice offer a different realization of strongly correlated quantum entities, whereby these systems can be even tuned closer to theoretical models.

One of the most straightforward methods to numerically deal with the lattice (discrete) models of correlated particles, which are inherently many-body (MB) quantum systems, is exact diagonalization (ED) of small-size systems. In view of the absence of well-controlled analytical methods, ED method has been employed intensively to obtain results for static and dynamical properties of various models with different aims: (a) to search and confirm novel phenomena specific for strongly correlated systems, (b) to test theoretical ideas and analytical results, (c) to get reference results for more advanced numerical techniques.

MB quantum lattice models of interacting particles are characterized with a dimension of the Hilbert space given by the number of basis states  $N_{st} \propto K^N$  that is in turn exponentially increasing with the lattice size  $N$ , where  $K$  is the number of local quantum states. It is therefore clear that ED methods can treat fully only systems with limited  $N_{st}$ , i.e., both  $K$  and  $N$  must be quite modest.

Among the ED approaches the full ED within the Hilbert space of the model Hamiltonian, yielding all eigenenergies and eigenfunctions, is the simplest to understand, most transparent and easy to implement. In principle it allows the evaluation of any ground state (g.s.) property as well as finite temperature  $T > 0$  static or dynamic quantity, at the expense of very restricted  $N_{st}$ . In spite of that, it represents a very instructive approach but also remains essentially the only practical method when all exact levels are needed, e.g., for studies of level statistics.

Lanczos-based ED methods have already long history of applications since Cornelius Lanczos [1] proposed the diagonalization of sparse matrices using the iterative procedure, allowing for much bigger Hilbert spaces  $N_{st}$  relative to full ED. Lanczos diagonalization technique is at present a part of standard numerical linear algebra procedures [2, 3] and as such in solid state physics mainly used to obtain the g.s. energies and wavefunction with corresponding expectation values. The approach has been quite early on extended to calculation of the dynamical response functions within the g.s. [4]. The method has been in the last 20 years extensively used in connection with models related to high- $T_c$  materials, for which we can refer to an earlier overview [5].

The present review will focus on recent development of ED-based and Lanczos-based methods. The basics of the Lanczos method are presented in Sect. 1.2 and its application for g.s. properties in Sect. 1.3. One of already established generalizations is the finite-temperature Lanczos method (FTLM) [6, 7], reviewed in Sect. 1.4, which allows for the evaluation of  $T > 0$  static and dynamic properties within simplest models. Several extensions and modifications of the latter have been introduced more recently, in particular the low-temperature Lanczos method (LTLM) [8] and the microcanonical Lanczos method (MCLM) [9], particularly applicable within the high- $T$  regime.

Since the application of the ED methods there have been attempts and proposals for the proper choice of reduced basis which could allow for the study of bigger systems. While this is clearly very broad subject with most substantial

achievements in one-dimensional (1D) systems within the framework of the density-matrix renormalization-group (DMRG) idea, there are also successful applications in higher  $D > 1$  combined with the Lanczos procedure being reviewed in Sect. 1.5. Recently, there is also quite an intensive activity on studies of real-time evolution of correlated systems, both under the equilibrium and the non-equilibrium conditions that can be simulated using the ED and Lanczos-based methods, as discussed in Sect. 1.6.

## 1.2 Exact Diagonalization and Lanczos Method

### 1.2.1 Models, Geometries and System Sizes

ED-based methods are mostly restricted to simple models with only few local quantum states  $K$  per lattice site in order to reach reasonable system sizes  $N$ . Consequently, there are only few classes of MB models that so far exhaust the majority of ED and Lanczos-method studies, clearly also motivated and influenced by the challenging physics and relevance to novel materials and related experiments.

To get some feeling for available sizes reachable within the ED-based approaches, it should be reminded that in full ED routines the CPU time scales with the number of operations  $Op \propto N_{st}^3$ , while the memory requirement is related to the storage of the whole Hamiltonian matrix and all eigenvectors, i.e.,  $Mem \propto N_{st}^2$ . This limits at present stage of computer facilities the full ED method to  $N_{st} < 2 \cdot 10^4$  MB states. On the other hand, using the Lanczos-based iterative methods for the diagonalization of sparse matrices (Hamiltonians), CPU and memory requirements scale as  $Op, Mem \propto N_{st}$ , at least in their basic application, to calculate the g.s. and its wavefunction. In present-day applications this allows the consideration of much larger basis sets, i.e.,  $N_{st} < 10^9$ . Still, lattice sizes  $N$  reached using the Lanczos technique remain rather modest, compared to some other numerical approaches as the DMRG and quantum-Monte-Carlo (QMC) methods, if the full Hilbert basis space relevant for the model is used.

The simplest nontrivial class of MB lattice models are spin models, the prototype being the anisotropic Heisenberg model for coupled  $S = 1/2$  spins,

$$H = \sum_{\langle ij \rangle \alpha} J_{ij}^{\alpha\alpha} S_i^\alpha S_j^\alpha, \quad (1.1)$$

where the sum  $\langle ij \rangle$  runs over pairs of lattice sites with an arbitrary interaction  $J_{ij}^{\alpha\alpha}$  (being in principle anisotropic) and  $S_i^\alpha$  are component of local  $S = 1/2$  operator. The model has  $K = 2$  quantum states per lattice site and therefore allows for biggest  $N$  in the ED-based approaches where  $N_{st} \propto 2^N$  basis states. To reduce  $N_{st}$  as many symmetries and good quantum numbers as practically possible are used to decompose the Hamiltonian into separate blocks. Evident choice are sectors with

the ( $z$ -component of) total spin  $S_{tot}^z$  and the wavevector  $\mathbf{q}$  for systems with periodic boundary conditions, but further also rotational symmetries of particular lattices have been used. In this way system sizes up to  $N \sim 36$  (for largest and most interesting sector  $S_{tot}^z = 0$ ) have been reached so far using the Lanczos technique without any basis reduction.

On the basis of this simple model one can already discuss the feasibility of the Lanczos-based methods with respect to other numerical quantum MB methods. For the g.s. in 1D spin systems more powerful methods allowing for much bigger systems are DMRG and related approaches. For unfrustrated models in  $D > 1$  the QMC methods are superior for the evaluation of static quantities at any  $T$ . Still, Lanczos-based methods become competitive or at least not superseded for frustrated spin models (where QMC can run into minus-sign problem) or for dynamical properties at  $T > 0$ .

Next in complexity and very intensively studied prototype model is the  $t$ - $J$  model, representing strongly correlated itinerant electrons with an antiferromagnetic (AFM) interaction between their spins,

$$H = - \sum_{\langle ij \rangle s} (t_{ij} \tilde{c}_{js}^\dagger \tilde{c}_{is} + \text{H.c.}) + J \sum_{\langle ij \rangle} \mathbf{S}_i \cdot \mathbf{S}_j, \quad (1.2)$$

where due to the strong on-site repulsion doubly occupied sites are forbidden and one is dealing with projected fermion operators  $\tilde{c}_{is} = c_{is}(1 - n_{i,-s})$ . The model can be considered as a good microscopic model for superconducting cuprates which are doped Mott insulators and has been therefore one of the most studied using the Lanczos method [5]. For a theoretical and experimental overview of Mott insulators and metal-insulator transitions see Ref. [10].

It has  $K = 3$  quantum states per lattice site and besides  $S_{tot}^z$  and  $\mathbf{q}$ , also the number of electrons  $N_e$  (or more appropriate the number of holes  $N_h = N - N_e$ ) are the simplest quantum numbers to implement. Since the model reveals an interesting physics in  $D > 1$ , the effort was in connection with high- $T_c$  cuprates mostly on 2D square lattice. Here the alternative numerical methods have more drawbacks (e.g., minus sign problem in QMC methods due to the itinerant character of fermions) so Lanczos-based methods are still competitive, in particular for getting information on  $T > 0$  dynamics and transport. The largest systems considered with Lanczos method so far are 2D square lattice with  $N = 32$  sites and  $N_h = 4$  holes [11].

Clearly, one of the most investigated within the MB community is the standard single-band Hubbard model, which has  $K = 4$  states per lattice site. Due to the complexity  $N_{st} \propto 4^N$  the application of ED and Lanczos-based method is already quite restricted reaching so far  $N = 20$  sites [12] requiring already  $N_{st} \sim 10^9$  basis states. The model is also the subject of numerous studies using more powerful QMC method and various cluster dynamical-mean-field-theory (DMFT) methods for much larger lattices so Lanczos-based approaches have here more specific goals.

Since reachable lattices for above mentioned models are rather small it is important to choose properly their geometries. This is not the problem in 1D models, but becomes already essential for 2D lattices, analysed in connection with novel

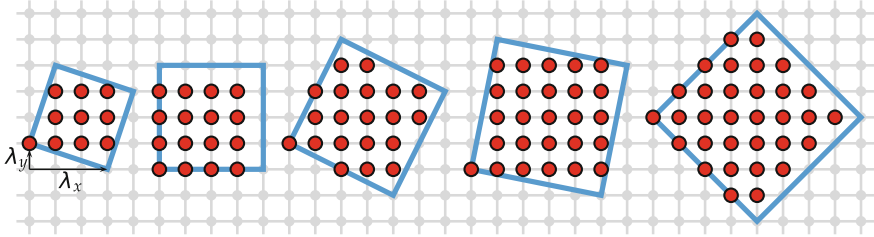


**Fig. 1.1** Tilted clusters used in 2D square-lattice studies

materials, in particular high- $T_c$  cuprates and related materials. In order to keep the periodic boundary conditions for 2D square lattice the choice of Pythagorean lattices with  $N = \lambda_x^2 + \lambda_y^2$  with  $\lambda_x, \lambda_y$  [13] has significantly extended available sizes. Some of frequently used are presented in Fig. 1.1. Taking into account only even  $N$  such lattices include  $N = 8, 10, 16, 18, 20, 26, 32, 36$  sites. While unit cells of such lattices are squares, it has been observed that they are not always optimal with respect to the number of next-nearest-neighbors and further nearest neighbors. It has been claimed and partly tested that better result are obtained with slightly deformed lattices (still with periodic boundary conditions) which at the same time offer an even bigger choice of sizes [14, 15].

### 1.2.2 Lanczos Diagonalization Technique

The Lanczos technique is a general procedure to transform and reduce a symmetric  $N_{st} \times N_{st}$  matrix  $A$  to a symmetric  $M \times M$  tridiagonal matrix  $T_M$ . From the chosen initial  $N_{st}$ -dimensional vector  $\mathbf{v}_1$  one generates an orthogonal basis of  $\{\mathbf{v}_1, \dots, \mathbf{v}_M\}$  vectors which span the Krylov space  $\{\mathbf{v}_1, \mathbf{A}\mathbf{v}_1, \dots, \mathbf{A}^{M-1}\mathbf{v}_1\}$  [1–3, 16].

In usual applications for the quantum MB system defined with the Hamiltonian operator  $H$  the Lanczos algorithm starts with a normalized vector  $|\phi_0\rangle$ , chosen as a random vector in the relevant Hilbert space with  $N_{st}$  basis states. The procedure generates orthogonal Lanczos vectors  $L_M = \{|\phi_m\rangle, m = 0 \dots M\}$  spanning the Krylov space  $\{|\phi_0\rangle, H|\phi_0\rangle, \dots, H^M|\phi_0\rangle\}$ . Steps are as follows:  $H$  is applied to  $|\phi_0\rangle$  and the resulting vector is split in components parallel to  $|\phi_0\rangle$ , and normalized  $|\phi_1\rangle$  orthogonal to it, respectively,

$$H|\phi_0\rangle = a_0|\phi_0\rangle + b_1|\phi_1\rangle. \quad (1.3)$$

Since  $H$  is Hermitian,  $a_0 = \langle\phi_0|H|\phi_0\rangle$  is real, while the phase of  $|\phi_1\rangle$  can be chosen so that  $b_1$  is also real. In the next step  $H$  is applied to  $|\phi_1\rangle$ ,

$$H|\phi_1\rangle = b'_1|\phi_0\rangle + a_1|\phi_1\rangle + b_2|\phi_2\rangle, \quad (1.4)$$

where  $|\phi_2\rangle$  is orthogonal to  $|\phi_0\rangle$  and  $|\phi_1\rangle$ . It follows also  $b'_1 = \langle\phi_0|H|\phi_1\rangle = b_1$ . Proceeding with the iteration one gets in  $i$  steps

$$H|\phi_i\rangle = b_i|\phi_{i-1}\rangle + a_i|\phi_i\rangle + b_{i+1}|\phi_{i+1}\rangle, \quad 1 \leq i \leq M, \quad (1.5)$$

where in Eq. (1.5) by construction there are no terms involving  $|\phi_{i-2}\rangle$  etc. By stopping the iteration at  $i = M$  and setting  $b_{M+1} = 0$ , the Hamiltonian can be represented in the basis of orthogonal Lanczos functions  $|\phi_i\rangle$  as the tridiagonal matrix  $H_M$  with diagonal elements  $a_i$ ,  $i = 0 \dots M$ , and off-diagonal ones  $b_i$ ,  $i = 1 \dots M$ . Such a matrix is easily diagonalized using standard numerical routines to obtain approximate eigenvalues  $\epsilon_j$  and corresponding orthonormal eigenvectors  $|\psi_j\rangle$ ,

$$|\psi_j\rangle = \sum_{i=0}^M v_{ji}|\phi_i\rangle, \quad j = 0 \dots M. \quad (1.6)$$

It is important to realize that  $|\psi_j\rangle$  are (in general) not exact eigenfunctions of  $H$ , but show a remainder. On the other hand, it is evident from the diagonalization of  $H_M$  that matrix elements

$$\langle\psi_i|H|\psi_j\rangle = \epsilon_j \delta_{ij}, \quad i, j = 0 \dots M, \quad (1.7)$$

are diagonal independently of  $L_M$  (but provided  $i, j \leq M$ ), although the values  $\epsilon_j$  can be only approximate.

If in the Eq. (1.5)  $b_{M+1} = 0$ , we have found a  $(M+1)$ -dimensional eigenspace where  $H_M$  is already an exact representation of  $H$ . This inevitably happens when  $M = N_{st} - 1$ , but for  $M < N_{st} - 1$  it can only occur if the starting vector is orthogonal to some invariant subspace of  $H$  which we avoid by choosing the input vector  $|\phi_0\rangle$  as a random one.

It should be recognized that the Lanczos approach is effective only for sparse Hamiltonians, characterized by the connectivity of each basis state with  $K_n \ll N_{st}$  basis states. All prototype discrete tight-binding models discussed in Sect. 1.2.1 are indeed of such a type in the local MB basis. Estimating the computation requirements, the number of operations  $Op$  needed to perform  $M$  Lanczos iterations scales as  $Op \propto K_n MN_{st}$ . The main restriction is still in memory requirements due to large  $N_{st}$ . A straightforward application of Eq. (1.5) would require the fast storage of all  $|\phi_i\rangle$ ,  $i = 0 \dots M$ , i.e., also the memory capacity  $Mem \propto MN_{st}$ . However, for the evaluation of the eigenvalues alone during the iteration, Eq. (1.5), only three  $|\phi_i\rangle$  are successively required, so this leads to  $Mem \propto 3N_{st}$ . If the Hamiltonian matrix is not evaluated on the fly (simultaneously), then also  $Mem \propto K_n N_{st}$  for the nonzero Hamilton matrix elements is needed.

The Lanczos diagonalization is in essence an iterative power method which is known to converge fast for the extreme lower and upper eigenvalues [2, 3], clearly in physical application most relevant is the search for the g.s. energy  $E_0$  and corresponding wavefunction  $|\Psi_0\rangle$ . Typically,  $M > 50$  are enough to reach very high

accuracy for both. It is evident that for such modest  $M \ll N_{st}$  one cannot expect any reliable results for eigenstates beyond the few at the bottom and the top of the spectrum. On the other hand, the Lanczos procedure is subject to roundoff errors, introduced by the finite-precision arithmetics which usually only becomes severe at larger  $M > 100$  after the convergence of extreme eigenvalues and is seen as the loss of the orthogonality of vectors  $|\phi_i\rangle$ . It can be remedied by successive reorthogonalization [2, 3, 16] of new states  $|\phi'_i\rangle$ , plagued with errors, with respect to previous ones. However this procedure requires  $Op \sim M^2 N_{st}$  operations, and can become computationally more demanding than Lanczos iterations themselves. This effect also prevents one to use the Lanczos method, e.g., to efficiently tridiagonalize full large matrices [3].

### 1.3 Ground State Properties and Dynamics

After  $|\Psi_0\rangle$  is obtained, the g.s. static properties can be evaluated in principle for any operator  $A$  as

$$\bar{A}_0 = \langle \Psi_0 | A | \Psi_0 \rangle. \quad (1.8)$$

Clearly, the procedure (1.8) for large basis is effective only if operator  $A$  is in the same basis also sparse, as it is in most cases of interest.

It is, however, the advantage of the Lanczos procedure that also g.s. dynamical functions can be calculated within the same framework [4]. Let us consider the dynamical (autocorrelation) response function

$$C(\omega) = \langle \Psi_0 | A^\dagger \frac{1}{\omega^+ + E_0 - H} A | \Psi_0 \rangle, \quad (1.9)$$

for the observable given by the operator  $A$  where  $\omega^+ = \omega + i\epsilon$ ,  $\epsilon > 0$ . To calculate  $C(\omega)$  one has to run the second Lanczos procedure with a new initial function  $|\tilde{\phi}_0\rangle$ ,

$$|\tilde{\phi}_0\rangle = \frac{1}{\alpha} A |\Psi_0\rangle, \quad \alpha = \sqrt{\langle \Psi_0 | A^\dagger A | \Psi_0 \rangle}. \quad (1.10)$$

Starting with  $|\tilde{\phi}_0\rangle$  one generates another Lanczos subspace  $\tilde{L}_{\tilde{M}} = \{|\tilde{\phi}_j\rangle, j = 0, \tilde{M}\}$  with (approximate) eigenvectors  $|\tilde{\psi}_j\rangle$  and eigenenergies  $\tilde{\epsilon}_j$ . The matrix for  $H$  in the new basis is again a tridiagonal one with  $\tilde{a}_j$  and  $\tilde{b}_j$  elements, respectively. Terminating the Lanczos procedure at given  $\tilde{M}$ , one can evaluate Eq.(1.9) as a resolvent of the  $H_{\tilde{M}}$  matrix expressed in the continued-fraction form [4, 5, 17],

$$C(\omega) = \frac{\alpha^2}{\omega^+ + E_0 - \tilde{a}_0 - \frac{\tilde{b}_1^2}{\omega^+ + E_0 - \tilde{a}_1 - \frac{\tilde{b}_2^2}{\omega^+ + E_0 - \tilde{a}_2 - \dots}}}, \quad (1.11)$$

terminating with  $\tilde{b}_{\tilde{M}+1} = 0$ , although other termination functions can also be employed and well justified.

We note that frequency moments of the spectral function

$$\begin{aligned} \mu_l &= -\frac{1}{\pi} \int_{-\infty}^{\infty} \omega^l \text{Im}C(\omega) d\omega = \langle \Psi_0 | A^\dagger (H - E_0)^l A | \Psi_0 \rangle \\ &= \alpha^2 \langle \tilde{\phi}_0 | (H - E_0)^l | \tilde{\phi}_0 \rangle, \end{aligned} \quad (1.12)$$

are exact for given  $|\Psi_0\rangle$  provided  $l \leq \tilde{M}$ , since the operator  $H^l, l < \tilde{M}$ , is exactly reproduced within the Lanczos (or corresponding Krylow) space  $\tilde{L}_{\tilde{M}}$ .

Finally,  $C(\omega)$  (1.11) can be presented as a sum of  $j = 0, \tilde{M}$  poles at  $\omega = \tilde{\epsilon}_j - E_0$  with corresponding weights  $w_j$ . As a practical matter we note that in analogy to Eq.(1.6)

$$w_j = |\langle \tilde{\psi}_j | A | \Psi_0 \rangle|^2 = \alpha^2 |\langle \tilde{\psi}_j | \tilde{\phi}_0 \rangle|^2 = \alpha^2 \tilde{v}_{j0}^2, \quad (1.13)$$

hence no matrix elements need to be evaluated within this approach. In contrast to the autocorrelation function (1.11), the procedure allows also the treatment of general correlation functions  $C_{AB}(\omega)$ , with  $B \neq A^\dagger$ . In this case matrix elements  $\langle \Psi_0 | B | \tilde{\psi}_j \rangle$  have to be evaluated explicitly. It should be also mentioned that at least lowest poles of  $C(\omega)$ , Eq.(1.11), should coincide with eigenenergies  $\omega = E_i - E_0$  if  $|\tilde{\phi}_0\rangle$  is not orthogonal to  $|\Psi_0\rangle$ . However, using  $\tilde{M} > 50$  spurious poles can emerge (if no reorthogonalization is used) which, however, carry no weight as also evident from exact moments (1.12).

In this chapter we do not intend to present an overview of applications of the full ED and Lanczos-type studies of g.s. static and dynamical properties of correlated systems. Such investigations have been numerous even before the high- $T_c$  era but intensified strongly with studies of prototype models relevant for high- $T$  cuprates [5] and other novel materials with correlated electrons. Although variety of models have been investigated they are still quite restricted in the number of local degrees and sizes.

## 1.4 Static Properties and Dynamics at $T > 0$

Before describing the Finite temperature Lanczos method (FTLM) we should note that the Lanczos basis is very useful and natural basis to evaluate the matrix elements of the type

$$W_{kl} = \langle n | H^k B H^l A | n \rangle, \quad (1.14)$$

where  $|n\rangle$  is an arbitrary normalized vector, and  $A, B$  are general operators. One can calculate this expression exactly by performing two Lanczos procedures with  $M = \max(k, l)$  steps. The first one, starting with the vector  $|\phi_0\rangle = |n\rangle$ , produces the Lanczos basis  $L_M$  along with approximate eigenstates  $|\psi_j\rangle$  and  $\epsilon_j$ . The second Lanczos procedure is started with the normalized vector  $|\tilde{\phi}_0\rangle \propto A|\phi_0\rangle = A|n\rangle$ , Eq.(1.10), and generates  $\tilde{L}_M$  with corresponding  $|\tilde{\psi}_j\rangle$  and  $\tilde{\epsilon}_j$ . We can now define projectors onto limited subspaces

$$P_M = \sum_{i=0}^M |\psi_i\rangle\langle\psi_i|, \quad \tilde{P}_M = \sum_{i=0}^M |\tilde{\psi}_i\rangle\langle\tilde{\psi}_i|. \quad (1.15)$$

Provided that  $(l, k) < M$  projectors  $P_M$  and  $\tilde{P}_M$  span the whole relevant basis for the operators  $H^k$  and  $H^l$ , respectively, so that one can rewrite  $W_{kl}$  in Eq.(1.14) as

$$W_{kl} = \langle \phi_0 | P_M H P_M H \dots H P_M B \tilde{P}_M H \dots \tilde{P}_M H \tilde{P}_M A | \phi_0 \rangle. \quad (1.16)$$

Since  $H$  is diagonal in the basis  $|\psi_j\rangle$  and  $|\tilde{\psi}_j\rangle$ , respectively, one can write finally

$$W_{kl} = \sum_{i=0}^M \sum_{j=0}^M \langle \phi_0 | \psi_i \rangle \langle \psi_i | B | \tilde{\psi}_j \rangle \langle \tilde{\psi}_j | A | \phi_0 \rangle (\epsilon_i)^k (\tilde{\epsilon}_j)^l. \quad (1.17)$$

It is important to note that matrix element expression (1.17) is exact, independent of how (in)accurate representation  $|\psi_i\rangle, \epsilon_i$  and  $|\tilde{\psi}_j\rangle, \tilde{\epsilon}_j$ , respectively, are to true system eigenvalues. The only condition remains that number of Lanczos steps is sufficient, i.e.,  $M > (l, k)$ .

#### 1.4.1 Finite Temperature Lanczos Method: Static Quantities

A straightforward calculation of canonical thermodynamic average of an operator  $A$  at  $T > 0$  (in a finite system) requires the knowledge of all eigenstates  $|\Psi_n\rangle$  and corresponding energies  $E_n$ , obtained, e.g., by the full ED of  $H$ ,

$$\langle A \rangle = \sum_{n=1}^{N_{st}} e^{-\beta E_n} \langle \Psi_n | A | \Psi_n \rangle \Big/ \sum_{n=1}^{N_{st}} e^{-\beta E_n}, \quad (1.18)$$

where  $\beta = 1/k_B T$ . Such direct evaluation is both CPU time and storage demanding for larger systems and is at present accessible only for  $N_{st} \sim 20000$ .

In a general orthonormal basis  $|n\rangle$  for finite system with  $N_{st}$  basis states one can express the canonical expectation value  $\langle A \rangle$  as

$$\langle A \rangle = \sum_{n=1}^{N_{st}} \langle n | e^{-\beta H} A | n \rangle \Bigg/ \sum_{n=1}^{N_{st}} \langle n | e^{-\beta H} | n \rangle, \quad (1.19)$$

The FTLM for  $T > 0$  is based on the evaluation of the expectation value in Eq. (1.19) for each starting  $|n\rangle$  using the Lanczos basis. We note that such a procedure guarantees correct high- $T$  expansion series (for given finite system) to high order. Let us perform the high- $T$  expansion of Eq. (1.19),

$$\begin{aligned} \langle A \rangle &= Z^{-1} \sum_{n=1}^{N_{st}} \sum_{k=0}^{\infty} \frac{(-\beta)^k}{k!} \langle n | H^k A | n \rangle, \\ Z &= \sum_{n=1}^{N_{st}} \sum_{k=0}^{\infty} \frac{(-\beta)^k}{k!} \langle n | H^k | n \rangle. \end{aligned} \quad (1.20)$$

Terms in the expansion  $\langle n | H^k A | n \rangle$  can be calculated exactly using the Lanczos procedure with  $M \geq k$  steps (with  $|\phi_0^n\rangle = |n\rangle$  as the starting function) since this is a special case of the expression (1.14). Using relation (1.17) with  $l = 0$  and  $B = 1$ , we get

$$\langle n | H^k A | n \rangle = \sum_{i=0}^M \langle n | \psi_i^n \rangle \langle \psi_i^n | A | n \rangle (\epsilon_i^n)^k. \quad (1.21)$$

Working in a restricted basis  $k \leq M$ , we can insert the expression (1.21) into sums (1.20), extending them to  $k > M$ . The final result can be expressed as

$$\begin{aligned} \langle A \rangle &= Z^{-1} \sum_{n=1}^{N_{st}} \sum_{i=0}^M e^{-\beta \epsilon_i^n} \langle n | \psi_i^n \rangle \langle \psi_i^n | A | n \rangle, \\ Z &= \sum_{n=1}^{N_{st}} \sum_{i=0}^M e^{-\beta \epsilon_i^n} \langle n | \psi_i^n \rangle \langle \psi_i^n | n \rangle, \end{aligned} \quad (1.22)$$

and the error of the approximation is  $O(\beta^{M+1})$ .

Evidently, within a finite system Eq. (1.22), expanded as a series in  $\beta$ , reproduces exactly the high- $T$  series to the order  $M$ . In addition, in contrast to the usual high- $T$  expansion, Eq. (1.22) remains accurate also for  $T \rightarrow 0$ . Let us assume for simplicity that the g.s.  $|\Psi_0\rangle$  is nondegenerate. For initial states  $|n\rangle$  not orthogonal to  $|\Psi_0\rangle$ , already at modest  $M \sim 50$  the lowest eigenstate  $|\psi_0^n\rangle$  converges to  $|\Psi_0\rangle$ . We thus have for  $\beta \rightarrow \infty$ ,

$$\langle A \rangle = \sum_{n=1}^{N_{st}} \langle n | \Psi_0 \rangle \langle \Psi_0 | A | n \rangle \Big/ \sum_{n=1}^{N_{st}} \langle n | \Psi_0 \rangle \langle \Psi_0 | n \rangle = \langle \Psi_0 | A | \Psi_0 \rangle / \langle \Psi_0 | \Psi_0 \rangle, \quad (1.23)$$

where we have taken into account the completeness of the set  $|n\rangle$ . Obtained result is just the usual g.s. expectation value of an operator.

The computation of static quantities (1.22) still involves the summation over the complete set of  $N_{st}$  states  $|n\rangle$ , which is clearly not feasible in practice. To obtain a useful method, a further essential approximation replaces the full summation over  $|n\rangle$  by a partial one over a much smaller set of random states [18, 19]. Such an approximation is analogous to Monte Carlo methods and leads to a statistical error which can be well estimated and is generally quite small. Let us first consider only the expectation value (1.19) with respect to a single random state  $|r\rangle$ , which is a linear combination of basis states

$$|r\rangle = \sum_{n=1}^{N_{st}} \eta_{rn} |n\rangle, \quad (1.24)$$

where  $\eta_{rn}$  are assumed to be distributed randomly. Then the random quantity can be expressed as

$$\begin{aligned} \tilde{A}_r &= \langle r | e^{-\beta H} A | r \rangle / \langle r | e^{-\beta H} | r \rangle \\ &= \sum_{n,m=1}^{N_{st}} \eta_{rn}^* \eta_{rm} \langle n | e^{-\beta H} A | m \rangle \Big/ \sum_{n,m=1}^{N_{st}} \eta_{rn}^* \eta_{rm} \langle n | e^{-\beta H} | m \rangle. \end{aligned} \quad (1.25)$$

Assuming that due to the random sign (phase) offdiagonal terms with  $\eta_{rn}^* \eta_{rm}$ ,  $m \neq n$  on average cancel for large  $N_{st}$ , we remain with

$$\bar{A}_r = \sum_{n=1}^{N_{st}} |\eta_{rn}|^2 \langle n | e^{-\beta H} A | n \rangle \Big/ \sum_{n=1}^{N_{st}} |\eta_{rn}|^2 \langle n | e^{-\beta H} | n \rangle. \quad (1.26)$$

We can express  $|\eta_{rn}|^2 = 1/N_{st} + \delta_{rn}$ . Random deviations  $\delta_{rn}$  should not be correlated with matrix elements  $\langle n | e^{-\beta H} | n \rangle = Z_n$  and  $\langle n | e^{-\beta H} A | n \rangle = Z_n A_n$ , therefore  $\bar{A}_r$  is close to  $\langle A \rangle$  with a statistical error related to the effective number of terms  $\bar{Z}$  in the thermodynamic sum, i.e.

$$\bar{A}_r = \langle A \rangle (1 + \mathcal{O}(1/\sqrt{\bar{Z}})), \quad (1.27)$$

$$\bar{Z} = e^{\beta E_0} \sum_n Z_n = \sum_{n=1}^{N_{st}} \langle n | e^{-\beta(H-E_0)} | n \rangle. \quad (1.28)$$

Note that for  $T \rightarrow \infty$  we have  $\bar{Z} \rightarrow N_{st}$  and therefore at large  $N_{st}$  very accurate average (1.28) can be obtained even from a single random state [18, 19]. On the other hand, at finite  $T < \infty$  the statistical error of  $\tilde{A}_r$  increases with decreasing  $\bar{Z}$ .

To reduce statistical error, in particular at modest  $T > 0$ , within the FTLM we sum in addition over  $R$  different randomly chosen  $|r\rangle$ , so that in the final application Eq.(1.22) leads to

$$\begin{aligned}\langle A \rangle &= \frac{N_{st}}{ZR} \sum_{r=1}^R \sum_{j=0}^M e^{-\beta\epsilon_j^r} \langle r | \psi_j^r \rangle \langle \psi_j^r | A | r \rangle, \\ Z &= \frac{N_{st}}{R} \sum_{r=1}^R \sum_{j=0}^M e^{-\beta\epsilon_j^r} |\langle r | \psi_j^r \rangle|^2.\end{aligned}\quad (1.29)$$

Random states  $|r\rangle = |\phi_0^r\rangle$  serve as initial functions for the Lanczos iteration, resulting in  $M$  eigenvalues  $\epsilon_j^r$  with corresponding  $|\psi_j^r\rangle$ . The relative statistical error is reduced by sampling (both for  $\langle A \rangle$  and  $Z$ ) and behaves as

$$\delta\langle A \rangle / \langle A \rangle = \mathcal{O}(1/\sqrt{R\bar{Z}}).\quad (1.30)$$

For general operator  $A$  the calculation of  $|\psi_j^r\rangle$  and corresponding matrix elements  $\langle \psi_j^r | A | r \rangle$  is needed. On the other hand, the calculation effort is significantly reduced if  $A$  is conserved quantity, i.e.,  $[H, A] = 0$ , and can be diagonalized simultaneously with  $H$ . Then

$$\langle A \rangle = \frac{N_{st}}{ZR} \sum_{r=1}^R \sum_{j=0}^M e^{-\beta\epsilon_j^r} |\langle r | \psi_j^r \rangle|^2 A_j^r.\quad (1.31)$$

In this case the evaluation of eigenfunctions is not necessary since the element  $\langle r | \psi_j^r \rangle = v_{j0}^r$ , Eq.(1.6), is obtained directly from eigenvectors of the tridiagonal matrix  $H_M^r$ . There are several quantities of interest which can be evaluated in this way, in particular the thermodynamic properties as internal energy, specific heat, entropy, as well as uniform susceptibility etc. [7, 20].

Taking into account all mentioned assumptions, the approximation  $\langle A \rangle$  (1.29) yields a good estimate of the thermodynamic average at all  $T$ . For low  $T$  the error is expected to be of the order of  $\mathcal{O}(1/\sqrt{R})$ , while for high  $T$  the error is expected to scale even as  $\mathcal{O}(1/\sqrt{N_{st}R})$ . Since arguments leading to these estimates are not always easy to verify, it is essential to test the method for particular cases.

#### 1.4.2 Finite Temperature Lanczos Method: Dynamical Response

The essential advantage of the FTLM with respect to other methods is nevertheless in the calculation of dynamical quantities. Let us consider the dynamical susceptibility

as given by the autocorrelation function  $C(\omega)$  (procedure for the general correlation function  $C_{AB}(\omega)$  is given in Ref. [7]),

$$\chi''(\omega) = \pi(1 - e^{-\beta\omega})\tilde{C}(\omega), \quad \tilde{C}(\omega) = \frac{1}{\pi}\text{Re} \int_0^{+\infty} dt e^{i\omega t} C(t), \quad (1.32)$$

with

$$C(t) = \langle A^\dagger(t)A(0) \rangle = \frac{1}{Z} \sum_n \langle n | e^{(-\beta+it)H} A^\dagger e^{-iHt} A | n \rangle. \quad (1.33)$$

Expanding the exponentials in analogy to static quantities, Eq.(1.20), we get

$$C(t) = Z^{-1} \sum_{n=1}^{N_{st}} \sum_{k,l=0}^{\infty} \frac{(-\beta + it)^k}{k!} \frac{(-it)^l}{l!} \langle n | H^k A^\dagger H^l A | n \rangle. \quad (1.34)$$

Expansion coefficients in Eq.(1.34) can be again obtained via the Lanczos method, as discussed in Sect. 1.4.1. Performing two Lanczos iterations with  $M$  steps, started with normalized  $|\phi_0^n\rangle = |n\rangle$  and  $|\tilde{\phi}_0^n\rangle \propto A|n\rangle$ , respectively, we calculate coefficients  $W_{kl}$  following the Eq.(1.17). We again note that (within the full basis  $|n\rangle$ ) the series are via  $W_{kl}$  exactly evaluated within the Lanczos basis up to order  $l, k \leq M$ . The latter yields through Eq.(1.34) a combination of  $(\beta, t)$  expansion, i.e. a combination of high- $T$ , short- $t$  (in frequency high- $\omega$ ) expansion to very high order. Extending and resuming series in  $k$  and  $l$  into exponentials, we get in analogy with Eq.(1.20)

$$C(t) = Z^{-1} \sum_{n=1}^{N_{st}} \sum_{i,j=0}^M e^{-\beta\epsilon_i^n} e^{it(\epsilon_i^n - \tilde{\epsilon}_j^n)} \langle n | \psi_i^n \rangle \langle \psi_i^n | A^\dagger | \tilde{\psi}_j^n \rangle \langle \tilde{\psi}_j^n | A | n \rangle, \quad (1.35)$$

Finally replacing the full summation with the random sampling the FTLM recipe for the correlation function is

$$\tilde{C}(\omega) = \frac{N_{st}}{ZR} \sum_{r=1}^R \sum_{i,j=0}^M e^{-\beta\epsilon_i^r} \langle r | \psi_i^r \rangle \langle \psi_i^r | A^\dagger | \tilde{\psi}_j^r \rangle \langle \tilde{\psi}_j^r | A | r \rangle \delta(\omega - \tilde{\epsilon}_{j^r} + \epsilon_i^r). \quad (1.36)$$

We check the nontrivial  $T = 0$  limit of above expression. If  $|r\rangle$  are not orthogonal to the g.s.  $|\Psi_0\rangle$ , then for large enough  $M$  the lowest-lying state converges to  $\epsilon_0^r \sim E_0$  and  $|\psi_0^r\rangle \sim |\Psi_0\rangle$ , respectively. In this case we have

$$\tilde{C}(\omega, T = 0) \approx \frac{N_{st}}{R} \sum_{r=1}^R \sum_{j=0}^M \langle \Psi_0 | A^\dagger | \tilde{\psi}_j^r \rangle \langle \tilde{\psi}_j^r | A | r \rangle \langle r | \Psi_0 \rangle \delta(\omega + E_0 - \tilde{\epsilon}_j^r) \quad (1.37)$$

At  $T \sim 0$  one needs in general  $M \sim 100$  in order that low-lying states relevant to Eq.(1.37) approach  $|\tilde{\psi}_j^r\rangle \rightarrow |\Psi_j\rangle$  and  $\tilde{\epsilon}_j^r \rightarrow E_j$ . Also a considerable sampling

$R > 1$  is required to get correct also amplitudes of separate peaks in the spectrum of Eq.(1.37) which are a subject of a statistical error due to the incomplete projection on different random  $|r\rangle$  in  $\langle\tilde{\psi}_j^r|A|r\rangle\langle r|\Psi_0\rangle$ . Similar statistical error can in fact appear also for static quantities in Eq.(1.29).

### 1.4.3 Finite Temperature Lanczos Method: Implementation

Most straightforward is the implementation of the FTLM for static quantities, Eq.(1.29). In particular for conserved quantities, Eq.(1.31), the computation load is essentially that of the g.s. Lanczos iteration repeated  $R$  times and only a minor changes are needed within the usual g.s. Lanczos code.

On the other hand, for the dynamical correlation function (1.36) the memory requirement as well as the CPU time is dominated mostly by the evaluation of the matrix element  $\langle\psi_i^r|A^\dagger|\tilde{\psi}_j^r\rangle$  where the operations scale as  $Op \propto RM^2N_{st}$  and memory as  $Mem \propto MN_{st}$ . This effectively limits the application of the FTLM to  $50 < M < 500$  where the lower bound is determined by the convergence of the g.s.  $|\Psi_0\rangle$ . Still, it should be noted that the calculation can be done simultaneously (without any additional cost) for all desired  $T$ , since matrix elements are evaluated only once. Evidently, one should use as much as possible symmetries of the Hamiltonian, e.g.,  $N_e$ ,  $S_{tot}^z$ ,  $\mathbf{q}$  to reduce effective  $N_{st}$  by splitting the sampling over different symmetry sectors.

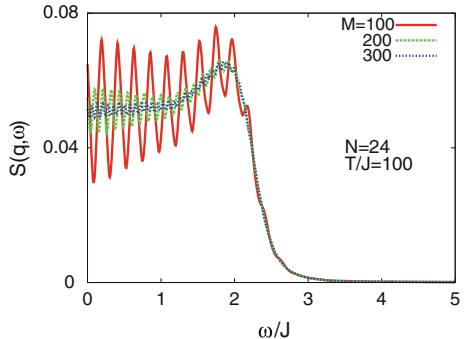
The effect of finite  $M$  is less evident. Since  $M \sim 100$  is enough to converge well few lowest levels, it is also generally satisfactory for reliable dynamical correlation functions at low  $T$ . At high  $T$ , however, one can observe very regular oscillations which are the artifact of the Lanczos iterations with  $M \ll N_{st}$ . Namely, the procedure generates between extreme eigenvalues quite equidistant spectrum of quasi-states with the level spacing  $\Delta\epsilon \sim \Delta E/M$ , where  $\Delta E$  is the full energy span of MB eigenstates. The effect is well visible in Fig. 1.2 where the high- $T$  result for the spin structure factor  $S(q = \pi, \omega)$  for the 1D Heisenberg model, Eq.(1.1), is presented for various  $M$ . It is evident that for the presented case ( $N = 24$  and  $\Delta E \sim 16J$ )  $M > 200$  is sufficient to obtain smooth spectra even for high  $T \gg J$ . However, larger  $M$  are advisable if sharper structures persist at high  $T$ .

The role of random sampling  $R$  is less important for intermediate and high  $T$  since the relative error is largely determined via  $\bar{Z}$  as evident from Eq.(1.28). Larger  $R \gg 1$  is necessary only for the correct limit  $T \rightarrow 0$  (for given system size) and for off-diagonal operators  $A$ .

One can claim that the FTLM in general obtains for all reachable systems results which are at any  $T$  very close to exact (full ED) results for the same finite (given  $N$ ) system and the accuracy can be improved by increasing  $M$  and  $R$ . Still, it remains nontrivial but crucial to understand and have in control finite size effects.

At  $T = 0$  both static and dynamical quantities are calculated from the g.s.  $|\Psi_0\rangle$ , which can be quite dependent on the size and on the shape of the system. At least in 1D for static quantities the finite-size scaling  $N \rightarrow \infty$  can be performed in a

**Fig. 1.2** High- $T$  spin structure factor  $S(q = \pi, \omega)$  for the 1D Heisenberg model, as calculated with different number of Lanczos steps  $M$



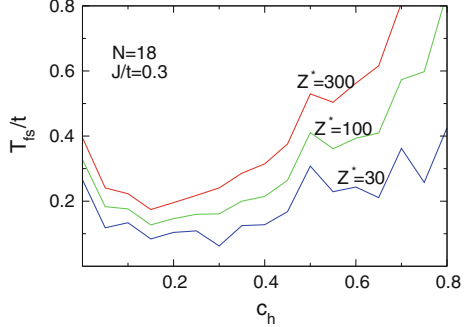
controlled way, although in this case more powerful methods as, e.g., the DMRG are mostly available. In higher dimensional lattices, e.g., in 2D systems finite-size scaling is practically impossible due to very restricted choice of small sizes and different shapes. Also g.s. ( $T = 0$ ) dynamical quantities are often dominated by few (typically  $N_p < M$ ) peaks which are finite-size dependent [5]. On the other hand,  $T > 0$  generally introduces the thermodynamic averaging over a large number of eigenstates. This directly reduces finite-size effects for static quantities, whereas for dynamical quantities spectra become denser. From Eq.(1.36) it follows that we get in spectra at elevated  $T > 0$  typically  $N_p \propto RM^2$  different peaks resulting in nearly continuous spectra. This is also evident from the example of a high- $T$  result in Fig. 1.2.

It is plausible that finite-size effects at  $T > 0$  become weaker. However, it should be recognized that there could exist several characteristic length scales in the considered physical (and model) system, e.g. the antiferromagnetic (AFM) correlation length  $\xi$ , the transport mean free path  $l_s$  etc. These lengths generally decrease with increasing  $T$  and results for related quantities get a macroscopic relevance provided that  $\xi(T), l_s(T) < L$  where  $L \propto N^{1/D}$  is the linear size of the system. However, there exist also anomalous cases, e.g., in an integrable system  $l_s$  can remain infinite even at  $T \rightarrow \infty$  [21, 22].

A simple criterion for finite size effects one can use the normalized thermodynamic sum  $\bar{Z}(T)$ , Eq. (1.28), which provides the effective number of MB states contributing at chosen  $T$  (note that for a system with a nondegenerate g.s.  $\bar{Z}(T = 0) = 1$ ). Finite-size temperature  $T_{fs}$  can be thus defined with the relation  $\bar{Z}(T_{fs}) = Z^*$  where in practice the range  $10 < Z^* < 50$  is reasonable. Clearly, the FTLM is best suited just for systems with a large density of low lying MB states, i.e., for large  $\bar{Z}$  at low  $T$ .

Since  $\bar{Z}(T)$  is directly related to the entropy density  $s$  and the specific heat  $C_v$  of the system, large  $\bar{Z}$  at low  $T$  is the signature of frustrated quantum MB systems which are generally difficult to cope with other methods (e.g., the QMC method). Such are typically examples of strongly correlated electrons with an inherent frustration, e.g., the doped AFM and the  $t$ - $J$  model, Eq. (1.2), in the strong correlation regime  $J < t$ . We present in Fig. 1.3 as an example the variation of  $T_{fs}$  in the 2D  $t$ - $J$  model with

**Fig. 1.3** Finite-size temperature  $T_{fs}$  versus hole doping  $c_h$  in the 2D  $t$ - $J$  model with  $J/t = 0.3$ , as calculated with the FTLM in system of  $N = 18$  sites [7]



the hole doping  $c_h = N_h/N$ , as calculated for different  $Z^* = 30 - 300$  for the fixed system of  $N = 18$  sites and  $J/t = 0.3$  as relevant for high- $T$  cuprates. It is indicative that  $T_{fs}$  reaches the minimum for intermediate (optimum) doping  $c_h = c_h^* \sim 0.15$ , where we are able to reach  $T_{fs}/t \sim 0.1$ . Away from the optimum doping  $T_{fs}$  is larger, i.e., low-energy spectra are quite sparse both for undoped AFM and even more for effectively noninteracting electrons far away from half-filling (for nearly empty or full band).

#### 1.4.4 Low Temperature Lanczos Method

The standard FTLM suffers at  $T \rightarrow 0$  from a statistical error due to finite sampling  $R$ , both for the static quantities, Eqs. (1.29) and (1.30), as well as for the dynamical correlations, Eqs. (1.36), and (1.37). The discrepancy can be easily monitored by the direct comparison with the g.s. Lanczos method, Eqs. (1.8, 1.11). To avoid this problem, a variation of the FTLM method, named Low-temperature Lanczos method (LTLM) has been proposed [8] which obtains correct g.s. result (for finite systems) independent of the sampling  $R$ .

The idea of LTLM is to rewrite Eq. (1.19) in a symmetric form

$$\langle A \rangle = \frac{1}{Z} \sum_{n=1}^{N_{st}} \langle n | e^{-\beta H/2} A e^{-\beta H/2} | n \rangle, \quad (1.38)$$

and insert the Lanczos basis in analogy with the FTLM, Eq. (1.19), now represented with a double sum

$$\langle A \rangle = \frac{N_{st}}{ZR} \sum_{r=1}^R \sum_{j,l=0}^M e^{-\beta(\epsilon_j^r + \epsilon_l^r)/2} \langle r | \psi_j^r \rangle \langle \psi_j^r | A | \psi_l^r \rangle \langle \psi_l^r | r \rangle, \quad (1.39)$$

The advantage of the latter form is that it satisfies the correct  $T = 0$  limit provided that the g.s. is well converged, i.e.,  $|\psi_0^r\rangle \sim |\Psi_0\rangle$ . It then follows from Eq.(1.39),

$$\langle A \rangle = \sum_{r=1}^R \langle r | \Psi_0 \rangle \langle \Psi_0 | A | \Psi_0 \rangle \langle \Psi_0 | r \rangle / \sum_{r=1}^R \langle \Psi_0 | r \rangle \langle r | \Psi_0 \rangle = \langle \Psi_0 | A | \Psi_0 \rangle, \quad (1.40)$$

for any chosen set of  $|r\rangle$ . For the dynamical correlations  $C(t)$  one can in straightforward way derive the corresponding expression in the Lanczos basis

$$\begin{aligned} \tilde{C}(\omega) &= \frac{N_{st}}{ZR} \sum_{r=1}^R \sum_{i,j,l=0}^M e^{-\beta(\epsilon_i^r + \epsilon_l^r)/2} \langle r | \psi_i^r \rangle \langle \psi_i^r | A^\dagger | \tilde{\psi}_j^{rl} \rangle \langle \tilde{\psi}_j^{rl} | A | \psi_l^r \rangle \langle \psi_l^r | r \rangle \\ &\times \delta(\omega - \tilde{\epsilon}_j^{rl} + \frac{1}{2}(\epsilon_i^r + \epsilon_l^r)). \end{aligned} \quad (1.41)$$

It is again evident that for  $T \rightarrow 0$  the sampling does not influence results being correct even for  $R = 1$  if the g.s.  $|\Psi_0\rangle$  is well converged for all starting  $|r\rangle$ . The payoff is in an additional summation over the new Lanczos basis sets  $|\tilde{\psi}_j^{rl}\rangle$  which need to be started from each  $A|\psi_l^r\rangle$  in Eq.(1.41) separately. Since the LTLM is designed for lower  $T$  there one can effectively restrict summations in  $(i, l)$  in Eq.(1.41) to much smaller  $M' \ll M$  where only lowest states with  $\epsilon_i^r, \epsilon_l^r \sim E_0$  contribute [8], and in addition use smaller  $M_1 \ll M$  for the basis  $|\tilde{\psi}_j^{rl}\rangle$ .

An alternative version for Lanczos-type approach [23] for dynamical quantities is not to start the second Lanczos run from  $A|r\rangle$  [7] or from  $A|\psi_l^r\rangle$  [8], but from

$$|\widetilde{Ar}\rangle = \sum_{l=0}^M A|\psi_l^r\rangle e^{-\beta\epsilon_l^r/2} \langle \psi_l^r | r \rangle. \quad (1.42)$$

In this way one obtains with the second Lanczos run the Lanczos eigenstates  $|\tilde{\psi}_k^r\rangle$ , which cover the relevant Hilbert space for starting random vector  $|r\rangle$  and the inverse temperature  $\beta$ . The resulting dynamical autocorrelation function is

$$\begin{aligned} \tilde{C}(\omega) &= \frac{N_{st}}{RZ} \sum_{r=1}^R \sum_{i,k=0}^M e^{-\beta\epsilon_i^r/2} \langle r | \psi_i^r \rangle \langle \psi_i^r | A^\dagger | \tilde{\psi}_k^r \rangle \langle \tilde{\psi}_k^r | \widetilde{Ar} \rangle \\ &\times \delta(\omega - \tilde{\epsilon}_k^r + \epsilon_i^r). \end{aligned} \quad (1.43)$$

In this way the sufficiency of only one random vector in the  $T = 0$  limit is reproduced, while at  $T > 0$  the algorithm has the same time efficiency as the FTLM, but with much smaller random sampling needed to reach the same accuracy (at least for low  $T$ ). However, the price paid is that results for each  $T$  need to be calculated separately, while within the FTLM all  $T$  (or  $T$  up to certain value within the LTLM) are evaluated simultaneously.

### 1.4.5 Microcanonical Lanczos Method

While most investigations in strongly correlated systems focus on the low- $T$  regime, there are systems where dynamical properties are nontrivial even at high  $T$ . Well known such case is the spin diffusion constant  $D_s(T)$  in the isotropic Heisenberg model, Eq. (1.1), which is not known by value and moreover not even its existence at any  $T > 0$ . Similar although somewhat less controversial is the case of transport quantities, both for integrable or generic nonintegrable models. Whereas the FTLM seems well adapted for studies of transport response functions, oscillations due to limited  $M$  can affect the crucial low- $\omega$  resolution as seen also in Fig. 1.2.

At elevated  $T$  it is therefore an advantage to use the Microcanonical Lanczos method (MCLM) [9], employing the fact from statistical physics that in the thermodynamic limit (for large system) the microcanonical ensemble should yield the same results as the canonical one. The shortcoming of the MCLM emerges since in finite systems statistical fluctuations are much larger within the microcanonical ensemble. Still, reachable finite-size systems have very high density of states in the core of the MB spectrum as probed by high  $T$ . Hence, statistical fluctuations are at high  $T$  effectively smoothed out in contrast to low- $T$  properties dominated by a small number of low lying MB states.

The implementation of the MCLM is quite simple and straightforward. One first determines the target energy  $\lambda = \langle H \rangle(T)$  which represents the microcanonical energy equivalent to the canonical average energy for chosen  $T$  and the system size  $N$ . Since  $\lambda$  is a parameter within the MCLM, one can relate it to  $T$  by performing either FTLM (simplified due to conserved quantity  $H$ ) on the same system or extrapolating full ED results (with linear dependence on  $N$ ) on small lattices. Next we find a representative microcanonical state  $|\Psi_\lambda\rangle$  for the energy  $\lambda$ . One convenient way within the Lanczos-type approach is to use the new operator

$$V = (H - \lambda)^2. \quad (1.44)$$

Performing Lanczos iterations with the operator  $V$  yields again the extremum eigenvalues, in particular the lowest one close to  $V \sim 0$ . In contrast to the g.s. procedure, the convergence to a true eigenstate cannot be reached in system sizes of interest even with  $M_1 \gg 100$ . The reason is extremely small eigenvalue spacing of operator  $V$  scaling as  $\Delta V_n \propto (\Delta E/N_{st})^2$ ,  $\Delta E$  being the whole energy span within the given system. Fortunately such a convergence is not necessary (even not desired) since the essential parameter is small energy uncertainty  $\sigma_E$ , given by

$$\sigma_E^2 = \langle \Psi_\lambda | V | \Psi_\lambda \rangle. \quad (1.45)$$

For small energy spread  $\sigma_E/\Delta E < 10^{-3}$  typically  $M_1 \sim 1000$  is needed. Again, to avoid storing  $M_1$  Lanczos wavefunctions  $|\phi_i\rangle$  Lanczos procedure is performed twice as described in Sect. 1.2.2, i.e., the second time with known tridiagonal matrix elements to calculate finally  $|\Psi_\lambda\rangle$  in analogy with Eq. (1.6). The latter is then used to

evaluate any static expectation average  $\langle A \rangle$  or the dynamical correlation function as in Eq.(1.9),

$$C(\omega, \lambda) = \langle \Psi_\lambda | A^\dagger \frac{1}{\omega^+ + \lambda - H} A | \Psi_\lambda \rangle. \quad (1.46)$$

The latter is evaluated again using Lanczos iterations with  $M_2$  steps starting with the initial wavefunction  $|\tilde{\phi}_0\rangle \propto A|\Psi_\lambda\rangle$  and  $C(\omega, \lambda)$  is represented in terms of continued fractions. Since the MB levels are very dense and correlation functions smooth at  $T \gg 0$  large  $M_2 \gg 100$  are needed but as well easily reachable to achieve high- $\omega$  resolution in  $C(\omega, \lambda)$ .

It is evident that the computer requirement for the MCLM both regarding the CPU and memory are essentially the same as for the g.s. dynamical calculations except that typically  $M_1, M_2 \gg 100$ . In particular requirements are less demanding than using the FTLM with  $M > 100$ . A general experience is that for systems with large  $N_{st} \gg 10000$  the MCLM dynamical results agree very well with FTLM results for the same system. It should be also noted that actual frequency resolution  $\delta\omega$  in  $C(\omega, \lambda)$ , Eq.(1.46), is limited by  $\delta\omega \sim \sigma_E$  which is, however, straightforward to improve by increasing  $M_1, M_2$  with typical values  $M_1, M_2 > 1000$ . One can also improve MCLM results for any  $T$  by performing an additional sampling over initial random starting  $|\phi_0\rangle$  as well as over  $\lambda$  with a probability distribution  $p(\lambda)$  simulating the canonical ensemble in a finite-size system, i.e., by replacing Eq.(1.46) with

$$C(\omega) = \sum_{\lambda} p(\lambda) C(\omega, \lambda). \quad (1.47)$$

#### 1.4.6 Statical and Dynamical Quantities at $T > 0$ : Applications

The FTLM has been designed to deal with simplest tight-binding models of strongly correlated electrons, at the time mostly with challenging microscopic electronic models of high- $T_c$  superconductors [6, 7], where besides superconductivity there is a variety of anomalous non-Fermi-like properties even in the normal state. Clearly of interest in this connection are prototype MB models as the Heisenberg model, Eq.(1.1), the  $t$ - $J$  model, Eq.(1.2) and the Hubbard model on the 2D square lattice. Unfrustrated Heisenberg model can be numerically studied on much bigger lattices with QMC and related methods. The 2D Hubbard model was and still is mostly subject of DMFT and QMC studies, since at half-filling or close to it the Lanczos methods are quite restricted due to large  $N_{st}$  even for modest sizes  $N \sim 16$ . Therefore one focus of Lanczos-based approaches was on the  $t$ - $J$  model being with some generalizations a microscopic representation of electronic properties of high- $T_c$  cuprates.

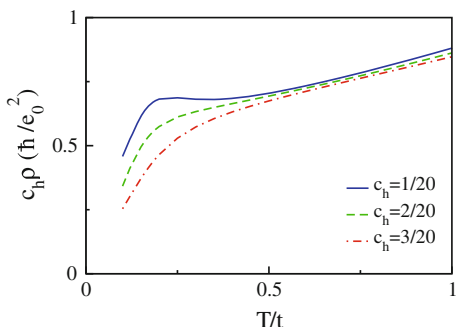
Thermodynamic quantities as chemical potential  $\mu$ , entropy density  $s$ , specific heat  $C_v$  are the easiest to implement within the FTLM. Their  $T$ - and (hole) doping  $c_h$ -dependence within the  $t$ - $J$  model on a 2D square lattice (calculated up to  $N = 26$  sites) reveal already very anomalous behavior of doped Mott insulators

[24] (as evident already from Fig. 1.3), confirmed also by results for more complete Hubbard model [25]. An introduction of next-neighbor hopping  $t'$  generates also an asymmetry in thermodynamic properties between hole-doped and electron-doped cuprates [26] as well quite dramatic influence of stripe order [27] consistent with the physics of cuprates.

The advantages of the FTLM and also its feasibility for the 2D  $t$ - $J$  model are even more evident in quite numerous studies of spin and charge dynamics at  $T > 0$  [7] which show good agreement with neutron scattering and NMR [20, 28–30], optical conductivity  $\sigma(\omega)$  and resistivity  $\rho(T)$  [31, 32], Hall constant  $R_H(T)$  [33] and a general non-Fermi-liquid behavior of cuprates [30], as well as the puzzling strong influence of nonmagnetic impurities [34]. As an example of a transport quantity hardly accessible by other methods we present in Fig. 1.4 the universal planar resistivity  $\rho(T)$ , as extracted from the dynamical conductivity  $\sigma(\omega \rightarrow 0) = 1/\rho$ , within the  $t$ - $J$  model for different doping levels  $c_h$  [32]. Result in Fig. 1.4 clearly shows a linear dependence below the pseudogap temperature  $T^*$  dependent on doping  $c_h$ . Another characteristic signature is a saturation (plateau) of  $\rho(T)$  at low doping and the universal trend at high  $T$ .

Spectral properties as manifested in single-particle spectral functions  $A(\mathbf{k}, \omega)$  are in the core of the understanding of cuprates, as well as of strongly correlated electrons in general. Here, even g.s. and low- $T$  properties are the challenge for numerical studies whereby the FTLM can be viewed as a controlled way to get reliable (macroscopic-like)  $T \rightarrow 0$  result, in contrast to quite finite-size plagued results obtained via g.s. Lanczos procedure [5]. Using the FTLM at  $T \sim T_{fs}$  with the twisted boundary condition can simulate a continuous wavevector  $\mathbf{k}$ . Using in addition the coarse graining averaging one can reach results for  $A(\mathbf{k}, \omega)$  [35–37] giving insight into the electron vs. hole doped angle-resolved photoemission experiments, quasi-particle relaxation and waterfall-like effects. A characteristic result of such studies is in Fig. 1.5 for the single-particle density of states  $\mathcal{N}(\omega) = \sum_{\mathbf{k}} A(\mathbf{k}, \omega)$  [35]. Here, the strength of the FTLM is visible in the high  $\omega$  resolution within the most interesting low- $\omega$  window. Interesting and reproducible are also nontrivial spectral shapes as the sharp peak close to  $\omega < 0$  and a broad shoulder for  $\omega \ll 0$ . Most important is,

**Fig. 1.4** Normalized 2D resistivity  $c_h \rho$  versus  $T/t$  within the  $t$ - $J$  model with  $J/t = 0.3$  for different hole concentrations  $c_h$  [32]



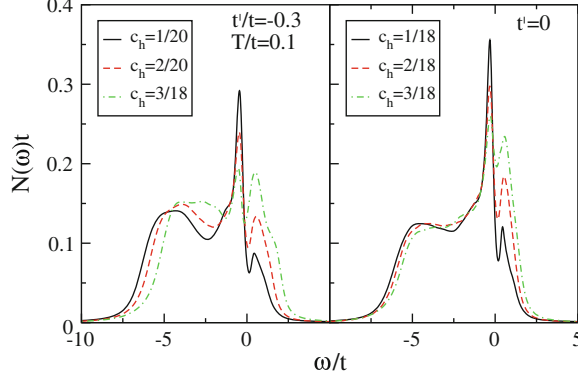


**Fig. 1.5** Density of states  $\mathcal{N}(\omega)$  for different dopings  $c_h$  within the extended  $t$ - $J$  model with n.n.n. hopping  $t' = -0.3t$  and  $t' = 0$ , respectively [35]

however, the evident pseudogap (observed also experimentally in cuprates) visible at  $\omega \sim 0$  in the low-doping regime.

Besides the challenging models for cuprates there have been also studies of static and dynamical properties of multiband and multiorbital models which either reduce to the generalized  $t$ - $J$  model [38] or to Kondo lattice models [39–41] and the Falicov-Kimball model [42]. While the increasing number of local basis states  $K$  clearly limits the applicability of ED-based methods, they are competitive in treating nontrivial frustrated spin models less suitable for the QMC and other methods, however closely related to physics of novel materials. Moreover, frustrated models are characterized by a large entropy density  $s$  and related low  $T_{fs}$  essential conditions for feasibility of FTLM results. Examples of such systems are the Shastry-Sutherland model [43, 44], 2D  $J_1$ - $J_2$  model [45], and properties of frustrated magnetic molecules [46–48].

Another class of problems which can be quite effectively dealt with the FTLM and MCLM approaches is the fundamental as well as experimentally relevant problem of transport in 1D systems of interacting fermions as realized, e.g., in quasi-1D spin-chain materials [49]. It has been recognized that the transport response at any  $T > 0$  crucially differs between integrable and nonintegrable systems. Since the 1D isotropic as well as anisotropic Heisenberg model, Eq. (1.1), is integrable it opens a variety of fundamental questions of anomalous transport in such systems, the effects of perturbative terms and impurities. Such fundamental questions on transport and low- $\omega$  dynamic response remain nontrivial even at high  $T$  [21, 22], hence the MCLM is the most feasible and straightforward method. It has been in fact first probed on the anomalous transport in 1D insulators [50] but further on used to study interaction-induced transport at  $T > 0$  in disordered 1D systems [51, 52], incoherent transport induced by a single either static [53] or dynamical spin impurity [54].

In Fig. 1.6 we present as an example the MCLM result for the dynamical spin conductivity in the anisotropic Heisenberg model, Eq.(1.1), where  $J^{zz} \neq J^{xx} = J^{yy} = J$  in the Ising-like (with the spin gap in the g.s.) regime  $\Delta = J^{zz}/J > 1$ .

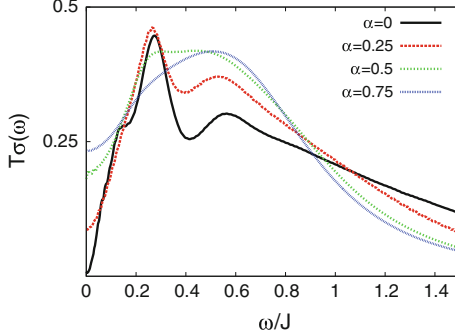


**Fig. 1.6** High- $T$  dynamical spin conductivity  $T\sigma(\omega)$  within the anisotropic Heisenberg model in the Ising-like regime  $\Delta = 1.5$  and various next-neighbor interaction  $\alpha = J_2^{zz}/J$  as calculated with the MCLM on a chain with  $N = 30$  sites

Results for the high- $T$  dynamical spin conductivity  $T\sigma(\omega)$  are shown for various next-neighbor (anisotropic) coupling  $\alpha = J_2^{zz}/J$ . First message is that the MCLM as the method is well adapted for the high  $\omega$  resolution (here using  $M_1 = M_2 = 2000$ ) and reaching large  $N = 30$  ( $N_{st} \sim 5.10^6$  in a single  $S^z = 0, q$  sector). Another conclusion is that the dynamics of such systems is very anomalous. For the integrable case  $\alpha = 0$  we find  $\sigma_0 = \sigma(0) \sim 0$  but also an anomalous finite-size peak at  $\omega_p \propto 1/N$  [50]. At the same time breaking integrability with  $\alpha > 0$  appears to lead to  $\sigma_0 > 0$  still approaching an ‘ideal’ insulator (insulating at all  $T$ ) for a weak perturbation  $\sigma_0(\alpha \rightarrow 0) \rightarrow 0$  [55].

## 1.5 Reduced Basis Lanczos Methods

The main shortcoming of ED approaches are finite-size effects that tamper calculations on small lattice systems. Exponentially growing Hilbert spaces represent the main obstacle against extending ED calculations to larger lattices. One way to extend ED calculations is to reduce the complete Hilbert space and keep only states that give a significant weight in the g.s. wavefunction or in the relevant Hilbert space, e.g., at  $T > 0$ . Here, the crucial step represents developing a feasible algorithm for the basis reduction.

One clear example of very effective basis construction is the DMRG method, most feasible for 1D correlated systems. Within this method, described in other chapters, some intermediate steps of ED diagonalization are frequently also performed via Lanczos iterations [56]. Moreover, there are recently developments which are extending the application of DMRG procedure to  $T > 0$  dynamical response [57, 58] involving more directly features of Lanczos-based approaches. In particular, recent finite- $T$  dynamical DMRG (FTD-DMRG) method [58] combines the DMRG selection of MB states and the LTLM procedure as described in Sect. 1.4.3

and in Eqs.(1.42), (1.43) to evaluate dynamical correlations at  $T > 0$ , both being effective at low  $T$ . So far the FTD-DMRG method has been applied to find novel features within the 1D  $J_1$ - $J_2$  model [59].

The ideas to find the reduced basis sets is, however, more general going beyond the 1D systems and has been successful in solving several problems of strongly correlated systems. Even before the discovery of high- $T_c$  superconductors that boosted research on models of correlated systems, Brinkman and Rice [60] developed a string representation of configurational space to compute the band renormalization and mobility in the atomic limit of the Hubbard model. The string picture was later used to compute single hole properties and to estimate hole-pair binding within the  $t$ - $J$  model by many authors [61–63]. In connection with ED calculations on finite lattices the truncation scheme based on the limitation of the maximal length of strings leads to slow convergence in terms of the number of reduced basis states [64] in the spin-isotropic limit of the  $t$ - $J$  model. Rather slow convergence is achieved also using a cluster diagonalization scheme together with the systematic expansion of the Hilbert space [65, 66].

The exact diagonalization method in limited functional space (EDLFS) was originally developed specifically for solving the problem of a single charge carrier (hole) doped in the AFM background [67]. The basic principle of the method is based on the above mentioned string picture, that emerges as a moving hole through the AFM background creates in its wake paths of overturned spins-strings. EDLFS was later generalized to include phonon degrees of freedom [68, 69]. For the purpose of presenting the method we start by considering the prototype  $t$ - $J$  model, Eq.(1.2), coupled to dispersionless optical phonons on a square lattice

$$\begin{aligned} H &= H_t + H_J + H_g + H_{\omega_0} \\ &= -t \sum_{\langle ij \rangle s} \tilde{c}_{is}^\dagger \tilde{c}_{js} + J \sum_{\langle ij \rangle} \left[ S_i^z S_j^z + \frac{\gamma}{2} (S_i^+ S_j^- + S_i^- S_j^+) \right] \\ &\quad + g \sum_i (1 - n_i) (a_i^+ + a_i) + \omega_0 \sum_i a_i^+ a_i, \end{aligned} \quad (1.48)$$

where  $t$  represents the nearest-neighbor hopping,  $a_i$  is the phonon annihilation operator,  $n_i = \sum_s n_{is}$  and all double sums run over the nearest neighbor pairs. The third term represents electron–phonon coupling  $g$  and the last the energy of Einstein-type phonons  $\omega_0$ .

The Néel state is the g.s. of the model when  $t = \gamma = g = 0$ . We construct the limited functional space (LFS) for one hole starting from a Néel state on an infinite 2D lattice with a hole placed in the origin and zero phonon degrees of freedom  $|\phi_0\rangle = c_0 |\text{Néel}; 0\rangle$ . We then proceed with the generation of new states, using the following generator

$$\{|\phi_l\rangle\} = \left( H_t + \sum_{i=1}^m H_g^i \right)^{n_s} |\phi_0\rangle, \quad (1.49)$$

where  $H_t$  and  $H_g$  are off-diagonal terms in Eq.(1.48), respectively. We select  $n_s = 1$ ,  $N_s$  and a fixed value of  $m$ . This procedure generates strings with maximum lengths given by  $N_s$  and phonon quanta at a maximal distance  $N_s - 1$  from the hole. Parameter  $m$  provides the creation of additional phonon quanta leading to a maximum number of phonons  $N_{ph} = mN_s$  in the system. Typically, larger  $N_{ph}$  are necessary to achieve convergence in the strong electron–phonon coupling (polaron) regime. While constructing LFS we take into account explicitly translational symmetry. I.e., we store only one out of (in principle) infinitely many translationally invariant states, called a parent state. However, the Néel state is a state with a broken translational symmetry so allowed translations are generated by two minimal translations  $\mathbf{r}_{1,2} = (1, \pm 1)$ . The basis wavefunctions are represented by one of the two nonequivalent hole positions  $\mathbf{r}_h$ , sets of strings, representing overturned spins relative to the Néel state (spin flips), and occupation numbers representing excited phonon quanta,

$$|\phi\rangle = |\mathbf{r}_h; \mathbf{r}_1, \mathbf{r}_2, \dots, \mathbf{r}_{N_{fl}}; n_{\mathbf{r}'_1}, n_{\mathbf{r}'_2}, \dots, n_{\mathbf{r}'_{N_s}}\rangle, \quad (1.50)$$

where  $\mathbf{r}_i$  represent spin-flip coordinates,  $n_{\mathbf{r}'_j}$  number of phonon quanta at site  $\mathbf{r}'_j$  and  $N_{fl} \leq N_s$  is the total number of spin flips.

Since the Hilbert space grows exponentially with  $N_s$  there exist many intuitive physically motivated restrictions optimizing LFS's for different parameter regimes to slow down the exponential growth. A systematic control over the growing Hilbert space can be achieved through realization that the diagonal energy of long strings grows linearly with  $N_s$ . Assuming that the contribution of long strings in the g.s. wave-function is negligible, we introduce an additional parameter  $N_b \leq N_s$  that restricts generation of long strings by imposing a condition under which all coordinates of spin flips satisfy  $|\mu_h - \mu_f| \leq N_b$ ;  $\mu = \{x, y\}$  where  $h$  and  $f$  refer to hole and spin-flip indexes, respectively. Application of this condition improves the quality of the LFS by increasing the number of states containing spin flips in the vicinity of the hole while keeping the total amount of states within computationally accessible limits.

Figure 1.7 represents a particular state generated using Eq.(1.49). Black and grey dots represent sites with spins ‘up’ and ‘down’, respectively. The hole starts at the position  $(-1, 1)$  in the direction  $(0, -1)$ , and travels along the path indicated by arrows. Crosses represent spin-flips and numbers represent excited phonon quanta, generated along the hole’s path. The effect of the parameter  $m$  is to set the maximal number of excited phonon quanta on indicated positions. In this particular parent the hole ends its path on the B-sublattice. Using allowed minimal translations, the position of the hole in the parent state is at  $\mathbf{r}_h = (1, 0)$ .

After the generation of LFS the full Hamiltonian in Eq.(1.48) is diagonalized within this LFS using the standard Lanczos procedure. The efficiency of the EDLFS method in case of the  $t$ - $J$  model and stability of results against varying  $N_s$  and  $N_b$  has been shown in detail in Ref. [67].

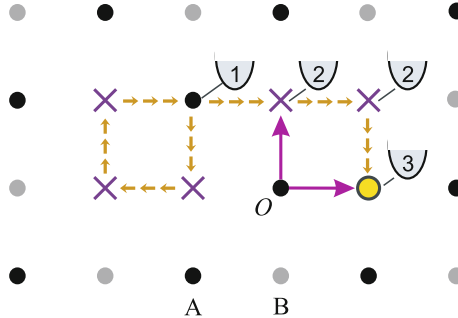


**Fig. 1.7** Schematic representation of a particular basis wavefunction obtained using  $N_s = 10$ ,  $m = 3$ , and  $N_b = 3$ . Circle represents the hole position, crosses, portray spin flips and numbers indicated excited phonon quanta. Dots represent lattice sites with no spin flips and zero excited phonon quanta. In this particular case,  $N_{fi} = 5$  and  $N_p = 8$ . Presented basis function is one of a total of  $N_{st} = 42.10^6$  states, generated using Eq. (1.49)

Besides reliable results obtained using the EDLFS there are other important advantages over most other methods: (a) it is highly efficient, (b) the method is free of finite-size effects, (c) it treats spin and lattice degrees of freedom on the same footing while preserving the full quantum nature of the problem, and (d) it allows for computation of physical properties at an arbitrary wavevector. Even though results depend on the choice of parameters defining the functional generator in Eq. (1.49), such as  $N_s$  and  $m$ , reliable results are obtained already for relatively small sizes of the Hilbert space  $N_{st}$ , typically up to three orders of magnitude smaller than in the case of exact diagonalization techniques. For most static as well as dynamic quantities convergence to the thermodynamic limit can be achieved with a systematic increase of  $N_s$  and  $m$ .

The EDLFS obviously has few limitations: (a) the method is limited to calculations in the zero-doping limit, e.g.,  $N_h = 1, 2$  mobile particles immersed in an infinite (AFM) background, (b) the spin anisotropy is inherently built in the method, and (c) due to the broken translational symmetry of the starting wavefunction, calculations are limited to the reduced AFM Brillouin zone.

Due to its high efficiency in dealing with spin fluctuation the method represents one of the few successful methods that allows the addition of lattice degrees of freedom to a correlated electron model. The EDLFS handles spin and lattice degrees of freedom by preserving the full quantum mechanical nature of the problem and enables a direct calculation of the dynamic response functions in terms of real frequency  $\omega$ .

The EDLFS can be rather in a straightforward way generalized for the study of the two-hole  $N_h = 2$  problem [70, 71]. ED studies in the  $t$ - $J$  model for  $N_h = 2$  were performed on a 2D square lattices up to  $N = 32$  sites [72, 73]. Still, the maximal distance between two holes remains rather small  $l_{\max} = \sqrt{N/2} = 4$ . Attempts to increase the lattices sizes beyond ED studies led authors to investigate various truncated basis approaches [64–66] and using small sets of variational wavefunctions with given rotational symmetries based on ‘string’ and ‘spin-bag’ pictures [74].

While the problem of two holes within the  $t$ - $J$  model represents a challenging problem, the addition of quantum phonons seems an almost unachievable task. Nevertheless, the EDLFS due to an efficient choice of LFS can handle this problem well. The construction of the LFS starts from a Néel state with holes located on neighboring sites and with zero phonon quanta. Such a state represents a parent state of a translationally invariant state. We generate new parent states in analogy with Eq.(1.49) by applying the generator of states

$$\{|\phi_l\rangle_a\} = \left( H_t + \tilde{H}_J + \sum_{i=1}^m H_g^i \right)^{n_s} |\phi_0\rangle \quad (1.51)$$

where  $\tilde{H}_J$  denotes the off-diagonal spin exchange term in Eq.(1.48) applied only to erase spin flips generated through application of  $H_t$ . This allows the creation of states with holes positioned further apart that are not connected with spin strings. Note that for larger  $N_s \geq 6$  some of such states would be generated even without evoking  $\tilde{H}_J$  term via the Trugman loops [61–63]. One of the advantages of this method in comparison to other approaches is that it allows much larger distances between the holes,  $l_{\max} = N_s + 1$ . Note also that the functional generator preserves as well the point-group symmetry.

As an example we present in Fig. 1.8 the probability of finding a hole pair at a distance  $r$

$$P(r) = \left\langle \sum_{\langle i \neq j \rangle} n_i^h n_j^h \delta(|\mathbf{r}_i - \mathbf{r}_j| - r) \right\rangle, \quad (1.52)$$

where  $n_i^h = 1 - n_i$  is the local hole density. In the case of dimensionless electron–phonon coupling  $\lambda = g^2/8\omega_0 t = 0$ , the maximal allowed distance between holes is  $l_{\max} = 13$  while for  $\lambda = 0.25$   $l_{\max} = 7$ , whereby results for  $\lambda = 0$  are consistent with previous findings using ED [72, 73], reduced-basis ED [65, 66], as well as string picture variational approaches [74].

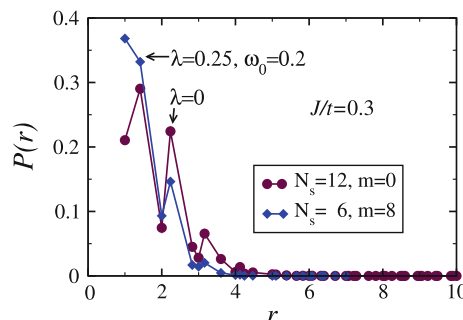


**Fig. 1.8** Probability  $P(r)$  of finding a hole pair at a distance  $r$  within the  $t$ - $J$ -Holstein model with  $J/t = 0.3$  and  $\omega_0/t = 0.2$ , evaluated for electron–phonon coupling parameters  $\lambda = 0$  and  $\lambda = 0.25$ . Different  $N_s$  and  $m$  as indicated in legends were chosen giving  $N_{st} \sim 7.10^6$  and  $N_{st} \sim 26.10^6$ , respectively. Both solutions correspond to a  $d$ -wave symmetry

## 1.6 Real Time Dynamics Using Lanczos Method

Research in the field of non-equilibrium dynamics of complex quantum systems constitutes a formidable theoretical challenge. When dealing with ED approaches or calculations in the reduced basis, the time evolution of the time-dependent Shrödinger equation,

$$i \frac{\partial \Psi(t)}{\partial t} = H(t) \Psi(t), \quad (1.53)$$

can be efficiently obtained using the time-dependent Lanczos technique, as originally described in Ref. [75] and later applied and analysed in more detail [76]. One of the straightforward reasons is that most commonly the Lanczos method is used to compute g.s. of MB Hamiltonian. Generalizing the method to time-dependent calculation represents only a minor change to already existing codes. Even though the method is most suitable for the time evolution of the time-independent Hamiltonian, it can nevertheless be applied even to the time-dependent case. The time evolution of  $|\Psi(t)\rangle$  is then calculated by step-wise change of time  $t$  in small time increments  $\delta t$ , generating at each step Lanczos basis of dimension  $M$  (typically  $M < 10$ ), to follow the evolution

$$|\Psi(t + \delta t)\rangle \simeq e^{-iH(t)\delta t} |\Psi(t)\rangle \simeq \sum_{l=1}^M e^{-i\epsilon_l \delta t} |\psi_l\rangle \langle \psi_l| \Psi(t)\rangle, \quad (1.54)$$

where  $|\psi_l\rangle, \epsilon_l, l = 0 \dots M$  are Lanczos eigenfunctions and eigenvalues, respectively, obtained via the Lanczos iteration started with  $|\phi_0\rangle = |\Psi(t)\rangle$ . The advantage of the time-evolution method following Eq. (1.54) is that it preserves the normalization of  $|\Psi(t + \delta t)\rangle$  for arbitrary large  $\delta t$ . The approximation of finite  $M$  in Eq. (1.54) is also correct at least to the  $M$ th Taylor-expansion order in  $\delta t$ . It is, however, important to stress that  $\delta t$  should be chosen small enough to take into account properly the time-dependence of  $H(t)$ . E.g., in the case of driving the system with an external constant electric field,  $\delta t/t_B \sim 10^{-3}$  where  $t_B$  is the Bloch oscillation period [55, 77–79].

So far, investigations of correlated driven systems under the influence of a driving electric field in 1D systems using the Lanczos time evolution method focused on generic systems, like the metallic and Mott-insulating regime within the 1D model of interacting spinless fermions [55, 77]. Even though rather small systems can be studied it has been established that steady state can be reached without any additional coupling to a heat bath, provided that the Joule heating of the system is properly taken into account.

The case of a single charge carrier in an inelastic medium driven by the external electric field in 1D as well as 2D has been investigated using EDLFS combined with a Lanczos-based time-evolution approach [77, 79–82]. The strength of EDLFS is in construction of the Hilbert space that enables not only an accurate description of the ground state of the single carrier system but it allows for enough extra inelastic (spin

or phonon) excitations to absorb energy, emitted by the field driven carrier, until the system reaches the steady state. This again enables a proper description of the steady state without coupling the system to an external thermal bath.

## 1.7 Discussion

Exact diagonalization based methods, both the full ED and Lanczos-type ED approach, are very extensively employed in the investigations of strongly correlated MB quantum systems in solid state and elsewhere. The reason for their widespread use are several: (a) unbiased approach to the MB problem without any simplifications or approximations, independent of complexity of the MB system, (b) relative simplicity of generating the codes for various models and observables, (c) easy and straightforward testing of codes, (d) direct interpretation of obtained quantum MB states and their possible anomalous structure and properties, (e) high pedagogical impact as a quick and at the same time very nontrivial introduction into the nature of MB quantum physics. Also the Lanczos-based methods described in this review, i.e., the g.s. Lanczos method for static and dynamic quantities, and somewhat more elaborate FTLM, MCLM, LTLM and EDLFS, require rather modest programming efforts in comparison with more complex numerical methods, e.g., the QMC- and DMRG- based methods, as described in other chapters.

Clearly, the main drawback of ED methods is the smallness of lattice sizes  $N$  determined by a limited number of basis states (at present  $N_{st} < 10^9$ ) treated with a Lanczos iteration procedure. The achievable  $N$  with ED methods appears quite modest in comparison with some established and recently developed numerical methods, as the QMC, DMRG, matrix-product-states methods etc. Still, in spite of very intensive development and advance of novel numerical methods in last two decades there are several aspects of strong-correlation physics, where ED-based methods are so far either the only feasible or at least superior to other methods. In this chapter we have focused mostly on Lanczos-based methods and applications where they are still competitive and get nontrivial results with a macroscopic validity:

- (a) MB g.s. and its properties of frustrated and complex models mostly so far do not offer alternative powerful methods except ED approaches, at least beyond  $D = 1$  systems where DMRG-based methods can be effectively applied,
- (b)  $T > 0$  static properties evaluated with Lanczos-based methods as the FTLM and the LTLM are as well most powerful and reliable for frustrated and complex system, in particular in systems with high degeneracies of MB states and large entropy at low  $T$ ,
- (c)  $T > 0$  Lanczos methods for dynamical quantities, as the FTLM and MCLM, yield for many models and geometries results superior to other methods or even the only accessible results in several cases. In particular the advantage of the latter methods is high  $\omega$  resolution at all temperatures beyond the finite size limit  $T > T_{fs}$ , the macroscopic-like results at low  $T$  with a proper scaling to  $T \rightarrow 0$ , and the

possibility of detailed studies of systems with nontrivial (anomalous) dynamics at any, in particular high  $T$ .

(d) Lanczos technique of ED is also the natural application within the methods with a restricted MB basis sets as the EDLFS and DMRG-type targeting as well as in the real-time evolution studies of strongly correlated systems.

## References

1. C. Lanczos, J. Res. Nat. Bur. Stand. **45**, 255 (1950)
2. B.N. Parlett, *The Symmetric Eigenvalue Problem* (Prentice Hall, Eaglewood Cliffs, 1980)
3. J.W. Demmel, *Applied Numerical Linear Algebra* (SIAM, Philadelphia, 1997)
4. R. Haydock, V. Heine, M.J. Kelly, J. Phys. C: Solid State Phys. **8**, 2591 (1975)
5. For a review, see E. Dagotto, Rev. Mod. Phys. **66**, 763 (1994)
6. J. Jaklič, P. Prelovšek, Phys. Rev. B **49**, 5065 (1994)
7. For a review, see J. Jaklič, P. Prelovšek, Adv. Phys. **49**, 1 (2000)
8. M. Aichhorn, M. Daghofer, H.G. Evertz, W. von der Linden, Phys. Rev. B **67**, 161103(R) (2003)
9. M.W. Long, P. Prelovšek, S. El Shawish, J. Karadamoglou, X. Zotos, Phys. Rev. B **68**, 235106 (2003)
10. For a review, see M. Imada, A. Fujimori, Y. Tokura, Rev. Mod. Phys. **70**, 1039 (1998)
11. P.W. Leung, Phys. Rev. B **73**, 14502 (2006)
12. T. Tohyama, Y. Inoue, K. Tsutsui, S. Maekawa, Phys. Rev. B **72**, 045113 (2005)
13. J. Oitmaa, D.D. Betts, Can. J. Phys. **56**, 897 (1978)
14. D.D. Betts, H.Q. Lin, J.S. Flynn, Can. J. Phys. **77**, 3535 (1999)
15. P.R.C. Kent, M. Jarrell, T.A. Maier, Th. Pruschke, Phys. Rev. B **72**, 060411 (2005)
16. J. Cullum, R.A. Willoughby, J. Comput. Phys. **44**, 329 (1981)
17. H. Mori, Prog. Theor. Phys. **34**, 423 (1965)
18. M. Imada, M. Takahashi, J. Phys. Soc. Jpn. **55**, 3354 (1986)
19. R.N. Silver, H. Röder, Int. J. Mod. Phys. C **5**, 735 (1995)
20. J. Jaklič, P. Prelovšek, Phys. Rev. Lett. **75**, 1340 (1995)
21. X. Zotos, P. Prelovšek, Phys. Rev. B **53**, 983 (1996)
22. For a review, see F. Heidrich-Meisner, A. Honecker, W. Brenig, Eur. Phys. J. **151**, 135 (2007) (Special Topics)
23. J. Kokalj, Ph.D. Thesis, University of Ljubljana, 2010 (unpublished)
24. J. Jaklič, P. Prelovšek, Phys. Rev. Lett. **77**, 892 (1996)
25. J. Bonča, P. Prelovšek, Phys. Rev. B **67**, 180502(R) (2003)
26. T. Tohyama, S. Maekawa, Phys. Rev. B **67**, 092509 (2003)
27. T. Tohyama, S. Maekawa, P. Prelovšek, Phys. Rev. B **67**, 180502 (2003)
28. Y. Shibata, T. Tohyama, S. Maekawa, Phys. Rev. B **64**, 054519 (2001)
29. P. Prelovšek, I. Sega, J. Bonča, Phys. Rev. Lett. **92**, 027002 (2004)
30. J. Bonča, P. Prelovšek, I. Sega, Phys. Rev. B **70**, 224505 (2004)
31. J. Jaklič, P. Prelovšek, Phys. Rev. B **50**, 7129 (1994)
32. M.M. Žemljič, P. Prelovšek, Phys. Rev. B **72**, 075108 (2005)
33. D. Veberič, P. Prelovšek, Phys. Rev. B **66**, 020408(R) (2002)
34. P. Prelovšek, I. Sega, Phys. Rev. Lett. **93**, 207202 (2004)
35. M.M. Žemljič, P. Prelovšek, Phys. Rev. B **75**, 104514 (2007)
36. M.M. Žemljič, P. Prelovšek, T. Tohyama, Phys. Rev. B **76**, 012502 (2007)
37. M.M. Žemljič, P. Prelovšek, T. Tohyama, Phys. Rev. Lett. **100**, 036402 (2008)
38. P. Horsch, J. Jaklič, F. Mack, Phys. Rev. B **59**, 6217 (1999)
39. K. Haule, J. Bonča, P. Prelovšek, Phys. Rev. B **61**, 2482 (2000)

40. P. Horsch, J. Jaklič, F. Mack, Phys. Rev. B **59**, 14149(R) (1999)
41. I. Zerec, B. Schmidt, P. Thalmeier, Phys. Rev. B **73**, 245108 (2006)
42. S. El Shawish, J. Bonča, D. Batista, Phys. Rev. B **68**, 195112 (2003)
43. S. El Shawish, J. Bonča, I. Sega, Phys. Rev. B **72**, 184409 (2005)
44. S. El Shawish, A. Ramšak, J. Bonča, Phys. Rev. B **75**, 205442 (2007)
45. B. Schmidt, P. Thalmeier, N. Shannon, Phys. Rev. B **76**, 125113 (2007)
46. J. Schnack, O. Wendland, Eur. Phys. J. B **78**, 535 (2010)
47. J. Schnack, C. Heesing, arXiv:1207.0299
48. M. Haertel, J. Richter, D. Ihle, J. Schnack, S.-L. Drechsler, Phys. Rev. B **84**, 104411 (2011)
49. For a review, see C. Hess, Eur. Phys. J. **151**, 73 (2007) (Special Topics)
50. P. Prelovšek, S. El Shawish, X. Zotos, M. Long, Phys. Rev. B **70**, 205129 (2004)
51. A. Karahalios, A. Metavitsiadis, X. Zotos, A. Gorczyca, P. Prelovšek, Phys. Rev. B **79**, 024425 (2009)
52. O.S. Barišić, P. Prelovšek, Phys. Rev. B **82**, 161106 (2010)
53. O.S. Barišić, P. Prelovšek, A. Metavitsiadis, X. Zotos, Phys. Rev. B **80**, 125118 (2009)
54. A. Metavitsiadis, X. Zotos, O.S. Barišić, P. Prelovšek, Phys. Rev. B **81**, 205101 (2010)
55. M. Mierzejewski, J. Bonča, P. Prelovšek, Phys. Rev. Lett. **107**, 126601 (2011)
56. For a review see U. Schollwöck, Rev. Mod. Phys. **77**, 259 (2005)
57. S. Sota, T. Tohyama, Phys. Rev. B **78**, 113101 (2008)
58. J. Kokalj, P. Prelovšek, Phys. Rev. B **80**, 205117 (2009)
59. J. Kokalj, P. Prelovšek, Phys. Rev. B **82**, 060406(R) (2010)
60. W.F. Brinkman, T.M. Rice, Phys. Rev. B **2**, 1324 (1970)
61. J.E. Hirsch, Phys. Rev. Lett. **59**, 228 (1987)
62. S.A. Trugman, Phys. Rev. B **37**, 1597 (1988)
63. B.I. Shraiman, E.D. Siggia, Phys. Rev. Lett. **60**, 740 (1988)
64. P. Prelovšek, X. Zotos, Phys. Rev. B **47**, 5984 (1993)
65. J. Riera, E. Dagotto, Phys. Rev. B **47**, 15346 (1993)
66. J. Riera, E. Dagotto, Phys. Rev. B **57**, 8609 (1998)
67. J. Bonča, S. Maekawa, T. Tohyama, Phys. Rev. B **76**, 035121 (2007)
68. J. Bonča, S. Maekawa, T. Tohyama, P. Prelovšek, Phys. Rev. B **77**, 054519 (2008)
69. L. Vidmar, J. Bonča, S. Maekawa, Phys. Rev. B **79**, 125120 (2009)
70. L. Vidmar, J. Bonča, S. Maekawa, T. Tohyama, Phys. Rev. Lett. **103**, 186401 (2009)
71. L. Vidmar, J. Bonča, Phys. Rev. B **82**, 125121 (2010)
72. P.W. Leung, Phys. Rev. B **65**, 205101 (2002)
73. A.L. Chernyshev, P.W. Leung, R.J. Gooding, Phys. Rev. B **58**, 13594 (1998)
74. P. Wróbel, R. Eder, Phys. Rev. B **58**, 15160 (1998)
75. T.J. Park, J.C. Light, J. Chem. Phys. **85**, 5870 (1986)
76. N. Mohankumar, S.M. Auerbach, Comput. Phys. Commun. **175**, 473 (2006)
77. M. Mierzejewski, P. Prelovšek, Phys. Rev. Lett. **105**, 186405 (2010)
78. M. Mierzejewski, L. Vidmar, J. Bonča, P. Prelovšek, Phys. Rev. Lett. **106**, 196401 (2011)
79. L. Vidmar, J. Bonča, M. Mierzejewski, P. Prelovšek, S.A. Trugman, Phys. Rev. B **83**, 134301 (2011)
80. L. Vidmar, J. Bonča, T. Tohyama, S. Maekawa, Phys. Rev. Lett. **107**, 246404 (2011)
81. J. Bonča, M. Mierzejewski, L. Vidmar, Phys. Rev. Lett. **109**, 156404 (2012)
82. D. Golež, J. Bonča, L. Vidmar, S.A. Trugman, Phys. Rev. Lett. **109**, 236402 (2012)

# Chapter 2

## The Density Matrix Renormalization Group

Adrian E. Feiguin

**Abstract** Since its creation in 1992, the density matrix renormalization group (DMRG) method has evolved and mutated. From its original formulation in a condensed matter context, it has been adapted to study problems in various fields, such as nuclear physics and quantum chemistry, becoming one of the dominant numerical techniques to simulate strongly correlated systems. In this chapter, we shall cover many technical aspects of the DMRG, from a “traditional”, or “conventional” perspective, describing the theoretical fundamentation, as well as the details of the algorithm.

### 2.1 Introduction

Variational methods rely on a trial wave function or ansatz derived from some physical insight. This wave-function may, or may not describe the actual ground state of a system, but if it does—even in an approximate way—we may gain some enormous knowledge. The Bethe ansatz is actually exact when applied to an integrable model, but it can also be an approximation such as in the case of  $SU(N)$  models [1–3]. Laughlin’s wave-function for the fractional quantum Hall state at filling fraction  $\nu = 1/3$  has more than 95 % accuracy [4]. The Hartree-Fock method can be formulated as a variational ansatz, as well as the BCS theory of superconductivity [5].

The Density Matrix Renormalization Group (DMRG) method [6, 7] is variational, but relies heavily on exact diagonalization and numerical renormalization group (NRG) ideas. It was introduced by Steve White in 1992 as a development of Wilson’s NRG [8, 9]. The premise is to obtain a wave-function that approximates the actual ground-state in a reduced Hilbert space, minimizing the loss of information. In a

---

A. E. Feiguin (✉)

Department of Physics, Northeastern University, Boston, MA 02115, USA  
e-mail: a.feiguin@neu.edu

certain way, it can be considered as an algorithm to compress the wave-function, same as classical compression algorithms work in digital imaging.

It is variational because the proposed solution has the very peculiar form of a “matrix-product state” (MPS) [10–13], and it also involves a truncation of the basis. However, no a priori assumptions are made about the form of the coefficients, or the underlying physics. The power of the method is precisely that it is “smart” enough to be able to find for us the best possible wave-function of that form, without any “external bias”. Even though the accuracy is finite, it is totally under control, and we can obtain results that are essentially exact (also referred-to as “quasi-exact”). Another ingredient is a block decimation process, similar to the one introduced by Wilson. However, the NRG technique has very limited applicability, while the DMRG can be used for a wide range of lattice problems.

The DMRG possesses features that make it extremely powerful: it is able to treat very large systems with hundreds of degrees of freedom, and to provide the most accurate results for ground-state energies and gaps in low dimensional systems. Reviews on the DMRG method abound [14–20]. For detailed lecture notes, we refer the reader to Refs. [18, 20].

## 2.2 Truncated Diagonalization: The Numerical Renormalization Group Idea

In this section we introduce the concept of “truncated diagonalization”. The idea is to diagonalize the Hamiltonian in a constrained Hilbert space. The questions to address are: how do we pick the states to keep, and the states to discard? Does this choice depend on the representation? Can we quantify the amount of “information” lost in the process? We shall start by describing a pretty unconventional diagonalization procedure that will help us introduce the main tools needed to build the DMRG algorithm. For illustration purposes we shall consider a one-dimensional chain of quantum spins described by the Heisenberg Hamiltonian.

### 2.2.1 Two-Spin Problem

The Hilbert space for the two-spin problem consists of four possible configurations of two spins

$$\{| \uparrow\uparrow \rangle, | \uparrow\downarrow \rangle, | \downarrow\uparrow \rangle, | \downarrow\downarrow \rangle\} \quad (2.1)$$

The problem is described by the Hamiltonian:

$$\hat{H} = \hat{S}_1^z \hat{S}_2^z + \frac{1}{2} \left[ \hat{S}_1^+ \hat{S}_2^- + \hat{S}_1^- \hat{S}_2^+ \right] \quad (2.2)$$

The corresponding matrix will have dimensions  $4 \times 4$ . In order to compute this matrix we shall use some simple matrix algebra to first obtain the single-site operators in the expanded Hilbert space. This is done by the following simple scheme: And operator  $O_1$  acting on the left spin, will have the matrix form:

$$\tilde{O}_1 = O_1 \otimes \mathbb{1}_2 \quad (2.3)$$

Similarly, for an operator  $O_2$  acting on the right spin:

$$\tilde{O}_2 = \mathbb{1}_2 \otimes O_2 \quad (2.4)$$

where we introduced the  $n \times n$  identity matrix  $\mathbb{1}_n$ . The product of two operators acting on different sites can be obtained as:

$$\tilde{O}_{12} = O_1 \otimes O_2 \quad (2.5)$$

It is easy to see that the Hamiltonian matrix will be given by:

$$H_{12} = S^z \otimes S^z + \frac{1}{2} [S^+ \otimes S^- + S^- \otimes S^+] \quad (2.6)$$

where we used the single spin ( $2 \times 2$ ) matrices  $S^z$  and  $S^\pm$ . We leave as an exercise for the reader to show that the final form of the matrix is:

$$H_{12} = \begin{pmatrix} 1/4 & 0 & 0 & 0 \\ 0 & -1/4 & 1/2 & 0 \\ 0 & 1/2 & -1/4 & 0 \\ 0 & 0 & 0 & 1/4 \end{pmatrix}, \quad (2.7)$$

Obtaining the eigenvalues and eigenvectors is also a straightforward exercise: two of them are already given, and the entire problem now reduces to diagonalizing a two by two matrix. We therefore obtain the well known result: The ground state  $|s\rangle = 1/\sqrt{2} [| \uparrow\downarrow \rangle - | \downarrow\uparrow \rangle]$ , has energy  $E_s = -3/4$ , and the other three eigenstates  $\{| \uparrow\uparrow \rangle, | \downarrow\downarrow \rangle, 1/\sqrt{2}[| \uparrow\downarrow \rangle + | \downarrow\uparrow \rangle]\}$  form a multiplet with energy  $E_t = 1/4$ .

### 2.2.2 Many Spins

Imagine now that we add a third spin to the right of our two spins. We can use the previous result to obtain the new  $8 \times 8$  Hamiltonian matrix as:

$$H_3 = H_2 \otimes \mathbb{1}_2 + \tilde{S}_2^z \otimes S^z + \frac{1}{2} [\tilde{S}_2^+ \otimes S^- + \tilde{S}_2^- \otimes S^+] \quad (2.8)$$

Here we used the single spin  $S_1^z$ ,  $S_1^\pm$ , and the ‘tilde’ matrices defined in Eqs. (2.3) and (2.4):

$$\tilde{S}_2^z = \mathbb{1}_2 \otimes S^z, \quad (2.9)$$

and

$$\tilde{S}_2^\pm = \mathbb{1}_2 \otimes S^\pm, \quad (2.10)$$

It is easy to see that this leads to a recursion scheme to construct the  $2^i \times 2^i$  Hamiltonian matrix the  $i$ th step as:

$$H_i = H_{i-1} \otimes \mathbb{1}_2 + \tilde{S}_{i-1}^z \otimes S^z + \frac{1}{2} \left[ \tilde{S}_{i-1}^+ \otimes S^- + \tilde{S}_{i-1}^- \otimes S^+ \right] \quad (2.11)$$

with

$$\tilde{S}_{i-1}^z = \mathbb{1}_{2^{i-2}} \otimes S^z, \quad (2.12)$$

and

$$\tilde{S}_{i-1}^\pm = \mathbb{1}_{2^{i-2}} \otimes S^\pm, \quad (2.13)$$

This recursion algorithm can be visualized as a left ‘block’, to which we add new ‘sites’ or spins to the right, one at a time, as shown in Fig. 2.1. The block has a ‘block Hamiltonian’,  $H_L$ , that is iteratively built by connecting to the new spins through the corresponding interaction terms.

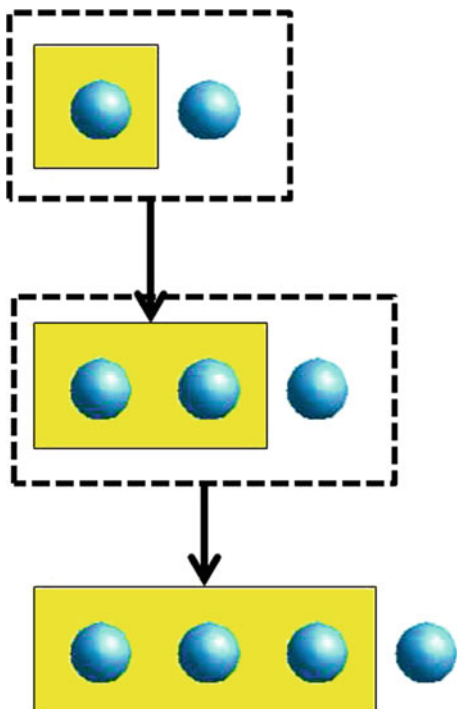
The process outlined above leads to a simple and elegant recursion scheme that allows one to construct the Hamiltonian matrix by using simple algebra. However, this idea is very impractical. The basis size, or the linear dimension of the matrix, grows with the number of spins  $N$  as  $2^N$ . It is clear that this matrix sizes soon become unmanageable by our computer. One way to deal with this problem is by using the symmetries of the Hamiltonian and the lattice to reduce the Hamiltonian into a block form. This leads to powerful algorithms that can diagonalize dozens of spins. However, this strategy also runs out of steam very soon. Another solution to deal with this exponential growth of the basis can be traced back to Wilson’s numerical renormalization group.

Suppose that we are able to diagonalize out Heisenberg spin chain, to obtain the ground state as:

$$|\Psi\rangle = \sum_{s_1, s_2, \dots, s_N} a_{s_1, s_2, \dots, s_N} |s_1, s_2, \dots, s_N\rangle \quad (2.14)$$

where the sum runs over all configurations of  $N$  spins. If we plot the weights  $|a_{s_1, \dots, s_N}|^2$  in decreasing order, we may find a structure like the one depicted in the left panel of Fig. 2.2: Most of the weight is concentrated on a couple of configurations, in our case  $|\uparrow\downarrow\uparrow\downarrow\dots\rangle$  and  $|\downarrow\uparrow\downarrow\uparrow\dots\rangle$ , and the rest of the weight is spread over a long tail. Usually only a few important states possess most of the weight, especially in ground states that resemble a classical state such as the antiferromagnet. One then might feel inclined to take a pair of scissors, and truncate the basis to a

**Fig. 2.1** Pictorial representation of the Hamiltonian building recursion explained in the text. At each step, the block size is increased by adding a spin at a time



few dozen states with largest weights, and get rid of the rest. However, this long tail of states with small weights are responsible for most of the interesting physics: the quantum fluctuations, and the difference in weight from one state to another in this tail cannot be necessarily ignored, since they are all of the same order of magnitude.

However, one may notice a simple fact: this is a basis dependent problem! What if, by some smart choice of basis, we find a representation in which the distribution of weights is such that all the weight on the tail is ‘shifted to the left’ on the plot, as shown on the right panel of Fig. 2.2. Then, if we truncate the basis, we would not need to worry about the loss of ‘information’. Of course, this is a nice and simple concept that might work in practice, if we knew how to pick the optimal representation. And as it turns out, this is not in principle an easy task. As we shall learn, what we need is a method for quantifying ‘information’.

### 2.2.3 A Simple Geometrical Analogy

Let us consider a vector in two dimensional space  $\mathbf{v} = (x, y)$ , as shown in Fig. 2.3. We need two basis vectors  $\hat{e}_1$  and  $\hat{e}_2$  to expand it as  $\mathbf{v} = x\hat{e}_1 + y\hat{e}_2$ . A simple 2D rotation by an angle  $\phi$  would be represented by an orthogonal matrix

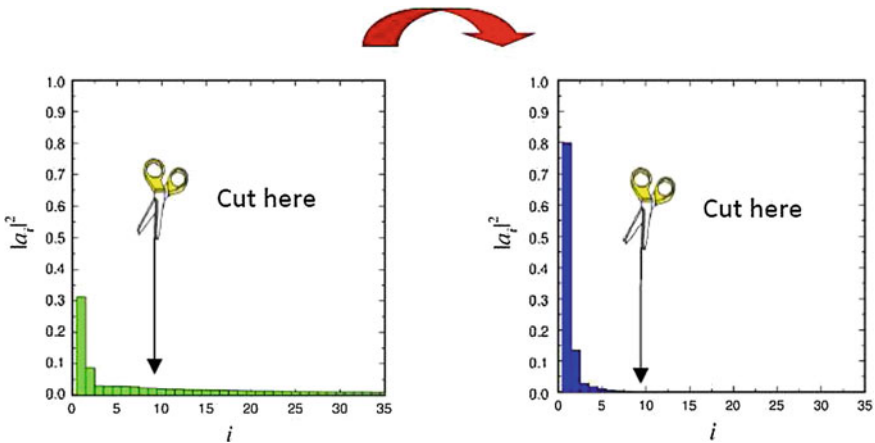
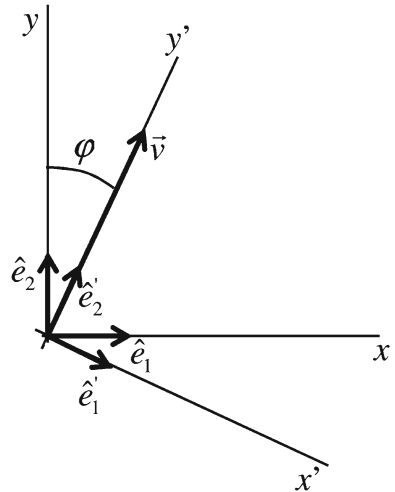


**Fig. 2.2** Schematic picture of the ideal basis truncation. Through a change of basis the ground-state weights are more concentrated in a few basis states, such that the loss of information after the truncation is minimal

**Fig. 2.3** Rotation by an angle  $\phi$  to a new reference system in the 2D plane



$$U = \begin{pmatrix} \cos \phi & \sin \phi \\ -\sin \phi & \cos \phi \end{pmatrix}, \quad (2.15)$$

After such a rotation, the new basis vectors will be  $\hat{e}'_1 = \cos \phi \hat{e}_1 + \sin \phi \hat{e}_2$ , and  $\hat{e}'_2 = -\sin \phi \hat{e}_1 + \cos \phi \hat{e}_2$ . If we pick the angle  $\phi$  such that  $\mathbf{v}$  is aligned along the new  $y'$ -axis, parallel to  $\hat{e}'_2$ , we find that we need only one component to describe the vector in the new basis:  $\mathbf{v} = (0, |v|)$ , or  $\mathbf{v} = |v| \hat{e}'_2$ . Therefore, we would feel inclined to eliminate the vector  $\hat{e}'_1$  from the basis. After truncating the basis, in order to rotate to the new one-dimensional space, we would use a rotation matrix:

$$U' = \begin{pmatrix} \cos \phi & \\ -\sin \phi & \end{pmatrix}, \quad (2.16)$$

which still is orthogonal. Now, we clearly see that unless a vector is parallel to  $\mathbf{v}$ , we would loose all information regarding the component orthogonal to  $\hat{e}'_2$ . In other words, this transformation does not preserve the norm, and therefore, it no longer is unitary. For the case of operators represented by  $2 \times 2$  matrices in the original basis, we find that they will be reduced to a  $1 \times 1$  matrix, a scalar, or just a simple change of scale. If we apply an operation on the vector, we have to deal with the fact that there will be some loss of information as a result. We would like to think that this loss of information is minimal, meaning that the contributions with support in the orthogonal manifold are very small. This simplified analogy illustrates the consequences one has to deal with when the basis is truncated.

### 2.2.4 The Case of Spins

Let us revisit the case of two spins, and look again at the eigenvectors of the Hamiltonian (2.7). By direct inspection we find that the states  $|+\rangle = |\uparrow\uparrow\rangle$  and  $|-\rangle = |\downarrow\downarrow\rangle$  are already eigenstates with eigenvalues  $E_{\pm} = 1/4$ . The other eigenstates can be found by diagonalizing the remaining  $2 \times 2$  matrix, yielding

$$\begin{aligned} |s\rangle &= \frac{1}{\sqrt{2}} [|\uparrow\downarrow\rangle - |\downarrow\uparrow\rangle] \\ |t\rangle &= \frac{1}{\sqrt{2}} [|\uparrow\downarrow\rangle + |\downarrow\uparrow\rangle] \end{aligned}$$

with eigenvalues  $E_s = -3/4$  and  $E_t = 1/4$  respectively. The transformation matrix, to rotate to this new basis is simple given by the eigenvectors in columns as:

$$U = \begin{pmatrix} 1 & 0 & 0 & 0 \\ 0 & 1/\sqrt{2} & 1/\sqrt{2} & 0 \\ 0 & -1/\sqrt{2} & 1/\sqrt{2} & 0 \\ 0 & 0 & 0 & 1 \end{pmatrix}, \quad (2.17)$$

If we focus on the  $|s\rangle$  and  $|t\rangle$  states, we see that the  $2 \times 2$  rotation matrix is equivalent to the geometric rotation Eq. (2.15) with an angle  $\phi = -\pi/4$ :

$$\begin{aligned} \hat{e}'_1 &= \frac{1}{\sqrt{2}} \hat{e}_1 - \frac{1}{\sqrt{2}} \hat{e}_2 \\ \hat{e}'_2 &= \frac{1}{\sqrt{2}} \hat{e}_1 + \frac{1}{\sqrt{2}} \hat{e}_2 \end{aligned}$$

The full transformation occurs in a four-dimensional space, but the two vectors  $|+\rangle$  and  $|-\rangle$  are untouched. Same as in the geometric case, the transformation preserves the norm (it is unitary!), and angles between basis states (it is an orthogonal transformation!), and we can use the eigenvectors as a new basis in which the Hamiltonian is already diagonal. In the course of these lecture we shall use slightly more complicated rotations, in which the states are eigenstates of a different matrix, not necessarily the Hamiltonian.

Now, we found that we do not need the basis states  $|+\rangle$  and  $|-\rangle$  to obtain the ground-state. By discarding these two states we simplify the calculation by reducing a  $4 \times 4$  eigenvalue problem to a  $2 \times 2$  problem. If we knew in advance that the ground-state was in the subspace with  $S_{total}^z = 0$  we could have formulated the problem directly in this subspace. This is a “trivial” truncation: if we are interested in a state with particular values of the quantum numbers, and if the Hamiltonian does not mix subspaces with different quantum numbers/symmetries, we can “block diagonalize” the Hamiltonian in each subspace separately.

Notice that the geometric analogy consists, in terms of spins, in truncating the Hilbert space to just one basis state  $|s\rangle$  in this case, the eigenvector of the Hamiltonian with the lowest eigenvalue.

### 2.2.5 The Block Decimation Idea

Let us try a simple idea, using the recursion scheme described above. At every step in the recursion, we add one spin on the right, and our basis dimension grows by a factor 2. At some point during this recursion, the matrix will be too large to deal with. So let us fix a maximum number of states that we want to keep,  $m$ . At certain point during the process, the basis dimension will become larger than  $m$ . It is here that we start applying the truncation rule: diagonalize the Hamiltonian matrix exactly, and keep only the  $m$  states with *lowest* eigenvalues (see Fig. 2.4).

As the system grows, the basis of the left block changes as we rotate to the new basis of eigenstates of the Hamiltonian. This is done by using a unitary transformation  $U$ . This matrix  $U$  is nothing else but the matrix with the eigenstates ordered in columns. Therefore, adding a spin to the block now involves two steps: (i) we need to build the ‘tilde’ operators as before, and (ii) rotate the Hamiltonian matrix and the tilde operators to the new basis (Fig. 2.5).

Let us assume that our old block before adding a site has a basis  $\{|\alpha_{i-1}\rangle\}$ , of dimension  $D_{i-1}$ , and the site has a basis  $\{|s_i\rangle\}$  of dimension  $d$ . The new block basis  $\{|\alpha_{i-1}, s_i\rangle\}$  has dimension  $d \times D_{i-1}$ , such that we can easily diagonalize it to obtain all the eigenvalues and corresponding eigenvectors  $\{|\alpha_{i+1}\rangle\}$ . We build the matrix  $U$  as the  $D_{i-1} \times D_i$  unitary matrix with the  $D_i = m$  eigenvectors with largest eigenvalues in the columns:

$$U_{\alpha_{i-1}s_i, \alpha_i} = \langle \alpha_{i-1} s_i | \alpha_i \rangle. \quad (2.18)$$

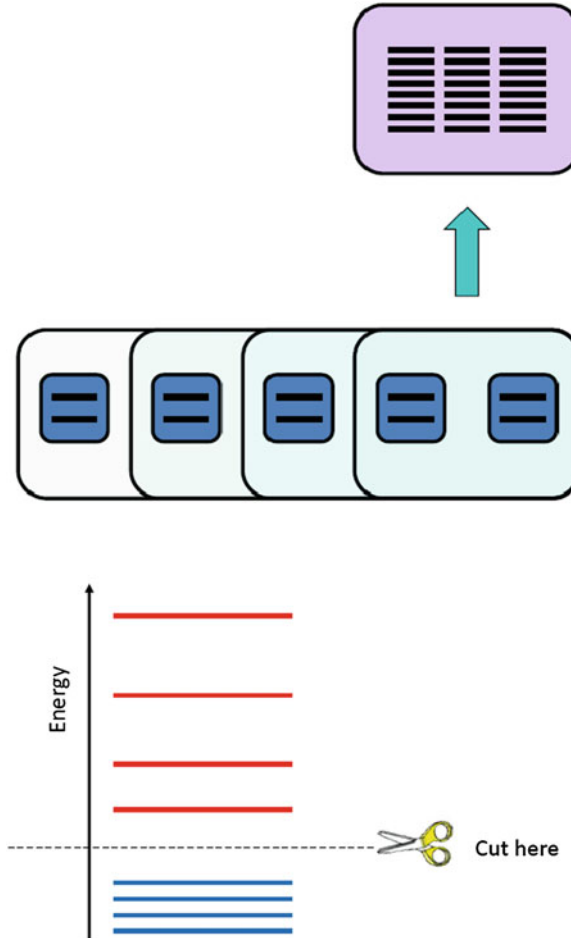


**Fig. 2.4** In the NRG scheme, we truncate the basis by keeping the  $m$  eigenstates of the Hamiltonian with the lowest eigenvalues

Before the rotation, the operators had matrix elements:

$$\tilde{O}_{\alpha_{i-1}s_i, \alpha'_{i-1}s'_i} = \langle \alpha_{i-1}s_i | \hat{O} | \alpha'_{i-1}s'_i \rangle. \quad (2.19)$$

We can now rotate all the tilde operators to the new basis as:

$$\begin{aligned} \tilde{O}_{\alpha_i, \alpha'_i} &= \langle \alpha_i | \hat{O} | \alpha'_i \rangle = \sum_{\alpha_{i-1}, s_i} \sum_{\alpha'_{i-1}, s'_i} \langle \alpha_i | \alpha_{i-1}s_i \rangle \langle \alpha_{i-1}s_i | \hat{O} | \alpha'_{i-1}s'_i \rangle \langle \alpha'_{i-1}s'_i | \alpha_i \rangle \\ &= \sum_{\alpha_{i-1}, s_i} \sum_{\alpha'_{i-1}, s'_i} (U^\dagger)_{\alpha_i, \alpha_{i-1}s_i} \tilde{O}_{\alpha_i, \alpha'_i} U_{\alpha'_{i-1}s'_i, \alpha'_i} \end{aligned} \quad (2.20)$$

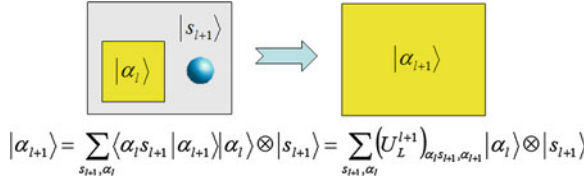


**Fig. 2.5** Adding a site to a block now involves a truncation and a change of basis

where the new matrices will have dimensions  $m \times m$ . we can now use these matrices to continue to block-growing process by adding another site. This can be repeated until the energy per site converges, or until we reach a desired system size.

It may seem that this new basis would be a natural choice is we assume that the physics of the problem is described by different manifolds with different energy scales. If we keep the lowest energy states and we get rid of the high energy states we can expect to get the low energy physics right. This in fact is the case in problems such as the Kondo and Anderson impurity problems [21]. However, in strongly correlated, many-body problems such as the Heisenberg chain, this scheme performs poorly.

## 2.3 The Density Matrix Truncation: The Kernel of the DMRG

The problem was solved by Steve White by using what he called the ‘density matrix truncation’. He realized (without knowing at the time) that instead of getting rid of high energy states, one has to redistribute the ‘entanglement’ and minimize the loss of information. However, the way he formulated the problem did not incorporate the idea of entanglement, a concept that entered the picture much later after quantum information ideas were used to understand why and when the DMRG actually works. Before introducing these ideas, we shall describe the original formulation of the density matrix truncation [6, 7].

In order to introduce this new concept, we are going to use a new scheme: We are going to use two blocks instead of one, a left block, and a right block, as shown in Fig. 2.6. We are going to grow both blocks simultaneously using the same procedure outlined previously: at every step we add one site at the right of the left block, and one site to the left of the right block. The ground state can then be written as:

$$|\Psi\rangle = \sum_{i,j} \Psi_{ij} |i\rangle |j\rangle, \quad (2.21)$$

where the sum runs over all the states of the left block  $|i\rangle$  and right block  $|j\rangle$ , with the corresponding coefficients  $\Psi_{ij}$ .

Now the idea is as follows: once we reach the desired basis dimension  $m$ , we shall rotate the left block to a new basis  $|i\rangle \rightarrow |\alpha\rangle$ . We want to pick these states  $|\alpha\rangle$  in such

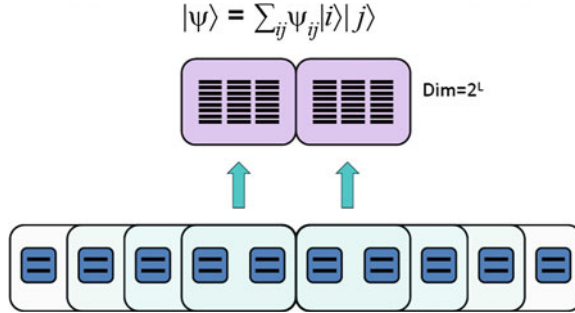


**Fig. 2.6** The DMRG modifies the NRG idea by adding a second block

a way that when we truncate the basis, the “distance” between the original ground state  $|\Psi\rangle$ , and the new, truncated, variational approximation  $|\tilde{\Psi}\rangle$ , is minimized:

$$S = \left| |\Psi\rangle - |\tilde{\Psi}\rangle \right|^2, \quad (2.22)$$

where

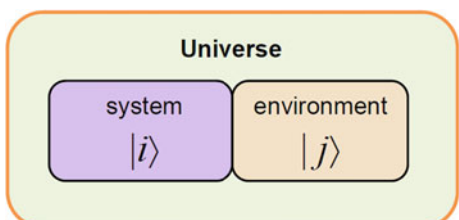
$$|\tilde{\Psi}\rangle = \sum_{\alpha=1}^m \sum_j \psi_{\alpha j} |\alpha\rangle |j\rangle. \quad (2.23)$$

We are going to anticipate the solution: pick the basis  $|\alpha\rangle$  given by the  $m$  eigenvectors of the reduced density matrix of the left block with the  $m$  largest eigenvalues. In order to justify this result, we first need to introduce some important concepts.

### 2.3.1 The Reduced Density Matrix

Imagine that we have a bipartite system, composed by subsystem  $A$  and subsystem  $B$ , as shown in Fig. 2.7. The Hilbert space of the system  $A + B$  will be given by the tensor product of the Hilbert spaces of the two subsystems:  $H_{A+B} = H_A \otimes H_B$ , and will have dimension  $D_{A+B} = D_A \times D_B$ . Assume that the state of our system is described by a normalized wave-function  $|\Psi\rangle$  that has support on  $H_{A+B}$ . We define

**Fig. 2.7** In the DMRG, one block acts as the environment for the second one



the reduced density matrix of subsystem  $A$  as

$$\hat{\rho}_A = \text{Tr}_B |\Psi\rangle\langle\Psi|. \quad (2.24)$$

Its corresponding matrix form is

$$\rho_{Aii'} = \langle i | \hat{\rho}_A | i' \rangle = \sum_j \langle ij | \Psi \rangle \langle \Psi | i' j \rangle = \sum_j \Psi_{ij} \Psi_{i'j}^* \quad (2.25)$$

This operator describes the density matrix of a mixed state, in which the system  $A$  is in contact with a bath or environment  $B$ . This is the price we have to pay for our ignorance of subsystem  $B$ .

The reduced density matrix has some nice properties:

- It is Hermitian (or symmetric in case of real matrices). This means that its eigenvalues are real.
- Its eigenvalues are non-negative.
- The trace equals to unity:  $\text{Tr} \rho_A = 1$ .
- Its eigenvectors  $|\alpha\rangle$  and eigenvalues  $\omega_\alpha$  form an orthonormal basis.

This means that the reduced density matrix can be re-defined in the new eigenvector basis as:

$$\hat{\rho}_A = \sum_\alpha \omega_\alpha |\alpha\rangle\langle\alpha|; \quad (2.26)$$

with  $\omega_\alpha \geq 0$  and  $\sum_\alpha \omega_\alpha = 1$ .

These same considerations are valid for the block  $B$ .

**Exercise:** Given a state  $|\Psi\rangle$  defined in  $A + B$ , show that the mean value of an observable  $\hat{O}_A$  acting on subsystem  $A$ , can be obtained as  $\langle \Psi | \hat{O}_A | \Psi \rangle = \text{Tr} \rho_A O_A$ .

### 2.3.2 The Singular Value Decomposition

Consider an arbitrary matrix  $\Psi$  of dimensions  $D_A \times D_B$ . One can prove that  $\Psi$  can be factorized as

$$\Psi = UDV^\dagger, \quad (2.27)$$

where  $U$  is a  $(D_A \times D_B)$  unitary matrix,  $V$  is a  $(D_B \times D_B)$  unitary matrix, and  $D$  is a  $(D_B \times D_B)$  diagonal matrix with real non-negative numbers along the diagonal, and zeroes elsewhere. Since  $U$  and  $V$  are unitary, they satisfy:

$$UU^\dagger = \mathbb{1};$$

$$V V^\dagger = \mathbb{1}.$$

Their columns are orthonormal vectors, so  $U$  and  $V$  can be regarded as rotation matrices. The diagonal matrix elements  $\lambda_\alpha$  of  $D$  are known as the “singular values” of  $\Psi$ .

### 2.3.3 The Schmidt Decomposition

Let us apply the SVD to our quantum wave-function  $|\Psi\rangle$  (2.21), and for illustration, let us assume that  $D_B \leq D_A$ . The coefficients  $\Psi_{ij}$  define a matrix  $\Psi$ . After a SVD, they can be re-written as:

$$\Psi_{ij} = \sum_{\alpha}^{D_B} U_{i\alpha} \lambda_{\alpha} (V^\dagger)_{\alpha j} = \sum_{\alpha}^{D_B} U_{i\alpha} \lambda_{\alpha} V_{\alpha j}^*. \quad (2.28)$$

The wave-function can now be expressed as:

$$\begin{aligned} |\Psi\rangle &= \sum_i^{D_A} \sum_j^{D_B} \sum_{\alpha}^{D_B} U_{i\alpha} \lambda_{\alpha} V_{\alpha j}^* |i\rangle |j\rangle \\ &= \sum_{\alpha}^{D_B} \left( \sum_i^{D_A} U_{i\alpha} |i\rangle \right) \lambda_{\alpha} \left( \sum_j^{D_B} V_{\alpha j}^* |j\rangle \right) \\ &= \sum_{\alpha}^{D_B} \lambda_{\alpha} |\alpha\rangle_A |\alpha\rangle_B, \end{aligned}$$

where we have defined the states  $|\alpha\rangle_A = \sum_i U_{i\alpha} |i\rangle$  and  $|\alpha\rangle_B = \sum_j V_{\alpha j}^* |j\rangle$ . Due to the properties of  $U$  and  $V$ , these states define a new orthogonal basis. This final expression is known as the “Schmidt decomposition” of the state  $\Psi$ , and the bases  $|\alpha\rangle$  as the “Schmidt bases”.

In general, we have that the state  $\Psi$  can be written in the new basis as:

$$|\Psi\rangle = \sum_{\alpha}^r \lambda_{\alpha} |\alpha\rangle_A |\alpha\rangle_B; \quad r = \min(D_A, D_B). \quad (2.29)$$

In the Schmidt basis, the reduced density matrices for the subsystems  $A$  and  $B$  are

$$\rho_A = \text{Tr}|\Psi\rangle\langle\Psi| = \sum_{\alpha} \lambda_{\alpha}^2 |\alpha\rangle_A \langle \alpha|, \quad (2.30)$$

and

$$\rho_B = \sum_{\alpha} \lambda_{\alpha}^2 |\alpha\rangle_B \langle \alpha| \quad (2.31)$$

At this point, we realize some interesting observations:

- The eigenvalues of the reduced density matrices are  $\omega_{\alpha} = \lambda_{\alpha}^2$ , the square of the singular values.
- The two reduced density matrices share the spectrum.
- The Schmidt bases are the eigenvectors of the reduced density matrices.

### 2.3.4 Optimizing the Truncated Wave-Function

We here go back to the original problem of optimizing the wave-function in a reduced basis. In order to solve it, we are going to reformulate the question as: Given a matrix  $\Psi$ , what is the optimal matrix  $\tilde{\Psi}$  with fixed rank  $m$  that minimizes the Frobenius distance between the two matrices? It turns out, this is a well known problem called the “low ranking approximation”.

If we order the eigenvalues of the reduced density matrix in decreasing order  $\omega_1, \omega_2, \dots, \omega_m, \dots, \omega_r$ , it is straightforward to see that the Frobenius distance between the two matrices is given by

$$S = \left| \Psi - \tilde{\Psi} \right|^2 = \sum_{m+1}^r \omega_i \quad (2.32)$$

This proves that the optimal basis is given by the eigenvectors of the reduced density matrix with the  $m$  largest eigenvalues.

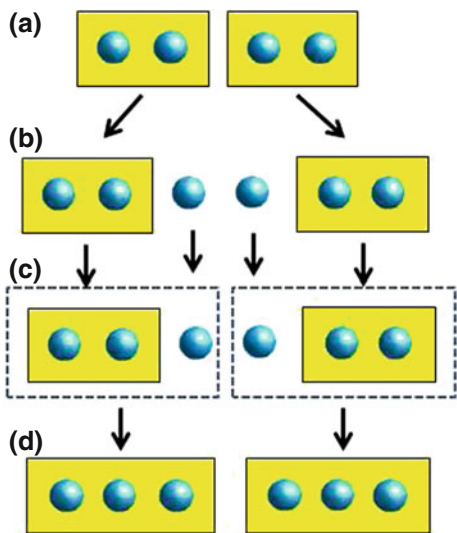
## 2.4 Infinite-Size DMRG

The above considerations allow us now to introduce the DMRG algorithm in a very natural way. We are going to present it in the traditional formulation, starting with the infinite-size algorithm, followed by the finite-size scheme.

The main idea behind the infinite-size algorithm consists in growing the left and right blocks by adding one site at a time. As we add sites, the basis of the blocks will grow, until we reach the desired maximum number of states  $m$ . At this point we need to start applying the density matrix truncation on both blocks. This process is repeated until we reach a desired system-size, or the error in the energy is below a pre-defined tolerance.

The algorithm illustrated in Fig. 2.8 could be outlined as below:

**Fig. 2.8** Step-by-step illustration of the block-growing scheme in the infinite-size DMRG algorithm: After obtaining the new blocks from the previous step (a), we add a new site to each block (b), we build the superblock and obtain the ground-state (c), and we calculate the reduced density-matrix, and rotate to the basis of the eigenvectors with  $m$  largest eigenvalues to build the new blocks for the next step (d)



- Build all the operator matrices for a single-site Hamiltonian, and the operators involved in the interactions between the site and the rest of the system.
- Start growing the blocks by adding single-sites, as outlined in the exact diagonalization section. We assume that the Hilbert space for the single site has dimension  $d$ .
- When the size of the blocks become larger than  $d \times m$ , we start applying the density matrix truncation as follows:
  1. Using a suitable library routine (Lanczos, Davidson), diagonalize the full Hamiltonian (sometimes called super-Hamiltonian) of the two blocks combined (sometimes referred to as superblock), to obtain the ground state  $|\Psi\rangle = \sum_{ij} \Psi_{ij} |i\rangle |j\rangle$ .
  2. Calculate the reduced density matrix of the left block, and right blocks. When the system is symmetric under reflections, we only need one of them.
  3. For each of the blocks, diagonalize the density matrix to obtain the full spectrum and eigenvectors.
  4. Truncate the basis by keeping only the  $m$  eigenvectors with the largest eigenvalues.
  5. Rotate the Hamiltonian and the operators involved in the interactions between blocks to the new basis.
  6. Add a new site to the left and right blocks, to build new blocks of dimension  $d \times m$ , and reiterate the diagonalization and truncation steps. Stop when we reach the desired system-size, or the error in the energy is below a pre-defined tolerance.

In the early days of DMRG it was assumed that this scheme would lead to a good approximation of the system properties in the thermodynamic limit. Today we know that the best way to reach the thermodynamic limit is by using the finite-size algorithm on systems of fixed length, and doing a careful finite-size analysis of the results.

Let us now explain some of these steps in more detail.

### 2.4.1 Adding a Single Site to the Block

Same as we did in the exact diagonalization section, we can add sites to the blocks by performing tensor products of the “tilde” operators on the block, and single-site operators.

Assume that we are in the  $i$ th iteration of the algorithm, with our left and right blocks having length  $i$ . Let us label our  $D_L$  basis states for the left block  $\{|\alpha_i\rangle\}$ , and our  $d$  basis states for the single site that comes to the right  $\{|s_{i+1}\rangle\}$  (see Fig. 2.9). When we add the site to the block, we obtain a new basis for the new combined block as  $|\alpha_{i+1}\rangle = |\alpha_i\rangle \otimes |s_{i+1}\rangle$ .

Let us assume for illustration purposes that we are dealing once more with the Heisenberg chain. All these ideas can be easily generalized to arbitrary models. Same as we did in the exact diagonalization section, we obtain the new Hamiltonian matrix for the combined block as:

$$H_{L,i+1} = H_{L,i} \otimes \mathbb{1}_2 + \tilde{S}_{L,i}^z \otimes S^z + \frac{1}{2} \left( \tilde{S}_{L,i}^+ \otimes S^- + \tilde{S}_{L,i}^- \otimes S^+ \right). \quad (2.33)$$

In this expression, the “tilde” operators are in the  $|\alpha_i\rangle$  basis, while the others are defined in the single-site basis.

A similar expression applies to the right block, which is obtained from the single site at position  $i + 2$ , with basis  $\{|s_{i+2}\rangle\}$  and dimension  $d$ , and the right block with

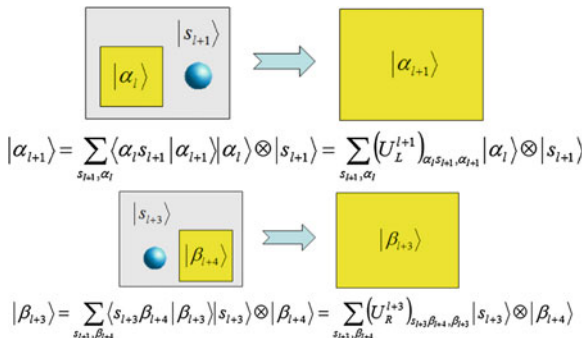


**Fig. 2.9** Adding sites to the blocks is done in the same way as in the NRG

basis  $\{|\beta_{i+3}\rangle\}$  and dimension  $D_R$ :

$$H_{R,i+2} = \mathbb{1}_2 \otimes H_{R,i+3} + S^z \otimes \tilde{S}_{R,i+3}^z + \frac{1}{2} (S^+ \otimes \tilde{S}_{R,i+3}^- + S^- \otimes \tilde{S}_{R,i+3}^+). \quad (2.34)$$

### 2.4.2 Building the Super-Hamiltonian

We now need to combine the left and right blocks to form the super-Hamiltonian:

$$\hat{H} = \hat{H}_{L,i+1} + \hat{H}_{R,i+2} + S_{i+1}^z S_{i+2}^z + \frac{1}{2} (S_{i+1}^+ S_{i+2}^- + S_{i+1}^- S_{i+2}^+) \quad (2.35)$$

where  $\hat{H}_{L(R)}$  where obtained above, and only involve terms in the left (right) block. The single sites at positions  $i+1$  and  $i+2$  were absorbed by the left and right blocks, respectively, so in order to build the interactions, we have to rotate the corresponding operators to the new basis of the blocks. This is again done in the same spirit of the “tilde” transformation:

$$\begin{aligned} H = & H_{L,i+1} \otimes \mathbb{1}_{D_R \times 2} + \mathbb{1}_{D_L \times 2} \otimes H_{R,i+2} \\ & + \mathbb{1}_{D_L} \otimes S^z \otimes S^z \otimes \mathbb{1}_{D_R} \\ & + \frac{1}{2} \mathbb{1}_{D_L} \otimes S^+ \otimes S^- \otimes \mathbb{1}_{D_R} \\ & + \frac{1}{2} \mathbb{1}_{D_L} \otimes S^- \otimes S^+ \otimes \mathbb{1}_{D_R} \end{aligned}$$

or:

$$\begin{aligned} H = & H_{L,i+1} \otimes \mathbb{1}_{D_R \times 2} + \mathbb{1}_{D_L \times 2} \otimes H_{R,i+2} \\ & + \tilde{S}_{L,i+1}^z \otimes \tilde{S}_{R,i+2}^z \\ & + \frac{1}{2} \tilde{S}_{L,i+1}^+ \otimes \tilde{S}_{R,i+2}^- \\ & + \frac{1}{2} \tilde{S}_{L,i+1}^- \otimes \tilde{S}_{R,i+2}^+ \end{aligned}$$

### 2.4.3 Obtaining the Ground-State: Lanczos Diagonalization

Once we have a superblock matrix, we can apply a library routine to obtain the ground state of the superblock  $|\Psi\rangle$ . The two algorithms widely used for this purpose are the Lanczos and Davidson diagonalization. Both are explained to great extent in Ref. [18], so we refer the reader to this material for further information. In these notes we will briefly explain the Lanczos procedure.

The basic idea of the Lanczos method [22, 23] is that a special basis can be constructed where the Hamiltonian has a tridiagonal representation. This is carried out iteratively as shown below. First, it is necessary to select an arbitrary seed vector  $|\phi_0\rangle$  in the Hilbert space of the model being studied. If we are seeking the ground-state of the model, then it is necessary that the overlap between the actual ground-state  $|\psi_0\rangle$ , and the initial state  $|\phi_0\rangle$  be nonzero. If no “a priori” information about the ground state is known, this requirement is usually easily satisfied by selecting an initial state with *randomly* chosen coefficients in the working basis that is being used. If some other information of the ground state is known, like its total momentum and spin, then it is convenient to initiate the iterations with a state already belonging to the subspace having those quantum numbers (and still with random coefficients within this subspace).

After  $|\phi_0\rangle$  is selected, define a new vector by applying the Hamiltonian  $\hat{H}$ , over the initial state. Subtracting the projection over  $|\phi_0\rangle$ , we obtain

$$|\phi_1\rangle = \hat{H}|\phi_0\rangle - \frac{\langle\phi_0|\hat{H}|\phi_0\rangle}{\langle\phi_0|\phi_0\rangle}|\phi_0\rangle, \quad (2.36)$$

that satisfies  $\langle\phi_0|\phi_1\rangle = 0$ . Now, we can construct a new state that is orthogonal to the previous two as,

$$|\phi_2\rangle = \hat{H}|\phi_1\rangle - \frac{\langle\phi_1|\hat{H}|\phi_1\rangle}{\langle\phi_1|\phi_1\rangle}|\phi_1\rangle - \frac{\langle\phi_1|\phi_1\rangle}{\langle\phi_0|\phi_0\rangle}|\phi_0\rangle. \quad (2.37)$$

It can be easily checked that  $\langle\phi_0|\phi_2\rangle = \langle\phi_1|\phi_2\rangle = 0$ . The procedure can be generalized by defining an orthogonal basis recursively as,

$$|\phi_{n+1}\rangle = \hat{H}|\phi_n\rangle - a_n|\phi_n\rangle - b_n^2|\phi_{n-1}\rangle, \quad (2.38)$$

where  $n = 0, 1, 2, \dots$ , and the coefficients are given by

$$a_n = \frac{\langle\phi_n|\hat{H}|\phi_n\rangle}{\langle\phi_n|\phi_n\rangle}, \quad b_n^2 = \frac{\langle\phi_n|\phi_n\rangle}{\langle\phi_{n-1}|\phi_{n-1}\rangle}, \quad (2.39)$$

supplemented by  $b_0 = 0$ ,  $|\phi_{-1}\rangle = 0$ . In this basis, it can be shown that the Hamiltonian matrix becomes,

$$H = \begin{pmatrix} a_0 & b_1 & 0 & 0 & \dots \\ b_1 & a_1 & b_2 & 0 & \dots \\ 0 & b_2 & a_2 & b_3 & \dots \\ 0 & 0 & b_3 & a_3 & \dots \\ \vdots & \vdots & \vdots & \vdots & \ddots \end{pmatrix} \quad (2.40)$$

i.e. it is tridiagonal as expected. Once in this form the matrix can be diagonalized easily using standard library subroutines. However, note that to diagonalize com-

pletely a Hamiltonian on a finite cluster, a number of iterations equal to the size of the Hilbert space (or the subspace under consideration) are needed. In practice this would demand a considerable amount of CPU time. However, one of the advantages of this technique is that accurate enough information about the ground state of the problem can be obtained after a small number of iterations (typically of the order of  $\sim 100$  or less).

Another way to formulate the problem is by obtaining the tridiagonal form of the Hamiltonian starting from a Krylov basis, which is spanned by the vectors

$$\left\{ |\phi_0\rangle, \hat{H}|\phi_0\rangle, \hat{H}^2|\phi_0\rangle, \dots, \hat{H}^n|\phi_0\rangle \right\} \quad (2.41)$$

and asking that each vector be orthogonal to the previous two. Notice that each new iteration of the process requires one application of the Hamiltonian. Most of the time this simple procedure works for practical purposes, but care must be payed to the possibility of losing orthogonality between the basis vectors. This may happen due to the finite machine precision. In that case, a re-orthogonalization procedure may be required.

Notice that the new super-Hamiltonian matrix has dimensions  $D_L D_R d^2 \times D_L D_R d^2$ . This could be a large matrix. In state-of-the-art simulations with a large number of states, one does not build this matrix in memory explicitly, but applies the operators to the state directly in the diagonalization routine.

#### 2.4.4 Density Matrix Truncation and the Rotation to the New Basis

The truncation process is similar to the one use in numerical renormalization group, but instead of using the matrix of eigenvectors of the Hamiltonian, we use the eigenvectors  $\{|\alpha\rangle\}, \{|\beta\rangle\}$  of the left and right reduced density matrix. Therefore, the new basis states for the left and right block are related to the states in the previous step as:

$$\begin{aligned} |\alpha_{i+1}\rangle &= \sum_{s_{i+1}, \alpha_i} \langle \alpha_i s_{i+1} | \alpha_{i+1} \rangle |\alpha_i s_{i+1}\rangle = \sum_{s_{i+1}, \alpha_i} (U_L)_{\alpha_i s_{i+1}, \alpha_{i+1}} |\alpha_i s_{i+1}\rangle \\ |\beta_{i+2}\rangle &= \sum_{s_{i+2}, \beta_{i+3}} \langle s_{i+2} \beta_{i+3} | \beta_{i+2} \rangle |s_{i+2} \beta_{i+3}\rangle = \sum_{s_{i+2}, \beta_{i+3}} (U_R)_{s_{i+2} \beta_{i+3}, \beta_{i+2}} |s_{i+2} \beta_{i+3}\rangle \end{aligned} \quad (2.42)$$

where

$$(U_L)_{\alpha_i s_{i+1}, \alpha_{i+1}} = \langle \alpha_i s_{i+1} | \alpha_{i+1} \rangle \quad (2.43)$$

and

$$(U_R)_{s_{i+2} \beta_{i+3}, \beta_{i+2}} = \langle s_{i+2} \beta_{i+3} | \beta_{i+2} \rangle. \quad (2.44)$$

If we keep only  $m$  states, the matrices  $U_{L(R)}$  will have dimensions  $D_{L(R)}d \times m$ . If the basis had already been truncated in the previous step, then  $D_L(R) = m$ .

We can now use these transformations to obtain the matrix elements for all the operators in the new truncated basis. For instance, an operator acting on a site inside the left block will be transformed as:

$$\begin{aligned}
(\tilde{O}_{L,i+1})_{\alpha_{i+1}, \alpha'_{i+1}} &= \langle \alpha_{i+1} | \hat{O} | \alpha'_{i+1} \rangle \\
&= \sum_{\alpha_i, s_{i+1}} \sum_{\alpha'_i, s'_{i+1}} \langle \alpha_{i+1} | \alpha_i s_{i+1} \rangle \langle \alpha_i s_{i+1} | \hat{O} | \alpha'_i s'_{i+1} \rangle \langle \alpha'_i s'_{i+1} | \alpha'_{i+1} \rangle \\
&= \sum_{\alpha_i s_{i+1}} \sum_{\alpha'_i s'_{i+1}} (U_L^\dagger)_{\alpha_{i+1}, \alpha_i s_{i+1}} (\tilde{O}_{L,i})_{\alpha_i s_{i+1}, \alpha'_i s'_{i+1}} (U_L)_{\alpha'_i s'_{i+1}, \alpha'_{i+1}},
\end{aligned} \tag{2.45}$$

and a similar expression can be obtained for operators in the right block.

#### 2.4.5 Storing Matrices and States

In order to optimize memory usage and performance, we can use the symmetries of the model to store all the matrices in block form. We have already noticed in the two-spin example that we can store the Hamiltonian in block diagonal form, with each block corresponding to a well defined symmetry sector, or quantum number. We can do the same with all our operators, with the main difference being that they may not be diagonal. For instance, the  $\hat{S}^z$  operator is diagonal, meaning that it does not mix subspaces with different quantum numbers. The  $\hat{S}^+$  operator mixes subspaces with the quantum number  $S^z$  differing by +1. So we can label the blocks by a pair of quantum numbers or, since we know how the operator changes the quantum numbers, we can use a single index. In the code implementation, we can store the blocks as a list of matrices. The main drawback is that we need a lookup table to find a block with given quantum numbers, but this can be done very efficiently. Notice that this idea can be applied to Hamiltonians that conserve the quantum numbers: if the model mixes different subspaces, we may need to store the full matrix.

The same idea applies to the state vectors. We can store them in a list of arrays, or matrices, each corresponding to a subspace with well defined quantum numbers.

### 2.5 The Finite-Size DMRG

As we mentioned before, the proper way to reach the thermodynamic limit with DMRG is by studying finite systems and performing a finite-size analysis. In order to study finite system, a generalization of the above ideas needs to be applied. The finite-size DMRG (illustrated in Fig. 2.10) can be summarized as follows:

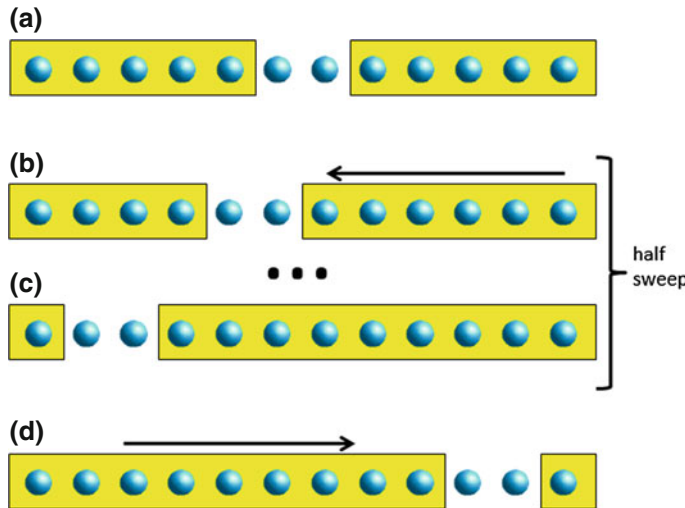


**Fig. 2.10** Schematic illustration of the finite-size DMRG algorithm: The infinite-size iteration stops when we reach the desired system size. Then, we start sweeping from left to right, and right to left. During the sweeping iterations, one block grows, and the other one “shrinks”. The shrinking block is retrieved from the blocks obtained in the previous sweep in the opposite direction, which are stored in memory or disk

- Run the infinite-size algorithm until the desired system size is reached. During this process, store all the left and right blocks, with their corresponding operators and basis transformations. This step is typically referred to as the “warmup”.
- Once the desired system size is reached we start performing “DMRG sweeps”, from right-to-left, and left-to-right to optimize the bases and improve accuracy. A left-to-right sweep is described as follows:
  1. Add a site to the left block using the same idea of the infinite-size DMRG. Since the total size of the system needs to be kept fixed, we need to “shrink” the right block. This is done by using the right block from the infinite-size step, or from the previous right-to-left sweep.
  2. Using a suitable library routine (Lanczos, Davidson), diagonalize the super Hamiltonian of the two blocks combined, same as for the infinite-size DMRG.
  3. Calculate the reduced density matrix of the left block.
  4. Diagonalize the density matrix to obtain the full spectrum and eigenvectors.
  5. Truncate the basis by keeping only the  $m$  eigenvectors with the largest eigenvalues.
  6. Rotate the Hamiltonian and the operators of the left block involved in the interactions between blocks to the new basis.

7. Iterate until reaching the far right end of the system, with a right block containing a single site. This completes the left-to-right sweep.
- Perform a right-to-left sweep, by growing the right block one site at a time, and using the left block from the previous left-to-right sweep.
  - Re-iterate the sweeping. Stop when the change in the energy is below a pre-defined tolerance. One typically stops at a point when both blocks have the same size, the “symmetric configuration”.

This sweeping process works in a similar fashion as a self-consistent loop, where we iteratively improve the solution. In fact, the DMRG can be formulated as a variational method, in which the variational parameters are continuously improved to minimize an energy functional. Intuitively a way to see it is by imagining a “demon” probing the environment around the block for the optimal states to improve the basis to represent the ground-state. These states are “absorbed” inside the block by the density matrix and its eigenvectors.

As described above, the shrinking block is replaced by the block from the previous sweep in the opposite direction. This means that all the information about the block and its operators needs to be stored, either in memory, or dumped on disk.

### ***2.5.1 Obtaining Quasi-Exact Results with the Finite-Size DMRG***

The DMRG accuracy is parametrized by a quantity called the “truncation error”, which is nothing but the residue of the trace of the density matrix after the truncation, Eq. (2.32). This is equal to the sum of the eigenvalues of the discarded states. How well the DMRG performs for a particular problem, and how many states we need to keep in order to achieve the desired accuracy will depend on the behavior of the eigenvalues of the density matrix, something that we will discuss in another section below. We say that the DMRG results are quasi-exact when the accuracy is strictly controlled by the truncation error, and can be improved by increasing the number of states kept  $m$ . However, even though the DMRG guarantees that we can obtain quasi-exact results, there are many other factors that need to be taken into account to make sure that the simulation has properly converged. Failing to do so may produce biased results. In order to avoid “mistakes” when using the DMRG, we should pay attention to the following:

- Applying the infinite-size DMRG to finite systems is not quasi-exact, and this has been the source of many mistakes in the past. Sweeping is an essential step in order to get accurate results, and multiple sweeps are typically required. A way to make sure that convergence is achieved is by looking at observables as we sweep, and making sure that they respect the symmetries of the problem. For instance, in a uniform spin chain, correlations from the end sites or the central sites should be

symmetric under reflections. Typically, observables do not converge as fast as the energy. Errors in the correlations tend to be higher than errors in the energy.

- A typical analysis of the results consists of looking at the behavior of the energy and observables as a function of the number of states kept  $m$ . Sometimes, in challenging situations that requires large numbers of states to converge, an extrapolation with  $m$  or the truncation error can be attempted.
- In cases where our computer power allows, we can typically guarantee well converged results by fixing the truncation error beforehand. We can ask the algorithm to automatically increase the number of states  $m$  such that the truncation error always lies within a tolerance.
- A finite-size scaling requires well converged results for every system size. Poor results for large system sizes can seriously bias the extrapolations and analysis.
- In some peculiar cases it may happen that the system gets trapped in a local minimum. This may occur for several reasons. A common one is doing the warmup or infinite-size sweep with too few states. This problem usually arises in calculations in momentum space, or with large barriers between energy manifolds, or in proximity to a first order first transition. A way to avoid this “sticking” problem is by adding a source of randomness in the density matrix that may induce the fluctuations necessary to escape the meta-stable state. Another possibility is by introducing fluctuations in some parameter of the model.
- Ultimately, the energy and ground-state are obtained by means of the Lanczos or Davidson diagonalization. It is essential that the diagonalization step is performed with an accuracy superior to the truncation error. Otherwise, the diagonalization errors will dominate over the truncation error, and the ground state will not have the expected accuracy, and may actually include a mixture of excited states (In fact, this may always happen to a certain extent, but a poor diagonalization may magnify the effects of the truncation).

### 2.5.2 Measuring Observables

Let us assume that we have a one-dimensional chain of certain length, and we want to measure correlations between observables acting on different sites,  $O_i$  and  $O'_j$ . Two cases can arise: (i) both sites are in separate blocks, or (ii) the two sites are inside the same block. Whether we find ourselves in situation (i) or (ii) will depend on the stage of the sweep. Sometimes we may find that the situation (i) will happen, and sometimes (ii). As we are going to see next, it is more convenient to measure the observables in case (i).

#### Operators in Separate Blocks

Let us assume a generic situation during the sweep where we find the two operators on separate blocks, as illustrated in Fig. 2.11. Let us denote the basis states for the

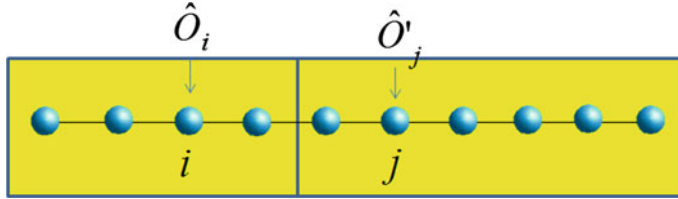


**Fig. 2.11** Setup for measuring observables acting on sites in separate blocks

left block as  $\{|\alpha\rangle\}$ , and for the right block as  $\{|\beta\rangle\}$ . The ground state wave-function will be given as:

$$|\Psi\rangle = \sum_{\alpha\beta} \langle\alpha\beta|\Psi\rangle |\alpha\beta\rangle = \sum_{\alpha\beta} \Psi_{\alpha\beta} |\alpha\beta\rangle. \quad (2.46)$$

It is easy to see that the correlation can be obtained as:

$$\begin{aligned} \langle \hat{O}_i \hat{O}'_j \rangle &= \langle \Psi | \hat{O}_i \hat{O}'_j | \Psi \rangle \\ &= \sum_{\alpha\beta, \alpha'\beta'} \Psi_{\alpha'\beta'}^* \Psi_{\alpha\beta} \langle \alpha' \beta' | \hat{O}_i \hat{O}'_j | \alpha \beta \rangle \\ &= \sum_{\alpha\beta, \alpha'\beta'} \Psi_{\alpha'\beta'}^* \Psi_{\alpha\beta} \langle \alpha' | \hat{O}_i | \alpha \rangle \langle \beta' | \hat{O}'_j | \beta \rangle \\ &= \sum_{\alpha\beta, \alpha'\beta'} \Psi_{\alpha'\beta'}^* \Psi_{\alpha\beta} (\tilde{O}_i)_{\alpha\alpha'} (\tilde{O}'_j)_{\beta\beta'}. \end{aligned} \quad (2.47)$$

## Operators in the Same Block

The situation with both operators in the same block is illustrated in Fig. 2.12. The proper way to calculate the correlations is by defining the composite product operator  $\hat{O}_{ij} = \hat{O}_i \hat{O}'_j$ . The correlation is then expressed as:

$$\begin{aligned} \langle \hat{O}_i \hat{O}'_j \rangle &= \langle \Psi | \hat{O}_i \hat{O}'_j | \Psi \rangle = \langle \Psi | \hat{O}_{ij} | \Psi \rangle \\ &= \sum_{\alpha\beta, \alpha'\beta'} \Psi_{\alpha'\beta'}^* \Psi_{\alpha\beta} \langle \alpha' | \hat{O}_{ij} | \alpha \rangle \langle \beta' | \beta \rangle \\ &= \sum_{\alpha\beta, \alpha'} \Psi_{\alpha'\beta}^* \Psi_{\alpha\beta} (\tilde{O}_{ij})_{\alpha\alpha'}. \end{aligned} \quad (2.48)$$

We clearly see that the composite operator has to be stored in the block, together with the individual operators. We need to represent it in the rotated basis the same as we do for the Hamiltonian when we do the truncation. Calculating this quantity

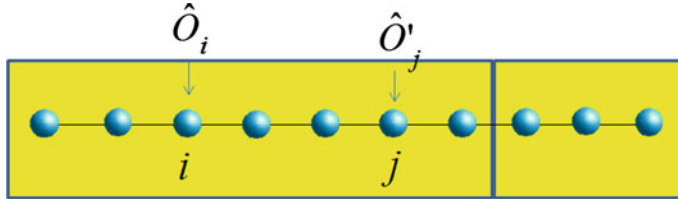


**Fig. 2.12** Setup for measuring observables acting on sites in the same block

as the product of two individual operators in the truncated basis is bad practice and should be avoided.

Clearly, storing and propagating the product operators for all pairs acting on sites  $i$  and  $j$  can be computationally very expensive. It is therefore convenient to store the individual operators, and calculate the correlations only when the operators are in separate blocks, as illustrated before.

### 2.5.3 Targeting States

It is important to point out that our basis has been optimized to accurately represent only the ground state. If we wanted to calculate other states, such as excited states, we need to build the density matrix using all these states as “target” states:

$$\rho = \sum_t w_t |\Psi_t\rangle \langle \Psi_t| \quad (2.49)$$

which is equivalent to the density matrix of a mixed state, with weights  $w_t$ , such that  $\sum_t w_t = 1$ . Finding a good combination of weights is a matter of trial and error, and it may depend on the particular problem. Generally, one picks all the weights to be equal.

When one targets multiple states, the number of DMRG states that we need to keep in order to represent them with enough accuracy grows in the same proportion.

### 2.5.4 Calculating Excited States

Sometimes we are interested in calculating excited states in sectors with different symmetry than the ground state. For instance, we may want to obtain the singlet-triplet gap by calculating the ground states in sectors with well defined total spin  $S = 0$  and  $S = 1$ . If we could use the symmetries of the Hamiltonian to be able to restrict our calculation to a sector with well-defined quantum numbers, then this should not be a problem. In these notes we are leaving the discussion on the use of

symmetries aside for the moment. So the problem now is to obtain the excited states, regardless of their quantum numbers. In this case we apply a simple trick that is also used in exact diagonalization calculations: At every step during the simulation, we target the ground state  $|\Psi\rangle$  of the Hamiltonian of interest  $\hat{H}$ , and the ground state  $|\Psi_1\rangle$  of the modified Hamiltonian:

$$\hat{H}' = \hat{H} + \Lambda |\Psi\rangle\langle\Psi|. \quad (2.50)$$

We have introduced a projector on the ground state that shifts its energy by an amount proportional to a constant  $\Lambda$ , that we pick to be sufficiently large. As a result, the ground state will be shifted in energy to the top of the spectrum, leaving the first excited state as the new ground state. As we explained before, in order to accurately represent both states, we need to use the density matrix:

$$\rho = \frac{1}{2}|\Psi\rangle\langle\Psi| + \frac{1}{2}|\Psi_1\rangle\langle\Psi_1|. \quad (2.51)$$

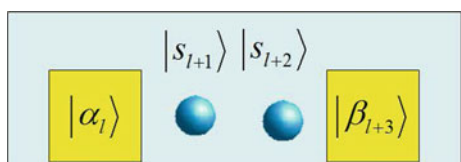
### 2.5.5 Wave-Function Prediction

At every step of the sweep we find that we have to obtain the ground-state of the Hamiltonian using some suitable diagonalization routine (Lanczos, Davidson). These algorithms converge iteratively to the ground-state, typically starting from some random seed. Depending on the accuracy wanted, one would have to perform a number of iterations, say between 20 and 100, applying the Hamiltonian to a new state at every iteration, until convergence is achieved. White [24] realized that the process could be sped up if we use the ground state from the previous step in the sweeping, as a starting seed for the diagonalization. All one would have to do is transform the old ground-state to the new basis. This process is usually referred to as “wave-function prediction” or “wave-function transformation”.

We assume we obtained the ground-state of our Hamiltonian, which before the change of basis is written as (see Fig. 2.13):

$$|\Psi\rangle = \sum_{\alpha_i, s_{i+1}, s_{i+2}, \beta_{i+3}} \langle \alpha_i s_{i+1} s_{i+2} \beta_{i+3} | \Psi \rangle | \alpha_i s_{i+1} s_{i+2} \beta_{i+3} \rangle \quad (2.52)$$

**Fig. 2.13** Four blocks used to represent the ground-state wave-function for the wave-function transformation



After the change of basis, we add a site to the left block, and we “spit out” one from the right block:

$$|\Psi\rangle = \sum_{\alpha_{i+1}, s_{i+2}, s_{i+3}, \beta_{i+4}} \langle \alpha_{i+1} s_{i+2} s_{i+3} \beta_{i+4} | \Psi \rangle |\alpha_{i+1} s_{i+2} s_{i+3} \beta_{i+4}\rangle \quad (2.53)$$

After some algebra, and assuming that  $\sum_{\alpha_i} |\alpha_i\rangle\langle\alpha_i| \approx 1$  and  $\sum_{\beta_i} |\beta_i\rangle\langle\beta_i| \approx 1$  after the truncation, one can readily obtain:

$$\begin{aligned} \langle \alpha_{i+1} s_{i+2} s_{i+3} \beta_{i+4} | \Psi \rangle &\approx \sum_{\alpha_i, s_{i+1} \beta_{i+3}} \langle \alpha_{i+1} | \alpha_i s_{i+1} \rangle \langle s_{i+3} \beta_{i+4} | \beta_{i+3} \rangle \langle \alpha_i s_{i+1} s_{i+2} \beta_{i+3} | \Psi \rangle \\ &= \sum_{\alpha_i, s_{i+1} \beta_{i+3}} (U_L^\dagger)_{\alpha_{i+1}, \alpha_i s_{i+1}} (U_R)_{s_{i+3} \beta_{i+4}, \beta_{i+3}} \langle \alpha_i s_{i+1} s_{i+2} \beta_{i+3} | \Psi \rangle \end{aligned} \quad (2.54)$$

This operation has relatively little computational cost, especially after considering that it will reduce the ground-state calculation to just a few Lanczos or Davidson iterations.

### 2.5.6 Generalization to Higher Dimensions and Complex Geometries

The DMRG method was originally introduced to study one dimensional systems. However, it can be extended to higher dimensions in a very straightforward way [25, 26]. Consider for simplicity a system of orbitals in a rectangular arrangement, as shown in Fig. 2.14, with first neighbor interactions, only. We can draw an imaginary path that scans through the lattice following a “snake”-like pattern. We can stretch the snake by putting all the orbitals aligned in a one-dimensional arrangement, and we obtain a system that we can study with the conventional DMRG. There is, however, a price tag to this simplification: the interactions now have long-range.

Other possible solutions have been explored in the literature. For instance, one could choose a vertical band composed by several sites along the  $y$  direction, and use the one-dimensional scheme in this super-site basis [27]. Another possibility is to use a different snake-like path that still adds one site at a time, but scans through the lattice more symmetrically [28]. Whatever the preferred solution is, in two-dimensional systems we always find the same barrier: entanglement grows with the size of the boundaries between left and right blocks. This affects the behavior of the density matrix spectrum, and as it turns out, we need to keep more DMRG states to achieve good results. The justification for this behavior will be explained in the following sections. For now, we simply point out that using “cylindrical” boundary conditions, with open boundary conditions along the  $x$  direction, and periodic along  $y$ , is the preferred setup for two-dimensional problems.

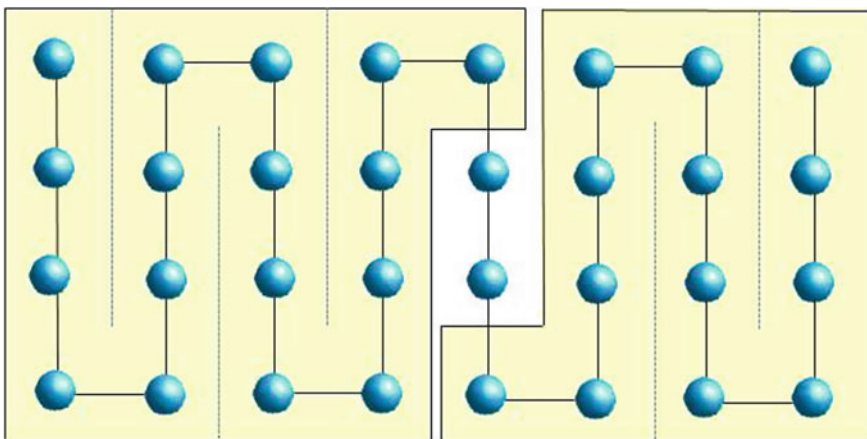


**Fig. 2.14** Generalizing the DMRG to 2d implies defining a one-dimensional path through the lattice

## 2.6 When and Why Does the DMRG Work?

While experimenting with the newly discovered method, Steve White noticed systems with periodic boundary conditions were ill-behaved: in order to achieve a given accuracy for a simple one-dimensional model with periodic boundary conditions would require, for instance  $O(10^4)$  states, while for the case of open boundary conditions, one could get away with just a fraction of those, say  $O(10^2)$ . He experimented with several approaches, but in the end, it seemed as though the only way to deal with this situation was by brute force, keeping lots of states. The reason for these different behaviors was somewhat a mystery, and it remained so until recently, when the quantum information community started exploring algorithms for simulating quantum many body problems (similar to the DMRG) [29, 30], and this behavior was finally understood. These ideas rely on the concept of “quantum entanglement” [31–33], and understanding how much information is needed to represent a quantum state faithfully can be quantified in terms of an “entanglement entropy” [34]. Quantum information could now explain why certain systems behaved in a certain way, depending on the geometry and topology of the lattice, by understanding the behavior of the spectrum of the reduced density matrices.

### 2.6.1 Entanglement

Entanglement is a property of quantum mechanical states composed of two or more “objects”: since in quantum mechanics the state of a system can be described as a linear superposition of basis states, we find that most of the time, we cannot describe

the state of an object, or a part of the system, without knowledge of the rest. To illustrate this idea let us consider the simple case of two spins, and assume there state can be described as:

$$|\Psi\rangle = |\uparrow\uparrow\rangle + |\uparrow\downarrow\rangle + |\downarrow\uparrow\rangle + |\downarrow\downarrow\rangle \quad (2.55)$$

We can readily see that this is equivalent to

$$\Psi\rangle = (|\uparrow\rangle + |\downarrow\rangle) \otimes (|\uparrow\rangle + |\downarrow\rangle) \quad (2.56)$$

Therefore, even though we started from a state that seemed to have a complicated structure, we found that in reality the two spins are not entangled: their wave-function can be written as the product of the states of the two individual spins. The two spins carry information individually, and knowing the state of one spin, does not tell us anything about the state of the second spin.

Instead, the following wave-function

$$|\Psi\rangle = |\uparrow\downarrow\rangle + |\downarrow\uparrow\rangle \quad (2.57)$$

cannot be separated: if we look at one spin, and it is pointing in one direction, we know that the other spin will be pointing in the opposite direction. In fact, for this particular example, the state of one spin carries *all* the information about the state of the second spin. We are going to see later that this case is referred to as the “maximally entangled” state of the two spins.

### 2.6.2 Entanglement and the Schmidt Decomposition

Let us assume that we define a partition in our system into parts  $A$  and  $B$ , same as we have been doing it all along during our discussion. The generic state of our system can be expressed, once more, as:

$$|\Psi\rangle = \sum_{ij} \Psi_{ij} |i\rangle |j\rangle, \quad (2.58)$$

where the states  $\{|i\rangle\}$  and  $\{|j\rangle\}$  live on parts  $A$  and  $B$ , and have dimensions  $D_A$  and  $D_B$ , respectively. This means that in order to describe the problem we need to know  $D_A \times D_B$  complex coefficients.

Let us re-formulate the original DMRG premise: Can we simplify this state by changing to a new basis? And... what do we mean by “simplifying” the state, anyway?

We have seen, that through a SVD decomposition, we can re-write the state as:

$$|\Psi\rangle = \sum_{\alpha}^r \lambda_{\alpha} |\alpha\rangle |\alpha\rangle \quad (2.59)$$

where  $r = \min(D_A, D_B)$ ,  $\lambda_{\alpha} \geq 0$ , and the states  $\{|\alpha\rangle_A\}$  and  $\{|\alpha\rangle_B\}$  form an orthogonal basis for the subsystems.

We notice right away, that if the Schmidt rank  $r = 1$ , then the wave-function reduces to a product state, “disentangling” the two subsystems.

How accurately or faithfully we will be able to represent the state by truncating the basis, will clearly depend on the behavior of the Schmidt coefficients  $\lambda_{\alpha}$ . If we recall that these are related to the eigenvalues of the reduced density matrices as  $\omega_{\alpha} = \lambda_{\alpha}^2$ , we conclude that the efficiency of the DMRG will be completely determined by the spectrum of the reduced density matrices, the so-called “entanglement spectrum”:

- If the eigenvalues decay very fast (exponentially, for instance), then we introduce little error by discarding the smaller ones.
- Few coefficients mean less entanglement. In the extreme case of a single non-zero coefficient, the wave-function is a product state and completely disentangled.
- The same way NRG minimizes the energy... DMRG minimizes the loss of information! The closer the state resembles a product state, the more efficient our truncation will be. Let us be clear, the amount of entanglement is in reality always the same, but when we rotate to a new basis, we pick it in such a way that the Schmidt coefficients are concentrated in as few states as possible, so we can discard the rest with a minimum loss of information.

### 2.6.3 Quantifying Entanglement

In order to quantify the entanglement, we define a quantity called the “entanglement entropy”. There are many definition, we shall pick the so called “von Neumann entanglement entropy”:

$$S = - \sum_{\alpha} \lambda_{\alpha}^2 \log \lambda_{\alpha}^2. \quad (2.60)$$

Or, in terms of the reduced density matrix:

$$S = -\text{Tr}(\rho_A \log \rho_A) = -\text{Tr}(\rho_B \log \rho_B). \quad (2.61)$$

To illustrate what this quantity represents, let us look again at the normalized state:

$$|\Psi\rangle = \frac{1}{\sqrt{2}} [|\uparrow\downarrow\rangle + |\downarrow\uparrow\rangle]. \quad (2.62)$$

We can obtain the reduced density matrix for the first spin, by tracing over the second spin

$$\rho = \begin{pmatrix} 1/2 & 0 \\ 0 & 1/2 \end{pmatrix} \quad (2.63)$$

We say that the state is “maximally entangled” when the reduced density matrix is proportional to the identity. The entanglement entropy in this case is:

$$S = -\frac{1}{2} \log \frac{1}{2} - \frac{1}{2} \log \frac{1}{2} = \log 2. \quad (2.64)$$

In general, if the rank of the Schmidt decomposition is  $r = \min(D_A, D_B)$ , then the entanglement spectrum will be  $\omega_\alpha = 1/r$ , and the entanglement entropy of the maximally entangled state will be  $S = \log r$ .

If the state is a product state:

$$|\Psi\rangle = |\alpha\rangle|\beta\rangle. \quad (2.65)$$

All the eigenvalues of the reduced density matrices will be  $\omega_\alpha = 0$  except for one  $\omega_1 = 1$ , and the entanglement entropy will be  $S = 0$ .

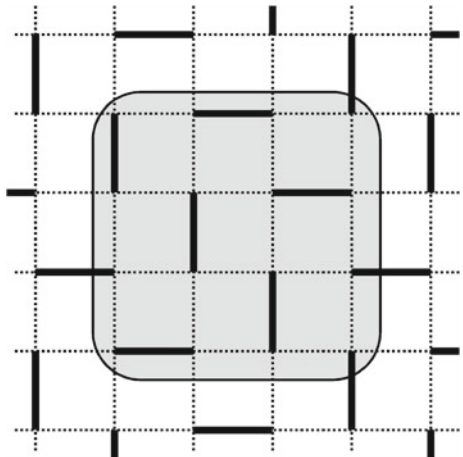
## 2.6.4 The Area Law

We know understand how to quantify the accuracy of the DMRG in terms of entanglement. What we still do not understand is why the DMRG performs so well in one-dimensional cases, and not so-well in two dimensions, and in systems with periodic boundary conditions. We can see that these issues have to be somehow related to the behavior of the entanglement spectrum, and there must be something that makes it behave in a particular way for some problems.

The study of the entanglement properties of quantum systems is a relatively new subject. It has recently become very relevant in condensed matter due to its ability to characterize quantum many body systems. As it turns out, it can be shown that the ground states of certain Hamiltonians, under certain conditions, obey what is called “area laws” for the entanglement entropy [35]. That is why the entanglement entropy is sometimes also called “geometric entropy”. This is now a topic of intense research and in these nodes we shall only described the main ideas in a qualitative way.

Consider the ground-state of a local Hamiltonian (with interactions limited to close neighbors). In two spacial dimensions, that is pictorially shown in Fig. 2.15. This state represents what is commonly known as a valence bond solid, in which some bonds form strong singlets (2.57). These singlets are represented in the figure by thick lines. Let us now draw an imaginary partition, as shown with the gray shaded area. The boundary lines will cut a number of singlets, proportional to the length, or perimeter of the partition. Since we know that the entanglement entropy between two spins forming a singlet is  $\log(2)$ , we conclude that the entanglement entropy between the enclosed region and the outside will be

**Fig. 2.15** Schematic representation of a valence bond solid. Thick lines represent singlets



$$S = \log(2) \times (\# \text{ of bonds cut}) \approx L \log(2) \quad (2.66)$$

Hence, the entanglement entropy is proportional to the area of the boundary separating both regions. This is the prototypical behavior of gaped systems, which we illustrate with this simple example [36]. The same ideas can be generalized to other contexts. Notice that this means that in *gaped* one-dimensional systems, the entanglement entropy between two pieces, left and right, is independent of the size of the partition (again, we are referring to models with short range interactions).

It can be shown using conformal field theory arguments [37, 38], that the entanglement entropy of *critical* (gapless) one-dimensional system with periodic boundary conditions obeys the law:

$$S \sim \frac{c}{3} \log(L) \quad (2.67)$$

where  $c$  is the “central charge” of the system, a measure of the number of gapless modes. For the case of open boundary conditions, a similar expression is obtained:

$$S \sim \frac{c}{6} \log(L) \quad (2.68)$$

The factor 2 arises from the simple fact that a system with periodic boundary conditions has *two* boundaries, compared to one in the case of open boundary conditions.

In general, most systems obey the area law, with some exceptions such as free fermions, or fermionic systems with a 1D Fermi surface [39–42].

### 2.6.5 Entanglement and the DMRG

In general, the number of DMRG state that we need to keep to represent a state is related to the entanglement entropy between the two blocks as [34, 43]:

$$m \approx \exp(S) \quad (2.69)$$

Therefore, we can predict the behavior or the algorithm for certain classes of systems:

- Gaped systems in 1D:  $m = \text{const.}$
- Critical systems in 1D:  $m \approx L^\alpha$ .
- Gaped systems in 2D:  $m = \exp(L)$ .
- Periodic boundary conditions in 1D: we need to keep the square of the states needed for open boundary conditions, since the boundary area is now doubled.

These rules of thumb give an idea of the computational cost of a simulation. However, the entanglement entropy is not the only factor that determines the behavior of the DMRG, but also the internal structure of the wave function which has the form of a matrix product state [10–13, 44]. This will be discussed in detail in a separate chapter of the book.

## 2.7 Outlook: DMRG and Tensor Network Methods

With the advent of matrix product state algorithms, and quantum information ideas, we have seen a remarkable progress in the computational field. A repeated question that arises is whether the variational approaches using MPS are more efficient, or “better” than conventional DMRG. The short answer is “not necessarily”. If one is interested in studying one-dimensional problems, all methods are basically equivalent. One may argue that MPS algorithms work better for periodic boundary conditions [45, 46], but the drawback is that the implementation of the MPS code suffers from normalization problems that may lead to some instabilities. It is possible to reformulate the DMRG as an MPS optimization code [47], that may lead to a hybrid solution. What is certain is that most of the people that have been working with the DMRG for decades, have very polished, optimized, state-of-the-art codes that are hard to beat with existent MPS codes. However, progress is rapidly being made, and ultimately, it may become a matter of taste. DMRG may be easier to generalize to arbitrary Hamiltonians, and general purpose codes exist and are freely available, such as the ALPS DMRG code [48–50]. On the other hand, MPS’s enjoy several advantages that in the end may make them the favorite choice: They are probably easier to understand intuitively; one only has to store local matrices; the structure of the wavefunction is easy to deal with algebraically; they are easy to extend to the thermodynamic limit in translational invariant problems [51–54]; overlaps between MPS’s are easy to calculate; and most importantly, the MPS structure makes them more suitable for massive parallelization, especially for time-evolution [55–57].

MPS's are extremely powerful objects, and we have been learning a great deal about entanglement [43], complexity [58–60], and the structure of the quantum world through them [61]. The concept can readily be extended to higher dimensions, with matrices being replaced by tensors, leading to complex structures: tensor networks. Several ideas exploiting tensor networks have been proposed, such as PEPS (projected entangled pair states) [54] and MERA (multi-scale entanglement renormalization ansatz) [62–65], with very promising results. However, until recent work [66], DMRG has always been more efficient at studying 2D problems [67]. The main reason for this is, once more, the lack of highly optimized code to deal with the tensor contractions in PEPS, which is a complex computational problem [68–70], and in the case of MERA, with the explicit breaking of the translational symmetry. But again, progress is rapidly being made, and we can anticipate a new wave of computational methods based on tensor network methods.

## References

1. F.D.M. Haldane, Phys. Lett. **80A**, 281 (1980)
2. T.C. Choy, Phys. Lett. **80A**, 49 (1980)
3. See also S.R. Manmana et al., Phys. Rev. A **84**, 043601 (2011)
4. R.B. Laughlin, Phys. Rev. Lett. **50**, 1395 (1983)
5. R. Schrieffer, *Theory of Superconductivity*, Advanced Books Classics (Perseus, Chicago, 1999)
6. S.R. White, Phys. Rev. Lett. **69**, 2863 (1992)
7. S.R. White, Phys. Rev. B **48**, 10345 (1993)
8. K.G. Wilson, Rev. Mod. Phys. **47**, 773 (1975)
9. R. Bulla, T.A. Costi, T. Pruschke, Rev. Mod. Phys. **80**, 395 (2008)
10. S. Ostlund, S. Rommer, Phys. Rev. Lett. **75**, 3537 (1995)
11. S. Rommer, S. Ostlund, Phys. Rev. B **55**, 2164 (1997)
12. H.A. Kramers, G.H. Wannier, Phys. Rev. **60**, 263 (1941)
13. R.J. Baxter, J. Math. Phys. **9**, 650 (1968)
14. I. Peschel, X. Wang, M. Kaulke, K. Hallberg (eds.), *Density-Matrix Renormalization—A New Numerical Method in Physics: Lectures of a Seminar and Workshop held at the Max-Planck-Institut für Physik*, Lecture Notes in Physics (Springer, Berlin, 1999)
15. U. Schollwöck, Rev. Mod. Phys. **77**, 259 (2005)
16. K. Hallberg, Density matrix renormalization: a review of the method and its applications, in *Theoretical Methods for Strongly Correlated Electrons*, CRM Series in Mathematical Physics, ed. by D. Senechal, A.-M. Tremblay, C. Bourbonnais (Springer, New York, 2003)
17. K. Hallberg, Adv. Phys. **55**, 477 (2006)
18. R.M. Noack, S.R. Manmana, Proceedings of the “IX. Training course in the physics of correlated electron systems and high-Tc superconductors”, Vietri sul Mare (Salerno, Italy, October 2004), AIP Conf. Proc. **789**, 93 (2005)
19. G. De Chiara, M. Rizzi, D. Rossini, S. Montangero, J. Comput. Theor. Nanosci. **5**, 1277 (2008)
20. A.E. Feiguin, Proceedings of the “XV. Training course in the physics of correlated electron systems”, Vietri sul Mare (Salerno, Italy, October 2010), AIP Conf. Proc. **1419**, 5 (2011)
21. A.C. Hewson, *The Kondo Problem to Heavy Fermions* (Cambridge University Press, Cambridge, 1997)
22. C. Lanczos, J. Res. Natl. Bur. Stand. **45**, 255 (1950)
23. D.G. Pettifor, D.L. Weaire (eds.), *The Recursion Method and Its Applications*, Springer Series in Solid State Sciences, vol. 58 (Springer, Berlin, 1985)

24. S.R. White, Phys. Rev. Lett. **77**, 3633 (1996)
25. R.M. Noack, S.R. White, D.J. Scalapino, The density-matrix renormalization group for fermion systems, in *Computer Simulations in Condensed Matter Physics*, vol. VII, ed. by D.P. Landau, K.K. Mon, H.B. Schüttler (Springer, Heidelberg, 1994), UCI-CMTHE-94-03
26. S. Liang, H. Pang, Europhys. Lett. **32**, 173 (1995)
27. M.S.L. du Croo de Jongh, J.M.J. van Leeuwen, Phys. Rev. B **57**, 8494 (1998)
28. T. Xiang, J.Z. Lou, Z.B. Zu, Phys. Rev. B **64**, 104414 (2001)
29. G. Vidal, Phys. Rev. Lett. **91**, 147902 (2003)
30. G. Vidal, Phys. Rev. Lett. **93**, 040502 (2004)
31. M.B. Plenio, S. Virmani, Quantum Inf. Comput. **7**, 1 (2007)
32. L. Amico, R. Fazio, A. Osterloh, V. Vedral, Rev. Mod. Phys. **80**, 517 (2008)
33. R. Horodecki, P. Horodecki, M. Horodecki, K. Horodecki, Rev. Mod. Phys. **81**, 865 (2009)
34. F. Verstraete, J.I. Cirac, Phys. Rev. B **73**, 094423 (2006)
35. J. Eisert, M. Cramer, M.B. Plenio, Rev. Mod. Phys. **82**, 277 (2010)
36. M.B. Hastings, J. Stat. Mech.: Theory Exp. **2007**, P08024 (2007)
37. P. Calabrese, J. Cardy, J. Stat. Mech.: Theory Exp. **2004**, P06002 (2004)
38. P. Calabrese, J. Cardy, Int. J. Quantum Inf. **4**, 429 (2006)
39. M.M. Wolf, Phys. Rev. Lett. **96**, 010404 (2006)
40. D. Gioev, I. Klich, Phys. Rev. Lett. **96**, 100503 (2006)
41. W. Li, L. Ding, R. Yu, T. Roscilde, S. Haas, Phys. Rev. B **74**, 073103 (2006)
42. T. Barthel, M.-C. Chung, U. Schollwöck, Phys. Rev. A **74**, 022329 (2006)
43. F. Verstraete, M.M. Wolf, D. Perez-Garcia, J.I. Cirac, Phys. Rev. Lett. **96**, 220601 (2006)
44. U. Schollwöck, Ann. Phys. **326**, 96 (2011)
45. F. Verstraete, D. Porras, J.I. Cirac, Phys. Rev. Lett. **93**, 227205 (2004)
46. See also P. Pippan, S.R. White, H.G. Evertz, Phys. Rev. B **81**, 081103 (2010)
47. I. McCulloch, J. Stat. Mech. **2007**, P10014 (2007)
48. B. Bauer et al. (ALPS collaboration), J. Stat. Mech. **2011**, P05001 (2011)
49. F. Albuquerque et al. (ALPS collaboration), J. Magnet. Magnet. Mater. **310**, 1187 (2007)
50. F. Alet et al. (ALPS collaboration), J. Phys. Soc. Jpn. Suppl. **74**, 30 (2005)
51. R. Orus, G. Vidal, Phys. Rev. B **78**, 155117 (2008)
52. I.P. McCulloch, arXiv:0804.2509
53. B. Pirvu, F. Verstraete, G. Vidal, Phys. Rev. B **83**, 125104 (2011)
54. J. Jordan, R. Orus, G. Vidal, F. Verstraete, J.I. Cirac, Phys. Rev. Lett. **101**, 250602 (2008)
55. M.C. Bañuls, M.B. Hastings, F. Verstraete, J.I. Cirac, Phys. Rev. Lett. **102**, 240603 (2009)
56. I. Pizorn, L. Wang, F. Verstraete, Phys. Rev. A **83**, 052321 (2011)
57. M.B. Hastings, J. Math. Phys. **50**, 095207 (2009)
58. N. Schuch, M.M. Wolf, F. Verstraete, J.I. Cirac, Phys. Rev. Lett. **100**, 030504 (2008)
59. N. Schuch, M.M. Wolf, F. Verstraete, J. Ignacio Cirac, Phys. Rev. Lett. **98**, 140506 (2007)
60. N. Schuch, I. Cirac, F. Verstraete, Phys. Rev. Lett. **100**, 250501 (2008)
61. F. Verstraete, J.I. Cirac, Phys. Rev. Lett. **104**, 190405 (2010)
62. G. Vidal, Phys. Rev. Lett. **99**, 220405 (2007)
63. G. Evenbly, G. Vidal, Phys. Rev. B **79**, 144108 (2009)
64. G. Evenbly, G. Vidal, Phys. Rev. Lett. **102**, 180406 (2009)
65. G. Vidal, in *Understanding Quantum Phase Transitions*, ed. by L.D. Carr (Taylor & Francis, Boca Raton, 2010)
66. P. Corboz, S.R. White, G. Vidal, M. Troyer, arXiv:1104.5463
67. S. Yan, D.A. Huse, S.R. White, Science **332**, 1173 (2011)
68. Gu Zheng-Cheng, Michael Levin, Xiao-Gang Wen, Phys. Rev. B **78**, 205116 (2008)
69. Z.Y. Xie, H.C. Jiang, Q.N. Chen, Z.Y. Weng, T. Xiang, Phys. Rev. Lett. **103**, 160601 (2009)
70. H.H. Zhao, Z.Y. Xie, Q.N. Chen, Z.C. Wei, J.W. Cai, T. Xiang, Phys. Rev. B **81**, 174411 (2010)

# Chapter 3

## Matrix Product State Algorithms: DMRG, TEBD and Relatives

**Ulrich Schollwöck**

**Abstract** The density-matrix renormalization group (DMRG) has established itself as the leading algorithm for the simulation of one-dimensional strongly correlated quantum systems and has been extended in various directions, from the calculation of ground states to e.g. the real- and imaginary-time evolution of quantum states, or to algorithms attempting to simulate two-dimensional quantum systems. While the original formulation of the DMRG algorithms was framed in well-known concepts of statistical mechanics (density matrices, decimation and others), it turned out that it is in many circumstances much more powerful to view this class of algorithms as natural manipulations of very special quantum mechanical state classes, the so-called matrix product states. In this chapter, both time-independent and time-dependent algorithms are presented in this framework, based on an introduction to matrix product states. I will also address the connection between matrix product states and quantum entanglement, which defines both the potential and the limitations of this class of algorithms.

### 3.1 Introduction

The study of strongly correlated quantum systems, where interaction effects cannot be neglected or treated in a simple effective way, is one of the major subfields of condensed matter or quantum many-body physics, as those systems are ubiquitous in nature: they range from Kondo systems through spin chains, spin ladders, two-dimensional (frustrated) quantum magnets, high- $T_c$  superconductors to compounds based on transition metals or rare earths and most recently ultracold dilute atomic gases with strong interactions due to the presence of Feshbach resonances or optical lattices [1]. The complex role of interactions typically implies that these systems are

---

U. Schollwöck (✉)

Department of Physics, University of Munich, Theresienstrasse 37, 80333 Munich, Germany  
e-mail: schollwoeck@lmu.de

quite hard to treat and a wealth of methods has been developed over the decades which usually allow to deal with certain aspects of these systems quite efficiently. Because of the difficulties many analytical methods face, numerical methods are of particular relevance for strongly correlated systems. Among those, the density-matrix renormalization group (DMRG), invented by White [2, 3] is now considered to be the leading method for the simulation of the statics and dynamics of one-dimensional strongly correlated quantum systems both at zero and finite temperature (for more recent reviews, see [4–6]). Recently the alternative view of DMRG as a variational method in the space of matrix product states [7–10] has become very important, because it allows for easy extensions of the method and a deeper conceptual understanding. In this chapter, I will first introduce and discuss matrix product states, introduce the most basic version of DMRG as a variational method, including the so-called infinite-system method for the initial build-up (in its improved MPS form), and discuss the reasons for its successes and limitations. From this I move on to an exposition of the time-dependent version of this method. Notations follow that of [6], where these and other algorithms are treated in much more detail than possible in this chapter. For an exposition of DMRG in its traditional framework, I would like to refer to the Sects. 1.7 and 4.6 in this book.

## 3.2 Ground State Calculations in One Dimension

### 3.2.1 Matrix Product States

Let us assume that our system consists of  $L$  sites on a one-dimensional chain with local state spaces  $\{|\sigma_i\rangle\}$  on site  $i$  of dimension  $d$  each. Then it can be shown (see e.g. [6]) that any quantum state

$$|\psi\rangle = \sum_{\sigma} c_{\sigma} |\sigma\rangle \quad (3.1)$$

where  $|\sigma\rangle = |\sigma_1, \sigma_2, \dots, \sigma_L\rangle$ , can be brought by a sequence of singular value decompositions (SVDs)—QR decompositions are also possible—exactly into the form of a *matrix product state (MPS)*, namely

$$|\psi\rangle = \sum_{\sigma} M^{\sigma_1} M^{\sigma_2} \dots M^{\sigma_{L-1}} M^{\sigma_L} |\sigma\rangle, \quad (3.2)$$

where on each lattice site  $i$  we introduce a set of  $d$  matrices  $M^{\sigma_i}$  labelled by the possible local states. To see this, let us briefly recall the key properties of an SVD (see e.g. [11]): for an arbitrary, rectangular matrix  $A$  of dimension  $(m \times n)$ , it provides a decomposition  $A = USV^{\dagger}$ , where the matrices  $U$ ,  $S$ , and  $V^{\dagger}$  have dimensions  $(m \times p)$ ,  $(p \times p)$  and  $(p \times n)$ , where  $p = \min(m, n)$ , the smaller of the two original dimensions. In addition, the three matrices have the following properties:  $U$  consists

of  $p$  orthonormal columns, which can be read as a set of orthonormal vectors (hence,  $U^\dagger U = I$ ); similarly,  $V^\dagger$  consists of  $p$  orthonormal rows, which again can be read as a set of orthonormal vectors (and  $V^\dagger V = I$ ); they are referred to as the left and right singular vectors.  $S$  is a non-negative diagonal matrix, with  $r \leq p$  positive singular values on the diagonal;  $r$  is the rank of  $A$ . In order to carry out the transformation into an MPS, we start by reshaping  $c_\sigma$  into a matrix  $\Psi_{\sigma_1, (\sigma_2 \dots \sigma_L)} := c_{\sigma_1 \dots \sigma_L}$  of dimension  $(d \times d^{L-1})$ . This is now singular value decomposed as

$$\Psi_{\sigma_1, (\sigma_2 \dots \sigma_L)} = \sum_{a_1} U_{\sigma_1, a_1} S_{a_1, a_1} V_{a_1, (\sigma_2 \dots \sigma_L)}^\dagger. \quad (3.3)$$

The  $U$ -matrix has dimension  $d \times d$ . As the next step, we reshape  $S_{a_1, a_1} V_{a_1, (\sigma_2 \dots \sigma_L)}^\dagger$  into a matrix  $\Psi_{(a_1 \sigma_2), (\sigma_3 \dots \sigma_L)}$  of dimension  $(d^2 \times d^{L-2})$ , where the row dimension may be smaller if singular values of the previous SVD happen to be zero. This is again singular value decomposed as

$$\Psi_{(a_1 \sigma_2), (\sigma_3 \dots \sigma_L)} = \sum_{a_2} U_{(a_1 \sigma_2), a_2} S_{a_2, a_2} V_{a_2, (\sigma_3 \dots \sigma_L)}^\dagger, \quad (3.4)$$

with the dimension of the  $U$ -matrix being  $d^2 \times d^2$ . If we continue this procedure to the end of the chain, we end up with a sequence of  $U$ -matrices as  $U_{\sigma_1, a_1}$ ,  $U_{(a_1 \sigma_2), a_2}$ ,  $U_{(a_2 \sigma_3), a_3}$ , and so on, with the last matrix being  $U_{(a_{L-1} \sigma_L), 1}$ , where the matrix is actually a vector (hence the dummy column index 1). The total state then reads

$$|\psi\rangle = \sum_{\sigma} \sum_{a_1, \dots, a_{L-1}} U_{\sigma_1, a_1} U_{(a_1 \sigma_2), a_2} \dots U_{(a_{L-2} \sigma_{L-1}), a_{L-1}} U_{(a_{L-1} \sigma_L), 1} |\sigma\rangle. \quad (3.5)$$

To simplify the notation, we now define the  $d$  matrices  $M^{\sigma_i}$  per site as  $M_{a_{i-1}, a_i}^{\sigma_i} := U_{(a_{i-1} \sigma_i), a_i}$  and use that the sum over the  $a_i$  is then nothing but a sequence of matrix multiplications of  $M^{\sigma_i}$  matrices to arrive at Eq.(3.2). Note that (if we introduce a dummy  $a_0 = 1$ ) the first and last site matrices are row and column vectors, such that the product of matrices yields a scalar, namely  $c_\sigma$ .

It is useful to introduce a graphical notation for MPS (see Fig. 3.1), where each matrix is represented by a blob with outgoing legs, namely a vertical physical leg and horizontal legs corresponding to the matrix indices. The rule is that all connected legs are contracted, leading to the MPS as defined above.

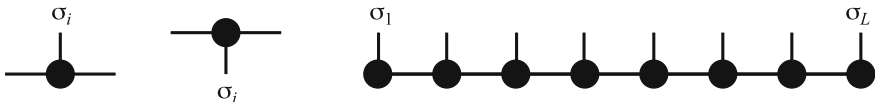


**Fig. 3.1** Definition of the graphical representation of an MPS constituent, a matrix  $M_{ab}^\sigma$ , of its complex conjugate, and of an MPS. Note that on the first and last sites the matrices reduce to row and column vectors (one horizontal leg only). The evaluation rule is to contract over all connected legs

If we review the above sequence of decompositions and the sizes of the  $U$ -matrices, the resulting  $M^\sigma$  matrix dimensions will be (at most)  $(1 \times d)$ ,  $(d \times d^2)$ ,  $\dots$ ,  $(d^{L/2-1} \times d^{L/2})$ ,  $(d^{L/2} \times d^{L/2-1})$ ,  $\dots$ ,  $(d^2 \times d)$ ,  $(d \times 1)$ : the  $M$ -matrices are always cut in the row dimension by a factor of  $d$  by the reshaping from the  $U$ -matrices; beyond the center of the chain, the column dimension will be smaller than the row dimension of the singular value decomposed matrix, hence the dimensions of the  $U$ -matrices will go down again. In systems of interest, where  $d^{L/2}$  will be exponentially large in system size, this exact representation is obviously useless in numerical practice. But let us assume for the moment that we consider MPS where matrix dimensions do not exceed some number  $D$ , which will be  $O(100)$  through  $O(1000)$ , and that these approximate MPS are a very close approximation to the exact quantum states of interest. Under this assumption, we may ask about quantum mechanics in this restricted set of MPS of dimension  $D$ .

Before we consider typical MPS operations we note that matrix product state representations of quantum states are not unique: Between any matrix pair  $M^{\sigma_i} M^{\sigma_{i+1}}$  we may insert  $I = XX^{-1}$ , where  $X$  is an invertible matrix of suitable dimensions, changing the local matrices to  $\tilde{M}^{\sigma_i} = M^{\sigma_i} X$  and  $\tilde{M}^{\sigma_{i+1}} = X^{-1} M^{\sigma_{i+1}}$ . One of the main usages of this is to bring MPS into *canonical form*: any MPS can be written in left-canonical form

$$|\psi\rangle = \sum_{\sigma} A^{\sigma_1} A^{\sigma_2} \dots A^{\sigma_{L-1}} A^{\sigma_L} |\sigma\rangle, \quad (3.6)$$

where the matrices  $A^{\sigma_i}$  are *left-normalized*,  $\sum_{\sigma_i} A^{\sigma_i \dagger} A^{\sigma_i} = I$ , or in right-canonical form

$$|\psi\rangle = \sum_{\sigma} B^{\sigma_1} B^{\sigma_2} \dots B^{\sigma_{L-1}} B^{\sigma_L} |\sigma\rangle, \quad (3.7)$$

where the matrices  $B^{\sigma_i}$  are *right-normalized*,  $\sum_{\sigma_i} B^{\sigma_i} B^{\sigma_i \dagger} = I$ , or in mixed-canonical form,

$$|\psi\rangle = \sum_{\sigma} A^{\sigma_1} A^{\sigma_2} \dots A^{\sigma_i} \Psi B^{\sigma_{i+1}} \dots B^{\sigma_{L-1}} B^{\sigma_L} |\sigma\rangle, \quad (3.8)$$

where the matrix  $\Psi$  is of matching dimensions; one can also contract e.g.  $A^{\sigma_i} \Psi \rightarrow M^{\sigma_i}$ , which generates a variety of ansatz classes for DMRG. To see how this can be done iteratively, consider a state which is already partially in left-canonical form on its left end,

$$|\psi\rangle = \sum_{\sigma} A^{\sigma_1} A^{\sigma_2} \dots A^{\sigma_i} M^{\sigma_{i+1}} \dots M^{\sigma_L} |\sigma\rangle. \quad (3.9)$$

Then one way of making  $M^{\sigma_{i+1}}$  at site  $i + 1$  left-normalized is to reshape the set of matrices  $M_{a_i, a_{i+1}}^{\sigma_{i+1}}$  into one matrix  $M_{(\sigma_{i+1} a_i), a_{i+1}}$ , which upon a singular value

decomposition reads  $\sum_{s_{i+1}} U_{(\sigma_i+1)a_i}, s_{i+1} S_{s_{i+1}, s_{i+1}} V_{s_{i+1}, a_{i+1}}^\dagger$ .  $U$  is reshaped into a set of matrices  $A_{a_i, s_{i+1}}^{\sigma_i}$ , which meet the left-normalization condition due to the column orthonormality of  $U$ .  $SV^\dagger$  is multiplied into  $M^{\sigma_{i+2}}$ , and the next iterative step occurs at site  $i+2$ . Similarly, one can start from the right to obtain right-normalized matrices. In fact, the proof of the representation in Eq. (3.2) generated left-normalized matrices right away, due to the orthonormality properties of the  $U$ -matrices.

If we divide the chain into blocks A and B and form states  $|a_i\rangle_A$  on block A formed from sites 1 through  $i$  and  $|a_i\rangle_B$  on block B formed from sites  $i+1$  through  $L$  as

$$|a_i\rangle_A = \sum_{\sigma_1, \dots, \sigma_i} (M^{\sigma_1} \dots M^{\sigma_i})_{1, a_i} |\sigma_1, \dots, \sigma_i\rangle \quad (3.10)$$

and similarly for  $|a_i\rangle_B$ , then the left- and right-normalization conditions correspond to orthonormality conditions  ${}_A\langle a_i | a'_i \rangle_A = \delta_{a_i, a'_i}$  and  ${}_B\langle a_i | a'_i \rangle_B = \delta_{a_i, a'_i}$  respectively. Generally, it is true that one can write

$$|a_{i+1}\rangle_A = \sum_{a_i, \sigma_{i+1}} M_{a_i, a_{i+1}}^{\sigma_{i+1}} |a_i\rangle_A |\sigma_{i+1}\rangle, \quad (3.11)$$

where  $M_{a_i, a_{i+1}}^{\sigma_{i+1}} = \langle a_i | \sigma_{i+1} | a_{i+1} \rangle$ . This establishes the connection between MPS notation and block growth  $i \rightarrow i+1$ , which—taking into account decimation of the states  $|a_{i+1}\rangle_A$ —makes the connection to RG growth steps; but this is not strictly necessary in anything that follows. In particular, it connects [12] to the important numerical renormalization group (NRG) method [13, 14].

In the mixed-canonical representation, the nature of the MPS as a systematic low-entanglement approximation to a quantum state becomes most obvious. If we do an SVD on  $\Psi = USV^\dagger$  and absorb matrices  $U$  and  $V^\dagger$  into the adjoining A and B-matrices, this does not change the orthonormality of the block states because of the properties of  $U$  and  $V^\dagger$ , but the state now takes the form

$$|\psi\rangle = \sum_{a_i}^r s_{a_i} |a_i\rangle_A |a_i\rangle_B, \quad (3.12)$$

where the sum runs over the  $r$  non-vanishing (positive) diagonal elements  $s_{a_i} = S_{a_i, a_i}$ , linking up states in A and B in pairwise fashion. This is the so-called Schmidt decomposition of a quantum state, with  $r$  being the Schmidt rank. If we have to cut the sum at some  $D < r$ , the quality of the approximation will depend on how rapidly the  $s_{a_i}$  decay; the optimal approximation is given by keeping the  $D$  largest  $s_{a_i}$ . But it is easy to see that at the same time the reduced density operators for A and B are given as  $\hat{\rho}_A = \text{Tr}_B |\psi\rangle\langle\psi| = \sum_{a_i} s_{a_i}^2 |a_i\rangle_A \langle a_i|$  and analogously  $\hat{\rho}_B$ . A good approximation is then possible if the eigenspectrum of the reduced density operators decays quickly. The spectrum is usually not known, but we may argue that a quickly decaying spectrum corresponds to small entanglement  $S_{A|B} = -\sum_a s_a^2 \log_2 s_a^2$ , and

MPS systematically approximate low-entanglement states well. Let us take that for granted and postpone the crucial question when this is actually the case to later, and focus on operations using MPS.

The most important operations on MPS are overlaps and expectation values. Let us consider the calculation of  $\langle \phi | \psi \rangle$ ; the generalization to  $\langle \psi | \hat{O} | \psi \rangle$  is completely obvious. We have

$$\langle \phi | \psi \rangle = \sum_{\sigma} \tilde{M}^{\sigma_1*} \dots \tilde{M}^{\sigma_L*} M^{\sigma_1} \dots M^{\sigma_L}, \quad (3.13)$$

where  $M$  and  $\tilde{M}$  form the states  $|\psi\rangle$  and  $|\phi\rangle$  respectively. Transposing the scalar formed from the  $\tilde{M} \dots \tilde{M}$  (which is the identity operation), we arrive at adjoints with reversed ordering:

$$\langle \phi | \psi \rangle = \sum_{\sigma} \tilde{M}^{\sigma_L\dagger} \dots \tilde{M}^{\sigma_1\dagger} M^{\sigma_1} \dots M^{\sigma_L}. \quad (3.14)$$

To represent this graphically, we introduce an inverted matrix-blob to correspond to the complex-conjugate matrix  $M^{\sigma_i*}$  (Fig. 3.1). In the resulting pictorial representation of the overlap calculation (Fig. 3.2), this calculation becomes then much simpler, if we follow the rule that all bond indices are summed over. To evaluate this expression efficiently, the following order of contractions is advisable:

$$\langle \phi | \psi \rangle = \sum_{\sigma_L} \tilde{M}^{\sigma_L\dagger} \left( \dots \left( \sum_{\sigma_2} \tilde{M}^{\sigma_2\dagger} \left( \sum_{\sigma_1} \tilde{M}^{\sigma_1\dagger} M^{\sigma_1} \right) M^{\sigma_2} \right) \dots \right) M^{\sigma_L}, \quad (3.15)$$

which contracts in  $O(LD^3)$  operations. In order to calculate an expectation value, say at site  $i$ , the sum to be evaluated there changes to

$$\sum_{\sigma_i, \sigma'_i} \hat{O}^{\sigma_i, \sigma'_i} M^{\sigma_i*} E M^{\sigma'_i}, \quad (3.16)$$

where  $E$  is the result of all the contractions up to site  $i - 1$ . Let me conclude by pointing out that, if we had carried out all matrix products for each  $\sigma$ -configuration and

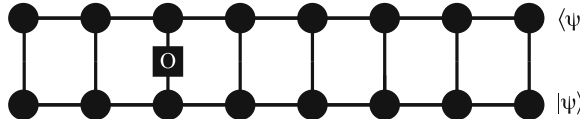


**Fig. 3.2** Graphical representation of the calculation of the norm of a state, potentially including an operator whose expectation value is calculated. Lines are contracted over iteratively, starting either from the *left* or *right*, for maximal efficiency

summed in the end, we would have ended up with an exponential number of operations. This shows the surmounting importance of the optimal ordering of contractions.

If we exploit left-normalization, it is easy to see that for  $\langle \psi | \psi \rangle$  matrix contractions collapse trivially to the identity  $I$  (similarly for right-normalization, if we rearrange the contractions to go from  $L$  to 1). In mixed-canonical notation, expectation values for operators that sit right next to the point where left- and right-normalized matrices meet become particularly efficient, as essentially all contractions become trivial.

Adding two matrix product states  $|\psi_1\rangle$  and  $|\psi_2\rangle$ , formed from matrices  $M_1^\sigma$  and  $M_2^\sigma$  is very simple. Then  $|\psi\rangle = |\psi_1\rangle + |\psi_2\rangle$  is formed from matrices  $M^\sigma = M_1^\sigma \oplus M_2^\sigma$ , i.e. matrices having the old ones as diagonal blocks, except on the first and last sites, where  $M^{\sigma_1} = [M_1^{\sigma_1} M_2^{\sigma_1}]$  and  $M^{\sigma_L} = [M_1^{\sigma_L} M_2^{\sigma_L}]^T$ . While MPS are therefore closed under addition, those of a specific dimension  $D$  are not, as matrix dimensions add under addition.

The last important operation on a matrix product state is its *compression*. Assume that some operation (like the application of a matrix product operator to a matrix product state, see below, or the addition of two MPS) generates an MPS of dimension  $D'$ , but we can only handle dimension  $D$  efficiently. How do we approximate  $|\psi\rangle$  by  $|\tilde{\psi}\rangle$ , an MPS of dimension  $D$ , such that the distance between the two states becomes minimal, i.e. the approximation becomes optimal? Essentially two techniques exist, one based on SVD and not necessarily optimal, but very often very close to it, and a variational technique, which is more complicated, but optimal.

Let us consider an MPS in mixed canonical representation, with  $S = \text{diag}(s_1, s_2, \dots)$ ,

$$|\psi\rangle = \sum_{\sigma} A^{\sigma_1} A^{\sigma_2} \dots A^{\sigma_\ell} S B^{\sigma_{\ell+1}} \dots B^{\sigma_{L-1}} B^{\sigma_L} |\sigma\rangle, \quad (3.17)$$

from which we read off the Schmidt decomposition  $|\psi\rangle = \sum_{a_\ell=1}^{D'} s_{a_\ell} |a_\ell\rangle_A |a_\ell\rangle_B$ , where the states on A and B form orthonormal sets respectively. We now look for the state  $|\tilde{\psi}\rangle$  that approximates  $|\psi\rangle$  best in the 2-norm and can be spanned by a smaller number of  $D$  states each in A and B. This is achieved by retaining the  $D$  largest  $s_{a_\ell}$ , and the compressed state simply reads  $|\psi\rangle = \sum_{a_\ell=1}^D s_{a_\ell} |a_\ell\rangle_A |a_\ell\rangle_B$ . If normalization is desired, the retained singular values must be rescaled.

This procedure rests on the orthonormality of the states on A and B, therefore can only be carried out at one bond, the one which connects blocks A and B of left- and right-normalized matrices. In order to shrink the state on all sites, we have to work our way through all mixed canonical representations, say from right to left, truncate, and shift the boundary between left- and right-normalized matrices by one site to the left, using techniques from creating a right-canonical state.

After the first step of right-canonicalization of a left-canonical state, it reads:

$$|\psi^{(L-1)}\rangle = \sum_{\sigma} A^{\sigma_1} \dots A^{\sigma_{L-1}} U S B^{\sigma_L} |\sigma\rangle, \quad (3.18)$$

where I have already reshaped  $B$ , which is right-normalized and guarantees that states formed as  $|a_{L-1}\rangle_B = \sum_{\sigma_L} (B^{\sigma_L})_{a_{L-1},1} |\sigma_L\rangle$  are orthonormal. But so are the states

$$|a_{L-1}\rangle_A = \sum_{\sigma_1 \dots \sigma_{L-1}} (A^{\sigma_1} \dots A^{\sigma_{L-1}} U)_{1,a_{L-1}} |\sigma_1 \dots \sigma_{L-1}\rangle, \quad (3.19)$$

as SVD guarantees  $U^\dagger U = 1$ : we are just doing a basis transformation within the orthonormal basis set constructed from the left-normalized  $A^{\sigma_i}$ . Hence, we have a correct Schmidt decomposition as

$$|\psi^{(L-1)}\rangle = \sum_{a_{L-1}} s_{a_{L-1}} |a_{L-1}\rangle_A |a_{L-1}\rangle_B. \quad (3.20)$$

The difference to a right canonization is now the truncation: matrices  $U$ ,  $S$  and  $B^{\sigma_L}$  are truncated (and singular values possibly renormalized) to  $\tilde{U}$ ,  $\tilde{S}$  and  $\tilde{B}^{\sigma_L}$  just as explained before: retain the  $D$  largest singular values.  $\tilde{B}^{\sigma_L}$  is still right-normalized. The next  $A^{\sigma_{L-1}}$  to the left,  $\tilde{U}$  and  $\tilde{S}$  are multiplied together to form  $M^{\sigma_{L-1}}$ . By reshaping, SVD and reshaping as

$$M_{i,j}^\sigma = M_{i,(\sigma,j)} = \sum_k U_{i,k} S_k B_{k,(\sigma,j)} = \sum_k U_{i,k} S_k B_{k,j}^\sigma \quad (3.21)$$

we obtain right-normalized  $B^{\sigma_{L-1}}$ , truncate  $U$ ,  $S$  and  $B^{\sigma_{L-1}}$  to  $\tilde{U}$ ,  $\tilde{S}$  and  $\tilde{B}^{\sigma_{L-1}}$ , and the procedure continues. At the end, the compressed MPS  $|\tilde{\psi}\rangle$  is right-normalized and given by  $\tilde{B}$ -matrices.

The disadvantage of the procedure is that there is a one-sided dependence of truncations on each other: truncations further to the left depend on those to the right, but not vice versa. If the truncation is small, the introduced additional inaccuracy is minor; however, for cases where large truncations may occur, the one-sidedness of the dependence might become too strong and the truncation far from optimal.

The optimal approach is to start from an ansatz MPS of the desired reduced dimension, and to minimize its distance to the MPS to be approximated iteratively, i.e. by changing its  $M^\sigma$  matrices iteratively. The matrices play the role of variational parameters.

Minimizing  $|||\psi\rangle - |\tilde{\psi}\rangle||_2^2$  with respect to  $|\tilde{\psi}\rangle$  is a highly multilinear optimization problem in the  $\tilde{M}^{\sigma_i}$ . But this can be done iteratively and linearly as follows. Starting with an initial guess for  $|\tilde{\psi}\rangle$  we sweep through the set of  $\tilde{M}^{\sigma_i}$  site by site, keeping all other matrices fixed and choosing the new  $\tilde{M}^{\sigma_i}$ , such that distance is minimized. Repeating this sweep through the matrices several times will lead to a converged optimal approximation.

The new  $\tilde{M}^{\sigma_i}$  is found by extremizing  $|||\psi\rangle - |\tilde{\psi}\rangle||_2^2$  with respect to  $\tilde{M}_{a_{i-1},q_i}^{\sigma_i*}$ , which only shows up in  $-\langle\tilde{\psi}|\psi\rangle + \langle\tilde{\psi}|\tilde{\psi}\rangle$ . We find

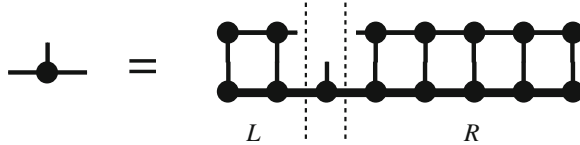


**Fig. 3.3** Equation for iterative compression of an MPS for a suitably normalized state. The *fatter* lines correspond to the state to be compressed, the *thinner* lines to the compressed state

$$\begin{aligned} & \frac{\partial}{\partial \tilde{M}_{a_{i-1}, a_i}^{\sigma_i *}} (\langle \tilde{\psi} | \tilde{\psi} \rangle - \langle \tilde{\psi} | \psi \rangle) \\ &= \sum_{\sigma_*} (\tilde{M}^{\sigma_1 *} \dots \tilde{M}^{\sigma_{i-1} *})_{1, a_{i-1}} (\tilde{M}^{\sigma_{i+1} *} \dots \tilde{M}^{\sigma_L *})_{a_i, 1} \tilde{M}^{\sigma_1} \dots \tilde{M}^{\sigma_i} \dots \tilde{M}^{\sigma_L} \\ &\quad - \sum_{\sigma_*} (\tilde{M}^{\sigma_1 *} \dots \tilde{M}^{\sigma_{i-1} *})_{1, a_{i-1}} (\tilde{M}^{\sigma_{i+1} *} \dots \tilde{M}^{\sigma_L *})_{a_i, 1} M^{\sigma_1} \dots M^{\sigma_i} \dots M^{\sigma_L} = 0. \end{aligned}$$

The sum over  $\sigma_*$  runs over the states of all physical sites except  $i$ . Assuming we keep  $|\tilde{\psi}\rangle$  at each iteration in mixed-canonical form,  $\tilde{A}^{\sigma_1} \dots \tilde{A}^{\sigma_{i-1}} \tilde{M}^{\sigma_i} \tilde{B}^{\sigma_{i+1}} \dots \tilde{B}^{\sigma_L}$ , the first term simplifies due to the normalization conditions to  $\tilde{M}^{\sigma_i}$ . Then we obtain the equation

$$\tilde{M}_{a_{i-1}, a_i}^{\sigma_i} = O_{a_{i-1}, a_i}^{\sigma_i}, \quad (3.22)$$

where  $O_{a_{i-1}, a_i}^{\sigma_i}$  is given by

$$\sum_{a'_{i-1} a'_i} L_{a_{i-1}, a'_{i-1}} M_{a'_{i-1}, a'_i}^{\sigma_i} R_{a_i, a'_i}, \quad (3.23)$$

with  $L$  and  $R$  as indicated in Fig. 3.3. In fact, calculating  $L$  and  $R$  is nothing but carrying out the first steps of an overlap calculation, starting from left or right. If one sweeps through the system from left to right and back one can build  $L$  and  $R$  iteratively from previous steps, which is the most efficient way.

To make this work for an entire chain, we have to shift the boundary between the left and right normalized matrices as we move through the chain. But this can be done by applying one step of left- or right-normalization (by SVD) to the matrices on a single site.

### 3.2.2 Matrix Product Operators

In the previous section, we have considered a local operator  $\hat{O}^{\sigma_i, \sigma'_i}$ , which ties in nicely with the local MPS notation. Keeping in mind operators like the Hamiltonian  $\hat{H}$  which consists of sums of (in practice usually) local terms of operator products,

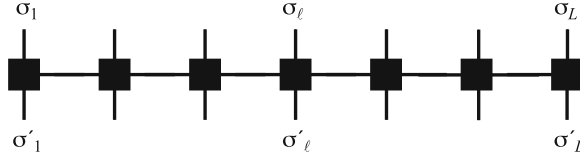


**Fig. 3.4** Graphical representation of a matrix product operator (MPO), with in- and outgoing (bottom and top) physical legs sticking out vertically

the natural question arises whether such operators can be expressed also in a form resembling an MPS. This is indeed the case and leads directly to *matrix product operators (MPOs)*. The most general operator acting on our  $L$ -site system is given as

$$\hat{O} = \sum_{\sigma, \sigma'} c_{\sigma, \sigma'} |\sigma\rangle\langle\sigma'|. \quad (3.24)$$

Interpreting the scalar coefficients as  $c_{(\sigma_1, \sigma'_1), \dots, (\sigma_L, \sigma'_L)}$ , we can by analogy to an MPS conclude that SVDs allow a decomposition as

$$\hat{O} = \sum_{\sigma, \sigma'} W^{\sigma_1 \sigma'_1} W^{\sigma_2 \sigma'_2} \dots W^{\sigma_L \sigma'_L} |\sigma\rangle\langle\sigma'|, \quad (3.25)$$

where at each lattice site we introduce a set of  $d^2$  matrices  $W^{\sigma_i \sigma'_i}$ . The previous statements about gauge degrees of freedom, orthonormalization types etc. generalize directly to MPOs.

The graphical representation of an MPO is also an obvious extension from the MPS case, with an ingoing physical leg going down and outgoing physical leg going up (Fig. 3.4).

The application of an MPO to an MPS is very elegant (Fig. 3.5):

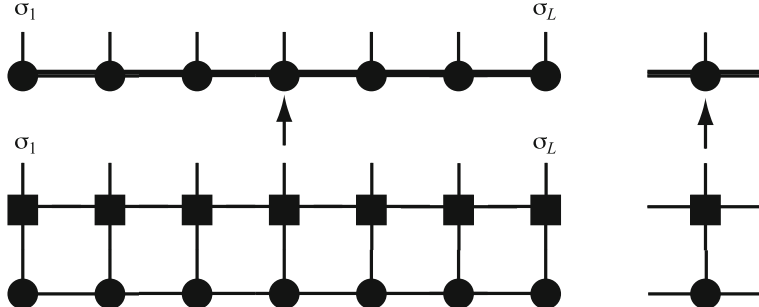


**Fig. 3.5** Graphical representation of the application of an matrix product operator (MPO) to an MPS. Matching legs are contracted over, the resulting MPS multiplies the dimensions of the underlying objects

$$\begin{aligned}
\hat{O}|\psi\rangle &= \sum_{\sigma, \sigma'} (W^{\sigma_1, \sigma'_1} W^{\sigma_2, \sigma'_2} \dots) (M^{\sigma'_1} M^{\sigma'_2} \dots) |\sigma\rangle \\
&= \sum_{\sigma, \sigma' \in \mathbf{a}, \mathbf{b}} \sum (W_{1, b_1}^{\sigma_1, \sigma'_1} W_{b_1, b_2}^{\sigma_2, \sigma'_2} \dots) (M_{1, a_1}^{\sigma'_1} M_{a_1, a_2}^{\sigma'_2} \dots) |\sigma\rangle \\
&= \sum_{\sigma, \sigma' \in \mathbf{a}, \mathbf{b}} (W_{1, b_1}^{\sigma_1, \sigma'_1} M_{1, a_1}^{\sigma'_1}) (W_{b_1, b_2}^{\sigma_2, \sigma'_2} M_{a_1, a_2}^{\sigma'_2}) \dots |\sigma\rangle \\
&= \sum_{\sigma \in \mathbf{a}, \mathbf{b}} \sum N_{(1, 1), (b_1, a_1)}^{\sigma_1} N_{(b_1, a_1), (b_2, a_2)}^{\sigma_2} \dots |\sigma\rangle \\
&= \sum_{\sigma} N^{\sigma_1} N^{\sigma_2} \dots |\sigma\rangle
\end{aligned}$$

The elegance stems from the observation that the form of the MPS remains invariant, with an increase of the matrix size: the new MPS matrices

$$N_{(b_{i-1}, a_{i-1}), (b_i, a_i)}^{\sigma_i} = \sum_{\sigma'_i} W_{b_{i-1} b_i}^{\sigma_i \sigma'_i} M_{a_{i-1} a_i}^{\sigma'_i}. \quad (3.26)$$

have the multiplied dimension of the MPS and the MPO. At the same time, like in the case of an overlap, the operation is only of small polynomial, not exponential complexity. Of course, it remains to show that it is in fact possible to construct the MPO of e.g. an Hamiltonian “by hand”, because the conceptual way of using an SVD might be exponentially complicated. But as we will see, this is no big problem indeed [15, 16].

Let us consider the following simple Hamiltonian

$$\hat{H} = \sum_{i=1}^{L-1} \left\{ \frac{J}{2} \hat{S}_i^+ \hat{S}_{i+1}^- + \frac{J}{2} \hat{S}_i^- \hat{S}_{i+1}^+ + J^z \hat{S}_i^z \hat{S}_{i+1}^z \right\}. \quad (3.27)$$

As this is a shorthand for sums of tensor products of operators while omitting all the identity operators on other sites, it is convenient to reconsider the building block  $W_{bb'}^{\sigma\sigma'}$  combined with its associated projector  $|\sigma\rangle\langle\sigma'|$  to become an operator-valued matrix  $\hat{W}_{b,b'} = \sum_{\sigma\sigma'} W_{b,b'}^{\sigma\sigma'} |\sigma\rangle\langle\sigma'|$  such that the MPO takes the simple form

$$\hat{O} = \hat{W}^{[1]} \hat{W}^{[2]} \dots \hat{W}^{[L]}. \quad (3.28)$$

In order to construct the MPO, we move through an arbitrary operator “string” appearing in  $\hat{H}$ : starting from the right end, the string contains unit operators, until at one point we encounter one of (in our example) 3 non-trivial operators. For the field operator, the string part further to the left may only contain unit operators; for the interaction operators, the complementary operator must follow immediately to complete the interaction term, to be continued by unit operators further to the

left. For book-keeping, we introduce 5 corresponding states of the string at some given bond: state 1: only units to the right, states 2, 3, 4: one  $\hat{S}^+$ ,  $\hat{S}^-$ ,  $\hat{S}^z$  just to the right, state 5: completed interaction somewhere to the right. Comparing the state of a string left and right of one site, only a few transitions are allowed:  $1 \rightarrow 1$  by the unit operator  $\hat{I}$ ,  $1 \rightarrow 2$  by  $\hat{S}^+$ ,  $1 \rightarrow 3$  by  $\hat{S}^-$ ,  $1 \rightarrow 4$  by  $\hat{S}^z$ . Furthermore  $2 \rightarrow 5$  by  $(J/2)\hat{S}^-$ ,  $3 \rightarrow 5$  by  $(J/2)\hat{S}^+$  and  $4 \rightarrow 5$  by  $J^z\hat{S}^z$ , to complete the interaction term, and  $5 \rightarrow 5$  for a completed interaction by the unit operator  $\hat{I}$ . Furthermore all string states must start at 1 to the right of the last site and end at 5 (i.e. the dimension  $D_W$  of the MPO to be) to the left of the first site. This can now be encoded by the following operator-valued matrices:

$$\hat{W}^{[i]} = \begin{bmatrix} \hat{I} & 0 & 0 & 0 & 0 \\ \hat{S}^+ & 0 & 0 & 0 & 0 \\ \hat{S}^- & 0 & 0 & 0 & 0 \\ \hat{S}^z & 0 & 0 & 0 & 0 \\ 0 & (J/2)\hat{S}^- & (J/2)\hat{S}^+ & J^z\hat{S}^z & \hat{I} \end{bmatrix} \quad (3.29)$$

and on the first and last sites

$$\hat{W}^{[1]} = [0 (J/2)\hat{S}^- (J/2)\hat{S}^+ J^z\hat{S}^z \hat{I}] \quad \hat{W}^{[L]} = \begin{bmatrix} \hat{I} \\ \hat{S}^+ \\ \hat{S}^- \\ \hat{S}^z \\ 0 \end{bmatrix}. \quad (3.30)$$

Inserting the explicit operator representations gives the desired  $W^{\sigma\sigma'}$ -matrices for the MPO. The MPO in this example has dimension  $D_W = 5$ . For longer-ranged Hamiltonians, further “intermediate states” have to be introduced: for

$$\hat{H} = J_1 \sum_i \hat{S}_i^z \hat{S}_{i+1}^z + J_2 \sum_i \hat{S}_i^z \hat{S}_{i+2}^z \quad (3.31)$$

the bulk operator would read

$$\hat{W}^{[i]} = \begin{bmatrix} \hat{I} & 0 & 0 & 0 \\ \hat{S}^z & 0 & 0 & 0 \\ 0 & \hat{I} & 0 & 0 \\ 0 & J_1 \hat{S}^z & J_2 \hat{S}^z & \hat{I}, \end{bmatrix} \quad (3.32)$$

as one can verify by working out the operator string paths allowed by this construction. Except for special cases like exponentially decaying interactions, which find a very compact representation [17, 18], the dimension of the MPO will grow with interaction range; however, we may always compress an MPO like an MPS to a smaller dimensional object with minimal loss of information.

### 3.2.3 The Variational MPS or Finite-System DMRG Algorithm

The so-called *variational MPS* (*vMPS*) or *finite-system DMRG algorithm* is, as the name indicates, a variational ground state search in the ansatz space of  $D$ -dimensional MPS. Historically, finite-system DMRG was not framed in the language of MPS, but rather in terms of the analysis of reduced density operators of subsystems (blocks) of the chain. If, on the other hand, one assumes that MPS are very efficient at encoding one-dimensional states (as we will discuss later), then the following algorithm for ground state searches in that state class follows naturally—and it then turns out that White [2] had the perfect intuition, as the algorithms are identical.

As increasing  $D$  leads to ansatz spaces that are supersets of the previous ones, the quality of approximation improves monotonically; in view of the exact MPS representation of quantum states the limit  $D \rightarrow \infty$  is exact. These two features allow for reliable extrapolation of results obtained for sequences of finite  $D$ .

Finding the ground state is equivalent to minimizing

$$E[|\psi\rangle] = \frac{\langle\psi|\hat{H}|\psi\rangle}{\langle\psi|\psi\rangle} \quad (3.33)$$

or, using a Lagrange multiplier  $\lambda$ , minimizing

$$\langle\psi|\hat{H}|\psi\rangle - \lambda\langle\psi|\psi\rangle. \quad (3.34)$$

Inserting the MPS encoding of  $|\psi\rangle$ , this turns into a highly multilinear problem in the variables  $M_{a_{i-1}, a_i}^{\sigma_i}$  which is unsolvable in numerical practice. But in fact, this problem can be turned into a sequence of linear problems, whose solutions will lead to an iterative improvement of the solution (in the sense that energy is monotonically lowered), where, with suitable numerical tricks, it can be ensured (in the sense of actual numerical practice) that the (energetically) optimal state in this ansatz class can be reached. One starts from a guess state, which can be picked either randomly (i.e.  $A^\sigma$  matrices with random entries) or be obtained from some warm-up algorithm such as the so-called *infinite-system* DMRG algorithm [2, 3]. This algorithm can also be brought into MPS form very efficiently [19], see our discussion below. We consider the MPS state provided by the initial guess and pick one site  $\ell$ , while all other sites remain inert. We then optimize energy with respect to the  $M^{\sigma_\ell}$  matrices belonging to this site. Then the variables appear in Eq. (3.34) only in quadratic form, for which the determination of the extremum is a benign linear algebra problem. This will lower the energy, and find a variationally better state, but of course not the optimal one. Now one continues to vary the matrix elements on another site for finding a state again lower in energy, moving through all sites multiple times, until the energy does not improve anymore.

Let us analyze the parts of Eq. (3.34). If we keep the state suitably mixed normalized, the normalization conditions imply that

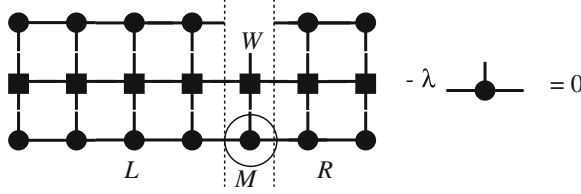


**Fig. 3.6** Standard eigenvalue problem for the optimization of  $M_{a_{\ell-1}, a_\ell}^{\sigma_\ell}$ . The unknown matrix is circled on the *left* network. The structure to the *left* of it is referred to as *L* in the text, the *right* structure as *R*

$$\langle \psi | \psi \rangle = \sum_{\sigma_\ell} \sum_{a_{\ell-1} a_\ell} M_{a_{\ell-1}, a_\ell}^{\sigma_\ell *} M_{a_{\ell-1}, a_\ell}^{\sigma_\ell}. \quad (3.35)$$

Considering  $\langle \psi | \hat{H} | \psi \rangle$  with  $\hat{H}$  in MPO language and taking the extremum of Eq.(3.34) with respect to  $M_{a_{\ell-1}, a_\ell}^{\sigma_\ell *}$  we find

$$\sum_{\sigma'_\ell} \sum_{a'_{\ell-1} a'_\ell} \sum_{b_{\ell-1} b_\ell} L_{b_{\ell-1}}^{a_{\ell-1}, a'_{\ell-1}} W_{b_{\ell-1}, b_\ell}^{\sigma_\ell, \sigma'_\ell} R_{b_\ell}^{a_\ell, a'_\ell} M_{a'_{\ell-1}, a'_\ell}^{\sigma'_\ell} - \lambda M_{a_{\ell-1}, a_\ell}^{\sigma_\ell} = 0, \quad (3.36)$$

with the mathematical objects as defined graphically in Fig. 3.6. This is in fact a very simple eigenvalue equation; if we introduce a matrix  $H$  by reshaping  $H_{(\sigma_\ell a_{\ell-1} a_\ell), (\sigma'_\ell a'_{\ell-1} a'_\ell)} = \sum_{b_{\ell-1}, b_\ell} L_{b_{\ell-1}}^{a_{\ell-1}, a'_{\ell-1}} W_{b_{\ell-1}, b_\ell}^{\sigma_\ell, \sigma'_\ell} R_{b_\ell}^{a_\ell, a'_\ell}$  and a vector  $v$  with  $v_{\sigma_\ell a_{\ell-1} a_\ell} = M_{a_{\ell-1}, a_\ell}^{\sigma_\ell}$ , we arrive at an eigenvalue problem of matrix dimension  $(dD^2 \times dD^2)$ ,

$$Hv - \lambda v = 0. \quad (3.37)$$

Solving for the lowest eigenvalue  $\lambda_0$  gives us a  $v_{\sigma_\ell a_{\ell-1} a_\ell}^0$ , which is reshaped back to  $M_{a_{\ell-1}, a_\ell}^{\sigma_\ell}$ ,  $\lambda_0$  being the current ground state energy estimate. In general,  $dD^2$  is too large for an exact diagonalization, but as we are only interested in the lowest eigenvalue and eigenstate, an iterative eigensolver that aims for the ends of the spectrum will do. Typical methods are the Lanczos or Jacobi-Davidson large sparse matrix solvers.

The optimal algorithm then runs as follows.

- Start from some initial guess for  $|\psi\rangle$ , which is right-normalized, i.e. consists of  $B$ -matrices only.
- Calculate the  $R$ -expressions iteratively for all site positions  $L - 1$  through 1 iteratively.
- *Right sweep:* Starting from site  $\ell = 1$  through site  $L - 1$ , sweep through the lattice to the right as follows: solve the standard eigenproblem by an iterative eigensolver for  $M^{\sigma_\ell}$ , taking its current value as starting point. It is crucial to take the current

value as starting point, because iterative eigensolvers perform optimally if provided with a good initial guess. In particular when convergence of the algorithm is close, matrices will not change much any more, and this procedure is extremely efficient. Once the solution is obtained, left-normalize  $M^{\sigma_\ell}$  into  $A^{\sigma_\ell}$  by SVD to maintain the desired normalization structure. The remaining matrices of the SVD are multiplied to the  $M^{\sigma_{\ell+1}}$  to the right, which will be the starting guess for the eigensolver for the next site. Build iteratively the  $L$  expression by adding one more site. Move on by one site,  $\ell \rightarrow \ell + 1$ , and repeat.

- *Left sweep:* Starting from site  $\ell = L$  through site 2, sweep through the lattice to the left as follows: solve the standard eigenproblem by an iterative eigensolver for  $M^{\sigma_\ell}$ , taking its current value as starting point. Once the solution is obtained, right-normalize  $M^{\sigma_\ell}$  into  $B^{\sigma_\ell}$  by SVD to maintain the desired normalization structure. The remaining matrices of the SVD are multiplied to the  $M^{\sigma_{\ell-1}}$  to the left, which will be the starting guess for the eigensolver for the next site. Build iteratively the  $R$  expression by adding one more site. Move on by one site,  $\ell \rightarrow \ell - 1$ , and repeat.
- Repeat right and left sweeps, until convergence is achieved. Convergence is achieved if energy converges, but the best test is (using MPO) to consider  $\langle \psi | \hat{H}^2 | \psi \rangle - (\langle \psi | \hat{H} | \psi \rangle)^2$  to see whether an eigenstate has been reached; this expression should approach 0 as closely as possible.

In this iterative process, the energy can only go down, as we continuously improve by varying the parameters. In fact, this most simple version of the ground state algorithm can be improved in terms of stability and performance but the core algorithm remains unchanged; for details, see e.g. [6].

In the exposition just given the link to true RG methods (with scaling and truncating) is not visible. It can however be put on a solid footing if one considers the reduced density operators of subsystems and takes those to the thermodynamic limit [7]. For these, a fixed point relationship holds. vMPS alias DMRG therefore sets up an RG flow in the space of reduced density operators, not in the space of Hamiltonians, as other RG methods would do.

### 3.2.4 *iDMRG—Infinite-System DMRG Revisited*

How can we build a suitable initial state for a vMPS procedure? The matrices might be chosen randomly and subjected to a suitable normalization before starting, but this random state will be far from a good guess, making vMPS inefficient. An alternative is provided by the method originally devised under the name of *infinite-system DMRG*, which is the starting point for finite-system DMRG (hence vMPS): a chain of length  $L$  is grown iteratively through lengths  $2 \rightarrow 4 \rightarrow \dots \rightarrow 2\ell \rightarrow \dots \rightarrow L$ , by starting from 2 initial sites and inserting pairs of new sites in the center. This method can not only be represented in the MPS language, but the MPS language allows interesting improvements beyond just providing a starting point for vMPS. This augmented method comes under the name of *iDMRG* [19].

It is convenient to label local states a bit differently from before to account for the iterative insertion of sites; we call the states of a chain of length  $2\ell$

$$|\sigma_1^A\rangle|\sigma_2^A\rangle\dots|\sigma_\ell^A\rangle|\sigma_\ell^B\rangle\dots|\sigma_2^B\rangle|\sigma_1^B\rangle.$$

Moreover, it will be very useful to give two labels to the matrices  $A$  and  $B$ , because the link between the matrices and the site on which they were generated will disappear.

Starting with a chain of 2 sites, the ground state wavefunction is  $|\psi_1\rangle = \sum_{\sigma_1^A \sigma_1^B} \Psi^{\sigma_1^A \sigma_1^B} |\sigma_1^A\rangle|\sigma_1^B\rangle$ . It can be worked out exactly. Reading  $\Psi^{\sigma_1^A \sigma_1^B}$  as matrix  $(\Psi_1)_{\sigma_1^A, \sigma_1^B}$ , it is singular-value decomposed as  $\Psi_1 = U_1 A^{[1]} V_1^\dagger$ . From this we read off

$$A_{1,a_1}^{[1]\sigma_1^A} = (U_1)_{\sigma_1^A, a_1} \quad B_{a_1, 1}^{[1]\sigma_1^B} = (V_1^\dagger)_{a_1, \sigma_1^B}. \quad (3.38)$$

Let me comment on the labeling: the double labeling by the site where the matrix was generated [1] and the local state  $\sigma_1$ , which implies the site, may seem overly pedantic, even though conceptually the label of a site and a state it takes are of course strictly different. As opposed to DMRG, in iDMRG the difference will come to bear, see below.  $A$  and  $B$  inherit left and right-normalization properties from  $U$  and  $V^\dagger$ , and the state takes the form

$$|\psi_1\rangle = \sum_{\sigma_1^A \sigma_1^B} A^{[1]\sigma_1^A} A^{[1]} B^{[1]\sigma_1^B} |\sigma_1^A \sigma_1^B\rangle. \quad (3.39)$$

If we now insert two sites, i.e. replace the matrix  $A^{[1]}$  by ansatz matrices labeled by the local states on those two sites for all local state configurations and sum over them; this is the most general ansatz possible. If we minimize the energy with respect to  $\hat{H}$ , we obtain

$$|\psi_2\rangle = \sum_{\sigma_1^A \sigma_2^A \sigma_2^B \sigma_1^B} A^{[1]\sigma_1^A} \Psi^{\sigma_2^A \sigma_2^B} B^{[1]\sigma_1^B} |\sigma_1^A \sigma_2^A \sigma_2^B \sigma_1^B\rangle, \quad (3.40)$$

where each  $\Psi^{\sigma_2^A \sigma_2^B}$  is a matrix with dimensions to match those of  $A$  and  $B$ , implicit matrix multiplications  $A\Psi B$  assumed. Note that in the minimization we keep matrices  $A$  and  $B$  fixed. Reshaping this set of  $\Psi$ -matrices into one,

$$(\Psi_2)_{(a_1^A \sigma_2^A), (a_1^B \sigma_2^B)} = (\Psi^{\sigma_2^A \sigma_2^B})_{a_1^A, a_1^B}, \quad (3.41)$$

SVD gives  $\Psi_2 = U_2 A^{[2]} V_2^\dagger$ , from which we can form

$$A_{a_1^A, a_2^A}^{[2]\sigma_2^A} = U_{(a_1^A \sigma_2^A), a_2^A} \quad B_{a_2^B, a_1^B}^{[2]\sigma_2^B} = V_{(a_1^B \sigma_2^B), a_2^B}^\dagger, \quad (3.42)$$

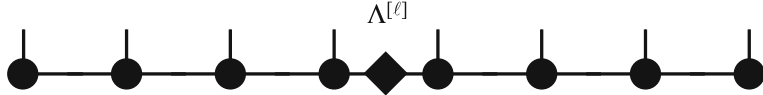


**Fig. 3.7** MPS structure generated by infinite-system DMRG at step  $\ell$ : a string of *left*-normalized  $A$ , a string of *right*-normalized  $B$ , joined by a diagonal singular value matrix  $\Lambda^{[\ell]}$ . Note that structurally the central unit does not repeat

such that

$$|\psi_2\rangle = \sum_{\sigma_1^A \sigma_2^A \sigma_2^B \sigma_1^B} A^{[1]\sigma_1^A} A^{[2]\sigma_2^A} A^{[2]} B^{[2]\sigma_2^B} B^{[1]\sigma_1^B} |\sigma_1^A \sigma_2^A \sigma_2^B \sigma_1^B\rangle. \quad (3.43)$$

At the  $\ell$ th step, the wavefunction will read

$$|\psi_\ell\rangle = \sum_{\sigma_1^A \dots \sigma_\ell^A \sigma_\ell^B \dots \sigma_1^B} A^{[1]\sigma_1^A} \dots A^{[\ell]\sigma_\ell^A} \Lambda^{[\ell]} B^{[\ell]\sigma_\ell^B} \dots B^{[1]\sigma_1^B} |\sigma_1^A \dots \sigma_\ell^A \sigma_\ell^B \dots \sigma_1^B\rangle \quad (3.44)$$

and look like in Fig. 3.7.

At each step we discard the smallest singular values and their associated singular vectors once matrix dimensions exceed  $D$ , which is equivalent to discarding the statistically most irrelevant contributions to the reduced density operators on chain parts A and B (left and right half).

At each step (new chain length) we can write down  $\hat{H}$  for that length as an MPO and do the energy minimization. Other operators find similar representations as in the finite-size case.

In finite-system DMRG (or vMPS), finding the ground state by an iterative solver like Lanczos is the most time-consuming part, and is improved by providing a good initial guess from the current wave function under consideration after suitable transformations. In the infinite-system method, the system changes at each iteration, hence we are talking about different wave functions in each iteration. Can we nevertheless find a speed-up by providing a good initial guess? Attempts at speeding up infinite-system DMRG have been made in the past, meeting with mixed success [20, 21]. The complete answer [19] builds on the identification of a structurally two-site repetitive “central” structure in the states:

$$A^{[\ell]\sigma_\ell^A} \Lambda^{[\ell]} B^{[\ell]\sigma_\ell^B} (\Lambda^{[\ell-1]})^{-1}. \quad (3.45)$$

Unfortunately, this result can be obtained very easily only in a different notation of MPS, which I cannot introduce here for lack of space. We will therefore simply take it for granted here, and build a state from repeating these state fragments. It is of course to be understood that repeating these state fragments does not generate the state they were taken from; the claim is just that in the thermodynamic limit  $\ell \rightarrow \infty$ ,

when all sites are created equal, this repetition can come close. In any case, the state fragments allow an educated guess what the state will look like! In the end, see below, we will only repeat the fragment once in the center, to add two new sites, as will be worked out below.

The identification of the “unit cell” of the state then allows us to define a good initial guess for the wave function in the next iteration of infinite-system DMRG [19], which avoids all the problems encountered by previous authors and leads to a dramatic speed-up even for small chains, where the underlying assumption that the chain center is representative of the physics of the thermodynamic limit state is certainly wrong: in order to grow the chain, we simply insert one unit cell, even though for small chains the idea that the state is just a repetition of these unit cells is not well verified—but even then so much better than a random guess. Starting from

$$|\psi_\ell\rangle = \sum_{\sigma} A^{[1]\sigma_1^A} \dots A^{[\ell-1]\sigma_{\ell-1}^A} (A^{[\ell]\sigma_\ell^A} A^{[\ell]} B^{[\ell]\sigma_\ell^B} [A^{[\ell-1]}]^{-1}) \\ \times A^{[\ell-1]} B^{[\ell-1]\sigma_{\ell-1}^B} \dots B^{[1]\sigma_1^B} |\sigma\rangle, \quad (3.46)$$

where the repeat unit has been bracketed out, the guess for the new chain with two additional sites (and local states  $|\sigma_{\ell+1}^A\rangle$  and  $|\sigma_{\ell+1}^B\rangle$ ) at the center will then read

$$|\psi_{\ell+1}^{\text{guess}}\rangle = \sum_{\sigma} A^{[1]\sigma_1^A} \dots A^{[\ell-1]\sigma_{\ell-1}^A} \\ \times (A^{[\ell]\sigma_\ell^A} A^{[\ell]} B^{[\ell]\sigma_{\ell+1}^A} [A^{[\ell-1]}]^{-1}) (A^{[\ell]\sigma_{\ell+1}^B} A^{[\ell]} B^{[\ell]\sigma_\ell^B} [A^{[\ell-1]}]^{-1}) \\ \times A^{[\ell-1]} B^{[\ell-1]\sigma_{\ell-1}^B} \dots B^{[1]\sigma_1^B} |\sigma\rangle \quad (3.47)$$

or, multiplying out,

$$|\psi_{\ell+1}^{\text{guess}}\rangle = \sum_{\sigma} A^{[1]\sigma_1^A} \dots A^{[\ell]\sigma_\ell^A} A^{[\ell]} B^{[\ell]\sigma_{\ell+1}^A} [A^{[\ell-1]}]^{-1} A^{[\ell]\sigma_{\ell+1}^B} A^{[\ell]} \\ B^{[\ell]\sigma_\ell^B} B^{[\ell-1]\sigma_{\ell-1}^B} \dots B^{[1]\sigma_1^B} |\sigma\rangle. \quad (3.48)$$

In this ansatz, we can now identify a guess for  $\Psi^{\sigma_{\ell+1}^A \sigma_{\ell+1}^B}$  as

$$\Psi_{\text{guess}}^{\sigma_{\ell+1}^A \sigma_{\ell+1}^B} = A^{[\ell]} B^{[\ell]\sigma_{\ell+1}^A} [A^{[\ell-1]}]^{-1} A^{[\ell]\sigma_{\ell+1}^B} A^{[\ell]}. \quad (3.49)$$

From this ansatz, we can then iteratively find the  $\Psi^{\sigma_{\ell+1}^A \sigma_{\ell+1}^B}$  that minimizes the energy in the infinite-system DMRG framework, generating from it  $A^{[\ell+1]\sigma_{\ell+1}^A}$ ,  $A^{[\ell+1]}$ , and  $B^{[\ell+1]\sigma_{\ell+1}^B}$ .

Alternatively, the ansatz can be brought into a more elegant form. At the moment,  $B$ -matrices show up on the  $A$ -side of the lattice and vice versa. But we can exploit our ability to canonize MPS, and canonize  $A^{[\ell]} B^{[\ell]\sigma_{\ell+1}^A}$  by SVD to

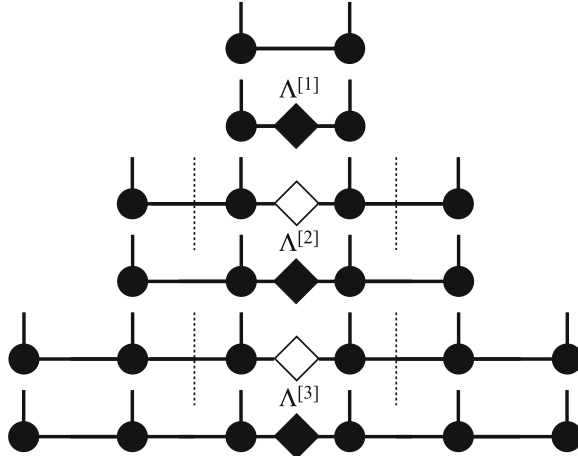


**Fig. 3.8** Summarizing representation of the infinite system algorithm including prediction. At each step, two more sites are introduced, with an ansatz (white) calculated from the last iteration, leading to a new singular value decomposition (black)

$A^{[\ell+1]\sigma_{\ell+1}} A_R^{[\ell]}$ , where  $A$  is derived from  $U$  and  $\Lambda$  from  $SV^\dagger$  in the way described before ( $\Lambda_a B_{ab}^\sigma = M_{a\sigma,b} = \sum_k U_{a\sigma,k} S_{k,k} (V^\dagger)_{k,b} = A_{ak}^\sigma \Lambda_{kb}$ ). Similarly, we do a canonization from the right on  $A^{[\ell]\sigma_{\ell+1}} A^{[\ell]}$  to obtain  $\Lambda_L^{[\ell]} B^{[\ell+1]\sigma_{\ell+1}}$ , where  $B$  is from  $V^\dagger$ . Then we have an ansatz

$$|\psi_{\ell+1}^{\text{guess}}\rangle = \sum_{\sigma} A^{[1]\sigma_1} \dots A^{[\ell+1]\sigma_{\ell+1}} \Lambda_{\text{guess}}^{[\ell+1]} B^{[\ell+1]\sigma_{\ell+1}} \dots B^{[1]\sigma_1} |\sigma\rangle, \quad (3.50)$$

where

$$\Lambda_{\text{guess}}^{[\ell+1]} = \Lambda_R^{[\ell]} [\Lambda^{[\ell-1]}]^{-1} \Lambda_L^{[\ell]}. \quad (3.51)$$

From this ansatz, we can then iteratively find the  $\Lambda^{[\ell+1]}$  that minimizes the energy, slightly modifying the minimization part of variational MPS for a single site. In general, the result will not have the diagonal form resulting from an SVD, because  $\Lambda_R$  and  $\Lambda_L$  are not diagonal to begin with. But an SVD on it yields two unitaries that can be absorbed into the neighbouring  $A$  and  $B$  without affecting their normalization properties, such that the final  $\Lambda^{[\ell+1]}$  is diagonal. In this form, the algorithm can be represented as in Fig. 3.8.

As shown by McCulloch [19], this prediction leads to a dramatic speedup of infinite-system DMRG which complements nicely prediction algorithms of finite-system DMRG: the overlap between the predicted and calculated state often approaches unity up to  $10^{-10}$  or so!

In this exposition, infinite-system DMRG was seen as a warm-up for finite-system DMRG (vMPS). However, it can be shown very neatly that this approach can also

be used to generate a thermodynamic limit version of DMRG, which is iDMRG proper [19], for which I refer to the literature and which has precursors in earlier approaches under the name of (product wave function renormalization group) PWFRG [22–24] which already contain part of the above ideas; iDMRG takes them to their natural completion [25, 26].

### 3.2.5 Why Does it Work and Why Does it Fail?

The performance of all MPS-based methods rests on whether a quantum state can be approximated well by an MPS with bonds of a manageable dimension  $D$ . As we can cut a state into two parts across such a bond, we have to consider bipartite quantum systems AB. Any state  $|\psi\rangle = \sum_{ij} \psi_{ij} |i\rangle_A |j\rangle_B$ , where the states  $|i\rangle_A$  and  $|j\rangle_B$  form orthonormal bases of dimensions  $N_A$  and  $N_B$  respectively. Thinking of the  $\psi_{ij}$  as entries of a rectangular matrix  $\Psi$  (dimension  $N_A \times N_B$ ), the reduced density matrices  $\rho_A$  and  $\rho_B$  take the form

$$\rho_A = \Psi \Psi^\dagger \quad \rho_B = \Psi^\dagger \Psi. \quad (3.52)$$

If we assume  $|\psi\rangle$  to be normalized, the eigenvalues  $w_a$  of  $\rho_A$  are non-negative, and sum to 1. This allows to interpret them directly as statistical weights. If we assume that we know  $|\psi\rangle$  exactly, the question of approximability reduces to how much statistical weight rests in the  $D$  eigenstates with the largest eigenvalues. In the few cases where this is the case, such analyses have been carried out in one and two dimensions starting with [27, 28]. They reveal that in one dimension for gapped systems eigenvalues  $w_a$  generically decay exponentially fast (roughly as  $e^{-c \ln^2 a}$ ), which explains the success of DMRG, but in two-dimensional stripe geometries of size  $L \times W$ ,  $L \gg W$ ,  $c \propto 1/W$ , such that with increasing width  $W$  (increasing two-dimensionality) the eigenspectrum decay is so slow as to make DMRG inefficient; this does however not preclude very powerful studies of not too wide stripe geometries, the most spectacular at the moment being the analysis of the kagome lattice [29, 30].

Usually, we have no clear idea about the eigenvalue spectrum; but it turns out that in such cases entanglement entropies can serve as “proxy” quantities, namely the von Neumann entanglement or entanglement entropy. It is given by the non-vanishing part of the eigenvalue spectrum of  $\rho_A$  as

$$S_{A|B} = -\text{Tr } \rho_A \log_2 \rho_A = - \sum_\alpha w_\alpha \log_2 w_\alpha. \quad (3.53)$$

If we now consider a bipartitioning where AB is in the thermodynamic limit and A of size  $L^D$ , with  $D$  the spatial dimension, the so-called *area laws* [31–35] predict that for *ground states* of short-ranged Hamiltonians with a gap to excitations entanglement entropy is not extensive, but proportional to the surface, i.e.  $S(A|B) \sim L^{D-1}$ , as opposed to thermal entropy. This implies  $S \sim \text{cst.}$  in one dimension and  $S \sim L$  in two dimensions. At criticality, a much richer structure emerges, which usually involves

the presence or absence of logarithmic corrections ( $S(L) \propto \log L$ ,  $S(L) \propto L \log L$  in 1D and 2D), see [32, 36–39]. It should be emphasized that these properties of ground states are highly unusual: in the thermodynamic limit, a random state out of Hilbert space will indeed show extensive, even maximal, entanglement entropy with probability 1. This shows that our methods work only in a tiny corner of Hilbert space, but also that this corner happens to contain states of crucial importance to us. From the perspective of ground state physics, the huge size of the Hilbert space is therefore only an illusion.

In a mathematically non-rigorous way one can now make contact between vMPS (alias DMRG) and the area laws of quantum entanglement: between two  $D$ -dimensional state spaces for A and B, as provided by a  $D$ -dimensional MPS, the maximal entanglement is  $\log_2 D$  in the case where all eigenvalues of  $\rho_A$  are identical and  $D^{-1}$  (such that  $\rho_A$  is maximally mixed); meaning that one needs a state of dimension  $2^S$  and more to encode entanglement  $S$  properly. This implies that for gapped systems in one dimension an increase in system size will not lead to a strong increase in  $D$ ; in two dimensions,  $D \sim 2^L$ , such that vMPS will fail even for relatively small system sizes, as resources, i.e. MPS dimensions, have to grow exponentially (this however does not exclude very precise results for small two-dimensional clusters or quite large stripes, as already mentioned). Critical systems in one dimension are borderline cases: the logarithmic correction makes them untreatable in the thermodynamic limit, but enough data for excellent finite-size extrapolations can be obtained. The ultimate reason why MPS are so useful is that they allow three things, namely the identification of the small-entanglement corner of Hilbert space, the parametrization of its states, and their efficient manipulation (like ground state searches in this corner for given Hamiltonians).

### 3.3 Time Evolution of Matrix Product States

The calculation of operators like  $e^{-i\hat{H}t}$  or  $e^{-\beta\hat{H}}$  is of central interest in quantum mechanics, for real-time evolutions of quantum states and for quantum statistical mechanics;  $\beta$  can be interpreted as an imaginary time. It is one of the most attractive features of MPS that such real or imaginary time evolutions can be encoded very neatly and efficiently. This holds both for pure and mixed states, important at finite temperature. In the following, I will focus on time evolution based on a Trotter decomposition of the evolution operators [40–44], explaining first the Trotter decomposition and the structure of the algorithm for pure states, then the representation of the Trotter decomposition by MPOs. After this, I will discuss the changes necessary for the simulation of the dynamics of mixed states.

### 3.3.1 Conventional Time Evolution: Pure States

#### Trotter Decompositions of Time Evolution

Let us assume that  $\hat{H}$  consists of nearest-neighbour interactions only, i.e.  $\hat{H} = \sum_i \hat{h}_i$ , where  $\hat{h}_i$  contains the interaction between sites  $i$  and  $i + 1$ . We can then discretize time as  $t = N\tau$  with  $\tau \rightarrow 0$ ,  $N \rightarrow \infty$  and (in the most naive approach) do a first-order Trotter decomposition as

$$e^{-i\hat{H}\tau} = e^{-i\hat{h}_1\tau} e^{-i\hat{h}_2\tau} e^{-i\hat{h}_3\tau} \dots e^{-i\hat{h}_{L-3}\tau} e^{-i\hat{h}_{L-2}\tau} e^{-i\hat{h}_{L-1}\tau} + O(\tau^2), \quad (3.54)$$

which contains an error due to the noncommutativity of bond Hamiltonians,  $[\hat{h}_i, \hat{h}_{i+1}] \neq 0$  in general; higher order decompositions will be discussed later in this section. All time evolutions on odd ( $e^{-i\hat{H}_{\text{odd}}\tau}$ ) and even ( $e^{-i\hat{H}_{\text{even}}\tau}$ ) bonds respectively commute among each other, and can be carried out at the same time. So we are looking for an MPO doing an infinitesimal time step on the odd bonds and for another MPO doing the same on the even bonds.

As any operator is guaranteed to be MPO-representable, let us assume for a moment that indeed we can construct these representation of infinitesimal time steps efficiently (see next section for the explicit construction). As we will see, the maximum bond dimension of the infinitesimal time step MPOs is  $d^2$  because the dimension of  $e^{-i\hat{h}\tau}$  is  $(d^2 \times d^2)$ . The application of the infinitesimal time step MPOs thus increases the bond dimensions from  $D$  up to  $d^2D$ . Repeated applications of the infinitesimal time evolution MPOs leads to an exponential growth of the matrix dimensions, which therefore have to be truncated after time steps.

The resulting time evolution algorithm takes a very simple form: starting from  $|\psi(t=0)\rangle$ , repeat the following steps:

- Apply the MPO of the odd bonds to  $|\psi(t)\rangle$ .
- Apply the MPO of the even bonds to  $e^{-i\hat{H}_{\text{odd}}\tau} |\psi(t)\rangle$ .
- Compress the MPS  $|\psi(t+\tau)\rangle = e^{-i\hat{H}_{\text{even}}\tau} e^{-i\hat{H}_{\text{odd}}\tau} |\psi(t)\rangle$  from dimensions  $d^2D$  to  $D$ , monitoring the error. Obviously, one may also allow for some compression error (state distance)  $\epsilon$  and choose a time-dependent  $D$ : it will typically grow strongly with time, limiting the reachable timescale. By analogy to the ground state calculations, all results should be extrapolated in  $D \rightarrow \infty$  or  $\epsilon \rightarrow 0$ .

After each time step, we may evaluate observables in the standard way,  $\langle O(t) \rangle = \langle \psi(t) | \hat{O} | \psi(t) \rangle$ . But we can do more: we can calculate time-dependent correlators as

$$\langle \hat{O}(t) \hat{P} \rangle = \langle \psi | e^{+i\hat{H}t} \hat{O} e^{-i\hat{H}t} \hat{P} | \psi \rangle = \langle \psi(t) | \hat{O} | \phi(t) \rangle \quad (3.55)$$

where  $|\psi(t)\rangle = e^{-i\hat{H}t} |\psi\rangle$  and  $|\phi(t)\rangle = e^{-i\hat{H}t} \hat{P} |\psi\rangle$ . If we take e.g.  $\hat{O} = \hat{S}_i^z$  and  $\hat{P} = \hat{S}_j^z$ , we can calculate  $\langle \hat{S}_i^z(t) \hat{S}_j^z \rangle$  and by a double Fourier transformation the structure function

$$S^{zz}(k, \omega) \propto \int dt \sum_n \langle \hat{S}_i^z(t) \hat{S}_{i+n}^z \rangle e^{ikn} e^{-i\omega t}, \quad (3.56)$$

where I have assumed translational invariance and infinite extent of the lattice for simplicity of the formula.

A simple improvement on the algorithm given above is to do a second-order Trotter decomposition

$$e^{-i\hat{H}\tau} = e^{-i\hat{H}_{\text{odd}}\tau/2} e^{-i\hat{H}_{\text{even}}\tau} e^{-i\hat{H}_{\text{odd}}\tau/2} + O(\tau^3), \quad (3.57)$$

where the error per timestep is reduced by another order of  $\tau$ . If we do not do evaluations after each time step, we can group half steps, and work at no additional expense compared to a first-order Trotter decomposition.

A very popular implementation of a fourth order-Trotter decomposition that originates in quantum Monte Carlo would be given by the following formula due to Suzuki [45, 46]:

$$e^{-i\hat{H}\tau} = \hat{U}(\tau_1)\hat{U}(\tau_2)\hat{U}(\tau_3)\hat{U}(\tau_2)\hat{U}(\tau_1), \quad (3.58)$$

where

$$\hat{U}(\tau_i) = e^{-i\hat{H}_{\text{odd}}\tau_i/2} e^{-i\hat{H}_{\text{even}}\tau_i} e^{-i\hat{H}_{\text{odd}}\tau_i/2} \quad (3.59)$$

and

$$\tau_1 = \tau_2 = \frac{1}{4 - 4^{1/3}}\tau \quad \tau_3 = \tau - 2\tau_1 - 2\tau_2. \quad (3.60)$$

Even smaller errors can be achieved at similar cost using less symmetric formulae [47]. This completes the exposition of the algorithm (an error analysis will be given at the end), and we now have to construct the MPOs.

## MPO for Pure State Evolution

Let us consider the Trotter step for all odd bonds of a chain:

$$e^{-i\hat{h}_1\tau} \otimes e^{-i\hat{h}_3\tau} \otimes \dots \otimes e^{-i\hat{h}_{L-1}\tau} |\psi\rangle, \quad (3.61)$$

each bond-evolution operator like  $e^{-i\hat{h}_1\tau}$  takes the form

$$\sum_{\sigma_1\sigma_2, \sigma'_1\sigma'_2} O^{\sigma_1\sigma_2, \sigma'_1\sigma'_2} |\sigma_1\sigma_2\rangle\langle\sigma'_1\sigma'_2|.$$

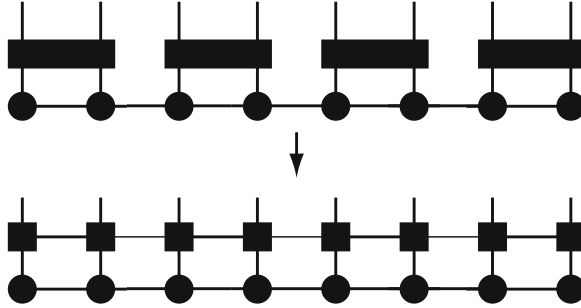


**Fig. 3.9** A Trotter step: On all odd bonds, an (infinitesimal) bond time evolution is carried out. This merges two sites, such that the simple product form of MPS is lost at first sight, but the time evolution can be translated into MPOs. As the time evolution factorizes, the MPOs have dimension 1 on all even bonds (thin lines)

Both in the pictorial and the explicit mathematical representation it is obvious that this operator destroys the MPS form (Fig. 3.9).

It would therefore be desirable to have  $O^{\sigma_1\sigma_2,\sigma'_1\sigma'_2}$  in some form containing tensor products  $O^{\sigma_1,\sigma'_1} \otimes O^{\sigma_2,\sigma'_2}$ , to maintain the MPS form. To this purpose, we carry out the procedure for decomposing an arbitrary state into an MPS, adapted to an operator (two indices per site). It works because there are so few indices; we are considering only two sites. One reorders  $O$  to group local indices and carries out a singular value decomposition:

$$\begin{aligned} O^{\sigma_1\sigma_2,\sigma'_1\sigma'_2} &= P_{(\sigma_1\sigma'_1),(\sigma_2\sigma'_2)} \\ &= \sum_k U_{\sigma_1\sigma'_1,k} S_{k,k} (V^\dagger)_{k,(\sigma_2\sigma'_2)} \\ &= \sum_k U_k^{\sigma_1\sigma'_1} \overline{U}_k^{\sigma_2\sigma'_2} \\ &= \sum_k U_{1,k}^{\sigma_1\sigma'_1} \overline{U}_{k,1}^{\sigma_2\sigma'_2} \end{aligned}$$

where  $U_k^{\sigma_1\sigma'_1} = U_{(\sigma_1\sigma'_1),k} \sqrt{S_{k,k}}$  and  $\overline{U}_k^{\sigma_2\sigma'_2} = \sqrt{S_{k,k}} (V^\dagger)_{k,(\sigma_2\sigma'_2)}$ . In the very last step of the derivation, we have introduced a dummy index taking value 1 to arrive at the form of an MPO matrix. The index  $k$  may run up to  $d^2$ , giving the bond dimension  $D_W$  of the MPO.

The MPO representing the operator in Eq.(3.61),  $U^{\sigma_1\sigma'_1} \overline{U}^{\sigma_2\sigma'_2} U^{\sigma_3\sigma'_3} \overline{U}^{\sigma_4\sigma'_4} \dots$ , factorizes on every second bond, as do the original unitaries. If one site does not participate in any bond evolution, we simply assign it the identity unitary as a  $(1 \times 1)$ -matrix:  $I_{1,1}^{\sigma,\sigma'} = \delta_{\sigma,\sigma'}$ . Then the global MPO can be formed trivially from local MPOs. The MPO for time evolution on all odd bonds would read  $U \overline{U} U \overline{U} U U \overline{U} \dots$ , whereas the even-bond time step reads  $I U \overline{U} U \overline{U} U U \overline{U} \dots I$  (Fig. 3.10).

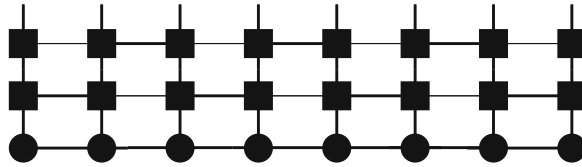


**Fig. 3.10** A complete first-order Trotter time step (odd and even bonds). *Fat* and *thin* lines correspond to dimension 1 and  $> 1$  on MPO bonds. The MPOs in the *top line* on the first and last site are trivial scalar identities 1

### 3.3.2 Conventional Time Evolution: Mixed States

#### Purification of Mixed States

Finite temperature calculations can be carried out based on the purification of an arbitrary mixed quantum state [44]: if we consider a mixed state in physical space  $P$  formed from orthonormal states, we can interpret it as the result of a partial trace over a Schmidt decomposition of a pure state on  $PQ$ , where  $Q$  is an auxiliary space:

$$\hat{\rho}_P = \sum_{a=1}^r s_a^2 |a\rangle_P \langle a|_P \rightarrow |\psi\rangle = \sum_{a=1}^r s_a |a\rangle_P |a\rangle_Q \quad \hat{\rho}_P = \text{Tr}_Q |\psi\rangle \langle \psi|. \quad (3.62)$$

The auxiliary state space can simply be taken as a copy of the original one, so finite-temperature density operators on a chain can be expressed as pure states on a ladder (see Fig. 3.11).

To calculate a thermal density operator  $\hat{\rho}_\beta = Z(\beta)^{-1} e^{-\beta \hat{H}}$ ,  $Z(\beta) = \text{Tr}_P e^{-\beta \hat{H}}$ , we write

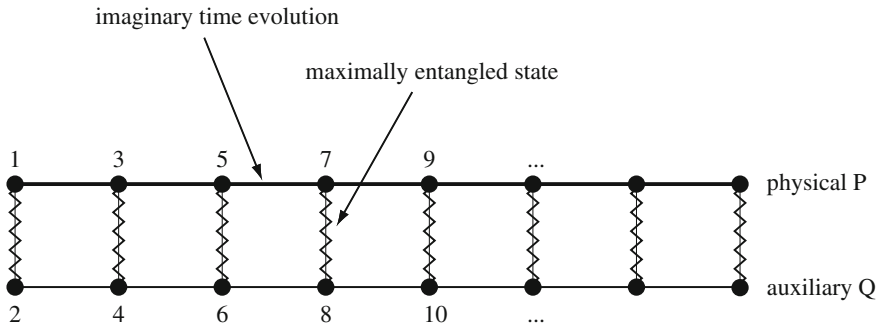


**Fig. 3.11** Schematic representation of finite-temperature simulations: instead of a chain, one sets up a ladder with an identical copy of the chain. Physical sites have odd, auxiliary sites have even labels. Equivalent sites on the physical and auxiliary leg are linked by maximally entangled states. To reach inverse temperature  $\beta$ , an imaginary time evolution is carried out up to “time”  $-i\beta/2$

$$\hat{\rho}_\beta = Z(\beta)^{-1} e^{-\beta \hat{H}} = Z(\beta)^{-1} e^{-\beta \hat{H}/2} \cdot \hat{I} \cdot e^{-\beta \hat{H}/2}. \quad (3.63)$$

The identity  $\hat{I}$  is nothing but  $Z(0)\hat{\rho}_0$ , the infinite temperature density operator times the infinite temperature partition function. Assume we know the purification of  $\hat{\rho}_0$  as an MPS,  $|\psi_{\beta=0}\rangle$ . Then

$$\begin{aligned} \hat{\rho}_\beta &= (Z(0)/Z(\beta))e^{-\beta \hat{H}/2} \cdot \text{Tr}_Q |\psi_0\rangle\langle\psi_0| \cdot e^{-\beta \hat{H}/2} \\ &= (Z(0)/Z(\beta))\text{Tr}_Q e^{-\beta \hat{H}/2} |\psi_0\rangle\langle\psi_0| e^{-\beta \hat{H}/2}. \end{aligned} \quad (3.64)$$

The trace over Q can be pulled out as the Hamiltonian does not act on Q. But the result means that we have to do an imaginary time evolution

$$|\psi_\beta\rangle = e^{-\beta \hat{H}/2} |\psi_0\rangle. \quad (3.65)$$

Expectation values are given by

$$\langle \hat{O} \rangle_\beta = \text{Tr}_P \hat{O} \hat{\rho}_\beta = (Z(0)/Z(\beta)) \text{Tr}_P \hat{O} \text{Tr}_Q |\psi_\beta\rangle\langle\psi_\beta| = (Z(0)/Z(\beta)) \langle\psi_\beta|\hat{O}|\psi_\beta\rangle. \quad (3.66)$$

$(Z(0)/Z(\beta)) = (d^L/Z(\beta))$  may seem difficult to obtain, but follows trivially from the expectation value of the identity,

$$1 = \langle \hat{I} \rangle_\beta = \text{Tr}_P \hat{\rho}_\beta = (Z(0)/Z(\beta)) \text{Tr}_P \text{Tr}_Q |\psi_\beta\rangle\langle\psi_\beta| = (Z(0)/Z(\beta)) \langle\psi_\beta|\psi_\beta\rangle, \quad (3.67)$$

hence  $Z(\beta)/Z(0) = \langle\psi_\beta|\psi_\beta\rangle$ , or, in complete agreement with standard quantum mechanics,

$$\langle \hat{O} \rangle_\beta = \frac{\langle\psi_\beta|\hat{O}|\psi_\beta\rangle}{\langle\psi_\beta|\psi_\beta\rangle}. \quad (3.68)$$

But this takes us right back to expressions we know how to calculate. All we have to do is to find  $|\psi_0\rangle$ , carry out imaginary time evolution up to  $-i\beta/2$ , and calculate expectation values as for a pure state. We can even subject the purified state  $|\psi_\beta\rangle$  to subsequent real time evolutions, to treat time dependence at finite  $T$ .

We can also do thermodynamics quite simply, as  $Z(\beta)/Z(0)$  is given by the square of the norm of  $|\psi_\beta\rangle$  and  $Z(0) = d^L$ . This means that we can obtain  $Z(\beta)$  by keeping the purified state normalized at all temperatures and by accumulating normalization factors as temperature goes down and  $\beta$  increases. From  $Z(\beta)$ , we have  $F(\beta) = -\beta^{-1} \ln Z(\beta)$ . At the same time,  $U(\beta) = \langle \hat{H} \rangle_\beta = \langle\psi_\beta|\hat{H}|\psi_\beta\rangle$ . But this in turn gives us  $S(\beta) = \beta(U(\beta) - F(\beta))$ . Further thermodynamic quantities follow similarly.

The purification of the infinite temperature mixed state is a simple MPS of dimension 1, because it factorizes (if we take one ladder rung as a big site):

$$\hat{\rho}_0 = \frac{1}{d^L} \hat{I} = \left( \frac{1}{d} \hat{I} \right)^{\otimes L}. \quad (3.69)$$

As  $\hat{\rho}_0$  factorizes, we can now purify the local mixed state on each physical site as a pure state on rung  $i$ , to get  $|\psi_{i0}\rangle$ , then  $|\psi_0\rangle = |\psi_{1,0}\rangle|\psi_{2,0}\rangle|\psi_{3,0}\rangle\dots$ , a product state or an MPS of dimension 1. If we consider some rung  $i$  of the ladder, with states  $|\sigma\rangle_P$  and  $|\sigma\rangle_Q$  on the physical site  $2i - 1$  and the auxiliary site  $2i$ , we can purify as follows:

$$\frac{1}{d} \hat{I} = \sum_{\sigma} \frac{1}{d} |\sigma\rangle_P \langle \sigma|_P = \text{Tr}_Q \left[ \left( \sum_{\sigma} \frac{1}{\sqrt{d}} |\sigma\rangle_P |\sigma\rangle_Q \right) \left( \sum_{\sigma} \frac{1}{\sqrt{d}} \langle \sigma|_P \langle \sigma|_Q \right) \right]. \quad (3.70)$$

Hence the purification is given by a maximally entangled state (entanglement entropy is  $\log_2 d$ ),

$$|\psi_{i0}\rangle = \sum_{\sigma} \frac{1}{\sqrt{d}} |\sigma\rangle_P |\sigma\rangle_Q. \quad (3.71)$$

It is easy to see that one can carry out local unitary transformations on both P and Q separately that leave that structure invariant. For example, for the purification of a spin-1/2 chain it is advantageous to use the singlet state as local purification,

$$|\psi_{i,0}\rangle = \frac{1}{\sqrt{2}} [|\uparrow_P \downarrow_Q\rangle - |\downarrow_P \uparrow_Q\rangle], \quad (3.72)$$

in case the program knows how to exploit good quantum numbers: this state would allow to conserve total  $S = 0$  and  $S^z = 0$  at the same time. In this case, the four A-matrices would read

$$A^{\uparrow_P \uparrow_Q} = 0 \quad A^{\uparrow_P \downarrow_Q} = 1/\sqrt{2} \quad A^{\downarrow_P \uparrow_Q} = -1/\sqrt{2} \quad A^{\downarrow_P \downarrow_Q} = 0, \quad (3.73)$$

and the purified starting state  $|\psi_0\rangle$  for  $\beta = 0$  is now given by a product of singlet bonds on a ladder. In fact, a SVD of reshaped matrix  $A_{\sigma,\sigma'}$  allows us to introduce truly site-local A-matrices, which have dimension  $(1 \times 2)$  on odd and  $(2 \times 1)$  on even sites:

$$A^{\uparrow_{2i-1}} = [1 \ 0] \quad A^{\downarrow_{2i-1}} = [0 \ -1] \quad A^{\uparrow_{2i}} = [0 \ 1/\sqrt{2}]^T \quad A^{\downarrow_{2i}} = [1/\sqrt{2} \ 0]^T. \quad (3.74)$$

In order to apply the pure state time evolution algorithm, it remains to find the MPO.

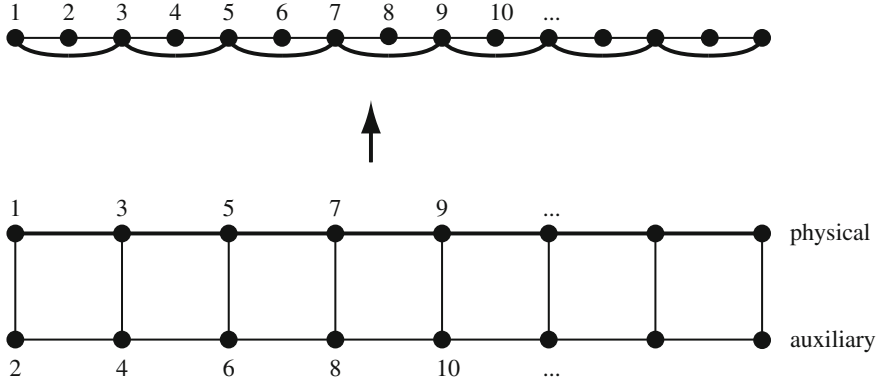


**Fig. 3.12** The time-evolution of mixed states on a chain can be seen as that of a pure state on a ladder, where the physical sites sit on the first leg and additional auxiliary sites on the second leg. This ladder is mapped to a chain. As the time evolution acts only on the physical states, next-nearest neighbour interactions arise

### MPO for Mixed State Evolution

The ladder appearing in mixed state simulations can be mapped to a chain (Fig. 3.12), where the physical Hamiltonian acts only on the odd sites, 1, 3, 5, . . . , and the auxiliary sites are even, 2, 4, 6, . . . . Then the only non-trivial time-evolution connects (1,3), (3,5), (5,7). There are several ways of dealing with such longer-ranged interactions, one explicitly constructing the longer-ranged interaction, the other using so-called swap gates, reducing it to a nearest-neighbour interaction.

The direct MPO description of the “longer-ranged” interaction (1, 3) involves necessarily a non-trivial tensor on site 2, whereas the site 4 is inert. Similarly for (3, 5), there is a non-trivial tensor on 4, but site 6 is inert. This suggests a Trotter decomposition (1, 2, 3, 4), (5, 6, 7, 8), . . . in the “odd” and (3, 4, 5, 6), (7, 8, 9, 10), . . . in the “even” steps.

The four-site evolution operator on sites 1 through 4 then reads

$$O^{(\sigma_1\sigma_2\sigma_3\sigma_4),(\sigma'_1\sigma'_2\sigma'_3\sigma'_4)} = O^{(\sigma_1\sigma_2\sigma_3),(\sigma'_1\sigma'_2\sigma'_3)} \cdot \delta_{\sigma_4,\sigma'_4} \quad (3.75)$$

and we can build the three-site unitary with only a slight modification of the two-site unitary which contains the actual physical time evolution:

$$O^{(\sigma_1\sigma_2\sigma_3),(\sigma'_1\sigma'_2\sigma'_3)} = O^{(\sigma_1\sigma_3),(\sigma'_1\sigma'_3)} \cdot \delta_{\sigma_2,\sigma'_2}. \quad (3.76)$$

This three-site unitary is now subjected to two SVDs. For the notation, we first shift down the indices and reorder sitewise. Reshaping with subsequent SVDs then iteratively isolates  $\sigma_3, \sigma'_3, \sigma_2, \sigma'_2$ , and  $\sigma_1, \sigma'_1$ :

$$\begin{aligned}
O_{(\sigma_1 \sigma_2 \sigma_3), (\sigma'_1 \sigma'_2 \sigma'_3)} &= P_{(\sigma_1 \sigma'_1 \sigma_2 \sigma'_2), (\sigma_3 \sigma'_3)} \\
&= \sum_{k_2} U_{(\sigma_1 \sigma'_1 \sigma_2 \sigma'_2), k_2} S_{k_2, k_2}^{[2]} (V_{23}^\dagger)_{k_2, (\sigma_3 \sigma'_3)} \\
&= \sum_{k_2} U_{(\sigma_1 \sigma'_1), (\sigma_2 \sigma'_2 k_2)} S_{k_2, k_2}^{[2]} (V_{23}^\dagger)_{k_2, (\sigma_3 \sigma'_3)} \\
&= \sum_{k_1, k_2} U_{(\sigma_1 \sigma'_1), k_1} S_{k_1, k_1}^{[1]} (V_{12}^\dagger)_{k_1, (\sigma_2 \sigma'_2 k_2)} S_{k_2, k_2}^{[2]} (V_{23}^\dagger)_{k_2, (\sigma_3 \sigma'_3)} \\
&= \sum_{k_1, k_2} W_{1, k_1}^{\sigma_1 \sigma'_1} W_{k_1, k_2}^{\sigma_2 \sigma'_2} W_{k_2, 1}^{\sigma_3 \sigma'_3}
\end{aligned}$$

where, with the introduction of dummy indices and the inert tensor on site 4:

$$W_{1, k_1}^{\sigma_1 \sigma'_1} = U_{(\sigma_1 \sigma'_1), k_1} \sqrt{S_{k_1, k_1}^{[1]}} \quad (3.77)$$

$$W_{k_1, k_2}^{\sigma_2 \sigma'_2} = \sqrt{S_{k_1, k_1}^{[1]} (V_{12}^\dagger)_{k_1, (\sigma_2 \sigma'_2 k_2)}} \sqrt{S_{k_2, k_2}^{[2]}} \quad (3.78)$$

$$W_{k_2, 1}^{\sigma_3 \sigma'_3} = \sqrt{S_{k_2, k_2}^{[2]} (V_{23}^\dagger)_{k_2, (\sigma_3 \sigma'_3)}} \quad (3.79)$$

$$W_{1, 1}^{\sigma_4 \sigma'_4} = \delta_{\sigma_4, \sigma'_4} \quad (3.80)$$

From this, MPOs for the entire chain can be formed as for the pure state time evolution. We have done nothing but the iterative decomposition of an MPO on 4 sites. Again, this is still manageable, as only 4 sites are involved.

Obviously, it is a straightforward step to write an evolution operator acting on all four bonds (1, 2), (1, 3), (2, 4) and (3, 4) and subject it to a similar sequence of SVDs, which would allow to consider pure state time-evolution on a real ladder.

Let me conclude with the remark that using MPO allows also other Trotter decompositions, e.g. decomposing the Heisenberg Hamiltonian in its  $x$ ,  $y$  and  $z$ -dependent parts, useful for long-range interactions [48].

### 3.3.3 tMPS, tDMRG, TEBD: Variations on a Theme

A bit before time evolution with MPS (tMPS) was developed, two other algorithms were introduced to simulate the real-time dynamics of one-dimensional quantum chains, time-evolving block decimation (TEBD) [40, 41] and real-time or time-dependent DMRG (tDMRG) [42, 43]. Both algorithms are also based on MPS, but are different from tMPS, when one looks more closely. All of them are however based on the idea of time-evolving an MPS which was first put forward in [40, 41] and therefore are minor variations on a theme. tDMRG and TEBD are mathematically equivalent,

i.e. should for exact arithmetic give the same results, whereas numerically they are clearly distinct algorithms, both carrying out operations that have no counterpart in the other method, with their respective advantages and disadvantages. Both methods share the central feature that time evolution and truncation are intertwined: after each single bond evolution, there is a truncation by SVD. By contrast, tMPS evolves all bonds first, and then truncates the entire state by compression of matrix dimensions  $d^2 D \rightarrow D$  by SVD or iteratively.

tMPS is the cleaner approach, but it can also be shown to be more precise. In fact, for real-time evolution it can be shown to relate to tDMRG or TEBD exactly as iterative variational compression to compression by SVD, which implies that for small state changes (e.g. for very small time steps) the difference goes down, as the interdependence of truncations becomes less severe, there being only very benign truncations. Hence, the difference between the three algorithms becomes only visible at the level of variational compression, which means that for small real time steps, where the difference between compression algorithms is small, all these issues do not matter. For a detailed discussion, consider [6].

### 3.3.4 How Far Can We Go?

In this section, I have described basic algorithms for the time evolution of pure and mixed states. There were two sources of error. One of them is the Trotter decomposition, which for an  $n$ th order decomposition generated an error  $O(\tau^{n+1})$  for each time step  $\tau$ . As there are  $t/\tau$  time steps, the error will ultimately be  $O(\tau^n t)$ , i.e. linear in time. This means it is only growing moderately in time and can be scaled down by smaller time steps and/or higher-order decompositions. This is common to all current methods [40–44]. In fact, there are other methods of calculating matrix exponentials such as the Krylov method [49] or lookahead procedures such as in [50], which reduce this error even more. In any case, it is not very worrisome in the long run.

On the other hand, there is the error due to the truncation of the blown-up bond dimensions of the MPS after each time step. This error is serious; early on it could be shown to lead to errors exponentially blowing up in time [51]. Yet truncation errors are only the symptom, not the fundamental problem: the real reason is that—following the Lieb-Robertson theorem—entanglement  $S$  can grow up to linearly in time for an out-of-equilibrium evolution of a quantum state:  $S(t) \leq S(0) + ct$ , where  $c$  is some constant related to the propagation speed of excitations in the lattice [52]. This linear bound is actually reached for many quantum quenches, where a Hamiltonian parameter is abruptly changed such that the global energy changes extensively. Both from  $D \sim 2^S$  and from a rigorous analysis [53] it follows that in such cases the matrix dimensions will have to go up exponentially in time,  $D(t) \sim 2^t$ , or that for fixed matrix dimensions precision will deteriorate exponentially. This reflects that typical starting states in quantum quenches are either product states ( $D = 1$ ) or area-law obeying ground states of some Hamiltonian. Upon a generic time evolution, the state will explore Hilbert space whose states are in general extensively entangled. The

gradual transformation upon time evolution from an area-law state to an extensive-entanglement state is captured by  $S(t) \leq S(0) + ct$ .

Nevertheless, in many circumstances matrix size growth is slow enough that numerical resources are sufficient to observe the time-dependent phenomenon of interest: Time-dependent DMRG has been used extensively in the meantime and found to open completely new perspectives on the non-equilibrium behaviour of strongly correlated one-dimensional systems.

## References

1. I. Bloch, J. Dalibard, W. Zwerger, Rev. Mod. Phys. **80**, 885 (2008)
2. S.R. White, Phys. Rev. Lett. **69**, 2863 (1992)
3. S.R. White, Phys. Rev. B **48**, 10345 (1993)
4. U. Schollwöck, Rev. Mod. Phys. **77**, 259 (2005)
5. K. Hallberg, Adv. Phys. **55**, 477 (2006)
6. U. Schollwöck, Ann. Phys. (NY) **326**, 96 (2011)
7. S. Ostlund, S. Rommer, Phys. Rev. Lett. **75**, 3537 (1995)
8. J. Dukelsky, M.A. Martín-Delgado, T. Nishino, G. Sierra, Europhys. Lett. **43**, 457 (1998)
9. H. Takasaki, T. Hikihara, T. Nishino, J. Phys. Soc. Jpn. **68**, 1537 (1999)
10. F. Verstraete, D. Porras, J.I. Cirac, Phys. Rev. Lett. **93**, 227205 (2004)
11. G.H. Golub, C.F. van Loan, C. F., Matrix Computations, 3rd edn. (Johns Hopkins University Press, Baltimore, 1996)
12. A. Weichselbaum, F. Verstraete, U. Schollwöck, J.I. Cirac, J. von Delft, Phys. Rev. B **80**, 165117 (2009)
13. K.G. Wilson, Rev. Mod. Phys. **47**, 773 (1975)
14. R. Bulla, T.A. Costi, T. Pruschke, Rev. Mod. Phys. **80**, 395 (2008)
15. I.P. McCulloch, J. Stat. Mech.: Theor. Exp. P10014 (2007)
16. G.M. Crosswhite, D. Bacon, Phys. Rev. A **78**, 012356 (2008)
17. G.M. Crosswhite, A.C. Doherty, G. Vidal, Phys. Rev. B **78**, 035116 (2008)
18. F. Fröwis, V. Nebendahl, W. Dür, Phys. Rev. A **81**, 062337 (2010)
19. I.P. McCulloch, Infinite size density matrix renormalization group, revisited (2008) arXiv:0804.2509.
20. U. Schollwöck, Phys. Rev. B **58**, 8194 (1998)
21. L.Q. Sun, J. Zang, S.J. Qin, Y. Lei, Phys. Rev. B **65**, 132412 (2002)
22. T. Nishino, K. Okunishi, J. Phys. Soc. Jpn. **64**, 4084 (1995)
23. Y. Hieida, K. Okunishi, Y. Akutsu, Phys. Lett. A **233**, 464 (1997)
24. K. Ueda, T. Nishino, K. Okunishi, Y. Hieida, R. Derian, A. Gendiar, J. Phys. Soc. Jpn. **75**, 014003 (2006)
25. H. Ueda, T. Nishino, K. Kusakabe, J. Phys. Soc. Jpn. **77**, 114002 (2008)
26. H. Ueda, A. Gendiar, T. Nishino, J. Phys. Soc. Jpn. **79**, 044001 (2010)
27. I. Peschel, M. Kaulke, Ö. Legeza, Ann. Phys. (Leipzig) **8**, 153 (1999)
28. K. Okunishi, Y. Hieida, Y. Akutsu, Phys. Rev. E **59**, R6227 (1999)
29. S. Yan, D.A. Huse, S.R. White, Science **332**, 1173 (2011)
30. S. Depenbrock, I.P. McCulloch, U. Schollwöck, Phys. Rev. Lett. **109**, 067201 (2012)
31. J.D. Bekenstein, Phys. Rev. D **7**, 2333 (1973)
32. M. Srednicki, Phys. Rev. Lett. **71**, 666 (1993)
33. C.G. Callan, F. Wilczek, Phys. Lett. B **333**, 55 (1994)
34. M.B. Plenio, J. Eisert, J. Dreissig, M. Cramer, Phys. Rev. Lett. **94**, 060503 (2005)
35. J. Eisert, M. Cramer, M.B. Plenio, Rev. Mod. Phys. **82**, 277 (2010)
36. G. Vidal, J.I. Latorre, E. Rico, A. Kitaev, Phys. Rev. Lett. **90**, 227902 (2003)

37. J.I. Latorre, E. Rico, G. Vidal, Quant. Inf. Comput. **4**, 48 (2004)
38. D. Gioev, I. Klich, Phys. Rev. Lett. **96**, 100503 (2006)
39. T. Barthel, M.-C. Chung, U. Schollwöck, U., Phys. Rev. A **74**, 022329 (2006)
40. G. Vidal, Phys. Rev. Lett. **91**, 147902 (2003)
41. G. Vidal, Phys. Rev. Lett. **93**, 040502 (2004)
42. A.J. Daley, C. Kollath, U. Schollwöck, G. Vidal, J. Stat. Mech.: Theor. Exp. P04005 (2004)
43. S.R. White, A.E. Feiguin, Phys. Rev. Lett. **93**, 076401 (2004)
44. F. Verstraete, J.J. Garcia-Ripoll, J.I. Cirac, Phys. Rev. Lett. **93**, 207204 (2004)
45. M. Suzuki, Prog. Theor. Phys. **56**, 1454 (1976)
46. M. Suzuki, J. Math. Phys. **32**, 400 (1991)
47. R.I. McLachlan, SIAM J. Sci. Comput. **16**, 151 (1995)
48. B. Pirvu, V. Murg, J.I. Cirac, F. Verstraete, New J. Phys. **12**, 025012 (2010)
49. P. Schmitteckert, Phys. Rev. B **70**, 121302 (2004)
50. A.E. Feiguin, S.R. White, Phys. Rev. B **72**, 020404 (2005)
51. D. Gobert, C. Kollath, U. Schollwöck, G. Schütz, Phys. Rev. E **71**, 036102 (2005)
52. P. Calabrese, J. Cardy, J. Stat. Mech.: Theor. Exp. P04010 (2006)
53. T. Osborne, Phys. Rev. Lett. **97**, 157202 (2006)

# Chapter 4

## Quantum Criticality with the Multi-scale Entanglement Renormalization Ansatz

Glen Evenbly and Guifre Vidal

**Abstract** The goal of this chapter is to provide an introduction to the multi-scale entanglement renormalization ansatz (MERA) and its application to the study of quantum critical systems. The MERA, in its scale-invariant form, is seen to offer direct numerical access to the scale-invariant operators of a critical theory. As a result, given a critical Hamiltonian on the lattice, the scale-invariant MERA can be used to characterize the underlying conformal field theory. The performance of the MERA is benchmarked for several critical quantum spin chains, namely Ising, Potts, XX and (modified) Heisenberg models, and an insightful comparison with results obtained using a matrix product state is made. The extraction of accurate conformal data, such as scaling dimensions and operator product expansion coefficients of both local and non-local primary fields, is also illustrated.

### 4.1 Introduction

Tensor network states are powerful variational ansätze that can be used to characterize the low-energy properties of quantum many-body systems on a lattice. The premise of tensor network approaches is to parameterize a many-body wave-function by using a collection of tensors connected into a network. The number of parameters required to specify these tensors is much smaller than the exponentially large dimension of

---

G. Evenbly (✉)

Institute for Quantum Information and Matter, California Institute of Technology,  
1200 E. California Blvd, Pasadena, CA 91125, USA  
e-mail: evenbly@caltech.edu

G. Vidal

Perimeter Institute for Theoretical Physics, 31 Caroline Street,  
Waterloo, ON N2L 2Y5, Canada  
e-mail: gvidal@perimeterinstitute.ca

the system's Hilbert space, in such a way that very large (and even infinite) lattices can be considered.

Tensor network states can be broadly classified into two sets according to the geometry of the underlying networks [1]. In the first set, the network reproduces the *physical geometry* of the system, as specified by the pattern of interactions in the Hamiltonian. For instance, the matrix product state (MPS) [2–4], an ansatz for  $D = 1$  dimensional systems, consists of a collection of tensors connected into a chain; similarly, its generalization for lattices in  $D > 1$  dimensions, known as projected entangled pair states (PEPS) [5–7], consists of a collection of tensors connected according to a  $D$  dimensional lattice. In contrast, a second class of tensor network states aim at reproducing the *holographic geometry* of the system. The latter spans an additional dimension used to parameterize the different length scales (or, equivalently, energy scales) relevant to the description of the many-body wavefunction. Thus the multi-scale entanglement renormalization ansatz (MERA) [8–23] for a lattice system in  $D$  dimensions consists of a network in  $D + 1$  dimensions.

The simplest and most widely employed tensor network state is the MPS. The MPS underlies the remarkable success of the density matrix renormalization group (DMRG) algorithm [24–27], which for almost two decades has dominated the numerical study of  $D = 1$  dimensional quantum systems, providing very accurate results for low energy properties. DMRG has not only become ubiquitous in condensed matter physics but has also found application in other fields involving quantum many-body systems, such as quantum chemistry [28]. Further algorithms based upon the MPS have also been developed, such as the time evolving block decimation (TEBD) [29, 30] algorithm, later reformulated as time-dependent DMRG [31, 32], which allows the simulation of certain low-energy *dynamics* for relatively long times.

In this chapter we discuss the application of the MERA to study critical systems in  $D = 1$  dimensions (although most of the present formalism is directly applicable to  $D > 1$  dimensions). Given the success of MPS-based methods such as DMRG and TEBD for quantum systems in  $D = 1$  dimensions, it is natural to ask whether an alternative approach is actually needed. A clear answer to this question is obtained by discussing the short-comings of the MPS representation for critical systems as well as by exploring the benefits of including scale invariance directly into a tensor network state, something that is possible with the MERA but not the MPS.

Critical systems typically lack a characteristic length scale and are thus invariant under changes of scale. One manifestation of scale invariance in critical systems is that correlators decay polynomially, in sharp contrast with gapped systems, where they decay exponentially with a characteristic correlation length. It is well-known, however, that an MPS with a finite bond dimension  $\chi$  (where  $\chi$  indicates the size of the tensors) can never properly capture the scale invariance of a critical state. Indeed, a duly optimized MPS possesses an intrinsic finite correlation length  $\zeta \approx \chi^\kappa$  [33, 34], where  $\kappa$  is a constant that depends on the universality class of the phase transition under consideration, such that correlators decay exponentially at length scales larger than  $\zeta$ . Thus, while the MPS can accurately approximate short-range properties of a critical ground state, it necessarily fails to capture its properties at asymptotically large distances. [In practice, however, the cost of MPS-based approaches scales only

as  $O(\chi^3)$  with the bond dimension  $\chi$ . This means that one can use a very large value of  $\chi$ , which often allows the critical behavior of a system to be accurately captured up to some very large length scale  $\zeta$ ].

On the other hand, the MERA can explicitly capture the scale invariance of critical systems [8, 10, 12, 15–17, 19, 22], a feature that has significant advantages, both conceptual and practical. Tensors in the MERA are organized in layers, where each layer corresponds to a different length (or energy) scale. In an infinite system, scale invariance is then easily enforced by choosing all layers of tensors to be identical. The resulting ansatz is referred to as the *scale-invariant* MERA. Certain structural properties of the scale-invariant MERA, such as the polynomial decay of correlators and the logarithmic growth of block entanglement entropy [1, 9], already hint at its suitability to represent critical systems.

In addition, this ansatz offers direct access to the scaling operators of a critical theory, namely those operators that transform into themselves under scale transformations. As a scale-invariant/covariant object, a scaling operator must act non-trivially on a region of the system that has no characteristic length scale. In a  $(1+1)$ -dimensional conformal field theory (CFT) [35–37] (corresponding to the continuum limit of a critical quantum system in  $D = 1$  spatial dimensions), the support of a scaling operator can therefore only be one of three possibilities: (i) an infinite line, (ii) a single point, or (iii) a semi-infinite line. The first type of support corresponds to a global internal symmetry of the CFT's Hamiltonian. The second type of support is seen to correspond to local scaling operators, associated to local excitations. Finally, the third type corresponds to non-local (or semi-local) scaling operators, associated e.g. to domain wall excitations. Going back to the lattice, scaling operators are distorted by the presence of a finite lattice spacing, but they can still be directly extracted from the scale-invariant MERA. Thus, on the lattice, (i) a global internal symmetry is implemented by an infinite string of identical single-site operators; (ii) local scaling operators are now supported on a small number of sites (the specific number depends on the MERA scheme); and (iii) non-local operators mix elements of the two previous objects: they consist of a semi-infinite string of identical single-site operators (the same ones that implement an internal symmetry) completed with some local operator at the end of the string. Importantly, the scaling dimensions and fusion rules of the scaling operators on the lattice are the same as in the continuum. As a result, a relatively simple and inexpensive calculation with the scale-invariant MERA can be used to obtain remarkably accurate estimates of the conformal data characterizing the underlying CFT.

The rest of the chapter is organized in sections as follows. Section 4.2 introduces the key aspects of entanglement renormalization, which is the renormalization group transformation for lattice models on which the MERA is based. We describe how local operators transform under the coarse-graining transformation and discuss basic aspects of the MERA, including the evaluation of the expectation value of local observables, and briefly compare different MERA implementations in  $D = 1$  dimensions. Section 4.3 addresses the role of spatial and internal symmetries in tensor network states, and compares how different symmetries can be enforced in MPS/PEPS and MERA. While translation invariance is naturally implemented in an MPS and

PEPS, it can only be approximately enforced on the MERA. Section 4.4 specializes on the implementation of scale invariance in the MERA and discusses how the scaling operators of a critical theory can be extracted from it. In Sect. 4.5 we demonstrate the performance of the scale-invariant MERA for a number of critical quantum spin chains, namely Ising, Potts, quantum XX and Heisenberg models. Specifically, Sect. 4.5.1 compares ground state energy and two-point correlators obtained with MERA and MPS. Interestingly, MPS and MERA approaches seem to complement each other. For a given computational cost, the MPS is seen to provide more accurate estimates of the expectation value of a local observable, such as the ground state energy. However, the MERA is seen to provide a better characterization of long-range properties, such as two-point correlators at long distances. The advantages of the scale-invariant MERA are then further illustrated in Sect. 4.5.2 by extracting, in the concrete context of the quantum Ising model, the conformal data (including scaling dimensions, fusion rules for scaling operators and central charge) of the underlying CFT.

## 4.2 Entanglement Renormalization and the MERA

In this section we first recall a few basic aspects of entanglement renormalization (ER), the coarse-graining transformation upon which the MERA is based. We then introduce the MERA and review a few of its features.

### 4.2.1 Foundations of Entanglement Renormalization

For concreteness, we mostly consider a specific implementation of ER that produces the so-called ternary MERA (where three sites are coarse-grained into one effective site). In Sect. 4.2.3 we also discuss other MERA schemes.

Let  $\mathcal{L}$  denote a  $D = 1$  dimensional lattice made of  $N$  sites, where each site is described by a Hilbert space  $\mathbb{V}$  of finite dimension  $d$ , so that the vector space of the lattice is  $\mathbb{V}_{\mathcal{L}} \cong \mathbb{V}^{\otimes N}$ . We consider a coarse-graining transformation  $U$  that maps lattice  $\mathcal{L}$  to a coarser lattice  $\mathcal{L}'$

$$U^\dagger : \mathbb{V}_{\mathcal{L}} \mapsto \mathbb{V}_{\mathcal{L}'} \quad (4.1)$$

where  $\mathcal{L}'$  is made of  $N/3$  sites, each with a vector space  $\mathbb{V}'$  of dimension  $\chi$ , so that  $\mathbb{V}_{\mathcal{L}'} \cong \mathbb{V}'^{\otimes N/3}$ , and where transformation  $U$  decomposes into local transformations, known as disentanglers  $u$  and isometries  $w$ ,

$$u^\dagger : \mathbb{V}^{\otimes 2} \mapsto \mathbb{V}^{\otimes 2}, \quad w^\dagger : \mathbb{V}^{\otimes 3} \mapsto \mathbb{V}', \quad (4.2)$$

according to Fig. 4.1a. More specifically, if we partition the initial lattice  $\mathcal{L}$  into blocks of three sites, then the disentanglers  $u$  are first applied across the boundaries

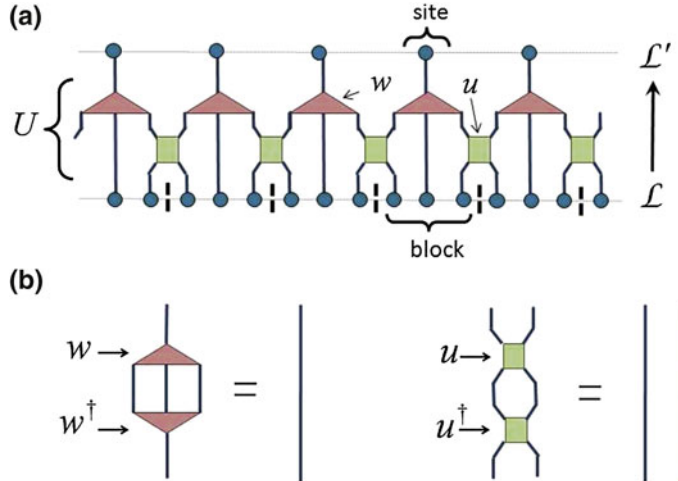


**Fig. 4.1** **a** The coarse-graining transformation  $U$ , a specific implementation of entanglement renormalization, is comprised of isometries  $w$  and disentanglers  $u$  and maps *blocks* of three sites from the initial lattice  $\mathcal{L}$  into a *site* of the coarser lattice  $\mathcal{L}'$ . **b** The tensors  $w$  and  $u$  are constrained to be isometric, see also Eq. 4.3

of neighboring blocks, followed by the isometries  $w$ , which map each block of three sites into a single effective site of the coarser lattice  $\mathcal{L}'$ . Disentanglers and isometries are required to satisfy isometric constraints, namely

$$u^\dagger u = \mathbb{I}^{\otimes 2}, \quad w^\dagger w = \mathbb{I}', \quad (4.3)$$

where  $\mathbb{I}$  and  $\mathbb{I}'$  are the identity operator in  $\mathbb{V}$  and  $\mathbb{V}'$ , respectively, see Fig. 4.1b. Note that, by construction, the disentangler  $u$  is also unitary, that is  $uu^\dagger = \mathbb{I}^{\otimes 2}$ . The dimension  $\chi$  of the Hilbert space  $\mathbb{V}'$  can be chosen to be different than  $d$ , provided that  $\chi \leq d^3$  (as demanded by the above isometric constraint on  $w$ ). In general, choosing a larger dimension  $\chi$ , i.e. retaining a larger effective Hilbert space  $\mathbb{V}'$  for each coarse-grained site, yields a more accurate RG transformation, one that better preserves the low energy properties of the system.

An important property of the coarse-graining transformation  $U$  is that it preserves *locality*. Let  $o(r_1, r_2)$  be a local operator defined on two contiguous sites  $(r_1, r_2)$  of lattice  $\mathcal{L}$ . Under coarse-graining, the operator  $o(r_1, r_2)$  becomes

$$U^\dagger o(r_1, r_2)U = \cdots \otimes \mathbb{I}' \otimes o'(r'_1, r'_2) \otimes \mathbb{I}' \otimes \cdots, \quad (4.4)$$

where the only non-trivial part of  $U^\dagger o(r_1, r_2)U$  is a new operator  $o'(r'_1, r'_2)$  supported on two contiguous sites  $(r'_1, r'_2)$  of lattice  $\mathcal{L}'$ . Notice that operator  $o'(r'_1, r'_2)$  remains local (i.e., it is supported on two sites) thanks to both the specific decomposition of  $U$  into disentanglers and isometries, and the isometric constraints of these tensors,

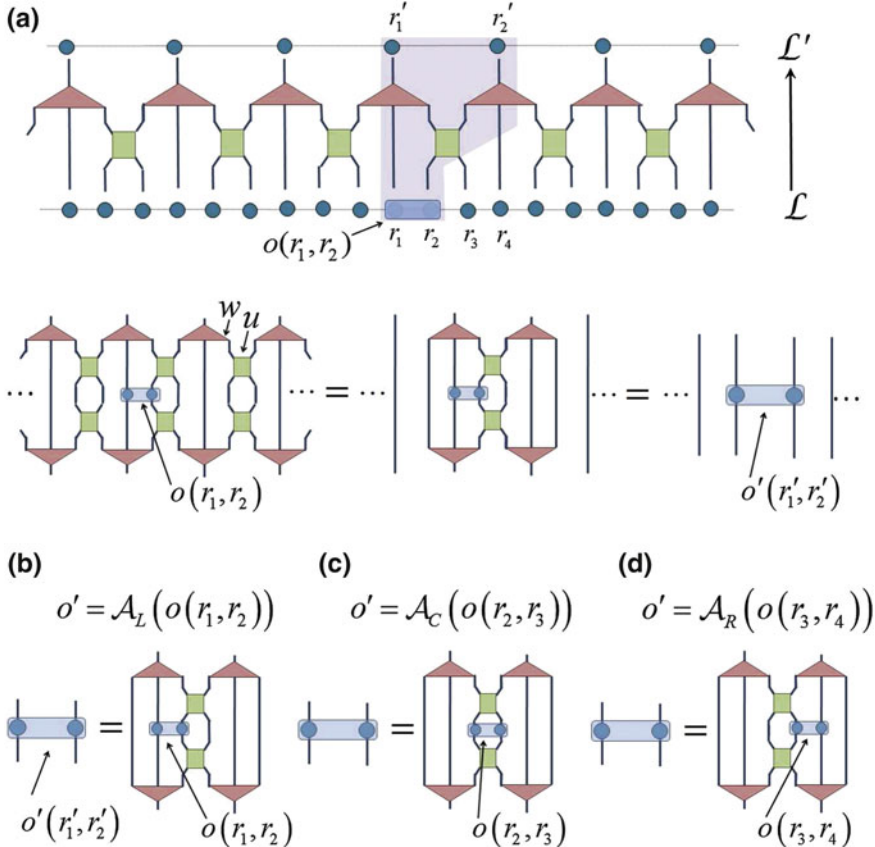


**Fig. 4.2** **a** Under coarse-graining with entanglement renormalization, an operator  $o(r_1, r_2)$  supported on two sites of lattice  $\mathcal{L}$  is transformed into a new operator  $o'(r'_1, r'_2)$  supported on two sites of the coarser lattice  $\mathcal{L}'$ , see Eq. 4.4. The coarse-graining of local operators can be implemented directly via the **b** *left*, **c** *center* and **d** *right* ascending superoperators, denoted  $\mathcal{A}_L$ ,  $\mathcal{A}_C$  and  $\mathcal{A}_R$  respectively. Notice that the coarse-graining of  $o(r_1, r_2)$  in **a** corresponds to application of the *left* ascending superoperator  $\mathcal{A}_L$

Eq. 4.3, which ensure that most of the tensors of  $U$  in  $U^\dagger o(r_1, r_2)U$  annihilate to identity with their conjugates in  $U^\dagger$ , as shown Fig. 4.2a. In view of this fact, it is most convenient to introduce left, center and right *ascending superoperators*  $\{\mathcal{A}_L, \mathcal{A}_C, \mathcal{A}_R\}$ , as shown Fig. 4.2b–d, which directly produce the two-site coarse-grained operator  $o'$  from the two-site operator  $o$ , as given by one of the following,

$$\begin{aligned} o'(r'_1, r'_2) &= \mathcal{A}_L(o(r_1, r_2)), \\ o'(r'_1, r'_2) &= \mathcal{A}_C(o(r_2, r_3)), \\ o'(r'_1, r'_2) &= \mathcal{A}_R(o(r_3, r_4)), \end{aligned} \quad (4.5)$$

where the specific choice of ascending superoperator to be used depends on the location of the operator  $o$  on the lattice  $\mathcal{L}$ .

We may now concatenate the coarse-graining transformation a number  $T$  of times to obtain a *sequence* of coarser lattices,

$$\mathcal{L}^{[0]} \xrightarrow{U^{[0]}} \mathcal{L}^{[1]} \xrightarrow{U^{[1]}} \dots \xrightarrow{U^{[T-1]}} \mathcal{L}^{[T]}, \quad (4.6)$$

where we use superscripts in square brackets to denote the level of coarse-graining, with the initial lattice  $\mathcal{L}^{[0]} \equiv \mathcal{L}$ . Then, for any local (i.e., two-site) operator  $o^{[0]} \equiv o$  defined on  $\mathcal{L}^{[0]}$ , the transformations  $\{U^{[\tau]}\}$  generate a sequence of local coarse-grained operators  $\{o^{[\tau]}\}$ , defined on lattices  $\{\mathcal{L}^{[\tau]}\}$ ,

$$o^{[0]} \xrightarrow{\mathcal{A}^{[0]}} o^{[1]} \xrightarrow{\mathcal{A}^{[1]}} \dots \xrightarrow{\mathcal{A}^{[T-1]}} o^{[T]}, \quad (4.7)$$

through application of the appropriate ascending superoperator  $\mathcal{A}$ , as per Eq. 4.5.

#### 4.2.2 Foundations of the MERA

We have just seen that the ER transformation  $U$  can be used to coarse-grain local operators, producing a renormalization group (RG) flow for local operators, Eq. 4.7. As a linear (isometric) map from  $\mathbb{V}_{\mathcal{L}}$  to  $\mathbb{V}_{\mathcal{L}'}$ ,  $U$  can of course also be used to coarse-grain quantum states. More important for us, however, is to consider an *inverse* RG flow of states. Let us assume that we have the sequence of ER transformations  $\{U^{[0]}, U^{[1]}, \dots, U^{[T-1]}\}$  which act on an initial lattice  $\mathcal{L}^{[0]}$  of  $N$  sites to eventually produce coarse-grained lattice  $\mathcal{L}^{[T]}$ . Then for a quantum state  $|\psi^{[T]}\rangle$  defined on lattice  $\mathcal{L}^{[T]}$ , the transformation  $U^{[T-1]}$  can be used to obtain a new state  $|\psi^{[T-1]}\rangle$ ,

$$|\psi^{[T-1]}\rangle \equiv U^{[T-1]} |\psi^{[T]}\rangle, \quad (4.8)$$

defined on the finer lattice  $\mathcal{L}^{[T-1]}$ . Through iteration of Eq. 4.8, one can further obtain increasingly fine-grained states, eventually reaching a state  $|\psi^{[0]}\rangle$  defined on  $\mathcal{L}^{[0]}$ ,

$$|\psi^{[0]}\rangle = U^{[0]} U^{[1]} \dots U^{[T-1]} |\psi^{[T]}\rangle. \quad (4.9)$$

Let us assume that the number of levels  $T$  is chosen  $T \approx \log_3(N)$ , such that the maximally coarse-grained lattice  $\mathcal{L}^{[T]}$  contains a small number of sites and hence the state  $|\psi^{[T]}\rangle$  can also be described with a small number of parameters. Then the multi-scale entanglement renormalization ansatz (MERA) is the class of states  $|\psi^{[0]}\rangle$  that can be represented as Eq. 4.9, for some choice of  $\{U^{[0]}, U^{[1]}, \dots, U^{[T-1]}\}$  and  $|\psi^{[T]}\rangle$ . For instance, Fig. 4.3 depicts the MERA, organized into  $T = 3$  layers, for a

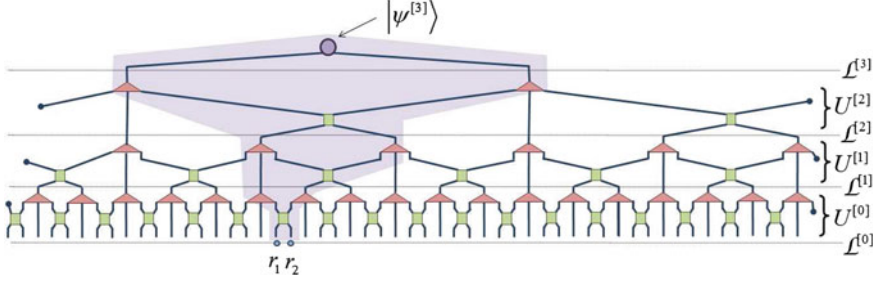


**Fig. 4.3** The ternary MERA for a lattice  $\mathcal{L}^{[0]}$  of  $N = 54$  sites. Each layer  $U^{[\tau]}$  of the MERA can be interpreted as a coarse-graining transformation between an initial lattice  $\mathcal{L}^{[\tau]}$  and a coarser lattice  $\mathcal{L}^{[\tau+1]}$ . The *past causal cone* of two sites  $(r_1, r_2)$  in lattice  $\mathcal{L}^{[0]}$  is shaded

state  $|\psi^{[0]}\rangle$  on a lattice of  $N = 54$  sites,

$$|\psi^{[0]}\rangle = U^{[0]} U^{[1]} U^{[2]} |\psi^{[3]}\rangle. \quad (4.10)$$

Let us now count variational parameters. We will assume for simplicity that for any value of  $\tau = 0, 1, \dots, T-1$ , the dimension of the local vector space  $\mathbb{V}^{[\tau]}$  is  $\chi$ . Recall that the transformations  $\{U^{[\tau]}\}$  themselves are comprised of local tensors, the disentanglers  $u$  and isometries  $w$ , each specified by  $\chi^4$  parameters. Since in an  $N$ -site lattice there are  $O(N)$  disentanglers  $u$  and isometries  $w$  (distributed in  $O(\log(N))$  layers), the MERA depends on  $O(N\chi^4)$  parameters. In Sect. 4.3 we will see that, through incorporation of spatial symmetries into the ansatz, this number can be reduced to  $O(\chi^4)$ , which is independent of  $N$  and allows for the study of infinite systems.

We have therefore established that the MERA can be specified with a number of parameters that is much smaller than the dimension of the Hilbert space  $\mathbb{V}_{\mathcal{L}}$ , which grows exponentially in the number  $N$  of sites. However, for this ansatz to be useful, we also need to be able to efficiently extract information about  $|\psi^{[0]}\rangle$  in Eq. 4.9. For any local operator  $o^{[0]}(r_1, r_2)$ , and due to the very peculiar causal structure of its tensor network, it is actually possible to efficiently compute the expectation value

$$\langle o^{[0]}(r_1, r_2) \rangle \equiv \langle \psi^{[0]} | o^{[0]}(r_1, r_2) | \psi^{[0]} \rangle \quad (4.11)$$

from the MERA. Let us define the *past causal cone* of a site in lattice  $\mathcal{L}^{[\tau]}$  as the set of tensors and indices that can affect the state on that site. By construction, in a MERA the causal cone of any site of  $\mathcal{L}^{[\tau]}$  is seen to involve just a constant (that is, independent of  $N$ ) number of sites of any other lattice  $\mathcal{L}^{[\tau']}$  for  $\tau' > \tau$ , a property that we refer to by saying that the past causal cone has bounded ‘width’. Figure 4.3 displays the past causal cone of two sites  $(r_1, r_2)$  in a ternary MERA, which only involves two sites of every lattice  $\mathcal{L}^{[\tau]}$ . This property allows for the efficient computation of local reduced density matrix  $\rho^{[0]}(r_1, r_2)$ , from which the expectation value

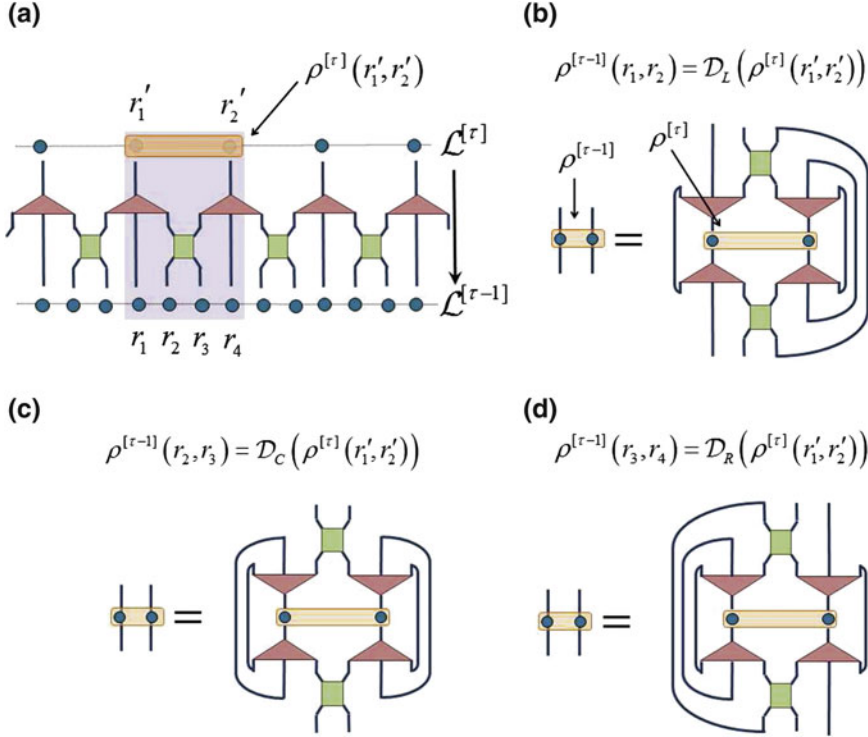


**Fig. 4.4** **a** The causal cone (shaded) of four sites ( $r_1, r_2, r_3, r_4$ ) in lattice  $\mathcal{L}^{[\tau-1]}$  involves two sites ( $r'_1, r'_2$ ) in lattice  $\mathcal{L}^{[\tau]}$ . Starting from the reduced density matrix  $\rho^{[\tau]}(r'_1, r'_2)$  on lattice  $\mathcal{L}^{[\tau]}$ , the reduced density matrix on any pair of contiguous from ( $r_1, r_2, r_3, r_4$ ) can be obtained using the **b left, c center and d right** descending superoperators, denoted  $\mathcal{D}_L, \mathcal{D}_C, \mathcal{D}_R$  respectively

$$\langle o^{[0]}(r_1, r_1) \rangle = \text{tr} \left( o^{[0]}(r_1, r_1) \rho^{[0]}(r_1, r_2) \right) \quad (4.12)$$

can be obtained. The computation of local reduced density matrices is simplified through the introduction of left, center and right descending superoperators,  $\{\mathcal{D}_L, \mathcal{D}_C, \mathcal{D}_R\}$ , which are the adjoints of the ascending superoperators of Eq. 4.5. Let us assume that we have the density matrix  $\rho^{[\tau]}(r'_1, r'_2)$  describing the state on two contiguous sites ( $r'_1, r'_2$ ) of lattice  $\mathcal{L}^{[\tau]}$ . Then, as shown Fig. 4.4, the descending superoperators may be used to compute the two-site reduced density matrix  $\rho^{[\tau-1]}$  on certain sites of the lattice  $\mathcal{L}^{[\tau-1]}$ ,

$$\begin{aligned} \rho^{[\tau-1]}(r_1, r_2) &= \mathcal{D}_L(\rho^{[\tau]}(r'_1, r'_2)), \\ \rho^{[\tau-1]}(r_2, r_3) &= \mathcal{D}_C(\rho^{[\tau]}(r'_1, r'_2)), \\ \rho^{[\tau-1]}(r_3, r_4) &= \mathcal{D}_R(\rho^{[\tau]}(r'_1, r'_2)). \end{aligned} \quad (4.13)$$

Thus, through repeated use of the appropriate descending superoperator in Eq. 4.13, we can compute the reduced density matrix  $\rho^{[0]}(r_1, r_2)$  of any two contiguous sites  $(r_1, r_2)$  of the original lattice  $\mathcal{L}^{[0]}$  by ‘lowering’ the density matrix through the appropriate causal cone. For instance, the reduced density matrix  $\rho^{[0]}(r_1, r_2)$  on the two sites  $(r_1, r_2)$  of lattice  $\mathcal{L}^{[0]}$  shown in Fig. 4.3 can be computed as

$$\rho^{[0]}(r_1, r_2) = \mathcal{D}_C \left( \mathcal{D}_L \left( \mathcal{D}_C \left( |\psi^{(3)}\rangle\langle\psi^{(3)}| \right) \right) \right). \quad (4.14)$$

The cost of calculating a local reduced density matrix  $\rho^{[0]}$ , as in the example of Eq. 4.14, is proportional to the number  $T \approx \log(N)$  of layers in the MERA, hence scales with system size  $N$  as  $O(\log(N))$ . Two point correlators can also be evaluated using similar manipulations, see Ref. [15].

### 4.2.3 Choice of MERA Scheme

There are many possible ways of implementing the MERA in  $D = 1$  dimensions, of which the ternary MERA described in Sect. 4.2.2 is just one example. Figure 4.5 displays a ternary MERA together with two other possible implementations: the binary MERA scheme (in terms of which the first ER proposals [8, 9] were formulated) and a modified binary MERA scheme (with half the amount of disentanglers as the previous binary scheme). While all MERA schemes function similarly on a conceptual level, the computational efficiency may differ between schemes. For instance, the cost of evaluating the expectation value of local observables as described Sect. 4.2.2 scales, in terms of the bond dimension  $\chi$ , as  $O(\chi^9)$  for the binary MERA, as  $O(\chi^8)$  for the ternary MERA and as  $O(\chi^7)$  for the modified binary MERA. On the other hand, the binary MERA scheme has more disentangling power than either the ternary or modified binary schemes and, for any given  $\chi$ , produces a more accurate representation of ground states. It is therefore not obvious which MERA implementation will give the best numeric results for a fixed computational budget. However, a direct comparison of performance, see Ref. [38], shows that the modified binary scheme of Fig. 4.5c is the most efficient scheme. Consequently, this scheme is used for the obtaining the numeric results presented in Sect. 4.5. However, for the sake of simplicity, we shall continue to discuss theoretical aspects of MERA in terms of the ternary MERA.

## 4.3 Symmetries in Tensor Network States

Consider a many-body state that is invariant under some symmetry transformation. In approximating this state with a tensor network state, we would like to preserve the original symmetry as much as possible. In this section we examine the types of

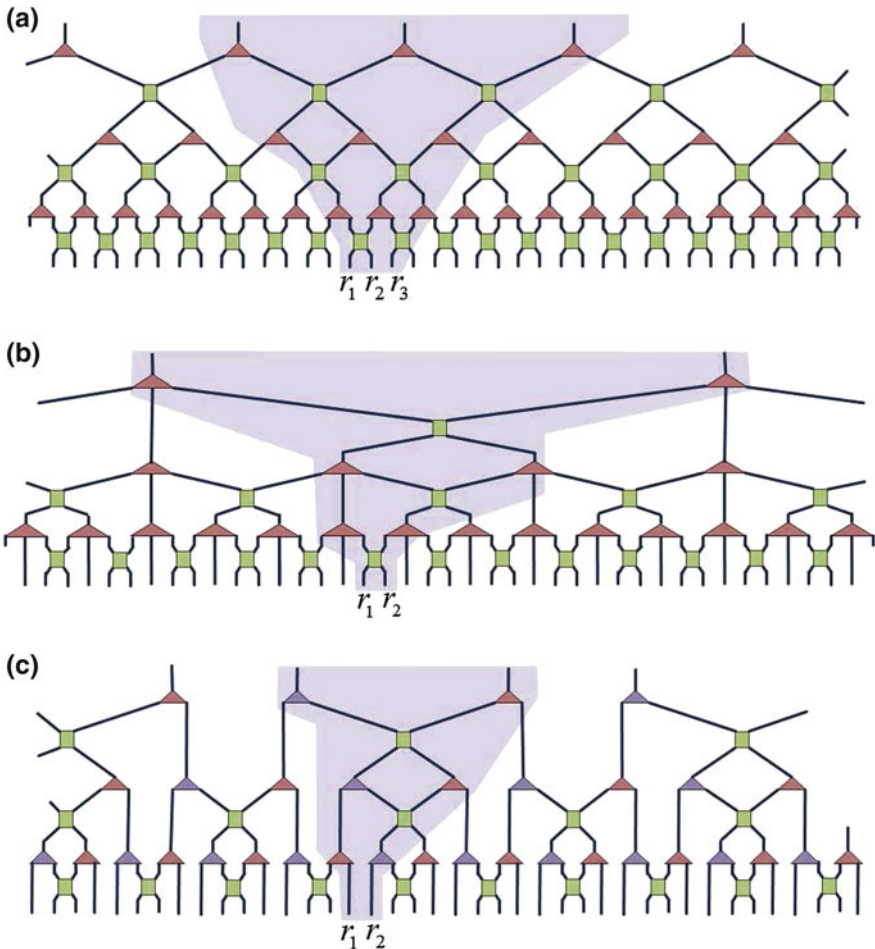


**Fig. 4.5** Three different MERA schemes for a  $D = 1$  dimensional lattice. An example of a causal cone is shaded for each scheme. **a** The binary MERA scheme, based upon a 2-to-1 coarse-graining step, has a causal width of three sites and a cost of contraction that scales with the bond dimension  $\chi$  as  $O(\chi^9)$ . **b** The ternary MERA scheme, based upon a 3-to-1 coarse-graining step, has a causal width of two sites and a cost of contraction that scales as  $O(\chi^8)$ . **c** The modified binary MERA scheme, equivalent to the binary MERA scheme with every second disentangler removed, has a causal width of two sites and a cost of contraction as  $O(\chi^7)$

symmetries that can be enforced upon the MPS and PEPS, and upon the MERA. We also examine whether the presence of the symmetry can be exploited for computational gain. We begin by discussing spatial symmetries, followed by global internal symmetries. The results are summarized in Table 4.1.

### 4.3.1 Spatial Symmetries

For simplicity we discuss only two typical spatial symmetries: invariance under translations in homogeneous systems and invariance under changes of scale in e.g. critical systems. Let us first consider them in the context of the MPS for  $D = 1$  dimensions and PEPS for  $D > 1$  dimensions (see Sects. 1.7 and 2.7 for an introduction to MPS).

In an inhomogeneous MPS/PEPS, one associates a different tensor  $A_r$  to each site  $r$  of the lattice  $\mathcal{L}$ . Hence, in a lattice made of  $N$  sites, the total number of tensors in the tensor network is also  $N$ . In the presence of translation invariance (either in a finite system with periodic boundary conditions or in an infinite system), this symmetry can be incorporated into the MPS/PEPS by choosing all the tensors to be a copy of the same tensor  $A$ , i.e.  $A_r = A$ , see Fig. 4.6a, b for an MPS. Translation invariance is in this way exactly preserved. It can also be exploited to reduce computational cost from  $O(N)$  to  $O(1)$ .

On the other hand, it is not clear how scale invariance could be enforced in these tensor networks. For an MPS this is unlikely to be possible at all because, as we mentioned earlier, a finite bond dimension  $\chi$  already implies the presence of an effective finite correlation length  $\zeta \approx \chi^\kappa$  [33, 34].

Let us now consider spatial symmetries in the MERA. Recall that a generic MERA on an  $N$  site lattice is arranged into  $T \approx \log(N)$  layers of tensors, and contains  $O(N)$  different tensors, as depicted in Fig. 4.6c. Suppose now that the state to be approximated by the MERA is translation invariant. Then we can choose all the tensors in each layer to be the same, so that layer  $U^{[\tau]}$  is characterized by a single pair of tensors  $u^{[\tau]}$  and  $w^{[\tau]}$ , see Fig. 4.6d. In this way translation invariance can be exploited to reduce computational costs from  $O(N)$  to  $O(\log(N))$ . Notice, however, that this choice of tensors does not enforce translation invariance, because the structure of the coarse-graining is not homogeneous (different sites are positioned in inequivalent positions with respect to the disentanglers and isometries). The final

**Table 4.1** Several symmetries that can be exactly enforced and/or whose presence can be exploited for computational gain with MPS/PEPS and MERA algorithms

	Enforceable	Exploitable
<i>Symmetries with MPS/PEPS</i>		
Translation invariance	Yes	Yes, cost: $O(N) \rightarrow O(1)$
Scale invariance	Unlikely	Unlikely
Internal symmetries (e.g. $\mathbb{Z}_2$ , $U(1)$ , $SU(2)$ )	Yes	Yes
<i>Symmetries with MERA</i>		
Translation invariance	Unknown	Yes, cost: $O(N) \rightarrow O(\log(N))$
Scale invariance	Yes	Yes, cost: $O(\log(N)) \rightarrow O(1)$
Internal symmetries (e.g. $\mathbb{Z}_2$ , $U(1)$ , $SU(2)$ )	Yes	Yes

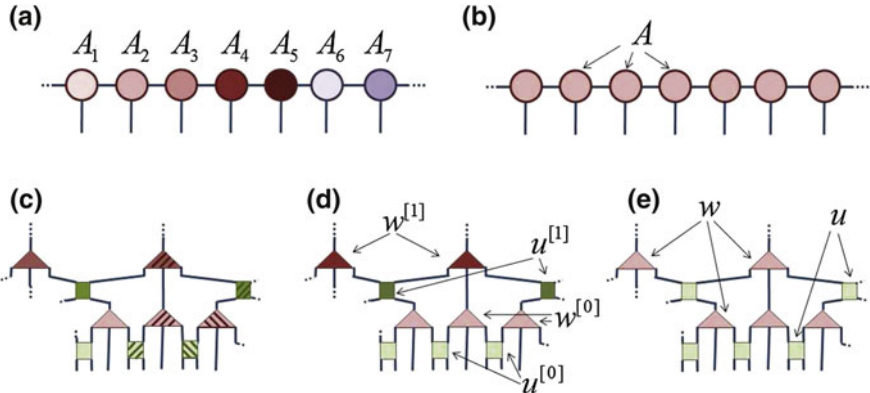


**Fig. 4.6** **a** An inhomogeneous MPS has an independent tensor  $A_r$  associated to each lattice site. **b** All the tensors in a translation invariant MPS are chosen to be copies of the same tensor  $A$ . **c** A generic MERA on an  $N$  site lattice contains  $O(N)$  different tensors. **d** Translation invariance can be exploited by choosing the tensors in each layer  $U^{[\tau]}$  of the MERA as copies of a single unique disentangler  $u^{[\tau]}$  and isometry  $w^{[\tau]}$ . For an  $N$  site lattice, this MERA contains  $O(\log N)$  different tensors. **e** Scale invariance can be incorporated into the MERA by further enforcing all layers to be identical, hence the entire MERA is described by a single  $u$  and  $w$

effect is examined in Fig. 4.7. A MERA characterized by a single pair of tensors  $u^{[\tau]}$  and  $w^{[\tau]}$  for each layer, where these tensors are filled with random coefficients (compatible with the isometric constraints of Eq. 4.3), is highly non-translation invariant, with e.g. oscillations in the expectation value of the energy of the order of 0.1 for the Hamiltonian  $H_{\text{Ising}}$  of Eq. 4.36. Still, these violations of translation invariance decrease significantly once the tensors are optimized so as to minimize the expectation value of the translation invariant Hamiltonian  $H_{\text{Ising}}$ . Indeed, they become of order  $10^{-5}$  for  $\chi = 4$  and decrease with increasing  $\chi$ . [In practice one can efficiently average the expectation value of a local observable over all possible lattice positions in order to further reduce the effect of these small violations of translation invariance]. We conclude that translation invariance can be exploited to reduce computational costs, but it can only be reproduced approximately. It is not known whether it can be enforced exactly.

Instead, enforcing scale invariance in the MERA is straightforward. This is accomplished by choosing all disentanglers and isometries to be copies of a single pair  $u$  and  $w$ , see Fig. 4.6e, which further reduces the number of parameters and the computational cost of MERA algorithms from  $O(\log(N))$  to  $O(1)$ , allowing infinite systems to be considered. The scale-invariant MERA will be discussed in more detail Sect. 4.4.

To summarize, in the MPS/PEPS we can enforce and exploit translation invariance but not scale invariance, whereas in the MERA we can enforce and exploit scale invariance but only exploit (i.e., we cannot enforce) translation invariance. Thus both MPS/PEPS and MERA have potential advantages over each other, depending

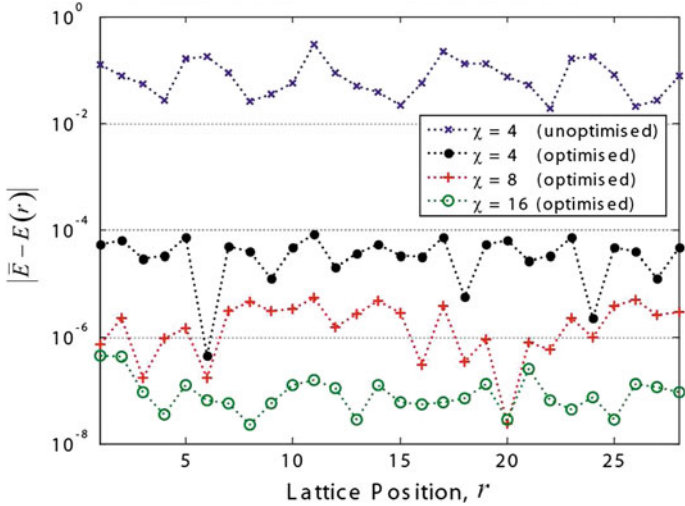


**Fig. 4.7** We investigate translation invariance in the scale-invariant MERA by comparing the bond energy  $E(r)$  over 30 contiguous lattice sites with the average bond energy  $\bar{E}$  from all sites, as measured with the critical Ising Hamiltonian,  $H_{\text{Ising}}$ , of Eq. 4.36. For a randomly initialized  $\chi = 4$  scale-invariant MERA, the large fluctuations of bond energies indicate the state is highly non-translationally invariant. Once the MERA has been optimized for the ground state of  $H_{\text{Ising}}$ , it more closely approximates translation invariance; bond energies now differ from the average by less than 0.1 %. As the bond dimension  $\chi$  of the MERA is increased, the optimized wavefunction better approximates translation invariance; for  $\chi = 16$  the bond energies differ from the average energy by less than 0.001 %

on whether exact translation invariance or exact scale invariance is more important for the problem under consideration.

### 4.3.2 Global Internal Symmetries

A second important class of symmetries are those involving internal degrees of freedom, such as  $\mathbb{Z}_2$  spin flips and  $U(1)$  or  $SU(2)$  spin rotations simultaneously applied on all the sites of a spin model. Such symmetries can be enforced and exploited in all tensor networks.

Let us assume that the Hamiltonian  $H$  of our lattice model is invariant under a symmetry group  $\mathcal{G}$ ,

$$\Gamma_g H \Gamma_g^\dagger = H, \quad \forall g \in \mathcal{G}, \quad (4.15)$$

where  $\Gamma_g \equiv \cdots V_g \otimes V_g \otimes V_g \cdots$  is an infinite string of copies of a matrix  $V_g$ , with  $V_g$  a unitary representation of  $\mathcal{G}$ , and let  $|\psi\rangle$  be the ground state of  $H$ , which

we will assume to have the same symmetry, i.e.  $\Gamma_g|\psi\rangle = |\psi\rangle$  (or, more generally,  $\Gamma_g|\psi\rangle = e^{i\phi}|\psi\rangle$ ). We can then ensure that the symmetry is also exactly preserved in a tensor network approximation to  $|\psi\rangle$  by using symmetry preserving tensors [39, 40]. For instance, for the MERA, we choose the disentanglers  $u$  and isometries  $w$  such that,

$$\begin{aligned}(V_g \otimes V_g)u(V_g \otimes V_g)^\dagger &= u, \\ (V_g \otimes V_g \otimes V_g)w(V_g)^\dagger &= w,\end{aligned}\tag{4.16}$$

where  $V_g$  acting on different indices may actually denote different (in general, reducible) representations of  $\mathcal{G}$ , see also Fig. 4.8. The use of symmetry preserving tensors implies that the tensors are block diagonal when viewed in a certain basis and thus contain less free parameters than generic tensors. This reduction in the number of parameters can be exploited to significantly decrease computational costs. Symmetries, and in particular a truncated version of the operator  $\Gamma_g$ , also play an important role in the description of non-local scaling operators, as discussed in Sect. 4.4.4.

## 4.4 Scale-Invariant MERA

We have already introduced the scale-invariant MERA: in a lattice  $\mathcal{L}$  with an infinite number of sites,  $N \rightarrow \infty$ , it consists of infinitely many layers of tensors, where all the disentanglers and isometries are copies of a unique pair  $u$  and  $w$ . In this section we enumerate two significant structural properties of the scale-invariant MERA and review how one can compute a local reduced density matrix, from which the expectation value of a local operator can be evaluated. Then we discuss the three types of scale-invariant (or covariant) objects one can extract from it.

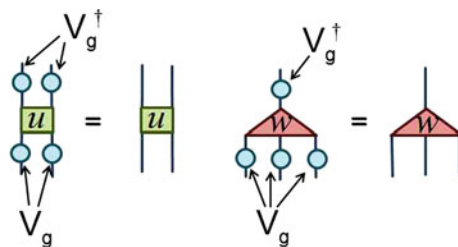


**Fig. 4.8** In order to preserve a (global) symmetry specified by symmetry group  $\mathcal{G}$ , the tensors  $u$  and  $w$  comprising the MERA are chosen to be invariant under the action of a unitary representation  $V_g$  of symmetry group  $\mathcal{G}$ , see also Eq. 4.16

### 4.4.1 Basic Properties

Two basic features of the scale-invariant MERA in  $D = 1$  dimensions match well-known properties of the ground state of a critical system. Firstly, the entanglement entropy  $S_L$  of a block of  $L$  contiguous sites can be seen to scale as the logarithm of  $L$  [9], which is compatible with the critical scaling [41, 42],

$$S_L \approx \frac{c}{3} \log(L), \quad (4.17)$$

where  $c$  is the central charge of the CFT. Secondly, correlation functions can be seen to decay polynomially [9],

$$\langle o(r_1)o(r_2) \rangle \approx \frac{1}{|r_1 - r_2|^q}, \quad (4.18)$$

as it is also expected of critical correlators. Interestingly, these two properties of the scale-invariant MERA follow from simple geometric considerations, namely by studying minimally connected regions and geodesic paths in the (discrete) holographic geometry generated by the tensor network [1].

### 4.4.2 Transitional Layers

In a practical computation (see e.g. [16, 38]) it is customary to consider a scale-invariant MERA with some small number  $M$  of translational layers  $\{U^{[0]}, \dots, U^{[M-1]}\}$ , which are characterized by  $M$  pairs of tensors  $\{(u^{[0]}, w^{[0]}), \dots, (u^{[M-1]}, w^{[M-1]})\}$  that are chosen independently of the single pair  $(u, w)$  characterizing the rest of layers (see Fig. 4.9 for an example with  $M = 2$ ). These transitional layers serve two main purposes. Firstly, they allow one to choose the bond dimension  $\chi$  of the scale-invariant layers independent of the local dimension  $d$  of the sites in the original lattice  $\mathcal{L}^{[0]}$ . Secondly they also allow to diminish the effect of RG irrelevant terms in the critical Hamiltonian  $H$  of the system. Such terms violate scale invariance but become less and less important at larger length scales. The number  $M$  of transitional layers required depends on the amplitude and scaling dimensions of the irrelevant operators present in  $H$ , and is often determined by trial and error. For the sake of simplicity, in the rest of this section we shall focus on the case of a purely scale-invariant MERA with no transitional layers.

### 4.4.3 Local Density Matrix

The computation of the (average) local density matrix

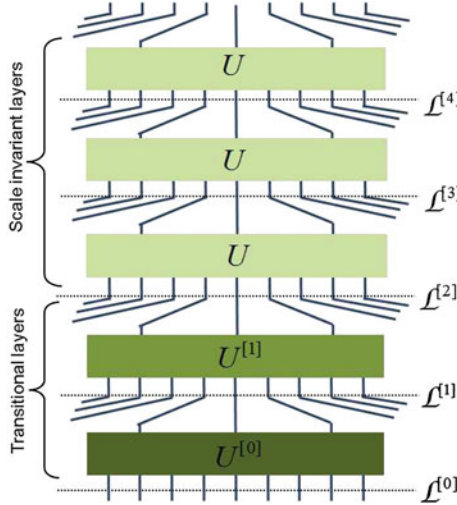


**Fig. 4.9** A scale-invariant MERA consists of a number  $M$  of transitional layers, here  $M = 2$  transitional layers  $U^{[0]}$  and  $U^{[1]}$ , followed by an infinite number identical of scaling layers  $U$ . Recall that each layer  $U^{[\tau]}$  is comprised of local isometric tensors, the disentanglers  $u^{[\tau]}$  and isometries  $w^{[\tau]}$ , as depicted Fig. 4.1a

$$\bar{\rho} \equiv \lim_{N \rightarrow \infty} \left( \frac{1}{N} \sum_{r=1}^N \rho(r, r+1) \right) \quad (4.19)$$

for two contiguous sites of lattice  $\mathcal{L}$  is of central importance in the present formalism. The density matrix  $\bar{\rho}$  is required both in order to extract the expectation value of a local operator  $o$  from the scale-invariant MERA and to optimize its tensors so as to approximate the ground state of a critical Hamiltonian  $H$ .

Here we consider the evaluation of the expectation value  $\langle o(r, r+1) \rangle$  of a local observable  $o(r, r+1)$ . As discussed in Sect. 4.3.1, the MERA is not manifestly translation invariant. Thus the expectation value  $\langle o(r, r+1) \rangle$  can *artificially* vary with the position of site  $r$  in the lattice. To mitigate this effect, rather than evaluating the expectation value at a particular lattice position  $r$  we will instead evaluate the average expectation value over all lattice sites,

$$\langle \bar{o} \rangle \equiv \lim_{N \rightarrow \infty} \left( \frac{1}{N} \sum_{r=1}^N \langle o(r, r+1) \rangle \right). \quad (4.20)$$

Notice that this average expectation value can be expressed in terms of the average two-site reduced density matrix  $\bar{\rho}$  introduced in Eq. 4.19,

$$\langle \bar{o} \rangle = \text{tr} (o(r, r+1) \bar{\rho}). \quad (4.21)$$

In Sect. 4.2.2 we described the use of the left, center and right descending superoperators,  $\{\mathcal{D}_L, \mathcal{D}_C, \mathcal{D}_R\}$ , to compute the reduced density matrix  $\rho^{[0]}(r, r+1)$  from a finite MERA. In particular, it was argued that obtaining the density matrix  $\rho^{[0]}(r, r+1)$  required application of a specific sequence of left, center and right descending superoperators that depended on the causal cone associated to sites  $(r, r+1)$ , see Eq. 4.14 for an example. The average density matrix  $\bar{\rho}$  can be seen to follow from using the average descending superoperator  $\bar{\mathcal{D}}$ , defined as

$$\bar{\mathcal{D}} \equiv \frac{1}{3} (\mathcal{D}_L + \mathcal{D}_C + \mathcal{D}_R), \quad (4.22)$$

in order to descend the density matrix through the ‘average’ causal cone. That is, given the average density matrix  $\bar{\rho}^{[\tau]}$  at level  $\tau$ , the average density matrix  $\bar{\rho}^{[\tau-1]}$  at lower level  $\tau - 1$  is obtained as

$$\bar{\rho}^{[\tau-1]} = \bar{\mathcal{D}} (\bar{\rho}^{[\tau]}). \quad (4.23)$$

In an infinite system,  $N \rightarrow \infty$ , the MERA has  $T \rightarrow \infty$  layers, and the average density matrix  $\bar{\rho}$  is obtained from

$$\bar{\rho} = \lim_{T \rightarrow \infty} (\underbrace{\bar{\mathcal{D}} \circ \cdots \circ \bar{\mathcal{D}}}_{T \text{ times}}) (\bar{\rho}^{[T]}), \quad (4.24)$$

where  $\bar{\rho}$  is simply the dominant eigen operator of the descending superoperator  $\bar{\mathcal{D}}$ , which is independent of  $\bar{\rho}^{[T]}$ . As a manifestation of scale invariance, this is also the two-site density matrix of any coarse-grained lattice  $\mathcal{L}^{[\tau]}$ , that is  $\bar{\rho}^{[\tau]} = \bar{\rho}$  for any  $\tau \geq 0$ . More details on the computation of  $\bar{\rho}$  can be found in Ref. [38].

#### 4.4.4 Scale-Invariant Objects

The scale-invariant MERA offers direct access to objects of a critical theory that are invariant (more generally, covariant) under a change of scale. In  $D = 1$  dimensions we can identify three classes of such objects, as depicted Fig. 4.10a–c. Next we discuss them in some detail.

#### Symmetry Transformations

Let us assume that the critical ground state is invariant under some symmetry group  $\mathcal{G}$ , as implemented by the symmetry transformations  $\Gamma_g \equiv \cdots V_g \otimes V_g \otimes V_g \cdots$  introduced in Eq. 4.15, where  $g \in \mathcal{G}$ . The first type of objects that transform into themselves under changes of scale correspond precisely to the infinite strings  $\Gamma_g$ , for which we have

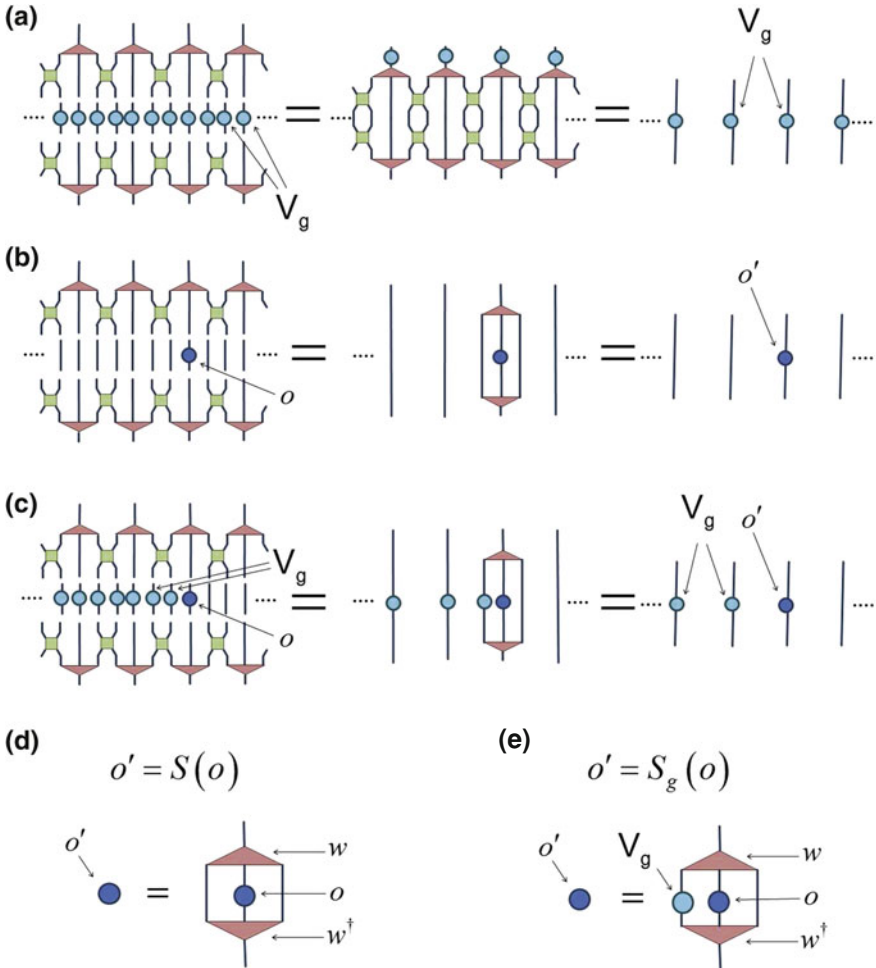


**Fig. 4.10** The three classes of scale-invariant/covariant objects for a  $D = 1$  dimensional lattice include **a** an infinite string of  $V_g$ , with  $V_g$  a unitary representation of symmetry group  $\mathcal{G}$  of the system, **b** local operators and **c** non-local operators, which consist of a local operator with a semi-infinite ‘tail’ of  $V_g$ . **d** Scaling superoperator  $S$  for local operators and **e** scaling superoperator  $S_g$  for non-local operators

$$\Gamma_g \xrightarrow{U^\dagger} \Gamma_g \quad (4.25)$$

Indeed, if we use symmetry preserving tensors in the MERA, as per Eq. 4.16, then the string  $\Gamma_g$  commutes with each layer  $U$  of the MERA,  $\Gamma_g U = U \Gamma_g$ , or equivalently the string  $\Gamma_g$  remains invariant under coarse-graining,  $U^\dagger \Gamma_g U = \Gamma_g$ , as shown in Fig. 4.10a.

## Local Scaling Operators

The second class of objects with a simple transformation rule under coarse-graining, which can be easily extracted from the scale-invariant MERA, are local scaling operators  $\phi_\alpha$ , fulfilling

$$\phi_\alpha \xrightarrow{U^\dagger} \lambda_\alpha \phi_\alpha, \quad (4.26)$$

where  $\lambda_\alpha$  is some constant.

For simplicity, here we focus on one-site scaling operators [One can also compute two-site scaling operators, but they lead to the same scaling dimensions and fusion rules]. As depicted in Fig. 4.10b, a one-site operator  $o$  located at certain points on the lattice is coarse-grained into another one-site operator  $o'$ . This coarse-graining can directly be implemented with the one-site ascending superoperator, which we call the (one-site) scaling superoperator  $\mathcal{S}$  in the scale-invariant setting,

$$o' = \mathcal{S}(o), \quad (4.27)$$

see also Fig. 4.10d. Iteration produces an RG flow for one-site operators:

$$o \xrightarrow{\mathcal{S}} o' \xrightarrow{\mathcal{S}} o'' \dots \quad (4.28)$$

The scaling operators  $\phi_\alpha$  and their corresponding scaling dimensions  $\Delta_\alpha$ ,

$$\mathcal{S}(\phi_\alpha) = \lambda_\alpha \phi_\alpha, \quad \Delta_\alpha \equiv -\log_3 \lambda_\alpha, \quad (4.29)$$

can then be obtained by simply diagonalizing the scaling superoperator  $\mathcal{S}$  [14, 16].

### 4.4.4.1 Non-Local Scaling Operators

Let us assume again that the critical ground state represented by the scale-invariant MERA is invariant under a symmetry group  $\mathcal{G}$ , as implemented by the symmetry transformations  $\Gamma_g \equiv \dots V_g \otimes V_g \otimes V_g \dots$  introduced in Eq. 4.15, where  $g \in \mathcal{G}$ , and that the tensors of the MERA have been chosen to preserve this symmetry, as per Eq. 4.16. We can then identify a third class of objects with a simple transformation rule under changes of scale, namely non-local scaling operators  $\phi_{g,\alpha}^\triangleleft$ , to be defined below, which fulfill

$$\phi_{g,\alpha}^\triangleleft \xrightarrow{U^\dagger} \lambda_{g,\alpha} \phi_{g,\alpha}^\triangleleft, \quad (4.30)$$

where  $\lambda_{g,\alpha}$  is some constant.

To see how these scaling operators come about [22], let us first introduce non-local operators  $o_g^\triangleleft$  of the form,

$$o_g^\triangleleft = \Gamma_g^\triangleleft \otimes o, \quad \Gamma_g^\triangleleft \equiv \underbrace{\cdots V_g \otimes V_g \otimes V_g}_{\infty} \quad (4.31)$$

where  $\Gamma_g^\triangleleft$  is a semi-infinite string made of copies of  $V_g$  and  $o$  is a one-site operator attached to the open end of  $\Gamma_g^\triangleleft$ . Notice that, under coarse-graining,  $o_g^\triangleleft$  can be mapped into another non-local operator  $o_g^{\triangleleft'}$  of the same type,

$$o_g^\triangleleft = \Gamma_g^\triangleleft \otimes o \xrightarrow{U^\dagger} o_g^{\triangleleft'} = \Gamma_g^\triangleleft \otimes o', \quad (4.32)$$

since the semi-infinite string  $\Gamma_g$  commutes with the coarse-graining everywhere except at its open end, as illustrated in Fig. 4.10c. Thus we can study the sequence of coarse-grained non-local operators  $o_g^\triangleleft \rightarrow o_g^{\triangleleft'} \rightarrow o_g^{\triangleleft''} \dots$  by just coarse-graining the local operator  $o$  with the modified one-site scaling superoperator  $\mathcal{S}_g$  of Fig. 4.10e,

$$o \xrightarrow{\mathcal{S}_g} o' \xrightarrow{\mathcal{S}_g} o'' \dots \quad (4.33)$$

In particular we can diagonalize the modified scaling superoperator  $\mathcal{S}_g$ ,

$$\mathcal{S}_g(\phi_{g,\alpha}) = \lambda_{g,\alpha} \phi_{g,\alpha}, \quad \Delta_{g,\alpha} \equiv -\log_3 \lambda_{g,\alpha}, \quad (4.34)$$

to obtain non-local scaling operators  $\phi_{g,\alpha}^\triangleleft$  of the form

$$\phi_{g,\alpha}^\triangleleft = \Gamma_g^\triangleleft \otimes \phi_{g,\alpha}. \quad (4.35)$$

Notice that for  $g = \mathbb{I}$  we recover the local scaling operators  $\phi_\alpha$  of Eq. 4.29.

Importantly, the scaling dimensions  $\Delta_\alpha$  and  $\Delta_{g,\alpha}$  of the both local and non-local scaling operators  $\phi_\alpha$  and  $\phi_{g,\alpha}^\triangleleft$  (as well as their operator product expansion coefficients, see Ref. [16]) are the same in the lattice than in the continuum. Therefore by extracting properties of the scaling operators on the lattice, we can characterize the CFT that describes the critical theory in the continuum. As demonstrated by the benchmark results of Sect. 4.5.2, a relatively simple and inexpensive MERA simulation can actually be used to obtain remarkably accurate conformal data of the underlying CFT.

## 4.5 Benchmark Results

In this section we benchmark the performance of the scale-invariant MERA by applying it to study of the ground state of several well-known quantum spin chains at criticality. The models we analyze are the critical Ising model [43, 44], the critical

three-state Potts models [45], the XX model [46] and a Heisenberg zig-zag chain [47] (the Heisenberg model with a next-nearest neighbor coupling), corresponding to the following Hamiltonians:

$$H_{\text{Ising}} = \sum_r (Z(r) - X(r)X(r+1)) \quad (4.36)$$

$$H_{\text{Potts}} = \sum_r (\tilde{Z}(r) - \tilde{X}(r)\tilde{X}^\dagger(r+1) - \tilde{X}^\dagger(r)\tilde{X}(r+1)) \quad (4.37)$$

$$H_{\text{XX}} = \sum_r (X(r)X(r+1) + Y(r)Y(r+1)) \quad (4.38)$$

$$H_{\text{Heis.Zig-Zag}} = \sum_r (S(r) \cdot S(r+1) + J_2 S(r) \cdot S(r+2)) \quad (4.39)$$

where  $X, Y, Z$  are Pauli matrices,  $S = [X, Y, Z]$ , and where  $\tilde{Z}, \tilde{X}$  are three-state Potts spin matrices given by

$$\tilde{Z} \equiv \begin{pmatrix} -1 & 0 & 0 \\ 0 & 2 & 0 \\ 0 & 0 & -1 \end{pmatrix}, \quad \tilde{X} \equiv \begin{pmatrix} 0 & 1 & 0 \\ 0 & 0 & 1 \\ 1 & 0 & 0 \end{pmatrix}. \quad (4.40)$$

The next-nearest neighbor coupling in the Heisenberg zig-zag chain is set at the critical value  $J_2 = 0.24116$ ; at this value the model is scale-invariant [47]. Note that, although the standard Heisenberg model (with  $J_2 = 0$ ) is quantum critical, the Hamiltonian contains a marginally irrelevant contribution that breaks scale invariance, which here we remove by adding the next-nearest neighbor coupling.

In the present calculation, we have used the modified binary MERA scheme, depicted in Fig. 4.5c, with either  $M = 2$  or  $3$  transition layers. This ansatz is optimized by minimizing the expectation value of the energy density for each of the above Hamiltonians, by using the optimization algorithm described in Ref. [38]. In terms of the bond dimension  $\chi_{\text{MERA}}$ , the cost of optimizing the modified binary MERA scales as  $O(\chi_{\text{MERA}}^7)$ , but can be reduced to  $O(\chi_{\text{MERA}}^6)$  through use of an approximation in the tensor network contractions, see Ref. [38]. We have computed the ground states of the four models over a range of values of  $\chi_{\text{MERA}}$  up to  $\chi_{\text{MERA}} = 150$ . Each simulation took under a week on a 3 GHz dual-core workstation with 32 Gb of RAM.

For purposes of comparison, we have also computed the ground state of the four critical spin chains using an infinite, translation invariant (with a 4-site unit cell) MPS. The MPS tensors are optimized with a variational approach similar to the iDMRG algorithm [48]. The computational cost scales with the bond dimension  $\chi_{\text{MPS}}$  of the MPS as  $O(\chi_{\text{MPS}}^3)$ . We have computed the ground states of the four models over a range of values of  $\chi_{\text{MPS}}$  up to  $\chi_{\text{MPS}} = 1536$ .

In both the MERA and MPS calculations we have employed symmetry preserving tensors, as described in Sect. 4.3.2, to enforce (some of) the global internal symmetries of these models. Specifically,  $\mathbb{Z}_2$  symmetric tensors have been used for the Ising model;  $\mathbb{Z}_3$  symmetric tensors have been used for the Potts model ( $\mathbb{Z}_3$  is a subgroup

of the full  $S_3$  symmetry of this model); and  $U(1)$  symmetric tensors have been used for both the quantum XX and Heisenberg zig-zag chains (again,  $U(1)$  is a subgroup of the full  $SU(2)$  symmetry of the Heisenberg zig-zag chain).

In the first part of the benchmark, Sect. 4.5.1, we compare ground energy and two-point correlators obtained from MERA and MPS, and discuss the relative merits of each approach. Then in Sect. 4.5.2 we demonstrate the extraction of conformal data from the scale-invariant MERA for the critical Ising model, following the approaches of Refs. [16, 22, 38].

### 4.5.1 Comparison with MPS

Here we compare the performances of MPS and scale-invariant MERA for the computation of ground state energy and two-point correlators.

#### Ground Energy

For both Ising and quantum XX models, the exact ground energy per site is  $E = -4/\pi$ , while for the three-state Potts and Heisenberg zig-zag chains we use an MPS with  $\chi_{\text{MPS}} = 1536$  to estimate the ground energy per site at  $E_{\text{Potts}} = -2.4359911239(1)$  and  $E_{\text{Heis.Z.Z.}} \approx -1.607784749(1)$ .

Figure 4.11 displays the relative error in the ground state energy per site,  $\Delta E \equiv (E_{\text{exact}} - E_{\text{numeric}})/E_{\text{exact}}$  for the models under consideration over a range of bond dimensions  $\chi$ , for both MERA and MPS. This figure reveals a number of interesting similarities between results obtained with MERA and MPS. Recall that the central charge  $c$  for these models is

$$c_{\text{Ising}} = \frac{1}{2}, \quad c_{\text{Potts}} = \frac{4}{5}, \quad c_{\text{XX}} = 1, \quad c_{\text{Heis.Z.Z.}} = 1, \quad (4.41)$$

Then a first observation is that for both MERA and MPS, for a given bond dimension  $\chi$  the larger the central charge  $c$  the larger the error in the energy is. A second similarity is that for both MERA and MPS the error  $\Delta E$  in the energy scales polynomially in  $\chi$ , i.e. to a good approximation,

$$\Delta E = a\chi^{-b}. \quad (4.42)$$

A linear fit in Fig. 4.11 produced the estimates for the coefficients  $a$  and  $b$  displayed in Table 4.2. In the large  $\chi$  regime, the error  $\Delta E$  is dominated by the coefficients  $b$ . Interestingly, the ratio  $b_{\text{MERA}}/b_{\text{MPS}}$  for the four models produces very similar results, namely 1.80, 1.74, 1.72, and 1.56 for the Ising, Potts, XX and Heisenberg zig-zag models respectively. Given that the average ratio is  $b_{\text{MERA}}/b_{\text{MPS}} \approx 1.72$ , we conclude that in the large  $\chi$  limit a similar error in the energy for MERA and MPS is

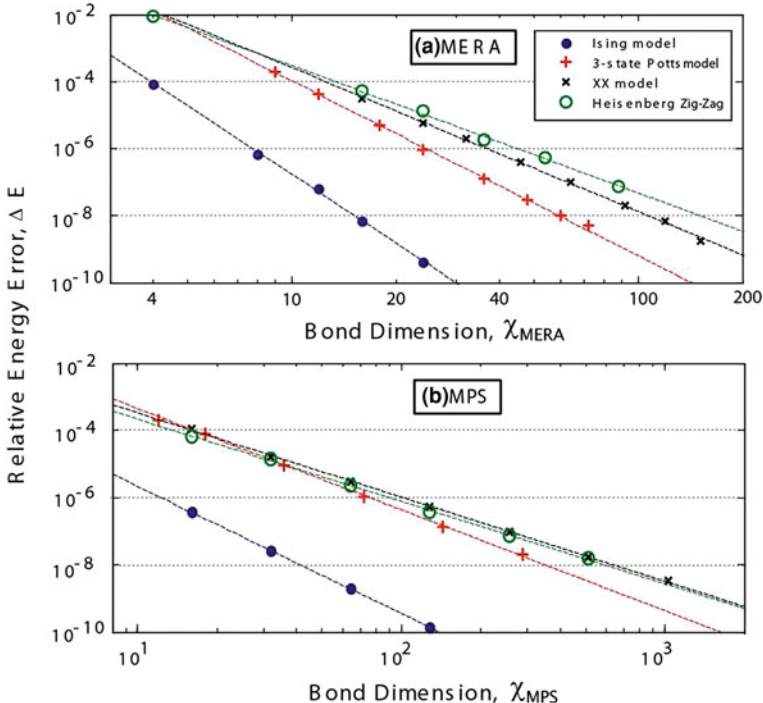


**Fig. 4.11** Relative energy error  $\Delta E$  in the ground state of critical spin models as a function of the tensor network bond dimension  $\chi$ , comparing **a** the scale-invariant MERA with **b** an infinite MPS. In all cases the energy error  $\Delta E$  appears to scale polynomially in  $\chi$  in accordance with Eq. 4.42

obtained if

$$\Delta E_{\text{MERA}}(\chi) \approx \Delta E_{\text{MPS}}(\chi^{1.72}), \quad (4.43)$$

that is, if  $\chi_{\text{MPS}} = (\chi_{\text{MERA}})^{1.72}$ . Taking into account that the number of variational parameters in the MERA and MPS scale as  $(\chi_{\text{MERA}})^4$  and  $(\chi_{\text{MPS}})^2$ , this comparison shows that in the large  $\chi$  limit the MPS requires less variational parameters than the scale-invariant MERA in order to obtain a similar accuracy in the ground state energy.

It is tempting to extend this comparison to computational costs. A first step in this direction is to note that each iteration in the optimization of MERA and MPS scales (naively) as  $(\chi_{\text{MERA}})^6$  and  $(\chi_{\text{MPS}})^3$ , from which it would be tempting to conclude that MPS algorithms require a lower computational budget than MERA algorithms to obtain the same accuracy in the ground state energy. However, there are important multiplicative prefactors  $k_{\text{MERA}}$  and  $k_{\text{MPS}}$  modifying the naive scaling of costs. In both cases, one is required to find the dominant eigenvector of a transfer matrix. But while in the case of the MERA this transfer matrix (or scaling superoperator)

**Table 4.2** Best fit coefficients to the functional form of Eq. 4.42 for the scaling of relative energy error in ground state MERA and MPS calculations

	(i) MERA		(ii) MPS	
	<i>a</i>	<i>b</i>	<i>a</i>	<i>b</i>
Ising Model ( $c = 1/2$ )	1.13	6.81	0.013	3.78
Potts Model ( $c = 4/5$ )	17.80	5.22	0.432	3.00
XX Model ( $c = 1$ )	5.25	4.30	0.103	2.50
Heisenberg Zig-Zag ( $c = 1$ )	1.89	3.80	0.059	2.44

The central charge  $c$  of the critical models is given for reference

has a well-defined gap, implying that  $k_{\text{MERA}}$  is essentially independent of  $\chi_{\text{MERA}}$ , in the case of the MPS the gap in the transfer matrix closes to zero with increasing  $\chi_{\text{MPS}}$ , and the prefactor  $k_{\text{MPS}}$  actually also grows with growing  $\chi_{\text{MPS}}$ . Therefore a proper comparison of computational costs requires first a careful characterization of the dependence of  $k_{\text{MPS}}$  in  $\chi_{\text{MPS}}$ , which is beyond the scope of the present chapter.

## Two-Point Correlators

Let us now compare the accuracy of two-point correlators produced by the scale-invariant MERA and MPS. For both approaches, we consider the ground state of the quantum XX model and compute the correlator,

$$C(d) \equiv \langle \hat{a}^\dagger(r) \hat{a}(r+d) \rangle \quad (4.44)$$

where  $\hat{a}$  is a fermionic operator defined in terms of spin operators as

$$\hat{a}(r) = \left( \prod_{m < r} Z(m) \right) \frac{X(r) - iY(r)}{2}. \quad (4.45)$$

The correlation function of Eq. 4.44 has the exact expression

$$C_{\text{exact}}(d) = \frac{-\sin(\pi d/2)}{\pi d}, \quad (4.46)$$

which is obtained from mapping the quantum XX model to a free-fermion model [49]. The correlation function  $C(d)$  decays polynomially, as expected from the ground state of a quantum critical model.

Figure 4.12a shows the correlations obtained with a scale-invariant MERA for  $\chi_{\text{MERA}} = \{16, 46, 96\}$  and with an MPS for  $\chi_{\text{MPS}} = \{24, 128, 512\}$ . These particular values of the bond dimension  $\chi$  have been chosen so that the tensor networks produce comparable errors in the ground state energy, namely

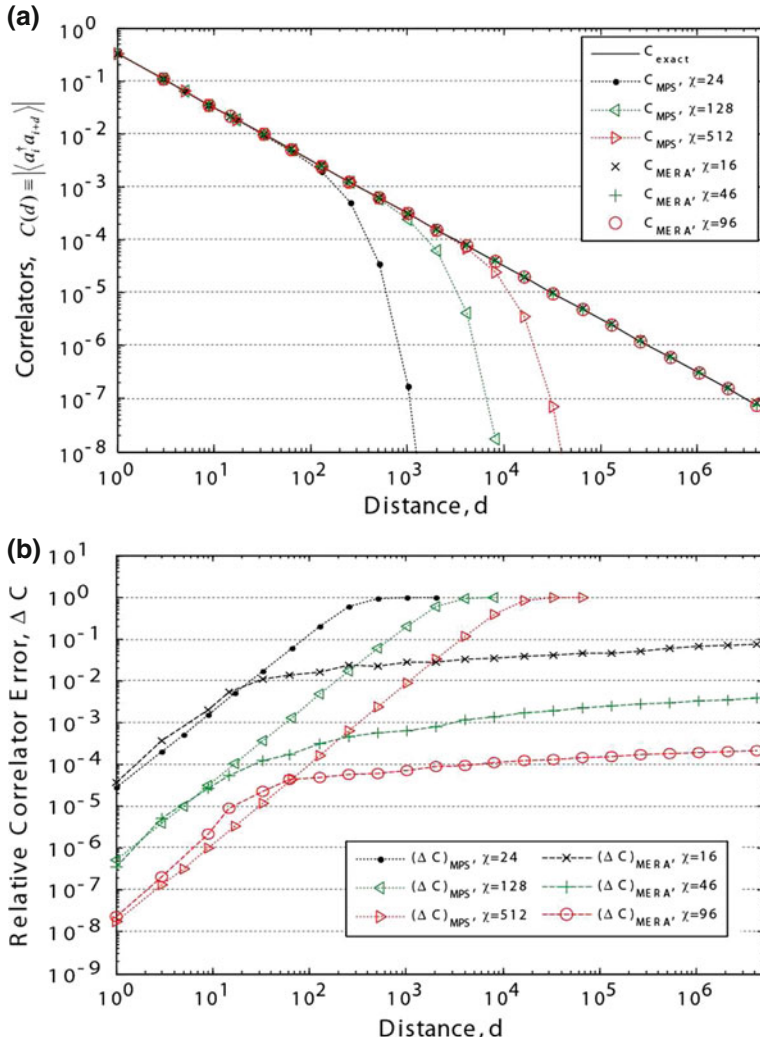


**Fig. 4.12** **a** The two-point correlator of fermion operators, as defined Eq. 4.44, in the ground state of the quantum XX model, comparing results from the scale-invariant MERA and infinite MPS with the exact correlators. Correlators from MPS approximate polynomial decay only until some finite length scale  $\zeta \approx \chi^{1.38}$ , while correlators from MERA remain polynomial at all length scales. **b** Relative error in correlators as defined Eq. 4.48

$$\begin{aligned}\Delta E_{\text{MERA}} (\chi_{\text{MERA}} = 16) &\approx \Delta E_{\text{MPS}} (\chi_{\text{MPS}} = 24) \approx 3.5 \times 10^{-5} \\ \Delta E_{\text{MERA}} (\chi_{\text{MERA}} = 46) &\approx \Delta E_{\text{MPS}} (\chi_{\text{MPS}} = 128) \approx 4.5 \times 10^{-7} \\ \Delta E_{\text{MERA}} (\chi_{\text{MERA}} = 96) &\approx \Delta E_{\text{MPS}} (\chi_{\text{MPS}} = 512) \approx 1.7 \times 10^{-8}. \end{aligned} \quad (4.47)$$

The figure illustrates quite clearly that while the MPS can only approximate polynomial correlations up to a finite length scale  $\zeta = \chi^\kappa$  [33], with  $\kappa \approx 1.38$  for the quantum XX model, correlations in the MERA decay polynomially at all length scales [9, 16]. Figure 4.12b displays the relative error in correlators,

$$\Delta C = \frac{|C_{\text{exact}} - C_{\text{numeric}}|}{|C_{\text{exact}}|}. \quad (4.48)$$

Here it is seen that a MERA and an MPS that produce the same accuracy in the ground state energy produce also similarly accurate correlators at short distances, but the relative error in the correlator grows much slower with distance in the case of the MERA. For instance, the  $\chi = 96$  MERA reproduces correlators up to  $d = 10^6$  sites with relative error  $\Delta C < 2 \times 10^{-4}$ , whereas the  $\chi = 512$  MPS, although possessing a similar ground energy, reproduces similarly accurate correlators only up to  $d \approx 100$  sites.

## Summary of Comparison

To summarize, we have seen that the MPS is more efficient than the scale-invariant MERA when it comes to ground state energies of critical Hamiltonians, in that it requires less variational parameters to achieve the same accuracy. However, the MERA produces better correlators at large distances, and it is therefore better suited to characterize asymptotic behaviors, such as the polynomial decay of correlations, from which one could in principle extract the critical exponents of the theory. However, as exemplified in Sect. 4.4.4 with the computation of scaling dimensions for local and non-local operators, critical exponents and other conformal data can actually be extracted more directly by analyzing the scaling superoperator. We illustrate this next.

### 4.5.2 Evaluation of Conformal Data: The Ising Model

As an example of extraction of conformal data from the scale-invariant MERA, here we identify the whole operator content (local and non-local primary fields) of the CFT corresponding to the quantum critical Ising model, reproducing the analysis of Ref. [22]. Similar results have also been obtained for the three-state Potts and quantum XX models in Refs. [16, 22].

The Hamiltonian  $H_{\text{Ising}}$  of Eq. 4.36 has a global internal  $\mathbb{Z}_2$  corresponding to flipping all the spins. That is,  $\mathcal{G} = \mathbb{Z}_2$  and  $g \in \{+1, -1\}$ , with  $V_{+1} = \mathbb{I}$  and  $V_{-1} = Z$ , and

$$\Gamma_{-1} H_{\text{Ising}} \Gamma_{-1}^\dagger = H_{\text{Ising}}, \quad \Gamma_{-1} \equiv \bigotimes_{m=-\infty}^{\infty} Z. \quad (4.49)$$

The tensors  $u$  and  $w$  that comprise the scale-invariant MERA are chosen to be parity preserving; each index  $i$  of tensors  $u$  and  $w$  decomposes as  $i = (p, \alpha_p)$ , where  $p$  labels the parity ( $p = +1$  for even parity and  $p = -1$  for odd parity) and  $\alpha_p$  labels the distinct values of  $i$  with parity  $p$ . For tensors  $u, w$  to be parity preserving it is ensured that, e.g.  $u_{i_1, i_2}^{j_1, j_2} = 0$  if  $p(i_1)p(i_2)p(j_1)p(j_2) = -1$ , in accordance with Eq. 4.16. An operator  $\mathcal{O}$  acting on the spin chain has parity  $p$  if

$$(\Gamma_{-1})\mathcal{O}(\Gamma_{-1})^\dagger = p\mathcal{O}. \quad (4.50)$$

The local scaling superoperator  $\mathcal{S}_{g=1}$  and the non-local scaling superoperator  $\mathcal{S}_{g=-1}$ , see Fig. 4.10d, e, are obtained from the optimized scale-invariant MERA with bond dimension  $\chi = 32$ . The scaling superoperator  $\mathcal{S}_{g=1}$  is diagonalized to find the local scaling operators  $\phi_{+1,\alpha}$  together with their scaling dimensions  $\Delta_{+1,\alpha}$ , while the scaling superoperator  $\mathcal{S}_{g=-1}$  is diagonalized to find the non-local scaling operators of the form

$$\phi_{-1,\alpha}^\triangleleft = \cdots Z \otimes Z \otimes Z \otimes \phi_{-1,\alpha}, \quad (4.51)$$

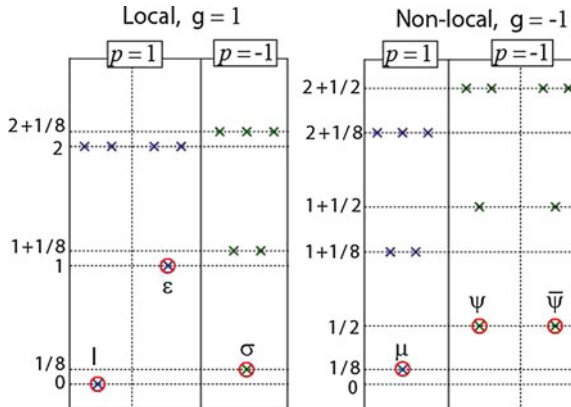
together with their scaling dimensions  $\Delta_{-1,\alpha}$ .

Table 4.3 compares the exact scaling dimensions of the primary fields of the Ising CFT and their numerical estimates obtained from the MERA, which reproduce the former with 4 to 6 digits of accuracy in all cases. In Fig. 4.13 we plot the scaling dimensions of magnitude  $\Delta \leq 2.5$  obtained from the scale-invariant MERA, which correspond to the primary fields and their descendants, organized both according to the locality  $g$  and the parity  $p$  of the corresponding scaling operators. Local scaling operators ( $g = +1$ ) with even parity ( $p = +1$ ) form the two conformal towers of the primary fields identity  $\mathbb{I}$  and energy  $\epsilon$  of the Ising CFT, whereas those with odd parity ( $p = -1$ ) form the conformal tower of the primary field spin  $\sigma$ . Non-local scaling operators ( $g = -1$ ) with even parity ( $p = +1$ ) form the conformal tower of the disorder operator  $\mu$ , and those with odd parity ( $p = -1$ ) are organized according to two towers corresponding to the fermion operators  $\psi$  and  $\bar{\psi}$ . The numerical results from the scale-invariant MERA are seen to accurately reproduce the smallest scaling dimensions, those with  $\Delta \leq 2.5$ , from all six conformal towers of the Ising CFT [36, 37].

We have also computed the OPE coefficients  $C_{\alpha\beta\gamma}$  for all primary fields, obtained by analyzing three-point correlators as described in Refs. [16]. Table 4.4 shows the numerical estimate of all non-vanishing OPE coefficients. Once again the results

**Table 4.3** Scaling dimensions of the primary fields of the Ising CFT

$\Delta^{\text{exact}}$	$\Delta_{\chi=32}^{\text{MERA}}$	Error (%)
$\Delta_\sigma = 0.125$	0.1249998	$2 \times 10^{-4}$
$\Delta_\epsilon = 1$	1.0001139	0.011
$\Delta_\mu = 0.125$	0.1250002	$2 \times 10^{-4}$
$\Delta_\psi = 0.5$	0.4999959	$8 \times 10^{-4}$
$\Delta_{\bar{\psi}} = 0.5$	0.4999963	$7 \times 10^{-4}$



**Fig. 4.13** A few scaling dimensions of the critical Ising model obtained from a  $\chi = 32$  scale-invariant MERA. The scaling dimensions are organized by the both locality  $g = \pm 1$  (local/non-local) and parity  $p = \pm 1$  (even/odd) of the corresponding scaling operators and together form the six conformal towers of the Ising CFT

**Table 4.4** OPE coefficients for the local and non-local primary fields of the Ising CFT

$C^{\text{exact}}$	$C_{\chi=32}^{\text{MERA}}$	Error (%)
$C_{\epsilon,\sigma,\sigma} = 1/2$	0.50008	0.016
$C_{\epsilon,\mu,\mu} = -1/2$	-0.49997	0.006
$C_{\psi,\mu,\sigma} = \frac{e^{-i\pi/4}}{\sqrt{2}}$	$\frac{1.00068 e^{-i\pi/4}}{\sqrt{2}}$	0.068
$C_{\bar{\psi},\mu,\sigma} = \frac{e^{i\pi/4}}{\sqrt{2}}$	$\frac{1.00068 e^{i\pi/4}}{\sqrt{2}}$	0.068
$C_{\epsilon,\psi,\bar{\psi}} = i$	1.0001 <i>i</i>	0.010
$C_{\epsilon,\bar{\psi},\psi} = -i$	-1.0001 <i>i</i>	0.010

match their exact values to within several digits of accuracy. Thus, not only have we been able to identify the *entire* field content  $\{\mathbb{I}, \epsilon, \sigma, \psi, \bar{\psi}, \mu\}$  of the Ising CFT from a simple and rather inexpensive analysis of a quantum spin chain, but we can now also identify all possible subsets of primary fields that close a subalgebra by inspecting Table 4.4. Indeed, it follows that we have the fusion rules

$$\epsilon \times \epsilon = \mathbb{I}, \quad \sigma \times \sigma = \mathbb{I} + \epsilon, \quad \sigma \times \epsilon = \sigma, \quad (4.52)$$

$$\mu \times \mu = \mathbb{I} + \epsilon, \quad \mu \times \epsilon = \mu, \quad (4.53)$$

$$\psi \times \psi = \mathbb{I}, \quad \bar{\psi} \times \bar{\psi} = \mathbb{I}, \quad (4.54)$$

$$\psi \times \bar{\psi} = \epsilon, \quad \psi \times \epsilon = \bar{\psi}, \quad \bar{\psi} \times \epsilon = \psi, \quad (4.55)$$

(as well as other, such as  $\sigma \times \mu = \psi + \bar{\psi}$ , etc) from where we see that  $\{\mathbb{I}, \epsilon\}$  and  $\{\mathbb{I}, \epsilon, \sigma\}$  close subalgebras of local primary fields, whereas  $\{\mathbb{I}, \epsilon, \mu\}$  and  $\{\mathbb{I}, \epsilon, \psi, \bar{\psi}\}$  close subalgebras that contain both local and non-local primary fields, where locality is relative to the spin variables.

## 4.6 Conclusions

In this chapter we have presented an introduction to the scale-invariant MERA and its application to the study of quantum critical systems. The main strength of MERA, when applied to quantum critical systems, is that it can explicitly incorporate scale invariance. This facilitates enormously the characterization of scaling dimensions (equivalently, critical exponents) and of other properties that characterize a quantum phase transition.

Direct comparison with an MPS shows that, while the later is more efficient at computing local observables such as the ground state energy, the MERA produces significantly more accurate correlators at long distances. In addition, from the MERA it is straightforward to identify the scaling operators of the theory, as well as their scaling dimensions and operator product expansion, producing accurate conformal data that can be used to unambiguously identify the underlying CFT.

Here we have considered homogeneous systems. However, the scale-invariant MERA has been successfully generalized to critical systems where translation invariance is explicitly broken, as it is the case of a critical system with a boundary, with an impurity, or the interface between two critical systems [50–52]. In all these scenarios translation invariance is no longer present, but exploitation of scale invariance still produces a MERA algorithm with a cost  $O(1)$  (that is, independent of the lattice size  $N$ ), and therefore infinite systems can be addressed. Again, scaling operators associated to boundaries, defects and interfaces can be easily extracted from the simulations.

Finally, much of the MERA formalism for critical systems in  $D = 1$  dimensions is also directly applicable to  $D = 2$  dimensions, including the characterization of scaling dimensions. However, due to significantly larger computational costs, so far only small values of  $\chi$  have been used in actual computations. Thus, further progress needs to be made in reducing computational costs before the scale-invariant MERA becomes a viable approach to quantum criticality also in  $D = 2$  dimensions.

## References

1. G. Evenbly, G. Vidal, Tensor Network States and Geometry. *J. Stat. Phys.* **145**, 891–898 (2011)
2. M. Fannes, B. Nachtergael, R.F. Werner, *Commun. Math. Phys.* **144**, 443 (1992)
3. S. Ostlund, S. Rommer, *Phys. Rev. Lett.* **75**, 3537 (1995)
4. S. Rommer, S. Ostlund, *Phys. Rev. B* **55**, 2164 (1997)
5. F. Verstraete, J.I. Cirac, arXiv:cond-mat/0407066v1 (2004)
6. V. Murg, F. Verstraete, J.I. Cirac, *Phys. Rev. A* **75**, 033605 (2007)
7. J. Jordan, R. Orus, G. Vidal, F. Verstraete, J.I. Cirac, *Phys. Rev. Lett.* **101**, 250602 (2008)
8. G. Vidal, *Phys. Rev. Lett.* **99**, 220405 (2007)
9. G. Vidal, *Phys. Rev. Lett.* **101**, 110501 (2008)
10. G. Evenbly, G. Vidal, *Phys. Rev. B* **81**, 235102 (2010)
11. L. Cincio, J. Dziarmaga, M.M. Rams, *Phys. Rev. Lett.* **100**, 240603 (2008)
12. G. Evenbly, G. Vidal, *New J. Phys.* **12**, 025007 (2010)
13. M. Aguado, G. Vidal, *Phys. Rev. Lett.* **100**, 070404 (2008)
14. V. Giovannetti, S. Montangero, R. Fazio, *Phys. Rev. Lett.* **101**, 180503 (2008)
15. G. Evenbly, G. Vidal, *Phys. Rev. B* **79**, 144108 (2009)
16. R.N.C. Pfeifer, G. Evenbly, G. Vidal, *Phys. Rev. A* **79**, 040301(R) (2009)
17. G. Evenbly, G. Vidal, *Phys. Rev. Lett.* **102**, 180406 (2009)
18. R. Koenig, B.W. Reichardt, G. Vidal, *Phys. Rev. B* **79**, 195123 (2009)
19. S. Montangero, M. Rizzi, V. Giovannetti, R. Fazio, *Phys. Rev. B* **80**, 113103 (2009)
20. G. Vidal, in *Understanding Quantum Phase Transitions*, ed. by L.D. Carr (Taylor & Francis, Boca Raton, 2010)
21. G. Evenbly, G. Vidal, *Phys. Rev. Lett.* **104**, 187203 (2010)
22. G. Evenbly, P. Corboz, G. Vidal, *Phys. Rev. B* **82**, 132411 (2010)
23. L. Cincio, J. Dziarmaga, A.M. Oles, *Phys. Rev. B* **82**, 104416 (2010)
24. S.R. White, *Phys. Rev. Lett.* **69**, 2863 (1992)
25. S.R. White, *Phys. Rev. B* **48**, 10345 (1993)
26. U. Schollwoeck, *Rev. Mod. Phys.* **77**, 259 (2005)
27. U. Schollwoeck, *Ann. Phys.* **326**, 96 (2011)
28. G.K.-L. Chan, J.J. Dorando, D. Ghosh, J. Hachmann, E. Neuscammman, H. Wang, T. Yanai, An introduction to the density matrix renormalization group ansatz in quantum chemistry. in *Frontiers in Quantum Systems in Chemistry and Physics*, ed. by S. Wilson, P.J. Grout, J. Maruani, G. DelgadoBarrio, P. Piecuch, vol. 18 of *Prog. Theor. Chem. Phys.* pp. 49–65, 2008
29. G. Vidal, *Phys. Rev. Lett.* **91**, 147902 (2003)
30. G. Vidal, *Phys. Rev. Lett.* **93**, 040502 (2004)
31. A.J. Daley, C. Kollath, U. Schollwoeck, G. Vidal, *J. Stat. Mech. Theor. Exp.* P04005 (2004)
32. S.R. White, A.E. Feiguin, *Phys. Rev. Lett.* **93**, 076401 (2004)
33. L. Tagliacozzo, T.R. de Oliveira, S. Iblisdir, J.I. Latorre, *Phys. Rev. B* **78**, 024410 (2008)
34. F. Pollmann, S. Mukerjee, A. Turner, J.E. Moore, *Phys. Rev. Lett.* **102**, 255701 (2009)
35. J. Cardy, *Scaling and Renormalization in Statistical Physics* (Cambridge University Press, Cambridge, 1996)
36. P. Di Francesco, P. Mathieu, D. Senechal, *Conformal Field Theory* (Springer, New York, 1997)
37. M. Henkel, *Conformal Invariance and Critical Phenomena* (Springer, New York, 1999)
38. See appendix of the preprint version of this Chapter, arXiv:1109.5334v1 (2011)
39. S. Singh, R.N.C. Pfeifer, G. Vidal, *Phys. Rev. A* **82**, 050301 (2010)
40. S. Singh, R.N.C. Pfeifer, G. Vidal, *Phys. Rev. B* **83**, 115125 (2011)
41. G. Vidal et al., *Phys. Rev. Lett.* **90**, 227902 (2003)
42. P. Calabrese, J. Cardy, *J. Stat. Mech.* P06002 (2004)
43. P. Pfeuty, *Ann. Phys.* **57**, 79–90 (1970)
44. T.W. Burkhardt, I. Guim, *J. Phys. A Math. Gen.* **18**, L33–L37 (1985)
45. J. Sólyom, P. Pfeuty, *Phys. Rev. B* **24**, 218 (1981)
46. E. Lieb, T. Schultz, D. Mattis, *Ann. Phys.* **16**, 407 (1961)

47. S. Eggert, Phys. Rev. B **54**, 9612 (1996)
48. I.P. McCulloch, arXiv:0804.2509v1 (2008)
49. J.I. Latorre, E. Rico, G. Vidal, Quant. Inf. Comput. **4**, 48–92 (2004)
50. G. Evenbly, R.N.C. Pfeifer, V. Pico, S. Iblisdir, L. Tagliacozzo, I.P. McCulloch, G. Vidal, Phys. Rev. B **82**, 161107(R) (2010)
51. P. Silvi, V. Giovannetti, P. Calabrese, G.E. Santoro, R. Fazio, J. Stat. Mech. L03001 (2010)
52. G. Evenbly, G. Vidal, in preparation

# Chapter 5

## The Time-Dependent Density Matrix Renormalization Group

Adrian E. Feiguin

**Abstract** The time-dependent DMRG is a remarkable and highly flexible tool to simulate real-time dynamics of strongly correlated systems. It can be used to calculate spectral functions, and to study systems far from equilibrium. In this chapter we describe how to generalize the DMRG method to solve the time-dependent Schrödinger equation, in both, real, and imaginary time. We illustrate these ideas with different applications such as transport problems in nano-structures, quantum quenches, and the calculation of time-dependent correlations functions.

### 5.1 Introduction

In this chapter we describe how to simulate the time-evolution of a quantum many-body state with the DMRG method (For reviews see Refs. [1–5]). The problem consists of simply solving the following the time-dependent Schrödinger equation:

$$i\hbar \frac{\partial}{\partial t} |\Psi(t)\rangle = \hat{H} |\Psi(t)\rangle, \quad (5.1)$$

which has a formal solution

$$|\Psi(t)\rangle = e^{-it\hat{H}} |\Psi(t=0)\rangle \quad (5.2)$$

The operator  $\hat{U}(t) = e^{-it\hat{H}}$  is the quantum-mechanical time-evolution operator.

Let us assume we know the eigenstates  $E_n$  and eigenvalues  $|n\rangle$  of the Hamiltonian  $\hat{H}$ . In this basis, the initial state can be expressed as:

---

A. E. Feiguin (✉)

Department of Physics, Northeastern University, Boston, MA 02115, USA  
e-mail: a.feiguin@neu.edu

$$|\Psi(t=0)\rangle = \sum_n c_n |n\rangle, \quad (5.3)$$

and the solution to our problem is simply given by:

$$|\Psi(t)\rangle = \sum_n c_n e^{-itE_n} |n\rangle. \quad (5.4)$$

In small systems, where full diagonalization of the Hamiltonian is viable, this solves our problem. However, in DMRG we work in a basis with the form of matrix product states, and in this basis the coefficients will be wildly oscillating functions of time with different frequencies. On top of that, we are working in a truncated basis that does not account for the full Hilbert space. On the one hand, we know that this breaks unitarity. But more worrisome, our wave-function will evolve in time and may “explore” or “drift” toward regions of the Hilbert space that we have not properly accounted for. So the challenge is to adapt our basis as time evolves, such that at every time-step, our wave-function is optimized to represent the actual exact solution of the time-dependent Schrödinger equation, in the same spirit as the original DMRG.

The first attempts of using the DRMG method for solving the time-dependent problem can be traced back to a seminal paper by Cazalilla and Marston [6–9]. After solving the time-independent problem using the infinite-system DMRG, they evolved the wave-function in time using Runge-Kutta (R-K) methods. This approach lacked some fundamental ingredients, and therefore it was not quasiexact: they used the infinite-system DMRG, and a fixed basis to evolve in time without sweeping. However, this work indicated the path toward the development of more sophisticated algorithms, and signified a remarkable first step. To illustrate its applicability, they simulated time-dependent transport in spinless chains, and they demonstrated that despite its limitations, the method worked well for moderate time ranges. Right after this work, Luo and collaborators [6–9] attempted to construct a quasiexact algorithm by targeting multiple states, keeping track of the entire story of the wave-function as it evolved in time (see Fig. 5.1). The problem with this idea is that keeping track of the entire history of the state with enough accuracy requires a large number of DMRG basis states, and becomes highly inefficient. However, this scheme becomes quasiexact if one adds sweeping and can control the errors introduced by the Runge-Kutta method.

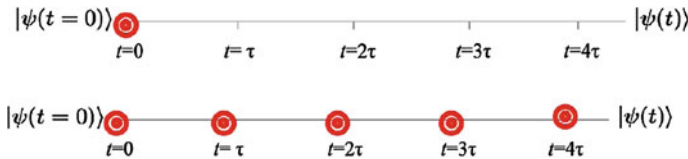


**Fig. 5.1** The *top* figure illustrates the original idea by Cazalilla and Marston: they would calculate the initial state, and evolve the wave-function in time without doing sweeping. The figure at the *bottom* shows Luo et al.’s idea of targeting the states at every time-step, keeping track of the entire time-evolution of the wave-function

## 5.2 The Adaptive Time-Dependent DMRG (tDMRG)

The crucial tipping point was the introduction by Vidal [10, 11] of the time-evolving block decimation method (TEBD). In rough terms, this method uses the time-evolution operator in imaginary time to project out the ground-state of a Hamiltonian in a matrix-product basis. The main innovation consisted in the idea of using the Suzuki–Trotter (S–T) decomposition of the time-evolution operator.

### 5.2.1 The Suzuki–Trotter Approach

Experts in quantum Monte Carlo are very familiar with the Suzuki–Trotter decomposition. When dealing with local Hamiltonians, with only nearest-neighbor interactions, it constitutes the most natural way to break-up the evolution operator. The idea is to evolve our ground state by successive applications of the evolution operator:

$$|\Psi(t)\rangle = (e^{-i\hat{H}\delta t} \dots e^{-i\hat{H}\delta t})|\Psi(0)\rangle \quad (5.5)$$

where our Hamiltonian  $\hat{H}$  can be decomposed as the sum of individual terms, each involving only nearest-neighbors:

$$\hat{H} = \hat{H}_1 + \hat{H}_2 + \hat{H}_3 \dots + \hat{H}_{L-1} \quad (5.6)$$

One would feel tempted to decompose the evolution operator as:

$$e^{-i\hat{H}\delta t} \neq e^{-i\hat{H}_1\delta t} e^{-i\hat{H}_2\delta t} \dots e^{-i\hat{H}_{L-1}\delta t} \quad (5.7)$$

But in general the “bond Hamiltonians” do not commute with their neighboring terms,  $[\hat{H}_i, \hat{H}_{i+1}] \neq 0$ , and as a consequence:

$$e^{-i(\hat{H}_1+\hat{H}_2)\delta t} \neq e^{-i\hat{H}_1\delta t} e^{-i\hat{H}_2\delta t} \quad (5.8)$$

In order to “cook up” a better break-up scheme, we start by grouping the terms into two pieces (see Fig. 5.2): a Hamiltonian  $\hat{H}_A = \hat{H}_1 + \hat{H}_3 + \dots$  containing only the odd terms, and a Hamiltonian  $\hat{H}_B = \hat{H}_2 + \hat{H}_4 + \dots$  containing the even terms. It is easy to see that all the terms inside  $\hat{H}_A$  and  $\hat{H}_B$  commute with each other, since they do not share any sites. Therefore, the evolution operator for the odd links can be *exactly* expanded as:

$$e^{-i\hat{H}_A\delta t} = e^{-i\hat{H}_1\delta t} e^{-i\hat{H}_3\delta t} \dots \quad (5.9)$$

and a similar result for  $\hat{H}_B$ .

$$\begin{aligned}\hat{H} &= \hat{H}_1 + \hat{H}_2 + \hat{H}_3 + \hat{H}_4 + \hat{H}_5 + \hat{H}_6 \\ \hat{H}_A &= \begin{array}{c} \text{---} \\ | \quad | \quad | \quad | \end{array} \hat{H}_1 + \hat{H}_3 + \hat{H}_5 \\ \hat{H}_B &= \begin{array}{c} \text{---} \\ | \quad | \quad | \quad | \end{array} \hat{H}_2 + \hat{H}_4 + \hat{H}_6\end{aligned}$$

**Fig. 5.2** Suzuki–Trotter break-up scheme: separate the Hamiltonian into two pieces, one containing the odd links, and one containing the even ones

One can show, that a first order S–T expansion can be expressed as:

$$e^{-i(\hat{H}_A+\hat{H}_B)\delta t} = e^{-i\hat{H}_A\delta t} e^{-i\hat{H}_B\delta t} + O(\delta t^2) \quad (5.10)$$

The second-order expansion is written as

$$e^{-i(\hat{H}_A+\hat{H}_B)\delta t} = e^{-i\hat{H}_A/2\delta t} e^{-i\hat{H}_B\delta t} e^{-i\hat{H}_A/2\delta t} + O(\delta t^3) \quad (5.11)$$

and fourth order expansion as:

$$\begin{aligned}e^{-i(\hat{H}_A+\hat{H}_B)\delta t} &= e^{-i\hat{H}_A\delta t\theta/2} e^{-i\hat{H}_B\delta t\theta} e^{-i\hat{H}_A\delta t(1-\theta)} e^{-i\hat{H}_B\delta t(1-2\theta)} \\ &\times e^{-i\hat{H}_A\delta t(1-\theta)} e^{-i\hat{H}_B\delta t\theta} e^{-i\hat{H}_A\delta t\theta/2} + O(\delta t^3)\end{aligned} \quad (5.12)$$

with  $\theta = 1/(2 - 2^{1/3})$ . This last expression is also known as the Forest-Ruth breakup [14, 15]. We point out that the error in the expansion is typically referred-to as the “Trotter error”.

The application of these operators reduces to taking two nearest neighbor sites, and evolving using a “bond evolution operator”  $e^{-i\hat{H}_i\delta t}$  (with the corresponding phases). These bond evolution operators have a very simple matrix representation. For instance, in the case of the Heisenberg model that concerns us:

$$\hat{H}_i = \hat{\mathbf{S}}_i \cdot \hat{\mathbf{S}}_{i+1} \quad (5.13)$$

Using a two-site basis:

$$|ss'\rangle = \{| \uparrow\uparrow\rangle, | \uparrow\downarrow\rangle, | \downarrow\uparrow\rangle, | \downarrow\downarrow\rangle\} \quad (5.14)$$

we can easily obtain the  $4 \times 4$  Hamiltonian matrix:

$$H_{i,i+1} = \begin{pmatrix} 1/4 & & & 0 \\ & -1/4 & 1/2 & \\ & 1/2 & -1/4 & \\ 0 & & & 1/4 \end{pmatrix}, \quad (5.15)$$

In order to obtain the exponential of the Hamiltonian matrix we follow these steps:

1. Diagonalize the matrix and calculate the eigenvalues and eigenvectors.
2. Calculate the exponential of  $\hat{H}$  in the diagonal basis, with the exponential of the eigenvalues along the diagonal.
3. Rotate back to the original basis using the transformation matrix with the eigenvectors as columns.

We leave it as an exercise for the reader to calculate the exponential of the matrix (5.15).

### 5.2.2 Evolution Using Suzuki–Trotter Expansions

As we have seen, we can reduce the time-evolution to successive applications of a  $d \times d$  matrix on pairs of sites, where  $d$  is the local dimension of the sites. This is a very fast and efficient operation. We only need to incorporate this idea in the context of the DMRG. We first realize that we always have two sites in between the DMRG blocks. It is therefore straightforward to apply the bond evolution operator to those two sites. If we express the operator matrix elements as:

$$\langle s'_i, s'_{i+1} | e^{-i\hat{H}_{i,i+1}\delta t} | s_i s_{i+1} \rangle = U_{s_i s_{i+1}}^{s'_i, s'_{i+1}} \quad (5.16)$$

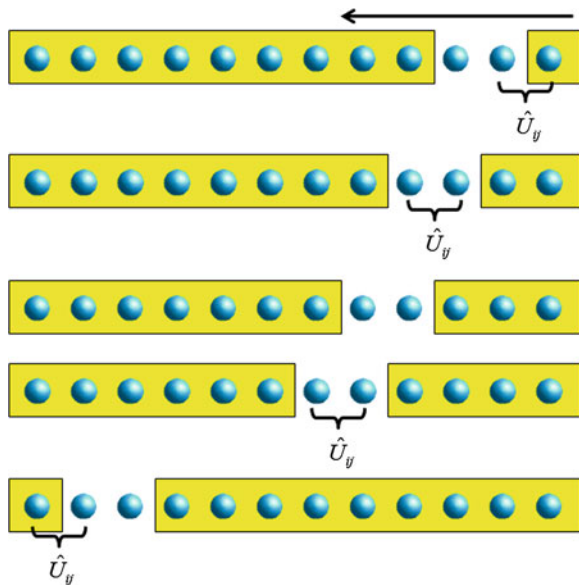
we obtain the wave function, after applying this operator as:

$$e^{-i\hat{H}_{i,i+1}\delta t} |\Psi\rangle = \sum_{\alpha_{i-1}\beta_{i+2}} \sum_{s_i, s_{i+1}} \sum_{s'_i, s'_{i+1}} \langle \alpha_{i-1} s_i s_{i+1} \beta_{i+2} | \Psi \rangle U_{s_i s_{i+1}}^{s'_i, s'_{i+1}} | \alpha_{i-1} s'_i s'_{i+1} \beta_{i+2} \rangle. \quad (5.17)$$

## 5.3 The tDMRG Algorithm

The implementation of the algorithm is very straightforward if we already count with a ground-state DMRG code that implements the ground-state prediction explained in a previous chapter [12, 13]. The idea is to initialize the state for the time-evolution, by calculating the ground-state of some Hamiltonian, for instance. We can choose to perturb the Hamiltonian by changing some parameter or adding a term to it, or we can also perturb the wave-function by applying some operator to it. We then evolve this initial state using the S–T breakup. There are two fundamental changes with respect

**Fig. 5.3** Illustration showing a *right-to-left* half-sweep during the time-evolution. The bond evolution operator is applied only to the odd links during this half-sweep. During the *left-to-right* half-sweep, only the even links will be evolved



to the ground-state scheme: (i) we turn off the Lanczos/Davidson diagonalization. This step will be replaced by the application of the evolution operator. (ii) we have to propagate the wave-function as we evolve in time, and sweep. This is done using the same transformation used for the wave-function prediction. The protocol (illustrated in Fig. 5.3) can be summarized as follows:

- Run the ground-state DMRG to calculate the initial state. We could choose it to be the ground-state of some particular Hamiltonian. Finish your simulation with a full sweep (from left to right, for instance).
- Introduce a perturbation to the problem: we could change the Hamiltonian (e.g. by changing the value of some parameter or adding some extra term) or to the state (e.g. by applying an operator).
- Turn off the Lanczos/Davidson diagonalization.
- Start the sweeping process, applying the bond evolution operator to the single sites. This will depend on whether you are applying the operator to the even links or odd links. You can choose to use the odd links when sweeping from left to right, and the even links when sweeping from right to left. If the two single sites correspond to the wrong partition, you iterate without doing anything to the state. At each step you have to:

1. Apply the bond evolution operator to the single sites, if the two sites correspond to the right partition. This step replaces the Lanczos/Davidson diagonalization.
  2. Increase the block size by adding a site, applying the density matrix truncation same as in the ground-state algorithm.
  3. Rotate all the operators to the new basis.
  4. Rotate the wave-function to the new basis, by using the wave-function prediction.
- Depending on the order of your S–T breakup, do as many half-sweeps as required to evolve one time-step.

Contrary to the ground-state DMRG, in which the wave-function transformation is merely a convenient trick to speed-up the calculation, the propagation of the wave-function is now the main purpose of the algorithm. Therefore, the wave-function will change, evolve in time at every-step of the sweep, and the DMRG states will accommodate accordingly to optimize the basis to faithfully represent it.

The number of half-sweeps required to evolve a single time-step will depend on the order of the S–T breakup. If we choose to use the second order expansion, we need three half-sweeps: (i) a right-to-left sweep applying the evolution operator to the even links (ii) a left-to-right sweep applying the evolution operator to the odd links, and (iii) another right-to-left sweep acting on the even links. Typically one would perform another half-sweep to do measurements, without evolving in time (we cannot measure at an intermediate step during the time-evolution!).

The initial state and the perturbation applied will depend on the problem of interest. We will discuss some typical examples in the following sections.

## 5.4 Time-Step Targeting Method

The application of the S–T break-up is limited to “nice” Hamiltonians with only nearest-neighbor iterations. If we want to study a problem with long range iterations, or with higher dimensionality, we need to find a different approach. One idea would be to modify the original proposal of Cazalilla and Marston, and Luo et al. [6–9] to adapt our basis in a similar fashion as the S–T approach, but without the computational cost of keeping track of the entire history of the state. In order to emulate the behavior of the S–T approach, we need to target *one time-step accurately*, before moving to the next step. To do so, we keep track of the states at some intermediate points between a time  $t$  and  $t + \delta t$  (See Fig. 5.4). Once we have performed a couple of half-sweeps to adapt the basis, we evolve one time-step.

In the original proposal [16], the time evolution was done by using Runge-Kutta integration. The intermediate states can be easily constructed as a spline, using the

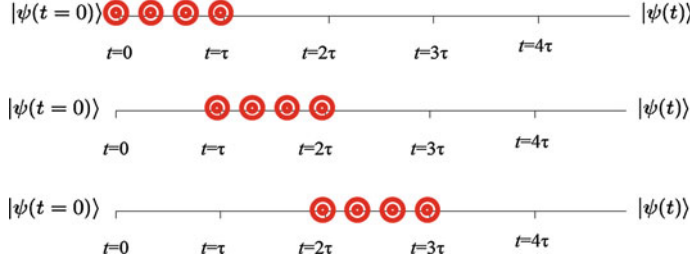


**Fig. 5.4** Time-targeting idea: at every time step, target four intermediate states to optimize the basis for the time evolution

same auxiliary vectors. The standard fourth order Runge-Kutta method relies on a set of four auxiliary vectors:

$$\begin{aligned} |k_1\rangle &= \delta t \hat{H}(t) |\Psi(t)\rangle \\ |k_2\rangle &= \delta t \hat{H}(t + \delta t/2) [|\Psi(t)\rangle + 1/2|k_1\rangle] \\ |k_3\rangle &= \delta t \hat{H}(t + \delta t/2) [|\Psi(t)\rangle + 1/2|k_2\rangle] \\ |k_4\rangle &= \delta t \hat{H}(t + \delta t) [|\Psi(t)\rangle + |k_3\rangle] \end{aligned} \quad (5.18)$$

The final state at time  $t + \delta t$  is given by:

$$|\Psi(t + \delta t)\rangle \approx |\Psi(t)\rangle + \frac{1}{6} [|k_1\rangle + 2|k_2\rangle + 2|k_3\rangle + |k_4\rangle] + O(\delta t^5) \quad (5.19)$$

We need to decide how to interpolate between these two states at times  $t$  and  $t + \delta t$ . We choose to target the states at times  $t$ ,  $t + \delta t/3$ ,  $t + 2\delta t/3$ , and  $t + \delta t$ . A way to interpolate between two time step is by using a spline, for instance. We can actually approximate the states at intermediate time by using the same auxiliary vectors defined above. The states at times  $t + \delta t/3$  and  $t + 2\delta t/3$  can be obtained, with an error of  $O(\delta t^4)$ , as

$$\begin{aligned} |\Psi(t + \delta t/3)\rangle &\approx |\Psi(t)\rangle + \frac{1}{162} [31|k_1\rangle + 14|k_2\rangle + 14|k_3\rangle - 5|k_4\rangle] \\ |\Psi(t + 2\delta t/3)\rangle &\approx |\Psi(t)\rangle + \frac{1}{81} [16|k_1\rangle + 20|k_2\rangle + 20|k_3\rangle - 2|k_4\rangle]. \end{aligned} \quad (5.20)$$

In practice we proceed as follows: we can choose one half-sweep to correspond to a time step. At every step during the sweeping iteration we calculate the four Runge-Kutta vectors. We obtain the new density matrix by targeting the four states  $|\Psi(t)\rangle$ ,  $|\Psi(t + \delta t/3)\rangle$ ,  $|\Psi(t + 2\delta t/3)\rangle$ , and  $|\Psi(t + \delta t)\rangle$ . We advance in time only on the last step of the half sweep. We could alternatively choose to perform more than one half-sweep to make sure that the basis is adequate to evolve one time-step. We typically find the a single half-sweep is sufficient. The method used to evolve in

time in this last step is arbitrary, and need not be the Runge-Kutta method. Whatever the method of choice is, the calculation cost of this last time is very small, so more sophisticated approaches are viable. Typically one could perform 10 iterations of the Runge-Kutta algorithm using a step  $\delta t/10$ . Alternatively, one could evolve using the exponential of the Hamiltonian in a Krylov basis, which is obtained by the same procedure as the Lanczos diagonalization. The advantage of this last approach is that the evolution is unitary, while Runge-Kutta breaks unitarity. However, we point out that the truncation to a finite number of DMRG states introduces non-unitarity anyway.

The target states can be weighted equally, or not. Tests using different combinations of weights indicate that the optimal choice is  $w_1 = w_4 = 1/3$  and  $w_2 = w_3 = 1/6$ .

## 5.5 Sources of Error

There are two fundamental sources of error: (i) The truncation error, and (ii) the error introduced in the time evolution by either S-T or the integration method of choice. The truncation error can in principle be controlled by keeping more DMRG states as the entanglement in the system grows. How the entanglement behaves during the time evolution is a topic of intense research, and will depend on the kind of perturbations introduced into the problem. We shall discuss this later. The Suzuki-Trotter error can also be controlled by using high order expansions or small time steps. In fourth-order schemes, such as Runge-Kutta or Forest-Ruth, the error is dominated by the truncation error.

For instance, in S-T simulations, the error typically decreases with increasing number of DMRG states, but it eventually plateaus and stays constant (see Fig. 5.5). This occurs when the error is dominated by the S-T error. On the other hand, in the

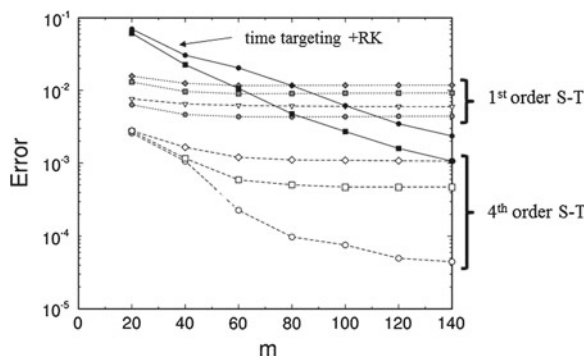


**Fig. 5.5** Error at time  $t = 8$  for the Haldane chain ( $L = 32$ ), as a function of the number of states kept  $m$ . We show results using a 1st order Suzuki-Trotter break-up (gray symbols), 4th order Suzuki-Trotter (empty symbols), and 4th order Runge-Kutta (filled symbols). See Ref. [16] for more details

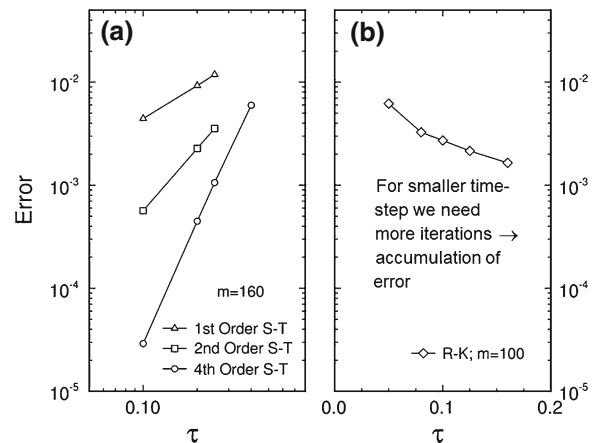
R-K simulations, the error steadily goes down, meaning that for the number of states kept in these simulations, the error is dominated by the truncation.

In the time-targeting schemes, we need to keep more DMRG states because we need the basis to optimize four different states at four different times. The general recipe to control the truncation error, both in ground-state, and time-dependent simulations, is to fix the truncation error below certain tolerance, and ask the algorithm to pick the optimal basis size to keep the error below that value. As mentioned before, the number of states needed to maintain a given tolerance may vary, and will typically grow. How fast it grows will depend on the particular problem. Sometimes it grows to a point when it becomes unmanageable by our computer. In that case we have two options: (i) stop the simulation (ii) continue with a fixed number of states. It is important to point out that option (ii) will likely produce biased results, and the simulation will no longer be quasi-exact.

A noteworthy fact is that even though the error in the R-K scheme is expected to grow as  $\delta t^4$ , it actually *decreases* with increasing time-step (See Fig. 5.6). This is due to the fact that the error accumulates with the number of steps: the larger the time-steps, the fewer iterations we need to reach a desired time, consequently the smaller is the accumulation of error.

The time-targeting scheme requires one half-sweep to evolve one time-step, while a fourth order S-T expansion will require seven. At the same time, R-K requires multiplying by the Hamiltonian several times per iteration during the sweep, while the S-T only requires a multiplication by a small matrix. On top of that, when evolving in time using S-T we only need to keep a fraction of the states, and we do not need to store the Hamiltonian, nor the operators needed to build the interactions between blocks. In general, S-T is always the optimal choice for Hamiltonians with nearest-neighbor interactions.

**Fig. 5.6** Error at time  $t = 8$  for the Haldane chain for different time steps  $\tau$ : **a** 1st, 2nd, and 4th order Suzuki-Trotter break-ups and  $m = 160$ ; **b** Runge-Kutta and  $m = 100$ . Time is in units of the Heisenberg exchange  $J$ . See Ref. [16] for more details



## 5.6 Comparing Suzuki–Trotter and Time-Step Targeting

Here we summarize the main facts to consider when picking a time-evolution method:

- S–T is fast and efficient for one-dimensional geometries with nearest-neighbor interactions.
- The S–T error is controlled by the Trotter error but can be reduced using higher order expansions of smaller time-steps.
- Time-step targeting methods can be applied to ladders, systems with complex geometries, and/or long-range interactions.
- Time-step targeting allows one to use larger time-steps, but it is computationally more expensive and requires keeping more DMRG states.
- In time-step targeting schemes it is convenient (and maybe a good practice), to perform an intermediate sweep to improve the basis before evolving in time.
- Time-evolution using R–K is non-unitary, which can be dangerous. A Krylov expansion is in principle the right choice. We have to remember, however, that unitarity is always broken by the DMRG truncation.

## 5.7 Evolution in Imaginary Time

The tDMRG method can easily be generalized to study time evolution in imaginary time [17–19]. The idea consists of enlarging the Hilbert space by adding auxiliary degrees of freedom called “ancillas” that are exact copies of the original, physical states. The use of auxiliary systems to study thermodynamics in quantum systems originated as a key idea in thermo field dynamics [17, 20–22]. Let the energy eigenstates of the system in question be  $\{n\}$ . We introduce an auxiliary set of fictitious states  $\{\tilde{n}\}$  in one-to-one correspondence with  $\{n\}$ , and define the unnormalized pure quantum state, in an enlarged Hilbert space,

$$|\psi(\beta)\rangle = e^{-\beta \hat{H}/2} |\psi(0)\rangle = \sum_n e^{-\beta E_n/2} |n\tilde{n}\rangle \quad (5.21)$$

where  $\tilde{n}$  is the matching state to  $n$ ,  $\beta$  is the inverse temperature, and  $|\psi(0)\rangle = \sum_n |n\tilde{n}\rangle$  is our thermal vacuum. Then the partition function is

$$Z(\beta) = \langle \psi | \psi \rangle \quad (5.22)$$

and we can obtain the exact thermodynamic average of an operator  $A$  (acting only on the real states), as

$$\langle A \rangle = Z(\beta)^{-1} \langle \psi | A | \psi \rangle. \quad (5.23)$$

At  $\beta = 0$ , the state  $\psi$  is the maximally entangled state between the real system and the fictitious system. It is easy to show that if we change basis from the energy

eigenstates  $n$  to some other arbitrary basis  $s$ ,  $\psi$  is still maximally entangled [20],  $|\psi(0)\rangle = \sum_s |s\tilde{s}\rangle$ . A natural basis to use is the site basis, where the state of each site  $i$  takes on a definite value  $s_i$ . One finds

$$|\psi(0)\rangle = \prod_i \sum_{s_i} |s_i\tilde{s}_i\rangle = \prod_i |I_i\rangle \quad (5.24)$$

defining the maximally entangled state  $|I_i\rangle$  of site  $i$  with its ancilla.

For practical purposes, it is useful to think of each ancilla as being the anti-site of its site. A state of the ancilla is given opposite quantum numbers to the corresponding state of the real site. In this way, the state of interest has both total charge and total  $z$  component of spin equal to zero. This is equivalent to applying a particle-hole transformation of the maximally entangled state: After the particle-hole transformation, the vacuum state becomes  $|I_i\rangle = \sum_{\{s_i\}} |\{s_i\}, \{\tilde{s}'_i\}\rangle$ , where the spin configurations  $\{\tilde{s}'\}$  are copies of  $\{s\}$  with all the spins reversed.

A useful example to see how these ideas work is to consider a single spin. We will square the Hilbert space by adding a second fictitious spin, our ancilla, and construct the following state:

$$|I_0\rangle = \frac{1}{\sqrt{2}} \left[ |\uparrow\tilde{\downarrow}\rangle + |\downarrow\tilde{\uparrow}\rangle \right] \quad (5.25)$$

This is the maximally entangled state between the spin and its ancilla. We can easily obtain the reduced density matrix of the physical spin by tracing over the ancilla, yielding:

$$\rho = \begin{pmatrix} 1/2 & 0 \\ 0 & 1/2 \end{pmatrix} \quad (5.26)$$

This is telling us that the physical spin is effectively at infinite temperature. Of course, temperature is ill defined for a single spin, but the thermal state of a spin at  $T = \infty$  is well defined. This also illustrates how the fictitious spin can act as an effective thermal bath for the physical one.

Next, we would want to build the thermal state for a chain of spins at infinite temperature. We simply multiply:

$$|\psi(0)\rangle = |I_0\rangle|I_0\rangle\dots|I_0\rangle. \quad (5.27)$$

We can build this state as the ground-state of an artificial “entangler” Hamiltonian acting on both, physical and fictitious spins:

$$\hat{H}_{aux} = \sum_i (\hat{S}_i^+ \hat{S}_i^- + \hat{\tilde{S}}_i^+ \hat{\tilde{S}}_i^-) \quad (5.28)$$

where the tilde operators act on the ancillas.

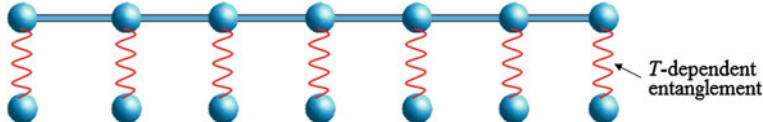


**Fig. 5.7** Illustration of the ancilla construction. Each *wiggly line* represent the quantum entanglement between a physical degree of freedom living on the chain, and its copy, or ancilla. The entanglement is temperature-dependent: it is maximum at infinite temperature, and zero at  $T = 0$ . The Hamiltonian—and the evolution operator—only acts on the physical degrees of freedom, and the ancillas only “evolve” through their entanglement with the physical spins

This idea can be generalized to particle-number conservation in fermionic systems. After applying the particle-hole transformation on the ancilla, we obtain the corresponding “anti-state”:  $|\uparrow, \downarrow\rangle$ ,  $|\downarrow, \uparrow\rangle$ ,  $|0, 2\rangle$ , and  $|2, 0\rangle$ .

The essence of the ancilla finite temperature method is to start in this local  $\beta = 0$  state, and evolve in imaginary time through a succession of temperatures  $\beta$  using the physical Hamiltonian acting only on the physical spins (see Fig. 5.7). The infinite temperature starting state has a correlation length of 0 and requires only one state per block. Since this state is a product state, the entanglement between left and right blocks is zero. As the system evolves in imaginary time, longer range entanglement is produced and the correlation length grows. The number of states needed for a given accuracy grows as the temperature decreases. It is most natural to slowly increase the size of the basis, in order to keep a roughly constant truncation error. One may wish to set a minimum basis set size to make the early evolution essentially exact with little computational cost.

The process outlined above is also called quantum purification of the state. Notice that we start from a product state of maximally entangled pairs, and we end at zero temperature with a state where the physical spins and the ancillas are completely decoupled: a product state between the ground-state of the physical spins, and the state of the ancillas.

## 5.8 Applications

Since the first seminal paper by Cazalilla and Marston [6–9] it became clear that a time-dependent DMRG method would enable one to study a whole zoo of new problems that were previously beyond reach. In their paper, they illustrated the first application to real-time transport through a resonant level. As soon as the more stable versions of the method were conceived, it was immediately applied to transport through quantum dots, and the calculation of spectral functions. When cold atom experiments started to provide a window into the atomic world, it was soon realized that it was an ideal playground to study non-equilibrium physics, and the tDMRG was used to study quenches, decoherence, and other interesting phenomena [23, 24].

Some generic scenarios that can be of interest can be grouped into the following classes:

- Start from a system in equilibrium (an eigenstate of the Hamiltonian), add a perturbation term to the Hamiltonian, and evolve under the new Hamiltonian.
- Start from a system in a state that is not an eigenstate, and evolve under the original Hamiltonian (“prepare and release”).
- Start from a system in equilibrium, and “drive it” with a time-dependent perturbation.
- Start from a system in equilibrium, and apply a perturbation to the state, for instance by “kicking it” with an operator. Evolve under the original Hamiltonian.

The first class of problems are typically referred-to as “quenches”. The last two are related to the calculation of response functions. Here I will illustrate examples of these applications in some detail.

### 5.8.1 Transport

Consider the case of a small interacting region connected to two reservoirs. We typically represent these reservoirs as non-interacting leads. The interacting region could be a quantum dot, for instance. We would like to learn the transport characteristics of the system by looking at its I–V characteristics. The generic setup was proposed by Cazalilla and Marston [6–9]: start from the system in the ground state, and apply a sudden bias difference to the two leads. This is done by shifting the chemical potential on the left and right leads by  $\pm V/2$ , where  $V$  is the external bias. One the bias is “turned on”, a current will start flowing through the system. Typically, after a transient, the current stabilized at a constant value, or plateau, corresponding to the steady state (see Fig. 5.8). We can then extract the full  $I - V$  characteristic of the problem by repeating the simulation for different values of the bias. Since the systems we study are finite and have open boundary conditions, the charge will eventually be reflected at the boundaries, and the current will “bounce back” in the opposite direction, changing sign. This gives us a window of time to reach the steady state where we can average and measure [25–31].

The transients have a duration that is related to the parameters of the problem, such as the coupling to the quantum-dot, the interactions in the dot, etc. Sometimes, we may find that for certain parameters the system does not reach a plateau before the current reverses. In such a case we have two options: (i) we can use longer leads, or (ii) we can use “damped boundary conditions” [32], or “Wilson leads” [26]. These solutions are very similar, and conceptually work in the same way: we tune the hopping matrix elements in the leads to decay with the distance from the dot, in such a way that the charge gets “trapped” at the boundaries, that act effectively as reservoirs, giving us more time to reach the steady state.

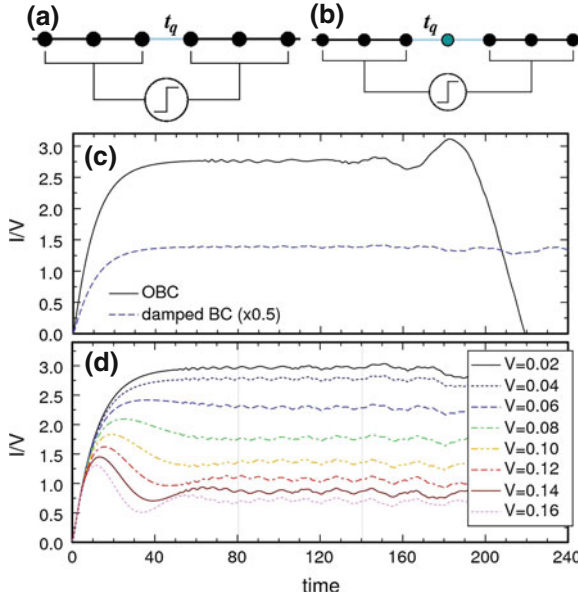


**Fig. 5.8** **a** Junction model consisting of a weak link connecting two interacting leads. **b** Quantum dot, or resonant level. **c** Current through a junction after a step bias is applied. We show results for different boundary conditions. **d** Time-dependent current though the same system, with damped boundary conditions, and different values of the bias  $V$ . Time is measured in units of the hopping  $t_q$

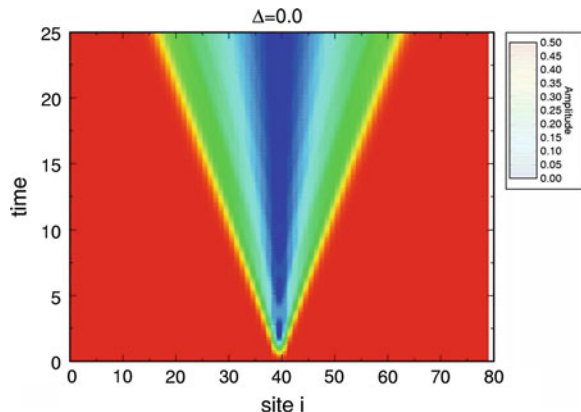
In general we want the algorithm to choose the number of states in such a way that the truncation error is always kept within a desired tolerance, say  $10^{-7}$ . How fast the number of states grows with time depends on the behavior of the entanglement entropy. This is an example of a sudden global quench, where the system is initialized in the ground state, and suddenly perturbed by the bias. We shall later see that the entanglement growth behaves for this class of problems.

An alternative approach to spin transport can be to initialize the system in a state that has all the spins on the left of the system polarized  $\uparrow$ , and the spins on the right,  $\downarrow$ . This can be achieved by using the ground state DMRG with an artificial Hamiltonian

$$\hat{H}' = \sum_{i=0}^{L/2-1} \hat{S}_i^z - \sum_{i=L/2}^{L-1} \hat{S}_i^z.$$

This creates a domain wall right at the center. We can then evolve the system under our original Heisenberg Hamiltonian, for instance, and look at the evolution of the spin. We will see wave fronts evolving in both directions, describing a “light-cone” in the  $x-t$  plane, as shown in Fig. 5.9. By measuring the slope of the boundaries, we can obtain the spin velocity. Another possibility is to create a Gaussian wave-packet with a given momentum and follow its evolution [30, 33].

**Fig. 5.9** Color density plot showing the absolute value of the spin polarization in a space-time representation, for a system that was initially fully polarized in opposite directions on *left* and *right* halves of the chain



### 5.8.2 Time-Dependent Correlation Functions

The knowledge of the excitation spectrum of a system allows for direct comparison with experiments, such as photoemission, or neutron scattering, for instance. The numerical evaluation of dynamical correlation functions is a very difficult task, since the methods are usually capable of calculating the ground-state, and maybe some low energy excitations. A number of techniques has been used in the past, however they all have very important limitations: exact diagonalization [34] is limited to small clusters, quantum Monte Carlo [35] suffers from the sign problem, and requires uncontrolled analytic continuations and the use of the max entropy approximation, and dynamical DMRG [36–38] is computationally very expensive.

For a decade or more, these limitations have in part prevented much progress in this area. However, the time-dependent DMRG method has the potential to tackle many open problems, due to its versatility and for being computationally less intensive. The time-dependent DMRG method can calculate time-dependent correlation functions with unprecedented accuracy, [16] providing a very good description of the entire spectrum of excitations with a single run, and with modest computational resources. This technique has been applied to a number of problems, such as the study of the spectral properties of a partially spin-polarized one-dimensional Hubbard chain [39], spin systems [40] and also in combination with imaginary time evolution to obtain the spectral properties of spin-incoherent Luttinger liquids [41], and spin systems [42]. In Fig. 5.10 we show the momentum resolved spectrum of a  $t - J$  chain to illustrate the remarkable capabilities of this algorithm, displaying all the distinctive features—spinon, and holon bands, shadow bands and continuum—with impressive resolution.

Imagine that we want to calculate a time-dependent correlation function that looks like

$$G(t) = \langle \psi | \hat{B}(t) \hat{A}(0) | \psi \rangle$$

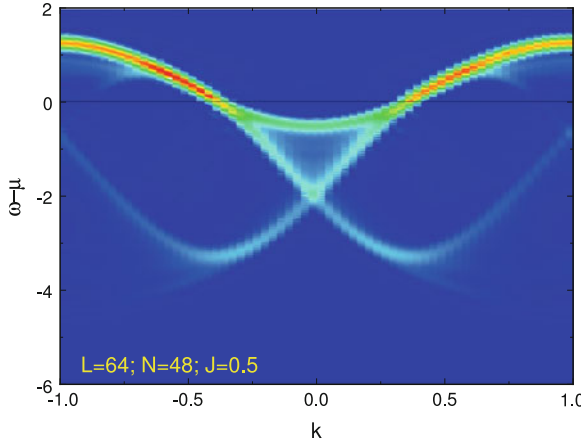


**Fig. 5.10** Momentum resolved spectrum of a  $t - J$  chain of  $L = 64$  sites, with  $J/t = 0.5$  and density  $n = 0.75$ , calculated with time-dependent DMRG, showing extremely well resolved spinon and holon bands, as well as shadow bands and continuum. Color density is proportional to the spectral weight, in linear scale

where  $|\psi\rangle$  is the ground state of the Hamiltonian  $\hat{H}$ . To obtain  $G(t)$  we follow the following steps:

- Using the conventional ground-state DMRG calculate  $|\psi\rangle$ . Turn off the Lanczos/Davidson diagonalization.
- During a half sweep, apply  $\hat{A}$  to  $|\psi\rangle$  to obtain  $|\phi\rangle = \hat{A}|\psi\rangle$ , targeting both  $|\psi\rangle$ , and  $|\phi\rangle$ .
- Start the time-evolution sweeps, evolving and targeting both states.
- Measure  $G(t)$  as  $\langle\psi(t)|\hat{B}|\phi(t)\rangle$ .

In the case presented here, since we have assumed that  $|\psi\rangle$  is the ground state, we can replace the time-evolution on this state by a multiplication by a phase  $\exp(-itE_0)$ .

If we are interested in obtaining the full momentum-resolved spectrum, we would want to calculate a correlator

$$G(x - x', t' - t) = i\langle\hat{O}(x', t')\hat{O}^\dagger(x, t)\rangle,$$

where  $O$  is an operator of interest. In practice we apply the operator  $\hat{A} = \hat{O}^\dagger(x = L/2)$  at the center site at time  $t = 0$  to obtain  $|\phi\rangle$ , and we apply  $\hat{B} = \hat{O}(x')$  on all the sites  $x'$  at every time step. This will yield the correlations in real space and time. Fourier transforming of these functions to momentum and frequency, will then yields the corresponding spectral weights as functions of momentum and frequency [12, 43]:

$$I(k, \omega) = \sum_n |\langle \psi_n | \hat{O}_k | \psi_0 \rangle|^2 \delta(\omega - E_n + E_0), \quad (5.29)$$

where  $E_0$  is the ground state energy, and the sum runs over all the eigenstates of the system, with energy  $E_n$ .

We typically study chains with an even number of sites. In order to recover the reflection symmetry, we may use  $G'(x) = 1/2(G(L/2 - x) + G(L/2 + x))$  instead of  $G(x)$ . In order to study small frequencies, or long time scales, one can perform an extrapolation in time using linear prediction methods, assuming that the form of the correlations can be deduced from some physics insight [43].

We should point out that the Fourier transform, as well as the linear momentum, are ill-defined in a system with open-boundary conditions. The scheme described here will work if the system is large enough such that we can ignore the effects of the boundaries, and we can assume that the system is translationally invariant near the center. We can also do it if we measure in short enough time ranges. No matter what we do, it is likely that the edges may introduce some perturbation in the form of Friedel oscillations. If the problem has an instability toward some sort of commensurate order, dimerization, spin or charge ordering, then the boundaries may lock the order and our artificial picture of translational invariance will be destroyed, making the application of the method nonviable.

## 5.9 The Enemy: Entanglement Growth

We have seen that the truncation error, or the number of states that we need to keep to control it, depends fundamentally on the entanglement entropy

$$S = S(t)$$

We need to understand its behavior if we want to learn how to fight it. In broad terms, the possible scenarios that we can find are:

- Global quench
- Local quench
- Periodic quench
- Adiabatic quench

When we apply such a perturbation to our system it no longer is in the ground state, but some superposition of excited states. Then, important questions arise, such as the relationship between thermalization and the properties of the system.

Without getting into that, we are going to try to characterize the basic behavior of the entanglement growth for each case. Although some specific demonstrations exist for particular cases, this behavior is believed to be very general and apply to a broad family of problems. Here, we shall use an intuitive picture to illustrate the main concepts without attempting formal proofs.

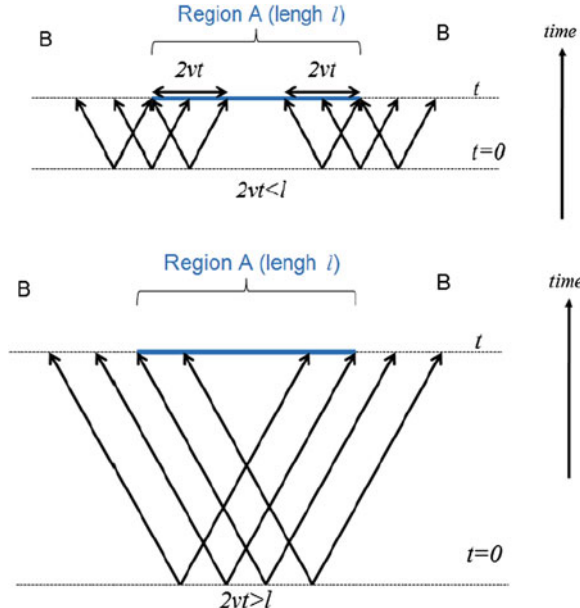


**Fig. 5.11** Illustration of the space-time evolution of the entanglement between two regions  $A$  and  $B$ , due to entangled quasi-particle pairs moving with velocity  $v$ . We assume that particles move along the light-cones, and we ignore scattering effects

### 5.9.1 Global Quench: Qualitative Picture

We are going to follow the reasoning described in Ref. [44]. Let us assume that at  $t = 0$  a perturbation is added to the Hamiltonian. This perturbation can be a change in the parameters (say  $J_z$  in the Heisenberg model), or an external magnetic field. This perturbation affects all the sites in the lattice, hence the “global” terminology. We are going to imagine that the perturbation acts as a source of quasi-particle excitations: we can picture quasi-particle pairs being emitted from all the sites on the lattice, which will be highly entangled (see Fig. 5.11). These excitations will propagate with a velocity  $v = dE/dk$ . Ignoring scattering effects, a particle produced at position  $x$ , will be at  $x + vt$  at time  $t$ . The wave-function at position  $x$  in the partition  $A$  in Fig. 5.11, will be entangled with that at position  $x'$  in partition  $B$ , if there is an entangled pair connecting both sites. The region covered by the entangled pairs will be of size  $2vt$ , and if we assume that the entanglement is proportional to the number of entangled pairs inside and outside of region  $A$ , then we obtain that the entropy grows linearly in time

$$S = S_0 + ct$$

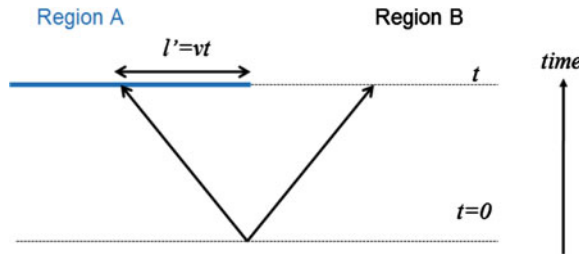


**Fig. 5.12** Illustration of the space-time evolution of the entanglement between *left* and *right* halves of a chain, due to entangled quasi-particle pairs created at the center of the system, moving with velocity  $v$  describing a light-cone

where  $c$  is some constant. When  $2vt = l$ , then the entanglement entropy saturates, and does no longer grow in time, reaching a constant value (see Fig. 5.11).

### 5.9.2 Local Quench: Qualitative Picture

To illustrate the case of a local quench, we are going to assume that the perturbation is introduced at the center of a one-dimensional chain. Following the previous considerations [45, 46], a quasiparticle pair will be created, entangling left and right halves of the chain, in a region of size  $vt$  on each side (see Fig. 5.12). In a critical system, we know that the entanglement is proportional to the log of the size of the entangled region:

$$S = S_0 + c \log(vt)$$

This corresponds to the worse case scenario. In a gaped system, the entropy will grow until the pair reaches a size comparable to the correlation length, and saturate at a constant value.

### 5.9.3 Computational Cost

After the above considerations, we find that the number of states needed for an efficient simulation grows as

- **Sudden global quench:**  $m \sim \exp(t)$ .
- **Sudden local quench:**  $m \sim t^\alpha$ .
- **Adiabatic quench:**  $m \sim \text{const.}$ , since we always remain close to the ground state.

## 5.10 Discussion

The time-dependent DMRG method has had a tremendous impact in several areas of physics, since it has enabled us to study of a whole new variety of problems: systems driven out of equilibrium by large biases or time-dependent perturbations, quantum quenches, quantum control, and non-equilibrium transport in nanodevices. It has also been very instrumental in the study of thermalization.

Since most experiments involve global quenches, research in the field has focused on this case, which is considerably more challenging –actually, it is the worse possible scenario. On the other hand, the calculation of correlations functions has the computational cost of a local quench, making the simulations extremely efficient with moderate computational resources.

The time-dependent DMRG has been used to study spectral functions at finite temperatures, by combining both evolution in real and imaginary time [41, 43]. Luckily this is a well behaved problem, in the sense that entanglement does not grow dramatically. Unfortunately, this does not occur in interesting problems such as transport and global quenches at finite-temperatures. It would be highly desirable to count with a method that could deal with these scenarios, which are currently out of reach.

Time evolution can also be used to find the ground-state of a system, and in fact this is the main idea behind the TEBD (time evolving block decimation) method [10, 11]. Techniques such as TEBD, and time-evolution with PEPS have the advantage that are easy to parallelize. However, if one counts with an efficient DMRG code that incorporates the wave-function prediction, it is relatively straightforward to implement time evolution with little effort.

## References

1. S.R. Manmana, A. Muramatsu, R.M. Noack, Time evolution of one-dimensional quantum many body systems, in *Contribution for the Conference Proceedings of the IX. Training Course in the Physics of Correlated Electron Systems and High-Tc Superconductors*, Vietri sul Mare (Salerno, Italy), October 2004. AIP Conference Proceedings, vol. 789, p. 269 (2005)
2. U. Schollwöck, J. Phys. Soc. Jpn. **74**(Supplement), 246 (2005)
3. U. Schollwöck, S.R. White, in *Effective Models for Low-dimensional Strongly Correlated Systems*, ed. by G.G. Batrouni, D. Poilblanc (AIP, Melville, 2006), p. 155
4. J.J. García-Ripoll, New J. Phys. **8**, 305 (2008)
5. A.E. Feiguin, in *Proceedings of the XV. Training Course in the Physics of Correlated Electron Systems*, Vietri sul Mare (Salerno, Italy), October 2010. AIP Conference Proceeding, vol. 1419, p. 5 (2011)
6. M.A. Cazalilla, J.B. Marston, Phys. Rev. Lett. **88**, 256403 (2002)
7. M.A. Cazalilla, J.B. Marston, Phys. Rev. Lett. **91**, 049702 (2003)
8. H.G. Luo, T. Xiang, X.Q. Wang, Phys. Rev. Lett. **91**, 049701 (2003)
9. H.G. Luo, T. Xiang, X.Q. Wang, Phys. Rev. Lett. **93**, 207204 (2004)
10. G. Vidal, Phys. Rev. Lett. **91**, 147902 (2003)
11. G. Vidal, Phys. Rev. Lett. **93**, 040502 (2004)
12. S.R. White, A.E. Feiguin, Phys. Rev. Lett. **93**, 076401 (2004)

13. A.J. Daley, C. Kollath, U. Schollwöck, G. Vidal, J. Stat. Mech.: Theor. Exp. P04005 (2004)
14. E. Forest, R.D. Ruth, Physica D **43**, 105 (1990)
15. I.P. Omelyan, I.M. Mryglod, R. Folk, Comput. Phys. Commun. **146**, 188 (2002)
16. A.E. Feiguin, S.R. White, Phys. Rev. B **72**, 20404 (2005)
17. A.E. Feiguin, S.R. White, Phys. Rev. B **72**, 20401 (2005)
18. F. Verstraete, J.J. Garcia-Ripoll, J.I. Cirac, Phys. Rev. Lett. **93**, 207204 (2004)
19. M. Zwolak, G. Vidal, Phys. Rev. Lett. **93**, 207205 (2004)
20. M. Suzuki, J. Phys. Soc. Jpn. **12**, 4483 (1985) and references therein
21. S.M. Barnett, P.L. Knight, Phys. Rev. A **38**, 1657 (1988)
22. S.M. Barnett, P.L. Knight, J. Opt. Soc. Am. B **2** 467 (1985)
23. F. Heidrich-Meisner, S.R. Manmana, M. Rigol, A. Muramatsu, A.E. Feiguin, E. Dagotto, Phys. Rev. A **80**, R041603 (2009)
24. F. Heidrich-Meisner, M. Rigol, A. Muramatsu, A.E. Feiguin, E. Dagotto, Phys. Rev. A **78**, 013620 (2008)
25. K.A. Al-Hassanieh, A.E. Feiguin, J.A. Riera, C.A. Busser, E. Dagotto, Phys. Rev. B **73**, 195304 (2006)
26. L.G.V. Dias da Silva, F. Heidrich-Meisner, A.E. Feiguin, C.A. Busser, G.B. Martins, E.V. Anda, E. Dagotto, Phys. Rev. B **78**, 195317 (2008)
27. A.E. Feiguin, P. Fendley, M.P.A. Fisher, C. Nayak, Phys. Rev. Lett. **101**, 236801 (2008)
28. F. Heidrich-Meisner, A.E. Feiguin, E. Dagotto, Phys. Rev. B **79**, 235336 (2009)
29. F. Heidrich-Meisner, I. Gonzalez, K.A. Al-Hassanieh, A.E. Feiguin, M.J. Rozenberg, E. Dagotto, Phys. Rev. B **82**, 205110 (2010)
30. P. Schmitteckert, Phys. Rev. B **70**, 121302(R) (2004)
31. E. Boulat, H. Saleur, P. Schmitteckert, Phys. Rev. Lett. **101**, 140601 (2008)
32. D. Bohr, P. Schmitteckert, P. Woelfle, Europhys. Lett. **73**, 246 (2006)
33. C. Kollath, U. Schollwöck, W. Zwerger, Phys. Rev. Lett. **95**, 176401 (2005)
34. Elbio Dagotto, Rev. Mod. Phys. **66**, 763 (1994)
35. J.E. Gubernatis, M. Jarrell, R.N. Silver, D.S. Sivia Phys. Rev. B **44**, 6011 (1991)
36. K. Hallberg, Phys. Rev. B **52**, R9827 (1995)
37. T.D. Kühner, S.R. White, Phys. Rev. B **60**, 335 (1999)
38. E. Jeckelmann, Phys. Rev. B **66**, 045114 (2002)
39. A.E. Feiguin, D.A. Huse, Phys. Rev. B **79**, 100507 (2009)
40. P. Bouillot, C. Kollath, A.M. Läuchli, M. Zvonarev, B. Thielemann, C. Rüegg, E. Orignac, R. Citro, M. Klanjsek, C. Berthier, M. Horvatić, T. Giamarchi, Phys. Rev. B **83**, 054407 (2011)
41. A.E. Feiguin, G. Fiete, Phys. Rev. B **81**, 075108 (2010)
42. T. Barthel, U. Schollwöck, S.R. White, Phys. Rev. B **79**, 245101 (2009)
43. S.R. White, I. Affleck, Phys. Rev. B **77**, 134437 (2008)
44. P. Calabrese, J. Cardy, J. Stat. Mech. P04010, (2005), ibid. Phys. Rev. Lett. **96**, 136801 (2006)
45. P. Calabrese, J. Cardy, J. Stat. Mech. P10004 (2007)
46. V. Eisler, I. Peschel, J. Stat. Mech. P06005, (2007)

# Chapter 6

## Loop Algorithm

Synge Todo

**Abstract** The loop algorithm for the world-line quantum Monte Carlo method on quantum lattice models is presented. After introducing the path integral representation that maps a quantum model to a classical one, we describe the continuous imaginary time limit, cluster algorithm, and the rejection free scheme, which are the major improvements on the quantum Monte Carlo technique during the last decades. By means of the loop algorithm, one can simulate various unfrustrated quantum lattice models of millions of sites at extremely low temperatures with absolute accuracy, being free from the critical and fine-mesh slowing down and the Suzuki-Trotter discretization error. We also discuss some technical aspects of the algorithm such as effective implementation and parallelization.

### 6.1 Introduction

The Markov chain Monte Carlo method is one of the most powerful tools in numerical investigation of phase transitions and critical phenomena in statistical and condensed matter physics [1, 2]. Especially, the world-line quantum Monte Carlo (QMC) method that is based on the quantum-classical mapping using the Suzuki-Trotter decomposition [3] has been developed over time, and successfully revealed diverse quantum phenomena, such as various types of long-range order, quantum liquids, valence bond crystals, quantum phase transitions, etc., in strongly correlated quantum lattice models [4].

One of the main advantages of the QMC method over other numerical ones, such as the exact diagonalization or the density matrix renormalization group method, is that it can treat rather large systems in any dimensions in *statistically exact* ways.

---

S. Todo (✉)

Institute for Solid State Physics, University of Tokyo, 7-1-26-R501 Port Island South,  
Kobe 650-0047, Japan  
e-mail: wistar@issp.u-tokyo.ac.jp

However, it is widely known that the conventional QMC method based on local updates of world-line configuration has the following serious problems: (i) It is usually nonergodic, or at least it is nontrivial to prove its ergodicity. (ii) As long as the local update is used, one can not change the topological numbers, such as the winding number of world lines in the real space and imaginary time directions. (iii) There is a systematic discretization error due to the Suzuki-Trotter decomposition. (iv) It suffers from the fine-mesh slowing down, as one increases the Trotter number to extrapolate the physical quantities into the continuous imaginary time limit. (v) It also suffers from the critical slowing down in the vicinity of the critical point. (vi) Offdiagonal correlations, e.g., Green's function, are not easy to measure. (vii) When the system incorporates long-range interactions, it becomes less efficient, i.e., the computational time for one Monte Carlo step grows in proportional to the system size squared. Note that the classical Monte Carlo methods also suffer from this problem. (viii) Finally, the notorious negative sign problem. It prevents us from simulating most of fermionic systems and frustrated spin/bosonic systems.

The loop algorithm invented in 1993 [5, 6] and its extensions solve (or at least reduce) most of the drawbacks in the conventional method [7, 8]. In the present chapter, we review the loop algorithm, emphasizing its key ingredients to success, the global cluster update and the rejection free scheme. In Sect. 6.2, also as an introduction for the following chapters in this book, the path integral representation of the lattice models and its continuous imaginary time limit are described in detail. In Sect. 6.3, the loop algorithm, a kind of cluster algorithm, is formulated based on the path integral representation. We discuss how the rejection free scheme for Monte Carlo trials is leveraged to construct an algorithm that works directly in the imaginary time continuum. Generalizations to a wider class of models as well as some technical aspects of the algorithm, such as implementation and parallelization, are also discussed. In Sect. 6.4, we explain how one can measure various physical quantities in the loop algorithm, which is common to the other QMC methods based on the path integral representation. In Sect. 6.5, we focus on the properties of loops themselves. We discuss the efficiency of the loop algorithm based on the pure loop representation, and present further extensions. Finally, conclusions and some remarks are presented in Section.

## 6.2 Path Integral Representation

### 6.2.1 Mapping to Classical System

The partition function  $Z$  and the expectation value of observable  $A$  of a lattice model, described by the Hamiltonian  $\mathcal{H}$ , are given by

$$Z = \text{Tr} \exp[-\beta \mathcal{H}] \text{ and} \quad (6.1)$$

$$\langle A \rangle = \frac{\text{Tr} A \exp[-\beta \mathcal{H}]}{\text{Tr} \exp[-\beta \mathcal{H}]}, \quad (6.2)$$

respectively, where  $\beta = 1/k_B T$  is the inverse temperature,  $T$  the temperature, and  $k_B$  the Boltzmann constant. One of the biggest problems in the statistical mechanics for quantum many-body systems is that the Hamiltonian as well as the observables are not c-numbers, but (typically) huge matrices.

In order to apply the Markov chain Monte Carlo technique and evaluate the expectation value (6.2), our first task is to represent (6.2) as

$$\langle A \rangle = \sum_c A(c) w(c) / \sum_c w(c) \quad (6.3)$$

with using c-numbers,  $w(c)$  and  $A(c)$ , where  $w(c)$  is the (unnormalized) weight of some “configuration”  $c$  and  $A(c)$  the “estimator” corresponding to the observable  $A$ . The mapping from the quantum system to the classical one is called “representation.” The standard way for achieving the quantum-classical mapping is the Suzuki-Trotter decomposition [3]. Before starting discussion on the many-body quantum lattice models, the main targets of the this book, we consider a simplest example to illustrate the most fundamental quantum-classical mapping and its continuous imaginary time limit.

### 6.2.2 Single Spin-1/2 in a Magnetic Field

The Hamiltonian of a single spin-1/2 in a magnetic field is given by

$$\mathcal{H} = \mathcal{H}_z + \mathcal{H}_x - C = -hS^z - \Gamma S^x - C, \quad (6.4)$$

where  $S^z$  and  $S^x$  are the spin-1/2 operators obeying the standard commutation relations, and the first and second terms represent the longitudinal and transverse external fields, respectively. We assume  $\Gamma \geq 0$  without loss of generality. A constant energy shift  $C$ , which does not affect physics, is introduced for later convenience. Although the Hamiltonian (6.4) can be easily diagonalized by choosing the quantum axis of the spin parallel to the external field, here we instead use a basis set in which  $S^z$  is diagonal ( $|\phi\rangle = |\uparrow\rangle$  or  $|\downarrow\rangle$  with  $S^z|\uparrow\rangle = \frac{1}{2}|\uparrow\rangle$  and  $S^z|\downarrow\rangle = -\frac{1}{2}|\downarrow\rangle$ ). In this basis, the Hamiltonian (6.4) is represented as the following matrix:

$$\mathcal{H} = \begin{pmatrix} -h/2 - C & -\Gamma/2 \\ -\Gamma/2 & h/2 - C \end{pmatrix}. \quad (6.5)$$

Although the continuous time path integral representation is commonly used in the modern world-line QMC, we first describe the discrete time formulation, where  $\beta$  is divided into  $M$  time steps,  $\Delta_\tau = \beta/M$ , as

$$Z = \text{Tr} \exp(-\beta \mathcal{H}) = \text{Tr} [\exp(-\Delta_\tau \mathcal{H})]^M = \text{Tr} T^M + O(\beta^2/M), \quad (6.6)$$

where we have introduced the quantum transfer matrix,  $T = 1 - \Delta_\tau \mathcal{H}$ . Since the Hamiltonian matrix  $\mathcal{H}$  will in general be hard to exponentiate, we have approximated the exponential factors,  $\exp(-\Delta_\tau \mathcal{H})$ , by a lowest order Taylor expansion. Inserting  $(M-1)$  sums over a complete set of states,  $\sum |\phi\rangle\langle\phi| = 1$ , between every  $T$ , we obtain

$$Z \approx \text{Tr} T^M = \sum_{\phi_M, \dots, \phi_1} \langle \phi_1 | T | \phi_M \rangle \langle \phi_M | T | \phi_{M-1} \rangle \cdots \langle \phi_2 | T | \phi_1 \rangle. \quad (6.7)$$

It is straightforward to confirm that the last expression is equivalent to the transfer matrix representation for the partition function of a one-dimensional ferromagnetic chain of classical Ising spins,  $\sigma_j = \pm 1$ , of length  $M$ :

$$-\beta_{\text{cl}} \mathcal{H}_{\text{cl}} = K_{\text{cl}} \sum_{j=1}^M \sigma_j \sigma_{j+1} + h_{\text{cl}} \sum_{j=1}^M \sigma_j \quad \text{with} \quad (6.8)$$

$$K_{\text{cl}} = -\frac{1}{2} \log(\Delta_\tau \Gamma/2) + \mathcal{O}(\Delta_\tau) \quad (6.9)$$

$$h_{\text{cl}} = \frac{1}{2} \Delta_\tau h + \mathcal{O}(\Delta_\tau^2) \quad (6.10)$$

besides a constant offset of the total energy.

### 6.2.3 Continuous Time Path Integral Representation

The discrete time expression (6.7) becomes exact in the continuous imaginary time limit  $\Delta_\tau \rightarrow 0$  (also known as Trotter limit). Although the number of spins in the mapped classical Ising chain increases as the imaginary time step is reduced, the average number of kinks (or domain walls) between ferromagnetic domains of parallel spins remains finite. This is due to the fact that the ferromagnetic coupling between two neighboring spins [Eq. (6.9)] becomes infinitely strong. Indeed, the average number of kinks in the continuous imaginary time limit is related to the energy and exactly estimated as  $(\beta \Gamma^2/2H) \tanh(\beta H/2)$  with  $H = \sqrt{h^2 + \Gamma^2}$  (see also Sect. 6.4.4). Therefore, it is more efficient to store only the position of kinks and the spin state of each domain, instead of storing spin state at every infinitesimal time step. Hereafter, we use a real number, *imaginary time*  $\tau$ , normalized between 0 and  $\beta$ , in order to specify the position of kinks along the imaginary time axis (Fig. 6.1).

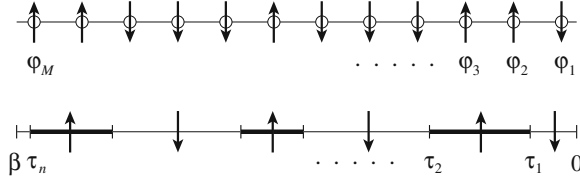


**Fig. 6.1** Discrete (*upper*) and continuous (*lower*) time path integral representations of single spin-1/2. In the latter, the position of kinks is specified by  $\tau$ , which takes a real number between 0 and  $\beta$

The path integral representation of the partition function in the continuous imaginary time limit can be derived more directly in terms of the time-dependent perturbation expansion [9]. Let us suppose that  $\mathcal{H}_0 = \mathcal{H}_z - C$  as the non-perturbative Hamiltonian and  $V = \mathcal{H}_x$  as perturbation. We define an operator  $U(\tau)$  that satisfies

$$e^{-\tau \mathcal{H}_0} U(\tau) = e^{-\tau(\mathcal{H}_0 + V)}. \quad (6.11)$$

Differentiating the both sides with respect to  $\tau$  and introducing the interaction representation,  $V(\tau) = e^{\tau \mathcal{H}_0} V e^{-\tau \mathcal{H}_0}$ , we obtain the following differential equation:

$$\frac{dU(\tau)}{d\tau} = -V(\tau)U(\tau) \quad (6.12)$$

with the initial condition  $U(0) = 1$ , or the integral equation:

$$U(\tau) = 1 - \int_0^\tau d\tau' V(\tau')U(\tau'). \quad (6.13)$$

By inserting the last equation into its own r.h.s. successively, we arrive at the following continuous time path integral representation:

$$\begin{aligned} Z &= \text{Tr}[e^{-\beta \mathcal{H}_0} U(\beta)] \\ &= \text{Tr}\left[e^{-\beta \mathcal{H}_0} \left(1 - \int_0^\beta d\tau_1 V(\tau_1) + \int_0^\beta d\tau_2 \int_0^{\tau_2} d\tau_1 V(\tau_2)V(\tau_1) - \dots\right)\right] \\ &= \text{Tr}\left[\sum_{n=0}^{\infty} (-1)^n \int_0^\beta d\tau_n \int_0^{\tau_n} d\tau_{n-1} \dots \int_0^{\tau_2} d\tau_1 e^{-(\beta-\tau_n)\mathcal{H}_0} V e^{-(\tau_n-\tau_{n-1})\mathcal{H}_0} \right. \\ &\quad \times V \dots V e^{-\tau_1 \mathcal{H}_0} \Big] \quad (6.14) \\ &= \sum_{n=0}^{\infty} (-1)^n \sum_{\phi_n, \dots, \phi_1} \int_0^\beta d\tau_n \int_0^{\tau_n} d\tau_{n-1} \dots \int_0^{\tau_2} d\tau_1 \langle \phi_1 | e^{-(\beta-\tau_n)\mathcal{H}_0} | \phi_1 \rangle \langle \phi_1 | V | \phi_n \rangle \\ &\quad \times \langle \phi_n | e^{-(\tau_n-\tau_{n-1})\mathcal{H}_0} | \phi_n \rangle \langle \phi_n | V | \phi_{n-1} \rangle \dots \langle \phi_2 | V | \phi_1 \rangle \langle \phi_1 | e^{-\tau_1 \mathcal{H}_0} | \phi_1 \rangle. \end{aligned}$$

Note that given  $\phi_1$ , the rest of spin states  $(\phi_2, \dots, \phi_n)$  are determined uniquely in the present single spin model, since the operator  $V$  always *flips* the spin from up to down, or *vice versa*. By introducing  $e^{-\tau E_0(\phi)} = \langle \phi | e^{-\tau \mathcal{H}_0} | \phi \rangle$  and using  $\langle \phi | V | \phi' \rangle = -\Gamma/2$ , each term in the last expression is further simplified as

$$\begin{aligned} w(c) d\tau_n \cdots d\tau_1 \\ = \left(\frac{\Gamma}{2}\right)^n e^{-(\beta-\tau_n)E_0(\phi_1)} e^{-(\tau_n-\tau_{n-1})E_0(\phi_n)} \cdots e^{-\tau_1 E_0(\phi_1)} d\tau_n \cdots d\tau_1, \end{aligned} \quad (6.15)$$

where  $c$  denotes a “configuration”  $(\tau_1, \dots, \tau_n, \phi_1, \dots, \phi_n)$ . Note that the expansion order  $n$  gives the number of kinks, and  $e^{-\tau E_0(\phi)} = e^{\pm \tau h/2 + \tau C}$  is the continuous imaginary time limit of the Boltzmann weight of a ferromagnetic domain of length  $\tau/\Delta_\tau$ , that is,  $e^{\pm \tau h/2 + \tau C} = \lim_{\Delta_\tau \rightarrow 0} (1 \pm \Delta_\tau h/2 + \Delta_\tau C)^{\tau/\Delta_\tau}$ .

Another useful continuous time path integral representation can be obtained by splitting the Hamiltonian into  $\mathcal{H}_0 = 0$  and  $V = \mathcal{H}$ . The weight of configuration  $c$  is then written as

$$\begin{aligned} w(c) d\tau_m \cdots d\tau_1 \\ = (-1)^m \langle \phi_1 | \mathcal{H} | \phi_m \rangle \langle \phi_m | \mathcal{H} | \phi_{m-1} \rangle \cdots \langle \phi_2 | \mathcal{H} | \phi_1 \rangle d\tau_m \cdots d\tau_1. \end{aligned} \quad (6.16)$$

Note that in addition to  $\phi_1$  one has to specify  $\phi_2, \dots, \phi_m$  explicitly in this representation, since the matrix  $\mathcal{H}$  is *branching*; it has two nonzero elements in each row or column. Also, the expansion order  $m$  is not necessarily equal to the number of kinks. This representation is used to formulate the directed loop algorithm in the continuous time path integral representation, while the worm algorithm (Sect. 10.3) is based on the former representation (6.15). As for the loop algorithm, however, either representation can be used as the starting point, and indeed the resulting algorithm is identical except for estimators of some physical quantities (Sects. 6.3.4 and 6.4.4).

Since the weight (6.16) does not depend on  $\tau_1, \dots, \tau_m$ , one can further simplify the expression by integrating it over the imaginary times:

$$Z = \sum_{m=0}^{\infty} \frac{(-\beta)^m}{m!} \sum_{\phi_m, \dots, \phi_1} \langle \phi_1 | \mathcal{H} | \phi_m \rangle \langle \phi_m | \mathcal{H} | \phi_{m-1} \rangle \cdots \langle \phi_2 | \mathcal{H} | \phi_1 \rangle. \quad (6.17)$$

This expression can be obtained more directly through the high-temperature series of  $\exp(-\beta \mathcal{H})$ . This is referred to as the (variable length) stochastic series expansion (SSE) representation [10], which will be explained in detail in Chap. 7. In what follows, we explain the cluster algorithms mainly in the path integral representation. We emphasize that the algorithms, however, can also be formulated in almost the same way in the SSE representation.

### 6.2.4 World-Line Representation of XXZ Spin Model

The continuous time path integral representation is straightforwardly applied to the many-body quantum lattice problems, such as quantum spin models, bosonic/fermionic Hubbard models,  $t$ - $J$  models, etc. Here, as a concrete example, we consider the spin-1/2 XXZ model:

$$\mathcal{H} = \sum_{\langle j,k \rangle} [J_z S_j^z S_k^z + \frac{J_{xy}}{2} (S_j^+ S_k^- + S_j^- S_k^+)], \quad (6.18)$$

where  $S_j^\pm = S_j^x \pm i S_j^y$  are the spin-1/2 ladder operators, and  $S_j^\alpha$  ( $\alpha = x, y, z$ ) the  $\alpha$ -component of spin operator at site  $j$ . The summation is taken over  $N_b$  bonds (pairs of neighbor sites) on a  $d$ -dimensional lattice of  $N$  sites. For  $J_z, J_{xy} > 0$ , the spin interaction is antiferromagnetic and neighboring spins prefer to align in antiparallel with one another. For  $J_z, J_{xy} < 0$ , on the other hand, the spin interaction is ferromagnetic. This Hamiltonian commutes with  $S_{\text{total}}^z = \sum_j S_j^z$ , and as a result  $S_{\text{total}}^z$  is conserved during the real/imaginary time evolution.

Now, we derive the path integral representation for the XXZ Hamiltonian (6.18) according to the formulation presented in the last subsection. The Hamiltonian is a  $2^N \times 2^N$  sparse matrix. We choose a basis set in which  $S_j^z$  ( $j = 1, \dots, N$ ) are all diagonal, i.e.,  $|\phi\rangle = |\phi^1, \dots, \phi^N\rangle = |\phi\rangle_1 \otimes \dots \otimes |\phi\rangle_N$ , where  $|\phi\rangle_j = |\uparrow\rangle_j$  or  $|\downarrow\rangle_j$  with  $S_j^z |\uparrow\rangle_j = \frac{1}{2} |\uparrow\rangle_j$  and  $S_j^z |\downarrow\rangle_j = -\frac{1}{2} |\downarrow\rangle_j$ . In terms of this basis set, we define the quantum transfer matrix as  $T = 1 - \Delta_\tau \mathcal{H}$ . For the continuous time representation, on the other hand, we split the Hamiltonian into a non-perturbative diagonal part  $\mathcal{H}_0$  and the remaining perturbation  $V$ . As discussed in Sect. 6.2.3, there are two typical ways of splitting the Hamiltonian. The first choice (splitting A) is

$$\mathcal{H}_0 = \sum_{\langle j,k \rangle} J_z S_j^z S_k^z \quad \text{and} \quad V = \sum_{\langle j,k \rangle} \frac{J_{xy}}{2} (S_j^+ S_k^- + S_j^- S_k^+), \quad (6.19)$$

where  $V$  is purely offdiagonal and has no diagonal elements. Another choice (splitting B) is

$$\mathcal{H}_0 = 0 \quad \text{and} \quad V = \mathcal{H}, \quad (6.20)$$

where all the terms are treated as perturbation.

The expression of the discrete and continuous time path integral representations for the present XXZ model are identical to Eqs. (6.7) and (6.14), respectively. In the present case, a “classical” configuration consists of  $M$  or  $n$  slices of  $d$ -dimensional array of  $N$  spins, which is tied up in a  $(d+1)$ -dimensional lattice. Furthermore, there are strong constraints for configurations to be allowed, i.e., to have nonzero weights, due to the sparseness of the matrices  $T$  or  $V$ ; a matrix element of  $T$  (or  $V$  in splitting B) is nonzero, iff  $|\phi\rangle$  and  $|\phi'\rangle$  are identical,  $|\phi\rangle = |\phi'\rangle$ , or they are identical

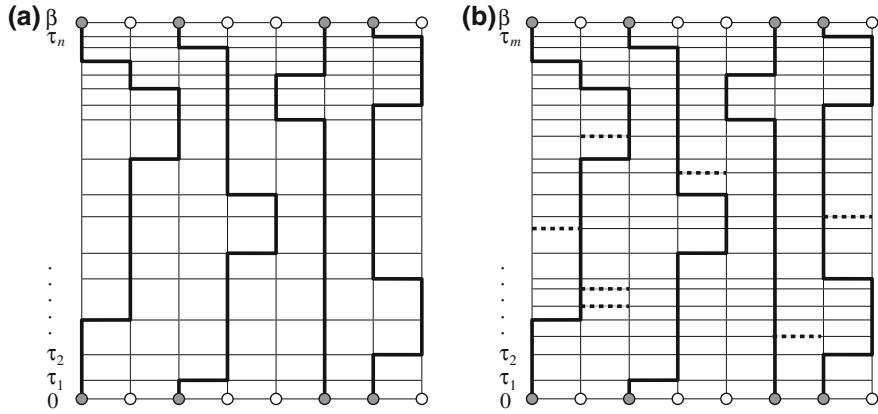


**Fig. 6.2** Examples of continuous time world-line configurations for the spin-1/2 XXZ chain for the case of operator splitting A (left) and B (right). The horizontal and vertical axes are the real space and imaginary time directions, respectively. The *vertical bold (thin) lines* denote up (down) spins. In the case of operator splitting A, a world line jumps at the imaginary time at which perturbation operators are inserted, while in the latter the operators can be either diagonal (*dotted horizontal lines*) or offdiagonal (*bold horizontal lines*)

except two spins that are swapped with one another, e.g.,  $|\phi\rangle = |\cdots \uparrow \cdots \downarrow \cdots\rangle$ ,  $|\phi'\rangle = |\cdots \downarrow \cdots \uparrow \cdots\rangle$ . These constraints for configurations can be depicted in terms of *world lines*; if one connects up spins by a line in the imaginary time direction, these lines form a set of closed loops. Examples of world-line configurations in the continuous time representation are shown in Fig. 6.2.

The offdiagonal elements of  $T$  are of  $O(\Delta_\tau)$ , while the diagonal ones are of order unity. Thus, the total number of *jumps* of world lines remains finite in the continuous imaginary time limit, and it is enough to store only the space-time position of jumps, as exactly the same as in the single spin case.

### 6.2.5 Negative Sign Problem

So far, we have assumed that all nonzero matrix elements of  $V$  are *negative*, which ensures that the overall weight of path integral configuration [Eqs. (6.15) or (6.16)] is always *positive*. If some of matrix elements are positive, however,  $w(c)$  would become negative, and it can not be considered as a weight for the Monte Carlo sampling any more.

As for the diagonal elements, this can be easily rectified by subtracting a large enough constant, i.e.,  $C$  in Eq. (6.4), making all diagonal elements negative, and hence the weights positive. The offdiagonal elements of  $V$ , on the other hand, always need to be negative, where a simple subtraction of a constant will not help. In the single spin-1/2 case [Eq. (6.4)], for example, the transverse field pointing to the negative  $x$ -axis

yields negative offdiagonal weights. Fortunately, this causes no problem since the number of offdiagonal weights is always even due to the periodic boundary condition in the imaginary time direction. Or, one can remove negative signs explicitly by rotating the spin by 180° around the spin quantization axis. The negative sign problem in the quantum antiferromagnet ( $J_{xy} > 0$ ) on a bipartite lattice can also be solved by a similar gauge transformation, rotating all the spins on one of two sublattices by 180° around the spin quantization axis, without changing the commutation relations. On non-bipartite lattices, such as the triangular or kagomé lattices, however, this trick will not work and these frustrated quantum magnets suffer from the negative sign problem.

When negative signs can not be removed by a simple gauge transformation, one has to run the simulation of a system, called “absolute system,” whose weight function is the absolute value of the original one, and take into account the sign of original weights through the reweighting technique:

$$\langle A \rangle = \frac{\sum_c A(c)w(c)}{\sum_c w(c)} = \frac{\sum_c A(c)S(c)|w(c)|}{\sum_c |w(c)|} \frac{\sum_c |w(c)|}{\sum_c S(c)|w(c)|} = \frac{\langle AS \rangle_+}{\langle S \rangle_+}, \quad (6.21)$$

where  $S(c) = \text{sgn}[w(c)]$  is the sign of  $w(c)$ , and  $\langle \cdot \rangle_+ = \sum_c |\cdot| / \sum_c |w(c)|$  denotes the Monte Carlo average evaluated in the absolute system.

The denominator at the rightmost side in Eq.(6.21) can be evaluated as a free energy difference:

$$\langle S \rangle_+ = \exp[-\beta(F - F_+)] \simeq \exp[-\beta N(f - f_+)], \quad (6.22)$$

where we approximate the free energy of the original (absolute) system,  $F$  ( $F_+$ ), by using the free energy density in the thermodynamic limit,  $f$  ( $f_+$ ). The relative error of the average sign is then estimated as

$$\epsilon = \frac{1}{\sqrt{N_{\text{MCS}}}} \frac{\sqrt{\langle S^2 \rangle_+ - \langle S \rangle_+^2}}{\langle S \rangle_+} \simeq \frac{\exp[\beta N \Delta f]}{\sqrt{N_{\text{MCS}}}}, \quad (6.23)$$

where  $N_{\text{MCS}}$  is the number of Monte Carlo steps and  $\Delta f = f - f_+ > 0$ . Thus, as the inverse temperature or the system size increase, the relative error grows exponentially and one needs exponentially long time to achieve a predetermined statistical accuracy.

## 6.3 Loop Algorithm

### 6.3.1 Markov Chain Monte Carlo

By the path integral representation, a quantum system is mapped to a classical system, to which one can apply a Monte Carlo method for classical lattice models. In the Markov chain Monte Carlo for a stationary distribution, the *balance condition* and the *ergodicity* must be imposed; the former ensures the invariance of a target distribution, while the latter does the convergence to the unique equilibrium distribution [11]. Although the *detailed balance condition* is usually placed as a sufficient condition for the total balance, an interesting optimization algorithm minimizing the rejection rate without the detailed balance has caught the attention these days [12].

For the single spin in a magnetic field, which is mapped to the classical Ising chain [Eq. (6.8)], single spin updates based on the standard Metropolis algorithm [13] or the heat-bath algorithm [14] can be used in a straightforward way. The single spin update, however, suffers from the slowing down (i.e., the acceptance rate of single spin flip gets lower and lower) at weak transverse field  $\beta\Gamma \ll 1$  (or  $K_{\text{cl}} \gg 1$ ). The same problem also occurs when the number of time slices  $M$  is increased, since the nearest neighbor interaction (6.9) becomes infinitely strong. Moreover, the computational time required to sweep the whole lattice diverges in proportional to  $M$ .

For the XXZ model, Monte Carlo update of world lines is more difficult; any attempts to flip a single spin at a space-time point will always be rejected due to the conservation law of the total  $S^z$ . In the following, we see that the nonlocal cluster update together with the rejection free scheme [15] can solve the slowing down problem as well as the computational time problem.

### 6.3.2 Swendsen–Wang Algorithm

The Swendsen–Wang algorithm [16] has been proposed for the classical Ising model in 1987. The main idea behind this algorithm is flipping clusters of spins instead of individual spins. As an example, let us consider a ferromagnetic Ising chain [Eq. (6.8)] with  $M = 10$  (Fig. 6.3). In the meantime, we consider the case where the magnetic field is absent ( $h_{\text{cl}} = 0$  or  $h = 0$ ). In the present example, the initial spin configuration  $c$  has two kinks between the ferromagnetic domains, and thus the Boltzmann weight is given by  $w(c) = e^{6K_{\text{cl}}}$ . Then, we label each bond as “connected” or “disconnected” according to the following rules: (i) Each satisfied bond is connected with probability  $(1 - e^{-2K_{\text{cl}}})$  or disconnected otherwise. (ii) Each unsatisfied bond (kink) is always disconnected. In Fig. 6.3, we have six spin clusters. Finally, we flip each cluster with probability 1/2, which results a new configuration  $c'$  with weight  $w(c') = e^{2K_{\text{cl}}}$ . Taking into account that there are six clusters in  $g$ , the transition probability from  $c$  to  $c'$  via  $g$  and that of its reverse process are given by  $T(c \rightarrow g \rightarrow c') = (1 - e^{-2K_{\text{cl}}})^4(e^{-2K_{\text{cl}}})^4/2^6$  and  $T(c' \rightarrow g \rightarrow c) = (1 - e^{-2K_{\text{cl}}})^4(e^{-2K_{\text{cl}}})^2/2^6$ ,

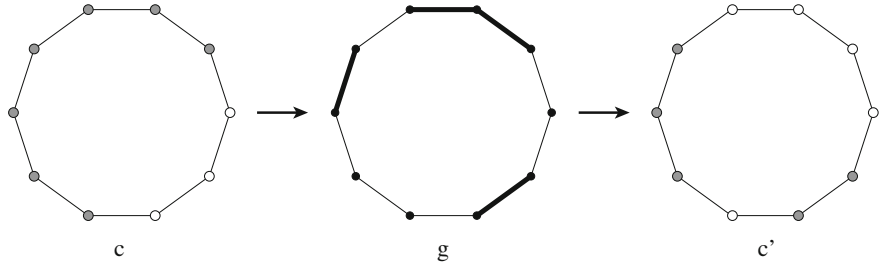


**Fig. 6.3** Example of Swendsen-Wang cluster update for a classical Ising chain of 10 sites. The *gray* (open) circles in  $c$  and  $c'$  denote up (down) spins. The *bold* (thin) lines in  $g$  denote the “connected” (“disconnected”) state

respectively. It is clear that the detailed balance condition  $w(c)T(c \rightarrow g \rightarrow c') = w(c')T(c' \rightarrow g \rightarrow c)$  is fulfilled in this specific case.

The Swendsen-Wang algorithm for the ferromagnetic model is ergodic. This is ensured by the fact that from any graph configuration, one can generate all up state with a finite probability. It is also easy to prove that the transition probability between two arbitrary configurations is always finite.

### 6.3.3 Kandel–Domany Framework

The Swendsen-Wang algorithm can be formulated in terms of so-called Kandel-Domany framework [17, 18]. In this framework, the original phase space is extended by introducing an auxiliary variable, called *graph*  $g$ , that represents a set of constraints on spin configurations.

In general, the weight of configuration  $c$  is a product of local weights:

$$w(c) = \prod_u w_u(c), \quad (6.24)$$

where  $u$  denotes “units” on which local weights are defined. For each unit, we introduce new weights  $w_u(c, g_u)$  that satisfy  $w_u(c, g_u) \geq 0$  for any  $c$  and  $g_u$ , and  $w_u(c) = \sum_{g_u} w_u(c, g_u)$  for any  $c$ . We further assume that  $w_u(c, g_u)$  does not depend on  $c$  whenever it is nonzero, i.e.,  $w_g(c, g_u)$  can be factored as

$$w_g(c, g_u) = \Delta_u(c, g_u) v_u(g_u) \quad \text{for any } c \text{ and } g_u \quad (6.25)$$

by introducing a binary function  $\Delta_u(c, g_u) = 0$  or  $1$ . We refer to  $\Delta_u(c, g_u)$  as *compatibility function*. The partition function can then be expressed as

$$Z = \sum_c \sum_g \prod_u w_u(c, g_u) = \sum_c \sum_g \prod_u \Delta_u(c, g_u) v_u(g_u), \quad (6.26)$$

which is called the generalized Fortuin-Kasteleyn representation [17, 18].

For the classical Ising model, it is natural to choose a bond as a unit. The local weight of bond  $u$  that connects sites  $j$  and  $k$  is decomposed as

$$w_u(c) = \exp(K_{\text{cl}} \sigma_j \sigma_k) = \sum_{g_u=0,1} (2\delta_{g_u,0} \delta_{\sigma_j, \sigma_k} \sinh K_{\text{cl}} + \delta_{g_u,1} e^{-K_{\text{cl}}}), \quad (6.27)$$

where  $\delta_{a,b}$  is the Kronecker delta. Defining

$$\Delta_u((\sigma_j, \sigma_k), g_u) = \begin{cases} \delta_{\sigma_j, \sigma_k} & \text{for } g_u = 0 \\ 1 & \text{for } g_u = 1, \text{ and} \end{cases} \quad (6.28)$$

$$v_u(g_u) = \begin{cases} 2 \sinh K_{\text{cl}} & \text{for } g_u = 0 \\ e^{-K_{\text{cl}}} & \text{for } g_u = 1, \end{cases} \quad (6.29)$$

one obtains the generalized Fortuin-Kasteleyn representation for the Ising model. In this representation,  $g_u = 0$  means that only parallel spin configurations ( $\uparrow\uparrow$  or  $\downarrow\downarrow$ ) are allowed on unit  $u$ . On the other hand, if  $g_u = 1$ , the neighboring spins can be either in parallel or in antiparallel. The local graphs ( $g_u = 0$  and 1) are thus represented symbolically as  and , respectively.

Once a generalized Fortuin-Kasteleyn representation (6.26) of the partition function has been obtained, the cluster algorithm follows immediately. Given a spin configuration  $c$  and graph configuration  $g$ , we choose a new graph configuration  $g'$  stochastically. If we employ the heat-bath-type update, the transition probability is given by

$$P_g((c, g) \rightarrow (c, g')) = P_g(g' | c) = \frac{w(c, g')}{w(c)} = \prod_u \frac{w_u(c, g'_u)}{w_u(c)}, \quad (6.30)$$

where  $w(c, g) = \prod_u w_u(c, g_u)$ . This update is called *labeling* or *breakup*. Since the probability is expressed as a product over the units, the assignment of graph variable  $g'_u$  to each unit can be performed independently. Next, we update the spin configuration by flipping clusters. Again using the heat-bath-type probability we obtain

$$P_c((c, g') \rightarrow (c', g')) = P_c(c' | g') = \frac{w(c', g')}{\sum_{c''} w(c'', g')} = \frac{\Delta(c', g')}{\sum_{c''} \Delta(c'', g')}, \quad (6.31)$$

where  $\Delta(c, g) = \prod_u \Delta_u(c, g_u)$ . Since  $\Delta(c, g)$  takes 0 or 1, the denominator of the rightmost side in Eq.(6.31) is nothing but the number of spin configurations

compatible to graph  $g'$ ; in the *flipping* process, a spin configuration will be chosen uniformly at random from those compatible to graph  $g'$ .

The detailed balance of the whole procedure is manifested by the fact that the expression for the amount of stochastic flow from  $c$  to  $c'$ :

$$w(c)P(c \rightarrow c') = w(c) \sum_{g'} P_c(c'|g') P_g(g'|c) = \sum_{g'} \left[ \frac{w(c, g')w(c', g')}{\sum_{c''} w(c'', g')} \right], \quad (6.32)$$

is symmetric about  $c$  and  $c'$ . Furthermore, the probability density function  $w(c, g)/Z$  is invariant by the labeling process as well as by the flipping process, i.e.,  $w(c, g)/Z$  is the equilibrium distribution in the extended phase space.

### 6.3.4 Continuous Imaginary Time Limit and Rejection Free Scheme

The graph weights and labeling probability can be obtained more directly in the quantum case. First, one should notice that the compatibility function (6.28) is represented as matrix elements of quantum operators as

$$\Delta_u((\phi, \phi'), g_u) = \begin{cases} \delta_{\phi, \phi'} = \langle \phi | 1 | \phi' \rangle & \text{for } g_u = 0 \\ 1 = \langle \phi | (1 + 2S^x) | \phi' \rangle & \text{for } g_u = 1. \end{cases} \quad (6.33)$$

Since the quantum transfer matrix can be decomposed into

$$T = 1 - \Delta_\tau \mathcal{H} = (1 - \Delta_\tau \Gamma/2) + (\Delta_\tau \Gamma/2)(1 + 2S^x), \quad (6.34)$$

one easily finds

$$v_u(g_u) = \begin{cases} 1 - \Delta_\tau \Gamma/2 & \text{for } g_u = 0 \\ \Delta_\tau \Gamma/2 & \text{for } g_u = 1, \end{cases} \quad (6.35)$$

which reproduces the labeling probability obtained in the last subsection.

In Sect. 6.2.3, we have seen that the average number of kinks remains finite even in the continuous imaginary time limit. It is also true for the number of cuts ( $g_u = 1$ ). Since  $v_u(1)$  is of  $O(\Delta_\tau)$ , while  $v_u(0)$  is of order unity, the average number of cuts will also stay finite in the continuous imaginary time limit. To be more precise, let us consider a uniform segment of up spins of unit length. The number of bonds in this segment is  $\Delta_\tau^{-1} = M/\beta$ , and it takes time of  $O(M)$  if one visits every bond one by one. However, since the acceptance ratio of inserting a cut becomes infinitesimal, almost all trials will be in vain. In order to sample such extremely rare events, a

*rejection free* scheme [15] will be extremely efficient. In this approach, instead of making trials one after another, we try to identify directly the next bond where the trial will be accepted; the probability of having no cuts in the imaginary time duration of length  $\tau$  is given by the exponential distribution with mean  $2/\Gamma$ :

$$f(\tau) = 1 - (1 - \Delta_\tau \Gamma/2)^{M\tau/\beta} \simeq 1 - \exp(-\Gamma\tau/2) \quad \text{for } M \gg \beta. \quad (6.36)$$

In other words, cuts will be inserted randomly with uniform density  $\Gamma/2$ . In practice, random numbers obeying the exponential distribution [Eq. (6.36)] are generated by using the inverse function method [19]. Thus, the Swendsen-Wang cluster algorithm for the single quantum spin problem can be implemented directly in the imaginary time continuum. One Monte Carlo step is described as follows: (i)  $\tau \leftarrow 0$ . (ii) Draw a random number  $r$  uniformly distributed in the interval  $(0, 1]$ , and  $\tau \leftarrow \tau - (2/\Gamma) \log r$ . (iii) If  $\tau > \beta$ , then go to step iv, otherwise insert a cut at imaginary time  $\tau$  and go to step ii. (iv) Assign a cut to each kink. (v) Identify clusters, flip spins on each cluster with probability  $1/2$ , and measure all the physical quantities of interest. This algorithm is free from the discretization error (apart from the accuracy of the floating point numbers in the processor). Furthermore, the labeling procedure (steps ii–iii) will terminate in a finite number of iterations  $\Gamma\beta/2$  on average.

If one adopt the second choice in splitting the Hamiltonian, i.e.,  $\mathcal{H}_0 = 0$  and  $V = \mathcal{H}$ , the matrix element (including the minus sign) is decomposed as

$$-\langle \phi | \mathcal{H} | \phi' \rangle d\tau = (C - \frac{\Gamma}{2}) \langle \phi | 1 | \phi' \rangle d\tau + \frac{\Gamma}{2} \langle \phi | (1 + 2S^x) | \phi' \rangle d\tau, \quad (6.37)$$

and thus we have  $v_u(0) = (C - \Gamma/2) d\tau$  and  $v_u(1) = \Gamma d\tau/2$ . Here,  $C$  should be equal to or greater than  $\Gamma/2$  to avoid negative signs. Thus, a cut will be assigned to the place where  $\mathcal{H}$  is located with probability  $v_u(1)/[v_u(0) + v_u(1)] = \Gamma/2C$ . Especially, if  $C$  is chosen as  $\Gamma/2$ , the labeling becomes *deterministic*, i.e., a cut is assigned with probability 1. However, this process is *not* ergodic, since the position of operators does not change. We should introduce another process that changes the imaginary time position as well as the number of operators.

In order to recover the ergodicity, we introduce so called *diagonal update*, inserting an operator at a certain imaginary time position and its reverse process, removing a diagonal operator. Since the weight of a diagonal operator,  $C d\tau$ , is infinitesimal, one can remove a diagonal operator with probability 1, while the insertion should be done according to the constant *density*  $C$ . Combining these diagonal updates with the above labeling probability, the overall density for inserting a cut is  $C \times (\Gamma/2C) = \Gamma/2$  irrespective of the choice for  $C$ , which is identical to the labeling density in the previous algorithm. As a result, the simulation code also becomes identical in these two representations, though the estimator for some observables may have a different form (see Sect. 6.4.4).

### 6.3.5 Loop Algorithm for XXZ Model

In the case of the XXZ model (6.18), one should notice that the difference between two arbitrary world-line configurations always forms a set of closed loops (see e.g., Fig. 6.4a, d) due to the conservation of total  $S^z$ . Thus, any allowed updates of world-line configuration should also be a combination of loop flips.

Let us consider a local Hamiltonian that connects sites  $j$  and  $k$ :

$$\mathcal{H}_{j,k} = J_z S_j^z S_k^z + \frac{J_{xy}}{2} (S_j^+ S_k^- + S_j^- S_k^+). \quad (6.38)$$

We assume that the local gauge transformation has already been performed in such a way that  $J_{xy}$  becomes negative. This local Hamiltonian is represented as a  $4 \times 4$  matrix in terms of the  $S^z$  basis set. The quantum transfer matrix  $T = 1 - \Delta_\tau \mathcal{H}$  has only six nonzero elements among  $2^4 = 16$ . In order to represent the conservation law symbolically, we introduce five local graphs as listed in Table 6.1, where the bold (dotted) lines can connect two space-time points iff the spins are parallel (antiparallel). For example, a configuration of crossing world lines  $[(|\phi\rangle, |\phi'\rangle) = (|\uparrow\downarrow\rangle, |\downarrow\uparrow\rangle)$  or  $(|\downarrow\uparrow\rangle, |\uparrow\downarrow\rangle)]$  is compatible with graphs 1 and 3 but not with 0, 2, and 4. Note that the graphs also represent possible updates that do not break the conservation law.

The compatibility between graphs and spin configurations is represented in the operator form as shown in the third column in Table 6.1. Now we have a matrix equation for the graph weights:

$$T = \sum_{g_u=0}^4 \Delta_u(g_u) v_u(g_u). \quad (6.39)$$

Since there are three independent equations for five unknown variables, solution is not unique. In Table 6.2, we list the standard solutions, where the number of graphs with nonzero weight is minimized, for each regime in the parameter space. Note that we need such solutions that the weights for graphs 1–4 are of  $O(\Delta_\tau)$  or zero while

**Table 6.1** Local graphs for XXZ model and corresponding compatibility matrices in the operator form

$g_u$	Graph	$\Delta_u(g_u)$
0		1
1		$\frac{1}{2} + 2S_1^z S_2^z + S_1^+ S_2^- + S_1^- S_2^+$
2		$\frac{1}{2} + 2S_1^z S_2^z$
3		$\frac{1}{2} - 2S_1^z S_2^z + S_1^+ S_2^- + S_1^- S_2^+$
4		$\frac{1}{2} - 2S_1^z S_2^z$

The horizontal and vertical directions of graphs represent the real space and the imaginary time, respectively. The bold and dotted lines in the graphs connect parallel and antiparallel spins, respectively

**Table 6.2** Standard solutions of the weight equation (6.39) for each regime in the parameter space; antiferromagnetic Ising (AFI), antiferromagnetic Heisenberg (AFH), XY, ferromagnetic Heisenberg (FH), and ferromagnetic Ising (FI)

	$v_u(1)/\Delta_\tau$	$v_u(2)/\Delta_\tau$	$v_u(3)/\Delta_\tau$	$v_u(4)/\Delta_\tau$
AFI ( $J_z > -J_{xy}$ )	0	0	$-\frac{1}{2} J_{xy}$	$\frac{1}{2} (J_z + J_{xy})$
AFH ( $J_z = -J_{xy}$ )	0	0	$\frac{1}{2} J_z$	0
XY ( $ J_z  < -J_{xy}$ )	$-\frac{1}{4} (J_z + J_{xy})$	0	$\frac{1}{4} (J_z - J_{xy})$	0
FH ( $J_z = J_{xy}$ )	$-\frac{1}{2} J_z$	0	0	0
FI ( $J_z < J_{xy}$ )	$-\frac{1}{2} J_{xy}$	$\frac{1}{2} (J_{xy} - J_z)$	0	0

Note that  $J_{xy} < 0$  is assumed. The weight of graph 0 is  $v_u(0) = 1 + O(\Delta_\tau)$  in all the cases

the weight for the trivial graph 0 is of order unity, in order that the algorithm will have a well defined continuous imaginary time limit.

Let us move onto a real problem, a spin model of  $N$  sites and  $N_b$  bonds. For this system, we introduce  $4N_b$  nontrivial graphs. Each graph has one of nontrivial local graphs 1–4 on a specific bond and vertical thick lines on other sites. Each compatibility operator  $\Delta_u(g_u)$  is thus a direct product of a bond compatibility operator (Table 6.1) acting on a bond and identity operators acting on other sites. The weight of each graph is given in Table 6.2 using the coupling constants of the corresponding bond. In addition to the nontrivial graphs, we introduce one trivial graph with weight of order unity representing the identity compatibility operator that only has vertical thick lines.

For example, if we choose splitting A for the continuous time path integral representation, one Monte Carlo step for the uniform Heisenberg antiferromagnet ( $J_z = |J_{xy}| = J$ ) is described as follows:

- (i)  $\tau \leftarrow 0$  and  $s \leftarrow (\phi_1^1, \phi_1^2, \dots, \phi_1^N)$ .
- (ii) Draw a random number  $r$  uniformly distributed in  $(0, 1]$ , and  $\tau' \leftarrow \tau - \rho^{-1} \log r$  with  $\rho = N_b J / 2$ .
- (iii) If there are offdiagonal operators between  $\tau$  and  $\tau'$ , assign graph 3 to each of them with probability 1, and update  $s$  by flipping spins accordingly.
- (iv) If  $\tau' > \beta$ , go to step vii.
- (v) Choose a bond uniformly at random. If graph 3 is compatible with the spin configuration at time  $\tau'$ , i.e., the spin states on both sides of the bond is antiparallel with each other, insert the graph 3 at time  $\tau'$ .
- (vi)  $\tau \leftarrow \tau'$  and go to step ii.
- (vii) Identify loops, flip them independently with probability 1/2, and update spin configurations at  $\tau = 0$  and series of operators accordingly.
- (viii) Perform measurement of physical quantities.

An example of one Monte Carlo step is illustrated in Fig. 6.4. For the ferromagnetic Heisenberg case ( $J_z = -|J_{xy}| = -J$ ), instead of graph 3, graph 1 is assigned to offdiagonal operators at step iii, and at step v, graph 1 is assigned iff spins are in parallel. For a non-uniform XXZ model, the total trial density of nontrivial operators  $\rho$  has to be replaced by a summation over  $4N_b$  graphs:

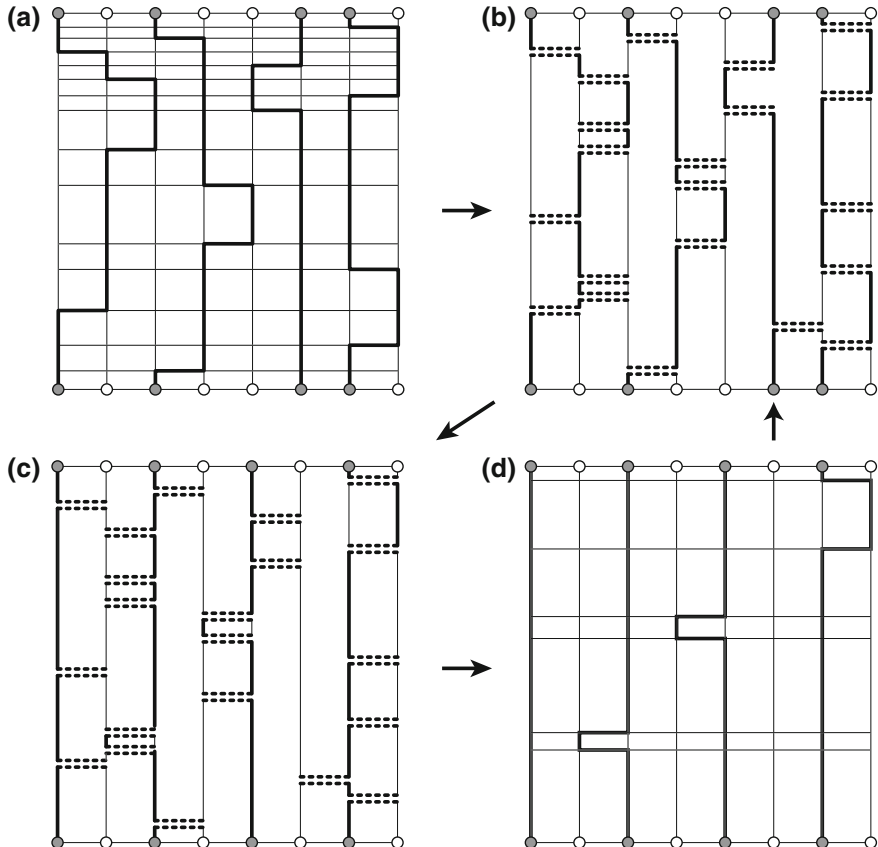


**Fig. 6.4** Example of loop update for spin-1/2 antiferromagnetic Heisenberg chain. World-line configuration (a) is updated to (d) via loop configuration (b) and (c). The horizontal and vertical axes are the real space and imaginary time directions, respectively. From (b) to (c), the loop involving the spin indicated by the upward arrow in (b) is flipped

$$\rho d\tau = \sum_{g_u \neq 0} v_u(g_u). \quad (6.40)$$

At step iii, graph 1 or 3 is assigned according to the probability  $v_u(1)/(v_u(1) + v_u(3))$  or  $v_u(3)/(v_u(1) + v_u(3))$ , respectively. Also, at step v, a graph is chosen among  $4N_b$  graphs according to their weights  $\{v_u(g)\}$  and will be inserted iff the graph is compatible with the spin state at  $\tau'$ . The remaining procedure does not change at all.

The ergodicity of the loop algorithm can be proved straightforwardly when  $v_u(1)$  is positive, as one always has a non-vanishing probability for constructing a graph that is identical to a given world-line configuration, and from such a graph configuration one can reach the ferromagnetically ordered reference state with a finite probability, or *vice versa*. That is, two arbitrary world-line configurations are connected with

each other within two Monte Carlo steps. For antiferromagnetic models on bipartite lattices, on the other hand, one can apply the same argument by choosing a classical Néel ordered state as a reference state. For frustrated antiferromagnets, the loop algorithm with a standard weight solution is not ergodic. Although the QMC on such models generally suffers from the severe negative sign problem, one can still ensure the ergodicity by adopting a non-standard solution with non-vanishing weight for graph 1 of the weight Eq. (6.39). We note that such a ergodic solution always exists for any combination of  $J_z$  and  $J_{xy}$ .

It is interesting to see that the present loop algorithm involves the Swendsen-Wang algorithm (Sect. 6.3.2) as a special limit. In the ferromagnetic Ising limit ( $J_z/|J_{xy}| \rightarrow -\infty$ ), the weight of offdiagonal operators vanishes and we have only straight world lines along the imaginary time axis. The weight of nontrivial graphs also vanishes except for graph 2 (the *freezing* graph) that locks in the neighboring spins parallel. Since the freezing graphs are inserted randomly with uniform density  $|J_z|/2$  between parallel world lines of length  $\beta$ , the probability for having at least one freezing graph on a bond is given by

$$\sum_{k=1}^{\infty} f(k; \beta|J_z|/2) = 1 - f(0; \beta|J_z|/2) = 1 - e^{-\beta|J_z|/2}, \quad (6.41)$$

where  $f(k; \lambda)$  is the probability mass function of the Poisson distribution with mean  $\lambda$ . This probability is identical to that for assigning a connected graph in the standard Swendsen-Wang algorithm (except for factor 4 in the exponent that comes from the difference in the normalization of spin length, i.e.,  $\sigma = \pm 1$  for the classical Ising model, while  $S^z = \pm 1/2$  for its quantum counterpart). Although one Monte Carlo step of this “quantum cluster algorithm” for the classical Ising model costs  $\beta$ -times more than the standard algorithm, it is still useful for formulating the order- $N$  method for long-range interacting classical spin models [20] as well as the Swendsen-Wang algorithm for higher-spin Ising models [21] (see also Sect. 6.3.7).

### 6.3.6 Implementation and Technical Aspects

In the practical implementation of the loop algorithm, we work directly in the imaginary time continuum. In order to represent world-line configurations as well as graph configurations, we store the spin state at  $\tau = 0$ , and space-time position and type of perturbation terms or nontrivial graphs. By inserting nontrivial graphs, the space-time is decomposed into many small fragments (vertical lines in Fig. 6.4b). Although each loop is a sequence of such fragments, it is more convenient to represent each loop by a rooted tree of fragments instead of a sequential list. During the loop identification procedure, trees are merged to build up loops by using the *union-find algorithm* [22]. It is proved that using two techniques, called *union-by-weight* and *path compression*, any sequence of  $m$  union and find operations on  $n$  objects can

be done in time of  $O(n\alpha(m, n))$ , where  $\alpha(m, n)$  is the inverse Ackermann function that grows extremely slow with increasing  $m$  and  $n$ . In any practical applications,  $\alpha(m, n)$  is less than 5 and one may regard it as a constant. Thus, the cost for one Monte Carlo step is virtually proportional to the space-time volume.

Since the autocorrelation time of the present loop algorithm is ideally short in many relevant models, the best parallelization strategy is running independent Markov chains with using different random number sequences on different processing nodes, as long as the memory requirement is not very strong. If the space-time volume exceeds  $\sim 10^7$ , however, the world-line configuration no longer fits in the memory of one node, and parallelization of each Markov chain becomes unavoidable.

In general, parallelization of the loop algorithm is far from trivial, since a number of global objects, loops, are built up and flipped in every Monte Carlo step. In order to parallelize the loop algorithm, first we have to determine how the information of world-line configuration is distributed to several processing nodes. In the continuous time loop algorithm, it is most natural to divide the  $(d + 1)$ -dimensional space-time into slices of same ‘thickness’ in the imaginary time direction. Each node stores only the spin directions at the bottom together with space-time position of world-line jumps in its own imaginary time window. The labeling procedure can be trivially parallelized and executed independently, since it requires local information only. On the other hand, identifying loops is nontrivial, since loops are global objects. The global union-find procedure is performed in two steps: (i) Each node identifies loops in its own imaginary time window. In this step, a number of loops are closed in the time window. However, there remain a number of unclosed loops, since they cross the imaginary time boundaries between the nodes. Then, (ii) these unclosed loops are merged gradually by using a binary-tree or butterfly algorithm [23, 24]. The theoretical efficiency of the present parallelized loop algorithm is evaluated as

$$P(N_p) = \frac{\beta N}{N_p} / \left[ \frac{\beta N}{N_p} + c N \log N_p \right] \simeq 1 - c \frac{N_p}{\beta} \log N_p \quad (6.42)$$

for  $\beta \gg N_p$ , where  $N_p$  is the number of processing nodes and  $c$  a system-dependent constant. Together with further techniques, such as thread parallelization in the real space directions, it has been shown that at least at low temperatures the parallelized loop algorithm scales fairly well up to about  $10^5$  processing cores on the state-of-the-art massively parallel supercomputers [25].

### 6.3.7 Generalizations

The present loop algorithm can be extended to more general interactions. In the XYZ model, the total  $S^z$  is not conserved due to the presence of pair creation  $S_j^+ S_k^+$  or annihilation  $S_j^- S_k^-$  operators. The loop algorithm, however, remains unchanged except that we have to introduce additional graphs, e.g., connecting parallel spins horizon-

tally, or antiparallel spins diagonally [5, 26]. The transverse external field,  $-\Gamma S_j^x$ , also breaks the total  $S^z$  conservation. In this case, as already seen in Sect. 6.2.3, we introduce site graphs that cut a world line in the imaginary time direction in addition to the bond graphs [27].

On the other hand, in the presence of the longitudinal external field,  $-hS_j^z$ , the partition function does not have a corresponding generalized Fortuin-Kasteleyn representation (6.26) any more, as a world-line configuration and its reversal share the same compatibility function  $\Delta(c, g)$ , but may have different weights with each other. One of the standard ways to incorporate the time-reversal asymmetry is ignoring the external field while assigning graphs, and then taking it into account separately in the loop flip procedure. Another way is using the so-called *ghost spin* technique [16]; we introduce a fictitious spin  $S_0^z$  that is fixed into *up* state ( $S_0^z = +1/2$ ), and represent the Zeeman term as an Ising interaction with this fictitious spin, i.e.,  $-2hS_0^zS_j^z$ . By this way, the longitudinal external field is included naturally in the labeling procedure. In flipping loops, spin direction on some loops will not be changed if the loop is *connected* with the fictitious spin. It is straightforward to show that these two approaches are equivalent as long as the longitudinal field is cooperative with the spin-spin interaction. If the external field competes against the spin-spin interaction, however, the algorithm quickly becomes inefficient as the temperature decreases [28] (see also Sect. 6.5.2).

The loop algorithm formulated originally for the SU(2) spin-1/2 case can also be extended to models with different symmetry and/or higher-spin representation. In the spin model with SU( $N$ ) symmetry, the local Hilbert space is  $N$ -dimensional. The algorithm remains unchanged except that the state of each spin is represented by a Potts variable that takes 1, 2, ..., or  $N$ . For the ferromagnetic SU( $N$ ) Heisenberg model, the Hamiltonian can be expressed by using the diagonal graph ( $g_u = 1$ ), while for the antiferromagnetic model the horizontal graph ( $g_u = 3$ ) is used instead [29]. As for the spin models in higher-spin representation ( $S \geq 1$ ), the generalized Fortuin-Kasteleyn representation is obtained by splitting each spin- $S$  into  $2S$  spin-1/2 *subspins*. As a result, the original model of  $N$  sites and  $N_b$  bonds is transformed into a spin-1/2 model of  $2SN$  sites and  $4S^2N_b$  bonds. In addition, we introduce a projection operator to each site in order to project onto the highest total spin states and recover the original dimension of the Hilbert space. Since the projection operator commutes with the transformed Hamiltonian, it is enough to insert a projection operator only at  $\tau = 0$  [30, 31].

The four-body interactions, such as the ring exchange,  $S_j^+S_k^-S_l^+S_m^- + S_j^-S_k^+S_l^-S_m^+$ , or the dimer-dimer interaction,  $(S_j \cdot S_k)(S_l \cdot S_m)$ , can also be treated by the loop algorithm. Since four-body terms introduce pair hopping of spins at the same imaginary time, we introduce the graphs with eight legs, each of which is a combination of two local graphs for the ordinary two-body interactions [32]. The biquadratic interaction in higher-spin models,  $(S_j \cdot S_k)^2$ , is also converted into the four-body interaction in the subspin representation [33].

Finally, we mention how the system with long-range interactions can be dealt with efficiently in the loop algorithm. In this case, as the total number of bonds grows as  $N_b \sim N^2$ , the computational time for one Monte Carlo step is also proportional

to  $N^2$  if one sweeps bonds sequentially. In the loop algorithm, however, this can be solved by exchanging the loops over real space and imaginary time [20]. Indeed, this has already been implemented in the pseudo code presented in p. 445; first, we note that although the total number of nontrivial graphs is proportional to  $N^2$ , the total density of nontrivial operators,  $\rho$  [Eq. (6.40)], is still of  $O(N)$  in unfrustrated models. (Otherwise, the system will not have a well defined thermodynamic limit.) Second, we modify step v in the pseudo code so that we choose a graph at random not uniformly, but with probability proportional to the weight of each graph. This can be done in a *constant* time by using Walker's method of aliases [34]. By combining these two techniques, one can update the world-line configuration in time proportional to the system size  $N$ . Non-uniform systems, e.g., the (unfrustrated) random bond Heisenberg model, can also be simulated efficiently by using the same technique. The present order- $N$  algorithm is extended to the long-range interacting classical Ising model by taking the strong anisotropic limit [20].

## 6.4 Measurements

### 6.4.1 Diagonal Operators and Correlation Functions

In order to evaluate the thermal average of some quantum operator  $A$  by the world-line QMC, we have to find the corresponding estimator  $A(c)$  [Eq. (6.3)]. If  $A$  is diagonal in the present  $S^z$  basis set,  $A(c)$  is simply given by

$$A(c) = A(\tau = 0) = \langle \phi_1 | A | \phi_1 \rangle. \quad (6.43)$$

For example, the  $z$ -component of the magnetization  $\langle \sum_j S_j^z \rangle$  and spin correlation function  $\langle S_j^z S_k^z \rangle$  belong to this class, and their estimators are given by  $\sum_j \phi_1^j$  and  $\phi_1^j \phi_1^k$ , respectively. The static structure factor at wavevector  $\mathbf{q}$ :

$$S_{A,B}(\mathbf{q}) = \frac{1}{N} \sum_{j,k} \langle A_j B_k \rangle e^{i\mathbf{q} \cdot (\mathbf{r}_j - \mathbf{r}_k)}, \quad (6.44)$$

which is the Fourier transform of correlation function, is also measured in a similar way. In practice, the evaluation of the double summation in Eq. (6.44) is performed in time of  $O(N)$  as

$$S_{A,B}(\mathbf{q}) = \frac{1}{N} \left\langle \left[ \sum_j A_j e^{-i\mathbf{q} \cdot \mathbf{r}_j} \right]^* \left[ \sum_j B_j e^{-i\mathbf{q} \cdot \mathbf{r}_j} \right] \right\rangle. \quad (6.45)$$

We note that as the system is imaginary time translational invariant, one may improve the statistics by taking an average over the imaginary time:

$$A(c) = \frac{1}{\beta} \int_0^\beta \langle \phi(\tau) | A | \phi(\tau) \rangle d\tau = \frac{1}{\beta} \sum_{\ell=1}^n (\tau_\ell - \tau_{\ell-1}) \langle \phi_\ell | A | \phi_\ell \rangle \quad (6.46)$$

instead of measuring only at  $\tau = 0$ . Here  $\tau_0 = \tau_n - \beta$ . Compared with the original zero-time estimator (6.43), the error bar of the  $\tau$ -averaged estimator (6.46) is expected to become smaller by a factor of  $\sqrt{\max(\beta\Delta, 1)}$ , where  $\Delta$  is the first excitation gap of the system. That is, if the inverse temperature  $\beta$  is larger than the correlation length in the imaginary time direction, i.e., the inverse gap  $\Delta^{-1}$ , the system is effectively divided into  $\beta\Delta$  statistically independent samples. When  $\beta$  is comparable with or smaller than  $\Delta^{-1}$ , on the other hand, spin configurations at different time slices correlate strongly, and thus the effective number of statistically independent samples will not increase even with the  $\tau$ -averaged estimator.

#### 6.4.2 Susceptibilities and Dynamical Structure Factors

A susceptibility  $\chi_{A,B}$  of diagonal operators  $A$  and  $B$  is defined as

$$\chi_{A,B} = \left. \frac{\partial \langle A \rangle}{\partial h_B} \right|_{h_B=0}, \quad (6.47)$$

where a field term  $(-h_B B)$  has been added to the Hamiltonian. By taking the derivative, we obtain the estimator for the susceptibility as an integration of the dynamical correlation functions:

$$\chi_{A,B} = \int_0^\beta d\tau \langle A(0)B(\tau) \rangle = \frac{1}{\beta} \int_0^\beta d\tau_1 \int_0^\beta d\tau_2 \langle A(\tau_1)B(\tau_2) \rangle, \quad (6.48)$$

where we use the imaginary time translational invariance. More generally, the estimator for the dynamical spin structure factor at wavevector  $\mathbf{q}$  and Matsubara frequency  $\omega_m = 2m\pi/\beta$  ( $m = 0, 1, 2, \dots$ ) is given by

$$\chi(\mathbf{q}, \omega_m) = \frac{1}{N\beta} \left\langle \left| \sum_j \int_0^\beta d\tau S_j^z(\tau) e^{-i(\omega_m \tau + \mathbf{q} \cdot \mathbf{r}_j)} \right|^2 \right\rangle. \quad (6.49)$$

In practice, one may use the following expression for  $\omega_m \neq 0$ :

$$\sum_j \int_0^\beta d\tau S_j^z(\tau) e^{-i(\omega_m \tau + \mathbf{q} \cdot \mathbf{r}_j)} = \frac{i}{\omega_m} \sum_{\ell=1}^n [e^{-i\omega_m \tau_\ell} - e^{-i\omega_m \tau_{\ell-1}}] \sum_j \phi_\ell^j e^{-i\mathbf{q} \cdot \mathbf{r}_j} \quad (6.50)$$

to avoid numerical integration over the imaginary time.

### 6.4.3 Correlation Length and Excitation Gap

The correlation function  $C_{A,B}(r)$  of diagonal operators  $A$  and  $B$  is in general a linear combination of exponentially damping functions:

$$C_{A,B}(r) = \sum_m C_{A,B}^{(m)} \cosh \left[ \frac{r - L/2}{\xi_{A,B}^{(m)}} \right], \quad (6.51)$$

where  $L$  is the linear extent of the lattice. The correlation length  $\xi_{A,B}$  is given by the largest one among  $\{\xi_{A,B}^{(m)}\}$ . In order to estimate  $\xi_{A,B}^{(m)}$  from the correlation function, we need to perform the inverse Laplace transform that is known to be extremely unstable to statistical noises in the raw data. Instead of the direct inverse Laplace transform or the method of least squares on the correlation function, the maximum entropy method [35] is widely used to obtain the spectral information. However, its accuracy depends greatly on the assumption made on the spectral function.

On the other hand, if we are interested in only the longest mode  $\xi_{A,B}$ , a series of the moment estimators are the method of choice [31, 36]. If the correlation function is single mode, its Fourier transform, i.e. the structure factor, is given by

$$S_{A,B}(\mathbf{Q} + \mathbf{q}) = \frac{S_{A,B}(\mathbf{Q})}{1 + |\mathbf{q}|^2 \xi_{A,B}^2}, \quad (6.52)$$

and thus the correlation length is estimated as

$$\xi_{A,B} = \frac{1}{|\mathbf{q}|} \sqrt{\frac{S_{A,B}(\mathbf{Q})}{S_{A,B}(\mathbf{Q} + \mathbf{q})} - 1}, \quad (6.53)$$

where  $\mathbf{Q}$  is the wavevector of dominant correlation, and  $\mathbf{q}$  is in practical chosen as the smallest possible wavevector on the reciprocal lattice, e.g.,  $\mathbf{q} = (2\pi/L, 0, 0)$ .

The excitation gap, which is the inverse of correlation length in the imaginary time direction, can also be estimated by the moment method for the dynamical spin structure factor:

$$\Delta^{-1} = \frac{1}{\omega} \sqrt{\frac{S_{A,B}(\mathbf{Q}, 0)}{S_{A,B}(\mathbf{Q}, \omega)} - 1}, \quad (6.54)$$

where we choose  $\omega = \omega_1 = 2\pi/\beta$ , the lowest Matsubara frequency.

Although these lowest order moment estimators have relatively large corrections of  $O(\xi_{A,B}^{(\ell)}/\xi_{A,B})$ , one can construct higher order estimators that have smaller corrections in a systematic way [31, 37]. Furthermore, if the operators  $A$  and  $B$  are chosen carefully enough, not only the smallest gap (the shortest correlation length), but also larger gaps (longer correlation lengths) are extracted very accurately. By using the series of lowest gaps, it becomes even possible to perform the *level spectroscopy analysis* [38], e.g., in order to determine the Kosterlitz-Thouless transition point, where the conventional finite-size scaling method will not work.

#### 6.4.4 Energy and Specific Heat

In Sect. 6.2.4, we have introduced two different splittings of the Hamiltonian into the non-perturbative and perturbation terms. Although for most of observables their estimators are identical in both representations, this is not the case for the energy as well as for the specific heat. The total energy is given by a derivative of the free energy with respect to the inverse temperature:

$$E = \langle \mathcal{H} \rangle = -\frac{\partial}{\partial \beta} \ln Z = -\frac{1}{Z} \frac{\partial Z}{\partial \beta}. \quad (6.55)$$

For splitting A, by differentiating the discrete time path integral representation of the partition function [Eq. (6.7)], we obtain

$$\frac{\partial Z}{\partial \beta} = \sum_{\phi_M, \dots, \phi_1} \sum_{i=1}^M f(\phi_{i+1}, \phi_i) \langle \phi_1 | T | \phi_M \rangle \langle \phi_M | T | \phi_{M-1} \rangle \cdots \langle \phi_2 | T | \phi_1 \rangle, \quad (6.56)$$

where

$$f(\phi, \phi') = \frac{\langle \phi | (-\mathcal{H}/M) | \phi' \rangle}{\langle \phi | (1 - \beta \mathcal{H}/M) | \phi' \rangle} = \begin{cases} -\mathcal{H}_0/M & \text{if } \phi = \phi' \\ 1/\beta & \text{if } \phi \neq \phi'. \end{cases} \quad (6.57)$$

Thus the total energy is expressed as

$$E = \frac{1}{\beta} \left\langle \int_0^\beta d\tau \mathcal{H}_0(\tau) \right\rangle - \frac{\langle n \rangle}{\beta} \quad (6.58)$$

using the number of offdiagonal operators  $n$ . The specific heat requires an additional derivative with respect to  $\beta$ :

$$\begin{aligned} C &= \frac{1}{N} \frac{\partial E}{\partial T} = -\frac{\beta^2}{N} \frac{\partial E}{\partial \beta} \\ &= \frac{1}{N} \left\langle \left( \int_0^\beta d\tau \mathcal{H}_0(\tau) - n \right)^2 \right\rangle - \frac{1}{N} \left\langle \int_0^\beta d\tau \mathcal{H}_0(\tau) - n \right\rangle^2 - \frac{\langle n \rangle}{N}, \end{aligned} \quad (6.59)$$

where the third term originates from the derivative of  $f(\phi, \phi')$  [Eq. (6.57)].

For splitting B, on the other hand,  $T$  is replaced by  $(-\Delta_\tau \mathcal{H})$  or 1 depending on whether an operator is present or not at each time slice. The former gives  $(-1/\beta)$ , while the latter does not contribute. The estimators in this case are simply obtained by setting  $\mathcal{H}_0 = 0$  and replacing  $n$  by  $m$ , the total number of diagonal and offdiagonal operators, in Eqs. (6.58) and (6.59):

$$E = -\frac{\langle m \rangle}{\beta} \quad \text{and} \quad C = \frac{1}{N} (\langle m^2 \rangle - \langle m \rangle^2 - \langle m \rangle). \quad (6.60)$$

Note that if one has subtracted a constant from the Hamiltonian to avoid negative signs (Sect. 6.2.5), the energy (6.60) will also shift by the same amount.

Generally, the statistical error of the specific heat diverges at low temperatures. This is caused by a serious cancellation between the three terms. The number of operators increases in proportional to the inverse temperature and its distribution obeys the Poisson distribution, where the variance is equal to its own mean. This results vanishing specific heat in the mean with diverging error bar.

#### 6.4.5 Spin Stiffness

The spin stiffness or helicity modulus (or the superfluid density in the bosonic language) is defined as the second derivative of the free energy with respect to twist angle  $\theta$  of the spins:

$$\rho_s = \frac{1}{L^2} \frac{\partial^2 F(\theta)}{\partial \theta^2} \Big|_{\theta=0} = -\frac{1}{L^2 \beta} \left[ \frac{1}{Z} \left( \frac{\partial^2 Z(\theta)}{\partial \theta^2} \right) - \left( \frac{1}{Z} \frac{\partial Z(\theta)}{\partial \theta} \right)^2 \right]_{\theta=0}. \quad (6.61)$$

We consider a one-dimensional nearest neighbor chain for the simplicity. In Eq. (6.61),  $Z(\theta)$  is the partition function of the *twisted* Hamiltonian in which the offdiagonal terms ( $S_j^+ S_{j+1}^- + S_j^- S_{j+1}^+$ ) are replaced by ( $e^{-i\theta} S_j^+ S_{j+1}^- + e^{+i\theta} S_j^- S_{j+1}^+$ ). The first derivative is evaluated as

$$\frac{1}{Z} \frac{\partial Z(\theta)}{\partial \theta} \Big|_{\theta=0} = \left\langle \int_0^\beta d\tau j_s(\tau) \right\rangle = i \langle \mathcal{N}_+ - \mathcal{N}_- \rangle, \quad (6.62)$$

where  $j_s = -i \sum_j (S_j^+ S_{j+1}^- - S_j^- S_{j+1}^+)$  is the spin current operator, and  $\mathcal{N}_+$  ( $\mathcal{N}_-$ ) are the number of right (left) jumps of up spins in the world-line configuration. One finds that the first derivative vanishes due to the symmetry. The second derivative is given by a canonical correlation of spin current operators. Thus, the spin stiffness is expressed in terms of  $\mathcal{N}_+$  and  $\mathcal{N}_-$  as

$$\rho_s = \frac{1}{\beta L^2} \langle (\mathcal{N}_+ - \mathcal{N}_-)^2 \rangle = \frac{1}{\beta} \langle W^2 \rangle, \quad (6.63)$$

where we use the fact that the difference between  $\mathcal{N}_+$  and  $\mathcal{N}_-$  is equal to the winding number of the world lines,  $W$ , multiplied by the system length  $L$ . Note that for the Heisenberg model we have to take into account the contribution from the  $z$ -component of spins and we have an extra factor  $3/2$ .

## 6.5 Loop Representation

### 6.5.1 Improved Estimators

In the loop algorithm, graph configuration  $g$  also carries a wealth of information on the physical properties of the system. In this section, we investigate the structure and properties of loops in detail and discuss the source of efficiency of the loop algorithm. To start with we present a neat trick, called *improved estimator*, that can be used in conjunction with the loop algorithm to reduce the error of measurements sometimes by orders of magnitude.

The idea behind the improved estimator is to measure the physical quantities not only for the world-line configuration, but also for all possible configurations generated from the current loop configuration [39]. In principle, given a standard estimator  $A(c)$ , the thermal average of the observable  $A$  can always be expressed as an average of  $A(g)$  over the graph variable  $g$ , where

$$A(g) = \sum_c A(c) \Delta(c, g) / \sum_c \Delta(c, g). \quad (6.64)$$

That is,  $A(g)$  is a simple average of  $A(c)$  over  $2^{N_c(g)}$  compatible world-line configurations, where  $N_c(g)$  is the number of loops. It is straightforward to show that  $A(g)$  is an unbiased estimator for  $A$ :

$$\begin{aligned} \langle A(g) \rangle_g &= \sum_g A(g) w(g) / Z = \sum_g \left[ \frac{\sum_c A(c) \Delta(c, g)}{\sum_c \Delta(c, g)} \right] \left[ \sum_c \Delta(c, g) v(g) \right] / Z \\ &= \sum_c A(c) \left[ \sum_g \Delta(c, g) v(g) \right] / Z = \langle A(c) \rangle_c. \end{aligned} \quad (6.65)$$

In general, it is quite expensive to calculate  $A(g)$  for a given  $g$ , since it is a summation over  $2^{N_c(g)}$  different world-line configurations. Fortunately, for many relevant observables, the evaluation of  $A(g)$  can be simplified drastically by the symmetries inherent to the original physical system. For example, the improved estimator for  $S_j^z$  is extremely simple, i.e.,  $S_j^z(g) = 0$ . This is because in the average over  $2^{N_c(g)}$  configurations,  $S_j^z = 1/2$  and  $-1/2$  appear  $2^{N_c(g)-1}$  times each and they are canceled out exactly.

Constructing the improved estimator for correlation functions is also straightforward. If two space-time points  $(j, \tau)$  and  $(k, \tau')$  belong to different loops, positive and negative contributions to the  $z$ -component of correlation function cancel out exactly due to the time-reversal symmetry. On the other hand, if the two space-time points belong to a same loop, contribution remains finite: In the ferromagnetic case ( $J_z \leq -|J_{xy}|$ ), all spins on a loop have a same direction, and thus contribution is always  $1/4$ . Similarly, in the antiferromagnetic case ( $J_z \geq |J_{xy}|$ ) on a bipartite lattice, the spin on a loop changes its direction when the loop jumps from one of the two sublattices to the other, and therefore contribution is  $1/4$  or  $-1/4$  depending on whether sites  $j$  and  $k$  are on the same sublattice or not. The present argument can also be extended to  $n$ -point functions ( $n = 3, 4, 5, \dots$ ).

Interestingly, in the case of easy-plane interaction ( $|J_z| \leq |J_{xy}|$ ), the size of loops corresponds not to the *diagonal* correlation but to the *offdiagonal* one, i.e., Green's function [40]. Formally, Green's function can be written as a ratio of partition functions,  $Z'/Z$ , where  $Z$  is the partition function of the system under consideration, and  $Z'$  is that of the system with a pair of kinks, i.e., discontinuities of world lines, at  $(j, \tau)$  and  $(k, \tau')$ . Although configurations with such kinks never appear during the simulation, we can virtually generate such configurations from the current graph configuration; iff the two points belong to a same loop, one can insert a pairs of cuts and flip partial loop between the cuts to generate a world-line configuration with two kinks. It contributes  $1/2$  to  $S_j^+(\tau)S_k^-(\tau')$ , and  $1/4$  to  $S_j^x(\tau)S_k^x(\tau')$ . Note that this virtual partial flip is used only for evaluating Eq. (6.64); we use the standard (closed) loop flip for updating the world-line configuration.

By integrating the correlation function over space-time, we obtain the simple and beautiful expression for the generalized susceptibility:

$$\chi(g) = \frac{1}{4\beta N} \sum_p V_p^2, \quad (6.66)$$

where the summation is taken over all loops and  $V_p$  denotes the volume (total length of fragments along the imaginary time) of each loop. The generalized susceptibility coincides with the ferromagnetic, transverse, and antiferromagnetic susceptibilities for  $J_z \leq -|J_{xy}|$ ,  $|J_z| \leq |J_{xy}|$ , and  $J_z \geq |J_{xy}|$ , respectively. In other words, the size of loops always represents the most divergent correlation in the whole parameter space.

Note that the argument presented here does not apply to the case where the longitudinal external field is present. In such a case, some of clusters are locked in by the

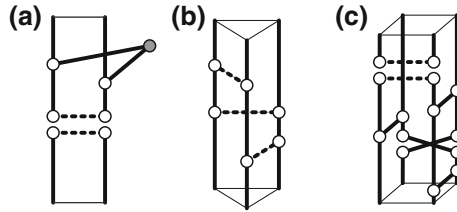


**Fig. 6.5** Example of avoided graphs: **a** Heisenberg antiferromagnet in a uniform external field. **b** Ising antiferromagnet on a triangle. **c** XY dimers coupled by Ising interaction. None of them have compatible world lines. The gray circle denotes the ghost spin. The bold (dotted) lines connect parallel (antiparallel) spins

ghost spin and thus we have to consider contribution from such clusters separately, and the size of clusters does *not* represent the relevant correlations any more. The same happens when the system is frustrated, i.e., there exist competing interactions.

### 6.5.2 Pure Loop Representation

The efficiency of the loop algorithm strongly depends on the structure of the phase subspace of  $g$ . In order to investigate in detail, we introduce the *pure loop representation* that is obtained by taking the summation over  $c$  in the extended Fortuin-Kasteleyn representation (6.26):

$$Z = \sum_c \sum_g \Delta(c, g) v(g) = \sum_g v(g) 2^{N_c(g)}, \quad (6.67)$$

where  $N_c(g)$  is the number of loops in  $g$ . The factor 2 comes from the fact that each loop has two corresponding spin configurations. This representation is analogous to the Fortuin-Kasteleyn representation of the Potts model [41]. The graph weight  $v(g)$  is a product of local graph weights. For example, for the Heisenberg antiferromagnet ( $J_z = |J_{xy}| = J$ ), it is simply given by  $v(g) = (J/2)^{k(g)}$  with  $k(g)$ , the number of horizontal graphs in  $g$ , besides a  $g$ -independent overall constant.

We have to be careful when we take the summation over  $g$  in Eq. (6.67), as some graphs may not have compatible world-line configurations (Fig. 6.5). Although such graphs have a non-vanishing weight  $v(g)$ , they can not be reached from any valid world-line configurations, and thus they never appear in the standard loop algorithm. In the pure loop representation, on the other hand, such avoided graphs should be excluded explicitly from the summation.

The existence of avoided graphs indicates that the phase subspace of  $g$  also has a restricted geometry. This may cause not only the complexity in taking the summation in the pure loop representation, but also the *exponential* slowing down, or *freezing*, in the loop algorithm. For example, the pure loop representations for the Heisenberg

antiferromagnet in a uniform longitudinal external field, the Ising antiferromagnet on a non-bipartite lattice, and the XY chains coupled by the Ising interchain coupling, all involve avoided graphs (Fig. 6.5), and they indeed exhibit serious slowing down at low temperatures.

Conversely, we conjecture that the loop algorithm will not suffer from the freezing, if its corresponding pure loop representation is *free*, i.e., no avoided graphs. If the Hamiltonian is expressed by using only the horizontal and crossing graphs (Table 6.1), and the cut graph for the transverse field, its pure loop representation is free. In this case, one can always choose the spin state on a loop so that it coincides with the direction of movement along the loop. Therefore, when one comes back to the original space-time position, the spin state can not be inconsistent. Similarly, when the Hamiltonian is expressed by using only graph 1 and 2 (or 3 and 4), the pure loop representation is free. The ferromagnetic model in a uniform longitudinal external field and the antiferromagnetic model on a bipartite lattice in a staggered field belong to this class, and they are actually free from the freezing problem.

The present argument applies even if the system has negative signs. The freezing problem is caused by *classical* (or diagonal) frustration in the system, and has little or nothing to do with *quantum* (or offdiagonal) frustration, though the latter problem is generally more serious.

We should note that the free pure loop representation does not necessarily mean the absence of any slowing down. It may still exhibit algebraic slowing down in the vicinity of the critical point, or exponential slowing down deep in the long-range ordered phase, especially when the loop update can not connect different ordered phases by a few Monte Carlo steps.

### 6.5.3 Pure Loop Algorithm

The pure loop representation is not merely a theoretical tool, but also useful for formulating another kind of loop algorithm, called *pure loop algorithm*. In this algorithm, graph configuration is updated directly by inserting or deleting a local graph without going through the world-line configurations. Since the overall graph weight  $v(g)$  as well as the number of loops  $N_c(g)$  will change by every insertion or deletion, one has to keep track of the information about the loop topology through the pure loop update. The algorithm may have advantages in recovering the ergodicity and avoiding the slowing down problem in some systems. Unfortunately, the pure loop update is much more complicated than the standard loop algorithm, and one Monte Carlo step will cost at least of  $O(N\beta \log N\beta)$ .

However, the pure loop algorithm has a potential for solving the negative sign problem in a wide range of applications. One promising candidate is the *meron cluster algorithm* [42]. First of all, in the world-line QMC for the spin/bosonic systems, the sign of world-line weight is determined by the parity of winding number of world lines around frustrated loops on the lattice. Moreover, contribution from each loop to the parity of winding number is independent; some loops change the world-line

sign, but the others do not. A loop in the former class is called “meron.” If there is at least one meron in the loop configuration, the improved estimator for the overall sign yields zero, as a meron contributes equally to +1 and −1. On the other hand, if there is no meron, the value of improved sign is non-vanishing. Furthermore, if there is a reference world-line configuration that has a positive weight and is compatible with any graph configurations, the improved sign takes either 0 or 1, that is, the negative sign is eliminated [42]. In practice, as graph configurations with zero improved sign still dominate, one has to introduce some extra weight, a function of the number of merons, in order to sample the zero-meron sector more frequently. The meron cluster algorithm solves the sign problem e.g., in the Heisenberg antiferromagnets in a staggered transverse field, or the Heisenberg models with unfrustrated interactions in  $z$ -component and frustrated (random) interactions in  $x$ - and  $y$ -components of spins. Unfortunately, in most interesting models, e.g., the Heisenberg antiferromagnets on kagomé or pyrochlore lattices, such a reference world-line configuration does not exist, and thus one still encounters negative signs even in the zero-meron sector.

More recently, another variant of the pure loop algorithm, *nested cluster algorithm*, has been proposed [43], which consists of two nested loop updates; the outer loop is the same as the original pure loop update, while in the inner loop only the update which does not change the footprint of each loop is allowed. As long as the typical cluster size is much smaller than the system size, by taking average on each cluster separately, the relative error is expected to scale linearly to the space-time volume instead of the exponential scaling. Thus, the nested cluster algorithm solves the negative sign problems [43] in the thermodynamic limit at high temperatures, or at zero temperature of gapped systems, though its availability has not yet been tested exhaustively.

## 6.6 Conclusion

The state-of-the-art loop algorithm and its extensions have been reviewed. In a variety of important quantum lattice models, such as the Heisenberg antiferromagnets on bipartite lattices without external field, the loop algorithm can reduce the autocorrelation time by several orders of magnitude, especially at low temperatures and/or in the vicinity of the critical point. It has already been applied to many quantum lattice models with great success [7, 8], e.g., the higher-spin Haldane chains [25, 31], phase transitions in extremely anisotropic magnets [44], randomly depleted magnets [45], etc. On the other hand, there still remain a number of unsolved algorithmic problems; the freezing problem induced by classical frustration, the negative sign problem due to quantum frustration, etc. As for the former, the worm algorithm (Sect. 10.3) and the directed loop algorithm (Sect. 6.3) solve the exponential slowing down caused by the freezing to a certain extent. Especially, they are more efficient for the spin systems in the competing magnetic field. In contrast to the loop algorithm, however, the algorithms based on worm update are hardly parallelized on modern parallel supercomputers. The negative sign problem is still common to all the existing QMC

algorithm except for few special cases. The real time dynamics as well as measuring exotic topological quantities also remain as a challenging problem for the world-line QMC method.

Finally, for those who are interested, ALPS/looper, a C++ implementation of the parallel continuous time loop algorithm, has been developed as a part of the ALPS project [46], and is freely available on the web [47].

The present author thanks K. Harada, N. Kawashima, Y. Motoyama, H. Suwa, and M. Troyer for stimulating discussions and helpful comments.

## References

1. C.P. Robert, G. Casella, *Monte Carlo Statistical Methods*, 2nd edn. (Springer, New York, 2004)
2. D.P. Landau, K. Binder, *A Guide to Monte Carlo Simulations in Statistical Physics*, 2nd edn. (Cambridge University Press, Cambridge, 2005)
3. M. Suzuki, Prog. Theor. Phys. **56**, 1454 (1976)
4. M. Suzuki (ed.), *Quantum Monte Carlo Methods in Condensed Matter Physics* (World Scientific, Singapore, 1994)
5. H.G. Evertz, G. Lana, M. Marcu, Phys. Rev. Lett. **70**, 875 (1993)
6. U.J. Wiese, H.P. Ying, Z. Phys. B **93**, 147 (1994)
7. H.G. Evertz, Adv. Phys. **52**, 1 (2003)
8. N. Kawashima, K. Harada, J. Phys. Soc. Jpn. **73**, 1379 (2004)
9. N.V. Prokof'ev, B.V. Svistunov, I.S. Tupitsyn, Sov. Phys. JETP **87**, 310 (1998)
10. A.W. Sandvik, J. Kurkijärvi, Phys. Rev. B **43**, 5950 (1991)
11. S.P. Meyn, R.L. Tweedie, *Markov Chains and Stochastic Stability* (Springer, New York, 1993)
12. H. Suwa, S. Todo, Phys. Rev. Lett. **105**, 120603 (2010)
13. N. Metropolis, A.W. Rosenbluth, M.N. Rosenbluth, A.H. Teller, E. Teller, J. Chem. Phys. **21**, 1087 (1953)
14. M. Creutz, Phys. Rev. D **21**, 2308 (1980)
15. A. Bortz, M. Kalos, J. Lebowitz, J. Comput. Phys. **17**(1), 10 (1975)
16. R.H. Swendsen, J.S. Wang, Phys. Rev. Lett. **58**, 86 (1987)
17. D. Kandel, E. Domany, Phys. Rev. B **43**, 8539 (1991)
18. N. Kawashima, J.E. Gubernatis, J. Stat. Phys. **80**, 169 (1995)
19. D.E. Knuth, *The Art of Computer Programming: Seminumerical Algorithms*, vol. 2, 3rd edn. (Addison Wesley, Reading, 1997), p. 121
20. K. Fukui, S. Todo, J. Comp. Phys. **228**, 2629 (2009)
21. S. Todo, K. Kato, Prog. Theor. Phys. Suppl. **138**, 535 (2000)
22. T.H. Cormen, C.E. Leiserson, R.L. Rivest, C. Stein, *Introduction to Algorithms*, 2nd edn. (MIT Press, Cambridge, 2001)
23. S. Todo, Prog. Theor. Phys. Suppl. **145**, 188 (2002)
24. S. Todo, in *Computer Simulation Studies in Condensed Matter Physics XV*, ed. by D.P. Landau, S.P. Lewis, H.B. Schüttler (Springer, Berlin, 2003), p. 89
25. S. Todo, H. Matsuo, H. Shitara (2012 preprint)
26. N. Kawashima, J. Stat. Phys. **82**, 131 (1996)
27. H. Rieger, N. Kawashima, Eur. Phys. J. B **9**, 233 (1999)
28. V.A. Kashurnikov, N.V. Prokof'ev, B.V. Svistunov, M. Troyer, Phys. Rev. B **59**, 1162 (1999)
29. K. Harada, N. Kawashima, M. Troyer, Phys. Rev. Lett. **90**, 117203 (2003)
30. K. Harada, M. Troyer, N. Kawashima, J. Phys. Soc. Jpn. **67**, 1130 (1998)
31. S. Todo, K. Kato, Phys. Rev. Lett. **87**, 047203 (2001)
32. R.G. Melko, A.W. Sandvik, Phys. Rev. E **72**, 026702 (2005)

33. K. Harada, N. Kawashima, J. Phys. Soc. Jpn. **70**, 13 (2001)
34. A.J. Walker, ACM Trans. Math. Softw. **3**, 253 (1977)
35. J.E. Gubernatis, M. Jarrell, R.N. Silver, D.S. Sivia, Phys. Rev. B **44**, 6011 (1991)
36. F. Cooper, B. Freedman, D. Preston, Nucl. Phys. B **210[FS6]**, 210 (1989)
37. H. Suwa, S. Todo, (2012 in preparation)
38. K. Okamoto, K. Nomura, Phys. Lett. A **169**, 433 (1992)
39. U. Wolff, Phys. Rev. Lett. **62**, 361 (1989)
40. R. Brower, S. Chandrasekharan, U.J. Wiese, Phys. A **261**, 520 (1998)
41. C.M. Fortuin, P.W. Kasteleyn, Physica **57**, 536 (1972)
42. S. Chandrasekharan, U.J. Wiese, Phys. Rev. Lett. **83**, 3116 (1999)
43. M. Nyfeler, F.J. Jiang, F. Kämpfer, U.J. Wiese, Phys. Rev. Lett. **100**, 247206 (2008)
44. C. Yasuda, S. Todo, K. Hukushima, F. Alet, M. Keller, M. Troyer, H. Takayama, Phys. Rev. Lett. **94**, 217201 (2005)
45. K. Kato, S. Todo, K. Harada, N. Kawashima, S. Miyashita, H. Takayama, Phys. Rev. Lett. **84**, 4204 (2000)
46. B. Bauer, et al., J. Stat Mech. p. P05001 (2011). <http://iopscience.iop.org/1742-5468/2011/05/P05001/>
47. <http://wistarria.comp-phys.org/alps-looper/>

# Chapter 7

## Stochastic Series Expansion Quantum Monte Carlo

Roger G. Melko

**Abstract** This chapter outlines the fundamental construction of the Stochastic Series Expansion, a highly efficient and easily implementable quantum Monte Carlo method for quantum lattice models. Originally devised as a finite-temperature simulation based on a Taylor expansion of the partition function, the method has recently been recast in the formalism of a zero-temperature projector method, where a large power of the Hamiltonian is applied to a trial wavefunction to project out the groundstate. Although these two methods appear formally quite different, their implementation via non-local *loop* or *cluster* algorithms reveals their underlying fundamental similarity. Here, we briefly review the finite- and zero-temperature formalisms, and discuss concrete manifestations of the algorithm for the spin 1/2 Heisenberg and transverse field Ising models.

### 7.1 Introduction

In the quest to understand the phenomenon of quantum systems in the thermodynamic limit, it is often one's ambition to simulate microscopic models on lattices of the largest sizes practically possible. In the context of quantum Monte Carlo (QMC), this means constructing a simulation methodology that is highly efficient, with favorable scaling properties, free of systematic errors or bias, yet capable of attacking the cornucopia of interesting quantum models which entice modern condensed matter, materials, atomic, molecular and optics, and quantum information scientists. Since QMC involves mapping a  $D$ -dimensional quantum system to  $D + 1$  dimensions, the

---

R. G. Melko (✉)

Department of Physics and Astronomy, University of Waterloo,  
Ontario N2L 3G1, Canada  
e-mail: rgmelko@uwaterloo.ca

Perimeter Institute for Theoretical Physics,  
Waterloo, Ontario N2L 2Y5, Canada

symmetry of the quantum Hamiltonian is often encoded directly into the structure of the simulation cell. Therefore, in order to facilitate a practitioner’s ability to examine a variety of physical Hamiltonians of interest, a QMC program should also be transparent and easy to implement, allowing flexibility to code in a wide range of different lattice models.

For many applications, the industry standard for simulation of lattice models of quantum spins and bosons (without the sign problem) has become SSE QMC, which stands for Stochastic Series Expansion.<sup>1</sup> Often, SSE simulations for ‘typical’ Hamiltonians can be straightforwardly implemented in a few thousand lines of code. This allows the programmer a high degree of control, facilitates optimization, and encourages algorithmic development. SSE programs scale with high efficiency, typically linear in the number of lattice sites and the inverse temperature:  $\mathcal{O}(N\beta)$ . This combination of favorable quantities enables a power, utility, and ease of use that is testified to by SSE QMC’s widespread adoption in a variety of applications in the physical sciences.

Modern SSE is based on some of the same principles as Handscomb’s method, namely Taylor expanding the partition function [1]. However, Handscomb (and others after him) only considered cases where the trace of the Hamiltonian could be computed analytically—a fact that caused the method to be considered limited in scope. The major advance, which propelled Handscomb’s method towards wide-spread applicability, was the realization that this trace could be stochastically *sampled*, like in worldline methods. Thus dubbed SSE, Sandvik [2, 3] pioneered not only the original, spin 1/2 version (used extensively to study the Heisenberg model [4]), but many extensions of the versatile framework, including the important recent recasting as a  $T = 0$  projector method [5, 6]. The SSE method has been applied to both spin 1/2 and higher spin models [2, 7] on a large variety of lattices, including partially-frustrated systems [8], models with long-range interactions [9], and a whole host of other manifestations of quantum magnetism. It has been adapted to boson Hamiltonians, both hard-core and soft-core, which has caused a proliferation of application on models of cold atoms trapped in optical lattices [10–12]. It has been generalized to study  $SU(N)$  symmetric models [13, 14], which has been instrumental in making connection with field-theoretic studies of universality and quantum phase transitions [15, 16]. Today, SSE simulations can routinely access simulation cells with a space-time volume  $N\beta$  larger than  $10^7$  [17]; its limitations it seems are only the imagination of the practitioner.<sup>2</sup>

The above are but a few examples of the success of SSE over the past twenty years. An exhaustive list would quickly fill all of the pages available in this volume. Instead, in this chapter, we describe the current broad framework of understanding of the SSE QMC method, outlining the modern approach to designing and implementing both  $T > 0$  and  $T = 0$  programs. The two simplest cases for spin 1/2 models, the isotropic Heisenberg model, and the Ising model in an applied transverse field, are discussed in detail.

<sup>1</sup> or alternatively, Sandvik’s *Simple and Efficient* QMC.

<sup>2</sup> and, of course, the infamous “sign problem”.

## 7.2 Quantum Monte Carlo Formalism

We begin by reviewing the foundational basis of the SSE methodology. Like any Monte Carlo method, the goal of SSE is to construct an importance sampling scheme, which ultimately leads to the computation of expectation values in the form of an arithmetic mean,

$$\langle \mathcal{O} \rangle = \frac{1}{N_{\text{mc}}} \sum_{t=0}^{N_{\text{mc}}} \mathcal{O}(x^t). \quad (7.1)$$

Here  $x^t$  is the configuration of the simulation cell at ‘time’ step  $t$  in a Markov Chain of length  $N_{\text{mc}} \rightarrow \infty$ . Each time step is one element of a random walk in a higher-dimensional configuration space, weighted with a probability distribution  $W(x)$  (where each  $W(x^t) > 0$ ), which samples all possible configurations when the number of steps is infinite. Because the random walk is an importance sampling through this weighted space, the arithmetic mean for finite- $N_{\text{mc}}$  corresponds to the estimate,

$$\langle \mathcal{O} \rangle = \frac{\sum_x \mathcal{O}_x W(x)}{\sum_x W(x)}. \quad (7.2)$$

This expectation value is the basis of many Markov Chain Monte Carlo (MCMC) procedures [18]. For the purposes of this chapter, the form of this expectation value provides a unified starting point for two different QMC formalisms with separate goals: calculating physical estimators at finite temperature, or calculating physical estimators at zero temperature.

We note here that the procedure we call “quantum Monte Carlo” simulation actually consists of two distinct steps [19]. First, we must derive the appropriate *representation* of the quantum mechanical model (i.e. lattice, basis states, and operators) such that this representation can be coded appropriately on a classical computer. This involves mapping a  $D$ -dimensional quantum lattice model to a  $D + 1$ -dimensional classical representation, which can be thought of as a highly non-trivial classical statistical mechanics problem. Strictly speaking, SSE can be thought of as a representation of  $\exp(-\beta H)$  together with some lattice basis; other representations exist, such as continuous-time or interaction representations [19]. Second, we must devise *updating schemes* that sample configurations of this representation, usually through some Metropolis procedure. Similar updating schemes may be used for different representations. In the next two sections, we will discuss the finite- $T$  and  $T = 0$  representations. In Sect. 7.2.3, we’ll outline some basic ideas behind updating schemes employed in the SSE, emphasizing the role of non-local updates.

### 7.2.1 Finite-Temperature Representation

For finite-temperature, Eq. 7.2 corresponds to the thermal average,

$$\langle \mathcal{O} \rangle = \frac{1}{Z} \text{Tr}\{\mathcal{O} e^{-\beta H}\}, \quad (7.3)$$

where  $\beta = 1/T$ , and the denominator is the partition function,

$$Z = \sum_x W(x) = \text{Tr}\{e^{-\beta H}\}. \quad (7.4)$$

The first step in the SSE approach is to write the trace in the partition function as a sum over diagonal matrix elements in a basis  $\{\alpha_0\}$ . Then, one can Taylor expand the exponential to get the expression,

$$Z = \text{Tr}\{e^{-\beta H}\} = \sum_{\alpha_0} \left\langle \alpha_0 \left| \sum_{n=0}^{\infty} \frac{\beta^n}{n!} (-H)^n \right| \alpha_0 \right\rangle. \quad (7.5)$$

We next insert a set of complete basis states as resolutions of the identity,  $\sum_{\alpha} |\alpha\rangle\langle\alpha|$  between the  $n$  products of  $-H$ ;

$$Z = \sum_{\{\alpha_i\}} \sum_{n=0}^{\infty} \frac{\beta^n}{n!} \langle \alpha_0 | -H | \alpha_1 \rangle \langle \alpha_1 | -H | \alpha_2 \rangle \cdots \langle \alpha_{n-1} | -H | \alpha_n \rangle, \quad (7.6)$$

where, importantly,  $\alpha_n = \alpha_0$  to keep the trace nonzero. Note the set of basis states  $\{\alpha_i\}$  in the sum is practically impossible to evaluate exactly; this motivates the use of an importance-sampling scheme. Then, the “weight” of a configuration,  $W(x)$ , is derived from this expression, and can be seen to be proportional to the product of  $n$  matrix elements. Each individual matrix element  $\langle \alpha_i | -H | \alpha_{i+1} \rangle$  is evaluated as a real number, and must be *positive* to be interpreted as a probability for use in a Metropolis scheme.

Note however that it is very possible for the above matrix elements to be negative, depending on the precise form of  $H$ . This is a manifestation of the so called “sign problem” [20]. It can essentially be avoided only in the case where all terms in the Hamiltonian have (or can be made to have) a negative sign in front of them. This can happen either intrinsically, e.g. with ferromagnetic interactions, or through a clever basis rotation, which is possible e.g. for antiferromagnetic interactions on bipartite lattices. In the examples we will consider in this chapter, resolution of the sign problem will be straightforward—however in general quantum lattice models, it can be quite inhibitive.

The next step is to write the Hamiltonian as a sum of elementary lattice operators,

$$H = - \sum_t \sum_a H_{t,a}, \quad (7.7)$$

where in our chosen representation the operators propagate the basis  $H_{t,a}|\alpha_i\rangle \rightarrow |\alpha_{i+1}\rangle$ , and all of the  $H_{t,a}$  are positive. The indices  $t$  and  $a$  refer to the operator “types” and the “lattice units” (e.g. bonds) over which the terms will be sampled (specific examples will be given below). We write the partition function as,

$$Z = \sum_{\{\alpha_i\}} \sum_{n=0}^{\infty} \sum_{S_n} \frac{\beta^n}{n!} \prod_{i=1}^n \langle \alpha_{i-1} | H_{t_i, a_i} | \alpha_i \rangle, \quad (7.8)$$

where  $S_n$  denotes a sequence of operator-indices specifying the  $n$  operators,

$$S_n = [t_1, a_1], [t_2, a_2], \dots, [t_n, a_n], \quad (7.9)$$

which must be importance sampled, along with the basis states  $\alpha$ , and the expansion power  $n$ .

As the final step, one can truncate the Taylor expansion at a maximum power  $M$ . This is not strictly necessary in principle, however it significantly facilitates implementation of the updating scheme. The truncation can be justified by ensuring that the chosen  $M$  is always greater than the largest  $n$  to occur in a numerical simulation,  $M > n_{\max}$ , for a given parameter set [4]. Working with a fixed  $M$  is possible to do if one inserts  $M - n$  “fill-in”, or null, operators  $H_{0,0} \equiv I$  into the operator list (where  $I$  is the identity operator). However, these operators do not occur in the evaluation of the partition function, and must be accounted for by dividing the final expression for  $Z$  by their contribution. To do so note that, statistically, the number of different way of picking the placement of the null operators in the expansion list is given by the binomial coefficient,  $\binom{M}{n} = M!/(M-n)!n!$ . One is required to divide our truncated partition function by this value, giving,

$$Z = \sum_{\alpha} \sum_{S_M} \frac{(\beta)^n (M-n)!}{M!} \prod_{i=1}^M \langle \alpha_{i-1} | H_{t_i, a_i} | \alpha_i \rangle, \quad (7.10)$$

where the sum over  $n$  is now implicitly included in the sampling of  $S_M$ .

We thus arrive at the final expression for the representation of the finite-temperature partition function in SSE, which can formally be related to path integral or world-line representations—resulting in the propagation (or expansion) dimension being identified with the imaginary time direction [19, 21]. With this SSE representation, we are free to devise updating methods adopted from classical Monte Carlo routines to generate the appropriate Markov Chain in the unified space of basis state ( $\alpha$ ) and operator/worldline ( $S_M$ ) configurations. This will be discussed in Sect. 7.2.3; first, however, we introduce the formally different  $T = 0$  starting point for QMC that,

nonetheless, results in a very similar SSE-type representation, amenable to analogous updating techniques as the  $T > 0$  representation here.

### 7.2.2 Zero-Temperature Projector Representation

At  $T = 0$ , Eq. 7.2 can alternatively be used as an estimate for the operator expectation value,

$$\langle \mathcal{O} \rangle = \frac{1}{Z} \langle \Psi | \mathcal{O} | \Psi \rangle, \quad (7.11)$$

where one aims to use some procedure to find  $\Psi$  as the ground-state wavefunction of a Hamiltonian [5]. The denominator of Eq. 7.2 is then the normalization, or inner product,

$$Z = \langle \Psi | \Psi \rangle. \quad (7.12)$$

In a “projector” QMC representation, the ground state wavefunction is estimated by a procedure where a large power<sup>3</sup> of the Hamiltonian is applied to a *trial* state, call it  $|\alpha\rangle$ . This can be seen by writing the trial state in terms of energy eigenstates  $|n\rangle$ ,  $n = 0, 1, 2 \dots$ ,  $|\alpha\rangle = \sum_n c_n |n\rangle$ , so that a large power of the Hamiltonian will project out the groundstate,

$$\begin{aligned} (-H)^m |\alpha\rangle &= c_0 |E_0|^m \left[ |0\rangle + \frac{c_1}{c_0} \left( \frac{E_1}{E_0} \right)^m |1\rangle \dots \right], \\ &\rightarrow c_0 |E_0|^m |0\rangle \quad \text{as } m \rightarrow \infty. \end{aligned} \quad (7.13)$$

Here, we have assumed that the magnitude of the lowest eigenvalue  $|E_0|$  is *largest* of all the eigenvalues. To achieve this, one may be forced to add a sufficiently large negative constant to the overall Hamiltonian (that we have not explicitly included). Then, from this expression, one can write the normalization of the groundstate wavefunction,  $Z = \langle 0 | 0 \rangle$  with two projected states (bra and ket) as,

$$Z = \langle \alpha | (-H)^m (-H)^m | \alpha \rangle, \quad (7.14)$$

for large  $m$ . The Hamiltonian is again written as a (negative) sum of elementary lattice interactions (Eq. 7.7), the indices  $t$  and  $a$  referring to the operator “types” and lattice “units” over which the terms will be sampled. In order to represent the normalization as a sum of weights,  $Z = \sum_x W(x)$ , motivated by Sect. 7.2.1 we can insert a compete resolution of the identity between each  $H_{t_i, a_i}$ ,

---

<sup>3</sup> Alternatively, with the imaginary-time evolution operator  $e^{-\beta H}$ , where  $\beta$  is large. The two methods are essentially equivalent however, since the exponential can be Taylor expanded.

$$Z = \sum_{\{\alpha\}} \sum_{S_m} \prod_{j=1}^{2m} \langle \alpha_\ell | H_{t_j, a_j} | \alpha_r \rangle. \quad (7.15)$$

We see that this has been cast in a form similar to Eq. 7.8, where the sum over the set  $\{\alpha\}$  and the operator list  $S_m$  must be done with importance sampling.

Note that, despite the similarity of Eq. 7.15 to its finite- $T$  analog, several important differences exist in this  $T = 0$  representation. First, although the convergence parameter  $2m$  is similar in magnitude to  $n$  in the “equivalent” finite- $T$  simulation, generally speaking this projector formalism only produces meaningful observables from Eq. 7.11 when the simulation is converged in  $m$ . Thus, although it is reasonable to think that the projector representation will result in a more efficient simulation for  $T = 0$ , in general one loses the advantage of interpreting  $m$  smaller than the converged value with some physical significance (i.e. finite temperature). Another important difference is that the simulation cell has lost its periodicity in the projection (or imaginary time) direction: i.e.  $|\alpha_\ell\rangle \neq |\alpha_r\rangle$  in Eq. 7.15. Thus, all estimators, either in terms of the basis state, or as expectation values of an operator, are evaluated in the “middle” of the projection—i.e. a distance  $m$  from either endpoint.

In Sects. 7.3 and 7.4 we will discuss the precise form of  $H_{t,a}$  used to represent the Heisenberg and transverse field Ising models, as well as the specific updating schemes for sampling the basis and operator space for both finite- $T$  and  $T = 0$  QMC frameworks. However before we turn to specific models, we discuss general strategies for developing updating schemes, to be used in MCMC sampling of the  $D + 1$  representations developed in the last two sections.

### 7.2.3 Local and Non-Local Updating Schemes

Now that we have presented two different ways of representing a  $D$  dimensional quantum lattice model by a  $D + 1$  classical statistical mechanical problem, we turn very generally to the problem of how the different configurations  $x$  are sampled in a MCMC scheme. The formation of any QMC simulation corresponds to addressing two questions in the procedure of updating a configuration  $x \rightarrow x'$ . First, how do the transition probabilities  $P(x \rightarrow x')$  depend on the weights  $W(x)$  such that detailed balance,

$$W(x)P(x \rightarrow x') = W(x')P(x' \rightarrow x), \quad (7.16)$$

is satisfied. Second, how are these configuration updates performed such that the simulation is ergodic (and efficient)?

We will assume that, for sign-problem free models, an updating scheme can always be found that satisfies detailed balance (indeed, all updates are constructed as such). The question of ergodicity is more subtle. In particular, since in the SSE representation the Hamiltonian is broken up into “types”,  $H_{t,a}$ , different update procedures are typically needed to properly sample each operator type (e.g. diagonal

or off-diagonal). These updates are roughly categorized into *local* and *non-local*, referring to the extent of the spatial or temporal region of the simulation cell that the update influences.

Local updates are familiar from classical Monte Carlo on spin systems, where the prototypical site update is simply the spin-flip  $\uparrow$  to  $\downarrow$ . These updates are possible (and recommended) in the SSE, but only at very high temperatures (or small  $m$ ), on physical lattice sites that remain unconnected by operators over the entire propagation direction. Rather, the term “local” update in QMC is generally referred to as such for involving one lattice unit (e.g. a bond). Local updates are typically used to sample diagonal operators in the  $S^z$  basis; however they can also be used to sample SU(2) singlet operators in the valence-bond basis (discussed below).

The term “non-local” update is a blanket term that can refer to several different procedures. Most common are so-called “loop” updates [22], which are essentially non-branching closed strings [23]. Loop updates have several functions: they facilitate sampling of off-diagonal operators, and also allow for fluctuations between different operators types in the simulation cell. Importantly, they are sometimes necessary for the ergodic sampling of certain estimators, such as the winding numbers, which spatially are related to quantities like the helicity modulus [24], and temporally to the uniform spin susceptibility or compressibility [25]. A variety of loop and worm algorithms have been discussed in the literature, the most important for SSE being the *directed loop* update [26]. In this review we will forgo a detailed discussion of transition probabilities in the construction of loop moves: instead we will focus entirely on so-called “deterministic” loop updates, which are available for certain Hamiltonians, e.g. the Heisenberg model discussed in the next section.

In addition to loop moves, the term “non-local” can also refer to updates in the  $D + 1$  simulation cell that do not form non-branching closed loops, but share the property of being extended over a larger space-time region. The most important of these are “cluster” updates, which unlike loops are allowed to branch with many legs over the simulation cell. In Sect. 7.4 we will discuss the simplest type of deterministic cluster update for the transverse field Ising model [9]. Cluster updates have also been designed in  $S^z$  preserving Hamiltonians, in particular the so-called J-K models with four-site exchange [27]. In these models, although the exact implementation details are a bit more complicated, the spirit of the cluster update is the same.

Remarkably, the form of the loop or cluster update depends very little on which representation of the SSE simulation cell is used, be it  $T = 0$  projector or  $T > 0$  partition-function based. Rather, it depends on the specific quantum Hamiltonian one wishes to implement. In order to make our discussion more concrete, we now abandon the general discussion of the SSE in favor of making pedagogical progress on specific spin 1/2 models. In Sect. 7.3, we will discuss implementations of the  $T = 0$  and  $T > 0$  SSE for the SU(2) symmetric Heisenberg model, which is sampled efficiently with deterministic loop updates. In Sect. 7.4, we similarly discuss SSE implementations of the transverse field Ising model, and the associated cluster update.

### 7.3 Spin-1/2 Heisenberg Model

Due to its important place in the history of the development of SSE, the literature describing algorithms for the spin-1/2 Heisenberg model,

$$H = \sum_{\langle ij \rangle} \mathbf{S}_i \cdot \mathbf{S}_j, \quad (7.17)$$

is extensive [1, 2, 4, 20, 23, 26]. We encourage the reader interested in implementation of the Heisenberg model to consult the appropriate authoritative reference. Here, we discuss the basic ideas of the SSE representation, together with the important local and loop updates, as a way of grounding the discussion. We therefore focus on the unifying framework of the zero- and finite-temperature simulations, instead of all possible implementation details for the plethora of variants of this important quantum many-body model.

The standard approach to simulating the Heisenberg Hamiltonian using an SSE representation is to employ the  $S^z$  basis. Using this basis, we begin by specifying the appropriate bond-decomposition for  $H_{t,a}$  (from Eq. 7.7) for Eq. 7.17. Namely, we use,

$$H_{0,0} = I, \quad (7.18)$$

$$H_{1,a} = \frac{1}{4} - S_i^z S_j^z, \quad (7.19)$$

$$H_{2,a} = \frac{1}{2}(S_i^+ S_j^- + S_i^- S_j^+), \quad (7.20)$$

from which matrix-element weights can be constructed to give  $W(x)$ . First note that, in the above bond decomposition, two facts are evident:

1. There has been a constant term 1/4 added to the diagonal operator  $H_{1,a}$ . This eliminates the offensive negative sign: however it adds a constant  $1/4 \times N_b$ , where  $N_b$  is the number of nearest-neighbor bonds, to the expectation value of the Hamiltonian (i.e. the energy).
2. There has been a *rotation* of the spin operators by  $\pi/2$  around the  $z$ -axis on one of the sublattices of a bipartite lattice. This ensures that the off-diagonal part of the Hamiltonian,  $H_{2,a}$ , remains positive-definite as required. Note however that this “trick” of eliminating the negative sign is only possible on bipartite lattices.<sup>4</sup>

The weight  $W(x)$  of a sampled configuration  $x$  is proportional to the product of all matrix elements in the SSE expansion. Each matrix element is calculated using the  $S^z$  basis: representing the  $S_i^z = +1/2$  eigenstate as  $| \bullet \rangle_i$  and  $S_j^z = -1/2$  as  $| \circ \rangle_j$ , the only non-zero matrix elements are,

---

<sup>4</sup> A generalization of this basis rotation on non-bipartite lattices would amount to a solution to the aforementioned “sign-problem”—and likely a Nobel prize for its architect.

$$\langle \bullet \circ | H_{1,a} | \bullet \circ \rangle = \langle \circ \bullet | H_{1,a} | \circ \bullet \rangle = \frac{1}{2}, \quad (7.21)$$

$$\langle \bullet \circ | H_{2,a} | \circ \bullet \rangle = \langle \circ \bullet | H_{2,a} | \bullet \circ \rangle = \frac{1}{2}. \quad (7.22)$$

We now see the choice of 1/4 in Eq. 7.19 to be judicious: the matrix elements contributing to the total weight of a configuration,  $W(x)$ , are equal when non-zero. This will significantly simplify sampling, we will now see for both the finite- $T$  and  $T = 0$  cases.

### 7.3.1 Finite-Temperature SSE in the $S^z$ Basis

It is common to call the space-time path that a  $S^z = +1/2$  state traces out in the  $D + 1$  dimension expansion a “worldline”. Figure 7.1 makes it evident that, in the SSE operator decomposition discussed above, the diagonal ( $H_{1,a}$ ) and off-diagonal ( $H_{2,a}$ ) operators affect the worldline path quite differently. Off-diagonal operators disturb it with a translation, while diagonal operators do not. Because of this, diagonal operators can be sampled in each propagation time-slice with *local* updates that replace  $H_{1,a}$  on a specific lattice bond  $a$  with the null operator  $H_{0,0}$ , or vice versa. The transition probabilities (in the Metropolis sense) associated with these “diagonal updates” are derived directly from Eqs. 7.10 and 7.16, by considering the ratio of weights  $W(x')/W(x)$ . One finds, to add a diagonal operator (thereby changing the power in the propagator list from  $n$  to  $n + 1$ ),

$$P(n \rightarrow n + 1) = \min\left(\frac{1}{2} \frac{N_b \beta}{(M - n)}, 1\right), \quad (7.23)$$

where the number of lattice bonds,  $N_b$ , enters in since the bond index  $a$  must be chosen at random for the insertion. The factor of 1/2 comes from the matrix elements 7.21—meaning one only inserts the operator if the  $S^z$  basis states are anti-aligned. If however the  $S^z$  states are aligned on the chosen bond index  $a$ , the matrix element (and hence the transition probability) is zero. Thus, the insertion is rejected and the algorithm moves on to the next propagation step. In a similar way, we can calculate the transition probably to remove an operator  $H_{1,a}$  from the list,

$$P(n \rightarrow n - 1) = \min\left(\frac{2(M - n + 1)}{N_b \beta}, 1\right). \quad (7.24)$$

These local updates are instrumental in changing the expansion order  $n$  (necessary to sample the sum  $\sum_n$  in Eq. 7.8). They also illustrate an important point: diagonal updates alone do nothing to sample *off-diagonal* operators  $H_{2,a}$ . For this, we must devise another updating scheme.

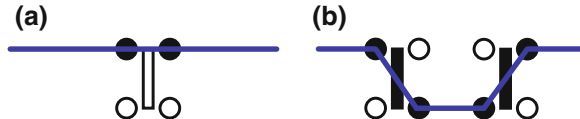


**Fig. 7.1** In (a), a particle worldline (blue) that encounters a two-site diagonal operator  $\langle \bullet \circ | H_{1,a} | \bullet \circ \rangle$  continues unmolested. In (b), a worldline that encounters an off-diagonal operator  $\langle \bullet \circ | H_{2,a} | \circ \bullet \rangle$  is translated by one lattice unit. If worldlines are to remain periodic in imaginary time, another off-diagonal operator  $\langle \circ \bullet | H_{2,a} | \bullet \circ \rangle$  is needed to translate the worldline back

Antiquated methods devised to sample  $H_{2,a}$  involved identifying diagonal operators that were “nearby” in the propagation direction, and updating them both to produce two off-diagonal operators such as in Fig. 7.1b [4]. Such approaches are the equivalent of local updates: they are found to be inefficient, as well as non-ergodic e.g. in the all-important winding number [24]. With the advent of the global *loop* move, such problems are relegated to history [23, 26].

In general, a loop move is constructed by creating a “defect” (or “head”) in the worldline configuration, and propagating that defect until it closes upon itself (i.e. finds its “tail”). The path of the defect through the space-time simulation cell passes through basis states (spins) and operators in  $D + 1$ . This path defines the loop, which itself is just a list of space-time lattice coordinates. A loop is said to be “flipped” if all spins on the path are flipped—which also changes the operator types associated with flipped spins (i.e. the matrix elements). This loop flipping generally accrues some change in weight. These weight changes can be absorbed into the process of creating the loop path, such that the propagation of the defect is subject to the Metropolis condition at every step (this is the *directed* loop [26]).

Quite generally, loop updates hold their power in the fact that one can typically avoid the cases where the algorithm samples “zero” (or low weight) contributions to the partition function. In some cases of higher symmetry like the Heisenberg model, simple loop algorithms can be constructed that have optimal properties in this regard. This comes from our choice of Eqs. 7.21 and 7.22, which forces non-zero matrix elements to have equal weights. In other words, if loops are constructed to only transition between non-zero matrix elements, the entire loop flip will involve no weight change:  $W(x')/W(x) = 1$ . Thus, a Swendsen-Wang (SW) algorithm can be employed, were all loops are constructed, and each flipped with probability 1/2 [28].

In Fig. 7.2 an abstraction of a finite- $T$  SSE simulation cell for the spin-1/2 Heisenberg model is shown, for a  $n = 6$  operator configuration. The propagation direction is horizontal—periodic boundary conditions in imaginary time are represented by arrows. Closed loops, eligible for flipping, are constructed from the paths formed by solid lines. In this case, the rules for a loop’s construction are simple: make the loop head follow a horizontal path, and when it reaches an operator (vertical bar), it turns its path in the opposite direction on the associated link. Given an operator position configuration (generally decided by the diagonal update above), the loop structure formed in this manner is fully determined—hence the name *deterministic*

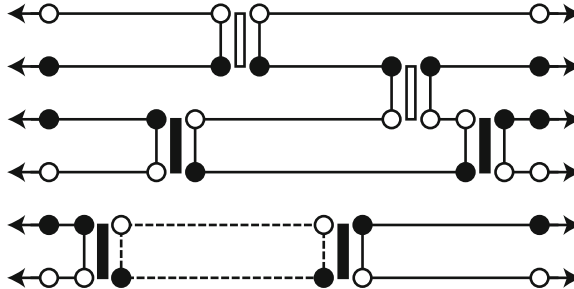


**Fig. 7.2** A  $D + 1$  SSE simulation cell snapshot for a six-site Heisenberg model. Lattice sites are arranged vertically in one-dimension: the propagation direction (imaginary time) is horizontal, with  $n = 6$  operators. Arrows represent periodic boundary conditions in the propagation direction. Solid lines are the fully-determined loop structure, where each loop can be formed and flipped with probability 1/2. If the dashed loop is flipped, it “straightens out” the worldline segment illustrated in Fig. 7.1b, changing the off-diagonal operators (filled bars) to diagonal operators (open bars)

loops. This allows for the straightforward application of the SW algorithm to determine whether loops are flipped, as discussed above.

Note the dashed lines in Fig. 7.2 highlighting one loop structure involving the bottom two lattice sites. The worldline for this configuration, which is not illustrated, would look similar to Fig. 7.1b. However, upon flipping the dashed loop, the worldline would straighten out to be entirely contained on the second-from-bottom site. By examining the structure of the other loops in this example, one can see that loop algorithms such as this are capable of making large-scale changes in the worldline configuration. Hence, among other features, loop updates are expected to vastly increase the efficiency of worldline sampling in an SSE QMC simulation.

The interested reader can distill many of the nuances regarding implementation of the Heisenberg model with finite- $T$  SSE from the literature. In particular, the loop updates occur within an abstracted simulation cell called a “linked list” [26]. The topology of the loop structure is fixed in each linked list; it is only the diagonal update which modifies the operator positions. Hence one again sees the necessity of both types of updates in an ergodic sampling of the Heisenberg model. The full SSE update procedure typically involves a three-step process: diagonal update, creation of the linked-list, and loop update.

We note that expectation values of physical quantities can be taken at various steps in this procedure. The simplest measurements involve quantities diagonal in the basis, such as the magnetization, that can be measured at any step in the periodic propagation direction. Expectation values of Hamiltonian operators, such as the energy, can be performed by counting the number and position of operators in the  $D + 1$  simulation cell; e.g.

$$E = -\frac{\langle n \rangle}{\beta}, \quad (7.25)$$

is the internal energy, up to the constant factor added to  $H_{1,a}$  [23]. Other quantities are determined by the change in worldline structure, and are easiest measured in the loop update itself—for example the equal-time Green’s function, which is measured by keeping track of the position of the loop propagating defect in the  $D + 1$  dimensional simulation cell [19, 29, 30].

It would be possible to discuss many more interesting and important details of the SSE representation, updating, and measurement procedure, however we refer the interested reader to the literature for these. Instead, we turn to a comparison of the basic structure of the loop-algorithm SSE code, described above, to the zero-temperature formulation of the same model. As we will see, despite their formally different starting points, this comparison reveals the underlying similarity of the two methods in the SSE QMC paradigm.

### 7.3.2 Zero-Temperature Projector in the Valence Bond Basis

The beginning point of the  $T = 0$  projection, as described in Sect. 7.2.2, is to choose a trial state  $|\alpha\rangle$ , and apply a large number of Hamiltonian operators to it. For the Heisenberg (or other SU(2) Hamiltonians) a particularly convenient class of trial states are lattice coverings in the “valence bond” (VB) basis [5, 6, 31, 32], which are lists of bonds (site-pairs) covering a (bipartite) lattice. That is,

$$|\alpha\rangle = |(a_1, b_1)(a_2, b_1) \dots (a_{N/2}, b_{N/2})\rangle, \quad (7.26)$$

where each index  $(a, b)$  labels the  $a$  and  $b$  sublattice coordinate associated with a singlet state  $(|\uparrow\downarrow\rangle - |\downarrow\uparrow\rangle)/\sqrt{2}$  connecting two of the  $N$  sites. This basis happens to be non-orthogonal and massively overcomplete. Also, one can see that it is suitable for sampling bond operators of the Heisenberg Hamiltonian, which can be written in the form of a singlet projection operator,

$$\frac{1}{4} - \mathbf{S}_i \cdot \mathbf{S}_j = \frac{1}{\sqrt{2}}(|\uparrow\downarrow\rangle - |\downarrow\uparrow\rangle) \frac{1}{\sqrt{2}}(|\uparrow\downarrow\rangle - |\downarrow\uparrow\rangle), \quad (7.27)$$

where the minus sign can again be removed by an operator rotation on bipartite lattices. With this, a  $T = 0$  QMC scheme satisfying Eq. 7.14 can quickly be constructed by noting that the projection operator serves to re-arrange the end-points of the valence bonds [5]. The resulting picture becomes very much like the finite-temperature SSE, where up-spins propagating from  $\langle\alpha_\ell|$  to  $|\alpha_r\rangle$  form “worldlines” that are re-arranged by the  $2m$  operators that occur in the propagation, Eq. 7.15. Indeed, the primary differences between this scheme and the finite temperature SSE are simply:

1. A fixed value of  $m$  is used in the  $T = 0$  projector method, whereas  $n$  in the finite- $T$  SSE necessarily fluctuates.
2. The  $T = 0$  simulation cell is not periodic in the propagation direction; rather, particle “worldlines” terminate at the boundaries  $\langle\alpha_\ell|$  and  $|\alpha_r\rangle$ .

Motivated by the loop algorithm of the finite- $T$  SSE, one can then proceed with a very similar sampling scheme. First, the singlet projection operator is broken up into diagonal and off-diagonal bond operators, Eqs. 7.19 and 7.20. At this stage, one sees that it is advantageous to consider the simulation to be taking place in a *combined* VB-spin basis, since these operators will only give non-zero matrix elements when spin states on the respective sublattices are opposite [33]. As a consequence of point 2 above, we will be interested in the “middle” states of the projection to take our expectation values. These can be seen to be dependent on the particular list of bond operators for a given sample  $r$ :

$$\left( \prod_{j=1}^m H_{t_j, a_j} \right)_r |\alpha_r\rangle \propto |V_r\rangle, \quad (7.28)$$

where the proportionality constant is the numerical value for the weight of the projection.

Now, sampling can occur in analogy to the finite- $T$  SSE with both a diagonal and a loop update. The diagonal update is significantly modified from the finite-temperature case, in part because no null ( $H_{0,0}$ ) operators are included in the  $T = 0$  projection. Then, the update proceeds by traversing the operator list  $\prod_{i=1}^{2m} H_{t_i, a_i}$ , and attempting the following transitions:

1. If an off-diagonal operator  $H_{2,a}$  acting on some bond  $a$  is encountered, move on to the next operator, making sure to keep track of the associated spin state.
2. If a diagonal operator  $H_{1,a}$  is present on some bond  $a$ , pick a random bond  $a'$  containing antiparallel spins, and move the operator to it.

The diagonal update being complete, one now performs the loop update, which because of the equal matrix elements of  $H_{1,a}$  and  $H_{2,a}$ , is executed in direct analogy to the finite- $T$  SSE case. The only difference is that loops no longer connect periodically in the propagation direction; instead, they follow the valence bonds when they encounter the trial states  $|\alpha_\ell\rangle$  or  $|\alpha_r\rangle$ . As illustrated in Fig. 7.3, the resulting schematic picture of the  $D + 1$  simulation cell is, besides this lack of periodicity, essentially equivalent to Fig. 7.2.

One other important difference occurs in the calculation of observables, Eq. 7.11, which based on the fact that our trial states have been projected from the left and right by  $m$  operators, must be measured in the *middle* of the simulation cell. Expectation values of the form Eq. 7.11 are therefore written,

$$\langle \mathcal{O} \rangle = \frac{\langle V_\ell | \mathcal{O} | V_r \rangle}{\langle V_\ell | V_r \rangle}, \quad (7.29)$$

where the states are the result of a projection from each endpoint, Eq. 7.28. Remarkably, many estimators can be written as a function of the loop structure that crosses the middle of the simulation cell as in Fig. 7.3 [6, 32, 33]. For example, the spin-spin correlation function  $\mathbf{S}_i \cdot \mathbf{S}_j$  gives a value of 0 when  $i$  and  $j$  belong to different loops

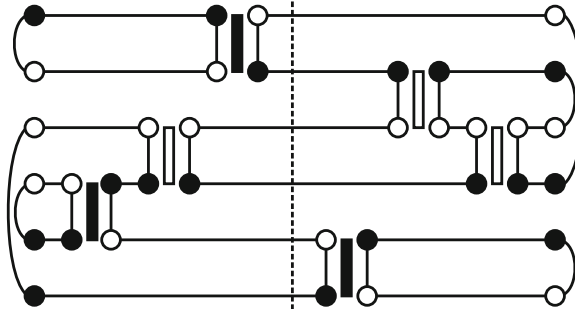


**Fig. 7.3** A  $D + 1$  projector simulation cell snapshot for a six-site Heisenberg model. Lattice sites are arranged vertically in one-dimension: at *left*, spin states are  $| \bullet \bullet \circ \circ \circ \circ \bullet \rangle$ , and at *right*,  $| \circ \bullet \bullet \circ \circ \bullet \circ \rangle$ . The propagation direction is horizontal, with  $m = 3$  operators. *Solid lines* are the fully-determined loop structure, which, when they encounter the trial states at the ends, propagate through the valence bonds (*curved lines*). The *dashed line* indicates the middle of the simulation cell, where expectation values must be measured

crossing the boundary, and either  $\pm \frac{3}{4}$  when they are in the same loop (depending on the sublattice of each spin). The expectation value of a sum of these operators for nearest neighbor pairs  $i, j$  (i.e. Eq. 7.17) can be sampled over the course of the simulation in order to obtain an estimate for the energy. Other examples of simple-to-calculate estimators include higher-order spin correlation functions (such as dimer-dimer correlation functions), the sublattice magnetization, and even the Renyi entanglement entropy in an extended simulation cell [34]. The reader is left to scour the literature for the precise procedure for calculating the expectation value of their favorite operator; we simply note here the important result that the overlap of the two valence-bond states is given by,

$$\langle V_\ell | V_r \rangle = 2^{N_{\text{loop}} - N/2}, \quad (7.30)$$

where  $N_{\text{loop}}$  is the number of loops crossing the middle of the projection (two in Fig. 7.3), and  $N$  the number of sites.

Much more discussion of the VB projector algorithm is possible, including using efficient trial states and state update, details of convergence, advanced measurement techniques, etc. However, we forgo these to continue with the broad theme of this chapter, connecting finite- $T$  and  $T = 0$  SSE. We therefore turn next to a specific implementation of a different model, to compare and contrast with the ideas introduced in this section.

## 7.4 Transverse Field Ising Model

The transverse field Ising model (TFIM) is one of the most well-studied quantum lattice model, due to the well-known mapping to a  $D + 1$  dimensional classical statistical mechanics problem, and its applicability to the field of quantum phase transitions [35]. A standard form for the Hamiltonian is,

$$H = -J \sum_{\langle i,j \rangle} \sigma_i^z \sigma_j^z - h \sum_i \sigma_i^x, \quad (7.31)$$

where  $\sigma_i$  is a Pauli spin operator, so that  $\sigma^z$  has eigenvalues  $\pm 1$ . In this equation, the first sum is over lattice *bonds*, while the second sum is over lattice *sites*. An SSE procedure for simulating the TFIM was first developed by Sandvik for the finite- $T$  representation [9]; this was subsequently adapted to a  $T = 0$  projector method, discussed in Sect. 7.4.2.

As with the Heisenberg model, both representations have a common starting point in the decomposition of the lattice Hamiltonian to bond (and site) operators. In this case,

$$H_{0,0} = I, \quad (7.32)$$

$$H_{-1,a} = h(\sigma_a^+ + \sigma_a^-), \quad (7.33)$$

$$H_{0,a} = h, \quad (7.34)$$

$$H_{1,a} = J(\sigma_i^z \sigma_j^z + 1). \quad (7.35)$$

Note that unlike the Heisenberg case, for the TFIM, the index  $a$  has two different meanings. Also, it is evident that some simple constants have been added to the Hamiltonian: the diagonal operator  $H_{0,a}$ , and also the  $+1$  in Eq. 7.35. The first results in matrix elements with equal weight for both site operators:

$$\langle \bullet | H_{-1,a} | \circ \rangle = \langle \circ | H_{-1,a} | \bullet \rangle = h, \quad (7.36)$$

$$\langle \bullet | H_{0,a} | \bullet \rangle = \langle \circ | H_{0,a} | \circ \rangle = h. \quad (7.37)$$

The latter ensures that the only non-zero matrix element for the bond operators are,

$$\langle \bullet \bullet | H_{1,a} | \bullet \bullet \rangle = \langle \circ \circ | H_{1,a} | \circ \circ \rangle = 2J. \quad (7.38)$$

These matrix elements form the basis of the SSE representation for the TFIM, by defining the weights  $W(x)$ . As for the Heisenberg model, the task is now to construct an updating procedure for QMC sampling. We will see below that a non-local update analogous to the deterministic loops will be possible; in this case however there will be branching *clusters* flipped with a SW procedure. These weights, and the updating procedure, will form a common framework for both the zero- and finite-temperature SSE procedures, outlined in the next two sections.

#### 7.4.1 Finite-Temperature SSE in the $S^z$ Basis

The finite- $T$  simulation cell is constructed in analogy to the Heisenberg model above, with  $n$  operators (of type 7.33 to 7.35) propagating the  $S^z$  basis state, and  $M - n$  null operators, 7.32. The sampling of Eq. 7.10 can then be carried out in a two-part update

sequence, similar to the Heisenberg model, but with several important differences. First, we discuss the equivalent of the *diagonal* update, and second, modifications of the non-local updating scheme which give us a *cluster* algorithm.

The diagonal update proceeds in the same spirit as Sect. 7.3.1. One traverses the list of all  $M$  operators in the propagation in sequence. If an off-diagonal operator  $H_{-1,a}$  is encountered, it is ignored (but the  $S^z$  spin associated with that site is flipped in the propagation). However, if another operator type is encountered, then a new Metropolis procedure is performed:

1. If a diagonal operator is encountered ( $H_{0,a}$  or  $H_{1,a}$ ), then it is removed with probability,

$$P = \min \left( \frac{M - n + 1}{\beta[hN + (2J)N_b]}, 1 \right), \quad (7.39)$$

where  $N$  is the number of sites, and  $N_b$  the number of bonds. One then goes to the next operator in the list (regardless of whether the removal is accepted or not).

2. If a null operator ( $H_{0,0}$ ) is encountered, try to insert a diagonal operator with the following procedure:

- (a) First the decision of what operator type to insert is made. One chooses to insert an operator of type  $H_{0,a}$  with probability,

$$P(h) = \frac{hN}{hN + (2J)N_b}, \quad (7.40)$$

or an operator of type  $H_{1,a}$  with probability,

$$P(J) = \frac{(2J)N_b}{hN + (2J)N_b}. \quad (7.41)$$

Note that  $P(h) + P(J) = 1$ .

- (b) After choosing a type, accept the addition of an operator with probability,

$$P = \min \left( \frac{\beta(hN + (2J)N_b)}{M - n}, 1 \right), \quad (7.42)$$

and randomly choose an appropriate bond or site to insert it. If it is a bond operator and the chosen bond has a local spin configuration that prevents the insertion of the operator (i.e. antiparallel spins) then we do not insert the operator and consider the move rejected.

It is clear that these local updates are again instrumental in changing the expansion order  $n$ , however they do not sample off-diagonal operators  $H_{-1,a}$ , and therefore must be combined with the use of some non-local update to produce an ergodic simulation.

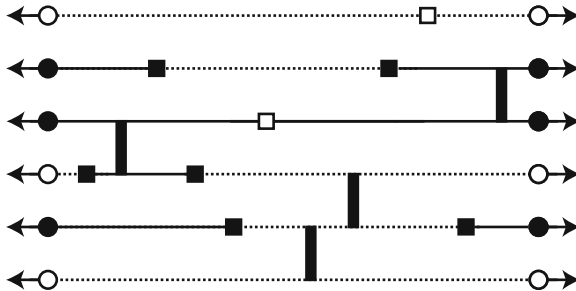


**Fig. 7.4** A  $D + 1$  SSE simulation cell snapshot for a six-site TFIM model. Lattice sites are arranged vertically in one-dimension: the propagation direction (imaginary time) is horizontal, with  $n = 12$  operators. Vertical bars are Ising bond operators  $H_{1,a}$ . Filled squares are off-diagonal site operators,  $H_{-1,a}$ , and open squares are diagonal site operators  $H_{0,a}$ . Arrows represent periodic boundary conditions in the propagation direction. Solid and dashed lines illustrate the spin states (spin up or down). Flipping all the spins associated with a cluster can be done with probability 1/2. This changes loop-terminating site operators  $H_{-1,a} \leftrightarrow H_{0,a}$ , but doesn't affect the bond operators or loop-internal site operators

We require a non-local update in analogy to the loop update of the Heisenberg model above. However, in this case, a branching *cluster* update is constructed. A cluster is formed in the  $D + 1$  simulation cell by grouping spins and operators together. It is built by starting e.g. with a site or bond operator, then finding the cluster that operator is a part of, according to a set of rules (Fig. 7.4). The two rules governing the building of clusters is: (1) clusters terminate on site-operators  $H_{-1,a}$  or  $H_{0,a}$ ; and (2) bond operators  $H_{1,a}$  belong to one cluster. This procedure continues until all clusters are identified.

The importance of including the trivial operator  $H_{0,a}$  now becomes apparent, since the matrix element of both the diagonal and off-diagonal single-site operators is  $h$ . Hence, switching between  $H_{0,a}$  and  $H_{-1,a}$  involves no weight change. With this, clusters constructed using the algorithm can be flipped with a SW procedure, as discussed previously for the Heisenberg model.

Like the loop algorithm of the Heisenberg model, we see that the topology of the cluster structure is fixed after each diagonal update. Flipping loops has the dual effect of sampling the *type* of site operator, and also sampling the spin configuration  $|\alpha\rangle$ ; however it is only the diagonal update which modifies the operator positions. The cluster update here is capable of making large-scale changes to the configuration of the simulation cell, however one again sees the necessity of both types of update in a fully ergodic sampling of the TFIM model.

We again refer the reader to seminal references for details of implementation, including the construction of the linked-list data structure which facilitates the practical construction of the clusters [9]. Note that measurements are again done in several different ways, either from the basis states directly (at any point in the propagation), by counting operators, or by looking at the cluster structure. We refer the reader to the relevant literature; instead, we now turn to a comparison of the cluster-algorithm TFIM code to a zero-temperature formulation of the same model.

### 7.4.2 Zero-Temperature Projector in the $S^z$ Basis

As realized recently [36], the finite- $T$  SSE representation of the TFIM can be straightforwardly cast in the form of a  $T = 0$  projector method. Unlike the Heisenberg model of Sect. 7.3.2, TFIM Hamiltonian operators cannot be represented as some generalized singlet projection operator, hence there is no analogous choice of basis which simplifies the sampling procedure. However, one can use a trial state which is an equal superposition of all spin states,  $|\alpha\rangle = \sum_{\{\sigma^z\}} \sigma^z$ , which simply involves storing a list of  $N$  spin states for the “left” and “right” trial state  $|\alpha_\ell\rangle$  and  $|\alpha_r\rangle$ . Note that  $\sigma^z$  configurations in the trial state are modified during the simulation by the cluster updates, as described below.

The  $D + 1$  dimensional projected simulation cell is built in a way similar to Sect. 7.3.2, where  $2m$  operators of the type 7.33 to 7.35 are sampled between the “end points” (i.e. the trial states). Recall, there are no null operators  $H_{0,0}$  in the projection scheme. Then, sampling occurs via two separate procedures as previously. First, the *diagonal update* where one traverses the list of all  $2m$  operators in the propagation direction in sequence. If an off-diagonal operator  $H_{-1,a}$  is encountered the  $\sigma^z$  spin associated with that site is flipped but no operator change is made. If a diagonal operator is encountered, the Metropolis procedure is:

1. The present diagonal operator,  $H_{0,a}$  or  $H_{1,a}$ , is removed.
2. A new operator *type* is chosen,  $t = 0$  or  $t = 1$ , corresponding to the insertion of either a diagonal  $h$  or a diagonal  $J$  operator. The transition probability to add  $H_{0,a}$  is,

$$P(h) = \frac{hN}{hN + (2J)N_b}. \quad (7.43)$$

Note,  $P(J) = 1 - P(h)$  as before.

3. If  $H_{0,a}$  is chosen, a site  $a$  is chosen at random, and the operator is placed there.
4. If  $H_{1,a}$  is chosen, a random *bond*  $a$  is chosen. The configurations of the two spins on this bond must be parallel for the matrix element to be nonzero. If they are not, then the insertion is rejected. Since no null operators are possible, steps (2)–(4) are repeated until a successful insertion is made.

The main differences between this diagonal update and that of Sect. 7.4.1 is the presence of null operators in the expansion list in the latter. However, as for the finite- $T$  SSE, one can see that this diagonal update is necessary in order to change the topology of the operator sequence in the simulation cell. In order to get fully ergodic sampling of the TFIM Hamiltonian operators, one must employ cluster updates as before.

In the  $T = 0$  projection, the cluster update is carried out in almost complete analogy to the finite- $T$  case, using a SW procedure. The main difference is that clusters terminate not only when they touch site operators, but also the spin states of the end point trial states  $|\alpha_\ell\rangle$  and  $|\alpha_r\rangle$ . We thus see how the cluster updates sample

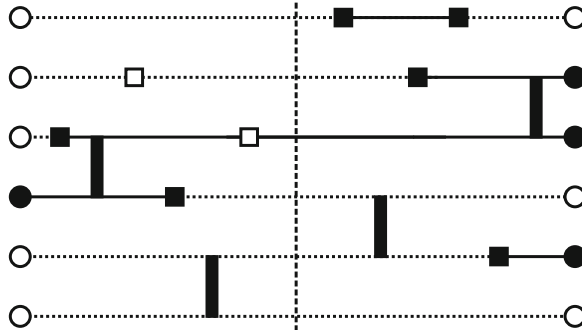


**Fig. 7.5** A  $D + 1$  projector simulation cell snapshot for a six-site TFIM model. Lattice sites are arranged vertically in one-dimension: the propagation direction (imaginary time) is horizontal, with  $m = 6$  operators. Vertical bars are Ising bond operators  $H_{1,a}$ . Filled squares are off-diagonal site operators,  $H_{-1,a}$ , and open squares are diagonal site operators  $H_{0,a}$ . Spin states are represented by solid or dashed lines (spin up or down). Flipping all the spins associated with each cluster can be done with probability 1/2. This changes site operators  $H_{-1,a} \leftrightarrow H_{0,a}$ , and also the spin states associated with  $|\alpha_\ell\rangle$  and  $|\alpha_r\rangle$

the trial state: the flipping of a cluster that extends all the way to the simulation cell end-points will flip the  $\sigma^z$  states associated with the state.

Similar to Sect. 7.3.2, measurements are made in principle in the middle of the projection, satisfying Eq. 7.11. For estimators involving basis states (e.g. the magnetization) or diagonal operators, the procedure is straightforward, and in some cases can incorporate the cluster structure at the middle of the projection. However, unlike the non-orthogonal VB basis, for off-diagonal operators, the naive expectation value can easily lead to an overlap of zero. This problem can be circumvented when operators are part of the Hamiltonian (e.g. the energy); in the interests of space however, we must leave the reader in suspense [36], or better yet, entice him or her to put down this volume, and discover the rewarding process of devising such estimators in this versatile and transparent SSE method.

## 7.5 Discussion

This chapter has aspired to give a basic flavor for the modern conceptual framework of Stochastic Series Expansion quantum Monte Carlo. Far from its first incarnations by Handscomb which were highly limited in scope, under Sandvik's tutelage it has blossomed into a widely adopted, highly general numerical framework for solving sign-problem free quantum lattice models. Remarkably, the pace of algorithmic development ceases to abate, as evident from the large number of new systems, symmetries, measurements, and models tackled almost daily with novel manifestations of the original SSE idea. Although this chapter focused on a pedagogical introduction to the framework of the simplest SSE simulations, the reader should not be fooled

by the apparent simplicity; these methods can quickly be expanded to tackle very sophisticated quantum lattice models of real interest to modern physics. Some of the most exciting recent research on exotic quantum phases and phase transitions has employed new variations of the SSE method; notable advances have recently been reviewed elsewhere [16].

Perhaps the most important take-home message of this chapter is the recent conceptual advances in unifying the traditional finite- $T$ , partition function-based SSE framework, with Sandvik's new zero-temperature projector perspective. Despite the initial apparent differences, particularly upon introduction of the valence bond projector method [5], the two paradigms have now almost completely converged, largely due to the understanding gained by considering the  $T = 0$  representation and updating procedure in terms of non-local loop structures [33]. It was the purpose of this review to emphasize this fact; the reader should be struck by the similarities between Figs. 7.2 and 7.3 for the Heisenberg SSE, and also Figs. 7.4 and 7.5 for the TFIM, which essentially differ from each other *only* in the periodicity of the boundary condition in the propagation direction.

As we move forward as a community, we can undoubtedly expect to rely more and more on SSE QMC as a mainstay of our research on quantum lattice models. This progress will likely come with a choice of  $T = 0$  or finite- $T$  frameworks for most Hamiltonians of interest. This, coupled with innovative sampling techniques, hardware advances, and of course unforeseen algorithm breakthroughs, will ensure the golden years of quantum many-body simulation still lie ahead.

**Acknowledgments** This work would not have been possible without the continuing collaboration of A. Sandvik, who is proprietor of almost every algorithmic advance outlined in the Chapter, and without who's willingness to communicate these ideas privately would have made this work impossible. I am also indebted to A. Kallin and S. Inglis for contributions to all sections of this chapter, especially the figures, and many critical readings.

## References

1. D.C. Handscomb, Proc. Cambridge Philos. Soc. **58**, 594 (1962)
2. A.W. Sandvik, J. Kurkijärvi, Phys. Rev. B **43**, 5950 (1991)
3. A.W. Sandvik, J. Phys. A **25**, 3667 (1992)
4. A.W. Sandvik, Phys. Rev. B **56**, 11678 (1997)
5. A.W. Sandvik, Phys. Rev. Lett. **95**, 207203 (2005)
6. K.S.D. Beach, A.W. Sandvik, Nucl. Phys. B **750**, 142 (2006)
7. P. Henelius, P. Fröbrich, P.J. Kuntz, C. Timm, P.J. Jensen, Phys. Rev. B **66**, 094407 (2002)
8. R.G. Melko, J. Phys. Condens. Matter **19**, 145203 (2007)
9. A.W. Sandvik, Phys. Rev. E **68**, 056701 (2003)
10. S. Wessel, F. Alet, M. Troyer, G.G. Batrouni, Phys. Rev. A **70**, 053615 (2004)
11. S. Wessel, F. Alet, S. Trebst, D. Leumann, M. Troyer, G.G. Batrouni, J. Phys. Soc. Jpn. Suppl. **74**, 10 (2005)
12. P. Pippan, H.G. Evertz, M. Hohenadler, Phys. Rev. A **80**, 033612 (2009)
13. K. Harada, N. Kawashima, M. Troyer, Phys. Rev. Lett. **90**(11), 117203 (2003)
14. N. Kawashima, Y. Tanabe, Phys. Rev. Lett. **98**, 057202 (2007)

15. R.K. Kaul, A.W. Sandvik, Phys. Rev. Lett. **108**, 137201 (2012)
16. R.K. Kaul, R.G. Melko, A.W. Sandvik, arXiv:1204.5405 (2012)
17. A.W. Sandvik, Phys. Rev. Lett. **104**, 177201 (2010)
18. J.S. Liu, *Monte Carlo Strategies in Scientific Computing* (Springer, Berlin, 2008)
19. F.F. Assaad, H.G. Evertz, in *Computational Many-Particle Physics (Lect. Notes Phys. 739)*, ed. by H. Fehske, R. Schneider, A. Weisse (Springer, Berlin, 2007), pp. 277–356
20. P. Henelius, A.W. Sandvik, Phys. Rev. B **62**, 1102 (2000)
21. N. Kawashima, K. Harada, J. Phys. Soc. Jpn. **73**, 1379 (2004)
22. H.G. Evertz, G. Lana, M. Marcu, Phys. Rev. Lett. **70**, 875 (1993)
23. A.W. Sandvik, Phys. Rev. B **59**, R14157 (1999)
24. E.L. Pollock, D.M. Ceperley, Phys. Rev. B **36**, 8343 (1987)
25. H. Evertz, Adv. Phys. **52**, 1 (2003)
26. O.F. Syljuåsen, A.W. Sandvik, Phys. Rev. E **66**, 046701 (2002)
27. R.G. Melko, A.W. Sandvik, Phys. Rev. E **72**, 026702 (2005)
28. R.H. Swendsen, J.S. Wang, Phys. Rev. Lett. **58**, 86 (1987)
29. N.V. Prokof'ev, B.V. Svistunov, I.S. Tupitsyn, Physics Letters A **238**(4–5), 253 (1998)
30. A. Dorneich, M. Troyer, Phys. Rev. E **64**, 066701 (2001)
31. S. Liang, B. Doucot, P.W. Anderson, Phys. Rev. Lett. **61**, 365 (1988)
32. A.W. Sandvik, K.S.D. Beach, in *Computer Simulation Studies in Condensed-Matter Physics XX*, ed. by D.P. Landau, S.P. Lewis, H.B. Schuttler (Springer, Berlin, 2008)
33. A.W. Sandvik, H.G. Evertz, Phys. Rev. B **82**, 024407 (2010)
34. M.B. Hastings, I. González, A.B. Kallin, R.G. Melko, Phys. Rev. Lett. **104**, 157201 (2010)
35. S. Sachdev, *Quantum Phase Transitions* (Cambridge University Press, Cambridge, 2011)
36. A.W. Sandvik, unpublished (2011)

# Chapter 8

## Variational Monte Carlo and Markov Chains for Computational Physics

Sandro Sorella

**Abstract** In this chapter the basic concepts of Markov-processes and Monte Carlo methods, as well as a detailed description of the variational Monte Carlo technique will be presented. Particular emphasis will be devoted to the apparent mystery of Monte Carlo techniques that allows us to sample a correlated many electron wave function defined in an Hilbert space that is exponentially large with the number  $N$  of electrons, in an affordable computational time, namely scaling with a modest power of  $N$ . This is a direct consequence of two key properties that are not common to all Monte Carlo techniques: (i) the possibility to define a Markov process and appropriate stochastic variables with a finite correlation time and variance, respectively; (ii) both these quantities should increase at most polynomially with  $N$ . In principle, the above properties should be proven a priori, because their numerical validations could be very difficult in practice. It will be shown that this is the case for the simplest variational Monte Carlo technique for quite generic wave functions and model Hamiltonians.

### 8.1 Introduction

In recent years we have been spectators of a very rapid growth of computer power, especially in the realization of massively parallel computers allowing to distribute several independent tasks of an algorithm over a basically unlimited number of processors. This opportunity will preserve for several decades the so called Moore's law of a constant exponential increase of computer power, despite the performances of the chip has almost reached a saturation within the silicon based technology. This new scenario, will allow us in the near future to perform computations that were essentially impossible before, but only by means of algorithms that involve scalable communications, as opposed to intrinsically limited sequential algorithms, that will probably survive this change only when the hope of quantum computation will

---

S. Sorella (✉)  
SISSA, Via Bonomea n.245, Trieste, Italy  
e-mail: sorella@sissa.it

become a bit more realistic than an academic exercise, done for fun by R. Feynmann in 1982, and still continuing to enjoy several people, without any meaningful application in computational physics so far. In electronic calculations the Monte Carlo method is the method that fulfills perfectly this requirement of scalability, because it requires a minimum amount of memory per processor and more importantly the communications remain minimal especially for high accuracy calculations. Without entering into the details of the various Monte Carlo techniques, nowadays the basic reason that, in my opinion, limits the spread out of quantum Monte Carlo in the various scientific disciplines, such as chemistry biology and physics, is the difficulty to obtain very accurate results, to the point when the statistical errors of the various target quantities become negligible. In quantum Monte Carlo statistical errors can be reduced simply by replicating the same calculation in several processors, the amount of reduction being inversely proportional to the square root of the number of processors. In this way we are not far from the date when we will obtain Monte Carlo calculations as accurate as non stochastic algorithms, and no need of statistical elaboration of the data will be necessary.

Let me emphasize further this concept, by taking as an example the present reluctance of chemists to accept Monte Carlo among the most promising and accurate techniques to deal with electronic correlation. It is clear, by reading their papers, that they really like to have methods able to fill a table with several digits, even when the last digits do not mean much, being overshooted by their approximations, such as basis sets and type of method used (e.g. Hartree-Fock or coupled clusters to mention some of them). On the other hand, I understand their point of view: with their techniques, anybody from different labs and using different computers can reproduce the same amount of irrelevant digits, though irrelevant, they are important for the sake of reliability and reproducibilities of the results. In the Monte Carlo methods, instead, nowadays often we do not have enough statistical accuracy to make clear statement about the “relevant digits” of some calculation, as, for instance, it is at present prohibitive to obtain the chemical accuracy in the total energy of a quite big molecule.

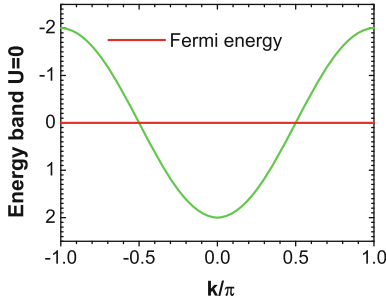
I believe that the present limitation represents only a transient period, because the progress in the parallel computation namely goes just in the right direction for the Monte Carlo methods. While the other sequential methods suffer, a reduction of the statistical error by a factor inversely proportional to the square root of processors is just guaranteed within the Monte Carlo methods. Thus the future in computer science represents a fantastic opportunity for statistical methods like quantum Monte Carlo.

## 8.2 Quantum Monte Carlo: The Variational Approach

### 8.2.1 *Introduction: Importance of Correlated Wave Functions*

The simplest and most famous Hamiltonian where the electron-electron correlations play an important role is the Hubbard model:

**Fig. 8.1** Electron band for the  $U = 0$  one dimensional Hubbard model at half-filling. All states below the Fermi energy are occupied. A metallic behavior is implied by standard band theory but the ground state of the model is a Mott insulator for  $U > 0$  [1]



$$H = -t \sum_{\langle i,j \rangle} \sum_{\sigma} (c_{i\sigma}^{\dagger} c_{j\sigma} + H.c.) + U \sum_i n_{i\uparrow} n_{i\downarrow}, \quad (8.1)$$

where  $c_{i\sigma}^{\dagger}$  ( $c_{i\sigma}$ ) creates (destroys) an electron with spin  $\sigma$  on the site  $i$ ,  $n_{i,\sigma} = c_{i\sigma}^{\dagger} c_{i\sigma}$  is the electron number operator (for spin  $\sigma$ ) at site  $i$ , and the symbol  $\langle i, j \rangle$  indicates nearest-neighbor sites. Finally, the system is assumed to be finite, with  $L$  sites, and with periodic boundary conditions.

A particularly important case is when the number  $N$  of electrons is equal to the number of sites  $L$ , a condition that is usually called *half filling* (see Fig. 8.1). In this case, the non-interacting system has a metallic ground state: for  $U = 0$ , the electronic band is half filled and, therefore, it is possible to have low-energy charge excitations near the Fermi surface. In the opposite limit, for  $t = 0$ , the ground state consists in having one electron (with spin up or down) on each site, the total energy being zero. Of course, since the total energy does not depend on the spin direction of each spin, the ground state is highly degenerate (its degeneracy is exactly equal to  $2^N$ ). The charge excitations are gapped—the lowest one corresponding to creating an empty and a doubly occupied site, with an energy cost of  $U$ —and, therefore, the ground state is insulating. This insulator state, obtained in the limit of large values of  $U/t$ , is called *Mott insulator*. In this case, the insulating behavior is due to the strong electron correlation, since, according to band theory, one should obtain a metal due to an odd number of electrons per unit cell. Because of the different behavior of the ground state in the two limiting cases,  $U = 0$  and  $t = 0$ , a metal-insulator transition is expected to appear for intermediate values of  $U/t$ . Actually, in one dimension, the Hubbard model is exactly solvable by using the so-called *Bethe Ansatz* [1], and the ground state is found to be an insulator for all  $U/t > 0$ , but, in the 2D honeycomb lattice [2, 3] or frustrated lattices [4, 5] one expects that the insulating state appears only for  $(U/t)$  above some positive critical value  $(U/t)_c$ .

Hereafter, we define an electron configuration  $|x\rangle$  as a state where all the electron *positions* and *spins* along the  $z$ -axis are defined. For instance in the one-dimensional Hubbard model, an electron configuration is determined by the position  $r_i$  of  $N$  electrons and their spins  $\sigma_i = \pm \frac{1}{2}$

$$|x\rangle = |\uparrow, \uparrow\downarrow, 0, 0, \downarrow, \dots\rangle = c_{r_1, \sigma_1}^{\dagger} c_{r_2, \sigma_2}^{\dagger} c_{r_3, \sigma_3}^{\dagger} c_{r_4, \sigma_4}^{\dagger} \cdots c_{r_N, \sigma_N}^{\dagger} |0\rangle, \quad (8.2)$$

where on each site we can have no particle (0), a singly occupied site ( $\uparrow$  or  $\downarrow$ ) or a doubly occupied site ( $\uparrow\downarrow$ ). Notice also that, due to the canonical anticommutation rules for fermions, also the order is important in the above definition of a configuration  $x$ , because an arbitrary permutation of the operators can change the overall sign of  $|x\rangle$ . We use the convention that the first fermion appears to the leftmost place and all the others in increasing order from left to right. The state  $|x\rangle$  we have written is nothing but a Slater determinant in position-spin space, where the number of doubly occupied sites  $D = \sum_i n_{i,\uparrow} n_{i,\downarrow}$  is a well defined number.

The  $U = 0$  exact ground state solution of the Hubbard model,  $|\Psi_0\rangle$ , can be expanded in terms of the complete set of configurations  $|x\rangle$ :

$$|\Psi_0\rangle = \prod_{k \leq k_F, \sigma} c_{k,\sigma}^\dagger |0\rangle = \sum_x |x\rangle \langle x| \Psi_0 \rangle. \quad (8.3)$$

In order to employ the above expansion, and to extend the wave function to generic mean field states it is more convenient to write the orbitals of the Slater determinant in a formal way:

$$|\Psi_0\rangle = \prod_{j=1}^N \left( \sum_{r,\sigma} \psi_j(r, \sigma) c_{r,\sigma}^\dagger \right) |0\rangle \quad (8.4)$$

as in the simplest case of Eq.(8.3) the real space orbitals with momentum  $k_j$  and spin  $\sigma_j$  are given by  $\psi_j(r, \sigma) = \frac{1}{\sqrt{L}} e^{ik_j r} \delta_{\sigma_j, \sigma}$  (or using sine and cosine functions for simpler real orbitals).

In the case of  $U/t \gg 1$ , this very simple wave function is not a good variational state, and the reason is that the configurations with doubly occupied states have too much weight. Indeed it is simple to verify that the average density of doubly occupied sites is 1/4 for the state  $|\Psi_0\rangle$ . Therefore, by increasing  $U/t$ , all the configurations with one or more doubly occupied sites will be “projected out” from the  $U = 0$  ansatz  $|\Psi_0\rangle$ , simply because they have a very large (of order of  $U/t$ ) average energy. A simple correlated wave function that is able to describe, at least qualitatively, the physics of the Mott insulator is the so-called *Gutzwiller wave function*. In this wave function the uncorrelated weights  $\langle x| \Psi_0 \rangle$  are modified according to the number of doubly occupied sites in the configuration  $|x\rangle$ :

$$|\Psi_g\rangle = e^{-gD} |\Psi_0\rangle = \sum_x |x\rangle e^{-g\langle x|D|x\rangle} \langle x| \Psi_0 \rangle \quad (8.5)$$

All these weights  $\langle x| \Psi_0 \rangle$  can be computed numerically by evaluating a Slater determinant  $|A|$  of a square matrix  $A$ , therefore with at most  $L^3$  floating point operations, where the  $N \times N$  matrix is given by:

$$A_{k,j} = \psi_k(r_j, \sigma_j). \quad (8.6)$$

For  $g = \infty$ , only those configurations  $|x\rangle$  without doubly occupied sites remain in the wave function, and the state is correctly an insulator with zero energy expectation value.

The importance of electronic correlation in the Gutzwiller wave function is clear: in order to satisfy the strong local constraint of having no doubly occupied sites, one has to expand the wave function in terms of a huge number of Slater determinants (in position-spin space), each satisfying the constraint. This is the opposite of what happens in a weakly correlated system, where at most a few Slater determinants (appropriately chosen) can describe qualitatively and also quantitatively the ground state.

### 8.2.2 Expectation Value of the Energy

Once a correlated wave function is defined, as in Eq. (8.5), the problem of computing the expectation value of the Hamiltonian (the variational energy) is very involved, because each configuration  $|x\rangle$  in the expansion of the wave function will contribute in a different way, due to the Gutzwiller weight  $\exp(-g\langle x|D|x\rangle)$ . In order to solve this problem numerically, we can use a Monte Carlo sampling of the huge Hilbert space containing  $4^L$  different configurations. To this purpose, using the completeness of the basis,  $\mathbf{1} = \sum_x |x\rangle\langle x|$ , we can write the expectation value of the energy, for the most general complex wave function  $\Psi_g$ , in the following way:

$$E_g = \frac{\langle \Psi_g | H | \Psi_g \rangle}{\langle \Psi_g | \Psi_g \rangle} = \frac{\langle \Psi_g | \mathbf{1} H | \Psi_g \rangle}{\langle \Psi_g | \mathbf{1} | \Psi_g \rangle} = \frac{\sum_x \langle \Psi_g | x \rangle \langle x | H | \Psi_g \rangle}{\sum_x \langle \Psi_g | x \rangle \langle x | \Psi_g \rangle} = \frac{\sum_x e_L(x) |\psi_g(x)|^2}{\sum_x |\psi_g(x)|^2}, \quad (8.7)$$

where  $\psi_g(x) = \langle x | \Psi_g \rangle$  and  $e_L(x)$  is the so-called *local energy*:

$$e_L(x) = \frac{\langle x | H | \Psi_g \rangle}{\langle x | \Psi_g \rangle}. \quad (8.8)$$

Though the Hilbert space of the Hubbard model is huge, the computation of the local energy is always polynomial in  $L$ , because the application of the Hamiltonian to a given configuration, generates only a finite number of Slater determinants  $H|x\rangle = -\sum_j t_j |x_j\rangle + UD|x\rangle$ , where the index  $j$  runs over all the nearest neighbor bonds where we can hop either a spin up or a spin down, ( $t_j = t$  if the hopping is allowed by the Pauli principle  $t_j = 0$  otherwise), thus amounting at most to  $2N_b$  different Slater determinants  $x_j$ , where  $N_b = dL$  is the number of bonds of the Hamiltonian, and  $d$  indicates the dimensionality of the lattice. Since the computation of all the resulting overlaps  $\langle x_j | \Psi_g \rangle$  in Eq. (8.8) is just given by the computation of at most  $2N_b$  Slater determinants of the type  $\langle x_j | \Psi_0 \rangle$  times the corresponding Gutzwiller factor  $\exp(-g\langle x_j | D | x_j \rangle)$ , everything requires at most  $2dL^4$  operations, if we neglect the time for computing the Gutzwiller factor, amounting to a much smaller number of operations  $\simeq L^2$ .

More efficient algorithms are based on the Sherman-Morrison algebra, allowing us to reduce the amount of computation involved to  $L^3$ . Essentially within these faster algorithms one computes each of the  $2dL$  ratios:

$$r_j = \frac{\langle x_j | \Psi_g \rangle}{\langle x | \Psi_g \rangle} \quad (8.9)$$

in  $\simeq N^2$  operations by using the inverse of the matrix  $A$  corresponding to the original configuration  $x$ , and computed once for all in  $N^3$  operations. In our experience we have also seen that a further improvement in efficiency can be obtained by updating the  $N \times 2L$  matrix:

$$W_{i,r,\sigma} = \sum_k A_{i,k}^{-1} \psi_k(r, \sigma) \quad (8.10)$$

In this way the ratio  $r_j$  corresponding to hop an electron with spin  $\sigma$  from  $r$  to  $r'$  is simply given by  $r_j = W(i, r', \sigma)$ , where  $i$  corresponds to the spin  $\sigma$  electron of the configuration  $x$  such that  $r_i = r$ . More details are given in Appendix, where all the algebra of fermion determinants, together with the Sherman-Morrison algebra is derived also for non expert in the field.

After all these technicalities, it is clear that we can generally recast the calculation of  $E_g$  as the average of a computable (in polynomial time) random variable  $e_L(x)$  over a probability distribution  $p_x$ <sup>1</sup> given by:

$$p_x = \frac{|\psi_g(x)|^2}{\sum_x |\psi_g(x)|^2}. \quad (8.11)$$

As we will show in the following, it is possible to define a stochastic algorithm (Markov chain), which generates a sequence of configurations  $\{|x_n\rangle\}$  distributed according to the desired probability  $p_x$ . Then, since the local energy can be easily computed for any given configuration, with at most  $L^3$  operations, we can evaluate the expectation value of the energy as the mean of the random variable  $e_L(x)$  over the visited configurations:

$$E_g = \frac{1}{M} \sum_{n=1}^M e_L(x_n). \quad (8.12)$$

This approach is very general and can be extended (with essentially the same definitions) to continuous systems (replace summations with multidimensional integrals), and to general Hermitian operators  $\hat{O}$  (for instance the doubly occupied site number  $D$ ), the corresponding local estimator, replacing  $e_L(x)$  in Eq. (8.12), being analogously defined:

<sup>1</sup> It is worth noticing here that  $p_x$  is generally easy to calculate up to a normalization constant, which is instead very complicated, virtually impossible, to calculate. In the present case, for instance,  $\psi_g^2(x)$  is assumed to be simple, but  $\sum_x \psi_g^2(x)$  involves a sum over the huge Hilbert space of the system, and is therefore numerically inaccessible in most cases.

$$O_L(x) = \frac{\langle x | \hat{O} | \Psi_g \rangle}{\langle x | \Psi_g \rangle}. \quad (8.13)$$

However, not all the operators can be computed in polynomial time.<sup>2</sup> With Monte Carlo we can estimate efficiently and with arbitrary small statistical accuracy  $\epsilon$  only the ones for which  $M$  is bounded by a (big) constant  $C \propto \epsilon^{-2}$  times a small power  $p$  of  $L$ , namely

$$M \leq C(\epsilon)L^p. \quad (8.14)$$

### 8.2.3 Finite Variance Property

As anticipated in the introduction one of the most important property of an efficient statistical method is that expectation values are obtained by averaging random variables with finite and small variance. We remind the reader that the variance of a stochastic variable defined over the probability  $p_x$  is just the square of its standard deviation, namely the square of its statistical error.

At this point we just notice that the average square of the local energy  $\langle |e_L(x)|^2 \rangle$ <sup>3</sup> corresponds to the exact quantum average of the Hamiltonian squared. Indeed:

$$\frac{\langle \Psi_g | H^2 | \Psi_g \rangle}{\langle \Psi_g | \Psi_g \rangle} = \frac{\sum_x \langle \Psi_g | H | x \rangle \langle x | H \Psi_g \rangle}{\sum_x \langle \Psi_g | x \rangle \langle x | \Psi_g \rangle} = \frac{\sum_x |e_L(x)|^2 |\psi_g(x)|^2}{\sum_x |\psi_g(x)|^2} = \langle |e_L(x)|^2 \rangle. \quad (8.15)$$

where here and henceforth we indicate with  $\langle O(x) \rangle$  the average of the random variable  $O(x)$  over the probability  $p_x$ , namely  $\langle O(x) \rangle = \sum_x p_x O(x)$ , so that we can also write  $E_g = \langle e_L(x) \rangle$ . Thus, the variance of the random variable  $e_L(x)$ , namely  $\text{Var}[e_L(x)] = \langle |e_L(x)|^2 \rangle - \langle e_L(x)^2 \rangle$ , is exactly equal to the quantum variance of the Hamiltonian on the variational state  $|\Psi_g\rangle$ :

$$\text{Var}[e_L(x)] = \sum_x p_x |e_L(x) - \langle e_L(x) \rangle|^2 = \frac{\langle \Psi_g | (H - E_g)^2 | \Psi_g \rangle}{\langle \Psi_g | \Psi_g \rangle} \quad (8.16)$$

From the above equation, since each bond of a lattice Hamiltonian is bounded by a constant  $\Lambda_H$ , e.g. for the Hubbard model  $\Lambda_H = 2|t| + 2|U|$ , we can safely bound the variance of the local energy by:

<sup>2</sup> For instance  $e^K$  is an example of an operator, whose expectation value cannot be computed in polynomial time (here  $K$  is for instance the kinetic energy operator). Indeed the statistical fluctuations of this operator are exponentially large for generic variational wave function  $\Psi_g$ , requiring an exponentially large  $M$ , namely  $M \geq CL^p$  for any finite  $p$  and  $C$ , and  $L$  large enough.

<sup>3</sup> Whenever the wave function  $\Psi_g$  is complex, the local energy is also complex, and all the forthcoming analysis applies, by considering that the local energy is a complex random variable, whose variance is the sum of the variance of its real and imaginary part. Notice also that the mean value of  $e_L(x)$  is real as it corresponds to the expectation value of the energy.

$$\text{Var}[e_L(x)] \leq \frac{\langle \Psi_g | H^2 | \Psi_g \rangle}{\langle \Psi_g | \Psi_g \rangle} \leq \Lambda_H^2 N_b^2 \sim L^2 \quad (8.17)$$

A closer inspection, using the cluster property, namely that the bond-bond hamiltonian correlations (e.g. local kinetic energy at a given bond) should decay with the distance between bonds, implies also a more strict (but less rigorous) inequality:

$$\text{Var}[e_L(x)] \sim L \quad (8.18)$$

The fact that the variance of the local energy is not only finite but increases slowly with the system size  $L$ , immediately implies that the standard deviation  $\sigma$  of  $E_g$  obtained after averaging the local energy  $e_L$  over a Markov chain of length  $M$  is given by:

$$\sigma \simeq K \sqrt{\tau L / M} \quad (8.19)$$

where  $K$  is a constant independent on  $L$  and  $\tau$  is the number of steps required by the Markov chain to generate a statistically independent sample. Here we arrive at the simple and important conclusion that, if  $\tau$  is also bounded, the statistical method requires a polynomial length  $M$  of the Markov chain to obtain a given statistical accuracy. It is important to remark for instance that, in order to get a given accuracy in the energy per site  $\sigma = \epsilon L$ , the length of the Markov chain is given by:

$$\begin{aligned} M &\leq C(\epsilon)/L \\ C(\epsilon) &= \frac{K^2 \tau}{\epsilon^2} \end{aligned} \quad (8.20)$$

which implies  $p = -1$  in Eq. (8.14), namely that the length of the Markov chain can be taken shorter and shorter when the size increases provided the correlation time  $\tau$  does not increase, which is typically the case for fully gapped systems. In this case the Monte Carlo method is especially convenient even for fermionic systems because, though the cost of the local energy scales as  $L^3$ , the overall amount of computation  $\simeq ML^3$  to obtain a given statistical accuracy in the energy per site scales only with  $L^2$ .

In general not all quantities and not all Markov chains have nice polynomial complexity. For instance one can use Monte Carlo to compute the normalization of the probability distribution  $Z = \sum_x \Psi_g(x)^2$ , by generating randomly configuration  $x$  with equal probability. However it is easy to realize that in this case the random variable  $\Psi_g(x)^2$  will have exponentially large variance as:

$$\frac{(\langle \Psi_g(x)^4 \rangle - \langle \Psi_g(x)^2 \rangle^2)}{\langle \Psi_g(x)^2 \rangle^2} \sim \exp(\sim L)$$

This follows from the fact that, for a many body wave function only  $\log |\Psi_g(x)|$  has fluctuations bounded by  $L$ , and therefore its exponential has exponential fluctuations.<sup>4</sup> In this case therefore, for computing  $Z$ , the Monte Carlo method is just as inefficient as the obvious method of summing the wave function square over the full Hilbert space.

Once again we remark here that it is not a general rule in Monte Carlo that we can evaluate quantities defined in an exponentially large Hilbert space with a polynomial time. In variational Monte Carlo this is given by the particularly smart choice to include in the weight  $p_x$  all the exponentially large fluctuations of the many body wave function, a scheme that was first proposed by McMillan [6]. This is why, I believe, variational Monte Carlo is a very simple, but nevertheless very robust and efficient technique.

We conclude this section, by emphasizing another important feature of the variational approach, the so-called *zero variance property*.

Suppose that the variational state  $|\Psi_g\rangle$  coincides with an exact eigenstate of  $H$  (not necessarily the ground state), namely  $H|\Psi_g\rangle = E_g|\Psi_g\rangle$ . Then, it follows that the local energy  $e_L(x)$  is constant:

$$e_L(x) = \frac{\langle x | H | \Psi_g \rangle}{\langle x | \Psi_g \rangle} = E_g \frac{\langle x | \Psi_g \rangle}{\langle x | \Psi_g \rangle} = E_g. \quad (8.21)$$

Therefore, the random variable  $e_L(x)$  is independent on  $|x\rangle$ , which immediately implies that its variance is zero, and its mean value  $E_g$  coincides with the exact eigenvalue. Clearly the closer is the variational state  $|\Psi_g\rangle$  to an exact eigenstate, the smaller the variance of  $e_L(x)$  will be, namely the constant  $C$  will be suppressed in Eq. (8.19), and this is very important to reduce the statistical fluctuations and improve the numerical efficiency.

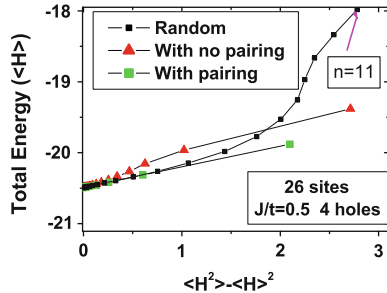
From the variational principle, the lower the energy is the better the variational state will be, but, without an exact solution or other inputs, it is hard to judge how accurate the variational approximation is. On the contrary, the variance is very useful, because the smallest possible variance, equal to zero, is known *a priori*, and in this case the variational state represents an exact eigenstate of the hamiltonian.

As shown in Ref. [7] it is possible to define, by means of a stochastic implementation of the Lanczos algorithm, a sequence of variational states that systematically converge to the exact ground state as can be clearly displayed in a plot of the energy as a function of its variance. As a matter of fact, the extrapolation to zero variance with few Lanczos steps allows us, in most cases, to reach very accurate estimates of the energy, as shown in Fig. (8.2).

---

<sup>4</sup> In order to convince ourselves of this property with a more careful analysis, we can just assume that  $\log|\Psi_g(x)|$  is a Gaussian random variable with given mean value and variance  $\simeq L$ . Then the statement immediately follows after simple integration of Gaussian functions.

**Fig. 8.2** Energy as a function of variance in the t-J model, showing that, for good variational wave functions, only few Lanczos steps are required to obtain a very good estimate of the exact ground state energy



### 8.3 Markov Chains: Stochastic Walks in Configuration Space

In the first section we have emphasized one of the two main points of this chapter. We know want to tackle the more important problem that the correlation time  $\tau$  in the expression (8.19) for the standard deviation should also be finite. This is a much more difficult task, but is general enough, to be presented in an introduction to the variational Monte Carlo method. As we will see in the following, in all the forthcoming section, it will be rigorously proven that the correlation time  $\tau$  is finite, but no rigorous statement bounding the length of the correlation time will be possible.

A Markov chain is a non deterministic dynamics, for which a random variable, denoted by  $x_n$ , evolves as a function of a discrete iteration time  $n$ , according to a stochastic dynamics given by:

$$x_{n+1} = F(x_n, \xi_n). \quad (8.22)$$

Here  $F$  is a known given function, independent of  $n$ , and the stochastic nature of the dynamics is due to the  $\xi_n$ , which are random variables (quite generally,  $\xi_n$  can be a vector whose coordinates are independent random variables), distributed according to a given probability density  $\chi(\xi_n)$ , independent on  $n$ . The random variables  $\xi_n$  at different iteration times are independent (they are independent realizations of the same experiment), so that, e.g.,  $\chi(\xi_n, \xi_{n+1}) = \chi(\xi_n)\chi(\xi_{n+1})$ . In the following, for simplicity of notations, we will indicate  $x_n$  and  $\xi_n$  as simple random variables, even though they can generally represent multidimensional random vectors. Furthermore, we will also consider that the random variables  $x_n$  assume a discrete set of values,<sup>5</sup> as opposed to continuous ones, as in the latter case multidimensional integrals should replace the much simpler summations. After that substitutions the generalization to continuous systems is rather obvious.

It is simple to simulate a Markov chain on a computer, by using the so-called *pseudo-random number generator* for obtaining the random variables  $\xi_n$ , and this is the reason why Markov chains are particularly important for Monte Carlo

<sup>5</sup> For instance  $\{x_n\}$  defines the discrete Hilbert space of the variational wave function in a finite lattice Hamiltonian.

calculations. Indeed, we will see that, by using Markov chains, we can easily define random variables  $x_n$  that, after the so called “equilibration time”, namely for  $n$  large enough, will be distributed according to any given probability density  $\bar{\rho}(x_n)$  (in particular, for instance, the one which is required for the variational calculation in Eq. (8.11)).

The most important property of a Markov chain is that the random variable  $x_{n+1}$  depends only on the previous one,  $x_n$ , and on  $\xi_n$ , but not on quantities at time  $n - 1$  or before. Though  $\xi_{n+1}$  and  $\xi_n$  are independent random variables, the random variables  $x_n$  and  $x_{n+1}$  are *not independent*; therefore we have to consider the generic joint probability distribution  $f_n(x_{n+1}, x_n)$ , and decompose it into the product of the marginal probability

$$\rho_n(x_n) = \sum_{x_{n+1}} f_n(x_{n+1}, x_n) \quad (8.23)$$

of the random variable  $x_n$ , namely the probability to have  $x_n$  regardless the value of  $x_{n+1}$ , times the conditional probability  $K(x_{n+1}|x_n)$  defined basically from the following equation:

$$f_n(x_{n+1}, x_n) = K(x_{n+1}|x_n) \rho_n(x_n). \quad (8.24)$$

implying immediately that  $K$  is normalized, i.e.  $\sum_{x_{n+1}} K(x_{n+1}|x_n) = 1$ , easily verified by summing both sides of the above equation, and using the definition of marginal probability. Therefore  $K$  represents the probability to find the configuration  $x_{n+1}$  once at the iteration  $n$  of the Markov chain the configuration is constrained to be at  $x_n$ .

For readers non familiar with probability notations, one has only to remind that  $K$  is nothing but a function of two variables  $x_n$  and  $x_{n+1}$ . At variance of common functions of two arguments the left argument is different from the right one since the function  $K$  is normalized only with respect to the left argument, and that's why one uses the pipe instead of the comma in order to distinguish the two arguments of a conditional probability. Apart from this technical notations, the most important property of the conditional probability  $K$  is that it does not depend on  $n$ , as a consequence of the Markovian nature of Eq. (8.22), namely that the function  $F$  and the probability density  $\chi$  of the random variable  $\xi_n$  do not depend on  $n$ .

We are now in the position of deriving the so-called *Master equation* associated to a Markov chain. Indeed the marginal probability of the variable  $x_{n+1}$  is given by  $\rho_{n+1}(x_{n+1}) = \sum_{x_n} f(x_{n+1}, x_n)$ , so that, using Eq. (8.24), we get:

$$\rho_{n+1}(x_{n+1}) = \sum_{x_n} K(x_{n+1}|x_n) \rho_n(x_n). \quad (8.25)$$

Thus the Master equation allows us to calculate the evolution of the marginal probability  $\rho_n$  as a function of  $n$ , since the conditional probability  $K(x'|x)$  is uniquely determined by the stochastic dynamics in Eq. (8.22). More precisely, though the actual value of the random variable  $x_n$  at the iteration  $n$  is not known deterministi-

cally, the probability distribution of the random variable  $x_n$  is instead known *in all details*, in principle, at each iteration  $n$ , once an initial condition is given, for instance at iteration  $n = 0$ , through a  $\rho_0(x_0)$ . The solution for  $\rho_n(x_n)$  is then obtained iteratively by solving the Master equation, starting from the given initial condition up to the desired value of  $n$ .

### 8.3.1 Detailed Balance and Effective Hamiltonian

At this point a quite natural question arises, concerning the existence of a limiting distribution reached by  $\rho_n(x)$ , upon iterating the Master equation for sufficiently large  $n$ : Does  $\rho_n(x)$  converge to some limiting distribution  $\bar{\rho}(x)$  as  $n$  gets large enough? The question is actually twofold: (i) Does it exist a stationary distribution  $\bar{\rho}(x)$ , i.e., a distribution which satisfies the Master equation (8.25) when plugged in both the right-hand and the left-hand side? (ii) Starting from a given arbitrary initial condition  $\rho_0(x)$ , under what conditions it is guaranteed that  $\rho_n(x)$  will converge to  $\bar{\rho}(x)$  as  $n$  increases? The first question (i) requires:

$$\bar{\rho}(x_{n+1}) = \sum_{x_n} K(x_{n+1}|x_n) \bar{\rho}(x_n). \quad (8.26)$$

In order to satisfy this stationarity requirement, it is sufficient (but not necessary) to satisfy the so-called *detailed balance* condition:

$$K(x'|x) \bar{\rho}(x) = K(x|x') \bar{\rho}(x'). \quad (8.27)$$

This relationship indicates that the number of processes undergoing a transition  $x \rightarrow x'$  has to be exactly compensated, to maintain a stable stationary condition, by the same amount of reverse processes  $x' \rightarrow x$ ; the similarity with the Einstein's relation for the problem of radiation absorption/emission in atoms is worth to be remembered.

It is very simple to show that the detailed balance condition allows a stationary solution of the Master equation. Indeed, if for some  $n$  we have that  $\rho_n(x_n) = \bar{\rho}(x_n)$ , then:

$$\rho_{n+1}(x_{n+1}) = \sum_{x_n} K(x_{n+1}|x_n) \bar{\rho}(x_n) = \bar{\rho}(x_{n+1}) \sum_{x_n} K(x_n|x_{n+1}) = \bar{\rho}(x_{n+1}), \quad (8.28)$$

where we used the detailed balance condition (8.27) for the variables  $x' = x_{n+1}$  and  $x = x_n$ , and the normalization condition for the conditional probability  $\sum_{x_n} K(x_n|x_{n+1}) = 1$ .

The answer to question (ii) is quite more complicated in general. In this context it is an important simplification to consider that the conditional probability function  $K(x'|x)$ , satisfying the detailed balance condition (8.27), can be written in terms of a symmetric function  $\tilde{H}_{x',x} = \tilde{H}_{x,x'}$  apart for a similarity transformation:

$$K(x'|x) = -\bar{H}_{x',x} \psi_0(x')/\psi_0(x) \quad (8.29)$$

where  $\bar{H}_{x',x} < 0$  and  $\psi_0(x) = \sqrt{\rho(x)}$  is a positive function which is non zero for all configurations  $x$ , and is normalized  $\sum_x \psi_0^2(x) = 1$ . Though the restriction to satisfy the detailed balance condition is not general, it basically holds in many applications of the Monte Carlo technique, as we will see in the following.

The function  $\bar{H}_{x',x}$ , being symmetric, can be thought as the matrix elements of an effective Hamiltonian with non positive off diagonal matrix elements. The ground state of this fictitious hamiltonian will be bosonic (i.e. non negative for each element  $x$ ) for well known properties of quantum mechanics that we will briefly remind here. This “bosonic” property of the ground state will be very useful to prove the convergence properties of a Markov chain described by (8.29). Indeed due to the normalization condition  $\sum_{x'} K(x', x) = 1$ , the positive function  $\psi_0(x)$  is just the bosonic ground state of  $\bar{H}$  with eigenvalue  $\lambda_0 = -1$ . We indicate with  $\lambda_M$  also the maximum eigenvalue and prove also that  $\lambda_M < 1$ .

It is simple to show that no eigenvalue  $\lambda_i$  of  $\bar{H}$  can be larger than 1 in modulus, namely  $|\lambda_i| \leq 1$ . Indeed suppose it exists an eigenvector  $\psi_i(x)$  of  $H$  with maximum modulus eigenvalue  $|\lambda_i| > 1$ , then:

$$|\lambda_i| = \left| \sum_{x,x'} \psi_i(x) (-\bar{H}_{x,x'}) \psi_i(x') \right| \leq \sum_{x,x'} |\psi_i(x)| (-\bar{H}_{x,x'}) |\psi_i(x')| \quad (8.30)$$

Thus  $|\psi_i(x)|$  may be considered a trial state with expectation value of the energy larger or equal than  $|\lambda_i|$  in modulus. Since the matrix  $\bar{H}$  is symmetric, by the well known properties of the minimum/maximum expectation value, this is possible only if the state  $\psi_{Max}(x) = |\psi_i(x)|$  with all non negative elements is also an eigenstate with maximum eigenvalue  $|\lambda_i|$ . By assumption we know that  $\psi_0(x)$  is also an eigenstate with all positive elements and therefore the assumption of  $|\lambda_i| > 1$  cannot be fulfilled as the overlap between eigenvectors corresponding to different eigenvalues has to be zero and instead  $\sum_x \psi_0(x) \psi_{Max}(x) > 0$ . Thus we conclude that  $|\lambda_i| \leq 1$  for all eigenvalues and, if the equality holds for some  $i$ , namely  $|\lambda_i| = 1$ , this is possible only if  $\lambda_i = -1$ , otherwise  $\psi_{Max}(x)$  would correspond to the maximum eigenvalue  $\lambda_M = 1$ , that is not possible for the same orthogonality condition between eigenvectors corresponding to different eigenvalues  $\lambda_0 = -1$  and  $\lambda_M = 1$ . Therefore  $\psi_0(x)$  is a bosonic ground state of  $\bar{H}$ , that can be at most degenerate, and  $\lambda_M < 1$ , as we have anticipated.

The possibility to have a degenerate ground state of  $\bar{H}$  would not lead to a unique stationary distribution, because, as it is obvious, any arbitrary linear combination of the degenerate ground state manifold defines a stationary equilibrium distribution  $\rho_0 = \psi_0^2$ . Therefore a further assumption is required to show that a unique equilibrium density distribution  $\bar{\rho}(x)$  can be reached for large  $n$ .

The second important condition that should be satisfied in order to generate the desired equilibrium probability  $\rho_0$  is that the Markov chain should be *ergodic*, i.e., any configuration  $x'$  can be reached, in a sufficiently large number of Markov iterations,

starting from any initial configuration  $x$ . This implies that  $\psi_0(x)$  is the *unique* ground state of  $\bar{H}$ , a theorem known as the Perron-Frobenius. To prove this theorem, we notice first that if a ground state  $\psi_0(x) \geq 0$  is non negative for any  $x$ , then it has to be strictly positive  $\psi_0(x) > 0$ . In fact suppose  $\psi_0(x) = 0$  for some  $x = x_0$ . By using that  $\psi_0$  is an eigenstate of  $\bar{H}$ , we have:

$$\sum_{x(\neq x_0)} \bar{H}_{x_0,x} \psi_0(x) = \lambda_0 \psi_0(x_0) = 0$$

so that, in order to fulfill the previous condition,  $\psi_0(x) = 0$  for all configurations connected to  $x_0$  by  $\bar{H}$ , since  $\psi_0(x)$  is non negative and  $-\bar{H}_{x_0,x}$  is strictly positive. By applying iteratively the previous condition to the new configurations connected with  $x_0$ , we can continue, by using ergodicity, to have that

$$\bar{\psi}_0(x) = 0$$

for *all* configurations, and this is not possible for a normalized eigenstate.

Now suppose that there exists another ground state  $\psi'_0(x)$  of  $\bar{H}$  different from  $\psi_0(x)$ . Then, by linearity and for any constant  $\lambda$ , also  $\psi_0(x) + \lambda\psi'_0(x)$ , if non-vanishing, is a ground state of  $\bar{H}$ , so that by the previous discussion also the state  $\bar{\psi}(x) = |\psi_0(x) + \lambda\psi'_0(x)|$  is a non negative ground state of  $\bar{H}$ . However the constant  $\lambda$  can be chosen to have  $\bar{\psi}(x) = 0$  for a particular configuration  $x = x_0$ , as we have shown that  $\psi_0(x) \neq 0$  for all  $x$ . This is not possible unless  $\bar{\psi}(x) = 0$  for all  $x$ , because otherwise  $\bar{\psi}(x) \geq 0$  would be a non negative eigenstate that vanishes for  $x = x_0$ , which contradicts what we have proved at the beginning for these particular ground state wave functions. Therefore,  $\bar{\psi}(x) = 0$  for all  $x$  implies that  $\psi_0(x)$  and  $\psi'_0(x)$  differ at most by an overall constant  $-\lambda$  and we finally conclude that  $\psi_0(x)$  is the unique ground state of  $\bar{H}$ .

We have finally derived that if ergodicity and detailed balance hold, the ground state of the fictitious hamiltonian  $\bar{H}$  (8.29) is unique and equal to  $\psi_0(x)$  with eigenvalue  $\lambda_0 = -1$ , and  $\lambda_M < 1$ . This implies, as readily shown later on, that any initial  $\rho_0(x)$  will converge in the end towards the limiting stationary distribution  $\bar{\rho}(x) = \psi_0(x)^2$ . In fact:

$$\rho_n(x') = \sum_x \psi_0(x') [ -\bar{H}]_{x',x}^n / \psi_0(x) \rho_0(x) \quad (8.31)$$

where the  $n$ th power of the matrix  $\bar{H}$  can be expanded in terms of its eigenvectors:

$$[ -\bar{H}]_{x',x}^n = \sum_i (-\lambda_i)^n \psi_i(x') \psi_i(x) \quad (8.32)$$

Since  $\psi_0(x)$  is the unique eigenvector with eigenvalue  $\lambda_0 = -1$ , by replacing the expansion (8.32) in (8.31) we obtain:

$$\rho_n(x) = \psi_0(x) \sum_i \psi_i(x) (-\lambda_i)^n \left[ \sum_{x'} \psi_i(x') \rho_0(x') / \psi_0(x') \right] \quad (8.33)$$

Thus for large  $n$  only the  $i = 0$  term remains in the above summation and all the other ones decay exponentially as  $|\lambda_i| < 1$  for  $i \neq 0$ . It is simple then to realize that for large  $n$

$$\rho_n(x) = \psi_0^2(x) \quad (8.34)$$

as the initial distribution is normalized and:

$$\left[ \sum_{x'} \psi_0(x') \rho_0(x') / \psi_0(x') \right] = \sum_{x'} \rho_0(x') = 1$$

Summarizing, if a Markov chain satisfies detailed balance and is ergodic, then the equilibrium distribution  $\bar{\rho}(x)$  will be always reached, for large enough  $n$ , independently of the initial condition at  $n = 0$ . The convergence is always exponential and indeed the dynamic has a well defined finite correlation time  $\tau = \text{Max}_{i \neq 0} - \ln \lambda_i$  corresponding to the first excitation of the hamiltonian matrix  $\tilde{H}_{x',x}$ .

It is not possible to quantify rigorously the length of the correlation time but, since the effective hamiltonian  $\tilde{H}$  associated to the Markov chain, is usually very similar to the physical one,<sup>6</sup> namely containing only nearest neighbor hoppings, we can use physical insights to guess how the gap  $\Delta \simeq \frac{1}{\tau}$  scales as a function of the number of electrons and/or lattice sites  $L$ :

- Standard band insulators or non conventional ground state with a finite gap to all excitations. In this case the correlation time is essentially independent of  $L$ , and the Monte Carlo method is mostly effective.
- Gapless phases due for instance to broken symmetry phase of matter (e.g. superconducting, magnetic etc.) or simple metals, or gapless spin liquids. In such a case we can estimate how the gap scales with the system size by assuming that the gapless excitations have a well defined dynamical critical exponent  $z$ . In a model with translation symmetry and physical spatial dimension  $d$  this is equivalent to know how the excitation spectrum  $\epsilon_k$  behaves at small momenta, namely  $\epsilon_k \simeq |k|^z \simeq L^{-z/d}$  (as the minimum non zero value of  $|k|$  is  $2\pi/L^{1/d}$ ), so that for instance  $z = 1$  ( $z = 2$ ) for the quantum antiferromagnet (ferromagnet) and the superconductor in a short range model (as the plasmon is gapless). The lowest gap  $\Delta$  to the physical excitations has to contain an elementary one with non zero momentum and therefore scales to zero with a law depending only on the dynamical critical exponent  $z$ , implying that:

---

<sup>6</sup> Since we have shown that the effective Hamiltonian has eigenvalues bounded by 1, whereas the physical Hamiltonian has extensive eigenvalues  $\simeq L$ , in the following discussion we assume that the gap of the effective Hamiltonian is also scaled by  $1/L$  that may be simply compensated from the choice to employ of the order of  $L$  Markov steps before computing a new value of the local energy, requiring always  $\simeq L^3$  operations.

$$\tau \simeq L^{z/d} \quad (8.35)$$

We arrive therefore quite generally to the conclusion that, within the variational Monte Carlo technique, the computer time (CPU) required for evaluating the energy per site, or any intensive thermodynamic quantity, with a given accuracy  $\epsilon$ , scales with  $L$  as:

$$CPU \simeq L^{2+z/d} \quad (8.36)$$

where we have inserted Eq. (8.35) in Eq. (8.20), and used that the cost for computing the local energy is  $\simeq L^3$  for fermionic systems (see Appendix). In practice the method has always polynomial complexity provided the dynamical critical exponent is finite.

- From the above argument an exponentially hard case is possible only in exceptional cases, when the Hamiltonian  $H$  has an exponentially small gap  $\Delta \simeq \exp(-\sim L)$ , namely a divergent dynamical critical exponent  $z$ . To my knowledge, among translationally invariant models without disorder, only the spectrum of the Heisenberg model in the Kagome' lattice [8] seems to display an exponentially large number of singlet excitations before the triplet gap, implying a singlet gap decreasing at least exponentially with the number of spins  $L$ . However this scenario has recently been ruled out by DMRG calculation on much larger cluster sizes [9].

On the other hand, in disordered systems, a very simple hamiltonian exists that have a full gap in all phases but at the critical point:

$$H = \sum_i J_i S_i^z S_{i+1}^z + h_i S_i^x \quad (8.37)$$

This model is defined with appropriate random couplings  $J_i$  and  $h_i$  [10–12], and close to the critical point the typical gap scales as:

$$\Delta \simeq \xi^{-z}, \quad (8.38)$$

where  $\xi$  is the correlation length and both  $z$  and  $\xi$  diverge at the critical point. Exactly at the critical point the quantum Monte Carlo becomes therefore an exponentially hard method. However it is clear from the above discussion and the present knowledge of quantum many-body physics that an infinite dynamical critical exponent  $z$  cannot define a stable phase apart for particular critical points, and this represents in most cases an irrelevant limitation. I believe in fact that the main purpose of numerical simulation of quantum many-body systems is to characterize non trivial phases of matter, that are genuinely driven by strong electron correlation and are stable against small perturbations (i.e. far from a critical point). The problem of phase transition and critical behavior, seems too much difficult for numerical methods, as it is much better understood by conventional field theory and renormalization group approaches.

As a result of the above considerations and the rigorous statements proved so far, we can fairly introduce the Metropolis algorithm [13], as a general and powerful Monte Carlo tool, used in particular for sampling in a polynomial time an exponentially large Hilbert space, within the variational quantum Monte Carlo method.

## 8.4 The Metropolis Algorithm

Suppose we want to generate a Markov chain such that, for large  $n$ , the configurations  $x_n$  are distributed according to a given probability distribution  $\bar{\rho}(x)$ . We want to construct, accordingly, a conditional probability  $K(x'|x)$  satisfying the detailed balance condition Eq. (8.27) with the desired  $\bar{\rho}(x)$ . How do we do that, in practice? In order to do that, Metropolis and collaborators introduced a very simple scheme [14]. They started considering a transition probability  $T(x'|x)$ , defining the probability of going to  $x'$  given  $x$ , which can be chosen with great freedom, as long as ergodicity is ensured, without any requirement of detailed balance. In order to define a Markov chain satisfying the detailed balance condition, the new configuration  $x'$  generated by the chosen transition probability  $T(x'|x)$  is then accepted only with a probability:

$$A(x'|x) = \text{Min} \left\{ 1, \frac{\bar{\rho}(x')T(x|x')}{\bar{\rho}(x)T(x'|x)} \right\}, \quad (8.39)$$

so that the resulting conditional probability  $K(x', x)$  is given by:

$$K(x'|x) = A(x'|x) T(x'|x) \quad \text{for } x' \neq x. \quad (8.40)$$

The value of  $K(x'|x)$  for  $x' = x$  is determined by the normalization condition  $\sum_{x'} K(x'|x) = 1$ . The proof that detailed balance is satisfied by the  $K(x'|x)$  so constructed is quite elementary, and is left to the reader. It is also simple to show that the conditional probability  $K(x'|x)$  defined above can be casted in the form (8.29), for which, in the previous section, we have proved that the equilibrium distribution can be always reached after many iterations. In particular:

$$\psi_0(x) = \sqrt{\bar{\rho}(x)} \quad (8.41)$$

$$\tilde{H}(x', x) = -A(x'|x)T(x'|x)\psi_0(x)/\psi_0(x') \quad (8.42)$$

In fact from the definition of the acceptance probability (8.39), it is simple to verify that  $\tilde{H}$  in (8.41) is symmetric and that the results of the previous section obviously hold also in this case.

Summarizing, if  $x_n$  is the configuration at time  $n$ , the Markov chain iteration is defined in two steps:

1. A *move* is proposed by generating a configuration  $x'$  according to the transition probability  $T(x'|x_n)$ ;

2. The move is *accepted*, and the new configuration  $x_{n+1}$  is taken to be equal to  $x'$ , if a random number  $\xi_n$  (uniformly distributed in the interval  $(0, 1]$ ) is such that  $\xi_n \leq A(x'|x_n)$ , otherwise the move is *rejected* and one keeps  $x_{n+1} = x_n$ .

The important simplifications introduced by the Metropolis algorithm are:

1. It is enough to know the desired probability distribution  $\bar{\rho}(x)$  up to a normalization constant, because only the ratio  $\frac{\bar{\rho}(x')}{\bar{\rho}(x)}$  is needed in calculating the acceptance probability  $A(x'|x)$  in Eq. (8.39). This allows us to avoid a useless, and often computationally prohibitive, normalization (e.g., in the variational approach, the normalization factor  $\sum_x \psi_g^2(x)$  appearing in Eq. (8.11) needs not be calculated).
2. The transition probability  $T(x'|x)$  can be chosen to be very simple. For instance, in a one-dimensional example on the continuum, a new coordinate  $x'$  can be taken with the rule  $x' = x + a\xi$ , where  $\xi$  is a random number uniformly distributed in  $(-1, 1)$ , yielding  $T(x'|x) = 1/2a$  for  $x - a \leq x' \leq x + a$ . In this case, we observe that  $T(x'|x) = T(x|x')$ , a condition which is often realized in practice. Whenever the transition probability is symmetric, i.e.,  $T(x'|x) = T(x|x')$ , the factors in the definition of the acceptance probability  $A(x'|x)$ , Eq. (8.39), further simplify, so that

$$A(x'|x) = \text{Min} \left\{ 1, \frac{\bar{\rho}(x')}{\bar{\rho}(x)} \right\}.$$

In the particular example of the Hubbard model, and typically any lattice model, in order to define  $T(x'|x) = T(x|x')$  one can generate randomly a bond and the spin  $\sigma$  of the electron to be moved. Since ratio of determinants can be computed very efficiently, as discussed in Appendix, it is not very important that the acceptance rate is quite small in this case, as most of the computation is spent only when the move is accepted.

3. As in the example shown in the previous point, the transition probability  $T(x'|x)$  allows us to impose that the new configuration  $x'$  is very close to  $x$ , at least for  $a$  small enough. In this limit, all the moves are always accepted, since  $\bar{\rho}(x')/\bar{\rho}(x) \approx 1$ , and the rejection mechanism is ineffective. A good rule of thumb to speed up the correlation time  $\tau$ , i.e., the number of iterations needed to reach the equilibrium distribution, is to tune the transition probability  $T$ , for instance by increasing  $a$  in the above example, in order to have an average acceptance rate  $\langle A \rangle = 0.5$ , which corresponds to accepting, on average, only half of the total proposed moves. This criterium is usually the optimal one for computational purposes, but it is not a general rule.

## 8.5 Stochastic Minimization of the Energy

In this section we introduce the *stochastic reconfiguration* method for the minimization of the total energy, a method that can be easily applied to lattice models [7] and recently extended also to continuous ones [15].

Let  $\Psi_g(\alpha^0)$  be the wave function depending on an initial set of  $p$  variational parameters  $\{\alpha_k^0\}_{k=1,\dots,p}$ . Consider now a small variation of the parameters  $\alpha_k = \alpha_k^0 + \delta\alpha_k$ . The corresponding wave function  $\Psi_g(\alpha)$  is equal, within the validity of the linear expansion, to the following one:

$$\Psi'_g(\alpha) = \left( \Psi_g(\alpha^0) + \sum_{k=1}^p \delta\alpha_k \frac{\partial}{\partial\alpha_k} \Psi_g(\alpha^0) \right) \quad (8.43)$$

Therefore, by introducing local operators defined on each configuration  $x$  as the logarithmic derivatives with respect to the variational parameters<sup>7</sup>:

$$O^k(x) = \frac{\partial}{\partial\alpha_k} \ln \Psi_g(x) \quad (8.44)$$

and for convenience the identity operator  $O^0 = 1$ , we can write  $\Psi'_g$  in a more compact form:

$$|\Psi'_g(\alpha)\rangle = \sum_{k=0}^p \delta\alpha_k O^k |\Psi_g\rangle, \quad (8.45)$$

where  $|\Psi_g\rangle = |\Psi_g(\alpha_0)\rangle$  and  $\delta\alpha_0 = 1$ . However, as a result of the iterative minimization scheme we are going to present,  $\delta\alpha_0 \neq 1$ , and in that case the variation of the parameters will be obviously scaled

$$\delta\alpha_k \rightarrow \frac{\delta\alpha_k}{\delta\alpha_0} \quad (8.46)$$

and  $\Psi'_g$  will be proportional to  $\Psi_g(\alpha)$  for small  $\frac{\delta\alpha_k}{\delta\alpha_0}$ .

Our purpose is to set up an iterative scheme to reach the minimum possible energy for the parameters  $\alpha$ , exploiting the linear approximation for  $\Psi_g(\alpha)$ , which will become more and more accurate close to the convergence, when the variation of the parameters is smaller and smaller. At a given iteration, we project the wave function change produced by the operator  $\Lambda I - H$  in the linear space defined above, by means of a formal projection operator  $P$ , such that  $P^2 = P$ , that satisfies

$$\langle \Psi_g | O_k P = \langle \Psi_g | O_k \quad (8.47)$$

<sup>7</sup> For the wave function defined in Eq. 8.5, to the Gutzwiller variational parameter  $g$  is associated an operator  $O_g(x) = -\langle x|D|x\rangle$ , namely minus the number of doubly occupied sites in the configuration  $|x\rangle$ .

for any  $k = 0, \dots, p$ . In this way, the state

$$|\Psi'_g\rangle = P(\Lambda - H)|\Psi_g\rangle \quad (8.48)$$

where  $\Lambda$  is a suitable large shift has an energy lower than  $\Psi_g$  [7], provided the constant shift  $\Lambda$  is large enough, as we assume. In a continuous system, even if its energy is unbounded from above,  $\Lambda$  can be finite due to the projection  $P$  because the Hamiltonian diagonalized in the basis (8.47) is bounded from above as in a lattice system. In order to determine the coefficients  $\{\delta\alpha_k\}_{k=1,\dots,p}$  corresponding to  $\Psi'_T$  defined in Eq. 8.48, we can overlap both sides of Eq. (8.48) with the set of states  $\langle\Psi_g|O_k$  for  $k = 0, 1, \dots, p$ , so that, reminding Eq. (8.47), we are led to solve the following conditions:

$$\langle\Psi_g|O^k(\Lambda - H)|\Psi_g\rangle = \langle\Psi_g|O^k|\Psi'_g\rangle \quad \text{for } k = 0, \dots, p \quad (8.49)$$

Hence, by substituting in the above equation the expansion of  $\Psi'$  in the form given by Eq. (8.45), we arrive at the a simple linear system:

$$\sum_l \delta\alpha_l s_{l,k} = f^k, \quad (8.50)$$

where  $s_{l,k} = \frac{\langle\Psi_g|O^l O^k|\Psi_g\rangle}{\langle\Psi_g|\Psi_g\rangle}$  is the covariance matrix and  $f^k = \frac{\langle\Psi_g|O^k(\Lambda - H)|\Psi_g\rangle}{\langle\Psi_g|\Psi_g\rangle}$  is the known term; both  $s_{l,k}$  and  $f^k$  are computed stochastically by the same Monte Carlo sampling used for the calculation of the energy, namely by generating configurations according to the probability  $p_x$  defined in Eq. (8.11), and by averaging the estimators  $O_k(x)O_{k'}(x)$  and  $O_k(x)(\Lambda - e_L(x))$  for the matrix elements  $s_{k,k'}$  and the force components  $f_k$ , respectively. Better sampling are also possible in this case, as the estimator of the forces  $f_k$  and the matrix  $s_{k,k'}$  may acquire infinite variance and may be problematic in some cases.<sup>8</sup> This problem can be solved by a simple reweighting technique, as discussed in Ref. [16]. With this formulation, with or without the mentioned reweighting technique, there is no difficulty to optimize the Jastrow and the Slater part of the wave function at the same time.

After the system (8.50) has been solved, we update the variational parameters

$$\alpha_k = \alpha_k^{(0)} + \frac{\delta\alpha_k}{\delta\alpha_0} \quad \text{for } k = 1, \dots, p \quad (8.51)$$

and we obtain a new trial wave function  $\Psi_g(\alpha)$ . By repeating this iteration scheme several times, one approaches the convergence when  $\frac{\delta\alpha_k}{\delta\alpha_0} \rightarrow 0$  for  $k \neq 0$ , and in this limit the conditions (8.49) implies the Euler equations of the minimum energy. Obviously, the solution of the linear system (8.50) is affected by statistical errors, yielding statistical fluctuations of the final variational parameters  $\alpha_k$  even when

---

<sup>8</sup> In Fig. 8.3, one can see a jump around the iteration 50, that is due to an infinite variance problem occurring in the variational parameter of the mean-field Hamiltonian.

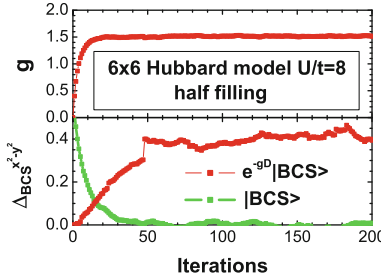


**Fig. 8.3** Convergence of the BCS pairing function as a function of the iteration steps for the 2D Hubbard model at  $U/t = 8$  for the  $6 \times 6$  cluster at half-filling ( $\Delta t = 0.05$  in Eq. 8.54). A finite value of the BCS pairing function is obtained *only* when the Gutzwiller correlation term  $g$  (*upper panel*) is optimized together with variational parameter  $\Delta_{BCS}^{x^2-y^2}$  appearing in the mean field Hamiltonian given by:  $H_{BCS} = -\sum_{k,\sigma} (\cos k_x + \cos k_y) c_{\sigma,k}^\dagger c_{k,\sigma} + \Delta_{BCS}^{x^2-y^2} \sum_k (\cos k_x - \cos k_y) c_{k,\uparrow}^\dagger c_{-k,\downarrow}^\dagger + \text{h.c.}$

convergence has been reached, namely when the  $\{\alpha_k\}_{k=1,\dots,p}$  fluctuate without drift around an average value. As is illustrated in Fig. (8.3) we perform several iterations in that regime; in this way, the variational parameters can be determined more accurately by averaging them over all these iterations and by evaluating also the corresponding statistical error bars. In this way one can perform an accurate finite size scaling of the variational parameters (see Fig. 8.4) to establish for instance whether the d-wave pairing remains at finite doping and in the thermodynamics limit, implying a d-wave superconducting ground state, at least within the simplest correlated wave function. In this picture we also see the main advantage of the variational approach: when the correlated part of the wave function (the Gutzwiller term) is optimized together with the mean-field like one (the gap function in the BCS Hamiltonian) a qualitatively new effect can be obtained, namely that there is tendency to form d-wave electron pairs in a model with only repulsive interactions.<sup>9</sup>

It is worth noting that the solution of the linear system (8.50) depends on  $\Lambda$  only through the  $\delta\alpha_0$  variable  $\delta\alpha_0 = f_0 - \sum_{k>0} \delta\alpha_k s_{0,k}$ . Therefore the constant  $\Lambda$  indirectly controls the rate of change in the parameters at each step, i.e. the speed of the algorithm for convergence and the stability at equilibrium: a too small value will produce uncontrolled fluctuations for the variational parameters, a too large one will allow convergence in an exceedingly large number of iterations. The choice of  $\Lambda$  can be controlled by evaluating the change of the normalized wave function at each step as:

$$\Delta\Psi = \left| \frac{\Psi'_g}{|\Psi'_g|} - \frac{\Psi_g}{|\Psi_g|} \right|^2 = \sum_{k \neq 0, k' \neq 0} \delta\alpha_k \delta\alpha_{k'} \bar{s}_{k,k'} \quad (8.52)$$

<sup>9</sup> For a technical description on how to compute the operator  $O_k(x)$  in Eq. (8.44), namely when the variational parameter of the determinantal part ( $\Delta_{BCS}^{x^2-y^2}$ ) is defined in terms of a mean field Hamiltonian, see for instance Ref. [17].

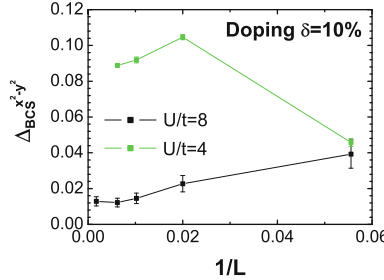


**Fig. 8.4** Finite size scaling of the d-wave BCS parameter for the 2D square lattice Hubbard model at  $U/t = 4$  and  $U/t = 8$  and 10 % doping. In this case the BCS hamiltonian defined in the previous figure contains also the chemical potential, that is also optimized together with  $\Delta_{BCS}^{x^2-y^2}$  and the Gutzwiller parameter  $g$ . Notice that the BCS pairing appears to go to zero or to an extremely small value at weak coupling

where the reduced overlap matrix, for  $k, k' \neq 0$ , is given by:

$$\bar{s}_{k,k'} = s_{k,k'} - s_{0,k}s_{0,k'} = \langle (O_k(x) - \langle O_k \rangle)(O_{k'}(x) - \langle O_{k'} \rangle) \rangle \quad (8.53)$$

Actually it is possible to formulate the minimization procedure, as a constrained minimization: the minimum of the energy is searched with the constraint that  $\Delta\Psi$  is fixed to a small value. By using a simple Lagrange multiplier  $\mu$ , by minimizing  $E_g + \mu\Delta\Psi$ , it is simple to obtain a solution independent of  $\Lambda$ :

$$\delta\alpha_k = \Delta t \sum_{k'} \bar{s}_{k,k'}^{-1} \bar{f}_{k'} \quad (8.54)$$

where  $\bar{f}_k = -\langle O_k(x)(e_L(x) - E_g) \rangle$  and  $\Delta_t = \frac{1}{\mu}$  small enough. Notice also that if  $\mu = \delta\alpha_0$ , Eq. (8.50) is consistent with the above one, meaning that, as anticipated,  $\Lambda$  implicitly defines the amplitude of the step  $\Delta\Psi$  at each iteration.

For large number of parameters the positive definite matrix  $\bar{s}$  can become very ill conditioned, namely the largest eigenvalue divided by the smallest one is a big number. Thus an important tip to improve the stability and the efficiency of the calculation is the regularization of the inversion in Eq. (8.54) [18]. This may be achieved by scaling the strictly positive diagonal elements of the matrix  $\bar{s}$  by a factor slightly larger than one:

$$\bar{s}_{k,k} \rightarrow (1 + \epsilon)\bar{s}_{k,k} \quad (8.55)$$

with  $\epsilon > 0$  (e.g.  $\epsilon = 10^{-3}$ ).

The ill conditioned nature of the matrix  $\bar{s}$  is intrinsic and essentially unavoidable for an accurate parametrization of a correlated wave function, where variational parameters define an highly non linear space. When this condition number is very

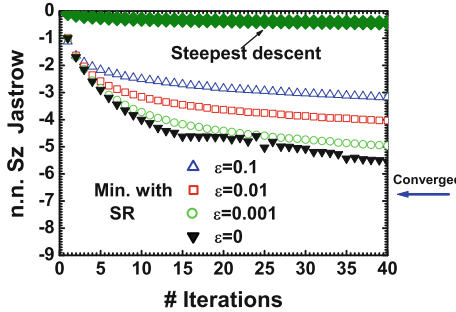


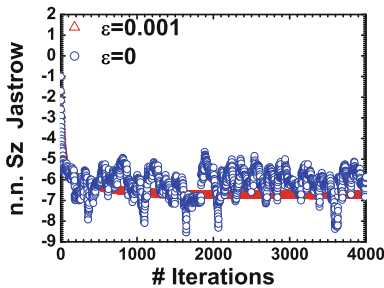
**Fig. 8.5** Convergence of the nearest neighbor spin Jastrow factor in the 1D 150-sites Heisenberg ring. During the optimization all independent 74 parameters of the spin Jastrow factor are optimized. Each iteration is obtained by averaging all quantities necessary, such as the matrix  $\bar{s}$  and the vector  $f_k$  in Eq. (8.54), over  $M = 2500 \gg 74$  samples, each generated by applying 300 Metropolis single particle attempts. Both in the stochastic reconfiguration method (SR) and in the steepest descent the amplitude of the step  $\Delta t$  is optimized and chosen about a factor two smaller than the maximum possible for a stable and convergent optimization of the energy (as well known if  $\Delta t$  is too large the methods are not stable even without statistical errors)

large, the standard steepest descent method<sup>10</sup> is very inefficient as shown in Fig. (8.5), simply because some direction in this non linear space can be changed only extremely slowly, with a speed inversely proportional to the condition number. As it is also shown in the same picture, the much better speed of convergence of the iterative method described by Eq. (8.54) is not affected much by the proposed regularization of the inverse (Eq. 8.55). On the other hand this is highly recommended because the matrix  $s$  is known only statistically and already a small value of  $\epsilon$  prevents unnecessary large fluctuations in the variational parameters. We remark here, that  $\epsilon$  does not introduce any bias in the calculation of the optimal wave function, because in absence of statistical errors, a stationary solution is reached only when  $\delta\alpha_k = 0$  in Eq. (8.54), implying that  $f_k = 0$  ( $\bar{s}$  is positive definite), namely the Euler conditions of minimum energy. For finite statistical error, a non zero value of  $\epsilon$  greatly reduces the error bars of the variational parameters, enhancing the efficiency of the optimization (see Fig. 8.6). Indeed if we define the efficiency as the inverse of the computer time necessary to have the chosen variational parameter within a given error bar, this is enhanced by about a factor 1000 compared to the  $\epsilon = 0$  case. In other words with  $\epsilon = 10^{-3}$  we need one thousand less computer time to obtain the wave function optimized with the same quality. Notice also that, in this case, the described method with  $\epsilon = 0.001$  is about 20 times more efficient than the recent more complicated minimization techniques (not shown), requiring also the derivative of the local energy with respect to all the variational parameters [19, 20].

We conclude this section by remarking that only after considering the non linear dependency of the variational parameters by means of the matrix  $\bar{s}$  it is possible

<sup>10</sup> This is obtained by applying the iteration given by Eq. (8.54) without using the matrix  $\bar{s}$ , namely  $\delta\alpha_k = \Delta t f_k$ .

**Fig. 8.6** Same as in Fig. 8.5 for several iterations, showing the different performances of the two methods



to optimize a large number of parameters (before '90s correlated wave functions contained only few parameters), provided the number of samples  $M$  used to evaluate this matrix is much larger than its dimension  $p$  given by the total number of variational parameters. The reason why  $M \geq p$ , is easily understood, because if a small number of sampling  $M < p$  is used, the resulting matrix  $\bar{s}$  is rank-deficient with a number  $p - M$  of exactly zero eigenvalues, despite the fact the matrix  $\bar{s}$  should be strictly positive definite if all the parameters are independent. This shows that this rank-deficiency is spurious and simply produced by the too small statistics for  $M < p$ . With the restriction  $M > \sim p$ , we notice that the variational Monte Carlo method becomes substantially slower when the number of parameters is large, and growing with some power of the system size. So far it is possible to optimize a number of parameters  $p \simeq L$ , yielding an algorithm scaling with the fourth power of the system size  $CPU \simeq L^4$  as opposed to the much cheaper computational cost (Eq. 8.36) for a parameter free variational wave function (like the Laughlin's one for the fractional quantum Hall effect).

## 8.6 Conclusion

In this chapter, we have described the simplest quantum Monte Carlo technique in a rigorous way, emphasizing how is possible to sample an exponentially large Hilbert space with an amount of computer time that remains feasible even for large number of electrons. Several improvement along this line are possible and should be mentioned:

- Systematically convergent improvements of the variational guess by the Lanczos algorithm. This technique was introduced by Heeb and Rice [21] and was later generalized in Ref. [7]. It allows us to apply a small number  $q$  of Lanczos iterations to a generic variational wave function of the standard type, with a computational cost scaling as  $M \times L^{q+2}$ , that is considerably larger than the standard cost  $M \times L^3$  only for  $q > 1$ . Obviously the method is not feasible for large  $q$ , but very accurate calculations can be obtained especially when the starting  $q = 0$  wave function is particularly good (see again Fig. 8.2). In particular the variance extrapolated energy obtained with few lanczos iterations represents the most simple and effec-

tive method to estimate the exact ground state energy of a model Hamiltonian on a lattice. Generalization to continuous model of this powerful technique is not possible because, due to Coulomb singularity, the standard Lanczos algorithm does not work in the present formulation.

- Fixed node Diffusion Monte Carlo, and is recent extension to lattice models [22–24]. Basically in order to avoid the exponential growth of the signal to noise ratio, due to so called “fermion sign problem”, an approximate projection to the ground state is employed by requiring that only the amplitudes of the wave function and not its phases (or signs) change during the projection  $\Psi_g \rightarrow e^{-\tau H} \Psi_g$ , that clearly for  $\tau \rightarrow \infty$  filters out the exact ground state component of  $\Psi_g$ . This method is more accurate than the variational Monte Carlo described here, in the sense that the corresponding energy is below the variational estimate, and nevertheless represents a rigorous upper bound. It is a bit slower, from a factor two on lattice models, to a factor 10 in continuous systems, with a clear improvement of the variational energy estimate, closer to the exact value (when known) by at least a factor two.
- Release nodes, by directly sampling the sign one can deal with the exact projection  $\Psi_g \rightarrow e^{-\tau H} \Psi_g$  with no approximation. In this way one can achieve for small cluster sizes or small number of electrons, exact ground state answers, with an exponentially large computer time [25]. It is a pity that this method has not been applied to lattice model yet, considering that the uniform electron gas problem was essentially solved exactly with this technique, at least for not too large values of  $r_s$ .

For fermions, there are not Monte Carlo methods that allow us to obtain an exact solution of the many-body wave function in a polynomial computational time. Nevertheless, in lattice model calculations, the variance extrapolation based on few lanczos iterations seems the most practical and efficient technique to estimate the exact energy and various correlation functions.

We conclude this chapter by showing the extraordinary good performances that can be obtained by fixed Node Diffusion Monte Carlo in modern Petaflop supercom-

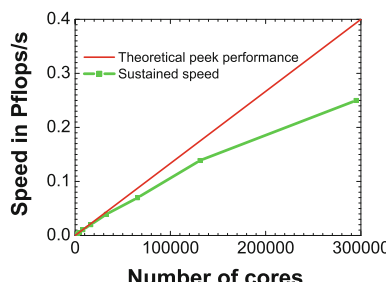


**Fig. 8.7** Speed performance of the standard Lattice diffusion Monte Carlo as a function of the number  $n_c$  of cores at the JuGene supercomputer in Jülich, Germany. Theoretical scaling neglecting communication time is  $\propto n_c$  (continuous line). By including the communication time a bit slower scaling is theoretically expected  $n_c / \ln n_c$ , which seems to be consistent with our test

puters. In Monte Carlo the amount of communications is minimal, when the paradigm to replicate independent calculations on different processors is adopted. With Diffusion Monte Carlo some communication is necessary, but the scaling is extraordinarily good as shown in Fig. (8.7). Since the major limitation of Monte Carlo is so far due in my opinion to the too large statistical errors that can be obtained in a conventional computer, the present fantastic improvements in the number of processors and performances represent a great opportunity, especially for the young generations, to establish quantum Monte Carlo as the method for strongly correlated systems and for electronic structure calculations, with robust predictive power, and fully ab initio many-body wave function based approach.

## Appendix

### Some Efficient Algebra for Determinants

The basic algebra for implementing all calculations with fermions is given by the well known rule for computing the overlap of two arbitrary  $N$  – particle Slater determinants of the form given in Eq. (8.4):

$$\langle \Psi | \Phi \rangle = \text{Det} S = |S| \quad (8.56)$$

where  $S$  is the overlap matrix between the orbitals  $\psi_i(r, \sigma)$  and  $\phi_i(r, \sigma)$  of the two Slater determinant  $|\Psi\rangle$  and  $|\Phi\rangle$ , respectively. Indeed the matrix elements of  $S$  are given by:

$$S_{i,j} = \sum_{r,\sigma} \psi_i^*(r, \sigma) \phi_j(r, \sigma) \quad (8.57)$$

Everything can be obtained by using the above equation, that is simple to derive using the canonical commutation rules and that  $c_{r,\sigma}|0\rangle = 0$  for all  $r, \sigma$ , namely that the vacuum is annihilated by all the destruction operators.<sup>11</sup>

#### A.1 Efficient Calculation of Determinant Ratios

In particular, let us try to describe how to get the ratio of two determinants appearing in Eq. (8.9) corresponding to a single particle move  $r, \sigma \rightarrow r', \sigma'$ :

$$|x'\rangle = c_{r',\sigma'}^\dagger c_{r,\sigma} |x\rangle \quad (8.58)$$

<sup>11</sup> All the forthcoming algebra is useful also for BCS wave functions, since after a simple particle-hole on the spin down electrons:  $c_{i,\downarrow}^\dagger \rightarrow c_{i,\downarrow}$  [26], the BCS wave function turns in a simple Slater Determinant with  $L$  orbitals written in the form given by Eq. (8.4).

Since  $|x\rangle$  is a Slater determinant in position space,  $x'$  is also a non vanishing Slater determinant in position space provided  $c_{r,\sigma}$  annihilates some creation operator  $c_{r_j,\sigma_j}^\dagger$  appearing in the definition of  $|x\rangle = \left( \prod_{j=1}^N c_{r_j,\sigma_j}^\dagger \right) |0\rangle$  (see Eq. 8.2) for  $j$  equal to some integer  $k$  such that  $r_k = r$  and  $\sigma_k = \sigma$ , and that  $r', \sigma'$  does not coincide with any of such operators as  $(c_{r_j,\sigma_j}^\dagger)^2 = 0$  for fermions. Under the above assumptions  $x'$  differs from  $x$  only for the replacement of the position and spin of the  $k$ th operator  $c_{r,\sigma}^\dagger \rightarrow c_{r',\sigma'}^\dagger$ , as all the other operators commute with  $c_{r',\sigma'}^\dagger c_{r,\sigma}$ . Then we can apply Eq. (8.56) to compute each of the two determinants:

$$r = \frac{|A'|}{|A|} \quad (8.59)$$

where the matrix  $A'$  differs from  $A$  only for the position of the  $k$ -th column, namely:

$$\begin{aligned} A_{i,j} &= \psi_i(r_j, \sigma_j) \\ A'_{i,j} &= A_{i,j} + \delta_{j,k}(\psi_i(r', \sigma') - \psi_i(r, \sigma)) \end{aligned} \quad (8.60)$$

We can now multiply the RHS of the above equation for the identity  $AA^{-1}$  and obtain that  $A' = AT$  where  $T$  is a very simple matrix that can be written in terms of the matrix  $W$  defined in Eq. (8.10).

$$T_{i,j} = \delta_{i,j} + (W_i(r', \sigma') - \delta_{i,k}) \delta_{j,k} \quad (8.61)$$

The determinant of this matrix is very simple to calculate as it contains only one non trivial column, and by applying the standard expansion of the determinant over this column it is simple to realize that only the diagonal element of this column provides a non vanishing contribution. Then by applying that the determinant of a product of two matrix is the product of their determinants, we obtain a simple expression for the determinant ratio:

$$r = \frac{|A'|}{|A|} = |T| = W_k(r', \sigma') \quad (8.62)$$

Analogously the inverse of the matrix  $T$  can be easily guessed by simple inspection:

$$T_{i,j}^{-1} = \delta_{i,j} + g(W_i(r', \sigma') - \delta_{i,k}) \delta_{j,k} \quad (8.63)$$

Indeed by making the simple product  $T^{-1}T$  we get that the above expression is actually correct provided  $1 + g + g(W_k(r', \sigma') - 1) = 0$ , namely  $g = -1/W_k(r', \sigma')$ . Using the above simple expression we obtain the new values of the matrix  $W'$  that can be useful for the next Markov step:

$$W'_i(r, \sigma) = W_i(r, \sigma) - \frac{W_i(r', \sigma') - \delta_{i,k}}{W_k(r', \sigma')} W_k(r, \sigma) \quad (8.64)$$

which takes  $N \times 2L$  operations. The above matrix can be updated during the Markov process, and allows to compute the local energy and the determinant ratio for the Metropolis algorithm in a very efficient way. Each time the new position is accepted the cost for updating the matrix  $W$  is optimal and correspond to standard linear algebra operations that can be further optimized using the technique described below.

## A.2 Delayed Updates

The basic operation in Eq.(8.64) is the so called rank-1 update of a generic  $N \times 2L$  matrix:

$$W'_{i,j} = W_{i,j} + a_i b_j \quad (8.65)$$

This operation can be computationally inefficient, when, for large size, the matrix  $W$  is not completely contained in the cache of the processor.<sup>12</sup> A way to overcome this drawback is to delay the update of the matrix  $W$ , without loosing its information. This can be obtained by storing a set of left and right vectors and the initial full matrix  $W^0$ , from which we begin to delay the updates:

$$W_{i,j} = W_{i,j}^0 + \sum_{l=1}^m a_i^l b_j^l \quad (8.66)$$

as, each time we accept a new configuration, a new pair of vectors  $a_i^{m+1}$  and  $b_j^{m+1}$  can be easily computed in few operations in term of  $W^0$ ,  $a_i^l$ ,  $b_j^l$   $l = 1, \dots, m$ , by substituting Eq.(8.66) into the RHS of Eq.(8.64):

$$a_i^{m+1} = -\frac{W_i(r', \sigma') - \delta_{i,k}}{W_k(r', \sigma')} \quad (8.67)$$

$$b_{r,\sigma}^{m+1} = W_k(r, \sigma). \quad (8.68)$$

where here the index  $j$  of the vector  $b$  has been replaced by the pair  $r, \sigma$  running over  $2L$  values. Notice that the number of operations required to evaluate the above expressions in term of  $W$  written in the form (8.66) is  $\simeq m(2L + N)$ , negligible compared to the full update for  $m \ll L$ .

In this way we can find an optimal  $m = k_{rep}$ , when we can evaluate the full matrix  $W_{i,j}$  by a standard matrix multiplication:

$$W = W^0 + AB^T \quad (8.69)$$

---

<sup>12</sup> For more fancy implementation of the algorithm see e.g. Ref. [27].

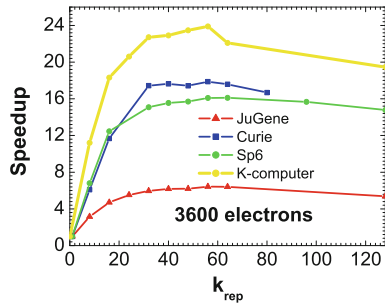


**Fig. 8.8** Speedup obtained by using delayed updates in quantum Monte Carlo for a variational wave function containing 3600 electrons in the Hubbard model at half filling. With the same number of Metropolis updates and calculation of the local energies the algorithm described in this appendix is several times faster compared with the conventional one ( $k_{rep} = 1$ ). Test calculations were done in the JuGene supercomputer in Jülich (maximum speedup 6.4 with  $k_{rep} = 56$ ), in the Curie machine (maximum speedup 17.9 with  $k_{rep} = 56$ ) hosted in Bruyères-le-Châtel France, in the K-computer hosted in Kobe Japan (maximum speedup 23.9 for  $k_{rep} = 56$ ), and in the sp6-CINECA (maximum speedup 16.1 for  $k_{rep} = 64$ ) in Bologna

where  $A$  and  $B$  are  $N \times k_{rep}$  and  $2L \times k_{rep}$  matrices made of the  $l = 1, 2, \dots, k_{rep}$  column vectors  $a_i^l$  and  $b_j^l$ , respectively. After this standard matrix-matrix product one can continue with a new delayed update with a new  $W^0 = W$ , by initializing again to zero the integer  $m$  in Eq.(8.66). The clear advantage of this is that after a cycle of  $k_{rep}$  Markov steps the bulk of the computation is given by the evaluation of the matrix-matrix product in Eq. (8.69), that is much more efficient and is not cache limited compared with the  $k_{rep}$  rank-1 original updates of  $W$  given in Eq.(8.64). With the  $k_{rep}$  delayed algorithm, once the optimal  $k_{rep}$  is found one can improve the speed of the variational Monte Carlo code by about an order of magnitude for large number of electrons (see Fig. 8.8).

## References

1. E.H. Lieb, F.Y. Wu, Phys. Rev. Lett. **20**, 1445 (1968)
2. Z.Y. Meng, T.C. Lang, S. Wessel, F.F. Assaad, A. Muramatsu, Nature **464**, 2010 (2010)
3. S. Sorella, E. Tosatti, Europhys. Lett. **19**, 699 (1992)
4. D. Duffy, A. Moreo, Phys. Rev. B **55**, R676 (1997)
5. L.F. Tocchio, F. Becca, A. Parola, S. Sorella, Phys. Rev. B **78**, R041101 (2008)
6. W.L. McMillan, Phys. Rev. **138**, A442 (1965)
7. S. Sorella, Phys. Rev. B **64**, 024512 (2001)
8. P. Lecheminant, B. Bernu, C. Lhuillier, L. Pierre, P. Sindzingre, Phys. Rev. B **56**, 2521 (1997)
9. S. Yan, D.A. Huse, S.R. White, ArXiv:cond-mat, p. 1011.6114 (2011)
10. D.S. Fisher, Phys. Rev. Lett. **69**, 534 (1992)
11. D.S. Fisher, Phys. Rev. B **50**, 3799 (1994)
12. D.S. Fisher, Phys. Rev. B **51**, 6411 (1995)
13. N. Metropolis, A.W. Rosenbluth, M.N. Rosenbluth, A.H. Teller, J. Chem. Phys. **21**, 1087 (1953)

14. N. Metropolis, A.W. Rosenbluth, M.N. Rosenbluth, A.N. Teller, E. Teller, Equation of state calculations by fast computing machines. *J. Chem. Phys.* **21**, 1078 (1953)
15. M. Casula, S. Sorella, *J. Chem. Phys.* **119**, 6500 (2003)
16. C. Attaccalite, S. Sorella, *Phys. Rev. Lett.* **100**, 114501 (2008)
17. S. Yunoki, S. Sorella, *Phys. Rev. B* **74**, 014408 (2006)
18. M. Casula, S. Sorella, D. Rocca, *J. Chem. Phys.* **127**, 014105 (2007)
19. S. Sorella, *Phys. Rev. B* **71**, R241103 (2005)
20. C. Umrigar, J. Toulouse, C. Filippi, S. Sorella, R. Henning, *Phys. Rev. Lett.* **98**, 110201 (2007)
21. E.S. Heeb, T.M. Rice, *Europhys. Lett.* **27**, 673 (1994)
22. S. Sorella, L. Capriotti, *Phys. Rev. B* **61**, 2599 (2000)
23. D.F.B. ten Haaf, H.J.M. van Bemmelen, J.M.J. van Leeuwen, W. van Saarloos, D.M. Ceperley, *Phys. Rev. B* **51**, 13039 (1995)
24. N. Trivedi, D.M. Ceperley, *Phys. Rev. B* **41**, 4552 (1990)
25. D.M. Ceperley, B.J. Alder, *J. Chem. Phys.* **81**, 5833 (1984)
26. M. Ogata, H. Shiba, *J. Phys. Soc. Jpn.* **58**, 2836 (1989)
27. P.K.V.V. Nukala et al., *Phys. Rev. B* **80**, 195111 (2009)

# Chapter 9

## Coupled Cluster Theories for Strongly Correlated Molecular Systems

Karol Kowalski, Kiran Bhaskaran-Nair, Jiří Brabec and Jiří Pittner

**Abstract** The basic aspects of coupled cluster (CC) theories are reviewed from the perspective of its applicability to molecular systems with strong many-body correlation effects. In practice strong correlation refers to systems where the corresponding wavefunctions are characterized by multiconfigurational character corresponding to collective excitations from the reference function/functions. Several CC formalisms specifically designed to tackle these situations are discussed. These include single reference CC methodologies accounting for high-rank excitations and multireference CC approaches. Special attention is paid to non-iterative methods, which provide a widely accepted compromise between accuracy and numerical cost. We also discuss major theoretical and computational challenges which have to be addressed for the future developments of CC methodologies.

### 9.1 Introduction

Many aspects of computational chemistry require accuracies that can only be met by a very limited class of methods that properly account for the instantaneous interactions between electrons or correlation effects in molecules. In particular, these accuracies

---

K. Kowalski (✉) · K. Bhaskaran-Nair

William R. Wiley Environmental Molecular Sciences Laboratory, Battelle,  
Pacific Northwest National Laboratory, Richland, Washington 99352, USA  
e-mail: karol.kowalski@pnnl.gov

K. Bhaskaran-Nair

e-mail: Kiran.BhaskaranNair@pnnl.gov

J. Brabec · J. Pittner

J. Heyrovský Institute of Physical Chemistry, Academy of Sciences  
of the Czech Republic, CZ-18223 Prague 8, Czech Republic  
e-mail: jiri.brabec@jh-inst.cas.cz

J. Pittner

e-mail: jiri.pittner@jh-inst.cas.cz

are needed to bridge the gap between theory and experiment in a profound way. Among the many methods that describe correlation effects, the coupled cluster (CC) formalism [1–6] has evolved into a widely used and very accurate method for solving the electronic Schrödinger equation. Compared with other formalisms such as perturbative methods or approaches based on the linear expansion of the wavefunction, the main advantage of the CC formalism lies in the fact that the correlation effects are very efficiently encapsulated in the exponential form of the wavefunction. This enables one to describe the correlated motion of one or two (or more) electron pairs simultaneously. A simple consequence of this feature is the size-extensivity of the resulting energies, or equivalently a proper scaling of energy with the number of electrons. This feature is essential for describing complicated chemical processes. Although the CC formalism was initially proposed in nuclear physics, it was quickly adopted by quantum chemists and since the late sixties there has been steady development which has spawned a variety of CC methodologies. Notably, in the last decade this formalism has been “readopted” by the nuclear physics theory community [7]. This clearly demonstrates the universal applicability of the method across a broad gamut of length and energy scales.

The dawn of peta-scale computer architectures offers a unique opportunity to validate and apply accurate yet numerically expensive many body-theories to large molecular systems. The single-reference CC (SRCC) methods accounting for high-rank excitations and multireference coupled-cluster methods (MRCC) fall into this category. These methods provide a means to properly treat correlation effects for electronic states characterized by strong correlation effects. Several problems such as bond-breaking processes, poly-radical species, transition metal compounds, low-spin open-shell states, and reactions involving potential energy surfaces crossing are characterized by strong correlation effects where the use of high-order methods is crucial.

The purpose of this chapter is to provide a short review of the interplay between sophisticated theoretical formulations and the opportunities offered by cutting-edge computer architectures in dealing with steep polynomial scaling of CC methods. To properly address the challenges emerging at the nexus of CC theory and computer science, three essential components have to be discussed, including: (1) efficient theories for encapsulating correlation effects in strongly correlated regime, (2) symbolic algebra systems for deriving and automatic code generation for second-quantized expressions underlying CC theories, (3) efficient parallel tools supporting distributed data programming models. We will also highlight our recent theoretical/computational developments. The authors are also aware that area is too broad even to be partially covered by this review. We refer interested readers to many excellent reviews on the subject [8–16].

## 9.2 Single Reference CC (SRCC) Methods

We start with the electronic Schrödinger equation, which describes the behavior of electrons in the field of a fixed nuclear frame (Born-Oppenheimer approximation)

$$H|\Psi\rangle = E|\Psi\rangle. \quad (9.1)$$

Hence the electronic Hamiltonian ( $H$ ) and the electronic wavefunction ( $|\Psi\rangle$ ) depend parametrically on the nuclear coordinates of all nuclei defining a given system.

The main purpose of advanced many-body methods is to go beyond the independent particle model such as the Hartree Fock (HF) method and to account for the correlation energy  $\Delta E_{\text{corr}}$  defined as the difference between exact ( $E$ ) and HF ( $E_{HF}$ ) energies

$$\Delta E_{\text{corr}} = E - E_{HF}. \quad (9.2)$$

Although contributing less than 1 % of the total energy  $E$ , inclusion of the correlation energy is an absolute prerequisite for understanding molecular structure, chemical reactions, and bond-forming/bond-breaking processes. Therefore, a substantial effort has been invested to develop efficient theoretical approaches capable of accounting for the correlation effects stemming from the instantaneous interactions between electrons.

Among the various methods approximating the electronic wavefunction (the WF approaches) such as truncated configuration interaction (CI) methods or many-body perturbation theory (MBPT) based approaches, the coupled cluster approach, for its accuracy in describing correlation effects, has attained a special position. The single reference CC wavefunction parametrization is based on the exponential Ansatz [1-4]

$$|\Psi\rangle = e^T |\Phi\rangle, \quad (9.3)$$

where  $T$  is the cluster operator and  $|\Phi\rangle$  is the reference function represented in the form of a single Slater determinant (usually  $|\Phi\rangle$  corresponds to the HF determinant). The cluster operator can be represented as a sum of its many-body components

$$T = \sum_{n=1}^N T_n \quad (9.4)$$

where  $N$  represents the total number of correlated electrons and  $T_n$  operators can be written in the second quantization language as follows

$$T_n = \sum_{i_1 < \dots < i_n; a_1 < \dots < a_n} t_{a_1 \dots a_n}^{i_1 \dots i_n} c_{a_1}^+ \dots c_{a_n}^+ c_{i_n} \dots c_{i_1}. \quad (9.5)$$

The creation/annihilation operators  $c_p^+$ / $c_q$  satisfy standard anticommutation relations

$$\{c_p^+, c_q\} = \delta_{pq}, \{c_p^+, c_q^+\} = \{c_p, c_q\} = 0. \quad (9.6)$$

As always, we will denote occupied (unoccupied) spinorbitals in the reference function  $|\Phi\rangle$  by  $i, j, k, \dots (a, b, c, \dots)$  or by  $i_1, i_2, \dots (a_1, a_2, \dots)$ . When the string of creation/annihilation operators  $c_{a_1}^+ \dots c_{a_n}^+ c_{i_n} \dots c_{i_1}$  acts on the reference function it produces an excited Slater determinant  $|\Phi_{i_1 \dots i_n}^{a_1 \dots a_n}\rangle$  defined as

$$|\Phi_{i_1 \dots i_n}^{a_1 \dots a_n}\rangle = c_{a_1}^+ \dots c_{a_n}^+ c_{i_n} \dots c_{i_1} |\Phi\rangle. \quad (9.7)$$

The cluster amplitudes  $t_{a_1 \dots a_n}^{i_1 \dots i_n}$  and CC energy can be obtained by substituting (9.5) into the Schrödinger Eq. (9.1)

$$He^T |\Phi\rangle = Ee^T |\Phi\rangle. \quad (9.8)$$

By premultiplying both sides of Eq.(9.8) by  $e^{-T}$  and using Baker-Campbell-Hausdorff formula

$$e^{-B} A e^B = A + [A, B] + \frac{1}{2!} [[A, B], B] + \frac{1}{3!} [[[A, B], B], B] + \dots, \quad (9.9)$$

one can show that Eq. (9.8) can be cast into the following form

$$(He^T)_C |\Phi\rangle = E |\Phi\rangle, \quad (9.10)$$

where subscript “C” designates connected diagrams of a given operator expression. By projecting Eq. (9.10) onto all possible excited configurations  $|\Phi_{i_1 \dots i_n}^{a_1 \dots a_n}\rangle$  one can decouple the equations for the cluster amplitudes

$$\langle \Phi_{i_1 \dots i_n}^{a_1 \dots a_n} | (He^T)_C | \Phi \rangle = 0 \quad (9.11)$$

from the equation for the energy, obtained by projecting (9.10) onto the reference function

$$E = \langle \Phi | (He^T)_C | \Phi \rangle. \quad (9.12)$$

For single reference CC theories, the connected form of the corresponding Eq. (9.11) assures the additive separability of the energy in the non-interacting subsystem limit (NSL). However, this is only the case when the reference function dissociates into the antisymmetrized product of Slater determinants corresponding to each subsystem.

Once all excitations are accounted for, the resulting full CC formalism is equivalent to the exact full configuration interaction (FCI) method based on the linear expansion for the wavefunction,

$$|\Psi\rangle = (1 + C)|\Phi\rangle = (1 + C_1 + C_2 + \dots + C_N)|\Phi\rangle. \quad (9.13)$$

This equivalence leads to the well-known relations between CC and FCI excitation operators  $T_n$  and  $C_n$ , respectively, i.e.,

$$C_1|\Phi\rangle = T_1|\Phi\rangle, \quad (9.14)$$

$$C_2|\Phi\rangle = (T_2 + \frac{1}{2!}T_1^2)|\Phi\rangle, \quad (9.15)$$

$$C_3|\Phi\rangle = (T_3 + T_1T_2 + \frac{1}{3!}T_1^3)|\Phi\rangle, \quad (9.16)$$

$$C_4|\Phi\rangle = (T_4 + T_1T_3 + \frac{1}{2!}T_2^2 + \frac{1}{2!}T_1^2T_2 + \frac{1}{4!}T_1^4)|\Phi\rangle. \quad (9.17)$$

...

The above formulas show that the higher-order  $C$  excitations can be approximated by the products of cluster operators. For example, for closed shell systems the  $C_4$  operator can be approximated by the product of  $T_2$  operators. This important result is in line with the perturbative expansion for the ground-state wavefunction. The possibility of approximating higher-order excitations by products of cluster operators is yet another hallmark of the CC formalism.

### 9.2.1 Standard Approximations

The SRCC parametrization introduces a hierarchical structure of approximations corresponding to the truncation of the cluster operator expansion at a certain excitation level  $m_A$  ( $m_A < N$ ), i.e.,

$$T = \sum_{n=1}^{m_A} T_n. \quad (9.18)$$

The inclusion of doubly- (D), singly- (S), triply- (T), quadruply- (Q), pentuply- (P), etc. excited clusters leads to the following approximations: CCD ( $T = T_2$ ) [4], CCSD ( $T = T_1 + T_2$ ) [17], CCSDT ( $T = T_1 + T_2 + T_3$ ) [18–20], CCSDTQ ( $T = T_1 + T_2 + T_3 + T_4$ ) [21, 22], CCSDTQP ( $T = T_1 + T_2 + T_3 + T_4 + T_5$ ) [23] etc., which in the limit of  $N$ -tuply excitations is equivalent to the FCI method. In order to assure that there are equal numbers of equations as there are unknown cluster amplitudes, Eq. (9.10) is projected onto the excited configurations generated by the action of the approximate cluster operator on the reference function. For example, the CCSDT amplitude equations are defined as follows

$$\langle \Phi_i^a | (He^{T_1+T_2+T_3})_C | \Phi \rangle = 0 \quad \forall_{i,a}, \quad (9.19)$$

$$\langle \Phi_{ij}^{ab} | (He^{T_1+T_2+T_3})_C | \Phi \rangle = 0 \quad \forall_{i < j; a < b}, \quad (9.20)$$

$$\langle \Phi_{ijk}^{abc} | (He^{T_1+T_2+T_3})_C | \Phi \rangle = 0 \quad \forall_{i < j < k; a < b < c}. \quad (9.21)$$

**Table 9.1** The differences between the CC and FCI energies (in millihartree) for several molecular systems for geometries close to the equilibrium ones

Molecule (basis set)	CCSD	CCSDT	CCSDTQ	CCSDTQP
HF (DZP)	3.006	0.265	0.018	0.000
H <sub>2</sub> O (cc-pVDZ)	3.774	0.493	0.019	0.003
N <sub>2</sub> (cc-pVDZ)	12.522	1.431	0.155	—
CH <sub>4</sub> (MINI)	0.243	0.053	0.000	0.000

Results were compiled based on Refs. [24, 25]

**Table 9.2** Numerical scaling of standard single reference approximations

Method	Cluster operator	Numerical scaling
CCD	$T = T_2$	$n_o^2 n_u^4$
CCSD	$T = T_1 + T_2$	$n_o^2 n_u^4$
CCSDT	$T = T_1 + T_2 + T_3$	$n_o^2 n_u^5$
CCSDTQ	$T = T_1 + T_2 + T_3 + T_4$	$n_o^2 n_u^6$
CCSDTQP	$T = T_1 + T_2 + T_3 + T_4 + T_5$	$n_o^2 n_u^7$

The parameters  $n_o$  and  $n_u$  refer to the number of occupied and unoccupied spinorbitals, respectively

Due to the pairwise structure of the electronic Hamiltonian, the expressions for the approximate CC energies ( $E^{(A)}$ ) assumes the same functional form in CCSD, CCSDT, CCSDTQ, CCSDTQP, etc. approximations

$$E^{(A)} = \langle \Phi | (H e^{T_1 + T_2})_C | \Phi \rangle. \quad (9.22)$$

An important consequence associated with the projective nature of the CC equations is the non-variational character of the CC energies. The inclusion of higher-order clusters leads to systematic improvements in the calculated ground-state energies and is especially important for systems with strong quasidegeneracy effects. Table 9.1 shows the CC energies for the HF, H<sub>2</sub>O, N<sub>2</sub>, CH<sub>4</sub> molecules obtained for geometries close to the equilibrium ones. One can see a rapid convergence of the CC results with the excitation rank of the cluster operator. Unfortunately, the inclusion of higher-order excitations comes at the high price associated with the construction of the relevant CC working equations (see Table 9.2). For example, doubling the size of the system (and assuming that the same basis set is employed) results in  $2^6 = 64$  fold increase of the numerical effort of the CCSD calculations and  $2^{10} = 1024$  fold more expensive calculations with the CCSDTQ method, which makes high-order CC approximations prohibitively expensive even for relatively small systems.

The following sections will discuss possible ways of dealing with the unfavorable scaling of the CC methods, which embraces two major areas: (1) theoretical developments of perturbative methods capable of cost reduction associated with the inclusion of higher order clusters and (2) development of efficient numerical algorithms capable of taking advantage of leadership class computer architectures. Before we discuss these areas, we will first present a discussion of the multiple solutions to the CC equations and iterative methods for obtaining physically interpretable solutions.

### 9.2.2 Solvability of the CC Equations

The CC equations constitute a system of strongly coupled nonlinear polynomial equations, which for Hamiltonians defined by pairwise interactions can be expressed as

$$\begin{aligned} \mathbf{F}(\mathbf{t})_I = & a_I + \sum_J b_{IJ} t_J + \sum_{J < K} c_{IJK} t_J t_K \\ & + \sum_{J < K < L} d_{IJKL} t_J t_K t_L + \sum_{J < K < L < M} e_{IJKLM} t_J t_K t_L t_M, \end{aligned} \quad (9.23)$$

where the  $t_I$  variables represent cluster amplitudes. Two natural questions arise: (1) how does one obtain the ground-state solution? and (2) how does one interpret the multiple solutions to the CC equations? The latter question is equivalent to establishing relationships between the multiple solutions corresponding to approximate theory and solutions of the full CC approach (or FCI approach).

The first attempt to analyze the multiple solutions of the CC equations was carried out by Zivković and Monkhorst [26], who employed the continuation approach to categorize various singular points corresponding to equations connecting CI and CC theories. Since then, multiple solutions have been analyzed for various SRCC formulations [27–29]. The first rigorous studies of the full solution set to the approximate CC equations for realistic model systems (epitomizing the basic features of true molecular systems) have been performed with the homotopy method

$$\mathbf{H}(\mathbf{x}, \lambda) = (1 - \lambda)\mathbf{G}(\mathbf{x}) + \lambda\mathbf{F}(\mathbf{x}) \quad (9.24)$$

where  $\mathbf{F}(\mathbf{x}) = 0$  is the target system of polynomial equations for which one wants to determine all geometrically isolated solutions [30–34]. The special choice of the  $\mathbf{G}(\mathbf{x})$  function ( $\mathbf{G}_i(\mathbf{x}) = x_i^{d_i} - \alpha_i$ ,  $\deg(F_i) \leq d_i$ , where  $\deg(F_i)$  is polynomial degree of  $i$ -th component of the  $\mathbf{F}(\mathbf{x})$  function) and the Transversality Theorem [35] assure that all solutions of the  $\mathbf{F}(\mathbf{x}) = 0$  problem can be obtained by analytical continuation of certain solutions of the  $\mathbf{G}(\mathbf{x}) = \mathbf{0}$  problem. Numerical studies have led to several interesting conclusions:

- SRCC theories can only be used to describe one state (the ground state). Most of the solutions lack a clear physical interpretation.
- In the spinorbital formulations, solutions to approximate CC approaches can break the symmetry of the reference function (spin symmetry or symmetry associated with the subsystem particle number conservation in the non-interacting subsystem limit) [31–33].
- The embedding procedures ( $\beta$ -nesting algorithm of Ref. [34]) have helped to establish the relationships between the approximate ground-state CC solutions and the ground-state solution corresponding to the full CC (or FCI) method in the form of the *Fundamental Theorem of  $\beta$ -Nested Equations* [36]. This theorem

provides the theoretical foundation for the method of moments of coupled cluster equations (MMCC) and ensuing renormalized CC methods [37].

Since the ground state is the main target of SRCC formulations, several methods have been tailored for the purpose of solving CC equations [38, 39]. Currently, the most widespread approach is based on the adaptation of the DIIS procedure (Direct Inversion in the Iterative Subspace) originally formulated by Pulay for solving Hartree-Fock equations [40]. The essential idea of DIIS is to minimize the norm of the residual vector

$$\mathbf{r} = \sum_{i=1}^m \alpha_i \mathbf{e}_i, \quad (9.25)$$

where vectors  $\{\mathbf{e}_i\}_{i=1}^m$  are the corrections to vectors of cluster amplitudes obtained in  $m$  iterations  $\{\mathbf{t}_i\}_{i=1}^m$ . The new  $\mathbf{t}$  vector for the next DIIS microcycle (composed of  $m$  iterations) is then represented as

$$\mathbf{t} = \sum_{i=1}^m \alpha_i \mathbf{t}_i. \quad (9.26)$$

The currently used variants of the DIIS procedure allow one to significantly reduce the number of iterations compared with the original Jacobi method.

To counter severe problems plaguing SRCC theories in the presence of quasidegeneracy effects, several regularization techniques have been proposed to deal either with the singularities of the specific form of the CC equations or divergent nature of the perturbative expansion. In particular, the Tikhonov regularization [41] has been applied by Taube and Bartlett to regularize the linear CCSD (L-CCSD) equations [42] (only the first and second terms are retained on the r.h.s. of Eq. (9.23)) in the vicinity of singular point, commonly occurring in quasidegenerate situations. For example, for linear CCD (L-CCD) equations the doubly excited cluster amplitudes are regularized as follows

$$t_{a_1 a_2}^{i_1 i_2 (n+1)} = \frac{\epsilon_{i_1 i_2}^{a_1 a_2}}{(\epsilon_{i_1 i_2}^{a_1 a_2})^2 + \omega^2} \langle \Phi_{i_1 i_2}^{a_1 a_2} | V_N + V_N T_2^{(n)} | \Phi \rangle, \quad (9.27)$$

where  $\epsilon_{i_1 i_2}^{a_1 a_2}$  represents the orbital energy differences and  $\omega^2$  is a positive number.

### 9.2.3 Perturbative Inclusion of Higher-Order Clusters

The single reference variant of the linked cluster theorem [43–47] provides a natural link between MBPT and SRCC theories. SRCC theory can be viewed as an infinite resummation of the perturbative expansion, where the cluster amplitudes and energy are expressed through connected diagrams only. MBPT techniques enable one to

build a hierarchical structure of particular correlation effects. For example, in the Møller-Plesset formulation of MBPT the cluster amplitudes for canonical HF orbitals appears in the following orders (denoted as superscripts):

$$T_2 = T_2^{(1)} + T_2^{(2)} + \dots \quad (9.28)$$

$$T_1 = T_1^{(2)} + T_1^{(3)} + \dots \quad (9.29)$$

$$T_3 = T_3^{(2)} + T_3^{(3)} + \dots \quad (9.30)$$

$$T_4 = T_4^{(3)} + T_4^{(4)} + \dots \quad (9.31)$$

...

which clearly indicates that the leading correlation effects are associated with exciting electron pairs. Perturbation theory also establishes recursive dependencies between cluster operators at various orders/ranks, which can be used to express high-rank clusters in terms of the low-rank ones, e.g.,

$$T_3^{(2)}|\Phi\rangle = R_3^{(0)} V_N T_2^{(1)}|\Phi\rangle, \quad (9.32)$$

where  $V_N$  is the two-body part of the Hamiltonian in normal ordered form  $H_N = H - \langle\Phi|H|\Phi\rangle = F_N + V_N$ , and  $R_3^{(0)}$  is a three-body resolvent operator

$$R_3^{(0)} = \sum_{i < j < k; a < b < c} \frac{|\Phi_{ijk}^{abc}\rangle\langle\Phi_{ijk}^{abc}|}{\epsilon_i + \epsilon_j + \epsilon_k - \epsilon_a - \epsilon_b - \epsilon_c}, \quad (9.33)$$

where  $\epsilon$ 's refer to the HF orbital energies. It has become clear that going beyond models involving single and double excitation is necessary for achieving chemical accuracy in thermochemistry and spectroscopic calculations. Chemical accuracy is typically defined as errors not exceeding 1 kcal/mol (see for example Ref. [48]). Intensive effort towards developing economical CC methods including triply (and higher) excited clusters is reflected by two classes of methods: (1) iterative CCSDT-n [49–53] and (2) non-iterative CCSD[T] [54, 55] and CCSD(T) [56] approaches, where the  $T_3$  amplitudes are expressed perturbatively in terms of  $T_2$  ones only. Due to their simplicity and robustness, non-iterative methods have been the focus of significant theoretical efforts for more than two decades. In the CCSD(T) approach, which is widely accepted as a “gold standard” of high-accuracy calculations, the ground-state energy is obtained by adding to the CCSD energy 4-th and 5-th order contributions

$$E^{\text{CCSD}(T)} = E^{\text{CCSD}} + \langle\Phi|T_2^+ V_N \bar{T}_3|\Phi\rangle + \langle\Phi|T_1^+ V_N \bar{T}_3|\Phi\rangle, \quad (9.34)$$

where  $\bar{T}_3$  is obtained from the formula (9.32) with  $T_2^{(1)}$  replaced by  $T_2$  obtained in the CCSD calculations. In the above expression we have also assumed that the canonical HF reference is used. The CCSD(T) reduces the  $n_o^3 n_u^5$  scaling of the CCSDT method

**Table 9.3** Comparison of HF, CCSD, and CCSD(T) molecular properties for the H<sub>2</sub>O and CO<sub>2</sub> molecules described by the TZ(2df, 2pd) basis set

Property	HF	CISD	CCSD	CCSD(T)	Expt.
<b>H<sub>2</sub>O molecule</b>					
$r_e(O - H)$	0.9402	0.9530	0.9568	0.9594	0.9578
$\theta_e(H - O - H)$	106.4	104.8	104.5	104.2	104.5
$\omega_1$	4134	3937	3874	3835	3832
$\omega_2$	1745	1676	1662	1650	1649
$\omega_3$	4235	4039	3981	3944	3943
<b>CO<sub>2</sub> molecule</b>					
$r_e(C - O)$	1.1349	1.1467	1.1558	1.1629	1.160
$\omega_1$	1513	1442	1389	1345	1354
$\omega_2$	779	729	697	672	673
$\omega_3$	2556	2502	2432	2391	2397

All results were taken from Ref. [60]. Equilibrium distances ( $r_e$ ) and angles ( $\theta_e$ ) are given in Ångstroms and degrees, respectively, while harmonic vibrational frequencies ( $\omega$ ) are reported in cm<sup>-1</sup>

to  $n_o^3 n_u^4$  while maintaining the same memory requirements as in the CCSD case. Similar ideas have been applied to account for quadruply excited clusters (CCSD(TQ) approaches of Refs. [57–59]). In Table 9.3 we compare the HF, CISD, CCSD, and CCSD(T) calculations for water and carbon dioxide molecules. First, the CC methods significantly improve the quality of the HF and CISD approaches. Second, CCSD(T) refines the CCSD results both for the equilibrium geometries and harmonic vibrational frequencies. The harmonic vibrational energies provide a good measure for the quality of the ground-state potential energy surface in the vicinity of the equilibrium geometry. It is remarkable to see that the CCSD(T) approach is capable of reducing harmonic vibrational frequencies to within 10 cm<sup>-1</sup>.

Several (T)-type formulations have been designed to address serious problems of the CCSD(T) method in describing bond breaking/forming processes. These problems result from the perturbative nature of the (T) energy corrections. An important class of methods extending the applicability of the CCSD(T) approach include the approaches [61–76] based on the use of bi-variational formalism that rely on the so-called left eigenvectors (or  $\Lambda$  operator) of the similarity transformed Hamiltonian  $\bar{H}$  ( $\bar{H} = e^{-T} H e^T$ ). These methods have been derived either by using perturbative partitioning of the  $\bar{H}$  operator or employing perturbative expansion for the CC functional [77–79]

$$E_{CC}(\Lambda, T) = \langle \Phi | (1 + \Lambda) \bar{H} | \Phi \rangle. \quad (9.35)$$

As explained by Taube and Bartlett [74, 75] a smaller magnitude of the  $\Lambda$  amplitudes (compared to  $T$  counterparts) provides a more balanced description of correlation effects compared with the CCSD(T) approach.

An alternative formalism to build efficient non-iterative schemes is offered by the MMCC functional [37]

$$\Lambda_{\text{MMCC}}(\Psi) = \langle \Psi | (He^T - E^{(A)}) | \Phi \rangle / \langle \Psi | e^T | \Phi \rangle. \quad (9.36)$$

When the trial wavefunction  $\langle \Psi |$  is replaced by the exact one, the value of the functional is equal to the correction ( $\delta^{(A)}$ ) which needs to be added to  $E^{(A)}$  to reproduce exact FCI energy. The many-body structure of  $\delta^{(A)}$ ,

$$\delta^{(A)} = \langle \Psi | e^T M | \Phi \rangle / \langle \Psi | e^T | \Phi \rangle, \quad (9.37)$$

has been utilized in constructing several types of corrections. The CC moment operator  $M$  can be expressed through the  $\bar{H}$  operator, i.e.,  $M|\Phi\rangle = Q\bar{H}|\Phi\rangle$ , where  $Q$  is the projection operator onto subspace of all excited configurations ( $Q = 1 - |\Phi\rangle\langle\Phi|$ ). Although early MMCC correction schemes to the CCSD energy, termed the completely renormalized CCSD(T) approach (CR-CCSD(T)) [36, 37],

$$\delta^{\text{CR-CCSD(T)}} = \langle \Psi^{\text{CR-CCSD(T)}} | M_3 | \Phi \rangle / \langle \Psi^{\text{CR-CCSD(T)}} | e^{T_1+T_2} | \Phi \rangle, \quad (9.38)$$

were not size-extensive, it was demonstrated that the CR-CCSD(T) approach can significantly improve the performance of the CCSD(T) method far from equilibrium geometries. Several formulations were designed to reinstate size-extensivity of the renormalized approaches including locally renormalized methods (LR-CCSD(T)) [80] and CR-CC( $m_A, m_B$ ) approaches by Piecuch and Włoch [81]. The CR-CC (2,3) approach is capable of providing nearly CCSDT level of accuracy for wide range of internuclear geometries. However, both LR-CCSD(T) and CR-CC( $m_A, m_B$ ) methods are not invariant under the separate rotations of the occupied and unoccupied orbitals.

Yet another approach to build efficient non-iterative corrections is offered by the regularization of the generating functional based energy expansion [82]:

$$E = E^{(A)} + \sum_{J; J \neq 0} \bar{M}_J^{(A)} \left[ \frac{\partial}{\partial S_J} W(\Sigma, S) \right] |_{S^{(A)}=T^{(A)}; S^{(R)}=0}, \quad (9.39)$$

where the energy is a function of the generating functional  $W(\Sigma, S)$ , which corresponds to the connected part of the overlap between exact and auxiliary wavefunctions in the CC parametrization ( $\Sigma$  and  $S$  refer to the exact and auxiliary cluster operators). The Js in summation (9.39) correspond to the strings of occupied and unoccupied spinorbital indices defining excited configurations. The connected form of the generating functional makes the expansion for the exact energy manifestly size-extensive. However, expansion (9.39) is valid when  $\gamma(\Sigma, S)$  ( $W(\Sigma, S) = \ln(1 + \gamma(\Sigma, S))$ ), satisfies the condition  $|\gamma(\Sigma, S)| < 1$ , which is the case for weakly correlated systems. To extend the applicability of the formula (9.39) to strong correlation limit Kowalski et al. [83] introduced a regularization parameter (cutoff)  $x$  into the  $\gamma(\Sigma, S)$  ( $\gamma(\Sigma, S, x)$ ) so that the  $|\gamma(\Sigma, S, x)| < 1$  condition is satisfied. The regularized version of the CCSD(T) approach improves the quality of the CCSD(T) method in describing bond breaking processes.

### 9.2.4 Parallel Implementations of the SRCC Methods

The two major obstacles affecting the development and applicability of CC methods is their complex algebraic structure and their high numerical complexity (see Table 9.2). For example, switching from CCSD to CCSDT leads to increase in numerical complexity from  $n_o^2 n_u^4$  to  $n_o^3 n_u^5$  (in typical calculations it is assumed that  $n_o \ll n_u$ ). At the same time, the memory/storage requirements associated with storing CC amplitudes grow from  $\frac{1}{4} n_o^2 n_u^2$  to  $\frac{1}{36} n_o^3 n_u^3$ . There are two closely interrelated measures, which can jointly alleviate these problems as far as the canonical formulations of the CC methods are concerned: (1) the development of non-iterative methods, which reduces the numerical complexity of the CCSDT method to  $n_o^3 n_u^4$  maintaining at the same time the storage requirements of the CCSD approach. (2) The development of parallel codes to enable the CC calculations for large systems. While several perturbative algorithms have already been discussed in this section we will entirely focus on the numerical challenges faced in the development of the CC methods.

To deal with the complex algebraic structure involving multiple contractions between multidimensional tensors, various symbolic algebra systems have been developed to automate the process of deriving second-quantization-based equations, optimization of the operation count, and generation of optimized parallel computer codes. The first step requires an efficient implementation of the Wick theorem to generate all diagrams relevant to a given approximation. The next step is associated with the most efficient reduction of the numerical complexity of a given CC method. For example, recursive intermediates can be invoked to minimize the number of operations associated with calculating a simple tensor expression

$$R_j^i = A_k^i B_l^k C_j^l, \quad (9.40)$$

where the Einstein summation over repeated indices is assumed. If we assume that each index runs from 1 to  $L$ , then the cost of calculating all components of the  $R$  tensor by direct summation of all products is proportional to  $L^4$ . Instead, if one introduces the recursive intermediate (or auxiliary tensor  $I$ ) defined as

$$I_j^k = B_l^k C_j^l, \quad (9.41)$$

then

$$R_j^i = A_k^i I_j^k \quad (9.42)$$

and the overall cost of calculating  $R$ -tensor is reduced to  $L^3$ , which is achieved at the expense of storing the  $I$ -tensor in memory. For the CC equations, the problem is more complicated (see Fig. 9.1) and one has to find the best trade-off between memory and operation count requirements (more details on factorization techniques can be found in [84, 85]). An important role in finding the best compromise between the optimum memory versus cost strategies is played by automatic code generators such as TCE ( tensor contraction engine) [86, 87] or SIAL (super assembly instruc-

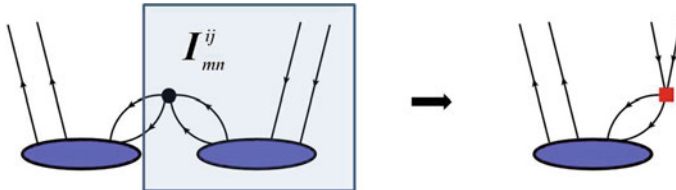


**Fig. 9.1** Factorization of the connected diagram contributing to the CCSD equations in projections onto doubly excited configurations  $|\phi_{ij}^{ab}\rangle$ . The corresponding algebraic expression  $\frac{1}{4}v_{mn}^{ef}t_{ef}^{ij}t_{ab}^{mn}$  is factorized to the form  $\frac{1}{2}I_{mn}^{ij}t_{ab}^{mn}$  where the intermediate  $I_{mn}^{ij}$  is defined as:  $I_{mn}^{ij} = \frac{1}{2}v_{mn}^{ef}t_{ef}^{ij}$  (Einstein summation convention is used). The initial cost of calculating this diagram is proportional to  $n_o^4 n_u^4$ . Once the intermediate  $I_{mn}^{ij}$  is utilized, the cost corresponds to  $2 \times n_o^4 n_u^2$ . The memory requirement associated with storing  $I_{mn}^{ij}$  is proportional to  $n_o^4$ . In the above Hugenholtz (unlabeled) diagram the cluster operator is represented by blue ovals, the two-body part of the Hamiltonian is represented by the black circle vertex, while the recursive intermediate  $I$  is symbolically represented by a red square

tion language) [89] used to automatically generate the CC codes in NWChem [88] and in ACES III [89] quantum chemistry packages. For various formulations of the symbolic algebra systems for CC theory the reader is referred to Refs. [90–96]. The TCE has been used to develop parallel implementations for a wide array of SRCC methods in NWChem including ground- and excited-state CC formulations and linear response CC methods. The execution granularity of the TCE codes is provided by the corresponding data representation which is based on the partitioning of the entire spinorbital domain into smaller subsets (tiles) containing spinorbitals corresponding to the same spin and spatial symmetries. The occupied and unoccupied tiles are designated as  $[i]$ ,  $[j]$ ,  $[k]$ , ... and  $[a]$ ,  $[b]$ ,  $[c]$ , ..., respectively. This division entails the partitioning of all tensors involved in the CC calculations including cluster amplitudes, recursive intermediates, and integrals. For example, the tensor corresponding to doubly excited amplitudes is stored in block form defined by smaller 4-dimensional tensors

$$t_{[a][b]}^{[i][j]} \quad (9.43)$$

representing a subset of doubly excited amplitudes defined by the indices belonging to the  $[i]$ ,  $[j]$ ,  $[a]$  and  $[b]$  tiles. Parallelization of the code, based on dynamic load balancing, occurs over the `do-loops` over occupied/unoccupied tiles. The units of parallel work are said to constitute a task pool—a collection of tasks that can be executed in parallel. The scalability of each section of the calculation is directly related to the size of its task pool. The maximum size of tiles ( $a_t$ ) can be used to tune the granularity of the CC code to given architecture specifications. The  $a_t$  parameter also defines the efficacy of `dgemm` calls [97] and local memory requirements. While for the iterative CCSD method the local memory demand is proportional to  $a_t^4$ , the analogous demand for the triples part amounts to  $2a_t^6$ . In order to overcome this bottleneck we have developed a version of the code where the 6-dimensional tensors can

be dynamically decomposed along the first two dimensions to match the available local memory. All parallel implementations of the non-iterative triples corrections for the ground- or excited-state formulations follow the non-iterative CCSD(T) algorithm:

```

corr=0.0d0
[a]=noab+1,noab+nvab
[b]=[a],noab+nvab
[c]=[b],noab+nvab
[i]=1,noab
[j]=[i],noab
[k]=[j],noab
dynamic load balancing: each task is assigned to the first
available process
calculate: A[a][b][c][i][j][k]
calculate: B[a][b][c][i][j][k]
calculate increments to the CCSD(T) correction
for a ∈ [a]; b ∈ [b]; c ∈ [c]; i ∈ [i]; j ∈ [j]; k ∈ [k]
corr=corr+λ × (Aabcijk + Babcijk)  $\frac{A_{ijk}^{abc}}{\epsilon_i+\epsilon_j+\epsilon_k-\epsilon_a-\epsilon_b-\epsilon_c}$ 
end of load balance assigned task
enddo
enddo
enddo
enddo
enddo
enddo

```

where noab and nvab refer to total number of occupied and virtual tiles and  $A_{ijk}^{abc}$  and  $B_{ijk}^{abc}$  tensors correspond to  $\langle \phi_{ijk}^{abc} | V_N T_2 | \phi \rangle$  and  $\langle \phi_{ijk}^{abc} | V_N T_1 | \phi \rangle$ , respectively. The weight coefficient  $\lambda$  depends on the occupied/unoccupied tiles. In the last step, values of corr are gathered from all cores. The usage of a distributed memory model in conjunction with a tool like Global Arrays [98–100] has enabled the development of very efficient non-iterative schemes. An excellent illustration of the progress achieved is given by two examples: (1) CCSD(T) calculations for the  $(\text{H}_2\text{O})_{24}$  and  $(\text{H}_2\text{O})_{17}$  clusters in the modified cc-pVTZ and aug-cc-pVTZ basis sets [101] for a total of 1224 and 1564 basis functions (see Refs. [102, 103] for details) and (2) recent scalability tests for the excited-state analogue of the CCSD(T) method (the CR-EOMCCSD(T) method [104]), where 94 % of parallel performance has been achieved when running on 210,000 cores (see Fig. 9.2). Recently, GPU (graphics processing units) implementations of the iterative [107] and non-iterative [108] methods have also been reported, showing great promise in accelerating CC calculations on massively parallel GPU computers.

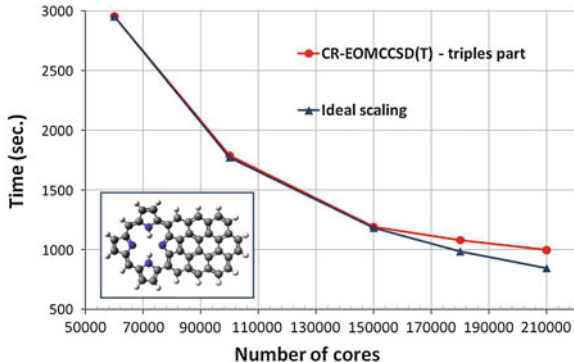


**Fig. 9.2** Scalability of the triples part of the CR-EOMCCSD(T) approach [105] for the FBP-f-coronene system (see the inset) with the Ahlrichs VTZ basis set (AVTZ) [106]. Timings were determined from calculations on the Jaguar Cray XT5 computer system at NCCS

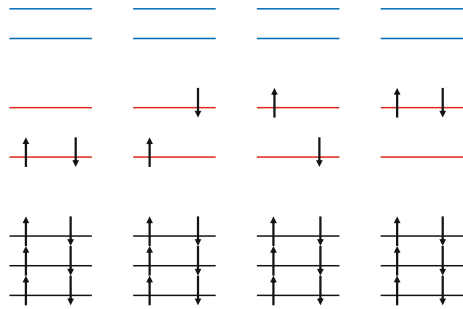
### 9.3 Multireference CC Theories

MRCC formalisms extend the applicability of CC methods to quasidegenerate situations, where several Slater determinants play an important role in the wavefunction description. In such situations SRCC methods experience problems which cannot be solved by perturbative inclusion of higher-rank cluster operators. These problems are commonly encountered in many chemical applications such as studies of bond-breaking processes, poly-radical species, transition metal compounds, low-spin open-shell states, and reactions involving potential energy surfaces crossing and symmetry breaking. In order to properly address problems associated with the inadequacy of single reference representations of the electronic wavefunctions, MRCC approaches based on the model space ( $\mathcal{M}_0$ ) concept have to be invoked. The  $M$ -dimensional model space is spanned ( $l_s$ ) by the most important Slater determinants  $|\Phi_\mu\rangle (\mu = 1, \dots, M)$

$$\mathcal{M}_0 = l_s \{ |\Phi_\mu\rangle \}_{\mu=1}^M \quad (9.44)$$

required to describe certain subset of electronic states (Fig. 9.3). In most formulations we deal with the complete model spaces (CMS) generated by all possible combinations of active electrons in active orbitals. The generalizations of the MRCC formalisms to incomplete or general model spaces (IMS/GMS) have also been considered. The main motivation behind the development of MRCC-based methods is to provide equally accurate descriptions of electronic states characterized by a very diversified configurational structure. Over the last few decades two major classes of the MRCC approaches have emerged: the Fock-space (FS-MRCC) [109–117] and Hilbert-space (HS-MRCC) [118–128] formulations (see also a recent review on the multireference CC methods [15]). While the FS-MRCC formalisms simultaneously

**Fig. 9.3** Schematic representation of the complete model space corresponding to two active electrons distributed over two active orbitals (red lines). Only determinants with  $M_S = 0$  are included in the model space



compute the energies of systems characterized by different number of electrons, the HS-MRCC methods describe the electron correlation effects within a given  $N$ -electron Hilbert space. In the following sections we will focus on the theoretical and computational aspects of the HS-MRCC approaches.

### 9.3.1 Wave Operator Formalism and Bloch Equation

The genuine forms of the MRCC theories or closely related multireference many-body perturbation theories (MR-MBPT) have been introduced on the basis of the wave operator formalism [129–132], where it is assumed that there exists a one-to-one mapping  $U$  (the wave operator) between model space  $\mathcal{M}_0$  and the so-called target space  $\mathcal{M}$

$$U : \mathcal{M}_0 \rightarrow \mathcal{M}, \quad (9.45)$$

where  $\mathcal{M}$  is spanned by the exact electronic wavefunctions  $|\Psi_p\rangle$

$$\mathcal{M} = ls\{|\Psi_p\rangle\}_{p=1}^M \quad (9.46)$$

satisfying the electronic Schrödinger equation

$$H|\Psi_p\rangle = E_p|\Psi_p\rangle \quad (p = 1, \dots, M). \quad (9.47)$$

The projection operators onto model space ( $P$ ) and its orthogonal complement in the Hilbert space ( $Q$ ) are defined as

$$P = \sum_{\mu=1}^M P_\mu, \quad P_\mu = |\Phi_\mu\rangle\langle\Phi_\mu|, \quad (9.48)$$

$$Q = 1 - P \quad (9.49)$$

We will further assume that no state from  $\mathcal{M}$  is orthogonal to  $\mathcal{M}_0$ , i.e., the projections  $|\tilde{\Phi}_p\rangle$

$$|\tilde{\Phi}_p\rangle = P|\Psi_p\rangle = \sum_{\mu=1}^M c_{p,\mu}|\Phi_{\mu}\rangle, \quad (9.50)$$

are linearly independent in  $\mathcal{M}_0$ , and the exact wavefunctions  $|\Psi_p\rangle$  can be approximated by linear combinations of reference functions  $|\Phi_{\mu}\rangle$ . The following conditions imposed on the form of the wave operator

$$PU = P, \quad UP = U, \quad (9.51)$$

guarantees its idempotency  $U^2 = U$ . The first condition in (9.51) is commonly referred to as the intermediate normalization condition. By projecting the Schrödinger equation (9.47) onto the model space

$$P(H - E_p)|\Psi_p\rangle = P(H - E_p)U|\tilde{\Phi}_p\rangle = 0, \quad (9.52)$$

one can see that the exact energy can be reproduced by diagonalizing effective Hamiltonian  $H^{\text{eff}}$ ,

$$H^{\text{eff}} = PHUP, \quad (9.53)$$

in the model space. Given the linear independence of the  $|\tilde{\Phi}_p\rangle$  vectors, the wave operator can be obtained from the Bloch equation [129]

$$HU = UH^{\text{eff}}. \quad (9.54)$$

The Bloch equation has become the basis for the State-Universal MRCC formulations (SU-MRCC). Having solved the Bloch equations for the wave operator, the  $p$ -th wavefunction can be represented as

$$|\Psi_p\rangle = \sum_{\mu=1}^M c_{p,\mu}U|\Phi_{\mu}\rangle, \quad (9.55)$$

where  $c_{p,\mu}$  coefficients are obtained through diagonalization of the effective Hamiltonian.

### 9.3.2 State-Universal MRCC Formulations

The Jeziorski-Monkhorst (JM) MRCC Ansatz [118] for electronic wavefunction provides a foundation for many Hilbert space MRCC formulations. In the state-universal formulation [118–128] the wave operator assumes the following exponential form

$$U = \sum_{\mu=1}^M e^{T^{(\mu)}} P_\mu, \quad (9.56)$$

where in order to assure the intermediate normalization condition the cluster operators for CMS have to satisfy the conditions

$$\langle \Phi_v | T^{(\mu)} | \Phi_\mu \rangle = 0 \quad \forall_{\mu, v}. \quad (9.57)$$

The above requirements imply that the internal excitations (or excitations within the model space) are excluded from the cluster operators. In other words the cluster operators generate the excitations from model space to its orthogonal complement ( $\mathcal{M}_0^\perp$ ).

The set of equations for unknown cluster amplitudes is obtained by introducing the JM Ansatz into the Bloch equation. After projecting Bloch equation from the right onto the  $|\Phi_\mu\rangle$  reference, premultiplying from the left by  $e^{-T^{(\mu)}}$ , and projecting the resulting equations onto the excited configurations from  $\mathcal{M}_0^\perp$ , one can arrive at a common form of the SU-MRCC equations

$$Q[e^{-T^{(\mu)}} H e^{T^{(\mu)}} |\Phi_\mu\rangle - \sum_{v \neq \mu} e^{-T^{(\mu)}} e^{T^{(v)}} |\Phi_v\rangle H_{v\mu}^{\text{eff}}] = 0, \quad (9.58)$$

where the first term on the left hand side (l.h.s.) of Eq. (9.58) is referred to as the direct term, while the second term, which couples the equations for various references, is referred to as the renormalization term. When the truncated form of the cluster operators is considered, for example defined by single and double excitations (SU-MRCCSD), i.e.,

$$T^{(\mu)} \simeq T_1^{(\mu)} + T_2^{(\mu)}, \quad (9.59)$$

then the working equations for the cluster amplitudes (or sufficiency conditions) are defined by projecting the SU-MRCC Eq. (9.58) onto the subspace  $\mathcal{M}_0^{(\mu)}$  (with associated projection operator  $Q^{(\mu)}$ ) of  $\mathcal{M}_0^\perp$  spanned by configurations obtained by acting with the cluster operators onto the corresponding reference functions:

$$(T_1^{(\mu)} + T_2^{(\mu)}) |\Phi_\mu\rangle. \quad (9.60)$$

In analogy with SRCC formulations, this procedure provides equal number of equations and unknown cluster amplitudes. Once the SU-MRCCSD equations given by,

$$Q^{(\mu)} [e^{-T_1^{(\mu)} - T_2^{(\mu)}} H e^{T_1^{(\mu)} + T_2^{(\mu)}} |\Phi_\mu\rangle - \sum_{v \neq \mu} e^{-T_1^{(\mu)} - T_2^{(\mu)}} e^{T_1^{(v)} + T_2^{(v)}} |\Phi_v\rangle H_{v\mu}^{\text{eff}}] = 0. \quad (9.61)$$

are solved, the energies of the  $M$ -state are obtained by diagonalizing effective Hamiltonian matrix, which for the CMS takes the form

**Table 9.4** Comparison of the SU-MRCCSD energies, obtained with the two dimensional model space, with energies of SRCC methods for the H8 model in DZ basis set [134]

$\alpha$	0.0001	0.001	0.01	0.1	0.5	1.0
$1^1A_g$ state						
CCSD	8.761	8.693	8.037	3.669	1.171	0.800
CCSDT	-8.771	-8.675	-7.644	-2.287	-0.033	0.026
SU-MRCCSD	-2.911	-2.913	-2.926	-2.294	-0.205	-0.291
$2^1A_g$ state						
SU-MRCCSD	9.979	9.980	10.028	9.817	11.535	24.989

Energies of the CC methods are reported as errors with respect to the FCI energies (all differences are expressed in millihartree). All results were taken from Ref. [128]

$$H_{\nu\mu}^{\text{eff}} = \langle \Phi_\nu | (He^{T_1^{(\mu)} + T_2^{(\mu)}})_C | \Phi_\mu \rangle. \quad (9.62)$$

Table 9.4 shows the results obtained with the single reference CCSD and CCSDT methods and SU-MRCCSD approach for the H8 model [133] (in DZ basis set [134]), which has been widely used as a test case for MRCC theories. The level of quasidegeneracy of the ground-state wavefunction can be controlled by a single geometry parameter  $\alpha$ . The geometries defined by  $\alpha < 0.1$  correspond to the strong quasidegeneracy effects in the ground state, while those given by  $\alpha > 0.1$  correspond to the nondegenerate case. The employed two dimensional model space provides a good description of the ground-state static correlation effects in the quasidegenerate situations. From Table 9.4 one can see that the quality of the CCSD and CCSDT ground-state energies significantly deteriorates in the quasidegenerate region (small  $\alpha$ 's). The SU-MRCCSD approach outperforms the SRCC methods in this region. For nondegenerate region ( $\alpha = 1.0$ ) the SU-MRCCSD energy is more accurate than CCSD and only slightly worse than CCSDT. However, the quality of the first excited singlet state does not match the quality of the ground state. This is especially seen for  $\alpha = 1.0$  region, where the model space is no longer adequate to provide zeroth order approximation to the  $2^1A_g$  state. These problems are usually attributed to the so-called intruder state problem, i.e. the detrimental effect of the configurations from  $\mathcal{M}_0^\perp$ , which are energetically close to some configurations from the model space. However, the nature of these problems is much broader and many issues confronting the SU-MRCC theories also stem from the existence of the multiple solutions to the SU-MRCC equations and accidental degeneracies in perturbative denominators.

### 9.3.3 Intruder State Problem

The genuine MRCC theories are inextricably linked with multireference many-body perturbation (MRMBPT) theory. In analogy with the SRCC case, the multireference generalizations of the linked cluster theorem [135, 136] have been used to examine the hierarchy of correlation effects in the quasidegenerate case. The intruder

state problems, which have been extensively reported over the last few decades, are usually linked to the lack of convergence of multireference many-body perturbation theory [137–141]. These problems have hampered the widespread use of MRCC/MRMBPT theories and have spawned significant efforts towards developing intruder-free MRCC algorithms. Several techniques have been introduced and tested including: generalizations of the SU-MRCC formalisms to the incomplete/general model spaces, State-Specific MRCC methods, intermediate Hamiltonian formulations, inclusion of higher-order effects, regularization techniques, to name a few.

The nature of these problems can be understood based on the perturbative analysis of the effective Hamiltonian  $H^{\text{eff}}(\lambda)$  as a function of the perturbation parameter  $\lambda$  in the perturbed Hamiltonian  $H(\lambda)$

$$H(\lambda) = H_0 + \lambda V, \quad (9.63)$$

where  $H_0$  and  $V$  represent the nonperturbed and perturbed parts of the Hamiltonian  $H$ . Following Schucan and Weidenmüller and using the extension of the von Neumann-Wigner noncrossing rule [142, 143], one can show that the radius of convergence ( $r_0$ ) for the effective interaction operator  $V^{\text{eff}}(\lambda)$ ,

$$H^{\text{eff}}(\lambda) = P H_0 P + V^{\text{eff}}(\lambda), \quad (9.64)$$

is defined by the position of the crossing  $x_c$  between internal (i.e. emanating from the model space for  $\lambda = 0$ ) and external (outside of model space for  $\lambda = 0$ ) eigenvalues of the perturbed Hamiltonian, i.e.,  $r_0 = |x_c|$ . This situation often occurs when some references from the model space are energetically close to some configurations from  $\mathcal{M}_0^\perp$ . Recently, it was also demonstrated that the nonlinear character of the Bloch equations and nonlinear parametrization of the wave operator can also lead to numerical problems which are commonly termed the intruder solution problem [144].

### 9.3.4 Incomplete/General Model Spaces

Although the use of CMS based SU-MRCC formulations leads to the connected form of the equations and the expressions for the effective Hamiltonian, the CMS based approaches are prone to the intruder state problem. Another unsettling problem arises due to the quick growth of the dimensionality of the CMS with the number of active orbitals. Therefore, it is desirable to have a connected form of the cluster amplitudes and effective Hamiltonian for the incomplete/general model space.

The first formulation of the SU-MRCC formulation for the incomplete model space was introduced by Meissner et al. [145–147] where the additional “internal” excitations, i.e. excitations from one to the other reference functions, were introduced to eliminate the disconnected terms in the coupling part of the equations for cluster amplitudes and for the effective interaction operator. Critical for the proof of the connected form of the cluster operators in the CMS case was showing that the

difference  $T^{(v)} - T^{(\mu)}$  in the coupling terms

$$\sum_{v \neq \mu} e^{-T^{(\mu)}} e^{T^{(v)}} |\Phi_v\rangle V_{v\mu}^{\text{eff}} = \sum_{v \neq \mu} (T^{(v)} - T^{(\mu)}) + \frac{1}{2} [T^{(v)}, T^{(\mu)}] \\ + \frac{1}{12} [[T^{(v)}, T^{(\mu)}], T^{(\mu)}] - \dots |\Phi_v\rangle V_{v\mu}^{\text{eff}} \quad (9.65)$$

can be expressed through diagrams carrying at least one spinorbital label that distinguishes references  $|\Phi_v\rangle$  and  $|\Phi_\mu\rangle$ . Through these indices the  $T^{(v)} - T^{(\mu)}$  expressions are “connected” with the matrix elements of the effective interaction  $V_{v\mu}$ , which depends on all spinorbitals distinguishing  $|\Phi_v\rangle$  and  $|\Phi_\mu\rangle$ . For the IMS this is no longer true (the excitation which produces the excited configuration from the  $\mathcal{M}_0$  when acting on  $|\Phi_\mu\rangle$  may lead back to the IMS when acting on the other reference  $|\phi_v\rangle$ ). In order to preserve the connectivity of the SU-MRCC equations Meissner et al. gave up the intermediate normalization in order to eliminate such disconnected contributions by introducing internal cluster amplitudes in  $T^{(v)}$  operator. These internal amplitudes are used to zero the problematic  $V_{v\mu}^{\text{eff}}$  terms, which results in a rigorous size-extensive formalism.

Another extension of the SU-MRCC formalism to the general model space was introduced by Paldus and Li [148–150], who by introducing additional internal excitations and the so-called *C-conditions* were able to maintain the intermediate normalization of the JM Ansatz. For each pair of references  $|\Phi_v\rangle$  and  $|\Phi_\mu\rangle$ , these internal excitations are defined from the conditions:

$$\langle \Phi_v | T^{(\mu)} | \Phi_\mu \rangle = -\langle \Phi_v | e^{T^{(\mu)}} | \Phi_\mu \rangle_{ADC}, \quad (9.66)$$

where the acronym *ADC* designates all disconnected clusters in the  $e^{T^{(\mu)}} |\Phi_\mu\rangle$  expansion. The above condition referred to as the *C-condition* leads to the intermediate normalization of the wave operator

$$\langle \Phi_v | e^{T^{(\mu)}} | \Phi_\mu \rangle = \delta_{v\mu}. \quad (9.67)$$

The C-condition based GMS SU-MRCC approach is size-consistent, and has been recently tested on a number of challenging ground- and excited-state problems. Due to the intricate logic, the biggest challenge in implementing GMS SU-MRCC theories is due to the renormalization terms. The explicit expressions for these terms were derived diagrammatically in Ref. [151].

### 9.3.5 State-Specific Methods

In contrast to the Bloch-equation-based SU-MRCC methods, the State-Specific MRCC methods (SS-MRCC) target only one electronic state. The main motiva-

tion behind the development of the SS-MRCC approaches was, as in the IMS/GMS-SU-MRCC cases, to alleviate the intruder-state problem. Additionally, the state-specific formulations offer more optimization parameters (cluster amplitudes) per state compared with the SU-MRCC methods. The SS-MRCC methods introduce the JM Ansatz directly into the electronic Schrödinger equation, which results in well known overcompleteness problems. Over the last decade several sufficiency conditions (or equations defining cluster amplitudes) have been discussed in the literature, including the original Brillouin-Wigner MRCC (BW-MRCC) methods introduced by Hubač, Pittner and co-workers, [152–158] Mk-MRCC methods by Mukherjee et al. [159–165] and Hanrath’s MExpT approach [166–168] (for other formulations see Refs. [169, 170]).

Introducing Ansatz (9.55) into the Schrödinger equation yields

$$\sum_{\mu=1}^M c_{\mu} (H - E) e^{T^{(\mu)}} |\Phi_{\mu}\rangle = 0, \quad (9.68)$$

where for the sake of simplicity we skipped the target state index  $p$ . Projecting this equation onto excited configurations from  $\mathcal{M}_0^\perp$  does not provide sufficient number of equations to determine all cluster amplitudes defining  $T^{(\mu)}$  operators. To address this problem several sufficiency conditions have been postulated. In the BW-MRCC theory the sufficiency conditions are extracted from (9.68) by requesting each component of the sum to be equal to zero

$$(H - E) e^{T^{(\mu)}} |\Phi_{\mu}\rangle = 0 \quad \forall_{\mu}, \quad (9.69)$$

or equivalently

$$(E - H_{\mu\mu}^{\text{eff}}) \langle \Phi_{\theta}^{(\mu)} | e^{T^{(\mu)}} | \Phi_{\mu} \rangle = \langle \Phi_{\theta}^{(\mu)} | H_N(\mu) e^{T^{(\mu)}} | \Phi_{\mu} \rangle_{C+DC,L}, \quad (9.70)$$

where  $\langle \Phi_{\theta}^{(\mu)} |$  are excited configurations corresponding to the excitations used to define cluster operator  $T^{(\mu)}$ . The  $H_N(\mu)$  operator represents the normal ordered Hamiltonian with respect to the  $\mu$ -th reference, i.e.,  $H_N(\mu) = H - \langle \Phi_{\mu} | H | \Phi_{\mu} \rangle$ . The subscript  $C + DC, L$  designates all connected diagrams and all linked, but disconnected diagrams. Assuming CMS and intermediate normalization of the wave operator, the effective Hamiltonian for the BW-MRCC approach assumes the same form as in the SU-MRCC case. The BW-MRCC equations can be easily implemented using spinorbital SRCC codes. In contrast to the Mk-MRCC approach (*vide infra*), the BW-MRCC formalism contains disconnected contributions.

In Mk-MRCC formulations the equations for amplitudes are obtained by introducing the reference-specific resolution of identity

$$1 = e^{T^{(\mu)}} (P + Q) e^{-T^{(\mu)}} \quad (9.71)$$

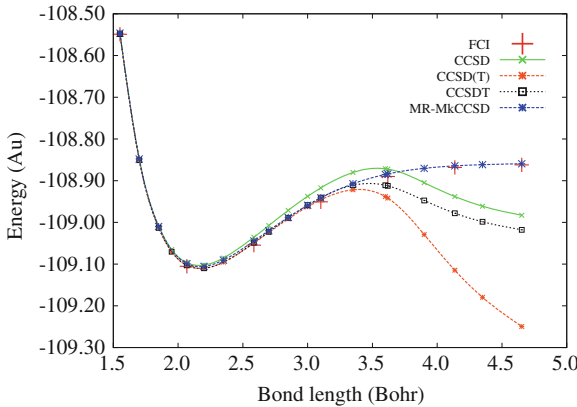


**Fig. 9.4** Comparison of SRCC and MRCC energies with the FCI ones for  $\text{N}_2$  molecule in the DZ basis set

in front of each term in summation (9.68). The Mk-MRCC sufficiency conditions are chosen in such a way that the following equations are satisfied

$$\langle \Phi_\theta^{(\mu)} | \bar{H}^{(\mu)} | \Phi_\mu \rangle c_\mu + \sum_{v \neq \mu} \langle \Phi_\theta^{(\mu)} | e^{-T^{(\mu)}} e^{T^{(v)}} | \Phi_\mu \rangle H_{\mu v}^{\text{eff}} c_v = 0 \quad \forall \mu. \quad (9.72)$$

The Mk-MRCC equations contain connected diagrams only and the approach is rigorously size-extensive. The compact form of the coupling terms has been derived by Evangelista et al. [162]. However, the main challenge in applying this approach to quasidegenerate systems is associated with very slow convergence of iterative procedures used to solve Mk-MRCC equations. The major contributing factor can be attributed to the presence of very small  $c_\mu$  coefficients for certain references spanning complete model space.

In Fig. 9.4 we illustrate typical problems encountered by SRCC formulations and the improvements offered by the Mk-MRCCSD (Mk-MRCC with singles and doubles) approach for the ground-state potential energy curve of the  $\text{N}_2$  molecule as in the Cartesian DZ basis set [134]. In the Mk-MRCCSD calculations the CMS defined by six active electrons and six active orbitals was used.

### 9.3.6 Inclusion of High-Order Clusters in MRCC Formalisms

As in the SRCC case, the inclusion of higher-rank clusters seems to be a natural way to increase the accuracy of the MRCC methods in the presence of intruder states. Consequently, the triply excited clusters have been included in several genuine MRCC formulations including BW-MRCCSDT [158] and Mk-MRCCSDT [163–165] formalisms. Although leading to systematic improvements of the MRCCSD energies,

the inclusion of triple excitations in MRCC theories is very challenging from a computational standpoint. Instead, as in the SRCC formulations, several strategies for incorporating triply excited cluster amplitudes in a non-iterative way have been intensively explored in the last decade. This effort has led to the emergence of two major classes of corrections. The first class, embracing both SU- and SS-MRCC formulations, augments the MRCCSD effective Hamiltonians to capture the effect of triply excited cluster amplitudes. This general strategy was first introduced by Balková and Bartlett [171] in the context of the SU-MRCC theory. In their approach (termed the MR-CCSD(T) method) terms due to triply excited amplitudes were added to the diagonal and off-diagonal elements of the SU-MRCCSD effective Hamiltonian. To get the perturbative estimates of triples the authors used the MRCC generalization of the CCSDT-1 formulas. Similar ideas have been adopted by Li and Paldus in the context of GMS MRCC [172] and by Pittner, Demel, Bhaskaran-Nair for the BW-MRCC and Mk-MRCC theories [173–175]. In these approaches, the general form of the corrected effective Hamiltonian  $H^{\text{eff}}(T)$  can be expressed as:

$$H_{\nu\mu}^{\text{eff}}(T) = \langle \Phi_\nu | (He^{T_1^{(\mu)} + T_2^{(\mu)}})_C | \Phi_\mu \rangle + \delta_{\nu\mu}(\bar{T}^{(\mu)}), \quad (9.73)$$

where  $\delta_{\nu\mu}(\bar{T}^{(\mu)})$  term depends on the  $\bar{T}_3^{(\mu)}$  operator representing perturbative approximation to the exact  $T_3^{(\mu)}$  operator. Due to the cost of the off-diagonal corrections, only diagonal corrections are numerically tractable in practical calculations. The MRCCSD(T) approaches provide further refinement of the MRCCSD methods especially in calculating spectroscopic constants and the heights of the transition barriers [174]. The non-iterative inclusion of triples also alleviates the problem of lack of unitary invariance of the MRCC theories with respect to the rotations of active orbitals [174]. Various choices for  $\bar{T}_3^{(\mu)}$  have been extensively discussed by Pittner et al. in Refs. [165, 174–176].

The second class of methodologies contains approaches where higher-order correlation effects are accounted for by using energy functionals. There are two main formulations:

- Multireference extension of the method of moments of coupled cluster equations [177, 178]. This approach utilizes the asymmetric form of the energy functional for the Bloch equations

$$\Lambda[\Psi, \chi] = \langle \Psi | (HU - UH^{\text{eff}}) | \chi \rangle / \langle \Psi | U | \chi \rangle, \quad (9.74)$$

to derive a hierarchy of the non-iterative approximations. In analogy with the SR MMCC theory, when the trial wavefunction  $|\Psi\rangle$  and model space state function  $|\chi\rangle$  are replaced by the exact wavefunction and eigenvector of the effective Hamiltonian, respectively, the value of this functional is equal to the energy difference between FCI energy and the energy obtained in approximate MRCC calculations. This approach was used to derive the triples corrections for the SU-MRCCSD approach (the completely renormalized SU-MRCCSD(T) approaches of Ref.

[178]). Recently, the MR MMCC formalism has been extended by Pittner and Piecuch to the Brillouin-Wigner-type and Rayleigh-Schrödinger-type MRCC theories [179].

- The Lagrangian formulations of the non-iterative corrections to the Mk-MRCC theories [180]. Although the resulting  $\Lambda$ -Mk-MRCCSD(T) method [180] provides an algebraic form of perturbative corrections to the effective Hamiltonian, their derivation is based on the constrained search for the stationary points of the Mk-MRCC Lagrangian

$$\begin{aligned} E(\Lambda^\mu, T^\mu, \mathbf{c}, \bar{\mathbf{c}}, E^{(A)}) = & \sum_{\mu, v=1}^M \bar{c}_\mu H_{\mu v}^{\text{eff}} c_v + \sum_{\mu=1}^M \bar{c}_\mu c_\mu \langle \Phi_\mu | \Lambda^\mu \bar{H}^\mu | \Phi_\mu \rangle \\ & + \sum_{\mu, v=1}^M \bar{c}_\mu H_{\mu v}^{\text{eff}} c_v \langle \Phi_\mu | \Lambda^\mu Y^{\mu v} | \Phi_\mu \rangle - E^{(A)} \left[ \sum_{\mu=1}^M \bar{c}_\mu c_\mu - 1 \right], \end{aligned} \quad (9.75)$$

where amplitudes defining  $\Lambda^\mu$  operators,  $\bar{c}_\mu$  coefficients, and scalar  $E^{(A)}$  refer to Lagrange multipliers. The calculation of the  $\Lambda$ -Mk-MRCCSD(T) correction involves iterative determination of the second-order of triply excited cluster amplitudes, which significantly increases the associated numerical overhead. Preliminary studies with the  $\Lambda$ -Mk-MRCCSD(T) approach have shown that the inclusion of the diagonal and off-diagonal corrections to the effective Hamiltonian significantly improves the quality of the Mk-MRCCSD formulations. Recently, it has also been demonstrated for the BeH<sub>2</sub> system that the MR MkCCSD(T<sub>u</sub>) approximation [176], which avoids the expensive iterative step for triply excited amplitudes, can produce results of the same quality as the  $\Lambda$ -Mk-MRCCSD(T) approach.

A very convenient theoretical platform for developing non-iterative corrections stems from the Universal State Selective formalism (USS) [181], which falls into the second class of methods. The USS approach is based on the asymmetric USS-MRCC functional defined as

$$E(\bar{\Psi}^{(1)}, \dots, \bar{\Psi}^{(M)}) = \sum_{\mu=1}^M \frac{\langle \bar{\Psi}^{(\mu)} | H e^{T^{(\mu)}} | \Phi_\mu \rangle}{\langle \bar{\Psi}^{(\mu)} | e^{T^{(\mu)}} | \Phi_\mu \rangle} c_\mu^2, \quad (9.76)$$

where  $\langle \bar{\Psi}_\mu |$  are the reference-specific trial wavefunctions. It can be shown that once the trial wavefunctions are replaced by the exact wavefunction, the value of the USS-MRCC is equal to the exact (FCI) energy (assuming that  $\sum_{\mu=1}^M c_\mu^2 = 1$ ). As discussed in Ref. [181] the form of the USS-MRCC functional can be greatly simplified by: (1) using a reference-specific form of the trial wave function  $\langle \bar{\Psi}_\mu |$  (see also Ref. [181] for details), i.e.,

$$\langle \bar{\Psi}^{(\mu)} | = \sum_{v=1}^M d_v^{(\mu)} \langle \Phi_v | (1 + \Lambda_v^{(\mu)}) e^{-T^{(\mu)}}, \quad (9.77)$$

where  $\Lambda_v^{(\mu)} = P_v \Lambda^{(\mu)} Q$  are the “de-excitation” correlation operators, and (2) by employing appropriate normalization conditions for the  $d_v^{(\mu)}$  coefficients, i.e.,

$$d_\mu^{(\mu)} = c_\mu. \quad (9.78)$$

Using (9.77) and (9.78) the USS-MRCC functional takes a simple form

$$E = E^{(A)} + \sum_{\mu, v=1}^M \Delta_v^{(\mu)} H_{v\mu}^{\text{eff}} c_\mu + \sum_{\mu, v=1}^M d_v^{(\mu)} \langle \Phi_v | \Lambda_v^{(\mu)} \bar{H}^{(\mu)} | \Phi_\mu \rangle c_\mu, \quad (9.79)$$

where the  $E^{(A)}$  is the energy obtained in the approximate MRCC calculations through the diagonalization of the corresponding effective Hamiltonian and  $\Delta_v^{(\mu)} = d_v^{(\mu)} - \bar{c}_v$  ( $\bar{c}_v$  coefficients are the components of the left eigenvector  $\bar{\mathbf{c}}$  of the effective Hamiltonian). Equivalently, Eq. (9.79) can be expressed using the formula

$$E = E^{(A)} + \text{Tr}[\Delta \mathbf{H}^{\text{eff}} \mathbf{M}] + \text{Tr}[\mathbf{D} \mathbf{H}^{\text{corr}} \mathbf{M}], \quad (9.80)$$

where  $\mathbf{H}^{\text{corr}}$  is the matrix representation of the correlation Hamiltonian operator  $H^{\text{corr}}$ ,

$$H^{\text{corr}} = \sum_{\mu, v=1}^M P_v \Lambda_v^{(\mu)} \bar{H}^{(\mu)} P_\mu. \quad (9.81)$$

The  $\Delta$ ,  $\mathbf{D}$ , and  $\mathbf{M}$  matrices are defined through the matrix elements  $\Delta_{\mu v} = \Delta_v^{(\mu)}$ ,  $D_{\mu v} = d_v^{(\mu)}$ ,  $M_{\mu v} = \delta_{\mu v} c_\mu$ . The  $\Lambda_v^{(\mu)}$  operators can be determined from reference-specific form of the left Bloch equations (see Ref. [181] for details). The use of the alternative form of the trial wavefunction (double exponential Ansatz)

$$\langle \bar{\Psi}^{(\mu)} | = \sum_{v=1}^M d_v^{(\mu)} \langle \Phi_v | e^{S_v^{(\mu)}} e^{-T^{(\mu)}}, \quad (9.82)$$

leads to several important features of the USS expansion (9.79). Assuming connectivity of the  $T^{(\mu)}$  and  $S_v^{(\mu)}$  operators and proper separability of the model space  $\mathcal{M}_0$  in the NSL into the tensor product of model spaces for the composite subsystems A and B, i.e.,  $(\mathcal{M}_0(A) \otimes \mathcal{M}_0(B))$ ,

$$\mathcal{M}_0(AB) = \mathcal{M}_0(A) \otimes \mathcal{M}_0(B), \quad (9.83)$$

one can prove (see Ref. [181]):

- connectivity of the effective and correlated Hamiltonians,
- additive separability of the USS functional in the NSL.

For these reasons the USS expansion can be utilized in constructing non-iterative corrections, which assures proper behavior of the energy in the dissociation limit. In recent studies [182], we have employed the simplest variant of the USS expansion in order to explore to what extent it can minimize the energy differences caused by a different choice of the sufficiency conditions for models employing single and double excitations (this feature will be referred to as the universality of the USS approach). For this purpose we applied a simple variant of the USS expansion (called the USS(2) approach) to BW-MRCCSD and Mk-MRCCSD approaches:

$$E^{\text{USS}(2)-X} = E^X + \sum_{\mu, \nu=1}^M c_\nu \langle \Phi_\nu | (T_1^{(\nu)} + T_2^{(\nu)})^+ (\bar{H}_1^{(\mu)} + \bar{H}_2^{(\mu)}) | \Phi_\mu \rangle c_\mu \quad (X = \text{BW, Mk}) \quad (9.84)$$

(we also considered the “diagonal” part of the formula (9.84) where  $\mu = \nu$  contributions are included only ( $E^{\text{D-USS}(2)-X}$  ( $X = \text{BW, Mk}$ ))). The USS(2) and D-USS(2) results for the H8 model in 6-31G basis set are shown in Fig. 9.5. Although the diagonal variant has the tendency to overshoot the FCI energies, both USS(2)-BW and USS(2)-Mk approaches provide a very balanced description of the correlation effects for the considered set of H8 geometries. Moreover, the differences between the USS(2)-BW and USS(2)-Mk energies are much smaller than the analogous differences between the original BW-MRCCSD and Mk-MRCCSD energies. These results provide a strong argument in favor of the universality of the USS methods.

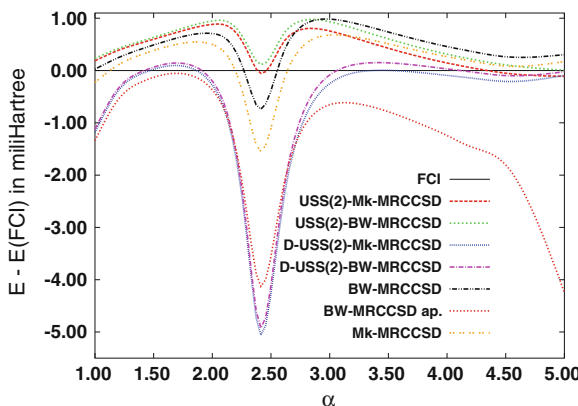


**Fig. 9.5** Errors of the MRCC energies (with respect to the FCI energies) for various geometries of H8 model. All calculations were performed for the 6-31G basis set [183]

### 9.3.7 Parallel Calculations with the MRCC Methods: Reference-Level Parallelism

The development of efficient implementations of the MRCC methodologies requires a thorough revision of the programming models used for coding SRCC theories. Recently, we have explored new algorithms based on the utilization of the reference-level parallelism and processor groups (PGs) to enable large scale MRCC calculations [184]. To understand basic tenets of this approach let us introduce basic terminology and notation. By processor group ( $G_i$ ) we mean a partitioning of the processor domain ( $D$ ) into smaller pieces, which can be symbolically expressed

$$D = \bigcup_{i=1, \dots, I} G_i \quad (9.85)$$

where  $I$  is the total number of the processor groups. We will assume that the number of processors in each group ( $S_i$ ) is the same and is equal to  $S$ , i.e.,

$$S_i = S = \frac{N_p}{I} \quad (i = 1, \dots, I). \quad (9.86)$$

In the above equation  $N_p$  stands for the total number of processors, which is a multiple of PGs number  $I$ . The key idea is to distribute the formation of reference-specific MRCC equations over various processor groups. This approach employs two-level parallelism: (1) reference-level parallelism, where each set of reference-specific equations (or their aggregate) is calculated on separate PG (2) task-level parallelism used to calculate given set of reference-specific equations. In the simplest case the work organization chart (symbolically designated by  $W$ ) corresponds to the situation when a single PG is delegated to calculate a single set of reference-specific equations ( $\mathbf{R}^{(\mu)}$ ) composed of the direct ( $\mathbf{F}^{(\mu)}$ ) and coupling ( $\mathbf{G}^{(\mu)}$ ) terms. In this case the number of PGs coincides with the size of the model space (i.e.,  $I = M$ ). A more general situation corresponds to the case when each PG  $G_i$  forms several ( $n_r(i)$ ) residual vectors  $\mathbf{R}^{(\mu)}$ . This can be symbolically denoted as

$$W = \bigcup_{i=1, \dots, I} W_i(n_r(i)), \quad (9.87)$$

where  $W_i$  refers to work-load on the corresponding processor group  $G_i$ . In order to provide best load balancing between the workloads on each PG it is natural to assume that

$$n_r = n_r(i) = \frac{M}{I} \quad (i = 1, \dots, I). \quad (9.88)$$

In the following, in order to report specific configurations of the processor groups used in the calculation, we will use the  $PG(n_r, I, S)$  notation. The schematic representation of our algorithm is shown in Fig. 9.6 In the first step, the domain  $D$  (or

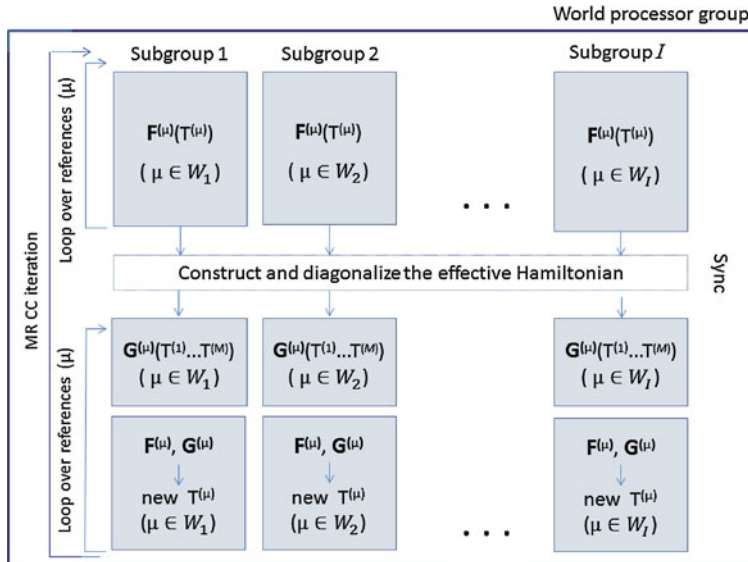


**Fig. 9.6** Schematic representation of processor-group based MRCC algorithms used to implement BW-MRCCSD and Mk-MRCCSD approaches

the world processor group) is partitioned into  $I$ -groups  $\{G_i\}_{i=1}^I$ . Each group calculates the corresponding subset of reference-specific MRCC equations and the subset of matrix elements of the effective Hamiltonian. In the second step, the effective Hamiltonian is formed and diagonalized to obtain the energy estimate in a given iteration cycle. In the third step, the processor groups are used to calculate coupling terms and to build the updates for the cluster amplitudes. In this process each processor group works on the cluster amplitudes for the subset of references delegated to a given PG. The reference-level parallelism was used to implement the BW-MRCCSD and Mk-MRCCSD approaches. Due to intensive communication associated with the calculation of the renormalization terms in the Mk-MRCCSD approach, all Mk-MRCCSD cluster amplitudes were stored in global arrays belonging to the so-called *world group*, i.e., they can be accessible by all PGs. The scalability tests performed for the  $\beta$ -carotene molecule in 6-31G basis set and employing CMS composed of 20 references show very good scalability across 24,000 processors (see Fig. 9.7). Using a similar approach, the BW-MRCCSD(T) and Mk-MRCCSD(T) diagonal corrections to effective Hamiltonian have recently been implemented. In analogy with the iterative methods the diagonal corrections  $\delta_{\mu\mu}(\bar{T}_3^{(\mu)})$  can be calculated on separate PGs.

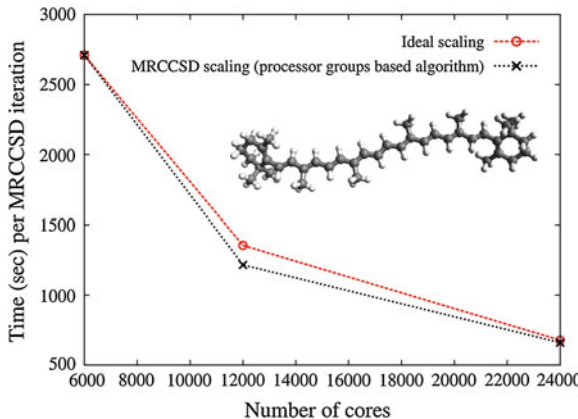


**Fig. 9.7** The scalability of the BW-MRCCSD implementation for  $\beta$ -carotene in 6-31G basis set [184]. All core electrons were kept frozen. The CMS used in our calculations contained 20 reference functions and was defined by four active electrons distributed among four active orbitals. The calculations were performed using 6000, 12000, and 24000 cores employing  $PG(4, 5, 1200)$ ,  $PG(2, 10, 1200)$ , and  $PG(1, 20, 1200)$  configurations, respectively. In these tests we used 6 cores per 12-core node of Jaguar system at ORNL

## 9.4 Conclusions

The tremendous progress achieved in the application of diversified CC formalisms to strongly correlated molecular systems is inextricably linked to the development of efficient theoretical algorithms for capturing complicated electron correlation effects and to efficient parallelization algorithms for optimization of the complex tensor expressions. The last factor includes the development of new parallel tools and domain specific languages, which has enabled the applicability of the accurate CC theories to systems with hundreds of correlated electrons.

Using CC implementations available in several computational chemistry packages such as ACES III, GAMESS [185], Molpro [186], NWChem, or PQS [187] one can perform accurate ground-state calculations using the CCSD(T) method for systems composed of 200–300 correlated electrons with 1300–1500 basis set function. Similar progress has also been achieved in high-precision calculations for molecular properties using linear response CC formulations and for excited states utilizing Equation-of-Motion CC method [188–190]. It has been demonstrated that the most numerically intensive non-iterative parts of the CCSD(T) and CR-EOMCCSD(T) approaches can take advantage of existing leadership-class computer architectures.

The extensions (or re-adaptation) of CC theory to nuclear physics, extended systems, and complex chemical systems are worth noting too [7, 191–194]. Although there has been significant progress, several outstanding problems at the nexus of the aforementioned domains still remain unanswered including the problem of simple and robust MRCC formulations for quasidegenerate systems and the problem of

reducing high numerical complexity of the CC methods based on the local character of the interactions. We believe that the integration of the existing peta-scale CC implementations with local CC formulations (see Ref. [195] and references therein) will pave the way towards very accurate exa-scale CC applications.

**Acknowledgments** One of us (KK) would like to thank the Editors for an invitation to contribute a chapter to the present volume. This work has been supported by the Extreme Scale Computing Initiative (KK, KBN), a Laboratory Directed Research and Development Program at Pacific Northwest National Laboratory. The Pacific Northwest National Laboratory is operated for the US Department of Energy by the Battelle Memorial Institute under Contract DE-AC06.76RLO-1830. J. B. and J. P. acknowledge the support of the Granting agency of the Czech Republic (Project No. 208/11/2222).

## References

1. F. Coester, Nucl. Phys. **7**, 421 (1958)
2. F. Coester, H. Kümmel, Nucl. Phys. **17**, 477 (1960)
3. H. Kümmel, in *Lectures on the Many-Body Problem*, ed by E.R. Caianiello (Academic Press, New York, 1962)
4. J. Čížek, Adv. Chem. Phys. **14**, 35 (1969)
5. J. Čížek, J. Paldus, Int. J. Quantum Chem. **5**, 359 (1971)
6. J. Paldus, J. Čížek, I. Shavitt, Phys. Rev. A **5**, 50 (1972)
7. D.J. Dean, M. Hjorth-Jensen, Phys. Rev. C **69**, 054320 (2004)
8. J. Paldus, in *New Horizons of Quantum Chemistry*, ed by P.-O. Löwdin, B. Pullman (Reidel, Dordrecht, 1983), p. 31
9. R.F. Bishop, Theoret. Chim. Acta **80**, 95 (1991)
10. R.J. Bartlett, in *Modern Electronic Structure Theory, Part I*, ed by D.R. Yarkony (World Scientific, Singapore, 1995), p. 1047
11. J. Paldus, X. Li, Adv. Chem. Phys. **110**, 1 (1999)
12. T.D. Crawford, H.F. Schaefer, Rev. Comput. Chem. **14**, 33 (2000)
13. P. Piecuch, K. Kowalski, I.S.O. Pimienta, M.J. McGuire, Int. Rev. Phys. Chem. **21**, 527 (2002)
14. R.J. Bartlett, M. Musiał, Rev. Mod. Phys. **79**, 291 (2007)
15. D.I. Lyakh, M. Musiał, V.F. Lotrich, R.J. Bartlett, Chem. Rev. **112**, 182 (2012)
16. I. Shavitt, R.J. Bartlett, *Many-Body Methods in Chemistry and Physics: MBPT and Coupled-Cluster Theory* (Cambridge University Press, Cambridge, 2009)
17. G.D. Purvis, R.J. Bartlett, J. Chem. Phys. **76**, 1910 (1982)
18. J. Noga, R.J. Bartlett, J. Chem. Phys. **86**, 7041 (1987)
19. J. Noga, R.J. Bartlett, J. Chem. Phys. **89**, 3401 (1988) (Erratum)
20. G.E. Scuseria, H.F. Schaefer III, Chem. Phys. Lett. **152**, 382 (1988)
21. S.A. Kucharski, R.J. Bartlett, Theoret. Chim. Acta **80**, 387 (1991)
22. N. Oliphant, L. Adamowicz, J. Chem. Phys. **95**, 6645 (1991)
23. M. Musiał, S.A. Kucharski, R.J. Bartlett, J. Chem. Phys. **116**, 4382 (2002)
24. M. Musiał, R.J. Bartlett, J. Chem. Phys. **122**, 224102 (2005)
25. M. Kállay, P.R. Surján, J. Chem. Phys. **113**, 1359 (2000)
26. T. Živković, H.J. Monkhorst, J. Math. Phys. **19**, 1007 (1978)
27. L. Adamowicz, R.J. Bartlett, Int. J. Quantum Chem. **217**, S19 (1985)
28. P. Piecuch, S. Zarabian, J. Paldus, J. Čížek, Phys. Rev. B **42**, 3351 (1990)
29. L. Meissner, A. Balková, R.J. Bartlett, Chem. Phys. Lett. **212**, 177 (1993)
30. K. Kowalski, K. Jankowski, Phys. Rev. Lett. **81**, 1195 (1998)
31. K. Kowalski, K. Jankowski, J. Chem. Phys. **110**, 3714 (1999)

32. K. Kowalski, K. Jankowski, *J. Chem. Phys.* **110**, 9345 (1999)
33. K. Kowalski, K. Jankowski, *J. Chem. Phys.* **111**, 2940 (1999)
34. K. Jankowski, K. Kowalski, *J. Chem. Phys.* **111**, 2952 (1999)
35. E.L. Allgower, K. Georg, *Numerical Continuation Methods* (Springer, Berlin, 1990)
36. P. Piecuch, K. Kowalski, in *Computational Chemistry: Reviews of Current Trends*, ed by J. Leszczynski (World Scientific, Singapore, 2000), p. 1
37. K. Kowalski, P. Piecuch, *J. Chem. Phys.* **113**, 18 (2000)
38. G.D. Purvis, R.J. Bartlett, *J. Chem. Phys.* **75**, 1284 (1981)
39. P. Piecuch, L. Adamowicz, *J. Chem. Phys.* **100**, 5857 (1994)
40. P. Pulay, *Chem. Phys. Lett.* **73**, 393 (1980)
41. P.C. Hansen, *Rank-Deficient and Discrete Ill-Posed Problems: Numerical Aspects of Linear Inversion, SIAM Monographs on Mathematical Modeling and Computation*, (Society for Industrial and Applied Mathematics, Philadelphia, 1998)
42. A.G. Taube, R.J. Bartlett, *J. Chem. Phys.* **130**, 144112 (2009)
43. K.A. Brueckner, *Phys. Rev.* **97**, 1353 (1955)
44. K.A. Brueckner, *Phys. Rev.* **100**, 36 (1955)
45. J. Goldstone, *Proc. Roy. Soc. London* **A239**, 267 (1957)
46. I. Lindgren, J. Morrison, *Atomic Many-Body Theory* (Springer, Berlin, 1982)
47. W. Kutzelnigg, *Int. J. Quantum Chem.* **109**, 3858 (2009)
48. K.A. Peterson, D. Feller, D.A. Dixon, *Theoret. Chem. Acc.* **131**, 1079 (2012)
49. Y.S. Lee, R.J. Bartlett, *J. Chem. Phys.* **80**, 4371 (1984)
50. Y.S. Lee, S.A. Kucharski, R.J. Bartlett, *ibid.* **81**, 5906 (1984)
51. Y.S. Lee, S.A. Kucharski, R.J. Bartlett, *J. Chem. Phys.* **82**, 5761 (1985) (Erratum)
52. J. Noga, R.J. Bartlett, M. Urban, *Chem. Phys. Lett.* **134**, 126 (1987)
53. G.W. Trucks, J. Noga, R.J. Bartlett, *ibid.* **145**, 548 (1988)
54. M. Urban, J. Noga, S.J. Cole, R.J. Bartlett, *J. Chem. Phys.* **83**, 4041 (1985)
55. S.J. Cole, R.J. Bartlett, *J. Chem. Phys.* **86**, 873 (1987)
56. K. Raghavachari, G.W. Trucks, J.A. Pople, M. Head-Gordon, *Chem. Phys. Lett.* **157**, 479 (1989)
57. S.A. Kucharski, R.J. Bartlett, *J. Chem. Phys.* **108**, 5243 (1998)
58. S.A. Kucharski, R.J. Bartlett, *J. Chem. Phys.* **108**, 5255 (1998)
59. S.A. Kucharski, R.J. Bartlett, *J. Chem. Phys.* **108**, 9221 (1998)
60. J.R. Thomas, B.J. DeLeeuw, G. Vacek, T.D. Crawford, Y. Yamaguchi, H.F. Schaefer III, *J. Chem. Phys.* **99**, 403 (1993)
61. J.F. Stanton, *Chem. Phys. Lett.* **281**, 130 (1997)
62. J.F. Stanton, J. Gauss, *J. Chem. Phys.* **103**, 1064 (1995)
63. J.F. Stanton, J. Gauss, *Theoret. Chim. Acta* **93**, 303 (1996)
64. T.D. Crawford, J.F. Stanton, *Int. J. Quantum Chem.* **70**, 601 (1998)
65. S.A. Kucharski, R.J. Bartlett, *J. Chem. Phys.* **108**, 5243 (1998)
66. S.R. Gwaltney, M. Head-Gordon, *Chem. Phys. Lett.* **323**, 21 (2000)
67. S.R. Gwaltney, C.D. Sherrill, M. Head-Gordon, A.I. Krylov, *J. Chem. Phys.* **113**, 3548 (2000)
68. S.R. Gwaltney, M. Head-Gordon, *J. Chem. Phys.* **115**, 2014 (2001)
69. S.R. Gwaltney, E.F.C. Byrd, T. Van Voorhis, M. Head-Gordon, *Chem. Phys. Lett.* **353**, 359 (2002)
70. S. Hirata, M. Nooijen, I. Grabowski, R.J. Bartlett, *J. Chem. Phys.* **114**, 3919 (2001)
71. S. Hirata, M. Nooijen, I. Grabowski, R.J. Bartlett, *J. Chem. Phys.* **115**, 3967 (2001)
72. Y.J. Bomble, J.F. Stanton, M. Kallay, J. Gauss, *J. Chem. Phys.* **123**, 054101 (2005)
73. M. Källay, J. Gauss, *J. Chem. Phys.* **123**, 214105 (2005)
74. A.G. Taube, R.J. Bartlett, *J. Chem. Phys.* **128**, 044110 (2008)
75. A.G. Taube, R.J. Bartlett, *J. Chem. Phys.* **128**, 044111 (2008)
76. H. Koch, O. Christiansen, P. Jørgensen, A.M. Sanchez de Merás, *J. Chem. Phys.* **106**, 1808 (1997)
77. J.S. Arponen, *Ann. Phys. (N.Y.)* **151**, 311 (1983)
78. E.A. Salter, G.W. Trucks, R.J. Bartlett, *J. Chem. Phys.* **90**, 1752 (1989)

79. H. Koch, P. Jørgensen, *J. Chem. Phys.* **93**, 3333 (1990)
80. K. Kowalski, P. Piecuch, *J. Chem. Phys.* **122**, 074107 (2005)
81. P. Piecuch, M. Włoch, *J. Chem. Phys.* **123**, 224105 (2005)
82. K. Kowalski, P.-D. Fan, *J. Chem. Phys.* **130**, 084112 (2009)
83. K. Kowalski, M. Valiev, *J. Chem. Phys.* **131**, 234107 (2009)
84. S.A. Kucharski, R.J. Bartlett, *Theoret. Chim. Acta* **80**, 387 (1991)
85. J.F. Stanton, J. Gauss, J.D. Watts, R.J. Bartlett, *J. Chem. Phys.* **94**, 4334 (1991)
86. S. Hirata, *J. Phys. Chem. A* **107**, 9887 (2003)
87. A.A. Auer, G. Baumgartner, D.E. Bernholdt, A. Bibireata, V. Choppella, D. Cocirva, X.Y. Gao, R.J. Harrison, S. Krishnan, C.C. Lam, Q.D. Lu, M. Nooijen, R.M. Pitzer, J. Ramanujam, P. Sadayappan, A. Sibirakov, *Mol. Phys.* **104**, 211 (2006)
88. M. Valiev, E.J. Bylaska, N. Govind, K. Kowalski, T.P. Straatsma, H.J.J. Van Dam, D. Wang, J. Nieplocha, E. Aprà, T.L. Windus, W. de Jong, *Comput. Phys. Commun.* **181**, 1477 (2010)
89. V.F. Lotrich, N. Flocke, M. Ponton, A.D. Yau, A. Perera, E. Deumens, R.J. Bartlett, *J. Chem. Phys.* **128**, 194104 (2008)
90. T.D. Crawford, T.J. Lee, H.F. Schaefer III, *J. Chem. Phys.* **107**, 7943 (1997)
91. P. Jankowski, B. Jeziorski, *J. Chem. Phys.* **111**, 1857 (1999)
92. C.L. Janssen, H.F. Schaefer III, *Theoret. Chim. Acta* **79**, 1 (1991)
93. X. Li, J. Paldus, *J. Chem. Phys.* **101**, 8812 (1994)
94. M. Kállyay, P.R. Surján, *J. Chem. Phys.* **115**, 2945 (2001)
95. M. Nooijen, V.F. Lotrich, *J. Mol. Struct. (Thoechem)* **547**, 253 (2001)
96. A. Engels-Putzka, M. Hanrath, *J. Chem. Phys.* **134**, 124106 (2011)
97. J. Dongarra, *Int. J. High Perform. Comput. Appl.* **16**, 115 (2002)
98. J. Nieplocha, R.J. Harrison, R.J. Littlefield, *The Global Array Programming Model for High Performance Scientific Computing* (SIAMNews, September, 1995)
99. J. Nieplocha, R.J. Harrison, R.J. Littlefield, *J. Supercomput.* **10**, 197 (1996)
100. J. Nieplocha, B. Palmer, V. Tipparaju, M. Krishnan, H. Trease, E. Aprà, *Int. J. High Perform. Comput. Appl.* **20**, 203 (2006)
101. T.H. Dunning Jr., *J. Chem. Phys.* **90**, 1007 (1989)
102. E. Aprà, A.P. Rendell, R.J. Harrison, V. Tipparaju, W.A. de Jong, S.S. Xantheas, in *Proceedings of the Conference on High Performance Computing Networking, Storage and Analysis* (ACM, Portland, 2009)
103. S. Yoo, E. Aprà, X.C. Zeng, S.S. Xantheas, *J. Phys. Chem. Lett.* **1**, 3122 (2010)
104. K. Kowalski, P. Piecuch, *J. Chem. Phys.* **120**, 1715 (2004)
105. K. Kowalski, S. Krishnamoorthy, R. Olson, V. Tipparaju, E. Aprà, Scalable implementations of accurate excited-state coupled cluster theories: application of high-level methods to Porphyrin-based systems. Paper presented at the Supercomputing 2011 conference, Seattle, 12–18 Nov 2011
106. A. Schafer, H. Horn, R. Ahlrichs, *J. Chem. Phys.* **97**, 2571 (1992)
107. A.E. DePrince III, J.R. Hammond, *J. Chem. Theory Comput.* **7**, 1287 (2011)
108. W. Ma, S. Krishnamoorthy, O. Villa, K. Kowalski, *J. Chem. Theory Comput.* **7**, 1316 (2011)
109. D. Mukherjee, R.K. Moitra, A. Mukhopadhyay, *Mol. Phys.* **33**, 955 (1977)
110. A. Mukhopadhyay, R.K. Moitra, D. Mukherjee, *J. Phys. B* **12**, 1 (1979)
111. H. Reitz, W. Kutzelnigg, *Chem. Phys. Lett.* **66**, 111 (1979)
112. M.A. Haque, D. Mukherjee, *J. Chem. Phys.* **80**, 5058 (1984)
113. A. Haque, U. Kaldor, *Chem. Phys. Lett.* **117**, 347 (1985)
114. B. Jeziorski, J. Paldus, *J. Chem. Phys.* **90**, 2714 (1989)
115. J.F. Stanton, R.J. Bartlett, C.M.L. Rittby, *J. Chem. Phys.* **97**, 5560 (1992)
116. L. Meissner, *J. Chem. Phys.* **108**, 9227 (1998)
117. M. Musiał, R.J. Bartlett, *J. Chem. Phys.* **121**, 1670 (2004)
118. B. Jeziorski, H.J. Monkhorst, *Phys. Rev. A* **24**, 1668 (1981)
119. L. Meissner, K. Jankowski, J. Wasilewski, *Int. J. Quantum Chem.* **34**, 535 (1988)
120. B. Jeziorski, J. Paldus, *J. Chem. Phys.* **88**, 5673 (1988)

121. J. Paldus, L. Pylypov, B. Jeziorski, in *Many-Body Methods in Quantum Chemistry, Lecture Notes in Chemistry*, vol. 52, ed by U. Kaldor (Springer, Berlin, 1989), p. 151
122. P. Piecuch, J. Paldus, *Theoret. Chim. Acta* **83**, 69 (1992)
123. J. Paldus, P. Piecuch, L. Pylypov, B. Jeziorski, *Phys. Rev. A* **47**, 2738 (1993)
124. P. Piecuch, J. Paldus, *Phys. Rev. A* **49**, 3479 (1994)
125. S.A. Kucharski, R.J. Bartlett, *J. Chem. Phys.* **95**, 8227 (1991)
126. A. Balková, S.A. Kucharski, L. Meissner, R.J. Bartlett, *Theoret. Chim. Acta* **80**, 335 (1991)
127. A. Balková, S.A. Kucharski, R.J. Bartlett, *Chem. Phys. Lett.* **182**, 511 (1991)
128. S.A. Kucharski, A. Balková, P.G. Szalay, R.J. Bartlett, *J. Chem. Phys.* **97**, 4289 (1992)
129. C. Bloch, *Nucl. Phys.* **6**, 329 (1958)
130. F. Jørgensen, *Mol. Phys.* **29**, 1137 (1975)
131. C.E. Soliverez, *Phys. Rev. A* **24**, 4 (1981)
132. P. Durnad, *Phys. Rev. A* **28**, 3184 (1983)
133. K. Jankowski, L. Meissner, J. Wasilewski, *Int. J. Quantum Chem.* **28**, 931 (1985)
134. T.H. Dunning Jr, *J. Chem. Phys.* **53**, 2823 (1970)
135. B.H. Brandow, *Rev. Mod. Phys.* **39**, 771 (1967)
136. B.H. Brandow, *Adv. Quantum Chem.* **10**, 187 (1977)
137. S. Zarabian, J. Paldus, *Int. J. Quantum Chem.* **38**, 761 (1990)
138. J.P. Finley, R.K. Chaudhuri, K.F. Freed, *J. Chem. Phys.* **54**, 343 (1996)
139. R.K. Chaudhuri, K.F. Freed, G. Hose, P. Piecuch, K. Kowalski, M. Włoch, S. Chattopadhyay, D. Mukherjee, Z. Rolík, Á. Szabados, G. Toth, P.R. Surján, *J. Chem. Phys.* **122**, 134105 (2005)
140. M.R. Hoffmann, D. Datta, S. Das, D. Mukherjee, Á. Szabados, Z. Rolík, P.R. Surján, *J. Chem. Phys.* **131**, 204104 (2009)
141. Á. Szabados, *J. Chem. Phys.* **134**, 174113 (2011)
142. T.H. Schucan, H.A. Weidenmüller, *Ann. Phys.* **73**, 108 (1972)
143. T.H. Schucan, H.A. Weidenmüller, *Ann. Phys. ibid* **76**, 483 (1973)
144. K. Kowalski, P. Piecuch, *Phys. Rev. A* **61**, 052506 (2000)
145. L. Meissner, R.J. Bartlett, *J. Chem. Phys.* **91**, 4800 (1989)
146. L. Meissner, S.A. Kucharski, R.J. Bartlett, *J. Chem. Phys.* **91**, 6187 (1989)
147. L. Meissner, R.J. Bartlett, *J. Chem. Phys.* **92**, 561 (1990)
148. X. Li, J. Paldus, *J. Chem. Phys.* **119**, 5320 (2003)
149. X. Li, J. Paldus, *J. Chem. Phys.* **119**, 5334 (2003)
150. X. Li, J. Paldus, *J. Chem. Phys.* **119**, 5346 (2003)
151. J. Paldus, X. Li, N.D.K. Petracca, *J. Math. Phys.* **35**, 215 (2004)
152. I. Hubač, in *New Methods in Quantum Theory*, NATO ASI Series 3: High Technology vol 8, ed by A. Tsipis, V.S. Popov, D.R. Herschbach, J.S. Avery, (Kluwer, Dordrecht, 1996), pp. 183–202
153. J. Mášik, I. Hubač, *Adv. Quantum Chem.* **31**, 75 (1999)
154. J. Pittner, P. Nachtigall, P. Čársky, J. Mášik, I. Hubač, *J. Chem. Phys.* **110**, 10275 (1999)
155. J. Pittner, *J. Chem. Phys.* **118**, 10876 (2003)
156. J. Pittner, X. Li, J. Paldus, *Mol. Phys.* **103**, 2239 (2005)
157. J. Pittner, O. Demel, *J. Chem. Phys.* **122**, 181101 (2005)
158. O. Demel, J. Pittner, *J. Chem. Phys.* **128**, 104108 (2008)
159. U.S. Mahapatra, B. Datta, D. Mukherjee, *Mol. Phys.* **94**, 157 (1998)
160. U.S. Mahapatra, B. Datta, D. Mukherjee, *Adv. Quantum Chem.* **30**, 163 (1998)
161. U.S. Mahapatra, B. Datta, D. Mukherjee, *J. Chem. Phys.* **110**, 6171 (1999)
162. F.A. Evangelista, W.D. Allen, H.F. Schaefer III, *J. Chem. Phys.* **127**, 024102 (2007)
163. F.A. Evangelista, A.C. Simmonett, W.D. Allen, H.F. Schaefer III, J. Gauss, *J. Chem. Phys.* **128**, 124104 (2008)
164. S. Das, D. Mukherjee, M. Kállay, *J. Chem. Phys.* **132**, 074103 (2010)
165. K. Bhaskaran-Nair, O. Demel, J. Pittner, *J. Chem. Phys.* **132**, 154105 (2010)
166. M. Hanrath, *J. Chem. Phys.* **123**, 084102 (2005)
167. M. Hanrath, *Chem. Phys. Lett.* **420**, 426 (2006)
168. M. Hanrath, *Theoret. Chem. Acc.* **121**, 187 (2008)

169. U.S. Mahapatra, S. Chattopadhyay, *J. Chem. Phys.* **133**, 074102 (2010)
170. L. Kong, *Int. J. Quantum Chem.* **109**, 441 (2009)
171. A. Balková, R.J. Bartlett, *J. Chem. Phys.* **101**, 8972 (1994)
172. X. Li, J. Paldus, *J. Chem. Phys.* **124**, 034112 (2006)
173. O. Demel, J. Pittner, *J. Chem. Phys.* **124**, 144112 (2006)
174. K. Bhaskaran-Nair, O. Demel, J. Pittner, *J. Chem. Phys.* **129**, 184105 (2008)
175. O. Demel, K. Bhaskaran-Nair, J. Pittner, *J. Chem. Phys.* **133**, 134106 (2010)
176. K. Bhaskaran-Nair, O. Demel, J. Smydke, J. Pittner, *J. Chem. Phys.* **134**, 154106 (2011)
177. K. Kowalski, P. Piecuch, *J. Mol. Struct. (Thoechem)* **547**, 191 (2001)
178. K. Kowalski, P. Piecuch, *Mol. Phys.* **102**, 2425 (2004)
179. J. Pittner, P. Piecuch, *Mol. Phys.* **107**, 1209 (2009)
180. F.A. Evangelista, E. Prochnow, J. Gauss, H.F. Schaefer III, *J. Chem. Phys.* **132**, 074107 (2010)
181. K. Kowalski, *J. Chem. Phys.* **134**, 194107 (2011)
182. J. Brabec, H.J.J. van Dam, J. Pittner, K. Kowalski, *J. Chem. Phys.* **136**, 124102 (2012)
183. W.J. Hehre, R. Ditchfield, J.A. Pople, *J. Chem. Phys.* **56**, 2257 (1972)
184. J. Brabec, J. Pittner, H.J.J. van Dam, E. Aprà, K. Kowalski, *J. Chem. Theory Comput.* **8**, 487 (2012)
185. M.W. Schmidt, K.K. Baldridge, J.A. Boatz et al., *J. Comput. Chem.* **14**(1993), 1347 (1993)
186. H.-J. Werner, P.J. Knowles, R. Lindh, et al., MOLPRO is a package of ab initio programs
187. J. Baker, K. Wolinski, M. Malagoli et al., *J. Comput. Chem.* **30**, 317 (2009)
188. J.R. Hammond, K. Kowalski, W.A. de Jong, *J. Chem. Phys.* **127**, 144105 (2007)
189. K. Kowalski, J.R. Hammond, W.A. de Jong, A.J. Sadlej, *J. Chem. Phys.* **129**, 226101 (2008)
190. K. Kowalski, R.M. Olson, S. Krishnamoorthy, V. Tippurajju, E. Aprà, *J. Chem. Theory Comput.* **7**, 2200 (2011)
191. W. Förner, R. Knab, J. Čížek, J. Ladik, *J. Chem. Phys.* **106**, 10248 (1997)
192. M. Yu, S. Kalvoda, M. Dolg, *Chem. Phys.* **224**, 121 (1997)
193. P. Reinhardt, *Theoret. Chem. Acc.* **104**, 426 (2000)
194. S. Hirata, R. Podeszwa, M. Tobita, R.J. Bartlett, *J. Chem. Phys.* **120**, 2581 (2004)
195. H.-J. Werner, M. Schütz, *J. Chem. Phys.* **135**, 144116 (2011)

# Chapter 10

## Diagrammatic Monte Carlo and Worm Algorithm Techniques

Nikolay Prokof'ev

**Abstract** This chapter reviews basic principles of Diagrammatic Monte Carlo and Worm Algorithm techniques. Diagrammatic Monte Carlo establishes generic rules for unbiased sampling of well defined configuration spaces when the only source of errors is of statistical origin due to finite sampling time, no matter whether configuration parameters involve discrete, as in the Ising model, or continuous, as in Feynman diagrams or lattice path integrals, variables. Worm Algorithms allow one to sample efficiently configuration spaces with complex topology and non-local constraints which cause severe problems for Monte Carlo schemes based on local updates. They achieve this goal by working with the enlarged configuration space which includes configurations violating constraints present in the original formulation.

### 10.1 Introduction

Statistical properties of large systems cannot be obtained by direct enumeration of the exponentially growing configuration space, or  $\nu$ -space for brevity. A variety of numerical approaches employ mathematical formulations which, if solved, would reproduce the same statistical predictions as the original model. Path integrals, high-temperature expansions, and Feynman diagrams belong to this category of methods. In this chapter I will concentrate on the Monte Carlo (MC) sampling technique [1] which is, arguably, among the most powerful universal tools designed to deal with large and complex  $\nu$ -spaces. Often, complex topology and non-local constraints on the configuration space, severely reduce efficiency of Monte Carlo simulations based on standard local updates. This leads to ergodicity problems when relevant sectors of  $\nu$ -space can not be sampled in a reasonable computation time. A somewhat related difficulty facing conventional MC schemes is calculations of correlation functions

---

N. Prokof'ev (✉)

Physics Department, University of Massachusetts, Amherst, MA 01003, USA  
e-mail: prokofev@physics.umass.edu

which have no direct representation in the configuration space employed for the evaluation of the partition function.

In what follows I will explain the general idea of how Worm Algorithms (WA) deal with topological constraints by going to the enlarged configuration space, and present illustrative results for specific cases. It is important to realize that MC sampling of well defined  $\nu$ -spaces can be done without systematic errors (i.e. the only source of error bars is of statistical origin due to finite sampling time), no matter whether configuration parameters involve discrete, as in the Ising model, or continuous, as in Feynman diagrams or lattice path integrals, variables. In essence, Diagrammatic Monte Carlo (DiagMC) is the generic prescription of how to arrange an unbiased sampling of  $\nu$ -spaces with arbitrary and ever changing number of continuous variables. WA and DiagMC were implemented originally as two complementary approaches to improve efficiency of Monte Carlo simulations in quantum lattice models. They turned out to be rather independent methods with their own domains of applicability, and thus I will proceed with presenting them separately.

## 10.2 Diagrammatic Monte Carlo

In the most abstract form one is interested in knowing some quantity  $Q(\mathbf{y})$  as a function of  $\mathbf{y}$  (in general, the multi-dimensional variable  $\mathbf{y}$  may include both continuous and discrete components) when the answer is expressed in terms of a series of multi-dimensional integrals/sums:

$$Q(\mathbf{y}) = \sum_{n=0}^{\infty} \sum_{\xi} \int \dots \int d\mathbf{x}_1 \dots d\mathbf{x}_n D(n, \xi, \mathbf{x}_1, \dots, \mathbf{x}_n; \mathbf{y}), \quad (10.1)$$

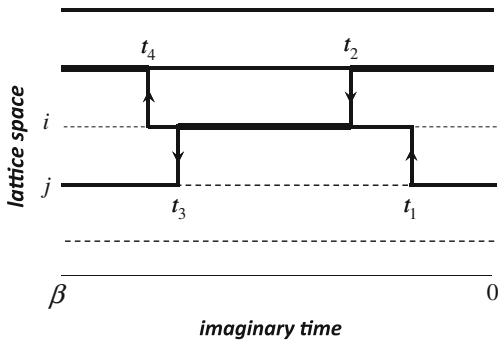
with  $D$  being some known function of its arguments. The ‘diagram order’  $n$  controls the number of ‘internal’ integration/summation variables  $\{\mathbf{x}_1, \dots, \mathbf{x}_n\}$ , and the ‘topology’ index  $\xi$  labels different terms of the same order in the series. The most familiar example, as the name of the technique suggests, would be Feynman diagrams for the many body system illustrated in Fig. 10.1. Strict diagrammatic rules relate graphical representation to the corresponding mathematical expression for the function  $D$ : up to a phase factor, it is given by the product of functions which are associated with the graph lines  $D = \prod_{\text{lines}} F_{\text{line}}(\mathbf{x}_{\text{line}}; \mathbf{y})$ . For example, in momentum-imaginary time representation for the system of electrons interacting with the pairwise potential  $V(\mathbf{r})$  the dotted lines are associated with the Fourier transform  $V(\mathbf{q})$ , and the solid lines are associated with the single-particle propagators  $G_0(\mathbf{p}_i, t)$ .

There are well-established diagrammatic series for other quantities of interest such as self-energies, polarization operators, pair-propagators, current-current and other correlation functions, etc. Numerous alternative formulations of quantum and classical statistics are mathematically identical to Eq. (10.1). When the partition

$$\begin{aligned}
G_\sigma(p, \tau) = & \frac{p}{0} \xrightarrow{t} + \frac{p}{0} \xrightarrow{t_1} \frac{p}{t} + \frac{p}{0} \xrightarrow{t_1} \frac{p-q}{t_2} \xrightarrow{t} + \\
& + \frac{p}{0} \xrightarrow{t_1} \frac{p-q_1}{t_3} \xrightarrow{q_1} \frac{p-q_2-q_1}{t_2} \xrightarrow{q_2} \frac{p-q_2}{t_4} \xrightarrow{p} + \frac{p}{0} \xrightarrow{t_1} \frac{p-q}{t_3} \xrightarrow{k} \frac{p-q}{t_2} \xrightarrow{k-q} \frac{p}{t} +
\end{aligned}$$

**Fig. 10.1** Graphical representation of the diagrammatic expansion for the Green's function in the interacting many-body system

**Fig. 10.2** Graphical representation of the lattice path-integral for interacting particles (bosons) hopping between the sites. It is generated by the expansion of the partition function in the number of hopping transitions. Line thickness is proportional to the occupation number



function of a lattice system, e.g. the Hubbard model, is written as a path-integral one has to sum over the number of hopping transitions and their order, as well as to integrate over their positions in time. Thus any particular path can be viewed as a ‘diagram’ understood broadly as a graphical representation of some term in the series expansion, see Fig. 10.2. Regardless of the origin of Eq. (10.1), it can be viewed as a mathematical expression for the answer in terms of a series of multi-dimensional integrals.

Let us denote the collection of all external and internal parameters which allow for a complete characterization of the diagram as  $\nu = (n, \xi, \mathbf{x}_1, \dots, \mathbf{x}_n; \mathbf{y})$ , and call it the ‘configuration space’; a particular set of parameters has to be viewed then as a point in  $\{\nu\}$ . Accordingly, the modulus of  $D_\nu$  will be called the configuration ‘weight’. Since in general the  $D$ -function is not sign-positive, we will need to introduce also the configuration ‘phase’,  $\varphi_\nu = \arg D_\nu$  (in general, the diagram phase is not necessarily equal to 0 or  $\pi$ ).

### 10.2.1 Updates

The MC process of generating diagrams with probabilities proportional to their weight is based on the conventional Markov-chain updating scheme [2, 3] implemented directly in the space of continuous variables. All updates are broadly classified as type-I and type-II. The number of continuous variables is preserved in type-I updates which perform sampling of diagrams of the same order  $n$ . A typical example would be changing the topology of lines in the diagram with the corresponding change of their parameters as dictated by the conservation laws, see Fig. 10.3a. Its implementation is straightforward: select at random any pair of consecutive interaction vertexes and exchange them places. An acceptance ratio for the corresponding update,  $R_{\nu \rightarrow \nu'}$ , is given by the ratio of the diagram weights,

$$R_{\nu \rightarrow \nu'} = D_{\nu'}/D_{\nu}, \quad (10.2)$$

which is easily calculated since  $D_{\nu}$  is the product of  $F_{\text{line}}$ -functions and only three of them change their values in this update. Type-I updates can be also used to change internal and external variables, see Fig. 10.3b. For example, one may select at random some interaction vertex and propose a new time,  $t_i'$ , associated with this vertex from the (arbitrary) probability density  $T(t_i')$ . The acceptance ratio for this update is given by the ratio of probabilities for suggesting the  $\nu \rightarrow \nu'$  and  $\nu' \rightarrow \nu$  moves in the statistical ensemble

$$R_{\nu \rightarrow \nu'} = \frac{D_{\nu'}}{D_{\nu}} \frac{T(t_i)dt}{T(t_i')dt} = \frac{D_{\nu'}}{D_{\nu}} \frac{T(t_i)}{T(t_i')} \cdot \frac{dt}{dt}. \quad (10.3)$$

The simplest implementation of this update would be to have non-zero  $T(t_i)$  only on the time interval determined by times of the previous and following interaction vertexes (times  $t_3$  and  $t_4$  in the Figure). The probability distribution  $T(t)$  should be optimized for the best acceptance ratio without compromising ones ability to use it for fast generation of random variables. Clearly, there are numerous other possibilities for type-I updates which are standard for MC simulations of multidimensional integrals. For pedagogical reasons I also mention differential measures  $dt$  to underline that they cancel out in the detailed balance Equation for acceptance ratio.

Type-II updates change the diagram order  $n \leftrightarrow n + m$  and thus require that new variables are proposed from some (arbitrary) probability density distribution  $W(\nu; \mathbf{x}_{n+1}, \dots, \mathbf{x}_{n+m})$ . For example, to implement the transformation illustrated in Fig. 10.3c we need to propose time positions  $t_3$  and  $t_4$  for the new interaction line along with the momentum transfer  $\mathbf{q}_2$  from the normalized probability distribution  $W(\nu; \mathbf{q}, t_1, t_2)$ . The detailed balance equation for a pair of updates which increase/decrease the diagram order by  $m$  reads

$$\begin{aligned} r_{n \rightarrow n+m} u_{n \rightarrow n+m} D_{\nu} W(\mathbf{x}_{n+1}, \dots, \mathbf{x}_{n+m})(d\mathbf{x})^{n+m} = \\ r_{n+m \rightarrow n} u_{n+m \rightarrow n} D_{\nu'}(d\mathbf{x})^{n+m}. \end{aligned} \quad (10.4)$$

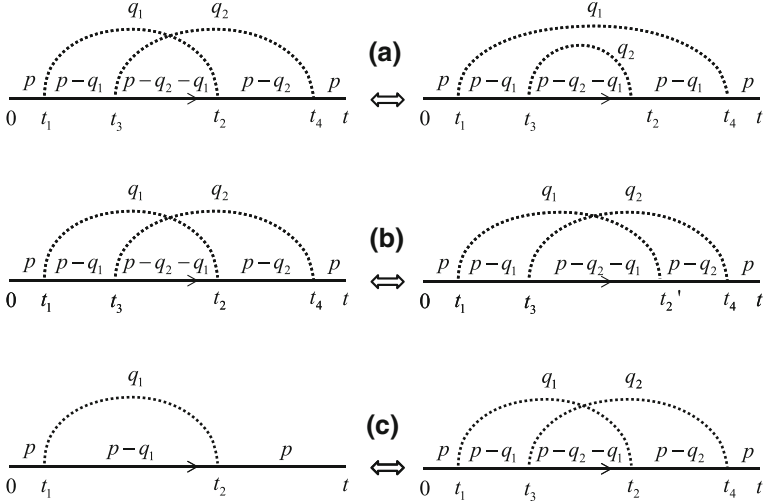


**Fig. 10.3** Local updates in the configuration space of Feynman diagrams. Type-I updates: **a** changing the diagram topology, **b** changing the value of the internal variable  $t_2$ . Type-II update **c** is changing the diagram order

where  $u_{n \rightarrow n+m}$  and  $u_{n+m \rightarrow n}$  are algorithm specific probabilities of proposing where and how new diagram structures are added and removed, respectively, while  $r_{n \rightarrow n+m}$  and  $r_{n+m \rightarrow n}$  are the probabilities of accepting an update. An acceptance ratio,  $R_{\nu \rightarrow \nu'} = r_{n \rightarrow n+m}/r_{n+m \rightarrow n}$ , to go from configuration  $\nu$  of order  $n$  to configuration  $\nu'$  of order  $n+m$  is then

$$R_{\nu \rightarrow \nu'} = \frac{u_{n \rightarrow n+m}}{u_{n+m \rightarrow n}} \frac{D_{\nu'}}{D_{\nu} W(\nu; \mathbf{x}_{n+1}, \dots, \mathbf{x}_{n+m})}. \quad (10.5)$$

As expected, all differential measures cancel in the acceptance ratio ensuring that working with arbitrary and changing number of continuous variables can be generically done without encountering systematic errors, i.e. the answer is guaranteed to converge to the exact value. Note, that the ratio of the diagram weights,  $D_{\nu'}/D_{\nu}$ , is some model specific function of  $\nu$  and new variables  $\mathbf{x}_{n+1}, \dots, \mathbf{x}_{n+m}$ . The optimal choice of  $W$  is then between how easily and efficiently it can be used for seeding new variables and the largest (on average) acceptance ratio.

It is relatively straightforward to design a set of type-I and type-II updates which satisfy an ergodicity requirement that given two arbitrary configurations  $\nu$  and  $\nu'$  contributing to the answer it takes a finite number of updates with non-zero acceptance ratios to transform one configuration into another. At this point I would like to stress that DiagMC is fundamentally different from enumerating/listing all diagrams with  $n \leq n_{max}$  and then computing the corresponding multidimensional integrals in each diagram one-by-one using classical MC methods. In DiagMC the diagram order, its topology, and all internal and external variables are treated on equal footing; namely,

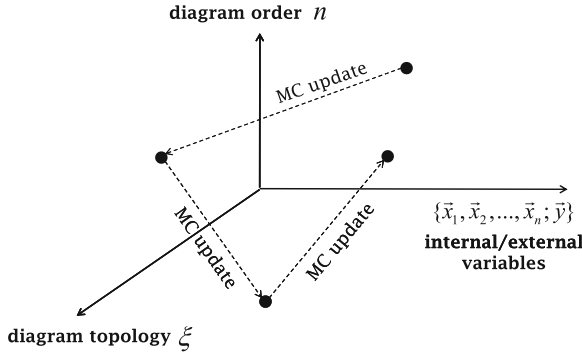


**Fig. 10.4** An illustration of the DiagMC process. Note that all configuration parameters are treated in the simulation protocol on equal footing

all configuration space parameters are sampled randomly from the probability distribution  $D_\nu$  and each diagram represents a point, not an integral, in the configuration space, see Fig. 10.4. One may wonder where did all the integrals go and what makes configuration space points with different differential measures contributing similarly to the answer (e.g. every diagram for the Green's function in Fig. 10.1 contributes  $e^{i\varphi_\nu}$  to  $G(\mathbf{p}, t)$ , and every diagram for the partition function  $Z$  in Fig. 10.2 contributes unity to  $Z$ )? Formally, all integrals of interest are silently hidden in normalization unities for  $W$ -functions in Eq. (10.5). With the normalization condition mentioned explicitly we have

$$R = \frac{u_{n \rightarrow n+m}}{u_{n+m \rightarrow n}} \left( \int d\mathbf{x}^m W(\nu; \mathbf{x}_{n+1}, \dots, \mathbf{x}_{n+m}) \right) \frac{D_{\nu'}}{D_\nu W(\nu; \mathbf{x}_{n+1}, \dots, \mathbf{x}_{n+m})}, \quad (10.6)$$

with straightforward interpretation of the second term as an integrated contribution of the higher-order diagram with fictitious weight  $W$ . The last term in the acceptance ratio is then the standard ‘rejection’ correction accounting for the difference between the true and fictitious weights.

### 10.2.2 Advantages and Potential Problems

If the diagram weight is sign positive (this is a typical case for interacting lattice bosons and un-frustrated spin Hamiltonians in the path-integral representation for the partition function, electron-phonon polarons, impurity solvers and determinant representations of fermionic models with local interactions at special filling factors, see e.g. [4], etc.) one can routinely handle diagrams up to very large order, as large as several million. I am not aware of any fundamental drawbacks of DiagMC under

such circumstances; intellectual challenge and technical sophistication in developing an efficient approach count as a plus. There are numerous examples of successful applications of the DiagMC method.

Sign-alternating diagram weights are usually associated with the sign-problem. Indeed, most MC schemes work with a chunk of matter, i.e. they simulate behavior of a finite number of degrees of freedom and work with their partition function. In this situation the CPU time required for obtaining results with good error bars scales exponentially with the  $(d + 1)$ -dimensional volume of the system. In higher dimensions of space and low temperature the calculation becomes inaccurate well before the results can be extrapolated to the thermodynamic limit.

The essence of the sign-problem, however, depends on the mathematical representation used for obtaining the final answer. Remarkably, in the space of connected Feynman diagrams in the many-body system the sign-problem as we know it is essentially gone, and sign-alternation of diagrams of the same order is *required* (!) for the method to be meaningful, i.e. it is more appropriate to speak of the sign-blessing! In what follows I explain the origin of this radical change in our perception of sign-alternating contributions.

To begin with, connected Feynman diagrams are typically formulated in the thermodynamic limit already, thus there is no infinite system size limit to take. The diagrams themselves have exactly the same structure in any dimension of space and at arbitrary temperature (within the same phase). This is because they are representing contributions to the free energy density, or the logarithm of the partition function. In most cases modern computers allow one to obtain good error bars by sampling contributions from all diagrams up to relatively high order even if their weights are sign-alternating. Moreover, the calculation can be run in the self-consistent mode when infinite geometrical series are automatically absorbed into the renormalized propagators and interaction lines, i.e. when all diagrams are of the ‘skeleton type’ [5, 6]. The final solution is then recovered by extrapolating results to the infinite diagram order limit. Even if the series are divergent but have finite convergence radius the extrapolation procedure can be done reliably provided enough terms in the series are known.

The most serious objection to the Feynman’s diagrammatic technique raised in the literature is series convergence. Indeed, for series with zero convergence radius calculating higher-order diagrams in the absence of small parameters is considered as a useless task. Dyson’s argument [7] links asymptotic properties of series in terms of bare coupling  $g$  to pathological properties of the model in the complex  $g$ -plane. Consider, for example, fermions in continuous space with repulsive inter-particle potential. Changing sign of the potential leads to the system collapse and divergent energy density in the thermodynamic limit meaning that expansion in the bare coupling has zero convergence radius. There are three important counter-considerations though:

- (i) There are interesting models which are not subject to this argument because they remain stable for any complex  $g$  (lattice fermions, spin models, resonant fermions in the zero-range limit, etc.);

- (ii) with appropriate regularization the series can be made to have a finite convergence radius and then re-summation techniques and extrapolation in the regularization parameter may work;
- (iii) the diagrammatic technique allows one to sum certain geometric series analytically and re-formulate diagrams in terms of renormalized objects (skeleton diagrams); convergence properties of skeleton series is an un-solved mathematical problem.

The other argument stating that all skeleton series in the many-body system have zero convergence radius is based on counting the diagram numbers [8]. One can show that the number of skeleton graphs of order  $n$  scales as  $n!2^n n^{3/2}$ . This creates an impression that their combined contribution also scales factorially and thus the resulting series are always asymptotic. This is exactly where the sign-blessing phenomenon enters the scene. Sign-alternation of same-order diagrams may lead to their mutual cancelation with accuracy inverse proportional to  $1/n!$  and ultimate series convergence. What we find in practice is exactly this sign-blessing phenomenon: for both the Fermi Hubbard model at  $U/t = 4$  [9] and resonant fermions [10] the series are either convergent or subject to the re-summation protocol.

There are numerous examples of key systems in nearly all disciplines of science: Standard model, Coulomb gasses, Hubbard model, frustrated magnetism, localization, charged polymers, just to name a few. For many decades researchers are trying to achieve their detailed understanding and find techniques to perform reliable calculations of basic properties. Though an enormous progress has been made, no systematic method exists to address these systems in their full complexity. Remarkably, it is possible to formally write answers for all models mentioned above in terms of series of Feynman diagrams but in the absence of small parameters there is no hope to deal with them analytically. The unique feature of DiagMC is to deviate from the standard MC approach aimed at simulations of larger and larger system sizes and apply it directly to the series of irreducible Feynman diagrams. Among advantages one may mention that results are obtained for the thermodynamic system at any temperature, lattice/continuous and short-range/long-range systems can be dealt with by the same approach, the simulation can be easily implemented for self-consistent skeleton graphs and combined with any existing analytical answer accounting for partial summation of selected graphs. Successful developments in this direction have enormous potential in providing a universal tool for addressing fundamental questions across several disciplines.

### 10.3 Worm Algorithm

Worm Algorithm is an updating strategy based on enlarged configuration space. Often, the original formulation of the problem, e.g. for the partition function, is either not fine-tuned to deal with the critical modes of the system or features non-local constraints on the configuration space. Such constraints are rather typical. For example, Feynman's path-integrals for interacting particles consist of many-body

trajectories which are periodic in imaginary time  $0 \leq \tau \leq \beta = 1/T$ , i.e. individual trajectories form loops on the  $\beta$ -cylinder. Moreover, in a system with periodic boundary conditions and in the superfluid phase some trajectories form macroscopically large loops which span the entire system and form the so-called winding cycles [11]. Statistical properties of such classical systems as the Ising- and  $XY$ -models can also be formulated in the loop language. Finally, connected Feynman diagrams are composed of loops with momentum/frequency conservation at each vertex; skeleton diagrams are even more restrictive in that they do not admit sub-structures which can be absorbed into renormalized lines (and vertexes). Clearly, in the presence of global constraints purely local updating schemes are simply non-ergodic, if possible at all. Local updates are also suffering from the critical slowing down when the nature of critical fluctuations is closely linked to constrained configurations. This is the case of the superfluid and Ising transitions in models mentioned above.

Worm Algorithm is based on two major ideas:

**1.** The configuration space is enlarged to include configurations violating constraints present in the original formulation. For definiteness, let us denote the original configuration space as  $Z$ -space and the configuration space with violated constraints as  $G$ -space. For example, in the path-integral representation one admits configurations with one open line, as if someone started drawing a new loop but is not finished yet. Often, this is not merely an algorithmic trick since an open line is representing an important correlation function, such as the Green's function [12, 13] (with several worms one may calculate multi-particle off-diagonal correlations as well [14, 15]). From time to time the two ends of the open line come close and get connected thus making a loop and transforming  $G$ -path into  $Z$ -path. In Monte Carlo, drawing and erasing processes are balanced and are complementary to each other.

**2.** All major updates in the  $G$ -space are local and are performed through the endpoints of the open line. Formally, there is no need to have updates transforming one  $Z$ -configuration to another  $Z$ -configuration though one may add them at will if they help code efficiency.

In what follows I will discuss two cases: the simplest realization of WA for the Ising model with generalizations to other classical and quantum models, and WA for simulations of skeleton Feynman diagrams. While in the former example WA naturally derives from the configuration space of the order-parameter correlation function, in the latter example the  $G$ -space is absolutely un-physical and is introduced for purely algorithmic purposes.

### 10.3.1 Ising and XY Models

I start with the textbook derivation of the loop representation (also known as the high-temperature expansion for the partition function) for the Ising model,  $-H/T = K \sum_{\langle ij \rangle} \sigma_i \sigma_j$ , where  $\sigma_i = \pm 1$  are spin variables on a cubic lattice and  $\langle ij \rangle$  stands for pairs of nearest-neighbor sites, or bonds. Using factorization of the global Gibbs exponent into Gibbs factors for each bond and identity

$$e^{K\sigma_i\sigma_j} = \cosh(K) (1 + \tanh(K)\sigma_i\sigma_j) = \cosh(K) \sum_{N_b=0}^1 (\tanh(K)\sigma_i\sigma_j)^{N_b}, \quad (10.7)$$

one can express the partition function as (the subscript  $b$  is used to label lattice bonds)

$$Z = \sum_{\{\sigma_i\}} \prod_{b=\langle ij \rangle} e^{K\sigma_i\sigma_j} = \cosh^{dN}(K) \sum_{\{\sigma_i\}} \prod_{b=\langle ij \rangle} \sum_{N_b=0}^1 \tanh^{N_b}(K) (\sigma_i\sigma_j)^{N_b}. \quad (10.8)$$

Here  $N$  is the number of lattice sites and  $d$  is the dimension of space. By changing summation over  $\{N_b = 0, 1\}$  and  $\{\sigma_i = \pm 1\}$  places we obtain

$$Z = \cosh^{dN}(K) \sum_{\{N_b\}} \left( \prod_b \tanh^{N_b}(K) \right) \left( \prod_i \sum_{\sigma_i=\pm 1} \sigma_i^{L_i} \right) \equiv 2^N \cosh^{dN}(K) \sum_{\{N_b\}}^{\text{loops}} W[\{N_b\}], \quad (10.9)$$

with the bond configuration weight  $W[\{N_b\}] = (\prod_b \tanh^{N_b}(K))$ . The ‘loops’ label on the sum represents the constraint that the sum of all bond numbers incident on every lattice site,  $L_i = \sum_{b=\langle ij \rangle} N_b$ , has to be even; otherwise  $\sum_{\sigma_i=\pm 1} \sigma_i^{L_i}$  is zero.

Each term in the sum over allowed bond configurations has a clear graphical representation—just draw a line along each bond with  $N_b = 1$ . The requirement that  $L_i = \sum_{b=\langle ij \rangle} N_b$  must be even is equivalent to demanding that the allowed configurations of lines are composed of closed un-oriented loops, since loops always contribute an even number to  $L_i$ , see the left panel in Fig. 10.5. In close analogy with the partition function, the configuration space of the spin–spin correlation function  $G_{IM}/Z = \langle \sigma_I \sigma_M \rangle$  is that of closed loops with one open line ‘originating’ at site  $I$  and ‘terminating’ at  $M$ , see the right panel in Fig. 10.5. The difference between  $G$  and  $Z$  expansions is that on sites  $I$   $M$  the values of  $L_i$  are increased by unity due to  $\sigma_I$  and  $\sigma_M$  variables leading to the requirement that the sum of bond numbers incident on  $I$  and  $M$  sites is odd.

The idea of WA is to unite configuration spaces for  $Z$  and  $G$  and to perform updates through the ends of the disconnected line (for the Ising model  $Z = G_{I=M}$ ). The algorithm consists of just one update and is simpler in implementation than the single spin-flip scheme:

- If  $I = M$ , select at random a new lattice site  $j$  and assign  $I = M = j$ ; otherwise skip this step. [In other words, put your pencil/eraser anywhere]. Select at random the direction (bond) to shift  $M$  to a nearest-neighbor site, let it be  $k$ , and propose to change the bond number from  $N_b$  to  $N'_b = \text{mod}_2(N_b + 1)$ . Accept the move

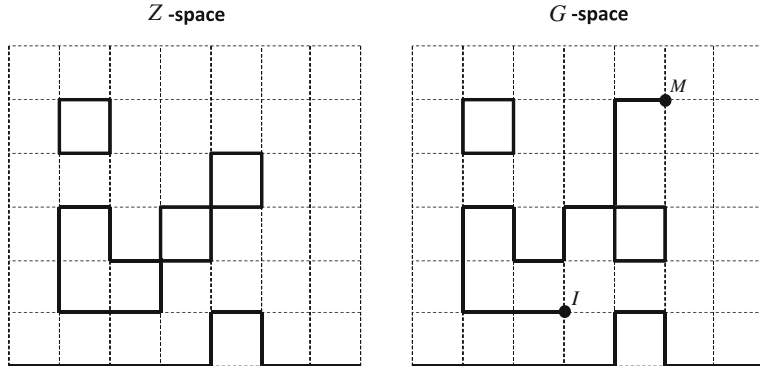


**Fig. 10.5** Graphical representation of the high-temperature expansion for the partition function (left-panel) and spin–spin correlation function (right panel) for the Ising model

with probability  $R = \max[1, \tanh^{N'_b - N_b}(K)]$ . This is a complete description of the entire algorithm!

Ergodicity is guaranteed because a finite number of steps is required to erase any initial trajectory and then to draw a new one, line after line. The efficiency is ultimately linked to the fact that WA works directly with the correlation function of the order parameter field. Every configuration contributes unity to the statistics of  $G_{I,M}$ .

Generalizations to other classical statistical models are straightforward [13]. For the  $XY$  model the bond exponential is replaced by the expansion

$$e^{K \cos(\theta_i - \theta_j)} = \sum_{N_b=-\infty}^{\infty} F(N_b) e^{i N_b (\theta_i - \theta_j)}, \quad (10.10)$$

with positive Fourier coefficients  $F(N_b)$ . This leads to the partition function

$$\begin{aligned} Z = & \left( \prod_i \int_0^{2\pi} \frac{d\theta_i}{2\pi} \right) \left( \prod_b \sum_{N_b=-\infty}^{\infty} F(N_b) e^{i N_b (\theta_i - \theta_j)} \right) = \\ & \sum_{\{N_b\}} \left( \prod_b F(N_b) \right) \prod_i \int_0^{2\pi} \frac{d\theta_i}{2\pi} e^{i L_i \theta_i}, \end{aligned} \quad (10.11)$$

where  $L_i = \sum_j N_{<ij>}$  with the convention that  $N_{<ij>} = -N_{<ji>}$ . This last rule comes from the trivial observation that on a given bond  $(\theta_i - \theta_j) = -(\theta_j - \theta_i)$  formally equivalent to changing the sign of  $N_b$  in (10.10). Graphically, each term in the expansion can be represented by lines with arrows drawn along the bonds with the line thickness proportional to  $|N_b|$  and direction pointing from  $i$  to  $j$  if  $N_{<ij>}$  is positive (from  $j$  to  $i$  if  $N_{<ij>}$  is negative). It is conventional to call  $N_b$  a ‘current’ number along the bond. Clearly, to have a non-vanishing contribution of the  $\{N_b\}$

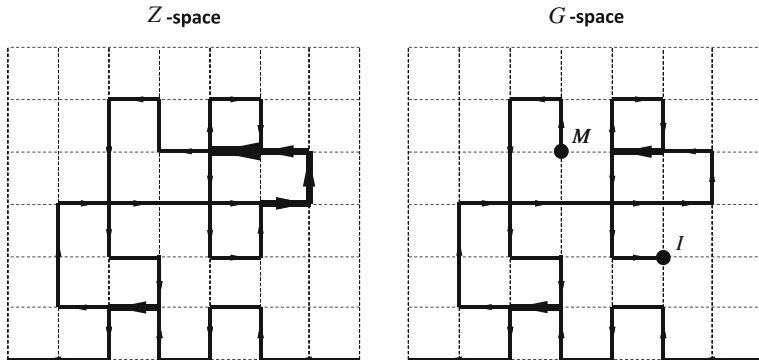


**Fig. 10.6** Graphical representation of the high-temperature expansion for the partition function (left-panel) and spin–spin correlation function (right panel) for the XY model

configuration to  $Z$  we must require that  $L_i$  is zero on all sites. In other words, the flux of currents entering the site must be equal to the flux of currents exiting the site,  $\sum_j N_{<ij>} = 0$ ; this is also known as a zero-divergence constraint. To satisfy it all allowed current configurations must consist then of closed loops which may self-intersect and overlap. A typical  $Z$ -configuration is shown in the left panel of Fig. 10.6.

The most important difference between the  $XY$  and Ising models is that loops are oriented in the  $XY$  case. This changes the universality class of the phase transition, but has no effect whatsoever on WA! To set up the algorithm we introduce the configuration space of the spin–spin correlation function  $G_{IM}/Z = \langle e^{i\theta_I} e^{-i\theta_M} \rangle$ . As before, due to extra  $e^{i\theta_I}$  and  $e^{-i\theta_M}$  factors the  $L_I$  and  $L_M$  numbers are increased/decreased by unity leading to the conditions  $\sum_j N_{<Ij>} = -1$  and  $\sum_j N_{<Mj>} = 1$ . Graphically this translates into one current line being absorbed/generated at  $I/M$  sites. Due to current conservation at all other sites it means that we can always draw a current line with unit flux originating at  $M$  and terminating at  $I$ , i.e. there is one open line in the  $G$ -configuration, see right panel in Fig. 10.6.

The rest is very much the same as for the Ising model. In the combined  $Z$  and  $G$  configuration space all updates are performed through the ends of the open line. The complete algorithm is as follows (it is hard to imagine anything simpler):

- If  $I = M$ , select at random a new lattice site  $j$  and assign  $I = M = j$ ; otherwise skip this step. Select at random the direction (bond) to shift  $M$  to a nearest-neighbor site, let it be  $k$ , and propose to change the bond number from  $N_{<Mk>}$  to  $N_{<Mk>} - 1$ . Accept the move with probability  $R = F(N_{<Mk>} - 1)/F(N_{<Mk>})$ .

One immediately realizes that the same algorithm will work for any statistical model defined on configurations consisting of closed loops with bond currents characterized by integers  $N_b$ . One may also add couplings between the currents originating from the same site; this will only change the acceptance ratio for the updates, but not the WA strategy. Thus, e.g.

$$Z = \sum_{\{N_b\}}^{\text{loops}} \exp \left\{ - \sum_b E(N_b) - \sum_i \tilde{E}(\{N_{<i,j>}\}) \right\}, \quad (10.12)$$

with arbitrary bond energy function  $E(N_b)$  and on-site interaction  $\tilde{E}(\{N_{<i,j>}\})$ , as well as its multi-component generalizations, can be dealt with in the same fashion. One may further complicate the local structure of the energy functional to include inter-site (and inter-bond) couplings, etc. This type of models are obtained after one does high-temperature expansions for single- and multi-component lattice field theories with  $U(1)$  and higher symmetries.

### 10.3.2 Path-Integral Representation

Let me now briefly discuss WA for the system of interacting lattice bosons with the configuration space shown in Fig. 10.2. In continuous imaginary time, things are getting technically more involved but all cases considered below are fully covered by the generic rules of the diagrammatic MC discussed above. I thus will not elaborate on the explicit procedures used to select the trajectory interval to be updated, explicit forms of the probability distributions used to seed new variables, or acceptance ratios. I will concentrate instead on the scheme concepts.

The path-integral configuration space of the Green's function contains two additional space-time points  $\mathcal{I}$  and  $\mathcal{M}$  at which one particle is annihilated and created, respectively. The rest is done in close analogy with the classical case, except that switching between the  $Z$ - and  $G$ -spaces is now accomplished with two pairs of separate complementary updates. The scheme presented below is ergodic but one should feel free to supplement it with additional procedures. It is sufficient to describe updates performed with the  $\mathcal{M}$ -end of the open worldline; updates involving the  $\mathcal{I}$ -end follow immediately from the time reversal symmetry.

*Open/Close.* This pair of updates takes us back and forth between the  $Z$ - and  $G$ -spaces by selecting at random some flat interval on the many-body trajectory and erasing a small part of it (*open*) or drawing an additional worldline piece between the end-points (*close*). These updates are illustrated in the upper panel of Fig. 10.7. In the (*open*) update the path interval characterized by time-independent occupation numbers on a given site is selected at random from the list of such intervals, and new imaginary times for the end-points  $\tau_I < \tau_M$  are seeded from the normalized probability distribution  $W(\tau_I, \tau_M)$  defined on the  $(\tau_{\text{in}}, \tau_{\text{fin}})$  interval. The distribution function  $W$  is arbitrary, and this freedom should be used to optimize the acceptance ratio  $R \propto D_{\text{new}}/[D_{\text{old}} W(\tau_I, \tau_M)]$ . In the (*close*) update one establishes whether  $\mathcal{I}$  and  $\mathcal{M}$  are connected by an interval with time-independent occupation numbers on a given site, and if so, proposes to eliminate them by ‘connecting the dots’. I skip here further technical details (such as data structure) which include standard programming tools, as well as explicit expressions for acceptance ratios, which are following from the generic rules described in the first section (since end-points represent

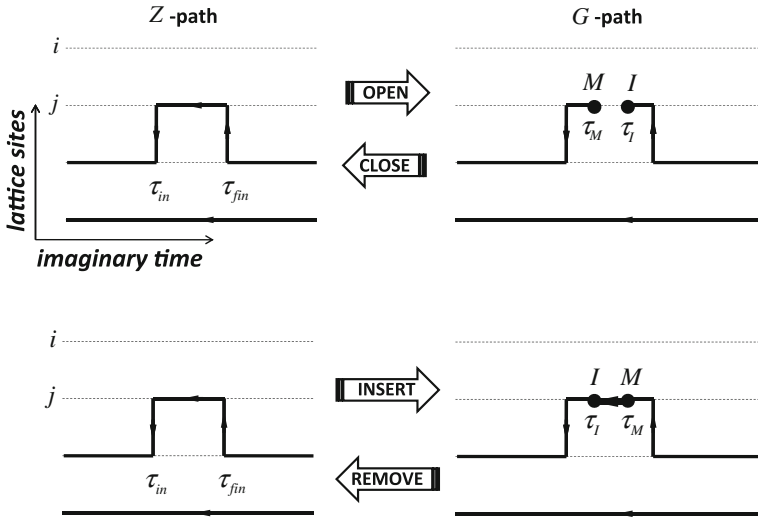


**Fig. 10.7** Open/Close (upper panel) and Insert/Remove (lower panel) pairs of updates which switch between the  $Z$  and  $G$  lattice path-integral configurations

particle creation and annihilation operators they contribute appropriate  $\sqrt{n}$  and  $\sqrt{n+1}$  factors to the configuration weight).

*Insert/Remove.* The only difference between the (*Insert/Remove*) and (*close*) pairs is that now end-points are created by adding (instead of erasing) an additional piece of the worldline (*insert*) and deleted by erasing (instead of adding) a trajectory connecting two ends (*remove*), see the lower panel in Fig. 10.7. Note that in accordance with this prescription the time ordering of  $\tau_I$  and  $\tau_M$  is reversed.

*Move.* Updates in the  $G$ -space literally implement the draw-and-erase idea. In the (*Move*) procedure  $\mathcal{M}$  point is shifted along the time axis,  $\tau_M \rightarrow \tau'_M$  within the interval  $(\tau_{in}, \tau_{fin})$  determined by changes of the occupation numbers on a given site, see upper panel in Fig. 10.8.

*Jump/anti-Jump.* This complementary pair of updates adds and deletes kinks on the trajectory and results in the motion of end-points in space. Without changing the time position of  $\mathcal{M}$ , we place it on the neighboring site and connect worldlines of the two sites involved in the update in such a way that the rest of the path remains intact. This requires adding/removing a kink immediately before or after  $\tau_M$ , the new time variable for the kink position is drawn from the probability density  $T(\tau_k)$  defined either on the  $(\tau_{in}, \tau_M)$  or  $(\tau_M, \tau_{fin})$  interval, see the lower panel in Fig. 10.8. Note the difference between the two cases. When the kink is inserted to the left of  $\mathcal{M}$ , the transformation can be interpreted as re-drawing of the same worldline. When the kink is inserted to the right of  $\mathcal{M}$ , we reconnect existing worldlines and place an end-point to the neighboring trajectory—this ensures that any line can be updated in the long run.

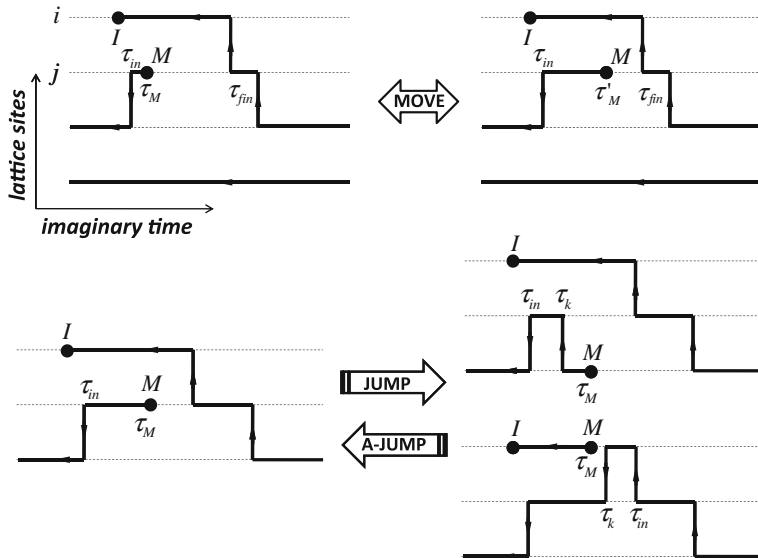


**Fig. 10.8** Move (upper panel) and Jump/anti-Jump (lower panel) updates performed in the  $G$ -space

This concludes the description of the algorithm for lattice path-integrals. Such properties as density, energy, density-density correlations, etc. are computed using standard rules when the configuration is in the  $Z$ -path sector. Every  $G$ -configuration makes a direct (unity) contribution to the statistics of  $G(\tau_M - \tau_I, i_M - i_I)$ .

Though WA is a local Metropolis scheme, its performance, remarkably, is similar to (or better than) the best cluster methods at the critical point, i.e. it does not suffer from the critical slowing down problem. It has no problem of producing loops winding around the system, allows efficient simulations of off-diagonal correlations, grand canonical ensembles, disordered systems, etc.

Continuous and lattice path-integrals are essentially identical in terms of the topology and meaning of their respective configuration spaces; the only technical difference is that now spatial coordinates characterizing trajectories are continuous while the imaginary time is discrete, i.e. the trajectory is defined by a set of ‘beads’ linked to each other. A complete description of updates and estimators for physical quantities can be found in Ref. [16]. [In continuous space the decomposition of the many-body path into individual worldlines is unique and this actually simplifies things at the programming level]. It is sufficient to simply draw updates and supplement them with the description of probabilistic decisions made to propose a particular transformation; since in all cases we know how to compute the path contribution to the statistics of  $Z$  or  $G$  the graphics can always be converted to precise mathematical expressions for the acceptance ratios.

Figures 10.9 and 10.10 show an ergodic set of updates which would allow one to efficiently simulate continuous space systems. The *Open/Close* and *Insert/Remove*

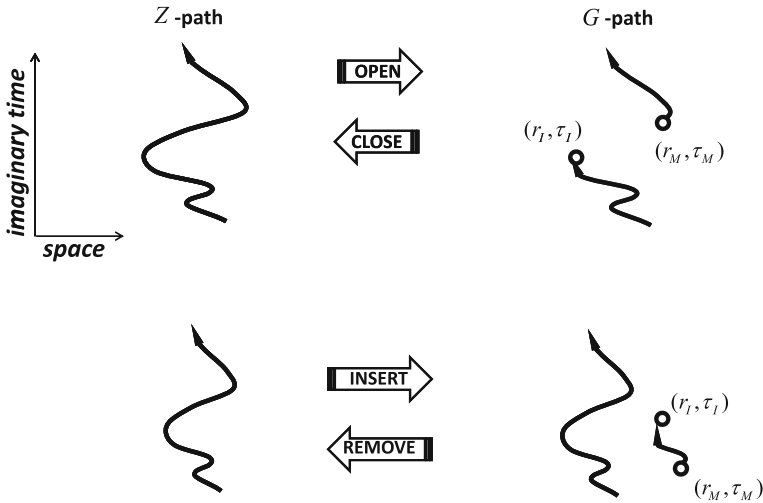


**Fig. 10.9** The upper and lower panels illustrate transformations performed by the *Open/Close* and *Insert/Remove* pairs of updates respectively on the continuous-space path thus switching between the *Z* and *G* configurations

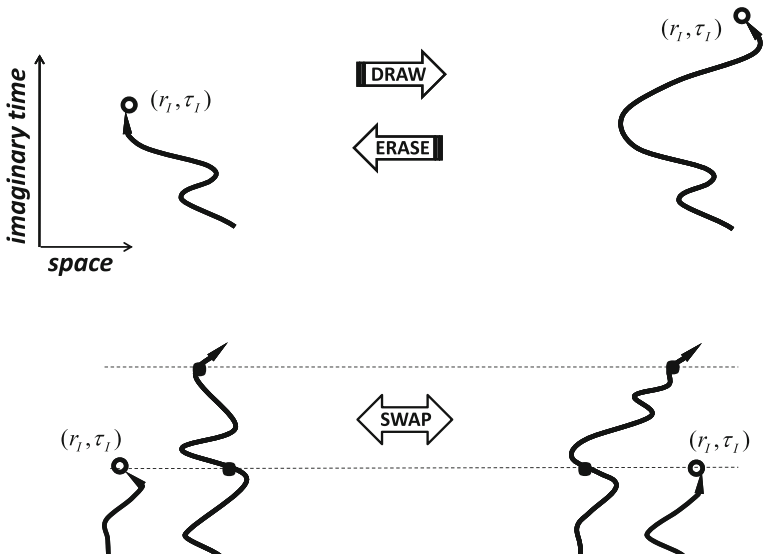


**Fig. 10.10** The upper and lower panels illustrate transformations performed by the *Draw/Erase* and *Swap* updates respectively on the continuous-space *G*-path

pairs of updates are reminiscent of similar updates in lattice systems. The *Draw/Erase* pair naturally combines in one update both space and time motion of the end-point and is a literal implementation of the draw-and-erase algorithm. The *Swap* update is equivalent to the version of the *Jump* update which involves reconnection of individual worldlines. In *Swap* all modifications of the path are restricted to occur between the two dashed lines, see Fig. 10.10.

### 10.3.3 Wandering Amongst the Feynman Diagrams

Consider now the configuration space of connected Feynman diagrams for free energy in the generic interacting many-body system. In momentum and/or frequency representation, the internal variables of all lines have to satisfy momentum and/or frequency conservation laws at each vertex (for brevity I will refer to such conservation laws by mentioning momentum only). Topologically, this rule is identical to stating that independent internal variables are assigned to closed loops formed by the graph lines—indeed, loop structure guarantees that the same momentum enters and exists every vertex. The other important consideration restricting topology of the configuration space is the possibility of performing DiagMC in a self-consistent fashion by considering only skeleton diagrams, and accounting for the renormalization of all graph lines in the form of Dyson-type equation. In this setup, irreducible skeleton graphs are not allowed to contain structures which can be interpreted as contributions to line renormalizations, (full skeleton technique includes also renormalized vertex functions and imposes additional restrictions).

If one is to perform MC sampling of this configuration space it appears that conservation laws and irreducibility conditions are simply incompatible with local updates, i.e. there is no way to satisfy the necessary requirements without knowing the global structure of the entire diagram. This is where WA idea of introducing fictitious diagrams and performing local updates through special end-points comes to rescue. In the example considered below fictitious diagrams have no physical meaning and constitute a purely algorithmic trick.

The non-physical diagrams feature two vertices,  $\mathcal{M}$  and  $\mathcal{I}$ , with conservation laws being violated by amount  $\mathbf{w}$  at  $\mathcal{M}$  and  $-\mathbf{w}$  at  $\mathcal{I}$ . The best way to visualize the idea of WA in this case is to imagine that  $\mathcal{M}$  and  $\mathcal{I}$  are end-points of an unphysical line connecting them which carries the extra momentum  $\mathbf{w}$ , see Fig. 10.11. Let us call it the ‘worm momentum’. An update switching between physical and un-physical spaces by selecting at random one of the lines in the graph is illustrated in Fig. 10.11. The parameters involved in the conservation laws for the selected line are then changed by random amount  $\mathbf{w}$  proposed from the probability density  $f(\mathbf{w})$ . An update taking the diagram back to the physical space simply checks that  $\mathcal{M}$  and  $\mathcal{I}$  are connected by a single line and proposes to change the momentum of this line accordingly by adding  $\mathbf{w}$ . More specific details and explicit acceptance ratios for the entire algorithm dealing with the Fermi-Hubbard model can be found in Ref. [17].

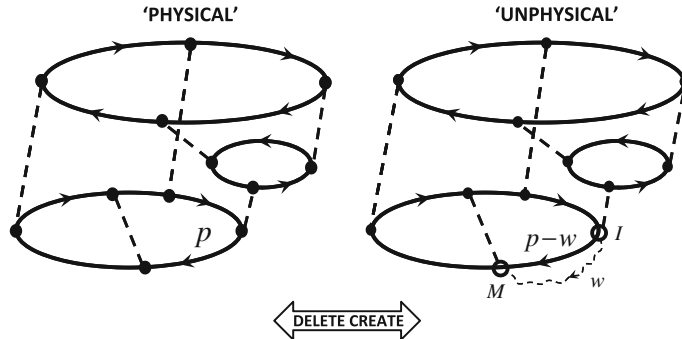


**Fig. 10.11** Creating and deleting special vertexes  $\mathcal{M}$  and  $\mathcal{I}$  in which the momentum conservation laws are violated by amount  $\pm w$ . One can imagine restoring conservation laws by drawing a hypothetical line between  $\mathcal{M}$  and  $\mathcal{I}$  which carries the missing amount of momentum

The rest of the updates are performed in unphysical space and constitute a set of local transformations always involving  $\mathcal{M}$  or  $\mathcal{I}$  or both. The simplest of them involves moving the end-point along any of the graph lines attached to it and changing its momentum accordingly (excluding cases when this leads to placing  $\mathcal{M}$  and  $\mathcal{I}$  on the same vertex). This ‘diffusive’ motion ensures that any vertex of the connected graph can be reached and parameters of all lines eventually changed. When worms are finally removed, one effectively changes momentum along some loop structure in the graph.

The crucial advantage of WA is that all necessary structural transformations of the diagrams can also be performed through worm ends using local updates only. For example, one can consider two out-going propagators originating from  $\mathcal{M}$  and  $\mathcal{I}$  vertexes and swap their destination vertexes places while keeping their momenta intact. This certainly changes the topology of the diagram. The update is purely local and conservation laws are handled properly by adjusting the value of the worm momentum, see the upper panel in Fig. 10.12.

Similarly, it is now possible to add and remove vertexes without knowing the global structure of the diagram, see the lower panel in Fig. 10.12. Conservation laws are satisfied by running an extra momentum  $\mathbf{q}$  along the loop involving the vertex to be added/removed and two propagators connecting it to the end-points. Depending on the Hamiltonian in question one may design additional updates to sample the corresponding configuration space but they can always be made local with the help of worms.

Even if diagrams are formulated in real space and time domains and conservation laws are absent, it still makes sense to introduce auxiliary momentum variables for all lines (nothing at all in the physical diagram depends on these variables) with the corresponding momentum conservation at each vertex. This allows one to perform an instantaneous check of the diagram for irreducibility. Indeed, in the irreducible diagram no two lines are allowed to have the same momentum which is a simple operational rule equivalent to the requirement that no part of the diagram can be

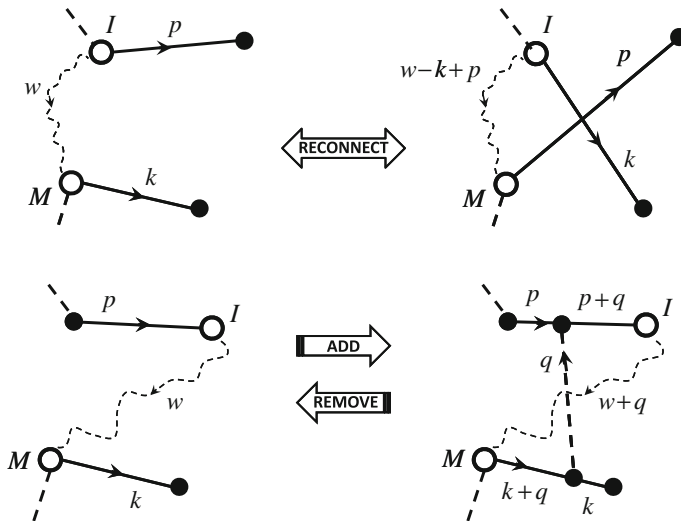


**Fig. 10.12** Commuting propagators originating from  $\mathcal{M}$  and  $\mathcal{I}$  points (*upper panel*) and adding/removing an interaction vertex (*lower panel*) with simultaneous change of the worm momentum  $w$

interpreted as line renormalization. In local updates only a small number of lines change their momentum states, thus if all momenta are stored in the so called ‘hash table’ one can check for the momentum coincidence condition with minimal effort, i.e. with effort which does not scale with the size and complexity of the diagram.

## References

1. N. Metropolis, A.W. Rosenbluth, M.N. Rosenbluth, A.H. Teller, E. Teller, Equation of state calculations by fast computing machines. *J. Chem. Phys.* **21**(6), 1087–1092 (1953)
2. N.V. Prokof’ev, B.V. Svistunov, Polaron problem by diagrammatic quantum monte carlo. *Phys. Rev. Lett.* **81**(12), 2514–2517 (1998)
3. A.S. Mishchenko, N.V. Prokof’ev, A. Sakamoto, B.V. Svistunov, Diagrammatic quantum monte carlo study of the fröhlich polaron. *Phys. Rev. B* **62**(10), 6317–6336 (2000)
4. E. Gull, A.J. Millis, A. Lichtenstein, A.N. Rubtsov, M. Troyer, P. Werner, Continuous-time monte carlo methods for quantum impurity models, arXiv:1012.4474 (2010)
5. N. Prokof’ev B. Svistunov, Bold diagrammatic monte carlo technique: when the sign problem is welcome. *Phys. Rev. Lett.* **99**(25), 250201 (2007)
6. N.V. Prokof’ev, B.V. Svistunov, Bold diagrammatic monte carlo: a generic sign-problem tolerant technique for polaron models and possibly interacting many-body problems. *Phys. Rev. B* **77**(12), 125101 (2008)
7. F.J. Dyson, Divergence of perturbation theory in quantum electrodynamics. *Phys. Rev.* **85**(4), 631–632 (1952)
8. L.G. Molinari, N. Manini, Enumeration of many-body skeleton diagrams. *Euro. Phys. J. B* **51**(3), 331–336 (2006)

9. E. Kozik, K. Van Houcke, E. Gull, L. Pollet, N. Prokof'ev, B. Svistunov, M. Troyer, Diagrammatic monte carlo for correlated fermions. *Euro. Phys. Lett.* **90**(1), 10004 (2010)
10. K. Van Houcke, F. Werner, E. Kozik, N.V. Prokof'ev, B.V. Svistunov, M.J.H. Ku, A.T. Sommer, L.W. Cheuk, A. Schirozek, M. Zwierlein, Feynman diagrams versus Fermi-gas Feynman emulator. *Nat. Phys.* **8**, 366 (2012). doi:[10.1038/nphys2273](https://doi.org/10.1038/nphys2273)
11. R.P. Feynman, Space-time approach to non-relativistic quantum mechanics. *Rev. Mod. Phys.* **20**(2), 367–387 (1948)
12. N. Prokof'ev, B. Svistunov, I. Tupitsyn, Worm algorithm in quantum monte carlo simulations. *Phys. Lett. A* **238**(4–5), 253–257 (1998)
13. N. Prokof'ev, B. Svistunov, Worm algorithms for classical statistical models. *Phys. Rev. Lett.* **87**(16), 160601 (2001)
14. A. Kuklov, N. Prokof'ev, B. Svistunov, Superfluid-superfluid phase transitions in a two-component Bose-Einstein condensate. *Phys. Rev. Lett.* **92**(3), 030403 (2004)
15. S.G. Söyler1, B. Capogrosso-Sansone, N.V. Prokof'ev, B.V. Svistunov, Sign-alternating interaction mediated by strongly correlated lattice bosons. *New J. Phys.* **11**(7), 073036 (2009)
16. M. Boninsegni, N.V. Prokof'ev, B.V. Svistunov, Worm algorithm and diagrammatic monte carlo: a new approach to continuous-space path integral monte carlo simulations. *Phys. Rev. E* **74**(3), 036701 (2006)
17. K. Van Houcke, E. Kozik, N. Prokof'ev, B. Svistunov, Diagrammatic monte carlo, in *Computer Simulation Studies in Condensed Matter Physics*, vol. XXI, ed. by D.P. Landau, S.P. Lewis, H.B. Schuttler (Springer, Heidelberg, 2008)

# Chapter 11

## Fermionic and Continuous Time Quantum Monte Carlo

Emanuel Gull and Matthias Troyer

**Abstract** Diagrammatic “continuous-time” algorithms for fermionic systems are algorithms that evaluate the diagrammatic perturbation series of interacting many-body systems stochastically. The algorithms involve no approximations and are numerically exact for convergent series, as they appear, for example, in the description of finite lattice problems and quantum impurity models. Among other advantages the various formulations of continuous-time algorithms are able to accurately describe systems with general, complex multi-orbital structures as they appear in the theoretical description of a wide range of transition metal and actinide compounds.

### 11.1 Introduction

In this chapter we give an introduction to modern continuous time quantum Monte Carlo (CT-QMC) methods for fermions. This chapter closely follows a recent review [1] both in notation and content. For pedagogic reasons we here focus on simple models and refer to the review [1] for the general case and further details.

The algorithms that we will cover will be applicable both to lattice models and to quantum impurity problems. As a representative for lattice models we will consider the prototypical Hubbard model with Hamiltonian

$$H = -t \sum_{\langle i,j \rangle} \sum_{\sigma=\uparrow,\downarrow} (c_{i,\sigma}^\dagger c_{j,\sigma} + c_{j,\sigma}^\dagger c_{i,\sigma}) + U \sum_i n_{i,\uparrow} n_{i,\downarrow}, \quad (11.1)$$

where  $c_{i,\sigma}^\dagger$  creates a fermion on site  $i$  with spin  $\sigma$  and  $n_{i,\sigma} = c_{i,\sigma}^\dagger c_{i,\sigma}$ .

---

E. Gull (✉)

Department of Physics, University of Michigan, Ann Arbor, MI 48109-1040, USA  
e-mail: egull@umich.edu

M. Troyer

Institut f. Theoretische Physik, ETH, 8093 Zurich, Switzerland  
e-mail: matthias.troyer@itp.phys.ethz.ch

Quantum impurity models describe “impurity” states (depending on the context usually ‘d’-orbitals of a transition metal, ‘f’-orbitals of a heavier element, or some auxiliary correlated subspace) embedded in a non-interacting medium. The simple Anderson impurity model is given by

$$H_{\text{QI}} = H_{\text{loc}} + H_{\text{bath}} + H_{\text{hyb}}, \quad (11.2)$$

where

$$H_{\text{loc}} = H_{\text{loc}}^0 + H_{\text{loc}}^I, \quad (11.3)$$

$$H_{\text{loc}}^0 = \sum_{ab} E^{ab} d_a^\dagger d_b, \quad (11.4)$$

$$H_{\text{loc}}^I = \sum_{pqrs} I^{pqrs} d_p^\dagger d_q^\dagger d_r d_s + \dots, \quad (11.5)$$

$$H_{\text{bath}} = \sum_{k\alpha} \varepsilon_{k\alpha} c_{k\alpha}^\dagger c_{k\alpha}, \quad (11.6)$$

and

$$H_{\text{hyb}} = \sum_{k\alpha b} V_k^{\alpha b} c_{k\alpha}^\dagger d_b + \text{H.c..} \quad (11.7)$$

Here the operators  $d_a^\dagger$  create fermions on the “impurity” site and the operators  $c_{k,a}^\dagger$  create fermions with momentum  $k$  in the non-interacting embedding medium. The indices  $a$  combine both orbital and spin degrees of freedom.

Quantum impurity models appear also in the solution of the dynamical mean field theory (DMFT) [2–4] equations. Much of the early push for CT-QMC methods came from the demand for unbiased, numerically exact impurity solvers for DMFT and this is still the area where CT-QMC algorithms are used most frequently. For a detailed introduction to DMFT we refer the reader to the reviews [5, 6] and lecture notes [7] on the subject, as well as to the reviews on extensions to real materials [6, 8, 9] and clusters [10].

The basic idea of the CT-QMC methods [1] is the stochastic sampling of time-dependent perturbation theory. One splits the Hamiltonian  $H = H_a + H_b$  into two parts, writes the partition function  $Z = e^{-\beta H}$  in the interaction representation with respect to  $H_a$  and expands in powers of  $H_b$ , thus ( $T_\tau$  is the time ordering operator)

$$\begin{aligned} Z &= \text{Tr } T_\tau e^{-\beta H_a} \exp \left[ - \int_0^\beta d\tau H_b(\tau) \right] \\ &= \sum_k (-1)^k \int_0^\beta d\tau_1 \dots \int_{\tau_{k-1}}^\beta d\tau_k \text{Tr} [e^{-\beta H_a} H_b(\tau_k) H_b(\tau_{k-1}) \dots H_b(\tau_1)]. \end{aligned} \quad (11.8)$$

The trace evaluates to a number and diagrammatic Monte Carlo methods [11] enable a sampling over all orders  $k$ , all topologies of the paths/diagrams and all times  $\tau_1, \dots, \tau_k$  in the same calculation. Because the method is formulated in continuous time from the beginning, time discretization errors do not arise and therefore do not have to be controlled. Provided the spectrum of the perturbation term is bounded from above the contributions of very large orders are exponentially suppressed by the factor  $\frac{1}{k!}$  originating from the expansion of an exponential. Thus the sampling process does not run off to infinite order and no truncation of the diagram order is needed.

In the impurity model context several types of expansion have been formulated. Here we focus on the hybridization expansion CT-HYB ( $H_b = H_{\text{hyb}}$ , Eq.(11.7)) [12], the interaction expansion CT-INT ( $H_b = H_{\text{loc}}^I$ , Eq. (11.5)) [13], and the continuous-time auxiliary field method CT-AUX ( $H_b = H_{\text{loc}}^I$  [14] but with an additional auxiliary field decomposition).

The advantage of the hybridization expansion is that arbitrarily complicated impurity interactions can easily be treated; the disadvantage is that because  $[H_{\text{hyb}}, H_{\text{loc}}] \neq 0$  at least one of the operators is non-diagonal so the expansion generically requires the manipulation of matrix blocks whose size grows exponentially with the number of impurity orbitals. The present state of the art is that five spin-degenerate orbitals can be treated. Various truncation and approximation schemes provide limited access to larger problems but as the number of orbitals is increased the difficulties rapidly become insurmountable.

CT-INT and CT-AUX are variations of an “interaction expansion”. They are sometimes referred to as “weak coupling” expansions, but this is a misnomer—the expansion is in powers of the interaction but is not (in principle) restricted to small interactions. The series is always convergent for nonzero temperature and finite number of orbitals. In CT-INT and CT-AUX the scaling with number of impurity orbitals is not exponential, so much larger systems can be treated. However, these methods are most suited to Hubbard-like models with a single local density-density interaction and are ideal for lattice models such as the Hubbard model. More complicated interactions typically require multiple expansions in all interaction vertices and if the interactions do not commute (as is the case for the components of the spin exchange) the difficulties increase.

While all of the expansions are based on the same general idea, there are significant differences in the specifics of how the expansion is arranged, the measurements are done and the errors are controlled. We therefore devote a separate section to each expansion, and refer the reader to a recent review [1] for more information and implementation issues.

## 11.2 Diagrammatic Monte Carlo

### 11.2.1 Monte Carlo Basics

In this subsection we recall some basic results pertaining to the Monte Carlo evaluation of high dimensional integrals. For reader unfamiliar with Monte Carlo, the books by Landau and Binder [15] and Krauth [16] give an extensive introduction to the technique.

In statistical physics we face the issue of evaluating sums over very high dimensional phase spaces or configuration spaces  $\mathcal{C}$ . Monte Carlo techniques are the only practical methods of evaluation of such high-dimensional sums or integrals. A crucial quantity is the partition function,  $Z$ , which we will write formally as an integral over configurations  $\mathbf{x} \in \mathcal{C}$  with weight  $p(\mathbf{x})$ :

$$Z = \int_{\mathcal{C}} d\mathbf{x} p(\mathbf{x}). \quad (11.9)$$

In a classical system  $\mathbf{x}$  might be a point in phase space with a Boltzmann weight  $p(\mathbf{x}) = \exp(-\beta E(\mathbf{x}))$ , where  $E(\mathbf{x})$  is the energy of the configuration  $\mathbf{x}$ . In the quantum problems described here  $\mathbf{x}$  will represent a particular term in a diagrammatic partition function expansion. The expectation value of a quantity  $A$  is given by the average, over the configuration space  $\mathcal{C}$  with weight  $p$ , of a quantity  $\mathcal{A}(\mathbf{x})$ :

$$\langle A \rangle_p = \frac{1}{Z} \int_{\mathcal{C}} d\mathbf{x} \mathcal{A}(\mathbf{x}) p(\mathbf{x}). \quad (11.10)$$

The auxiliary quantity  $\mathcal{A}(\mathbf{x})$  depends on the specific representation chosen in a particular algorithm. The average (11.10) can be estimated in a Monte Carlo procedure by selecting  $M$  configurations  $\mathbf{x}_i$  with a probability  $p(\mathbf{x})/Z$  and averaging the contributions  $\mathcal{A}(\mathbf{x}_i)$ :

$$\langle A \rangle_p \approx \langle A \rangle_{MC} \equiv \frac{1}{M} \sum_{i=1}^M \mathcal{A}(\mathbf{x}_i). \quad (11.11)$$

According to the central limit theorem, if the number of configurations is large enough the estimate (11.11) will be normally distributed around the exact value  $\langle A \rangle_p$  with variance

$$(\Delta A)^2 \equiv \langle (A_{MC} - A_p)^2 \rangle = \frac{\text{Var } A}{M}. \quad (11.12)$$

It will sometimes be advantageous or necessary to sample from configurations  $\mathbf{x}_i$  with a distribution  $\rho(\mathbf{x})$  different  $p(\mathbf{x})$ . The expectation value  $\langle A \rangle_\rho$  in the ensemble then has to be reweighted:

$$\langle A \rangle = \frac{1}{Z} \int_{\mathcal{C}} d\mathbf{x} \mathcal{A}(\mathbf{x}) p(\mathbf{x}) = \frac{\int_{\mathcal{C}} d\mathbf{x} \mathcal{A}(\mathbf{x}) \frac{p(\mathbf{x})}{\rho(\mathbf{x})} \rho(\mathbf{x})}{\int_{\mathcal{C}} d\mathbf{x} \frac{p(\mathbf{x})}{\rho(\mathbf{x})} \rho(\mathbf{x})} \equiv \frac{\langle A \frac{p}{\rho} \rangle_{\rho}}{\langle \frac{p}{\rho} \rangle_{\rho}}. \quad (11.13)$$

To estimate this expectation value one needs to sample both the numerator and denominator and collect averages of  $\mathcal{A}(\mathbf{x}_i) p(\mathbf{x}_i)/\rho(\mathbf{x}_i)$  and  $p(\mathbf{x}_i)/\rho(\mathbf{x}_i)$ . Care must be taken in estimating the statistical errors of such ratios, since cross-correlations will make naïve error propagation unreliable. A jackknife or bootstrap procedure is needed. Integrals with general distributions such as Eqs. (11.9) and (11.13) are best sampled by generating configurations using a Markov process. A Markov process is fully characterized by a transition matrix  $W_{\mathbf{xy}}$  specifying the probability to go from state  $\mathbf{x}$  to state  $\mathbf{y}$  in one step of the Markov process. Normalization (conservation of probabilities) requires  $\sum_{\mathbf{y}} W_{\mathbf{xy}} = 1$ . Starting from an arbitrary distribution the Markov process will converge exponentially to a stationary distribution  $p(\mathbf{x})$  if two conditions are satisfied:

- *Ergodicity*: It has to be possible to reach any configuration  $\mathbf{x}$  from any other configuration  $\mathbf{y}$  in a finite number of steps: for all  $\mathbf{x}$  and  $\mathbf{y}$  there exists an integer  $N < \infty$  such that for all  $n \geq N$  the probability  $(W^n)_{\mathbf{xy}} \neq 0$ .
- *Balance*: Stationarity implies that the distribution  $p(\mathbf{x})$  fulfills the balance condition

$$\int_{\mathcal{C}} d\mathbf{x} p(\mathbf{x}) W_{\mathbf{xy}} = p(\mathbf{y}), \quad (11.14)$$

that is  $p(\mathbf{x})$  is a left eigenvector of the transition matrix  $W_{\mathbf{xy}}$ . A sufficient but not necessary condition usually used instead of the balance condition is the *detailed balance* condition

$$\frac{W_{\mathbf{xy}}}{W_{\mathbf{yx}}} = \frac{p(\mathbf{y})}{p(\mathbf{x})}, \quad (11.15)$$

which we will use below.

The first, and still most widely used, algorithm that satisfies detailed balance is the Metropolis-Hastings algorithm [17, 18]. There, an update from a configuration  $\mathbf{x}$  to a new configuration  $\mathbf{y}$  is proposed with a probability  $W_{\mathbf{xy}}^{\text{prop}}$  but accepted only with probability  $W_{\mathbf{xy}}^{\text{acc}}$ . If the proposal is rejected the old configuration  $\mathbf{x}$  is used again. The transition matrix is

$$W_{\mathbf{xy}} = W_{\mathbf{xy}}^{\text{prop}} W_{\mathbf{xy}}^{\text{acc}} \quad (11.16)$$

and the detailed balance condition (11.15) is satisfied by using the Metropolis-Hastings acceptance rate

$$W_{\mathbf{xy}}^{\text{acc}} = \min [1, R_{\mathbf{xy}}]. \quad (11.17)$$

with the acceptance ratio  $R_{\mathbf{xy}}$  given by

$$R_{\mathbf{xy}} = \frac{p(\mathbf{y}) W_{\mathbf{yx}}^{\text{prop}}}{p(\mathbf{x}) W_{\mathbf{xy}}^{\text{prop}}} \quad (11.18)$$

and  $R_{\mathbf{yx}} = 1/R_{\mathbf{xy}}$ . To simplify the notation we will often quote just  $R_{\mathbf{xy}}$ , and imply that  $\min[1, R_{\mathbf{xy}}]$  is the actual acceptance probability. Note that the acceptance ratio  $R_{\mathbf{xy}}$  includes both the weights and the proposal probabilities. In the following sections we will always specify both the proposal probabilities  $W_{\mathbf{xy}}^{\text{prop}}$  and the acceptance ratios  $R_{\mathbf{xy}}$ .

### 11.2.2 Diagrammatic Monte Carlo

The partition function Eq.(11.8) may be expressed as a sum of integrals originating from a diagrammatic expansion:

$$Z = \sum_{k=0}^{\infty} \sum_{\gamma \in \Gamma_k} \int_0^{\beta} d\tau_1 \dots \int_{\tau_{k-1}}^{\beta} d\tau_k w(k, \gamma, \tau_1, \dots, \tau_k), \quad (11.19)$$

which has the form of Eq.(11.9). The individual configurations are of the form

$$\mathbf{x} = (k, \gamma, (\tau_1, \dots, \tau_k)), \quad (11.20)$$

where  $k$  is the expansion or diagram order and  $\tau_1, \dots, \tau_k \in [0, \beta]$  are the times of the  $k$  vertices in the configuration. The parameter  $\gamma \in \Gamma_k$  includes all discrete variables, such as the topology of the diagram and spin, orbital, lattice site, and auxiliary spin indices associated with the interaction vertices.

A configuration  $\mathbf{x}$  has a weight

$$p(\mathbf{x}) = w(k, \gamma, \tau_1, \dots, \tau_k) d\tau_1 \dots d\tau_k, \quad (11.21)$$

which we will assume to be non-negative for now. The case of negative weights is discussed in Sect. 11.2.3. Although these weights are well-defined probability densities they involve infinitesimals  $d\tau$ , which one might worry could cause difficulties with proposal and acceptance probabilities in the random walk in configuration space. As Ref. [19] showed, this is not the case.

The algorithms presented here all express the partition function in the general form (11.19). To illustrate the sampling of such continuous-time partition function expansions we consider the very simple partition function

$$Z = \sum_{k=0}^{\infty} \int_0^{\beta} d\tau_1 \int_0^{\beta} d\tau_2 \cdots \int_0^{\beta} d\tau_k \frac{w(k)}{k!}, \quad (11.22)$$

which using time ordering can be rewritten as

$$Z = \sum_{k=0}^{\infty} \int_0^{\beta} d\tau_1 \int_{\tau_1}^{\beta} d\tau_2 \cdots \int_{\tau_{k-1}}^{\beta} d\tau_k w(k). \quad (11.23)$$

The distribution describing the probability of a diagram of order  $k$  with vertices at times  $\{\tau_j\}$  is (here we make the times explicit)

$$p((k, \tau_1, \dots, \tau_k)) = w(k) \prod_{i=1}^k d\tau_i. \quad (11.24)$$

In the following we will always assume time-ordering  $\tau_1 \leq \tau_2 \leq \dots \leq \tau_k$  and visualize the configurations using a diagrammatic representation as in Fig. 11.1.

Transitions between configurations  $\mathbf{x}$  and  $\mathbf{y}$  are realized by updates. They typically involve (i) updates that increase the order  $k$  by inserting an additional vertex at a time  $\tau$  and (ii) updates that decrease the order  $k$  by removing a vertex  $\tau_j$ . These insertion and removal updates are necessary to satisfy the ergodicity requirement and are often sufficient: we can reach any configuration from another one by removing all the existing vertices and then inserting new ones. Additional updates keeping the order  $k$  constant are not required for ergodicity but may speed up equilibration and improve the sampling efficiency. In some special circumstances, for example if all odd order diagrams have zero weight, updates which insert or remove multiple vertices are required.

In the following we will focus on the insertion and removal updates, illustrated in Fig. 11.2. For the insertion let us start from a configuration  $(k, \tau) = (k, \tau_1, \dots, \tau_k)$  of order  $k$ . We propose to insert a new vertex at a time  $\tau$  uniformly chosen in the interval  $[0, \beta]$ , to obtain a new time-ordered configuration  $(k+1, \tau') = (k+1, \tau_1, \dots, \tau, \dots, \tau_k) \equiv (k+1, \tau'_1, \dots, \tau'_{k+1})$ . The proposal rate for this insertion is given by the probability density

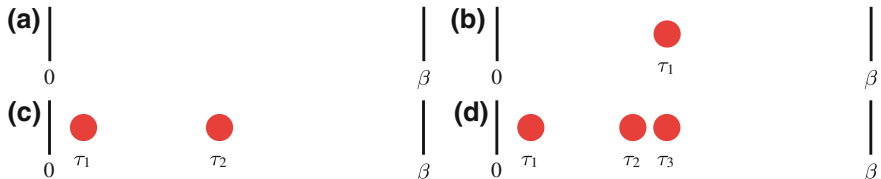
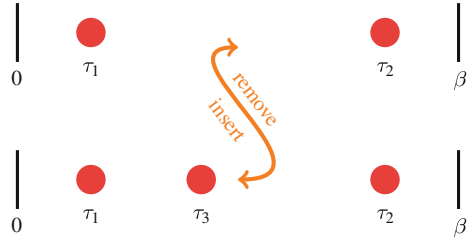


**Fig. 11.1** Diagrammatic representation of configurations  $\mathbf{x} = \{(k; \tau_1, \dots, \tau_k)\} \in \mathcal{C}$  showing examples with orders  $k = 0, 1, 2, 3$  and vertices (represented by dots) at times  $\tau_1, \dots, \tau_3$

**Fig. 11.2** An insertion update (*top to bottom*) inserting a vertex at time  $\tau_3$  and the corresponding removal update (*bottom to top*), removing the vertex at time  $\tau_3$



$$W_{(k, \tau), (k+1, \tau')}^{\text{prop}} = \frac{d\tau}{\beta}. \quad (11.25)$$

The reverse move is the removal of a randomly chosen vertex. The probability of removing a particular vertex to go back from  $(k+1, \tau')$  to  $(k, \tau)$  is just one over the number of available vertices:

$$W_{(k+1, \tau'), (k, \tau)}^{\text{prop}} = \frac{1}{k+1}. \quad (11.26)$$

To obtain the acceptance rates we first calculate the acceptance ratio

$$\begin{aligned} R_{(k, \tau), (k+1, \tau')} &= \frac{p((k+1, \tau'))}{p((k, \tau))} \frac{W_{(k+1, \tau'), (k, \tau)}^{\text{prop}}}{W_{(k, \tau), (k+1, \tau')}^{\text{prop}}} \\ &= \frac{w(k+1) d\tau'_1 \cdots d\tau'_{k+1}}{w(k) d\tau_1 \cdots d\tau_k} \frac{1/(k+1)}{d\tau/\beta} = \frac{w(k+1)}{w(k)} \frac{\beta}{k+1}. \end{aligned} \quad (11.27)$$

Observe that all infinitesimals cancel: the additional infinitesimal in the weight  $p((k+1, \tau'))$  is canceled by the infinitesimal of the proposal rate for insertions.

Equation (11.27) implies that the acceptance rates  $W^{\text{acc}}$  are well defined finite numbers given by

$$W_{(k, \tau), (k+1, \tau')}^{\text{acc}} = \min [1, R_{(k, \tau), (k+1, \tau')}], \quad (11.28)$$

$$W_{(k+1, \tau'), (k, \tau)}^{\text{acc}} = \min [1, 1/R_{(k, \tau), (k+1, \tau')}] . \quad (11.29)$$

The general scheme of diagrammatic Monte Carlo algorithms is illustrated in Fig. 11.3. One cannot stress often enough that measurements are performed again on the old configuration if the proposed update has been rejected.

### 11.2.3 The Negative Sign Problem

Until now we have assumed that the expansion coefficients of our partition function expansion are always positive. This has allowed us to interpret the weights as

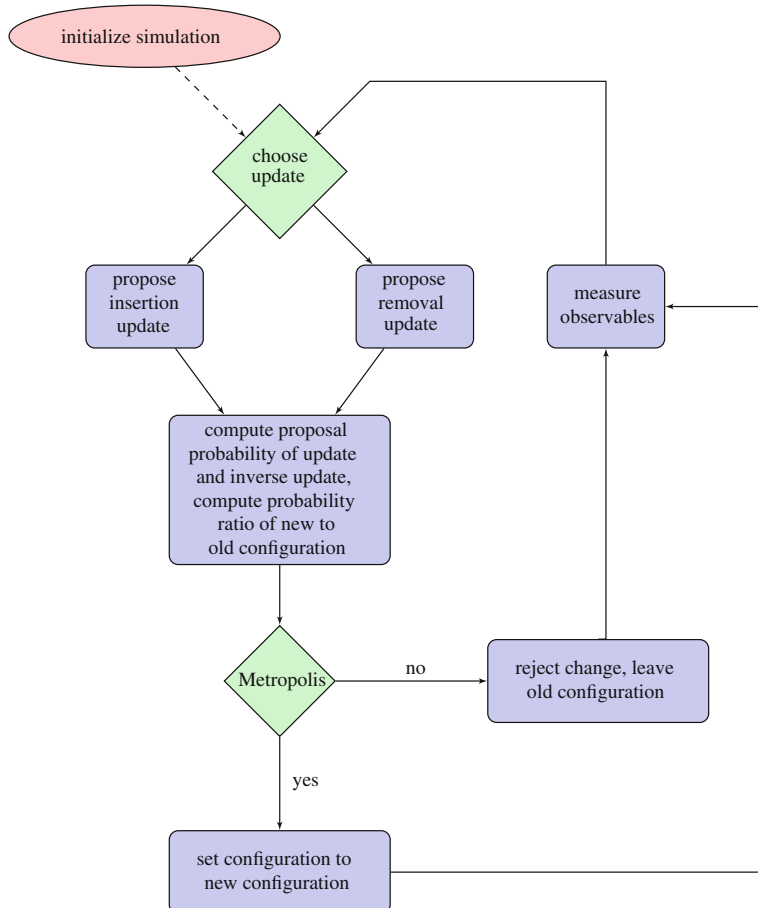


**Fig. 11.3** Continuous-time Quantum Monte Carlo flow diagram

probability densities on the configuration space and to perform a stochastic sampling of these configurations. If the weights  $p(\mathbf{x})$  become negative, as is often the case in fermionic simulations due to the anti-commutation relations between fermionic operators, they can no longer be regarded as probabilities. The common solution is to sample with respect to the absolute value of the weight  $\rho(\mathbf{x}) = |p(\mathbf{x})|$  and reweight the measurements according to Eq.(11.13). The ratio  $p(\mathbf{x})/\rho(\mathbf{x})$  is then just  $\text{sign}(p(\mathbf{x})) = p(\mathbf{x})/|p(\mathbf{x})|$ . This gives for the average (11.10)

$$\langle A \rangle = \frac{\langle A \cdot \text{sign} \rangle_{|p|}}{\langle \text{sign} \rangle_{|p|}}, \quad (11.30)$$

which can be evaluated by sampling numerator and denominator separately with respect to the positive weight  $|p(\mathbf{x})|$ .

While sampling with the absolute value and reweighing allows Monte Carlo simulations of systems with negative weights, it does not solve the “sign problem”. Sampling Eq.(11.30) suffers from exponentially growing errors. To see this let us consider the average sign which is just the ratio of the partition function  $Z$  and the partition function of a system with positive weights  $|p(\mathbf{x})|$  (sometimes termed the corresponding “bosonic” system). This ratio can be expressed through the difference  $\Delta F$  in free energies of these two systems

$$\langle \text{sign} \rangle = \frac{\int_{\mathcal{C}} d\mathbf{x} \text{sign}(\mathbf{x}) |p(\mathbf{x})|}{\int_{\mathcal{C}} d\mathbf{x} |p(\mathbf{x})|} = \frac{Z}{Z_{|p|}} = \exp(-\beta \Delta F), \quad (11.31)$$

and decreases exponentially as the temperature is lowered or the volume of the system increased.

The sign *problem* is thus the accurate measurement of this near-zero sign from individual measurements that are  $+1$  or  $-1$ , a *cancellation* problem. The relative error after  $M$  measurements

$$\frac{\Delta \text{sign}}{\langle \text{sign} \rangle} = \frac{\sqrt{\text{Var sign}/M}}{\langle \text{sign} \rangle} = \frac{\sqrt{(\langle \text{sign}^2 \rangle - \langle \text{sign} \rangle^2)/M}}{\exp(-\beta \Delta F)} \approx \frac{\exp(\beta \Delta F)}{\sqrt{M}} \quad (11.32)$$

grows exponentially with decreasing temperature and increasing system size.

The sign problem has been proven to be nondeterministic polynomial (NP) hard, and hence in general no polynomial time solution is believed to exist [20]. However, the severity of the sign problem (in the notation of Eq.(11.32) the magnitude of the coefficient  $\exp(\beta \Delta F)$ ) depends both on the model considered and on the representation chosen for the model. For example, due to symmetries, there is no sign problem in simulations of the attractive Hubbard model at equal population of up-spins and down-spins and in the repulsive Hubbard model at half filling. Yoo and coworkers proved that there is no sign problem in Hirsch-Fye simulations of the single impurity single orbital Anderson impurity model [21], and this proof can be straightforwardly extended to some multi-orbital models and adapted to the continuous time algorithms presented in this review. In our experience impurity models tend to have less severe sign problems than comparable finite-sized lattice models.

## 11.3 Interaction Expansion

### 11.3.1 Partition Function Expansion

The interaction expansion algorithm CT-INT was the first continuous-time impurity solver algorithm to be introduced [22]. We illustrate the method by considering the

single orbital single site Anderson impurity model which, for this expansion, is most conveniently formulated in terms of the action  $S = S_0 + S_U$  with

$$S_0 = - \sum_{\sigma} \iint_0^{\beta} d\tau d\tau' d_{\sigma}^{\dagger}(\tau) \mathcal{G}_{\sigma}^0(\tau - \tau')^{-1} d_{\sigma}(\tau'), \quad (11.33)$$

$$S_U = U \int_0^{\beta} d\tau n_{\uparrow}(\tau) n_{\downarrow}(\tau), \quad (11.34)$$

where  $\mathcal{G}_{\sigma}^0 = (i\omega_n - \epsilon_0 - \Delta_{\sigma})^{-1}$ , and  $\epsilon_0$  is the impurity energy level.

The expansion of the partition function in powers of  $U$  reads

$$\begin{aligned} Z/Z_0 &= 1 + \frac{(-U)}{1!} \int_0^{\beta} d\tau_1 \langle n_{\uparrow}(\tau_1) n_{\downarrow}(\tau_1) \rangle_0 \\ &\quad + \frac{(-U)^2}{2!} \int_0^{\beta} d\tau_1 d\tau_2 \langle n_{\uparrow}(\tau_1) n_{\downarrow}(\tau_1) n_{\uparrow}(\tau_2) n_{\downarrow}(\tau_2) \rangle_0 + \dots, \end{aligned} \quad (11.35)$$

where the notation  $\langle \dots \rangle_0 = \frac{1}{Z_0} \int \mathcal{D}[d^{\dagger}, d] e^{-S_0} [\dots]$  denotes an average in the non-interacting ensemble with quadratic action  $S_0$  (see low order terms in Fig. 11.4), and  $Z_0 = \int \mathcal{D}[d^{\dagger}, d] e^{-S_0}$ . Employing Wick's theorem [23] we may express the expectation value in terms of determinants of the non-interacting Green's function  $-\langle T d(\tau_i) d^{\dagger}(\tau_j) \rangle_0 = \mathcal{G}_{\sigma}^0(\tau_i - \tau_j)$ :

$$\langle n_{\uparrow}(\tau_1) n_{\downarrow}(\tau_1) n_{\uparrow}(\tau_2) n_{\downarrow}(\tau_2) \dots n_{\uparrow}(\tau_k) n_{\downarrow}(\tau_k) \rangle_0 = \det \mathbf{D}_k^{\uparrow} \det \mathbf{D}_k^{\downarrow}, \quad (11.36)$$

$$(\mathbf{D}_k^{\sigma})_{ij} = \mathcal{G}_{\sigma}^0(\tau_i - \tau_j). \quad (11.37)$$

Summing the contractions into a determinant instead of sampling them individually avoids a sign problem coming from the fermionic exchange in the single impurity case and lessens the sign problem in the case of clusters.

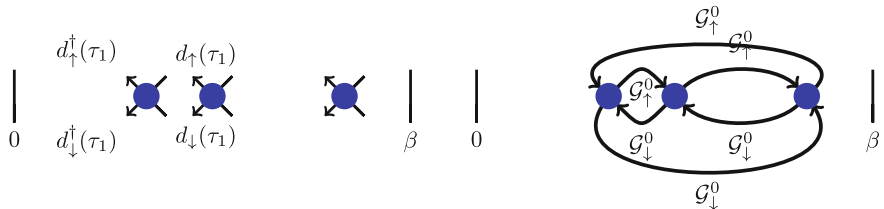


**Fig. 11.4** Depiction of a third order term in the weak coupling expansion. *Left panel* Hubbard interaction vertices denoted by circles. Each  $Un_{\uparrow}(\tau)n_{\downarrow}(\tau)$ -vertex has four operators. *Right panel* one possible contraction of the interaction vertices

We thus arrive at the following series for the partition function:

$$Z/Z_0 = \sum_{k=0}^{\infty} \frac{(-U)^k}{k!} \int_0^\beta d\tau_1 \dots d\tau_k \left( \prod_{\sigma} \det \mathbf{D}_k^{\sigma} \right). \quad (11.38)$$

Two “sign problems” may potentially occur in this expansion: an “intrinsic” sign problem arising from fermion exchange because the determinants might become negative and a “trivial” sign problem, arising for  $U > 0$  from the  $(-U)^k$  factor.

This “trivial” sign problem may be circumvented at the cost of introducing an auxiliary field [13, 24]  $s = \uparrow, \downarrow$  and expanding in powers of

$$S_U = \frac{U}{2} \int_0^\beta d\tau \sum_{s_\tau} (n_\uparrow(\tau) - \alpha_{s_\tau \uparrow}) (n_\downarrow(\tau) - \alpha_{s_\tau \downarrow}), \quad (11.39)$$

Expanding this action we get an additional random variable  $s_i = \uparrow, \downarrow$  at each vertex that needs to be sampled over. In the actual calculation it is best to take the parameter  $\alpha_{s\sigma} = 0.5 + \delta$  for  $s = \sigma$  and  $\alpha_{s\sigma} = -\delta$  otherwise [13]. In principle,  $\delta$  can be taken to be zero but setting it to a small positive value  $\delta \approx 0.01$  allows to avoid numerical instabilities due to nearly-singular matrices.

### 11.3.2 Updates

The series (11.38) and the corresponding one for (11.39) are of the type (11.19), and we can employ continuous-time sampling described in Sect. 11.2.2. We insert and remove interaction vertices on the imaginary time axis, corresponding to the terms  $U(n_\uparrow(\tau) - \alpha_{s_\tau \uparrow})(n_\downarrow(\tau) - \alpha_{s_\tau \downarrow})$ . Proposing a vertex insertion update with probability  $d\tau/(2\beta)$  (for the imaginary time location and the orientation of the auxiliary spin  $s_\tau$ ) and a removal update with probability  $1/(k+1)$  we obtain

$$R = \frac{\beta U}{(k+1)} \prod_{\sigma} \frac{\det \mathbf{D}_{k+1}^{\sigma}}{\det \mathbf{D}_k^{\sigma}}. \quad (11.40)$$

This update and its inverse are sufficient to be ergodic. In evaluating the determinant ratios the fast-update techniques described in Ref. [13, 25] should be used, since it allows to calculate the ratio  $R$  in  $O(k^2)$  operations, substantially faster than the naïve evaluation of determinants with  $O(k^3)$  operations.

### 11.3.3 Measurements

Monte Carlo averages are calculated using Eqs. (11.10) and (11.11), where the distribution  $p$  of Eq. (11.10) is given by the coefficients of Eq. (11.38). In particular, the Green’s function

$$G_\sigma(\tau - \tau') = -\frac{Z_0}{Z} \sum_{k=0}^{\infty} \frac{(-U)^k}{k!} \int d\tau_1 \dots d\tau_k \\ \times \left\langle T_\tau d_\sigma(\tau) d_\sigma^\dagger(\tau') n_{1\uparrow}(\tau_1) n_{1\downarrow}(\tau_1) \dots n_{k\downarrow}(\tau_k) \right\rangle_0 \quad (11.41)$$

is estimated by  $G_{\tau_1 \tau_1, \dots, \tau_k \tau_k}(\tau, \tau')$  (corresponding to  $A(\mathbf{x})$  in Eq.(11.10)):

$$G_\sigma(\tau - \tau') = \langle G_{\tau_1 \tau_1, \dots, \tau_k \tau_k}(\tau, \tau') \rangle_{MC}, \quad (11.42)$$

$$G_{\tau_1 \tau_1, \dots, \tau_k \tau_k}(\tau, \tau') = -\frac{\langle T_\tau d_\sigma(\tau) d_\sigma^\dagger(\tau') n_{1\sigma} n_{2\sigma} \dots n_{k\sigma} \rangle_0}{\langle n_{1\sigma} n_{2\sigma} \dots n_{k\sigma} \rangle_0}. \quad (11.43)$$

The  $\langle \dots \rangle_{MC}$  denotes a Monte Carlo average, while the  $\langle \dots \rangle_0$  denotes all possible Wick's contractions of one particular Monte Carlo configuration.

### 11.3.4 Generalizations

The interaction expansion is readily generalized to actions with a more complex interaction structure, in particular multi-orbital and multi-site (cluster) problems. For simple local density-density interactions the complexity rises as  $(N\beta U)^3$ , whereas in the case of completely general interactions the complexity is  $\propto (N^4 \beta)^3$  (symmetries reduce the number of interactions needed to be sampled in practice). The basic idea is to perform a multiple expansion in all interaction terms.

General multi-orbital and cluster problems away from particle-hole symmetry have a sign problem, and how decouplings that minimize it are best chosen in practice is currently an open problem [26].

Cluster problems are best solved by using the continuous-time auxiliary field algorithm [14]. In the single orbital Anderson impurity model case this expansion can be mapped onto the interaction expansions, but efficient numerical methods allow for fast simulations of large cluster impurity problems [27].

A generalization to phonons and retarded (or general non-local in time) interaction vertices has been proposed by Assad et al. [24]. Their method uses an expansion in generalized two-time vertices to stochastically sample an extended configuration space of phonon and electron diagrams.

Similarly, [28] investigated an extension to the superconducting phase of the attractive- $U$  Hubbard model.

## 11.4 Hybridization Expansion

### 11.4.1 Partition Function Expansion

The hybridization expansion CT-HYB [12, 29] is complementary to the weak-coupling expansion. It proceeds from Eq.(11.8) with  $H_b$  taken to be the hybridization term  $H_{\text{hyb}}$  and  $H_a = H_{\text{bath}} + H_{\text{loc}}$ . An advantage of this approach is that the average expansion order for a typical problem near the Mott transition is much smaller than for the interaction expansion [30].

The partition function in the interaction representation is

$$Z = \sum_{k=0}^{\infty} \int_0^{\beta} d\tau_1 \dots \int_{\tau_{k-1}}^{\beta} d\tau_k \int_0^{\beta} d\tau'_1 \dots \int_{\tau'_{k'-1}}^{\beta} d\tau'_k \\ \times \text{Tr} \left[ T_{\tau} e^{-\beta H_a} \tilde{H}_{\text{hyb}}(\tau_k) \tilde{H}_{\text{hyb}}^{\dagger}(\tau'_k) \dots \tilde{H}_{\text{hyb}}(\tau_1) \tilde{H}_{\text{hyb}}^{\dagger}(\tau'_1) \right]. \quad (11.44)$$

Inserting  $H_{\text{hyb}}$  and separating the bath and impurity operators we obtain

$$Z = \sum_{k=0}^{\infty} \int_0^{\beta} d\tau_1 \dots \int_{\tau_{k-1}}^{\beta} d\tau_k \int_0^{\beta} d\tau'_1 \dots \int_{\tau'_{k'-1}}^{\beta} d\tau'_k \sum_{\substack{j_1, \dots, j_k \\ j'_1, \dots, j'_k}} \sum_{\substack{p_1, \dots, p_k \\ p'_1, \dots, p'_k}} V_{p_1}^{j_1} V_{p'_1}^{j'_1*} \dots V_{p_k}^{j_k} V_{p'_k}^{j'_k*} \\ \times \text{Tr}_d \left[ T_{\tau} e^{-\beta H_{\text{loc}}} d_{j_k}(\tau_k) d_{j'_k}^{\dagger}(\tau'_k) \dots d_{j_1}(\tau_1) d_{j'_1}^{\dagger}(\tau'_1) \right] \\ \times \text{Tr}_c \left[ T_{\tau} e^{-\beta H_{\text{bath}}} c_{p_k}^{\dagger}(\tau_k) c_{p'_k}(\tau'_k) \dots c_{p_1}^{\dagger}(\tau_1) c_{p'_1}(\tau'_1) \right]. \quad (11.45)$$

We can now integrate out the bath operators  $c_p(\tau)$ , since they are non-interacting and the time-evolution (given by  $H_a$ ) no longer couples the impurity and the bath. Defining the bath partition function

$$Z_{\text{bath}} = \text{Tr} e^{-\beta H_{\text{bath}}} = \prod_{\sigma} \prod_p (1 + e^{-\beta \varepsilon_p}), \quad (11.46)$$

In the anti-periodic hybridization function  $\Delta$  defined as

$$\Delta^{ab}(i\omega_n) = \sum_{k\alpha} V_k^{*\alpha\alpha} (i\omega_n - \varepsilon_{k\alpha})^{-1} V_k^{\alpha b} \quad (11.47)$$

integrating out the bath operators leads to

$$\Delta_{lm}(\tau) = \sum_p \frac{V_p^{l*} V_p^m}{e^{\varepsilon_p \beta} + 1} \times \begin{cases} -e^{-\varepsilon_p(\tau-\beta)}, & 0 < \tau < \beta \\ e^{-\varepsilon_p \tau}, & -\beta < \tau < 0 \end{cases} \quad (11.48)$$

and to the determinant

$$\frac{1}{Z_{\text{bath}}} \text{Tr}_c \left[ T_\tau e^{-\beta H_{\text{bath}}} \sum_{p_1, \dots, p_k} \sum_{p'_1, \dots, p'_k} V_{p_1}^{j_1} V_{p'_1}^{j'_1 *} \dots V_{p_k}^{j_k} V_{p'_k}^{j'_k *} \right. \\ \left. \times c_{p_k}^\dagger(\tau_k) c_{p'_k}(\tau'_k) \dots c_{p_1}^\dagger(\tau_1) c_{p'_1}(\tau'_1) \right] = \det \Delta, \quad (11.49)$$

for an arbitrary product of bath operators. Here,  $\Delta$  is a  $k \times k$  matrix with elements  $\Delta_{lm} = \Delta_{j_l j_m}(\tau_l - \tau_m)$ . In practice, and in analogy to the interaction algorithm in the previous section, it will be more convenient to handle the inverse of this matrix  $\Delta$ , which we denote by  $\mathbf{M} = \Delta^{-1}$ .

The partition function expansion for the hybridization algorithm now reads (for time-ordered configurations)

$$Z = Z_{\text{bath}} \sum_k \iiint d\tau_1 \dots d\tau_k \sum_{j_1, \dots, j_k} \sum_{j'_1, \dots, j'_k} \\ \times \text{Tr}_d \left[ T_\tau e^{-\beta H_{\text{loc}}} d_{j_k}(\tau_k) d_{j'_k}^\dagger(\tau'_k) \dots d_{j_1}(\tau_1) d_{j'_1}^\dagger(\tau'_1) \right] \det \Delta. \quad (11.50)$$

In the case of multi-orbital models with density-density interactions the local Hamiltonian  $H_{\text{loc}}$  commutes with the occupation number operator of each orbital. We may therefore represent the time evolution of the impurity by collections of “segments” which represent time intervals in which an electron of a given flavor resides on the impurity. An example of such a segment configuration for a single orbital model (two spin flavors) is shown in Fig. 11.5.

Since the local Hamiltonian is diagonal in the occupation number basis the contribution of the trace factor can be computed for each segment configuration. For a model with  $n$  orbitals and a total length  $L_j$  of segments in orbital  $j$  and a total overlap

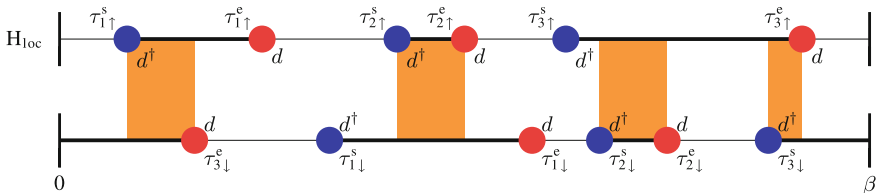


**Fig. 11.5** Segment representation of term in hybridization expansion of single orbital Anderson model. *Upper line* spin up orbital, *lower line* spin down orbital, *heavy line* orbital occupied, *light line* orbital empty. For each orbital, length of *black line* (occupied orbitals) determines the chemical potential contribution to the weight factor (11.51). *Shaded areas* regions where both up and down orbitals are filled, so the impurity is doubly occupied. The length of the *shaded area* enters into an overall weighting factor for the potential energy (Hubbard  $U$ )

$O_{ij}$  between segments of flavor  $i$  and  $j$  one obtains ( $s$  is a sign depending on the operator sequence)

$$w_{\text{loc}}(\mathbf{x}) = \text{Tr}_d[\dots] = se^{\mu \sum_j^n L_j} e^{-\sum_{i < j}^n (U_{ij} O_{ij})}, \quad (11.51)$$

except in the trivial case where there are no operators for certain flavors. In the latter case, several segment configurations, involving “full” and “empty” lines, contribute to the trace.

### 11.4.2 Updates

In order to sample Eq.(11.50) we perform a Monte Carlo simulation as described in Sect. 11.2.2. We explain the sampling procedure for the formulation with density–density interactions. The two basic updates required for ergodicity are the insertion and the removal of a segment.

Starting from a configuration of segments  $\mathbf{x}_k = \{(\tau_1^s, \tau_1^e), (\tau_2^s, \tau_2^e), \dots, (\tau_k^s, \tau_k^e)\}$  we attempt to insert a new segment  $s_{k+1}$  starting at  $\tau^s$  to obtain a configuration  $\mathbf{y}_{k+1}$ . This move is rejected if  $\tau^s$  lies on one of the existing segments, since we cannot create two identical fermions at the same site. Otherwise, we choose a random time uniformly in the interval  $[\tau^s, \tau^{s'}]$  of length  $l_{\max}$ , where  $\tau^{s'}$  is the start of the next segment in  $\mathbf{x}_k$ . For the reverse move, the proposal probability is given by the probability of selecting that given segment for removal.

Therefore the proposal probabilities are

$$W_{\mathbf{xy}}^{\text{prop}} = \frac{d\tau^2}{\beta l_{\max}}, \quad (11.52)$$

$$W_{\mathbf{yx}}^{\text{prop}} = \frac{1}{k+1}, \quad (11.53)$$

and the acceptance ratio becomes

$$R_{\mathbf{xy}} = \frac{p_y W_{\mathbf{yx}}^{\text{prop}}}{p_x W_{\mathbf{xy}}^{\text{prop}}} = \frac{\beta l_{\max}}{k+1} \frac{w_{\text{loc}}(\mathbf{y}) \det \Delta(\mathbf{y})}{w_{\text{loc}}(\mathbf{x}) \det \Delta(\mathbf{x})}. \quad (11.54)$$

### 11.4.3 Measurements

The single most important observable for quantum Monte Carlo impurity solvers is the finite temperature imaginary time Green’s function  $G_{lm}(\tau) = -\langle T_\tau d_l(\tau) d_m^\dagger(0) \rangle$ .

The series for this observable is

$$G_{lm}(\tau_l, \tau_m) = -Z_{\text{bath}} \sum_{k, \substack{j_1, \dots, j_k \\ j'_1, \dots, j'_k}} \int d\tau_1 \dots d\tau'_k \det \Delta_k \text{Tr}_d \left[ T_\tau e^{-\beta H_{\text{loc}}} d_l(\tau_l) d_m^\dagger(\tau_m) d_{j_k}(\tau_k) d_{j'_k}^\dagger(\tau'_k) \dots d_{j_1}(\tau_1) d_{j'_1}^\dagger(\tau'_1) \right]. \quad (11.55)$$

This shows that Green's function configurations at expansion order  $k$  are partition function configurations at expansion order  $k$  with additional  $d_l$  and  $d_m^\dagger$  operators or, alternatively, partition function operators at order  $k + 1$  with no hybridization line connecting to  $d_l(\tau_l)$  and  $d_m^\dagger(\tau_m)$ . In practice we obtain an estimator of  $G_{lm}(\tau_l, \tau_m)$  by identifying two operators  $d_l(\tau_l)$ ,  $d_m^\dagger(\tau_m)$  in a partition function configuration that are an imaginary time distance  $\tau = \tau_l - \tau_m$  apart, and removing the hybridization line connecting them. The insertion of local operators into a partition function configuration, as it is done in the interaction expansion formalism, is not ergodic in the hybridization expansion.

The size  $(k - 1) \times (k - 1)$  hybridization matrix  $\Delta_{k-1}^{\tau_l, \tau_m}$  of all hybridization operators except for  $d_l(\tau_l)$  and  $d_m^\dagger(\tau_m)$  corresponds to  $\Delta$  with the column/row  $s_l$  and  $s_m$  corresponding to the operators  $d_l$  and  $d_m^\dagger$  removed, and the weight of a Green's function configuration  $G_{lm}(\tau_l, \tau_m)$  is

$$\frac{p_{G_{lm}}}{Z} = \frac{\det \Delta_{k-1}^{\tau_l, \tau_m}}{\det \Delta}. \quad (11.56)$$

An expansion by minors or the inverse matrix formulas of Ref. [25] describe how such a determinant ratio is computed:

$$\frac{p_{G_{lm}}}{Z} = (\Delta)^{-1}_{s_m s_l} = M_{s_m s_l}. \quad (11.57)$$

We can bin this estimate into fine bins to obtain the Green's function estimator

$$G_{lm}(\tau) = \frac{1}{\beta} \left\langle \sum_{ij}^k M_{ji} \tilde{\delta}(\tau, \tau_m - \tau_l) \delta_{t(i)l} \delta_{t(j)m} \right\rangle_{\text{MC}}, \quad (11.58)$$

$$\tilde{\delta}(\tau, \tau') = \begin{cases} \delta(\tau - \tau'), & \tau' > 0 \\ -\delta(\tau - \tau' - \beta), & \tau' < 0, \end{cases} \quad (11.59)$$

with  $t(i)$  denoting the orbital index of the operator at row / column i. For a configuration at expansion order  $k$  we obtain a total of  $k^2$  estimates for the Green's function—or one for every creation-annihilation operator pair or every single element of the  $(k \times k)$ -matrix  $\mathbf{M} = \Delta^{-1}$ .

### 11.4.4 Generalizations

The hybridization expansion algorithm has been presented here for simple density–density interactions. A formulation suitable for more general interactions was originally derived in Ref. [29]. The scaling of the method is independent of the structure of the interactions but exponential in the number of local states (cluster sites or orbitals), and therefore only suitable for relatively small clusters and single-site multi-orbital problems. The ability to treat general interaction structures makes it the method of choice for multi-orbital problems.

Several refinements and extensions to the method have been proposed, most notably a “Krylov” extension [31] able to treat large orbital problems without truncation.

As in the case of the interaction expansion algorithm, an application to phonons has been presented [32]. Unlike in the interaction expansion, phonons as treated in [32] present essentially no additional numerical cost, but the formulation is far less general and at present limited to Holstein phonons.

An extension to Kondo-models with expansion directly in the Kondo couplings was developed by Otsuki et al. [33], and applications to a range of materials within the LDA+DMFT context were presented [34–36].

## 11.5 Applications

### 11.5.1 Nanoscience

Impurity models were initially designed to describe impurity atoms embedded in a host material. A typical problem is the description of *Co* atoms embedded in the bulk or deposited on the surface of *Cu*. Savkin et al. [37] studied a model problem of three interacting Kondo impurities on a metallic surface with CT-INT. The ability to treat general interactions beyond the density–density type allowed an accurate investigation of the interplay of Coulomb interactions, Heisenberg interactions, cluster geometry and inter-cluster hopping effects.

Gorelov et al. [26, 38] performed a realistic study of *Co* atoms embedded in *Cu* and of *Co* impurities deposited on the surface of *Cu*. They found that a complete treatment of the problem, including all inequivalent terms of the Coulomb interaction, was essential for obtaining physically relevant results.

Impurity models are also used to describe quantum dots coupled to external leads, “single molecule” conductors, and other devices occurring in nanotechnology [39]. These impurity models may have a complex internal interaction structure with interaction strengths beyond those accessible in weak-coupling perturbation theory, which makes them an ideal candidate for simulation with continuous-time algorithms.

One such application was presented by Wang and Millis [40] who investigated the imaginary time dependence of correlation functions of two-level two-lead quantum

dots to describe Fermi-liquid and non-Fermi-liquid phases and investigate a potential quantum critical point.

All of these simulations suffer from a severe fermionic sign problem caused by the off-diagonal structure of the hybridization function and, additionally in the interaction expansion, by alternating signs of the interaction terms. An appropriate basis choice can mitigate this sign problem to some extent, but a general sign free representation is not known.

### 11.5.2 Single Site Dynamical Mean Field Theory

One of the first applications that illustrated the strength of the CT-QMC approach examined the DMFT solution of the Hubbard model on a Bethe lattice in the infinite coordination number limit. The model exhibits a first-order metal-insulator transition with a large coexistence region. A comparison of the kinetic energy obtained by CT-HYB [12], exact diagonalization [41], and discrete time Hirsch-Fye QMC [42] is reproduced in Fig. 11.6. The CT-QMC method agrees with the other solutions, shows results down to very low  $T$  and does not suffer from the discretization issues evident in the Hirsch Fye solution.

The ability of CT-QMC to reach much lower temperature than previous QMC methods is caused by the fact that typical diagrammatic expansion orders are much smaller than the number of time slices needed to obtain accurate results in discrete time algorithms [30]. This is illustrated in Fig. 11.7, where average expansion orders

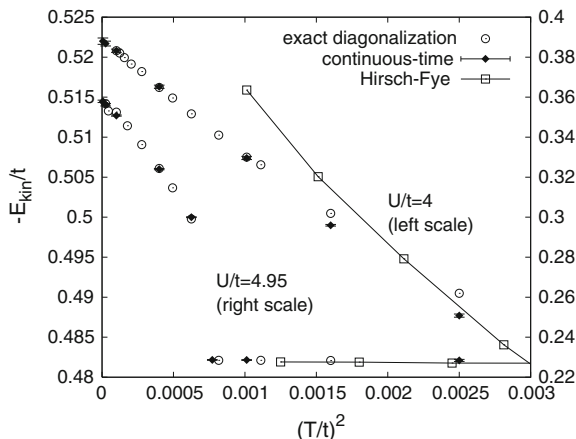


**Fig. 11.6** Kinetic energy obtained using the indicated impurity solvers plotted as a function of temperature for the Hubbard model with a semicircular density of states and bandwidth  $4t$  and interactions indicated. For  $U = 4t$  the model is in a strongly renormalized metallic phase, for  $U = 4.95t$  a low-T metal to higher T insulator transition occurs, visible as a jump in kinetic energy at  $(T/t)^2 \approx 0.0007$ . From Ref. [12]

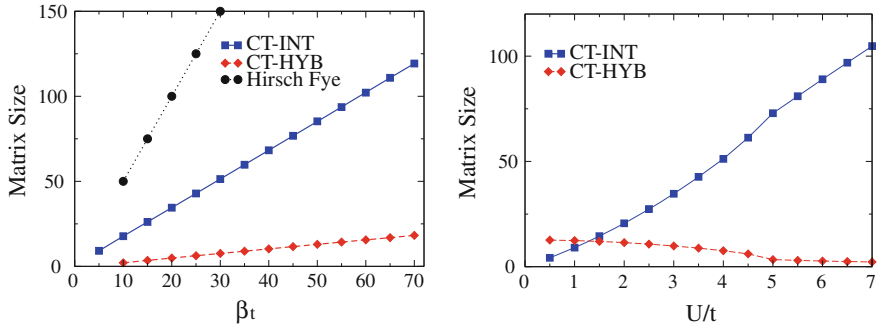


**Fig. 11.7** *Left panel* Bethe lattice, single site DMFT, scaling of matrix size with temperature at  $U/t = 4$  for the Hirsch-Fye, CT-INT and CT-HYB algorithms. For Hirsch-Fye, the resolution  $N = \beta U$  has been chosen as a compromise between reasonable accuracy and acceptable speed, while the average matrix size is plotted for the continuous-time solvers. *Right panel* scaling of matrix size with  $U/t$  for fixed  $\beta t = 30$ . The solutions for  $U \leq 4.5$  are metallic, while those for  $U \geq 5.0$  are insulating. The much smaller matrix size in the relevant region of strong interactions is the reason for the higher efficiency of the hybridization expansion method. From Ref. [30]

and time slices are shown as a function of  $\beta$  and  $U$ . In the absence of a sign problem all algorithms shown scale as the cube of the expansion order, which is linear in  $\beta$  and, in the case of CT-INT and CT-AUX, linear in  $U$  and the number of cluster sites.

### 11.5.3 Cluster DMFT

Single site DMFT, while exact in the infinite coordination number limit, neglects all spatial (or momentum) dependence that is often crucial in finite-dimensional systems. The pseudogap problem in high  $T_c$ , a suppression of the electronic spectral function at the Brillouin zone face but not at the zone diagonal, is a typical example of such a momentum-dependent phenomenon that is not well described by single site DMFT.

Cluster dynamical mean field methods [10] extend the method to include spatial correlations, either by considering periodic momentum-space clusters [43], or clusters in real space [44, 45]. These methods are summarized in previous chapters and in Ref. [10].

CT-QMC methods greatly increased the range of parameters that could be studied using moderate computational resources and removed the need for delicate  $\Delta\tau$  extrapolations.

A typical result, obtained in Ref. [46], is illustrated in Fig. 11.8: Plotted is the zero-frequency component of the Matsubara self-energy in  $k$ -space for a 2D Hubbard model at relatively weak interaction strength  $U = 4t$  (the total bandwidth is  $W = 8t$ ), as obtained by a numerically exact method [46] directly in the thermodynamic limit

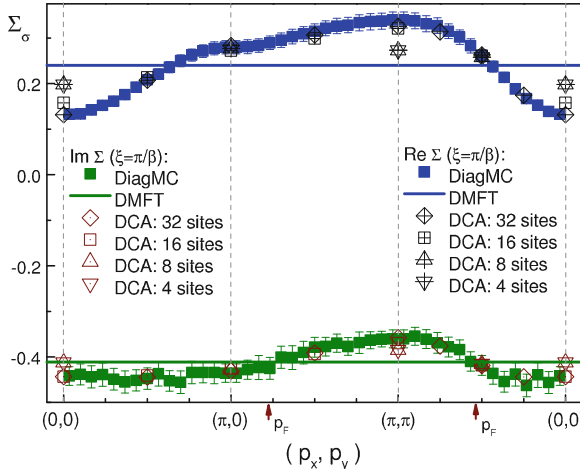


**Fig. 11.8** Comparison of momentum-dependence of the self-energy of the two-dimensional Hubbard model with parameters  $U/t = 4$ ,  $\mu/t = 3.1$  and  $T/t = 0.4$  calculated at the Matsubara frequency  $\omega_0 = \xi = \pi/\beta$  calculated for along the cut  $(0, 0) - (\pi, 0) - (\pi, \pi) - (0, 0)$  in the first Brillouin zone using a numerically exact “diagrammatic Monte Carlo” procedure and using CT-AUX simulations of single site and 4, 8, 16, and 32-site DCA DMFT approximations. From Ref. [46]

and DCA on clusters of size up to 32. We see that for increasing cluster size the DCA result (obtained with a CT-AUX [14] solver) approaches the exact solution.

Physics relevant to the pseudogap problem has been studied with continuous-time algorithms on clusters of size four [47–50], eight [51, 52], and sixteen [53–55]. A crucial discovery was that the pseudogap “phase” is a robust feature of the two-dimensional Hubbard model at intermediate correlation strength, and in particular does not require long ranged order.

### 11.5.4 Diagrammatics Beyond DMFT

Cluster methods approach the thermodynamic limit by enlarging the cluster size. This approach has two limitations: the choice of any small finite size cluster may bias the results, and the simulation of large clusters may become prohibitively expensive due to the algorithmic scaling and the fermionic sign problem.

Another route to the thermodynamic limit is provided by a diagrammatic sampling of corrections to the DMFT. Several methods have been implemented [56–59]. These methods are systematic diagrammatic expansions around single site DMFT. They have the advantage that short- and long-ranged correlations are treated simultaneously.

The main technical difficulty lies in the fact that two-particle quantities (vertex functions) need to be sampled. CT-QMC algorithms can measure vertex functions either directly in frequency space without the need for Fourier-transforming time-discretized values, or can expand them into efficient orthogonal bases [60] and are therefore ideally suited for these problems.

So far CT-QMC methods have mainly been applied to “Dual Fermion” simulations. Rubtsov et al. [61] studied the pseudogap regime of the doped Hubbard model with CT-INT. Hafermann et al. [62] summed particle-hole ladders in dual diagrams for the half-filled Hubbard model, revealing a pseudogap formed by antiferromagnetic correlations. Further investigation of extensions beyond DMFT is currently an active area of research.

### ***11.5.5 Lattice and Large Cluster DMFT Calculations and Extrapolations to the Infinite System***

Continuous-time algorithms can be applied both to the lattice problem of Eq. 11.1 on a finite lattice of  $N$  sites with some, usually periodic, boundary conditions; and to the cluster quantum impurity problems of Eq. 11.2. For simple models and in some regions of phase space (usually at high temperature or close to half filling) it is possible to reach large enough systems that finite size scaling to the infinite system is possible. In these cases the (finite size or cluster DMFT) approximation can be controlled and the behavior of the underlying infinite lattice problem is recovered. The results are numerically exact for the infinite system, with the only errors coming from the finite size extrapolation procedure. A crucial test is provided by comparing extrapolated results from isolated lattice and cluster DMFT calculations, which approach the infinite system size limit differently.

This procedure has recently been performed for the 3D Hubbard model above the Néel temperature  $T_N$ , where the full phase diagram at and away from half filling was computed using DCA (with CT-AUX), CT-INT on an isolated lattice, single site DMFT and high temperature series expansion [63]. Typical results for the entropy, comparing the different methods, are given in Fig. 11.9. Both the extrapolated DCA and the extrapolated lattice curves approach the results for the infinite system and hence agree within error bars, whereas simple approximations like the single-site DMFT and high-temperature series expansion show significant deviations.

The approach to the infinite system size limit can be seen directly in the self-energy: in cluster DMFT, enlarging the cluster size systematically reintroduces the momentum dependence of the self-energy until, for very large clusters, the full momentum dependence is resolved. Ref. [27] shows how DCA recovers this momentum dependence as a function of cluster size, for clusters of size 18–100.

A related calculation for the attractive case has been done for the BCS-BEC crossover in ultracold atomic systems, including an extrapolation to the dilute limit, to determine the universal critical temperature at resonance [64, 65]. These calculations

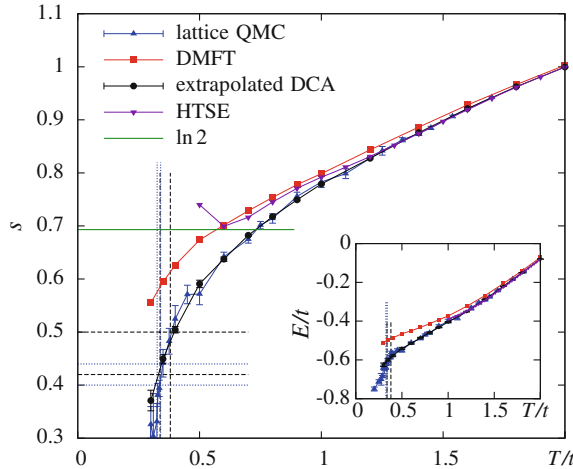


**Fig. 11.9** Entropy (*inset* energy) of the three-dimensional Hubbard model at  $U/t = 8$  computed with continuous-time QMC on an isolated lattice and on a cluster embedded in an effective medium (DCA), as well as high-temperature series expansion and single site DMFT values. The lattice QMC and DCA data are extrapolated to the infinite system size. From Ref. [63]

used a non-local worm-update, described in detail in Ref. [64], combined with continuous time simulations.

### 11.5.6 Applications to Real Materials

Many correlated electron materials contain transition metals, actinides, or rare-earth elements. The electronic states are subject to complicated interactions and exhibit a broad range of phases *beyond* what is observed in the single-orbital Hubbard model. A successful description of many of these systems has been achieved within the LDA+DMFT framework; the combination of band structure methods with ‘correlated’ DMFT methods [6, 8].

The treatment of such systems was computationally challenging: traditional QMC methods cannot decouple Hund’s coupling terms without encountering a severe sign problem and are therefore limited in practice to density–density interactions. There are too many states to apply exact diagonalization [41] or NRG [66] methods. Semi-analytic partial infinite resummation techniques like the non-crossing [67] or one-crossing [68] approximations are uncontrolled and in general not reliable in the regime of intermediate interaction strength [69].

This has changed with the advent of CT-QMC methods. In particular the CT-HYB method and the related CT-J method [34] have made the systematic study of single-site multi-orbital problems with realistic interactions possible. The general formulation and the application to two-orbital Hamiltonians of CT-HYB was pioneered by

Werner et al. [29], and the formalism optimized and extended to large multi-orbital systems by Haule [47]. Applications to model systems include the study of rotationally invariant three-orbital models [70, 71] and the discovery of a spin-freezing phase. In the real-materials context, CT-QMC methods were used to simulate heavy Fermion materials [34, 36, 72–74] and pnictide superconductors [75–78], as well as other correlated electron materials. In particular for the simulation of large multi-orbital systems these algorithms are now becoming the methods of choice.

### 11.5.7 Real-Time Dynamics

One of the most active and interesting domains of physics is the study of systems out of equilibrium: “quench” problems (the response to a sudden change of parameters), “driven” systems (under the influence of an external driving field), initial value problems, and systems in a nonequilibrium steady state (e.g. quantum dots with applied voltage) are typical subjects of interests. These systems are not described by the usual imaginary-time equilibrium formalism presented above and require an extension of the diagrammatic methods to the Keldysh double-contour.

Real-time CT-QMC methods were pioneered by Mühlbacher and Rabani who used a hybridization expansion method to study a problem of electrons coupled to phonons [79]. The non-equilibrium hybridization expansion was generalized to the case of electron-electron interactions in [80–83], while the real-time version of the CT-AUX method was given in [81, 84] and used in [85–88]. It is important to bear in mind that unlike in the equilibrium case, where the algorithms have been tried, tested and optimized, the nonequilibrium extensions of CT-QMC are still in an experimental stage. The methods which have been implemented so far are more-or-less straightforward adaptations of the equilibrium CT-QMC algorithms and significant improvements, e.g. by employing “bold” diagrammatic methods [69, 89] may be possible.

The basic theoretical task is to evaluate the expectation value of some operator  $\mathcal{O}$  at some time  $t$ , given that the system was prepared at time  $t = 0$  in a state described by the density matrix  $\rho_0$ . Using the Heisenberg representation the expectation value may be expressed mathematically as

$$\langle \mathcal{O}(t) \rangle = Tr \left[ \rho_0 e^{i \int_0^t dt' H(t')} \mathcal{O} e^{-i \int_0^t dt'' H(t'')} \right]. \quad (11.60)$$

A nonequilibrium situation may arise through a time dependence of  $H$  (as occurs for example in a system ‘pumped’ by a laser), through nonequilibrium correlations expressed by  $\rho_0$  (as occurs for a quantum dot with current flowing across it) or through an initial density matrix  $\rho_0$  which is different from the long-time (thermal equilibrium) limit, as occurs if a system is ‘quenched’ into a different state.

For a detailed discussion of the real-time algorithms, their applications, successes, and limitations, we refer the reader to the original papers [79, 82, 84], where the CT-AUX and CT-HYB real-time algorithms are derived, and to the review [1].

## 11.6 Outlook

In this chapter we have introduced continuous time algorithms for fermionic lattice models and quantum impurity problems. These recent developments have substantially broadened the range of models that can be addressed by quantum Monte Carlo methods, and have achieved impressive performance gains. Development is still continuing, such as with the development of bold-line methods [69], or related algorithms for bosonic quantum impurity problems [90]. A related development is that if diagrammatic quantum Monte Carlo methods, sampling only connected diagrams of the perturbation series for the self energy of an infinite system instead of the partition function of a lattice model [46]. Given the difficulty and complexity of fermionic simulations, further development of new simulation approaches based on various diagrammatic expansion techniques will be crucial for future progress.

**Acknowledgments** We would like to thank our many colleagues and collaborators who have enabled extraordinary progress in the field of diagrammatic Monte Carlo methods over the last few years. In particular we would like to thank A. Lichtenstein, A. J. Millis, A. Rubtsov, and P. Werner for co-authoring Ref. [1], which we followed for large parts of this chapter. E. G. acknowledges support by NSF-DMR-1006282.

## References

1. E. Gull et al., Rev. Mod. Phys. **83**(2), 349 (2011)
2. W. Metzner, D. Vollhardt, Phys. Rev. Lett. **62**(3), 324 (1989)
3. A. Georges, W. Krauth, Phys. Rev. Lett. **69**(8), 1240 (1992)
4. M. Jarrell, Phys. Rev. Lett. **69**(1), 168 (1992)
5. A. Georges, G. Kotliar, W. Krauth, M.J. Rozenberg, Rev. Mod. Phys. **68**(1), 13 (1996)
6. G. Kotliar, S.Y. Savrasov, K. Haule et al., Rev. Mod. Phys. **78**(3), 865 (2006)
7. A. Georges, Lectures on the physics of highly correlated electron systems VIII: Eighth training Course in the physics of correlated electron systems and high-Tc superconductors **715**(1), 3 (2004)
8. K. Held, Advances in physics **56**, 829 (2007)
9. K. Held, I.A. Nekrasov, G. Keller, V. Eyert, N. Bluemer, A.K. McMahan, R.T. Scalettar, T. Pruschke, V.I. Anisimov, D. Vollhardt, Phys. Status Solidi **243**(11), 2599 (2006)
10. T. Maier, M. Jarrell, T. Pruschke, M.H. Hettler, Rev. Mod. Phys. **77**(3), 1027 (2005)
11. N.V. Prokof'ev, B.V. Svistunov, Phys. Rev. Lett. **81**(12), 2514 (1998)
12. P. Werner, A. Comanac, L. de' Medici, et al. Phys. Rev. Lett. **97**(7), 076405 (2006)
13. A.N. Rubtsov, V.V. Savkin, A.I. Lichtenstein, Phys. Rev. B **72**(3), 035122 (2005)
14. E. Gull, P. Werner, O. Parcollet, M. Troyer, Europhys. Lett. **82**(5), 57003 (2008)
15. D.P. Landau, K. Binder, *A Guide to Monte Carlo Simulations in Statistical Physics* (Cambridge University Press, Cambridge, 2000)

16. W. Krauth, *Statistical Mechanics: Algorithms and Computations* (Oxford University Press, Oxford, 2006)
17. N. Metropolis, A.W. Rosenbluth, M.N. Rosenbluth, A.H. Teller, E. Teller, *J. Chem. Phys.* **21**(6), 1087 (1953)
18. W.K. Hastings, *Biometrika* **57**(1), 97 (1970)
19. N.V. Prokof'ev, B.V. Svistunov, I.S. Tupitsyn, *JETP Lett.* **64**, 911 (1996)
20. M. Troyer, U.J. Wiese, *Phys. Rev. Lett.* **94**(17), 170201 (2005)
21. J. Yoo, S. Chandrasekharan, R.K. Kaul, D. Ullmo, H.U. Baranger, *J. Phys. A* **38**(48), 10307 (2005)
22. A.N. Rubtsov, A.I. Lichtenstein, *JETP Lett.* **80**, 61 (2004)
23. G.C. Wick, *Phys. Rev.* **80**(2), 268 (1950)
24. F.F. Assaad, T.C. Lang, *Phys. Rev. B* **76**(3), 035116 (2007)
25. E. Gull, P. Werner, A. Millis, M. Troyer, *Physics Procedia* **6**, 31 (2010), In: Computer Simulations Studies in Condensed Matter Physics XXI - Proceedings of the 21st Workshop, Computer Simulations Studies in Condensed Matter Physics XXI
26. E. Gorelov, Electronic structure of multiorbital correlated systems. Ph.D. thesis, University of Hamburg 2007
27. E. Gull, P. Staar, S. Fuchs, P. Nukala, M.S. Summers, T. Pruschke, T.C. Schulthess, T. Maier, *Phys. Rev. B* **83**(7), 075122 (2011)
28. D.J. Luitz, F.F. Assaad, *Phys. Rev. B* **81**(2), 024509 (2010)
29. P. Werner, A.J. Millis, *Phys. Rev. B* **74**(15), 155107 (2006)
30. E. Gull, P. Werner, A. Millis, M. Troyer, *Phys. Rev. B* **76**(23), 235123 (2007)
31. A.M. Läuchli, P. Werner, *Phys. Rev. B* **80**(23), 235117 (2009)
32. P. Werner, A.J. Millis, *Phys. Rev. Lett.* **99**(14), 146404 (2007)
33. J. Otsuki, H. Kusunose, P. Werner, Y. Kuramoto, *J. Phys. Soc. Jpn.* **76**(11), 114707 (2007)
34. J. Otsuki, H. Kusunose, Y. Kuramoto, *Phys. Rev. Lett.* **102**(1), 017202 (2009)
35. J. Otsuki, H. Kusunose, Y. Kuramoto, *J. Phys. Soc. Jpn.* **78**, 034719 (2009)
36. M. Matsumoto, M.J. Han, J. Otsuki, S.Y. Savrasov, *Phys. Rev. Lett.* **103**(9), 096403 (2009)
37. V.V. Savkin, A.N. Rubtsov, M.I. Katsnelson, A.I. Lichtenstein, *Phys. Rev. Lett.* **94**(2), 026402 (2005)
38. E. Gorelov, T.O. Wehling, A.N. Rubtsov, M.I. Katsnelson, A.I. Lichtenstein, *Phys. Rev. B* **80**(15), 155132 (2009)
39. R. Hanson, L.P. Kouwenhoven, J.R. Petta, S. Tarucha, L.M.K. Vandersypen, *Rev. Mod. Phys.* **79**(4), 1217 (2007)
40. X. Wang, A.J. Millis, *Phys. Rev. B* **81**(4), 045106 (2010)
41. M. Caffarel, W. Krauth, *Phys. Rev. Lett.* **72**(10), 1545 (1994)
42. J.E. Hirsch, R.M. Fye, *Phys. Rev. Lett.* **56**(23), 2521 (1986)
43. M.H. Hettler, A.N. Tahvildar-Zadeh, M. Jarrell et al., *Phys. Rev. B* **58**(12), R7475 (1998)
44. G. Kotliar, S.Y. Savrasov, G. Pállsson, G. Biroli, *Phys. Rev. Lett.* **87**(18), 186401 (2001)
45. A.I. Lichtenstein, M.I. Katsnelson, *Phys. Rev. B* **62**(14), R9283 (2000)
46. E. Kozik, K.V. Houcke, E. Gull, L. Pollet, N. Prokof'ev, B. Svistunov, M. Troyer, *Europhys. Lett.* **90**(1), 10004 (2010)
47. K. Haule, *Phys. Rev. B* **75**(15), 155113 (2007)
48. H. Park, K. Haule, C.A. Marianetti, G. Kotliar, *Phys. Rev. B* **77**(3), 035107 (2008)
49. E. Gull, P. Werner, X. Wang, M. Troyer, A.J. Millis, *Europhys. Lett.* **84**(3), 37009 (6pp) (2008)
50. G. Sordi, K. Haule, A.M.S. Tremblay, *Phys. Rev. Lett.* **104**(22), 226402 (2010)
51. P. Werner, E. Gull, O. Parcollet, A.J. Millis, *Phys. Rev. B* **80**(4), 045120 (2009)
52. E. Gull, O. Parcollet, P. Werner, A.J. Millis, *Phys. Rev. B* **80**(24), 245102 (2009)
53. K. Mikelsons, A. Macridin, M. Jarrell, *Phys. Rev. E* **79**(5), 057701 (2009)
54. E. Khatami, K. Mikelsons, D. Galanakis, A. Macridin, J. Moreno, R.T. Scalettar, M. Jarrell, *Phys. Rev. B* **81**(20), 201101 (2010)
55. E. Gull, M. Ferrero, O. Parcollet, A. Georges, A.J. Millis, *Phys. Rev. B* **82**(15), 155101 (2010)
56. H. Kusunose, *J. Phys. Soc. Jpn.* **75**(5), 054713 (2006)
57. A. Toschi, A.A. Katanin, K. Held, *Phys. Rev. B* **75**(4), 045118 (2007)

58. C. Slezak, M. Jarrell, T. Maier, J. Deisz, *J. Phys. Condens. Matter* **21**(43), 435604 (2009)
59. A.N. Rubtsov, M.I. Katsnelson, A.I. Lichtenstein, *Phys. Rev. B* **77**(3), 033101 (2008)
60. L. Boehnke, H. Hafermann, M. Ferrero, F. Lechermann, O. Parcollet, Orthogonal polynomial representation of imaginary-time green's functions. *Phys. Rev. B* **84**, 075145 (2011)
61. A.N. Rubtsov, M.I. Katsnelson, A.I. Lichtenstein, A. Georges, *Phys. Rev. B* **79**(4), 045133 (2009)
62. H. Hafermann, G. Li, A.N. Rubtsov, M.I. Katsnelson, A.I. Lichtenstein, H. Monien, *Phys. Rev. Lett.* **102**(20), 206401 (2009)
63. S. Fuchs, E. Gull, L. Pollet, E. Burovski, E. Kozik, T. Pruschke, M. Troyer, *Phys. Rev. Lett.* **106**(3), 030401 (2011)
64. E. Burovski, N. Prokof'ev, B. Svistunov, M. Troyer, *New J. Phys.* **8**(8), 153 (2006)
65. E. Burovski, N. Prokof'ev, B. Svistunov, M. Troyer, *Phys. Rev. Lett.* **96**(16), 160402 (2006)
66. R. Bulla, T.A. Costi, T. Pruschke, *Rev. Mod. Phys.* **80**(2), 395 (2008)
67. H. Keiter, J. Kimball, *Int. J. Magn.* **1**, 233 (1971)
68. T. Pruschke, N. Grewe, *Z. Phys. B* **74**(4), 439 (1989)
69. E. Gull, D.R. Reichman, A.J. Millis, *Phys. Rev. B* **82**(7), 075109 (2010)
70. P. Werner, E. Gull, M. Troyer, A.J. Millis, *Phys. Rev. Lett.* **101**(16), 166405 (2008)
71. C.K. Chan, P. Werner, A.J. Millis, *Phys. Rev. B* **80**(23), 235114 (2009)
72. C.A. Marianetti, K. Haule, G. Kotliar, M.J. Fluss, *Phys. Rev. Lett.* **101**(5), 056403 (2008)
73. J.H. Shim, K. Haule, G. Kotliar, *Nature* **446**(7135), 513 (2007)
74. J.H. Shim, K. Haule, G. Kotliar, *Science* **318**(5856), 1615 (2007)
75. K. Haule, J.H. Shim, G. Kotliar, *Phys. Rev. Lett.* **100**(22), 226402 (2008)
76. M. Aichhorn, L. Pourovskii, V. Vildosola, M. Ferrero, O. Parcollet, T. Miyake, A. Georges, S. Biermann, *Phys. Rev. B* **80**(8), 085101 (2009)
77. A. Kutepov, K. Haule, S.Y. Savrasov, G. Kotliar, *Phys. Rev. B* **82**(4), 045105 (2010)
78. V. Brouet, F. Rullier-Albenque, M. Marsi, B. Mansart, M. Aichhorn, S. Biermann, J. Faure, L. Perfetti, A. Taleb-Ibrahimi, P. Le Fèvre, F. Bertran, A. Forget, D. Colson, *Phys. Rev. Lett.* **105**(8), 087001 (2010)
79. L. Mühlbacher, E. Rabani, *Phys. Rev. Lett.* **100**(17), 176403 (2008)
80. T.L. Schmidt, P. Werner, L. Mühlbacher, A. Komnik, *Phys. Rev. B* **78**(23), 235110 (2008)
81. P. Werner, T. Oka, A.J. Millis, *Phys. Rev. B* **79**(3), 035320 (2009)
82. M. Schiró, M. Fabrizio, *Phys. Rev. B* **79**(15), 153302 (2009)
83. M. Schiró, *Phys. Rev. B* **81**(8), 085126 (2010)
84. P. Werner, T. Oka, M. Eckstein, A.J. Millis, *Phys. Rev. B* **81**(3), 035108 (2010)
85. M. Eckstein, M. Kollar, P. Werner, *Phys. Rev. Lett.* **103**(5), 056403 (2009)
86. M. Eckstein, M. Kollar, P. Werner, *Phys. Rev. B* **81**(11), 115131 (2010)
87. N. Tsuji, T. Oka, P. Werner, H. Aoki, Dynamical band flipping in fermionic lattice systems: an ac-field driven change of the, interaction phys. *Rev. B* **81**, 115131 (2010)
88. N. Eurich, M. Eckstein, P. Werner, *Phys. Rev. B* **83**(15), 155122 (2011)
89. E. Gull, D.R. Reichman, A.J. Millis, unpublished (2011)
90. P. Anders, E. Gull, L. Pollet, M. Troyer, P. Werner, *Phys. Rev. Lett.* **105**(9), 096402 (2010)

# Index

## A

Accuracy, 52  
Additive separability, 240  
Adiabatic quench, 148  
Algorithm, 44  
Ancilla, 141–143  
Anderson model, 293  
Area laws, 61, 86  
Auxiliary field, 304  
Auxiliary field CT-QMC, 295

## B

Balance condition, 162  
BEC-BCS crossover, 314  
Biquadratic interaction, 172  
Bi-variational CC formalism, 246  
Bloch equation, 253  
Block, 38, 40  
Bold Monte Carlo, 316  
Bond evolution operator, 134  
Bond Hamiltonian, 133  
Boundary conditions, 57, 63, 144  
Bounded eigenvalues, 219  
Brillouin-Wigner MRCC, 258  
BW-MRCCSDT, 259

## C

CCD, 241  
CC exponential Ansatz, 239  
CC functional, 246  
CC generating functional, 247  
CC nonlinear polynomial equations, 243  
CC numerical complexity, 248  
C-conditions, 257

CC regularization techniques, 244  
CCSD, 241  
CCSD(T), 245  
CCSDT, 241  
CCSDT-n, 245  
CCSDTQ, 241  
CDMFT, 312  
Central charge, 62  
critical spin chains, 121  
Chemical accuracy, 245  
Chemical potential, 144  
Cluster DMFT, 305, 312, 314  
Cluster update, 192, 201, 203  
Coarse graining, 105  
Compatibility function, 163  
Completely renormalized CCSD(T)  
approach, 247  
Computational cost, 63  
Conditional probability, 217  
Condition number, 229  
Configuration space, 296  
Connected diagrams, 240  
Constrained minimization, 228  
Continued-fraction, 7  
Continuous imaginary time limit, 154,  
156–158, 165, 168  
Continuous systems, 212  
Continuous time path integral representation,  
156, 157, 159  
Continuous-time quantum Monte Carlo, 293  
Correlation energy, 239  
Correlation function, 147  
Correlation Hamiltonian, 262  
Correlations, 148  
Correlation time, 216  
Covariance matrix, 226

- C** (*cont.*)  
 Creation/annihilation operators, 239  
 CT-AUX, 295  
 CT-HYB, 295, 306  
 CT-INT, 295, 302  
 CT-J, 310  
 CT-QMC, 293
- D**  
 $D\Gamma A$ , 313  
 Damped boundary conditions, 144  
 Davidson, 136  
 DCA, 312, 314  
 Density matrix, 31, 40–42  
 Density-matrix renormalization group, 68. *See also* DMRG  
 Detailed balance, 191, 218, 297  
 Detailed balance condition, 162, 163, 165  
 Deterministic loop update, 192, 196, 200  
 Diagonalization, 32  
 Diagonal update, 194, 198, 201, 203  
 Diagrammatic Monte Carlo, 273, 274, 293, 296, 298, 314  
 Diffusion Monte Carlo, 231  
 DIIS, 244  
 Directed loop algorithm, 158, 182  
 Directed loop update, 192, 195  
 Discrete time path integral representation, 156, 157  
 Distance, 41  
 DMFT, 4, 293, 311  
 DMRG, 3, 31, 68
  - finite-system, 79
  - infinite-system, 81
  - time-dependent, 95. *See also* tDMRG
 Dual Fermion method, 313  
 Dynamical cluster approximation, 312  
 Dynamical correlation functions, 174  
 Dynamical mean field theory (DMFT), 293, 311  
 Dynamical response, 12  
 Dynamical spin structure factor, 174, 175  
 Dynamic load balancing, 249
- E**  
 EDLFS, 23  
 Effective Hamiltonian, 219, 253  
 Electronic Schrodinger equation, 238  
 Entanglement, 40, 58, 59, 63, 143, 148  
 Entanglement entropy, 60, 62, 86  
 Entanglement growth, 148–150  
 Entanglement renormalization, 102
- Entangler, 142  
 Entropy, 60  
 Entropy growth, 149, 150  
 Environment, 42  
 Ergodic, 219  
 Ergodicity, 154, 162, 166, 169, 181, 191, 220, 297  
 Estimator, 212  
 Euler conditions, 229  
 Exact diagonalization, 2  
 Excited states, 56  
 Expectation value, 187, 198  
 Exponentially hard, 222
- F**  
 Falicov-Kimball model, 21  
 Feynman diagrams, 273, 274, 289  
 Finite correlation time, 221  
 Finite-size DMRG, 50  
 Finite temperature Lanczos method, 9  
 Fock-space CC, 251  
 Fortuin-Kasteleyn representation, 180  
 Four-body interaction, 172  
 Fourier transform, 148  
 Freezing problem, 180, 181  
 Friedel oscillations, 148  
 Frobenius, 44  
 FTLM, 2, 9
- G**  
 Gaussian wave-packet, 145  
 Generalized Fortuin-Kasteleyn representation, 164, 172  
 Generalized susceptibility, 179  
 Ghost spin, 172, 180  
 Global arrays, 250  
 Global quench, 145, 148, 149  
 Green's function, 154, 179, 197  
 Gutzwiller wave function, 227
- H**  
 Hamiltonian, 32, 38  
 Handscomb's method, 186, 204  
 Heat-bath algorithm, 162  
 Heisenberg, 40  
 Heisenberg antiferromagnet, 168, 180, 182  
 Heisenberg model, 3, 193  
 Heisenberg quantum chain, 120  
 Helicity modulus, 177  
 Higher-spin representation, 170, 172  
 High-temperature expansion, 281

- Hilbert space, 216  
 Hilbert-space CC, 251  
 Holstein Phonons, 310  
 Homotopy method, 243  
 Hubbard model, 4, 293, 314  
 Hybridization expansion CT-QMC, 295, 306  
 Hybridization function, 306
- I**  
 iDMRG, 81  
 Ill conditioned, 228  
 Imaginary-time, 133, 141  
 Improved estimator, 178, 182  
 Infinite-size DMRG, 44  
 Infinite variance, 226  
 Incomplete model space, 256  
 Information, 35, 37, 40, 58  
 Interaction expansion CT-QMC, 295, 302  
 Intermediate normalization condition, 253  
 Internal cluster amplitudes, 257  
 Intruder state problem, 255  
 Ising model, 273, 281  
 Ising quantum chain, 120, 125  
     operator product expansion  
     coefficients of, 126  
     scaling dimensions of, 126  
 Iterative minimization, 225
- J**  
 Jeziorski-Monkhorst MRCC Ansatz, 253
- K**  
 Kandel-Domany framework, 163  
 Keldysh, 316  
 Kondo, 40  
 Kondo effect, 310  
 Kondo model, 310, 315  
 Krylov algorithm, 310  
 Krylov basis, 49
- L**  
 Lanczos, 5, 47, 48, 136, 139  
 Lanczos algorithm, 215, 230  
 Lattice QMC, 314  
 LDA+DMFT, 310, 315  
 Level spectroscopy analysis, 176  
 Lieb-Robertson theorem, 96  
 Light-cone, 145  
 Linear prediction, 148  
 Linear system, 227
- Linked cluster theorem, 244  
 Linked list, 196, 202  
 Local energy, 211, 229  
 Local quench, 148, 150  
 Long-range interaction, 154, 170, 172  
 Loop algorithm, 154, 162, 167  
 Loop update, 192, 195, 198  
 Low ranking approximation, 44  
 Low temperature Lanczos method  
     (LTLM), 2, 16
- M**  
 Moller-Plesset perturbation theory, 245  
 Many-body perturbation theory, 244  
 Marginal probability, 217  
 Markov chain, 212, 216, 219  
 Markov chain Monte Carlo, 153, 155, 162,  
     187, 191  
 Markov process, 297  
 Master equation, 217  
 Matrix, 33  
 Matrix-product, 32  
 Matrix product operator, 76. *See also* MPO  
 Matrix product state. *See also* MPS, 68  
 Matrix product states  
     ground energy of, 121  
     spatial symmetries in, 110  
     two-point correlators of, 123  
 MCLM, 2, 18  
 Measurement, 53  
 Meron cluster algorithm, 181  
 Method of moments of coupled cluster  
     equations, 244  
 Metropolis algorithm, 162, 187, 297  
 Microcanonical, 1  
 Microcanonical Lanczos method, 18  
 Mk-MRCC Lagrangian, 261  
 Mk-MRCC method, 258  
 Mk-MRCCSDT, 259  
 MMCC functional, 246  
 Model space, 251  
 Monte-Carlo, 133, 296  
 Mott insulators, 4  
 MPO, 76  
     graphical representation, 76  
     Hamiltonian as an, 77  
     mixed state evolution, 94  
     pure state evolution, 89  
 MPS, 32, 68  
     addition, 73  
     compression, 73  
     expectation values, 72  
     graphical notation, 69

- M** (*cont.*)  
 left-canonical, 70  
 left-normalized matrices, 70  
 mixed-canonical, 70  
 non-uniqueness, 70  
 normalization, 72  
 overlap, 72  
 right-canonical, 70  
 right-normalized matrices, 70  
 variational, 79
- MR-CCSD(T), 260
- Multiple CC solutions, 242
- Multireference CC formalism, 251
- Multireference extension of the method of moments, 260
- Multireference many-body perturbation theories, 252
- Multi-scale entanglement renormalization ansatz, 105  
 ascending superoperators of, 104  
 causal cone of, 106  
 conformal data from, 125  
 descending superoperators of, 107, 116  
 evaluation of expectation values from, 108, 115  
 global internal symmetries in, 112, 116  
 ground energy of, 121  
 scale-invariant form of, 113  
 spatial symmetries in, 110  
 two-point correlators of, 123
- N**  
 Nanoscience (CT-QMC), 310  
 Negative sign problem, 154, 160, 161, 170, 181, 182  
 Nested cluster algorithm, 182  
 Nonequilibrium CT-QMC, 316  
 Non-interacting subsystem limit, 240  
 Non-variational character of the CC method, 242  
 NRG, 31, 71  
 Numerical renormalization group, 71. *See also* NRG
- O**  
 Offdiagonal correlation, 154, 179  
 Operator, 33, 38
- P**  
 Parallel codes, 248  
 Parallelization, 171
- Parallel performance, 250  
 Particle-hole transformation, 143  
 Partition function, 188, 296  
 Path-integral, 285, 287  
 PEPS, 63  
 Periodic quench, 148  
 Perron Frobenius uniqueness, 219  
 Petaop supercomputers, 232  
 Phonons, 305, 310  
 Potts model-state, 120  
 Probability, 212  
 Processor groups, 264  
 Product state, 61  
 Product wave function renormalization group, 86. *See also* PWFRG  
 Projector QMC, 190  
 Pure loop algorithm, 181  
 Pure loop representation, 180  
 Purification, 91, 143  
 PWFRG, 86
- Q**  
 QMC, 3  
 Quantum transfer matrix, 156, 159, 165, 167  
 Quasi-exact, 52, 132  
 Quench, 144, 148  
 Quench problems, 316
- R**  
 Radius of convergence, 256  
 Random variables, 212, 216  
 Real time dynamics, 27  
 Real-time Monte Carlo, 316  
 Recursion, 38  
 Recursive intermediates, 248  
 Reduced basis Lanczos method, 22  
 Reduced density matrix, 42, 44, 61  
 Reference-level parallelism, 264  
 Regularization of CC energy, 247  
 Regularization of the inversion, 228  
 Rejection free scheme, 162, 165, 166  
 Relations between CC and FCI, 241  
 Renormalization group, 31  
 Reweighting technique, 161  
 Rotation, 36, 37, 43  
 Runge–Kutta, 132, 138–140
- S**  
 Scaling operators, 118, 126  
 Scaling superoperator local, 118

- non-local, 119
- Schmidt, 43, 44, 59
- Schmidt decomposition, 71
- Schmidt rank, 71
- SchrÖdinger equation, 131
- Series convergence, 279
- Sign blessing, 279
- Sign problem, 188, 193, 279, 300, 304
- Singular value, 43
- Singular value decomposition, 68. *See also* SVD
- Snake path, 57
- Spectral function, 8
- Spin stiffness, 177
- Standard deviation, 213
- State-specific MRCC methods, 257
- State Universal MRCCSD, 254
- Stationary distribution, 218
- Stochastic reconfiguration, 225
- Stochastic series expansion, 158
- Structure function, 88
- SU( $N$ ) symmetry, 172
- Sufficiency conditions, 259
- Superconductivity, 305
- Super-Hamiltonian, 47, 49
- Superuid density, 177
- Suzuki–Trotter, 133–135, 137, 140
- Suzuki–Trotter decomposition, 153–155
- SVD, 43, 60, 68
- Sweeping, 52, 132, 137
- Swendsen-Wang algorithm, 162, 195, 202
  
- T**
- Target, 139
- Targeting, 55
- Taylor expansion, 188
- tDMRG, 95, 135
- TEBD, 63, 95, 133, 151
- Temperature, 142, 143
- Tensor contraction engine, 248
- Tensor networks, 63
- Thermal density operator, 91
- Thermal state, 142
- Thermo field, 141
- Tilted clusters, 5
- Time-dependent perturbation expansion, 157
- Time-evolution, 131, 136
- Time-evolution operator, 133
- Time-evolving block decimation, 95. *See also* TEBD
- Time-targeting, 140
- $t\text{-}J$  model, 4
- Trotter error, 134, 139
  
- Transformation, 38
- Transient, 144
- Transport, 132, 144
- Transverse external field, 155, 160, 172, 181, 182
- Transverse field Ising model, 199
- Tridiagonal matrix, 49
- Trotter decomposition, 88
  - first order, 88
  - fourth order, 89
  - second order, 89
- Trotter limit, 156
- Truncation, 34, 38, 40, 49
- Truncation error, 52, 139, 145
  
- U**
- Union-find algorithm, 170
- Unitary invariance of the MRCC theories, 260
- Unitary transformation, 38
- Universal State Selective formalism, 261
- Updating schemes for QMC, 191
- USS(2), 263
  
- V**
- Valence bond basis, 197
- Variance, 213, 215
- Variational parameters, 227
- vMPS, 79
  
- W**
- Walker's method of aliases, 173
- Wave operator formalism, 252
- Wave-function prediction, 56
- Wilson leads, 144
- Worldline, 194, 196
- World-line configuration, 160, 167, 170
- World-line quantum Monte Carlo, 153, 156
- Worm algorithm, 158, 182, 273, 280, 289
  
- X**
- XX quantum chain, 120
  - two-point correlator of, 123
- XY model, 281, 283
- XXZ model, 159
- XYZ model, 171
  
- Z**
- Zero variance property, 215